Solute Transport in Flow Through Random Emergent Vegetation

Jesús Leonardo Corredor García

A thesis submitted in partial fulfilment of the requirements for the degree of Doctor of Philosophy

The University of Sheffield
Faculty of Engineering
Department of Civil and Structural Engineering

February 2023

ACKNOWLEDGEMENTS

The completion of this research, both as a personal and academic project, is a testimony to the help, support and influence of many great people to whom I will forever be indebted.

First, I would like to express my gratitude to Professors Ian Guymer and Virginia Stovin for the opportunity, and their unwavering support and trust throughout my PhD journey. Ian's enthusiasm for scientific exploration, drive to solve practical problems and learning spirit; together with Virginia's attention to detail, commitment to quality and motivation for improvement, have inspired the way I see research and all professional endeavours. May their lessons keep shaping my research career and guide me to improve everyday.

For the completion of this project, the unvaluable help and orientation from staff and colleagues has been crucial. Very special thanks go to all technicians in the Water Engineering Laboratory, particularly Mr. Joe Milner for his incredible support, efficiency and input during very demanding times. I would like to recognise and thank Dr. Fred Sonnenwald, for his support through enriching and encouraging discussions; and very specially to (now Dr.) Zhangjie Peng for her friendship, unvaluable support, great ideas and a making the PhD a very enjoyable experience.

It was through the love and support from my parents, Jesús and Blanca, and my brothers, Julio César and Camilo Andrés, that I could find the inspiration and strength to complete this very important project. Their resolute spirit to endure hardship, their countless lessons and excellent examples have accompanied me during this time. Despite the distance and the unforeseen circumstances during this endeavour, their love and all the caring and encouraging words have always remained intact in my heart. To them I dedicate this work.

I would like to thank all my friends in Sheffield for all the memorable moments and great experiences.

ABSTRACT

Aquatic vegetation governs a wide range of river processes, from flood control to nutrient exchange, and crucially, pollution dispersal and treatment. This thesis presents a comprehensive experimental study, using a random array of circular cylinders, of varying diameters, based on charactersations of real species, to simulate aquatic plants, and study mass transport in vegetated flows. Optical techniques—Particle Image Velocimetry (PIV) and Laser Induced Fluorescence (LIF)—were employed to obtain velocity and concentration fields at unprecedented spatial and temporal resolutions.

Concentration maps provided estimates of longitudinal and transverse dispersion coefficients over multiple reaches, and a comprehensive range of flows ($50 < Re_d < 1000$). Two distinct longitudinal dispersion regimes, separated at $Re_d \approx 400$, were found where different physical processes drive dispersion. For $Re_d < 400$ mixing is dominated by shear and thus cannot be considered strictly Fickian. For $Re_d > 400$ turbulent diffusion efficiently spreads mass locally and transport is mainly advective. Transverse dispersion is mainly determined by vegetation morphology, and not Reynolds number. Generally, solutes are seen to spread independently of initial conditions, as they quickly assimilate the average physical characteristics of vegetation.

Instantaneous velocity maps were obtained with PIV and glass cylinders to allow inter-stem visualisation. Mean maps show that flow heterogeneities are caused by complex stem interactions and not by a superposition of their individual effects. Dispersive fluxes grow with increasing Re_d, and become dominant drivers of large-scale dispersion at $Re_d > 300$. After this range, turbulent fluxes become less prominent as drivers of large scale dispersion, but small-scale mixing still increases with Re_d, thus reducing trapping times in recirculation zones.

In summary, the novel findings present a comprehensive picture of the main hydrodynamic features dominating dispersion in vegetation, and their dependence on Reynolds number. The novel inclusion of diameter and spacing distributions in the RandoSticks array reveals the existence of a range of characteristic flow scales broader than in uniform-diameter artificial systems. This variability suggests the existence of stem and wake interactions that have not been previously included in models for vegetation morphology and mixing, and further work is needed to characterise these effects, to develop more accurate, physically-based dispersion models.

TABLE OF CONTENTS

LIST OF FIGURES

LIST OF TABLES

LIST OF SYMBOLS

ACRONYMS

PIV: Particle Image Velocimetry

LIF: Laser Induced Fluorescence

ADE: Advection Diffusion Equation

LHS: Left Hand Side

RHS: Right Hand Side

MKE: Mean Kinetic Energy

TKE: Turbulent Kinetic Energy

DA: Double-Averaged

SPIV: Surface Particle Image Velocimetry

ADV: Acoustic Doppler Velocimetry

RANS: Reynolds Average Navier Stokes [equation]

DANS: Double-Average Navier Stokes [equation]

PVC: Polyvinyl Chloride

FoV: Field of View

BBL: Bouguer-Beer-Lambert [law]

CW: Continuous Wave [laser]

OD: Optical Density

AV: Artificial Vegetation

FFT: Fast Fourier Transform

RMS: Root-Mean-Square of the fluctuating component of a quantity

STD: Standard Deviation

Note: the acronym RMS is used exclusively to refer to the variation around the mean of any quantity, so it is equivalent to the standard deviation STD in this document.

FRAMES OF REFERENCE

$\{x, y, z\}$: Main Cartesian coordinates. x – streamwise, y – spanwise or transverse, and z – vertical directions

x_i : Cartesian coordinates in tensor notation. $x_i \equiv \{x_1, x_2, x_3\} = \{x, y, z\}$

u_i : Velocity components in tensor notation. $u_i \equiv \{u_1, u_2, u_3\} = \{u, v, w\}$

$\{u, v, w\}$: Main velocity components in u – streamwise, v – spanwise or transverse, and w – vertical directions

$\{U, V, W\}$: Main components of the time-averaged velocities in U – streamwise, V – spanwise or transverse, and W – vertical, directions

t : Time domain

τ : Auxiliary time domain

T : Time interval long enough to contain all scales of flow

AVERAGING FRAMEWORKS

$\overline{\theta}$: (Overbar) time-average of the instantaneous quantity θ

θ' : Turbulent fluctuation of the instantaneous quantity θ

γ_f : Phase-function, determining whether at a determined instant, a point is occupied by fluid $(= 1)$ or solid, i.e. obstruction $(= 0)$

$\langle\theta\rangle$: Spatial average over a volume of fluid only considering the fluid phase. Also called intrinsic spatial average

θ'' : Spatial fluctuations of the passive quantity θ, from the space average $\langle\theta\rangle$ over a volume of fluid, only considering the fluid phase.

$\langle\overline{\theta}\rangle$: Consecutive time- and space- average of the passive quantity in a control volume of fluid, only considering the space and time intervals occupied by the fluid phase

$\overline{\theta}''$: Spatial fluctuations around the mean value $\langle\overline{\theta}\rangle$, of the time-averaged quantity $\overline{\theta}$, over a volume of fluid, only considering the space and time intervals occupied by the fluid phase

$\overline{\langle\theta\rangle}$: Consecutive space- and time- average of the passive quantity in a control volume of fluid, only considering the space and time intervals occupied by the fluid phase

$\langle\theta\rangle'$: Temporal fluctuations around the mean value $\overline{\langle\theta\rangle}$, of the space-averaged quantity $\langle\theta\rangle$, over a volume of fluid, only considering the space and time intervals occupied by the fluid phase

$\langle\theta\rangle_x$: Space average of the passive quantity θ along the x-direction only

$\langle\theta\rangle_y$: Space average of the passive quantity θ along the y-direction only

V : Volume of fluid space large enough to cover the average morphological characteristics of emergent vegetation, covering the solid and fluid phase

V_f : Portion of V only containing the fluid phase

ϵ_f : Porosity in a multiphase (solid-fluid) field

$n_{f,i}$: Vector normal to the surface of the solid-fluid interfaces (i.e. surface of obstructions), pointing into the fluid phase, in the i-th direction

A_{fs} : Total area of the control volume occupied by the solid-fluid interface, i.e. obstruction surfaces

u_{fs}: Velocity at the solid-fluid interface

$\langle\theta\rangle_{s_{nc}>r^*}$: Conditional spatial average that considers contributions from obstructions with a centre further away than a distance r^*

GREEK CHARACTERS

Λ_i : Characteristic Lagrangian turbulent length scale

Λ_t : Estimate of the characteristic length scale of coherent turbulent structures, obtained from time (auto)correlation functions

Λ_{t2} : Characteristic length scale of shed vortices

Λ_{xy} : Characteristic length scale of coherent turbulent structures, obtained from space correlation functions

Φ_E : Quantum efficiency of a camera (ration of photons absorbed to electrons generated)

Φ_y : Quantum yield of a fluorescent substance (ratio of incident to emitted light/energy)

Ω_i : Time-averaged vorticity, $\Omega = \overline{\omega}$

α_a, α_b : Linear best-fit coefficients of the Re_d-dependent drag coefficient, C_D, function for an array of circular cylinders

α_w : Velocity-defect threshold defining the areas in which low velocities are associated with the existence of a recirculation zone (i.e. primary wake)

$\overline{\varepsilon}$: Direct dissipation of energy from the mean flow due to viscosity

$\langle\varepsilon\rangle$: Spatial average of TKE dissipation, both directly and through the turbulence cascade, due to viscosity

ε_w : Vorticity criterion to define the areas where vortex formation is stronger, and are thus connected to the existence of recirculation zones (i.e. primary wakes)

η_w : Attenuation coefficient due to clean water

κ_t^3 : Streamwise (i.e. temporal) Pearson skewness coefficient of the concentration distribution

κ_u^3 : Global Pearson skewness coefficient of the instantaneous, streamwise velocity field from a complete PIV record

κ_v^3 : Global Pearson skewness coefficient of the instantaneous, transverse velocity field from a complete PIV record

κ_y^3 : Transverse Pearson skewness coefficient of the concentration distribution

μ_u : Global average of the instantaneous, streamwise velocity field from a complete PIV record

μ_v : Global average of the instantaneous, transverse velocity field from a complete PIV record

μ_τ : Average light intensity value of a PIV image

ν_t : Eddy/turbulent viscosity

σ_{ji} : Dynamic stress component in the i-th direction, over the j-th face of a fluid element

σ_t^2 : Streamwise (i.e. temporal) variance of the concentration distribution

σ_u^2 : Global variance of the instantaneous, streamwise velocity field from a complete PIV record

σ_v^2 : Global variance of the instantaneous, transverse velocity field from a complete PIV record

σ_w : Standard deviation of the spatial velocity fluctuations, associated with the secondary wakes of obstructions in the flow field

σ_y^2 : Transverse variance of the concentration distribution

$\bar{\tau}$: Average trapping time of a passive solute, within the recirculation area of cylinder wakes (cf. primary wake)

$\tau_1,\ \tau_2$: (8bit) intensity maps corresponding to the same interrogation window at two consecutive PIV images

τ_{ji} : Shear stress component in the i-th direction, over the j-th face of a fluid element

τ_w : Boundary-layer induced shear stress

τ_{xy} : Shear stress component in 2D horizontal flows

$v'_{i,n}$: Lagrangian velocity in the i-th direction, of the n-th particle of a statistical ensemble

v_i^+ : Turbulence intensity of the Lagrangian velocity component v_i

ω_i : i-th component of the instantaneous vorticity field

ϵ_o : Absorptivity of light due to Rhodamine 6G concentration

ϵ_w : Fraction of the flow field occupied by recirculation areas (i.e. primary wakes)

Γ : (Upper) incomplete gamma function, defined as: $\Gamma(t,a) = \int_a^\infty x^{t-1}e^{-x}dx$. Note that the lower incomplete gamma function is defined over the limits $(0,a)$

β : Flume bed slope

$\beta(\tau)$: Frequency function for the sinusoidal component of the autocorrelation function $r(\tau)$

ε : Absorptivity (i.e. attenuation) coefficient of laser intensity

ε : Dissipation of energy due to viscosity at the smallest scales of turbulence

η : Laser power absorbance (due to fluorescence) along the laser beam

κ : Wavenumber

μ : Dynamic viscosity of water

ν : Kinematic viscosity of water

ξ : Auxiliary x domain

ρ : Density of water

φ : Solid volume fraction, i.e. portion of the flow field occupied by obstructions (solid phase)

ϵ : Absorption coefficient of the medium where laser light travels

$\epsilon(\tau)$: Envelope function of the autocorrelation function $r(\tau)$

LATIN CHARACTERS

$\langle\overline{f_D}\rangle_V$: Average drag force per unit of submerged cylinder height

$\langle\overline{f_D}\rangle$: Drag force, in the streamwise direction, caused by the average cylinder in the array

$\langle\overline{f_{Dx}}\rangle$: Total drag force considering the fluid density and fluid depth, in the vegetated array, caused by the presence of stems

$\widetilde{D_y}$: Transverse diffusion coefficient approximation using an Eulerian approximation to Taylor's theory of diffusion

$\widetilde{E_\iota}$: Turbulent energy (two-sided) spectrum. From the Eulerian Autocorrelation function

$\overline{S_{ij}}$: Rate-of-strain tensor for the time-averaged velocity field

$\overrightarrow{X_p}$: Vector coordinates of an array of illuminated seeding particles

$\langle\bar{t}\rangle$: Average travel time between consecutive LIF measurement points for all reaches tested

$\overline{t_i}$: 'Travel time' between injection and the centroid of the concentration profile at the i-th measurement point

T_2 : Characteristic period of the secondary shedding frequency

A_S : Projected surface area of a cylinder, perpendicular to the direction of mean flow

C_D : Drag coefficient for a circular cylinder

C_D^{form} : Drag coefficient associated with form drag force over a circular cylinder

C_D^{visc} : Drag coefficient associated with viscous drag force over a circular cylinder

C_n : (Estimated/calibrated) concentration value at the n-th pixel along the laser beam

D_{BL} : Dispersion by trapping in boundary layers

D_s : Shear dispersion coefficient. Dispersion attributed to spatial differences in time-averaged velocity only

D_t : Turbulent diffusion coefficient

$D_{x,g}$: Dispersion by acceleration between obstructions

$D_{x,s}$: Secondary wake dispersion (also, dispersion by differential advection)

$D_{x,v}$: Vortex trapping dispersion

D_x : Dispersion coefficient in the streamwise direction

$D_{y,m}$: Lateral dispersion coefficient caused by mechanical dispersion alone

D_y : Dispersion coefficient in the transverse direction

D_z : Dispersion coefficient in the vertical direction

$\overline{E}$: Mean Kinetic Energy

E' : Turbulent Kinetic Energy

E_i : Turbulent energy density spectrum. From the Eulerian Autocorrelation function

E_{ij} : Turbulent energy density cross-spectrum. From the Eulerian (two-point) Cross-correlation function $R_{ij}(\tau)$

F_D : Drag force over a single circular cylinder

F_D^{form} : Form (pressure) drag over a circular cylinder

F_D^{visc} : Viscous (shear) drag over a circular cylinder

$F_{reference}$: Reference force acting on a circular cylinder

I_1, I_2 : (8bit) intensity maps corresponding to consecutive PIV images

I_f : Emitted fluorescent light

I_l : Laser light intensity

I_n : (8bit) image intensity value at the n-th pixel along the laser beam

I_o : (8bit) image intensity value corresponding to the output laser power

L_h : Characteristic length scale of the flow associated (proportional) to the flow depth

L_X : Characteristic length scale of turbulence in the streamwise direction

M_n : n-th statistical moment of a concentration function

$P_{s_{nc}>r^*}$: Probability of finding a cylinder at a distance larger than r^*.

$P_{s_{nc}>5d}$: Probability of finding cylinders within $5d$ from each other

P_N : Nominal output laser power

P_b : Production of TKE due to buoyancy effects (only applicable in atmospheric flows)

P_n : (Estimated) laser power at the n-th pixel along the laser beam

P_o : Attenuated output laser power

P_s : Production of TKE due to velocity shear

P_w : Production of TKE due to obstructions' wakes

R_C : Contribution to the image correlation function $R(\vec{s})$ from the mean light intensity of two consecutive PIV images

R_D : Peak of the correlation coefficient map $R(\vec{s})$, which is found for the displacement vector that matches the same particles between two consecutive PIV images

R_F : Contribution to the correlation coefficient $R(\vec{s})$ from random contributions of non-matching particles between two consecutive PIV images

R_i : Eulerian velocity autocorrelation for the i-th component of velocity

R_{ij} : Eulerian velocity (two-point) correlation for the i-th and j-th components of velocity

R_t^2 : Best-fit coefficient between a model prediction and experimental measurements

S_f : Friction slope (i.e. slope of the vegetated flow energy line)

S_{ij} : Rate-of-strain tensor

S_t : Strouhal number, non-dimensional shedding frequency

S_{xy} : Rate of strain tensor in 2D horizontal flows

T_X : Characteristic temporal scale of turbulence in the streamwise direction

T_p : Pressure transport in the balance of TKE

T_t : Turbulent transport of TKE (only applicable in submerged vegetation/canopies)

U_∞ : Incident flow velocity (before it reaches the vegetated area)

U_{CL} : Time-averaged streamwise component of velocity along the wake centreline of a cylinder

U_p : Mean pore velocity, averaged over the volume occupied by fluid

U_p : Pore velocity computed as the double-averaged velocity from a PIV recording. Note that this quantity is used instead of U in chapters 6 and 7, as U_p is obtained from a spatial subsample, which, though large enough to cover the average macroscopic features of the vegetated field, it is not by definition the same

V_{CL} : Time-averaged transverse component of velocity along the wake centreline of a cylinder

X_i : Streamwise coordinate of the i-th measurement point, i.e. x-coordinate of the i-th camera.

X_i : Streamwise coordinate of the i-th measurement point, i.e. x-coordinate of the i-th camera.

X_{sc} : Local streamwise coordinates associated with a wake centreline

a^+ : Root-mean-square of the fluctuating quantity a'. $a^+ = \sqrt{\overline{a'^2}}$

$b_{1/2}$: Half width of the wake behind a circular cylinder

f_2 : Secondary shedding frequency, associated to the streamwise velocity signal along the wake centreline. Defined as 2 times the measured shedding frequency f_s

f_s : Shedding frequency, defined as the peak of the frequency spectrum measured at the end of the recirculation area (start of secondary wake)

f_x : Total drag force, per unit height and unit mass, in the vegetated array caused by the presence of obstructions, i.e. cylinders

g_i : Gravity as external force

$k_\perp$: Permeability of the vegetated flow field

$\tilde{p}$: “Gaussian propagator for the transverse diffusive motion”, a probability function introduced by White and Nepf (2003), expressing the likelihood of finding a particle, that is diffusing in a Gaussian manner, at specific points downstream

$q_{c,i}$: Flux of a passive scalar in the i-th direction

r^* : Minimum centre-to-centre distance between adjacent cylinder to allow turbulence to generate diffusion

$\vec{s}$: Displacement vector of PIV seeding particles between two consecutive images

s_{ij} : Rate-of-strain tensor from the turbulent fluctuations of velocity

s_n : Edge-to-edge distance between adjacent cylinders

s_{nc} : Centre-to-centre distance between adjacent cylinders

$\bar{t}$: Travel time between consecutive measurement points

t_{ci}: 'Travel time' between injection point and the centroid of the concentration profile at the i-th measurement point. The notation μ_t is also used to relate to the statistical moments of concentration functions

u^+ : Streamwise turbulence intensity (root-mean-square of the fluctuating turbulence component)

$u^\times$: Shear velocity

u_i^+ : Turbulence intensity

u_t : Characteristic velocity scale of turbulence in the dissipation range, i.e. Kolmogorov velocity scale

u_w'' : Wake induced spatial velocity fluctuations

v^+ : Transverse turbulence intensity (root-mean-square of the fluctuating turbulence component)

x_0 : Local coordinate associated to the start of a secondary wake for a single circular cylinder

x_A : Local coordinate system related to the secondary wake of the cylinder labelled A

x_B : Local coordinate system related to the secondary wake of the cylinder labelled B

y_c : Transverse centroid of the concentration distribution

y_{inj} : Lateral position of the injection, measured from the wall at the laser side, for the LIF experiments

y_x : Diffusive distance obtained from Taylor's proportionality relationship

h : Flow depth

T : Characteristic time scale of coherent turbulent structures, defined as the reciprocal of the characteristic shedding frequency

Δx : Streamwise distance between consecutive measurement points

C : Concentration of a passive scalar, i.e. solute, in a moving flow field

D : Molecular diffusion coefficient

E : Total kinetic energy of a differential volume of fluid

I : Light intensity (map) expressed as an (8bit) image grayscale value

OD : Attenuation of laser power from optical density filter

P : Laser light power

Pe : Péclet number expressing the ratio between mixing coefficients due to advection and diffusion

Q : Volumetric flow rate

$R(\vec{s})$: Correlation coefficient of the displacement vector, $\vec{s}$, of a set of illuminated particles between two consecutive PIV images

Re_d : Reynolds number associated to the mean cylinder diameter d, as characteristic length scale

Re_t : Turbulent Reynolds number, calculated using the eddy viscosity ν_t

Re : Reynolds number associated to the generic flow scale L

Sc_t : Turbulent Schmidt number

U : Mean (time-averaged) streamwise velocity

X : Lagrangian displacement, in the streamwise direction, of a fluid particle as a function of time

Y : Lagrangian displacement, in the transverse direction, of a fluid particle as a function of time

a : Frontal-facing area of vegetation (obstructions) per unit volume

$cs(\tau)$: Basis for a sinusoidal function

d : Circular cylinder diameter

f : Frequency

k : Turbulent Kinetic Energy only considering the horizontal, $\{x, y\}$, components of velocity

m : Stem number density (number of stems per square metre)

p : pressure

$r(\tau)$: Analytical autocorrelation function for periodic flow phenomena.

SPECIAL CHARACTERS

$\mathcal{P}$: Production of turbulent kinetic energy from the mean flow

$\mathcal{R}_i$: Lagrangian correlation function, relating the velocity of a fluid particle at different times during its motion

ℓ_t : Characteristic length scale of turbulence in the dissipation range, i.e. Kolmogorov length scale

l_R : Streamwise extent of the recirculation region

l_A : Attenuation length: streamwise extension of the velocity decay caused by the presence of an obstruction (i.e. cylinder)

Φ : Diameter measure

$\aleph$: Function representing the non-static component of the dynamic pressure acting on a volume of fluid. This function considers the sum of vertical and streamwise virtual stresses and their gradients. For the effects of this research, this quantity is considered negligible

PREFACE

This thesis is structured in a traditional format, such that the contents of each chapter build from the conclusions of previous ones. However, care has been taken to also allow the reader to understand each individual component without exhaustive background. The background theory underpining the current understanding of vegetated solute transport is presented in Chapter 2. A set of preliminary experiments designed to study the assumptions of previous longitudinal dispersion models, are presented in Chapter 3. The novel experimental system is explained in Chapter 4, and a thorough description of the set up process and calibrations is presented in Appendices A and B. Chapter 5 shows the results from concentration measurements and an analysis of the trends observed. The velocity maps obtained are presented and analysed in Chapter 6, and Chapter 7 presents a discussion of the relevant flow scales and their impact on large-scale mixing. The main findings are summarised and discussed in Chapter 8, and further steps given in Chapter 9.

During the course of this project, prior to its official submission, the following conference publications have arose from the work included in this document.

a. Corredor-Garcia, J. L., Delalande, A., Stovin, V., & Guymer I., (2020) 'On the Use of Surface PIV for the Characterization of Wake Area in Flows Through Emergent Vegetation', in Kalinowska, M., Mrokowska, M., and Rowiński, P. (eds) Recent Trends in Environmental Hydraulics. GeoPlanet: Earth and Planetary Sciences. Cham, Switzerland: Springer-Verlag, pp. 43–52.
b. Corredor-Garcia, J. L., Stovin, V., Guymer, I., (2022) 'Spatio-Temporal Characterization of Hydrodynamics and Mixing Processes in Obstructed Flows using Optical Techniques', Proceedings of the 39th IAHR World Congress, (June 2022), Granada, Spain. pp. 5140–5149. doi: 10.3850/IAHR-39WC2521716X20221035.

The first publication is extracted from the contents of Chapter 3.1, and the last one summarizes the contents in Chapter 4.

DECLARATION

I, the Author, confirm that the Thesis is my own work. I am aware of the University's Guidance on the Use of Unfair Means *(www.sheffield.ac.uk/ssid/unfair-means)*. This work has not been previously presented for an award at this, or any other, university.

Chapter 1. INTRODUCTION

1.1. Rationale

The presence of emergent vegetation dominates a wide range of physical, biochemical, geomorphological and restoration processes in various aquatic systems. Understanding flow resistance imposed by vegetation is important for flood modelling and management. Vegetated flows control the fluxes of many different suspended materials and solutes. Sediment transport through and between plant patches controls rates of erosion and deposition, which have consequences on river geomorphology. Nutrients, biological species and seeds are exchanged through vegetation elements for biota reproduction and conservation and water quality control. The latter is relevant for the construction of engineered wetlands for pollution treatment.

Acknowledging the importance of emergent vegetation flow systems, accurate modelling, management and design is crucial for their effective use and conservation. This requires a thorough characterisation of the vegetation elements and their interaction with the flow. The hydrodynamic processes occurring in these systems are a subset of the comprehensive and complicated area of fluid dynamics, alongside the complexities included in the foregoing cases, such as reaction rates, sediment transport and biological processes. Appropriate understanding of the physics behind plant-flow interactions underpins the success of their application, and can provide case studies for the comprehension of problems in fundamental fluid mechanics.

As can be seen, any study on emergent vegetation and its applications is necessarily multi-disciplinary. Broadly, the project 'Solute Transport in Flow Through Random Emergent Vegetation' belongs to the area of Environmental Fluid Dynamics, specifically in the intersection of fluid dynamics and solute transport. The physical phenomena of emergent vegetation systems are continuously explored in the subareas of these topics: turbulence, stability theory, stochastic transport, advection-diffusion, among others. Understanding the complexities of vegetated flows hinges on the possibility of developing representative numerical, field and laboratory studies, so that the main interactions, physical drivers, orders of magnitude and trends can be identified. From this knowledge, simplifying assumptions for practical applications and quantifiable evidence to contrast with existing theories can be developed.

Generally, investigations on flow and mixing use representations of vegetation that fall into one of two categories: realistic macrophytes including natural features such as leafs and branches, or simplified elements with known geometries. The former usually covers field studies and laboratory experiments with real species, or models aiming to represent them. The latter is used in numerical and simplified laboratory experiments, normally representing stalks and stems with circular cylinders, either in regular, staggered or random arrays. Both have provided useful insights into some of the relevant physical phenomena. Their main difference lies in the conflict between scalability/reproducibility and accuracy. Realistic systems provide bulk quantifications of vegetated reaches, more faithful to natural systems. However, quantifications of small-scale processes are usually overlooked, such that scaling the results becomes challenging. Simplified systems allow for a better characterisation of phenomena from single and interacting elements, to vegetated reaches. The latter approach is pursued in this work, as the aim is to enhance the understanding of the fundamental processes and how these are the result of interacting vegetation elements. Given the simplified nature of the vegetation array used in this study, the conclusions derived are limited to vegetation species with a morphology similar to the RandoSticks array, that is, rigid, cylindrical stalk-like elements e.g. reeds.

From hydrodynamic studies, it has been found that vegetation elements dominate the behaviour of their flow fields: they extract most of the energy from the mean flow through form and viscous drag, and, through instability regimes, create structures that prompt the development of a spectrum of flow structures. These structures distribute and dissipate energy across different scales, which ultimately dominate the rates of mass transfer and mixing. In vegetated solute transport, most experimental results and subsequent models are developed in the Fickian regime, which is achieved after solute clouds are significantly larger than representative scales of the flow (e.g stem diameter, cluster sizes), and disperse linearly with time. As will be presented, these results are still insufficient for accurate models, and the following research needs remain:

- **Vegetation characterisation:** there is a persistent gap between realistic and simplified experimental models. Most of the diversity of vegetation morphology is overlooked by the current uniform cylinder-based approaches. More realistic artificial models must account for variations in stem spacing and diameters.
- **Flow heterogeneity:** knowledge is still needed to describe how plant elements interact and produce the mean flow fields, and what defines the sizes and behaviours of features of vegetated flows such as wakes, recirculation zones and boundary layers.

- **Turbulent kinetic energy budgets in vegetated reaches:** current results are from point-based measurements or small areas covering few vegetation elements. More results are needed to define the sizes and life spans of energy-containing structures, i.e. flow scales, and the verification of hypotheses regarding, isotropy, homogeneity and energy production-dissipation relationships.
- **Fickian regimes in vegetated reaches:** No unifying, vegetation-dependent threshold has been defined to determine the time/length scales necessary for solutes to spread linearly, and thus for current models to be valid.
- **Comprehensive experimental results:** Addressing the previous research needs requires thorough characterisations of flow fields and solute traces in vegetated reaches. These obstructed flows limit the use of instrumentation for velocity field characterisations, such that reach-scale information is still absent from current experiments.

1.2. Objectives

The main objective of this research is to provide high-quality hydrodynamic and mass transport data, through Particle Image Velocimetry and Laser Induced Fluorescence experiments, respectively. From these, velocity and concentration fields are expected to resolve the behaviour of the flow and solute clouds, from single elements to comprehensive stem arrays. These results are expected to shed light on some of the fundamental processes overlooked thus far, and to verify and inform the main assumptions, models and theories of vegetated solute transport. The aim of this novel dataset is associated with the research needs via the following specific objectives.

- **Better represent vegetation through artificial arrays.** a novel artificial vegetation configuration is presented, called RandoSticks, which introduces the stem diameter distribution measured for the species Winter *Typha latifolia*, in addition to a random stem location distribution. The additional complexity of this configuration is expected to introduce realistic interactions to laboratory flow fields, such that interactions, sheltering and stem spacing variations, can better represent the phenomena overlooked on previous experimental approaches.
- **Provide accurate and representative mean hydrodynamic maps.** From the configuration proposed, velocity fields over a comprehensive range of flows will be obtained, and spanning an area large enough to cover a representative sample of vegetation elements. Mean maps of the main hydrodynamic quantities will be used to describe how the

interaction of stems define the features of the vegetated flow field, namely, wakes, recirculation zones and boundary layers. The main quantitative trends will be explored and assessed in the context of their impact on solute transport.

- **Spatial turbulence and flow scale characterisation.** Obtain full characterisations of velocity time series to derive the main turbulence quantities, localise important zones of turbulent energy production and derive relevant turbulent length scales. Given the area where these measurements will be obtained, the results will be used to explore the evolution of these quantities in the context of the double-averaged equations of motion.
- **Comprehensive range of concentration measurements for dispersion characterisation.** The velocity measurements will be coupled with concentration measurements, over a wider range of flow rates, and a comprehensive vegetated reach, to quantify dispersion for the RandoSticks configuration. Dispersion results will be compared with the main flow scales found, and alternatives to characterise the influence of vegetation distribution and their impact on mixing will be explored. Building on the relationship between concentration maps and probabilistic distributions, a relationship between statistical descriptors of concentration traces and the threshold to attain a Fickian regime will also be explored.

1.3. Methodology and Structure

The physical limitations of obstructed flows have limited the possibility to obtain extensive velocity and concentration fields. This project proposes a novel experimental set-up, with bespoke solutions for the acquisition of high-quality data, from which to address the research needs described above. At the end of this research it is expected that the final velocity and concentration information can help elucidate the main features of vegetated flows, verify the assumptions of previous models for vegetated dispersion and provide solid phenomenological principles from which to study these crucial systems, such that both researchers and practitioners can develop realistic and extensible models.

Given the scope of this research, the ambitious experimental plan proposed is divided into 2 main stages. 1) LIF experiments to estimate dispersion coefficients, to describe mixing in a range of flows spanning the regimes found in nature. This stage involves the use of an optical system, with 4 laser-camera measurement stations, to obtain 2D concentration maps that describe the transverse and longitudinal variation in concentration. 2) PIV experiments in a representative area of the flow field, with novel solutions to allow illumination within obstructed flows, to obtain spatio-temporal velocity fields, at high enough resolutions and frequencies to describe the spatial evolution of hydrodynamic quantities and turbulence quantities. Given this division of the experimental stage, the data will be analysed and presented in the following way:

Chapter 2 presents the literature review, summarising the findings from relevant previous studies that independently explored the physical phenomena involved in the study of hydrodynamics and mixing in emergent vegetation.

Chapter 3 presents the results of preliminary experiments, proposed and executed to study specific assumptions of the previous models for vegetated dispersion. Using Surface PIV measurements, the information needed to reproduce the most relevant model for streamwise dispersion is obtained. Some of the main assumptions are analysed in light of the experimental results, and a preliminary discussion is presented on some of the main physical factors overlooked in current approaches. Further, a study of velocity statistics, to introduce the idea of interacting wakes, and the importance of coherent structures in mass transfer is given. Finally, some important theoretical considerations are highlighted regarding the use of Eulerian measurements to represent theories of diffusion initially proposed in a Lagrangian frame of reference.

Chapter 4 concisely describes the vegetated array and the novel experimental configurations proposed to obtain the data described. The theoretical principles and the pre-processing techniques used for the experiments are described. A detailed, step-by-step account of the setting up process of the instrumentation, and calibration results, is given in Appendices A and B, for LIF and PIV, respectively.

Chapter 5 presents the results from the first experimental stage proposed above. First, a description of the methods used to pre-process and clean concentration profiles is given. This is intended as a benchmark to prepare concentration data for the calculation of dispersion coefficients, using both statistical approaches and optimisation procedures based on a routing solution of the ADE. The trends found for the statistical descriptors and concentration profiles help elucidate the behaviour of the mixing regime for each test. These results are further compared with characterisations of vegetation descriptors and previous estimates from artificial and natural vegetation.

Chapter 6 presents the maps of first and second order velocity statistics, such that the spatial variation of these quantities is contrasted with the known theory of obstructed flows (e.g. zones of turbulent production, evolution of vorticity). These results are further analysed in the context of the double-averaged momentum equation, and used to characterise drag forces and coefficients in the RandoSticks configuration.

Chapter 7 uses the velocity fields obtained, to explore different alternatives for the calculation of energy spectra, shedding frequencies and relevant length scales. These scales are analysed in probabilistic terms and compared with those found from the vegetation characterisation. Lastly, the results from Chapter 4, Chapter 6 and Chapter 7 are assembled, and the trends and magnitudes of dispersion coefficients and hydrodynamic scales (e.g. Reynolds stresses, dispersive fluxes) are compared over the range of Reynolds numbers analysed. Distincts dispersion regimes are identified and the dominant velocity terms for each one identified. Further consequences regarding the use of these conclusions for the design of experimental studies and development of analytical/empirical models are explored.

Chapter 2. LITERATURE REVIEW

2.1. Introduction

Flows in and around vegetation, present in a variety of ecosystems, control several key environmental processes for their subsistence and stability (Jadhav and Buchberger, 1995). They influence bed erosion and sediment deposition, mass and momentum exchange between vegetation and high conveyance streams (Nepf, 2012), and regulate solute transport and mixing. The latter determines the rates of nutrient uptake and biochemical reactions within vegetation (Nishihara and Terada, 2010), and its study can improve the control and design of natural and engineered vegetated systems for pollutant treatment and stormwater management (Shilton, 2000). There is, however, a considerable knowledge gap concerning the general understanding of fluid mechanics at relatively small scales (i.e. stem and inter-stem scales), its implications for mixing, and the principles under which dimensional analysis may be applied to upscale these concepts at the patch and reach scale.

This literature review presents a brief overview of the current understanding in hydrodynamics and solute transport in vegetation. Emphasis is given to general concepts of fluid dynamics, and the processes encountered in vegetated flows. Subsequently, a general review of the current, physically-based models for mass transport is given, and finally, previous approaches to model mass transport in vegetated systems are presented. This chapter concludes with a discussion on the limitations of previous relevant studies, alongside the most prominent knowledge gaps that motivated this research project.

2.2. Hydrodynamics

This review focuses on the particular subset of flows through emergent vegetation, which, for practicality is often represented as arrays rigid circular cylinders. The following descriptions of flow components and turbulence are presented from cases relevant to vegetated flows. Further, since this research has ultimately a practical, engineering aim, all flows are described under the assumption of incompressibility and constant viscosity.

All descriptions of fluid flow and mass transport are given in Cartesian coordinates, represented in 3D by the components $\{x, y, z\}$, where x is the direction of mean flow, y is the component perpendicular to x in the horizontal direction (i.e. parallel to the flow bed), and z represents the component perpendicular to the bed. The velocity components for $\{x, y, z\}$ are $\{u, v, w\}$, respectively; and the general Cartesian and velocity vectors will be represented by bold lowercase letters, or by an arrow above each letter, thus $\vec{u} = \boldsymbol{u} = \{u, v, w\}$, and $\vec{x} = \boldsymbol{x} = \{x, y, z\}$. Wherever convenient, Einstein summation convention will be used, in which an index indicates that a quantity must be considered over all Cartesian directions, and repeated indices represent a sum over all components of the repeated index (Synge and Schild, 1978). The connection between vector and tensor notation is: $x_i = \{x_1, x_2, x_3\} = \{x, y, z\}$, and $u_i = \{u_1, u_2, u_3\} = \{u, v, w\}$.

2.2.1. Mean and fluctuating velocity components

The mathematical framework for the study of fluid flow is represented by conservation equations. The first of which is the mass conservation equation or *continuity equation*, and is represented as follows (Currie, 2012)

$$\frac{\partial u_i}{\partial x_i} = \frac{\partial u}{\partial x} + \frac{\partial v}{\partial y} + \frac{\partial w}{\partial z} = 0 \qquad \textit{Eq. 2.2-1}$$

The second fundamental equation represents the momentum balance and is obtained from a force equilibrium applied over a differential fluid element. Considering body forces and gravity (g_i) only, we obtain the following expression for the momentum balance (Hinze, 1975)

$$\rho \frac{\partial u_i}{\partial t} + \rho \frac{\partial}{\partial x_j}\left(u_i u_j\right) = \frac{\partial}{\partial x_j} \sigma_{ji} - \rho g_i \qquad \textit{Eq. 2.2-2}$$

Where ρ is the fluid density, and the left hand side of Eq. 2.2-2 is a *material* or *substantial* derivative, which represents the change in momentum following a single differential volume of fluid along its motion path (Batchelor, 2000). The term σ_{ji} represents the stress component in the i-th direction applied over the j-th face of the differential volume. This stress component can be divided into an isotropic, symmetrical part, i.e. pressure p, and an antisymmetrical one, representing shear stresses τ_{ji}. Shear stress is defined for a Newtonian fluid as linearly proportional to the rate of strain, $\tau_{ji} = \mu 2 S_{ij}$ (Hinze, 1975); where the proportionality constant μ is the fluid viscosity. The resulting expression is the Navier-Stokes equation for incompressible flow (Currie, 2012)

$$\frac{du_i}{dt} + u_j \frac{\partial}{\partial x_j} u_i = -\frac{1}{\rho} \frac{\partial}{\partial x_i} p + \frac{\partial}{\partial x_j} \left(\nu 2 S_{ij} \right) - g_i \qquad \textit{Eq. 2.2-3}$$

ν is the kinematic viscosity and S_{ij} the rate-of-strain tensor, which is defined as the average velocity gradients for the plane ij, that is (Pope, 2000)

$$S_{ij} = \frac{1}{2} \left(\frac{\partial u_i}{\partial x_j} + \frac{\partial u_j}{\partial x_i} \right) ; \quad S_{xy} = \frac{1}{2} \left(\frac{\partial u}{\partial y} + \frac{\partial v}{\partial x} \right) \qquad \textit{Eq. 2.2-4}$$

Applying the continuity equation to the second differential term on the RHS of Eq. 2.2-3, a more concise expression for the Navier-Stokes equation is obtained

$$\frac{du_i}{dt} + u_j \frac{\partial}{\partial x_j} u_i = -\frac{1}{\rho} \frac{\partial}{\partial x_i} p + \nu \frac{\partial^2}{\partial x_j \partial x_j} u_i - g_i \qquad \textit{Eq. 2.2-5}$$

Eq. 2.2-5 represents a non-linear system of partial differential equations, whose analytical solution (even its existence) is beyond the reach of the current theory (Pope, 2000). Except for a few flow cases, quantities such as velocities, trajectories (i.e. streamlines) and positions of fluid particles cannot be predicted from analytical expressions; instead they follow random patterns that can be described only through statistical methods (Taylor, 1935). This randomness, with increased rates of momentum and mass transfer, three-dimensionality, rotational motions and viscosity-induced instabilities, is what characterise *turbulent motion* (Tennekes and Lumley, 1972). When the extent of this chaotic motion is low, and the movement of fluid particles resembles an idealised flow of parallel streamlines, the flow is said to be *laminar* (Batchelor, 2000). As the randomness of the motion increases, due to increased energy of the flow or induced instabilities, the flow transitions to a state of turbulence, which is the state of most flows in nature, and particularly in vegetated systems. The parameter used to quantify the state of this transition and the type of fluid motion is the *Reynolds number*, Re, defined as the ratio of kinetic to viscous forces in the flow,

$$Re = \frac{U\,L}{\nu} \qquad \textit{Eq. 2.2-6}$$

Where U and L represent characteristic velocity and length scales of the flow. In the case of flow past circular stems (cylinders), L is usually chosen to represent the stem diameter, d, and

U is the pore velocity U_p. Consequently, all references to Reynolds number included in this work, are understood to indicate the *stem Reynolds number*, $Re_d = U_p d/\nu$.

Experimentally, Reynolds (1883, 1895) showed that in the transition to turbulence, the initially laminar streamlines break down and form eddies that advect downstream with the mean flow, and the velocity behaves in a chaotic manner downstream. An image from his influential paper is presented in Figure 2.2-1.

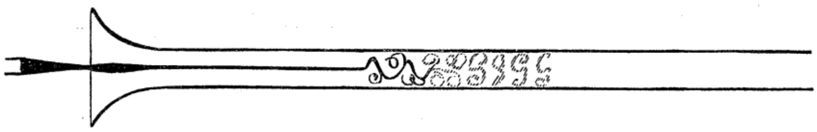

Figure 2.2-1 Experimental investigation of Reynolds (taken from Reynolds, 1883, p. 942), in which the transition from laminar to turbulent flow is identified. The transition is identified from the breakdown of a line of dye into distinct eddies, viewed against a sparkling light.

Whether velocity is measured for a single particle along its path, or a specific spatial point in the flow, a temporal profile similar to that shown in Figure 2.2-2 is found.

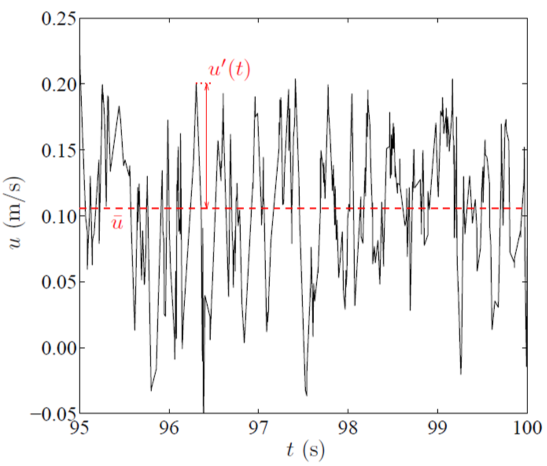

Figure 2.2-2 Graphical representation of Reynolds decomposition from a time series of longitudinal velocity (Ricardo, 2014)

Any property of the flow will behave similarly to Figure 2.2-2. For the velocity, u, and any property travelling with the flow, its instantaneous value can be expressed as the sum of the contribution from the mean value and a deviation therefrom (Reynolds, 1895; Monin and Yaglon, 1971).

$$u = U + u' \qquad \textit{Eq. 2.2-7}$$

U is the mean velocity component, obtained from a time average of the velocity record ($U = \overline{u}$). u' is the fluctuating component of the instantaneous velocity, characterised by random deviations from the mean, as shown in Figure 2.2-2. Details of the time averaging procedure and the criteria necessary to apply the decomposition shown in Eq. 2.2-7, are given in Section 2.2.5.

This decomposition is important for two main reasons, first it presents the averaging procedures and statistical framework used to describe turbulence. Second, it relates u_i' to the existence of eddies, which are features with structural consistency, intrinsic to all turbulent flows; and shown as the swirls sketched by Reynolds in Figure 2.2-1.

2.2.2. Turbulent Structures and Coherence

As shown in Figure 2.2-1 turbulence is characterised by the existence of eddies. Two questions with regards to these structures arise: what determines their formation and size? And, what controls their size and stability downstream?

Regarding the first question, turbulence is generated from instabilities caused by small perturbations; which, due to interactions between inertial and viscosity terms in the equations of motion (second terms on the LHS and RHS of Eq. 2.2-5, respectively), propagate rapidly owing to their nonlinearity (Tennekes and Lumley, 1972). Several types of instabilities exist, which are subject to intensive research in fundamental fluid mechanics, and are therefore beyond the scope of this thesis.

The current research focuses on vegetated flows, where stems are modelled as circular cylinders. For this case, flow past a fixed cylinder exhibits different types of transition and stability regimes for the structures developed. The influence of viscosity near the cylinder walls creates a *Boundary Layer*, that expands downstream from the incidence/stagnation point (A in Figure 2.2-3a), along the cylinder circumference (Schlichting and Gersten, 2000). The subsequent formation of vortices depends on the interaction between the boundary layer and the outer flow, which varies with Reynolds number, Re_d, and pressure gradient along the cylinder.

To illustrate the formation of vortices, Figure 2.2-3a shows the interaction between the flow and a cylinder at low Reynolds numbers ($Re_d = 13$). From point A to B, a local increase in velocity is coupled with a decrease in pressure; followed by a deceleration and pressure increase from points B to D. A sharp velocity gradient outwards from the boundary layer, induces a rotational instability that prompts flow separation at point C, between B and D (Schlichting and Gersten, 2000). This causes mass to 'roll up' in the form of two symmetric vortices at the back of the cylinder, creating a closed recirculation (separation) region whose longitudinal extent is given by the distance between points D and E (Gerrard, 1966; Berger and Wille, 1972). This initial form of recirculating eddies constitutes a stationary stable state for low Reynolds numbers, $10 < Re_d < 40$ (Gerrard, 1978).

This stable separation region scales with Re_d, until the length ($\overline{DE}$) reaches approximately 2 cylinder diameters ($2d$), which in turbulence-free incident flow occurs at $Re_d \approx 40$, (Roshko, 1954; Gerrard, 1978). After this threshold, the recirculation cell starts to oscillate, opening a pathway of mass exchange towards the outer flow, at point E (Figure 2.2-3a). This pathway leaves a trace with a sinusoidal variation that accelerates until the separation point in the boundary layer becomes unstable and behaves as a vortex sheet, thereby rolling up into alternating vortices that are then advected downstream. This alternating detachment of vortices forms a stable two-dimensional configuration at low-to-moderate Reynolds numbers, $70 < Re_d < 400$ (Gerrard, 1978), in the form of a parallel pair of vortex rows, with a phase shift, is known as the Kármán vortex street (Kármán, 1911), and shown in Figure 2.2-3b.

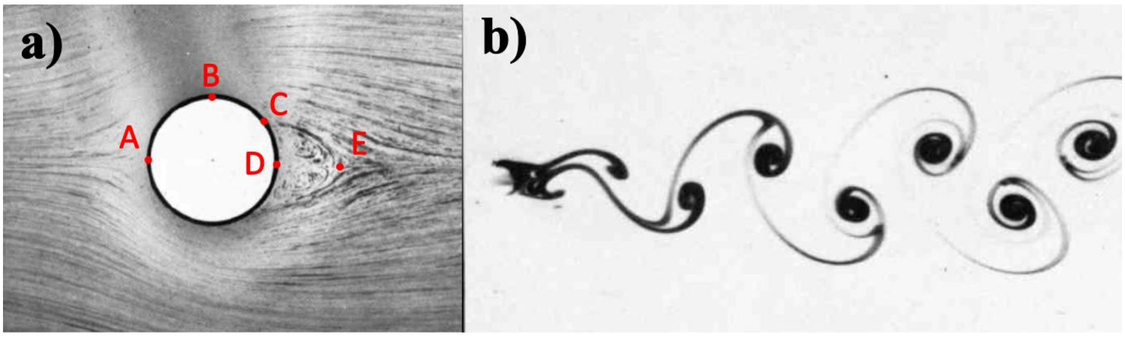

Figure 2.2-3 a) Flow separation at the rear of the circular cylinder at Re = 13, the stable stationary configuration generates two symmetric eddies rotating with opposite direction (Van Dyke, 1988) (A) Stagnation point, i.e. point where the incident velocity approaches zero at the surface of the body; (B) First point of peak negative pressure; (C) separation point; (E) rear of the cylinder; (E) end of recirculation cell. b) Development of a regular and stable Kármán vortex street visualised using electrolytic precipitation, Re_d = 105 (Van Dyke, 1988).

The configurations shown in Figure 2.2-3 are two-dimensionally stable for each regime, and the transition between the two, for turbulence-free incident flow occurs at $40 < Re < 70$. A delay in this transition is expected for shear flows and incoming turbulence (Kiya, Tamura and Arie, 1980; Khabbouchi *et al.*, 2014).

Physically, two-dimensional stability means that vortices are parallel to the cylinder. For increasing Re_d, this 2D stability is lost, and a transition to a 3D regime occurs in two stages.

First, vortices that are initially parallel, or slightly oblique (Williamson, 1988a), to the cylinder axis, break down and form closed loops ($170 < Re_d < 180$). At larger Re_d (~ 230-260) smaller vortices, with a strong streamwise component, develop in the near wake (Williamson, 1988b).

The transition to a fully 3D vortex shedding regime is accompanied by changes in the negative pressures behind the cylinder (Williamson, 1991). A laminar-turbulent transition occurs from moderate Reynolds numbers ($Re_d \approx 190$) in the near wake. This expands the range of vortex motions and scales (Williamson, 1996b, 1996c).

Different scales of motion, i.e. size of eddy, have frequencies associated with their vorticity (rotation) and thus a role in terms of energy flux, momentum transport, dissipation, and diffusion (Hinze, 1975; Townsend, 1980). Vortex stability depends on Re_d and distance downstream: large eddies from the vortex street will either be dissipated directly to viscosity, for $Re_d < 180$ (Williamson, 1991), or they will break down into smaller eddies, $Re_d > 180$, until turbulence becomes isotropic (Roshko, 1954), that is, the statistical properties of turbulence will be independent of any rotation of the coordinate system (Karman and Howarth, 1938).

The previous discussion shows that eddies are largely responsible for the energy transfer (see section 2.2.3) and diffusion of mass and momentum. Large-scale structures govern the turbulent behaviour of a cylinder wake, and are instrumental in the trapping, release and transport of scalar quantities such as pollutants, sediment and heat (Taylor, 1915). Referring back to the question of what factors determine the size and stability of these structures, there is not a complete understanding of the complex flow phenomena governing their life span. However, it is possible, through experimental methods, to study their consistency with time, which is usually referred to as *coherence*.

The term 'coherent structure' was first associated with the persistent features of large-scale motions in turbulent flows (Townsend, 1980; Liu, 1988), further refinements defined them as *masses of fluid with a phase-correlated vorticity* (Hussain, 1983), or simply put, as *organised spatial features which repeatedly appear and undergo a characteristic temporal life cycle* (Berkooz, Holmes and Lumley, 1993). Understanding their life cycle is of particular interest in the study of mass and momentum transport, particularly in vegetated flows. Several methods exist for the study of coherent structures, their temporal variation, is usually determined via the Proper Orthogonal Decomposition, POD, (Holmes *et al.*, 2012), and the Dynamic Mode Decomposition, DMD, (Schmid, 2010). Both are limited when used independently by the nonlinearity of the structures, which is associated with their formation mechanisms (Higham, 2017). These decomposition techniques work by extracting the main orthonormal modes of rotation in phase space, so that the turbulent field can be reconstructed based on these dominant modes (Holmes *et al.*, 2012).

As explained above, coherent structures carry energy transferred from the mean flow. The range of vortices is associated with a distribution of energy spanning the large (integral) scales, to the smallest microscales. The latter are of the same order of magnitude as viscosity, ν, and subject to deformation energy dissipation to heat (Hinze, 1975).

2.2.3. Energy Spectrum

As energy is abstracted from the mean flow through stem/cylinder drag (see Section 2.2.4), it is distributed across different structures, whose energy is associated with a frequency, thereby creating an spectrum of turbulence (Taylor, 1938). This spectrum is the result of transforming the turbulent velocity components into a frequency domain. Their amplitudes represent the contribution to the total flow energy. Before describing such transformation, it is necessary to recall how energy is quantified in turbulent flows.

Each turbulent velocity component contributes to the total energy of the flow. The total kinetic energy of a differential volume of fluid, per unit mass, is given by the following expression

$$E = \frac{1}{2}(u^2 + v^2 + w^2) = \frac{1}{2}(u_i u_i) \qquad \textit{Eq. 2.2-8}$$

Where the second definition is given using tensor notation. Applying the Reynolds decomposition, the total instantaneous energy is divided into mean and turbulent components, Then, time averaging Eq. 2.2-8 yields the total energy as the contribution from the Mean Kinetic Energy (MKE), $\overline{E}$, and Turbulent Kinetic Energy (TKE), E'. For reference, the term E' is used to define turbulent kinetic energy in a full 3D flow field. In vegetated flows, where the 2D simplification is applied, the same quantity is represented by k where $i \in (1, 2)$.

$$E = \overline{E} + E' = = \frac{1}{2}\overline{u_i}\,\overline{u_i} + \frac{1}{2}\overline{u_i' u_i'} \qquad \textit{Eq. 2.2-9}$$

The details of the decomposition in Eq. 2.2-9 are given in section 2.2.5. The equation for the rate of change of kinetic energy, per unit mass, of a fluid particle can be obtained by multiplying each of the expressions in Eq. 2.2-5 by u_i, and summing all equations together, thus obtaining (Pope, 2000)

$$\frac{\partial E}{\partial t} + u_j \frac{\partial E}{\partial x_j} + \frac{\partial}{\partial x_i}\left(\frac{u_i}{\rho} p - 2\nu u_j S_{ij}\right) = -2\nu S_{ij} S_{ij} \qquad \textit{Eq. 2.2-10}$$

The third term on the LHS represents the energy flux density of a differential element of fluid, which comprises the direct energy transfer by the displacement of particles, and pressure, molecular and internal friction effects (Monin and Yaglon, 1971). The term on the RHS, $2\nu S_{ij} S_{ij}$, results from the work done by viscous shear terms and represents viscous dissipation: the conversion of kinetic energy into heat (Pope, 2000).

Similar to the case of the equations of motion, the terms in Eq. 2.2-10 can be decomposed into mean and turbulent components (Eq. 2.2-9), which give expressions for the change in Mean (Eq. 2.2-11), and Turbulent (Eq. 2.2-12) Kinetic Energy, respectively

$$\frac{\partial \overline{E}}{\partial t} + \overline{u_j} \frac{\partial}{\partial x_j} \overline{E} + \frac{\partial}{\partial x_i}\left(\overline{u_i}\, \overline{u_i' u_j'} + \frac{\overline{u_i}\, \overline{p}}{\rho} - 2\nu\, \overline{u_j}\, \overline{S_{ij}}\right) = -\mathcal{P} + \overline{\varepsilon} \qquad \textit{Eq. 2.2-11}$$

$$\frac{\partial E'}{\partial t} + \overline{u_j} \frac{\partial}{\partial x_j} E' + \frac{\partial}{\partial x_i}\left(\frac{1}{2}\overline{u_i' u_j' u_j'} + \frac{\overline{u_i'\, p'}}{\rho} - 2\nu\, \overline{u_j'\, s_{ij}}\right) = \mathcal{P} + \varepsilon \qquad \textit{Eq. 2.2-12}$$

The term $\mathcal{P}$ represents a production of turbulent kinetic energy, and appears as a 'sink' (i.e. negative) term in the MKE (Eq. 2.2-11) and as a 'source' (i.e. positive) term in the TKE (Eq. 2.2-12, indicating that $\mathcal{P}$ entails a transfer of energy from the mean motion to the scales of turbulence, which are responsible for an increase in momentum transport (Pope, 2000), as can be seen from the definition of $\mathcal{P}$

$$\mathcal{P} = -\overline{u_i' u_j'} \frac{\partial \overline{u_i}}{\partial x_j} \qquad \textit{Eq. 2.2-13}$$

The instantaneous rate of strain tensor S_{ij} can also be subdivided into a mean and a fluctuation component,

$$S_{ij} = \overline{S_{ij}} + s_{ij} = \frac{1}{2}\left(\frac{\partial \overline{u_i}}{\partial x_j} + \frac{\partial \overline{u_j}}{\partial x_i}\right) + \frac{1}{2}\left(\frac{\partial u_i'}{\partial x_j} + \frac{\partial u_j'}{\partial x_i}\right) \qquad \textit{Eq. 2.2-14}$$

The terms $\overline{\varepsilon}$ and ε in Eq. 2.2-11 and Eq. 2.2-12 represent the dissipation of energy due to viscosity at the mean flow and turbulent (mainly at dissipative scales), respectively. For undisturbed turbulent flows (e.g. away from boundaries or obstructions), $\overline{\varepsilon}$, is several orders of magnitude smaller than $\mathcal{P}$, and is therefore negligible for all practical purposes (Pope, 2000). Dissipation terms are defined as follows

$$\overline{\varepsilon} = 2\nu\overline{S_{ij}}\ \overline{S_{ij}} \quad ; \quad \varepsilon = 2\nu\overline{s_{ij}\, s_{ij}} \qquad \textit{Eq. 2.2-15}$$

In vegetated flows, the presence of obstructions leads to enhanced dissipation of energy at the mean flow level, via viscous drag due to increased shear along cylinder surfaces, so $\overline{\varepsilon}$ can no longer be considered negligible (Nepf, 1999).

The largest scales of turbulent motion, i.e. *integral scales*, abstract energy from the mean flow and are responsible for most of the mass and momentum transport; therefore, most of the turbulent energy is contained in these scales. An intermediate range of scales, called the *inertial subrange*, is responsible for transferring energy from the integral scales, to the *dissipation range*, which contains the smallest eddies and where energy is dissipated under the action of viscosity. For vegetated flows, the identification of this inertial subrange from velocity data is still an open question (Nikora, 2000). Nonetheless, to quantify the dispersion of any scalar quantity, the focus must necessarily be placed on the integral scales.

Khintchine (1934) and Taylor (1938) reported the relationship between the velocity correlation function (Karman and Howarth, 1938) and the energy spectrum of velocities in the frequency space f. Before defining the spectral functions, it is necessary to introduce the correlation functions in time and space domain.

In general, the velocity signals covered in this thesis are considered stationary random processes (steady flow), meaning that mean values do not vary. If, as in Figure 2.2-2, a velocity signal contains a noticeable periodic component, correlation functions can reveal these features with respect to time and space.

The first correlation to consider is the *autocorrelation* function, which relates a signal with a shifted version of itself. It is defined as the covariance coefficient between the original and shifted signals. To maintain consistency with the hydrodynamics literature, the covariance is better expressed in terms of the turbulent component of velocity, which has zero mean. The autocorrelation function is used in fluid dynamics to describe the temporal evolution of the velocity signal at a single point in a flow field, and is therefore defined as

$$R_i(t^*) = \frac{\overline{u_i'(t), u_i'(t+t^*)}}{\overline{u_i'^2}} \qquad \textit{Eq. 2.2-16}$$

Eq. 2.2-16 requires the average period to be considerably larger than the largest flow scale (see Section 2.2.5). Two main properties can be derived from Eq. 2.2-16. First, the range of the autocorrelation function is, $-1 \leq R_i(\tau) \leq 1$, and second $R_i(\tau)$ is an even function of τ, that is $R_i(\tau) = R_i(-\tau)$. For periodic signals, the absolute maxima of $R_i(\tau)$ are approached when the peaks of the signal and its shifted version match. The values of τ where local maxima and minima of $R_i(\tau)$ are found, represent the characteristic period, and therefore frequency, of the dominant structures present in a velocity record.

Although evidence of flow features can be found via autocorrelations; knowledge regarding the stability and intrinsic features is unattainable. To compute the statistical relation between the ith velocity component at a point $\vec{x}$, and the jth velocity component of point $\vec{\xi}$, with a time lag τ, the general cross-correlation (cf. multi-point correlation) is defined as

$$R_{ij}(\vec{\xi}, \tau) = \frac{\overline{u_i'(\vec{x}, t), u_j'(\vec{x} + \vec{\xi}, t - \tau)}}{u_i^+(\vec{x}) u_j^+(\vec{x} + \vec{\xi})} \qquad \textit{Eq. 2.2-17}$$

The correlation function presented in Eq. 2.2-17 describes the characteristic period and thus frequencies, of the structures encoded in a velocity record. To find the contribution of each structure to the total turbulent energy E', the spectrum $E_i(f)$, which describes the proportion of energy contained in structures with frequency, f, is defined. (Taylor, 1938) found that this spectrum function $E_i(f)$ and the autocorrelation function $R_u(\tau)$ are Fourier transforms of one another, as shown in Eq. 2.2-18 and Eq. 2.2-19.

$$E_i(f) = 2\int_{-\infty}^{\infty} R_i(\tau) e^{-\boldsymbol{i}2\pi f \tau} d\tau \qquad \textit{Eq. 2.2-18}$$

$$R_i(\tau) = \frac{1}{2}\int_{-\infty}^{\infty} E_i(f) e^{\boldsymbol{i}2\pi f \tau} df \qquad \textit{Eq. 2.2-19}$$

$R_i(\tau)$ is an even function, so it is possible to redefine the limits of the energy spectrum equation, so that only positive values of the domain are considered, which are more consistent with experimental results[1].

$$E_i(f) = 4\int_0^\infty R_i(\tau)\cos(2\pi f\tau)\,d\tau \qquad \textit{Eq. 2.2-20}$$

The energy spectrum in Eq. 2.2-20, is a function of the velocity statistics of a single point. This can be extended to multi-point correlations. If mean velocity, U, is significantly larger than the turbulent velocity scales, i.e. turbulent structures at two points (within a distance ξ) remain unchanged, (Taylor, 1938) 'frozen turbulence hypothesis' applies, and the time component in Eq. 2.2-20 can be expressed as $\tau = \xi/U$, thus, yielding the spectrum in the wavenumber domain, κ. In generality, the spectrum from multipoint correlations should be defined in terms of either time or space. For the latter—the one used in this thesis—the wavenumber spectrum is calculated

$$E_{ij}(\kappa) = 2\int_0^\infty R_{ij}(\xi,0)e^{-i2\pi\xi\kappa}d\xi \qquad \textit{Eq. 2.2-21}$$

In addition to defining the distribution of energy across flow scales, spectral functions allow for the estimation of vortex shedding frequencies (Roshko, 1954). Finally, considering turbulent velocities as random functions implies that their Fourier transforms will be random functions as well, therefore, the relations between different scales can be expressed in statistical terms. The energy relations between different scales of turbulent motion led Kolmogorov (1941a, 1941b) to formulate his famous universal equilibrium theory, which can be summarised as follows.

For steady flows, no net change of kinetic energy with time occurs, therefore, an equilibrium between dissipation and production is expected. The smallest scales dissipate energy under the action of viscosity, so, a continuous input of energy is necessary to maintain an equilibrium. Times of characteristic large scales are several orders of magnitude bigger than those of microscales. It is hypothesised that both are statistically independent. Consequently, small scales depend only on viscosity and on the rate at which energy is transferred from the large

[1] Note that the function $E_i(f)$ refers to the one-sided spectrum, i.e. considering only $f \mid f \geq 0$. Parseval's theorem is originally defined for the double-sided, symmetrical spectrum $\widetilde{E}_i(f)$, then, $E_i(f) = 2\widetilde{E}_i(f)$.

scales. Similarly, intermediate and large scales will be independent of viscosity and dependent on the rate of transfer of energy and the energy abstraction rate from the mean flow, respectively. In other words, the range of eddies and the dissipation rate will adjust to both viscosity and the rate at which energy is fed into turbulence from the mean flow, to maintain equilibrium (Fischer *et al.*, 1979).

2.2.4. Drag and Shear

Having defined turbulent scales and their associated energy, the focus is now on the source of that energy transfer.

It is known, from Boundary Layer Theory, that viscous effects are dominant near solid surfaces. Boundary layers originate from the non-slip condition along the surfaces, which implies the existence of a dominant shear stress, τ_w, in this region. Most vegetated/obstructed flows are divided into boundary layers, where shear and viscosity are dominant, and an outer region which, for large Re_d, is dominated by advection.

For the case of circular cylinders, the hydrodynamic force is the combination of the effects of shear stress and pressure gradients, along the surface. Note that a transition from positive to negative pressures leads to the boundary layer instability described in section 2.2.2, and the subsequent vortex shedding. The hydrodynamic force acting on the body is divided into a *Lift* and a *Drag* component, which are perpendicular and parallel to the incident streamlines, respectively.

Circular cylinders are subject to a drag force, F_D, only, which is in turn composed of a viscous (from the shear stress) and a form (from the pressure gradient) component. Defining F_D analytically requires the velocity and pressure fields along the entire cylinder surface, which is experimentally unachievable. Alternatively, mechanical similitude allows the drag force to be scaled for different flow fields, in terms of a characteristic force and the same morphology.

The flow fields around two geometrically similar bodies are said to be *mechanically similar* if the streamline layout around both are similar. A property of mechanical similitude flows is that the ratio of forces acting on similar positions is constant for both flow fields (Schlichting and Gersten, 2000). Assuming a reference force common to all circular cylinders, this is defined as

$$\frac{F_D}{F_{reference}(x)} = C_D = constant \qquad \textit{Eq. 2.2-22}$$

The similarity constant, C_D, is the drag coefficient. The most convenient choice of the reference force is the stagnation pressure; defined, from Bernoulli's principle, as the pressure at the point where the vector normal to the cylinder surface and the incident streamlines are parallel, therefore

$$F_{reference}(x) = \frac{1}{2}\rho U A_S \qquad \textit{Eq. 2.2-23}$$

Where A_S is a characteristic area of the body, perpendicular to the direction of the mean flow. U is the incident mean velocity, ρ is the flow density. Through dimensional analysis it is known that the drag coefficient, C_D, is a function of Re_d only, and is defined as

$$C_D = \frac{F_D}{\frac{1}{2}\rho U A_S} \qquad \textit{Eq. 2.2-24}$$

Dividing F_D into the aforementioned viscous and form (pressure) components, respectively. A drag coefficient for each contribution, can be defined

$$C_D^{form} = \frac{F_D^{form}}{\frac{1}{2}\rho U A_S} \qquad C_D^{visc} = \frac{F_D^{visc}}{\frac{1}{2}\rho U A_S} \qquad \textit{Eq. 2.2-25}$$

It has been found that the dominant source of energy in flows through random arrays of cylinder-like elements, e.g. atmospheric canopy flow, is turbulent production due to drag imposed by solid boundaries (Raupach, Antonia and Rajagopalan, 1991; Kaimal and Finnigan, 1994; Finnigan, 2000). Another important source of energy in canopy flow is the effect of shear, which appears as a consequence of sharp velocity gradients, due to changes in the boundary conditions of the flow field. Furthermore, the action of cylinders in the flow field also induces heterogeneities leading to temporal and spatial fluxes of energy; vortex shedding being an example of the former, and wake interactions and vertical turbulent fluxes being examples of the latter.

To date, measurements of shear production in canopy flow (Raupach and Shaw, 1982; Raupach, Coppin and Legg, 1986; Raupach, Antonia and Rajagopalan, 1991) have associated this source of energy with the shear layer occurring in the interface between vegetated and non-vegetated regions, particularly in the vertical direction. To the author's knowledge, there are no experimental measurements of shear production at length scales comparable to the size of vegetation elements within the flow.

2.2.5. Averaging Frameworks

The previous sections presented hydrodynamics concepts that rely on the concept of averaging, mainly in the time and space domain. The concept of averaging is well-known. However, its application in fluid mechanics depends on certain conditions that will be covered in this section.

Consider a variable θ, which represents any scalar function for a specific point in the flow field (e.g. concentration, heat, velocity component, pressure, etc.), its time average $\overline{\theta}$ is defined as

$$\overline{\theta}(t) = \frac{1}{T} \int_{-T/2}^{T/2} \theta(t + t^{*}) \gamma_f (t + t^{*})\, dt^{*} \qquad \textit{Eq. 2.2-26}$$

Where T represents the recording time interval, and γ_f is a phase function where, for instants when the point is occupied by the fluid phase, it takes the value $\gamma_f = 1$; and $\gamma_f = 0$ otherwise. For this study, all flow fields analysed are steady, hence θ as a random process has the same mean parameters independent of the value of t. Additionally, the mean value $\overline{\theta}$ complies with the Reynolds decomposition presented in Eq. 2.2-7

$$\theta = \overline{\theta} + \theta' \qquad \textit{Eq. 2.2-27}$$

Eq. 2.2-26 and Eq. 2.2-27 are also valid for the case of unsteady flows. (Reynolds, 1895), formulated some conditions necessary to average the equations of motion. These were refined into the formal relations presented below (Monin and Yaglon, 1971, p. 207)

$$\overline{\theta + \psi} = \overline{\theta} + \overline{\psi} \qquad \textit{Eq. 2.2-28}$$

$$\overline{a\,\theta} = a\,\overline{\theta} \qquad \textit{Eq. 2.2-29}$$

$$\overline{a} = a \qquad \textit{Eq. 2.2-30}$$

$$\overline{\frac{\partial \theta}{\partial q}} = \frac{\partial \overline{\theta}}{\partial q} \qquad \textit{Eq. 2.2-31}$$

$$\overline{\overline{\theta}\,\psi} = \overline{\theta}\,\overline{\psi}\,, \qquad \textit{Eq. 2.2-32}$$

Where θ and ψ are scalar functions of the flow field, a is a constant and q represents any of the domain variables of the flow field scalar quantities, i.e. x_i or t. Clearly, the conditions presented in Eq. 2.2-28, Eq. 2.2-29 and Eq. 2.2-30 are automatically satisfied from properties of the integral operator. Eq. 2.2-31, is satisfied only for the time average in vegetated flows. Below the theorems for the application of Eq. 2.2-31 considering space averaging are given.

From the Reynolds decomposition (Eq. 2.2-27) and the condition presented in Eq. 2.2-32, the following consequences are obtained.

$$\overline{\overline{\theta}} = \overline{\theta}\,, \quad \overline{\theta'} = \overline{\theta - \overline{\theta}} = 0, \quad \overline{\overline{\theta}\,\overline{\psi}} = \overline{\theta}\,\overline{\psi}\,, \quad \overline{\overline{\theta}\,\psi'} = \overline{\theta}\,\overline{\psi'} = 0 \qquad \textit{Eq. 2.2-33}$$

Note that the validity of the identities in Eq. 2.2-33 requires the interval T to be considerably larger than the characteristic period of the largest integral flow scale, but small enough to avoid effects of the long-term variations in the mean flow (e.g. seasonal changes, tidal waves). Mathematically, (Monin and Yaglon, 1971) define this as a *spectral gap*, represented as an interval in the Fourier transform of θ where the values are zero between the characteristic frequencies of the long-term variations and turbulent fluctuations.

For a flow field where the foregoing conditions are satisfied, the Reynolds decomposition (Eq. 2.2-27) can be applied over the momentum equation (Eq. 2.2-5), thus obtaining the Reynolds-Averaged Navier Stokes equations (RANS)

$$\frac{\partial}{\partial t}\overline{u_i} + \overline{u_j}\frac{\partial}{\partial x_j}\overline{u_i} = -\frac{1}{\rho}\frac{\partial}{\partial x_i}\overline{p} + \frac{\partial}{\partial x_j}\left(\nu 2\overline{S_{ij}} - \overline{u_i'u_j'}\right) + \overline{g_i} \qquad \textit{Eq. 2.2-34}$$

The RANS equations represent the momentum balance over a period T, for a single point in the flow field, in an Eulerian frame of reference. This procedure introduces new virtual stresses (called Reynolds or turbulent stresses) representing the momentum contribution from turbulent fluctuations. However, Eq. 2.2-34 does not provide information regarding the spatial variation of velocities or stresses, or the correlation between flow quantities at different points; parameters that are essential in the analysis of mass dispersion in a flow field (Tanino and Nepf, 2008b).

A similar form of upscaling, in the spatial domain, is proposed in the Double Averaging (DA) framework, a methodology used for the analysis of flow phenomena in multiphase flow (Wilson and Shaw, 1977), atmospheric canopy flow (Raupach and Shaw, 1982; Finnigan, 2000), and recently formalised for its application in flow through vegetation and rough beds (Nikora *et al.*, 2007, 2013). The use of a formal methodology for spatial and temporal averages originates from the complexity of multiphase flows. The first consideration of the DA framework, is the definition of a spatial average over a discontinuous multiply connected domain. Considering again a generic flow scalar field, θ, the spatial average over a domain V, composed of a fluid and a solid (vegetation) phase, is defined as

$$\langle\theta\rangle = \frac{1}{V}\iiint\limits_{V} \theta\left(\vec{x}+\vec{\xi}\,\right)\gamma_f(\vec{x}+\vec{\xi}\,)d\xi_x d\xi_y d\xi_z \qquad \textit{Eq. 2.2-35}$$

Where $\gamma_f(\vec{x})$ is the fluid phase function defined over the spatial domain, such that for points lying in the fluid phase $\gamma_f = 1$, and $\gamma_f = 0$ otherwise. The use of a phase function allows for the definition of a porosity ϵ_f as an extension of the spatial average, thus

$$\epsilon_f = \frac{1}{V}\iiint\limits_{V} \gamma_f(\vec{x}+\vec{\xi}\,)\, d\xi_x d\xi_y d\xi_z = \frac{V_f}{V} \qquad \textit{Eq. 2.2-36}$$

V_f represents the fluid portion of the volume domain V. For simplicity, the product $d\xi_x d\xi_y d\xi_z$ will be expressed as $d\vec{\xi}$ from now on. This research is confined to the case of static vegetation elements, therefore, both the phase function γ_f, and the porosity ϵ_f, are independent of time.

Applying the spatial average to time-averaged quantities, e.g. $\overline{\theta}$, extends the idea of a Reynolds (temporal) decomposition of variables, to a double averaged one. The instantaneous variable θ is then divided into three components. A double averaged term, $\langle\overline{\theta}\rangle$ as shown in Eq. 2.2-37. $\overline{\theta}''$ represents the spatial deviation of the time-averaged values with respect to $\langle\overline{\theta}\rangle$. θ' is the time fluctuation presented in Eq. 2.2-27. These components relate to each other according to Eq. 2.2-37, inverting the averaging order leads to the decomposition in Eq. 2.2-38 (Nikora *et al.*, 2013).

$$\theta = \langle\overline{\theta}\rangle + \overline{\theta}'' + \theta' \qquad \textit{Eq. 2.2-37}$$

$$\theta = \overline{\langle\theta\rangle} + \langle\theta\rangle' + \theta'' \qquad \textit{Eq. 2.2-38}$$

Where the terms in Eq. 2.2-38 show the DA when the space average is done first. $\overline{\langle\theta\rangle}$ is the double average mean of θ, $\langle\theta\rangle'$ is the temporal fluctuation of each spatially-averaged quantity

$\langle\theta\rangle$ and θ'' represents the spatial variations around $\langle\theta\rangle$. To develop the flow equations from the double averaging (DA) framework, the conditions given in Eq. 2.2-28 to Eq. 2.2-33 must be satisfied. The first three are automatically valid from Eq. 2.2-36, and the requirements that V is larger than the length scales of the flow still applies, which makes the conditions presented in Eq. 2.2-32 and Eq. 2.2-33 valid. However, due to the discontinuity of the flow field, the condition in Eq. 2.2-31 cannot be mathematically attained. A relation between the derivatives and average quantities is necessary. For the case of $q = x_i$ (Eq. 2.2-31) (Whitaker, 1985) presented a solution for the spatial averaging theorem, now referred to as the *First Double-Averaging Theorem* (Nikora *et al.*, 2013)

$$\left\langle \overline{\frac{\partial \theta}{\partial x_i}} \right\rangle = \left\langle \frac{\partial \overline{\theta}}{\partial x_i} \right\rangle = \frac{1}{\epsilon_f} \frac{\partial}{\partial x_i} \epsilon_f \langle \overline{\theta} \rangle - \frac{1}{V_f} \iint_{A_{fs}} n_{f,i} \overline{\theta}(\vec{x} + \vec{\xi})\, d\vec{\xi} \qquad \textit{Eq. 2.2-39}$$

The term $n_{f,i}$ represents the ith component of the vector normal to the solid-phase interface (i.e. stem surfaces), pointing into the fluid. The integral term is defined over the sum of all the areas, A_{fs}, of the interfaces between stems and fluid.

A solution to the requirement in Eq. 2.2-31, for the case of $q = t$, was presented by Gray and Lee (1977), which solved the derivatives along the solid-fluid interfaces using the properties of the Dirac delta functions (Kinnmark and Gray, 1984); this solution is known as Reynolds theorem or the *Second Double-Averaging Theorem*.

$$\left\langle \overline{\frac{\partial \theta}{\partial t}} \right\rangle = \left\langle \frac{\partial \overline{\theta}}{\partial t} \right\rangle = \frac{1}{\epsilon_f} \frac{\partial}{\partial t} \epsilon_f \langle \overline{\theta} \rangle + \frac{1}{V_f} \iint_{A_{fs}} \overline{(\overrightarrow{u_{fs}} \cdot \overrightarrow{n_f}) \theta(\vec{x} + \vec{\xi})}\, d\vec{\xi} \qquad \textit{Eq. 2.2-40}$$

The variables of the dot product within the integral term represent the velocity of all points in the solid-fluid phase interface, $\overrightarrow{u_{fs}}$, and the vector normal to the interfaces, $\overrightarrow{n_f}$. Note that the stems are static and impermeable; therefore, the integral term in Eq. 2.2-40 will vanish for the effects of this research. To apply the DA framework for the continuity equation, the modified Reynolds decomposition is used (Nikora *et al.*, 2013) to obtain.

$$\frac{\partial}{\partial x_i} \epsilon_f \langle \overline{u_i} \rangle \;=\; 0 \qquad \textit{Eq. 2.2-41}$$

Similarly, decomposing the instantaneous variables, performing the double averages and applying the theorems to the differential terms in Eq. 2.2-5 yields the Double Average Navier Stokes (DANS) equation (Nikora *et al.*, 2007, 2013).

$$\epsilon_f \frac{\partial}{\partial t}\langle\overline{u_i}\rangle + \epsilon_f\langle\overline{u_j}\rangle\frac{\partial}{\partial x_j}\langle\overline{u_i}\rangle = -\frac{1}{\rho}\frac{\partial}{\partial x_i}\langle\overline{p}\rangle + \frac{\partial}{\partial x_j}\epsilon_f\left(\nu 2\langle\overline{S_{ij}}\rangle - \langle\overline{u_i}''\,\overline{u_j}''\rangle - \left\langle\overline{u_i'u_j'}\right\rangle\right) + \epsilon_f\langle\overline{g_i}\rangle + \left(\frac{1}{\rho}\right)\frac{1}{V}\iint_{A_{fs}} n_{f,i}\overline{p}\,dA - \frac{1}{V}\iint_{A_{fs}} n_{f,j}\nu\overline{S_{ij}}\,dA \qquad \text{Eq. 2.2-42}$$

The three additional terms in the DANS equation (cf. RANS Eq. 2.2-34) describe the hydrodynamic force induced by the presence of stems, and the dispersion of mass in flows through solid elements. The two integral terms for the streamwise component ($x_1 \equiv x$) are the form and viscous drag components, respectively (Tanino and Nepf, 2008a). The terms $\langle\overline{u_i}''\,\overline{u_j}''\rangle$ and $\left\langle\overline{u_i'u_j'}\right\rangle$, are correlations of velocity components along the averaging volume, and represent the net transfer of momentum due to spatial heterogeneity of the flow field and turbulence, respectively. The latter is the spatial average of the Reynolds stresses, and the former have been termed form-induced stresses and dispersive fluxes (Leonard and Luther, 1995; Giménez-Curto and Corniero Lera, 1996). These terms quantify the gradients of velocity that ultimately contribute to the differential displacement of mass particles and therefore of the dispersion coefficient of solutes in flow through vegetation.

2.3. Solute Transport

The previous sections focused on the fundamental concepts of vegetated hydrodynamics, particularly random cylinder arrays. One of the most important challenges in Environmental Fluid Mechanics is to understand how different mechanical processes in water bodies affect the fate and transport of substances (Socolofsky and Jirka, 2002). This section provides an overview of the current state of the art in the study of solute transport.

The spatial and temporal description of the flow field for this section is the same given in section 2.2, that is, a Cartesian frame of reference with the three main directions $\{x, y, z\}$ where x is oriented in the direction of the mean flow, y lies in a plane parallel to the bed and z is oriented upwards, normal to the bed. The quantity of interest in this section is concentration, C, of a passive substance, varying in space and time, $C = C(x, y, z, t)$. Tensor notation and the summation convention are used in this section when necessary.

2.3.1. Solute Transport Equation – ADE

Any solute in a flow field is subject to two main actions: advection and diffusion. The former refers to solute particles (e.g. sediments or pollutants) moving with the same direction and speed as the mean flow. Diffusion is associated with random turbulent motions and local concentration gradients (Socolofsky and Jirka, 2002).

A fixed injection of a passive solute increases its spatial extent with time, while the total mass remains constant. Solutes spread in aqueous media according to Fick's law, which follows the same principles as Fourier's law of heat conduction. This theory states that the flux of solutes along the ith direction, $q_{c,i}$, is proportional to the negative of the concentration gradient,

$$q_{c,i} = -D\frac{\partial C}{\partial x_i} \qquad \textit{Eq. 2.3-1}$$

where D, the proportionality constant, is called the isotropic, molecular *diffusion coefficient*. Eq. 2.3-1 is defined for mass flux in stationary fluid. Extending to the case of a moving flow field, advection and the gradient flux are superimposed (Fischer *et al.*, 1979), leading to the general mass flux,

$$q_{c,i} = u_i C - D\frac{\partial C}{\partial x_i} \qquad \textit{Eq. 2.3-2}$$

From the mass conservation principle applied to a differential element of fluid, using the flux defined in Eq. 2.3-2, the variation in concentration with respect to time and space, in a moving flow field, is obtained in the form of the Advection Diffusion Equation, ADE.

$$\frac{\partial C}{\partial t} + u_i\frac{\partial C}{\partial x_i} = \frac{\partial}{\partial x_i}\left(D\frac{\partial C}{\partial x_i}\right) \qquad \textit{Eq. 2.3-3}$$

The analytical solution of the general ADE (Eq. 2.3-3) requires knowledge of the velocity u_i, for all points in the flow field. This requires the solution of the complex hydrodynamic equations (Eq. 2.2-5). However, it is possible to simplify the general ADE, depending on the specific case study. The simplifications relevant to this research are related to flow through emergent vegetation. First, the flow is predominantly two-dimensional, and the concentration is considered uniformly distributed over the depth ($\partial C/\partial z = 0$). Further, based on the geometry of elements comprising the cylinder array, bed effects are assumed to have negligible effects on large-scale dispersion (Nepf, Mugnier and Zavistoski, 1997; Nepf, 2004). This first set of reductions leads to the following version of the ADE,

$$\frac{\partial C}{\partial t} + u\frac{\partial C}{\partial x} + v\frac{\partial C}{\partial y} = \frac{\partial}{\partial x}\left(D\frac{\partial C}{\partial x}\right) + \frac{\partial}{\partial y}\left(D\frac{\partial C}{\partial y}\right) \qquad \textit{Eq. 2.3-4}$$

Despite the simplification, an analytical solution to Eq. 2.3-4 still requires complete knowledge of u and v. To circumvent the complexity, the instantaneous variables are separated into time- and spatial-averages, together with fluctuations therefrom. In a similar way that such a decomposition generates virtual stresses in the momentum equations, the cross-products between concentration and velocity fluctuations generate directional fluxes. These fluxes represent the effects of turbulence and velocity heterogeneities, and are lumped into new, anisotropic and spatially independent coefficients, D_x and D_y, representing longitudinal and transverse dispersion, respectively. Further, the averaging removes any mean velocity component besides the mean streamwise velocity, $V = 0$ (Socolofsky and Jirka, 2002). The ADE becomes,

$$\frac{\partial C}{\partial t} + U\frac{\partial C}{\partial x} = D_x\frac{\partial^2 C}{\partial x^2} + D_y\frac{\partial^2 C}{\partial y^2} \qquad \textit{Eq. 2.3-5}$$

The consideration of a passive solute involves the additional requirement of a constant mass, independent of time, for pulse injections; and a rate of mass change as an initial condition for Eq. 2.3-4, for the case of continuous injections. The former is applied in this work as the experiments used pulse injections (see Chapter 4). Following these considerations, it is possible to find a 2D routing solution to the ADE equation, as derived by (Baek, Seo and Jeong, 2006).

$$\begin{aligned} C(X_2, y, t) = \int_0^W \int_{-\infty}^{\infty} & \frac{C(X_1, y^*, t^*)U}{4\pi(t_{c2} - t_{c1})\sqrt{D_x D_y}} \exp\left\{-\frac{U^2(t_{c2} - t_{c1} - t + t^*)^2}{4D_x(t_{c2} - t_{c1})}\right\} \\ & \times \exp\left\{-\frac{(y - y^*)^2}{4D_y(t_{c2} - t_{c1})}\right\} dt^* dy^* \end{aligned} \qquad \textit{Eq. 2.3-6}$$

For a routing solution to be valid, knowledge of the concentration profile at a first measurement point, $x^{(1)}$, is necessary. This can vary with respect to y and t. The other parameters needed to estimate concentration at a second point, $x^{(2)}$, are the travel times at the two measurement stations, $\overline{t_1}$ and $\overline{t_2}$, the mean velocity U, and the dispersion coefficients, D_y and D_x. The routing solution presented in Eq. 2.3-6 has two main purposes: first, to predict concentrations downstream from a measured profile, which requires knowledge of D_x, D_y and U. Second, from two known concentration, with separation $\Delta x = x^{(2)} - x^{(1)}$, it is possible to use Eq. 2.3-6 as an objective function to find best-fit estimates of D_x, D_y and U.

2.3.2. Dispersion and Diffusion

The previous section covered the fundamentals of the governing physically-based model for dispersion. Specifically, the simplified solution from which to calculate dispersion parameters, or make predictions. The purpose of this section is to study the physical drivers that define the dispersion coefficients D_x and D_y, their influence on the mixing of tracers in a flow, and the techniques used for their estimation.

The assumption of a reference system moving with velocity U, used to derive Eq. 2.3-6, implies that all points of the solute cloud move with the same speed, and diffuse depending on D_x and D_y. This assumes that molecular diffusion, and the dispersive effects of turbulence and shear are mutually independent, and as such can be lumped together into general *mixing* or *dispersion coefficients* (Fischer *et al.*, 1979). This section will cover the basics of turbulent and shear dispersion, and discuss the limitations of this 'lumped' approach in the quantification of D_x and D_y. It will be seen, that Eq. 2.3-6 is valid only after an initial length scale called the advective zone.

In solute transport, turbulence is treated as a random walk process, with a displacement scale given by the product of turbulent velocity $u'(t)$, and a time step dt. If a fluid particle is followed in a Lagrangian Frame of Reference, with a coordinate system moving with velocity U, the relative distance, X, between the origin of the frame of reference and the position of the particle at a specific time, will be a function of time. This relative displacement analogy was proposed by Taylor (1922) in his "theory of diffusion by continuous movements". From this initial postulate, he concluded that the change in the variance of displacement, $\overline{X^2}$, of particles moving in a turbulent flow is equal to the product of a turbulent velocity scale, defined as the turbulence intensity u^+ (i.e. mean-root-square of the turbulent velocity), and a characteristic length scale, L_X, analogous to the mixing length. The sequence of steps leading to this theory is shown in Eq. 2.3-7.

$$\frac{1}{2}\frac{d}{dt}\overline{X^2} = \overline{u'X} = \overline{u'(t)\int_0^t u'(t-t^*)dt^*} = \int_0^t \overline{u'(t)\,u'(t-t^*)}dt^*$$

$$= \overline{u'^2}\int_0^t \mathcal{R}_x(t^*)dt^* \text{ and if } t \to \infty\text{, then: } \overline{u'^2}\int_0^t \mathcal{R}_x(t^*)dt^* = u^+ L_X \qquad \textit{Eq. 2.3-7}$$

where all the terms in Eq. 2.3-7 represent the turbulence diffusion D_t. Note that the existence of a constant length scale L_X, depends on the integral of the Lagrangian autocorrelation $\mathcal{R}_x(t^*)$ being finite and reaching a constant value as $t \to \infty$. This means that $\mathcal{R}_x(t)$ must tend asymptotically to zero. Both conditions are in general satisfied after an initial time scale $T_X = L_X/u^+$. As said in Section 2.2.2 the larger flow scales of turbulence dominate most of the turbulent diffusion, and parameters L_X and T_X provide approximate values for their characteristic length and time scale.

Figure 2.3-1a shows 4 different instants of a cloud of dye diffusing in a turbulent flow, after a pulse injection. While the cloud of dye is smaller than the largest turbulent scales, it is shaped by the passing random structures, thus yielding different shapes for each experimental realisation. If several such realisations are made, an ensemble dispersive cloud is obtained as shown in Figure 2.3-1b (Fischer *et al.*, 1979).

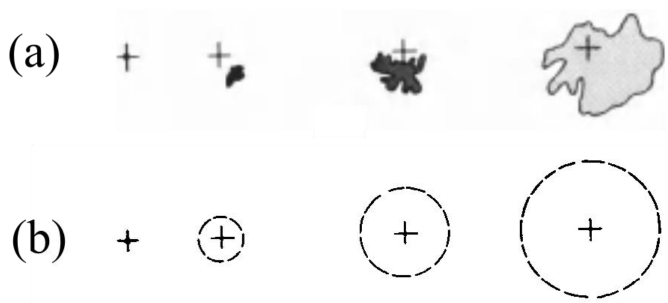

Figure 2.3-1. Effects of large scales of turbulence on diffusion. a) diffusion of a cloud of dye in a turbulent flow field. b) ensemble average of several tracer tests on the same conditions of (a). Reproduced from (Fischer et al., 1979)

Figure 2.3-1a shows that the ensemble cloud is bigger than each individual trace. However, after the cloud is larger than the characteristic length scales it will disperse normally, and the ensemble and each individual realisation will resemble each other closely. Following these considerations, dispersion can be divided into two distinct regimes. An initial regime where the spread of the cloud is dominated by the passing structures, followed by a Fickian regime, where Eq. 2.3-7 is constant and the variance of the cloud grows linearly. It will be shown below that the existence of these regimes is related to an equilibrium between turbulence and shear dispersion, hence giving the name of *advective zone* to the first regime, and *equilibrium zone* to the second one (Rutherford, 1994).

The previous description of turbulent diffusion implicitly requires homogeneity. In reality, the presence of boundaries and obstructions in emergent vegetation, creates a non-uniform mean velocity profile, with lower velocities in the neighbourhood of solid boundaries, and high conveyance regions away from them. Shear is defined by velocity gradients, and particles travelling along streamlines with different mean velocities will increase their relative distance with time.

Consider a particle moving along a streamline in shear flow. Due to molecular and turbulent diffusion, such a particle moves laterally and experiences the velocities at different points in the cross section. Similar to turbulent diffusion, different streamline velocities induces increases in the relative distance between particles (Fischer *et al.*, 1979). If a line source of dye is injected in a flow field with a non-uniform, time-averaged velocity profile (Figure 2.3-2a), the cross-sectional variations of velocity will determine the shape of the cloud (Figure 2.3-2b) and therefore the profile of cross-sectionally averaged concentration (Figure 2.3-2c)

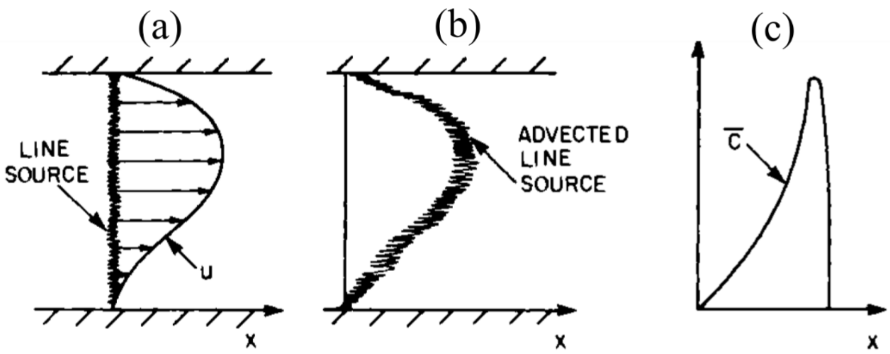

Figure 2.3-2. Graphical representation of the dispersion of mass due to shear dispersion. a) laterally constant line source of dye is injected into a flow field with a cross-sectional velocity profile. b) shape of the injected dye due to the effect of velocity gradients. c) cross-sectional mean concentration profile of dye. Source (Fischer *et al.*, 1979)

If the cross-sectional variations in time-averaged velocity are of comparable magnitude to advection velocity (e.g. laminar pipe flow), care must be taken when applying Eq. 2.3-6, as longer times are required to achieve Gaussian dispersion. For the case of laminar flow in a pipe, (Taylor, 1953) developed a model for shear flow dispersion under the premise of a scale large enough to smooth out lateral variations. To understand his analysis, let us take as a base the general two dimensional ADE given in Eq. 2.3-4 with $V = 0$ and $D_x = D_y = D$. Initially, time-averaged concentration and velocity fields will have cross-sectional variations, meaning that terms U and C can be expressed as a cross-sectional average and a deviation therefrom, i.e. $U = \langle U \rangle_y + U''$ and $C = \langle C \rangle_y + C''$. Also, advection is equal to $\langle U \rangle_y$, which means that all variations multiplied by $\langle U \rangle_y$ in the resulting equation can be neglected. The key assumption is that enough time has passed so that the function C'' is independent of time and space (Rutherford, 1994). After ancillary reductions, Eq. 2.3-8 is obtained.

$$U'' \frac{\partial}{\partial \xi} \langle C \rangle_y = D \frac{\partial^2}{\partial y^2} C'' \qquad \text{Eq. 2.3-8}$$

Where ξ represents the spatial coordinate of the advection direction. Solving Eq. 2.3-8 leads to an expression for the mean mass transfer in the streamwise direction, which is, in simple words, an analogous expression to the gradient flux relationship given in Eq. 2.3-1 but now for the cross-sectionally averaged concentration $\langle C \rangle_y$. If a mass balance of mean longitudinal dispersion is done, a modified form of the ADE is thus obtained

$$\frac{\partial}{\partial \tau} \langle C \rangle_y = D_s \frac{\partial^2}{\partial \xi^2} \langle C \rangle_y \qquad \text{Eq. 2.3-9}$$

Where D_s, is a (virtual) shear dispersion coefficient expressing the proportionality between the mean mass transfer in the streamwise direction, and the gradient of the averaged concentration. τ is obtained from the relation $\partial \xi / U''$. If only laminar flow is considered, D_s will be a function of the relative gradient and the molecular diffusion coefficient as follows

$$D_s = -\frac{1}{h} \int_0^h U'' \int_0^y \frac{1}{D} \int_0^y U''\, dy^* dy^* dy^* \qquad \text{Eq. 2.3-10}$$

Taylor (1954), extended this initial analysis, to turbulent flow in a pipe. After similar developments, the gradient flux relationship was found to be analogous in turbulent flows, with D_s now proportional to a turbulent velocity scale related to the mean turbulent shear, i.e. Kármán shear velocity $u^\times$, and a length scale related to the scale of the turbulent shear flow, e.g. a channel depth or width in case of surface flow.

$$D_s \propto \; L_h u^\times \qquad \text{Eq. 2.3-11}$$

The derivation of shear dispersion is based on Taylor's assumption of mean concentration gradients, in the streamwise direction, being much larger than small cross sectional concentration variations. This implies that after injection, the longitudinal extent of the cloud of dye is larger than L_h. This happens when molecular or turbulent diffusion have completely spread the cloud in the cross-sectional direction (Fischer *et al.*, 1979). Before this asymptotic case, the cloud of dye will develop a 'tail', i.e. skewness as a result of dominant shear, which will grow steadily until cross-sectional mixing and turbulent diffusion equilibrate each other (Rutherford, 1994). Once this condition is reached, the tail will slowly disappear and the cloud profile will resemble a Fickian (normal) diffusion profile.

The existing models for turbulent and shear dispersion are only valid after an equilibrium zone has been reached. This zone is reached once the solute cloud is considerably larger than—and hence unaffected by—turbulent integral scales and cross-sectional velocity gradients. This is manifested as a linear increase in the variance of the concentration profile, and a Fickian behaviour in the limit of very large times since injection (Fischer, 1973). Conversely, the region preceding this Fickian regime will be characterised by random dislocations of the cloud centroid (due to turbulence scales), and a tail proportional to the shear in the cross-sectional velocity profile (due to boundary-induces shear). The effect of these regimes on the variance and skewness (tail) is presented in Figure 2.3-3.

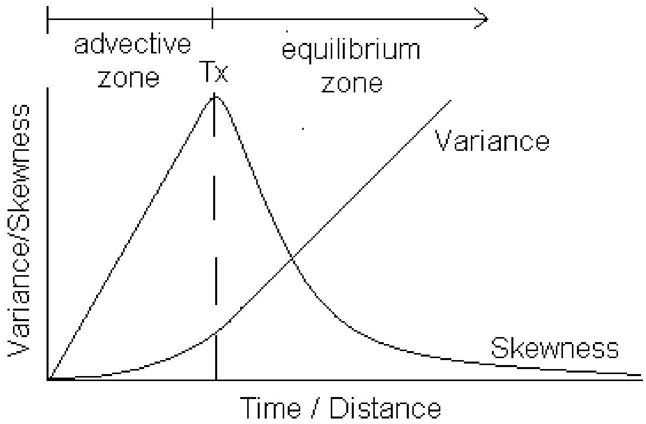

Figure 2.3-3. Effect of the advective and equilibrium zones on the variance and skewness (tail) of a concentration profile. Taken from Shucksmith, Boxall and Guymer (2007), source Rutherford (1994, p. 182).

Considering a real flow with both turbulence and shear components, it is expected that the equilibrium zone is reached after a time scale proportional to the Lagrangian time scale, T_X, determined by Taylor (1922). This time scale is also proportional to the ratio L_X^2/D_t (Fischer, 1967). However, of the handful of experiments and numerical simulations that have been conducted to measure the time scale of the advective zone, a lack of agreement in reported results is found (Shucksmith, Boxall and Guymer, 2007). From the experiments conducted by

(Shucksmith, Boxall and Guymer, 2007), some initial assessments are provided. First, the length of the advective zone seems to increase with discharge; second, the channel width has no bearing on the length of the advective zone. Lastly, the best estimator of the advective length is the skewness of the concentration profile, specifically the peak value indicating the transition to the equilibrium zone. Further, experiments conducted in rivers and laboratory channels report increases in the advective zone length due to sinuosity and cross-sectional variations (Guymer, 1998; Boxall and Guymer, 2007).

2.4. Mixing in Vegetated Flows

This section recapitulates previous concepts, in the context of mixing within emergent vegetation. To avoid confusion, the terms diffusion, dispersion and mixing are distinctly defined. *Diffusion* refers to processes that cause isotropic spreading of a solute. *Dispersion* defines processes that lump the effects of flow and boundary conditions along each direction independently. For instance, mechanical dispersion, is the result of obstructions and flow path tortuosity imposed by stems and causes predominantly lateral dispersion. *Mixing* will be defined as the aggregate effect of processes that contribute to the spread of a substance as a whole (Fischer *et al.*, 1979).

Mixing in vegetation is the result of several interacting processes, making any distinction unmanageable. Nonetheless, experimental evidence suggests that vegetated mixing can be divided into the following main processes: turbulent diffusion, mechanical dispersion, differential advection and trapping, each with a range of associated sub-processes. The existence of different mixing scales along stem wakes induces non-uniform turbulence production, shedding frequency and energy dissipation. In other words, turbulence in vegetated flow is anisotropic and heterogeneous, therefore, a localised difference in turbulence diffusion is expected. Differential advection encompasses dispersion caused by bed shear (Shucksmith, Boxall and Guymer, 2007; Sonnenwald *et al.*, 2017) and stem shear from acceleration and trapping zones (White and Nepf, 2003; Nepf, 2004; Serra, Fernando and Rodríguez, 2004). Trapping is associated with the existence of recirculation cells, boundary layers and dead zones, which, after temporarily capturing mass, release it at a lower rate than the mean flow and therefore contribute to the spreading of the concentration profile (Beer and Young, 1983; Young and Jones, 1991; Sonnenwald, Stovin and Guymer, 2019a).

Although the physics behind each mixing component are not entirely understood, previous studies have shed some light into the relationship between vegetated hydrodynamics and mixing in emergent vegetation. The following sections present the most important results regarding the hydrodynamics of vegetated flows, and their influence on the computation of mixing parameters.

2.4.1. Hydrodynamics of Vegetated Flows

The relevant results, to date, on the study of vegetation hydrodynamics are presented in this section. Shallow open channel flow can be considered as a vertically varying two-dimensional flow (Jirka and Uijttewaal, 2004), and the difference between a vegetated channel and a non-vegetated one lies in the relative difference between bed effects and stem turbulence production. Turbulence intensity increases with vegetation density (Nepf, Mugnier and Zavistoski, 1997; Ricardo, Franca and Ferreira, 2016), and vertical fluxes of momentum increase with stems, although the magnitudes of the transfer are still negligible (Ricardo, Franca and Ferreira, 2016). These two effects, mean that the vertical profile of mean velocity, $U(z)$, will become constant, away from the reduced bed boundary layer (Nepf, Sullivan and Zavitoski, 1997). Therefore, mean vertical shear ($dU/dz \approx 0$) is negligible within emergent vegetation. The most prominent results of the study of vegetated hydrodynamics are given in the same order as the concepts were presented in section 2.2, for consistency.

2.4.1.1. Mean quantities in vegetated flows

Vegetated flows present a strong horizontal heterogeneity which leads to differential advection. The term differential advection refers to the long term spatial variations of the velocity field, i.e. heterogeneities in the mean velocity maps. These variations are connected to the appearance of recirculation areas and therefore of trapping zones (Beer and Young, 1983). The spatial extent of these heterogeneities will consequently be proportional to the rate of spread of the concentration profile of a solute (Taylor, 1953). Mixing is proportional to both differential advection and mean shear, which are also proportional to one another (Rutherford, 1994). Figure 2.4-1 shows two examples of flow heterogeneities related to differential advection in vegetated flows, the velocity-defect behind stems is compensated by local acceleration zones between stems.

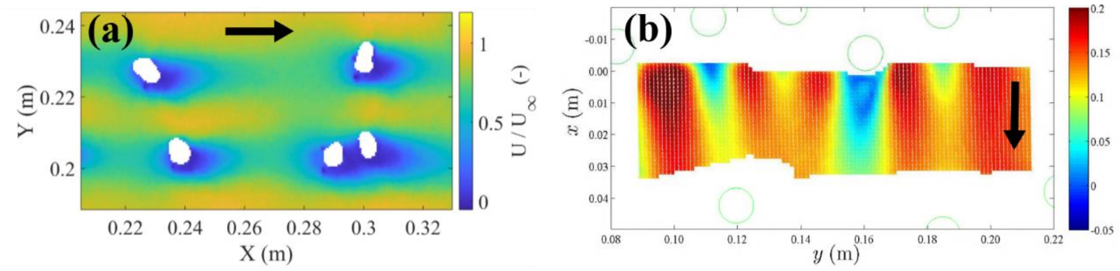

Figure 2.4-1 Flow visualization of differential advection. a) map of mean longitudinal velocity using Surface PIV (Corredor-Garcia et al., 2020); b) time-averaged longitudinal velocity map for a section of flow at mid-depth, using conventional PIV (Ricardo, 2014). Black arrows indicate the direction of flow.

Several studies have quantified the vertical variation of the mean flow features. For artificial emergent vegetation, (Nepf, Mugnier and Zavistoski, 1997) measured the relationship between U, W and distance downstream from the stem. These measurements were complemented by Ricardo, Franca and Ferreira (2016) and (Ricardo, 2014) for the double-averaged (DA) quantities. The effect of the recirculation zone can be seen in Figure 2.4-2c for the points marked with $\times$ symbols. Figure 2.4-2a shows a DA plot of $U(z)$, where the effect of the bed boundary layer is seen to be confined to a lower vertical extent for vegetated flows than for open channels. The profiles are vertically constant for the region dominated by stems. In the case of mean vertical velocity $W(z)$, shown in Figure 2.4-2b, the profile with the increase close to the bed reflects a low density configuration; for closely packed stems, the energy of the mean velocity is quickly transferred to turbulent motions and the vertical component of velocity is quickly damped, as shown for the other plots with a relatively flat distribution of $w(z)$.

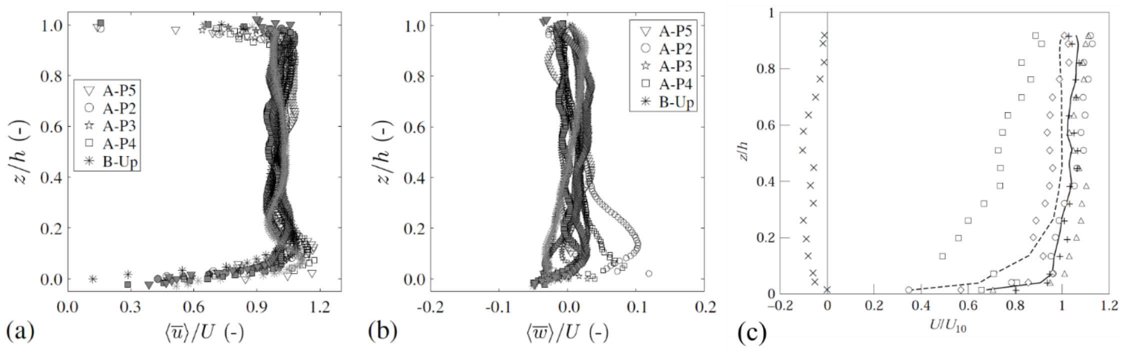

Figure 2.4-2 Vertical profiles of mean velocities for artificial vegetation. a) double averaged (time and area) longitudinal velocity as a function of vegetation density (Ricardo, Franca and Ferreira, 2016). b) double-averaged (time and area) profile of vertical velocity as a function of vegetation density (Ricardo, Franca and Ferreira, 2016)*. c) Vertical profiles of mean longitudinal velocity as a function of normalised distance downstream, $x^* = x/d$,* ($\times$) *0.5,* ($\square$) *3,* ($\diamond$) *11,* ($+$) *26,* (Δ) *34,* (O) *42* (Nepf, Mugnier and Zavistoski, 1997).

Care must be exercised when interpreting results from artificial vegetation (e.g. Figure 2.4-2), as real vegetation has a richer morphology and thus additional sources of resistance. Figure 2.4-3 shows vertical profiles of mean longitudinal velocity for real vegetation, specifically for winter *Typha* at several points within the same array (Figure 2.4-3a; West, 2016), salt marsh vegetation with vertical variation in frontal-facing area per unit volume, and therefore drag (Figure 2.4-3b; Lightbody and Nepf, 2006) and *Carex* and Reeds, for different growing stages (Figure 2.4-3c; Shucksmith, Boxall and Guymer, 2010). At a first glance, all profiles shown in Figure 2.4-3 show a considerably larger spread than the profiles shown in Figure 2.4-2a; these variations imply a larger resistance compared with artificial vegetation and a different turbulence regime.

Figure 2.4-3a and Figure 2.4-3b show that, although there is a large spread between the velocity profiles taken at different points, the general shape of the velocity curve is similar. This reinforces the idea of emergent vegetation being vertically uniform, and therefore, able to be modelled using a 2D approximation.

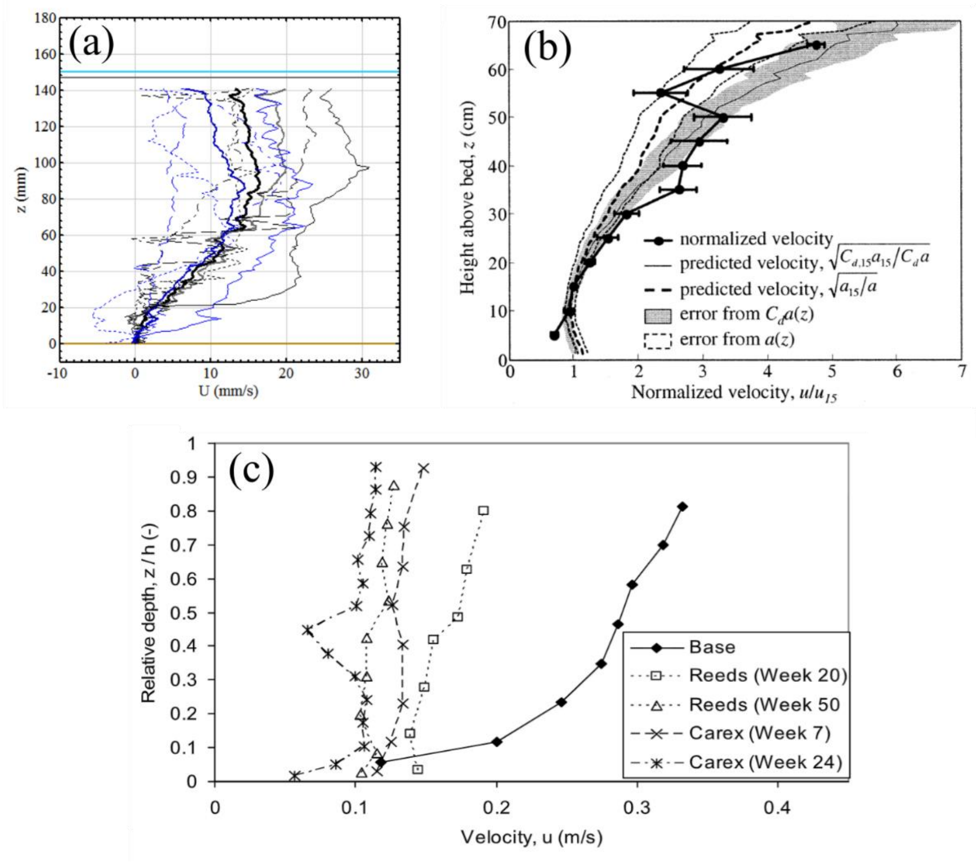

Figure 2.4-3 Vertical profiles of mean longitudinal velocity a) profiles of U(z) and ensemble average for different stems (West, 2016) b) vertical variation in mean longitudinal velocity as a function of vertical variation in frontal-facing area (Lightbody and Nepf, 2006b) *c) vertical variation in mean longitudinal velocity as a function of age, increase of resistance with age* (Shucksmith, Boxall and Guymer, 2010).

Artificial vegetation is usually represented as arrays of cylinders with a single diameter, which clearly unifies the response with respect to recirculation zone size (White and Nepf, 2003), wake width and shape of the velocity profile. It should be noted that variations in season, age and local density (i.e. clustering) generate a distribution of stems of different diameters (Sonnenwald *et al.*, 2017) which can explain the variance in the ensemble average of profiles shown (e.g. Figure 2.4-3a). This variation in stem diameter, which redefines the dominant length scale of the vegetation has, to the author's knowledge, been consistently overlooked.

2.4.1.2. Turbulence and coherent structures in vegetated flows

Turbulence is generated primarily at the stem scale, due to wake effects, which overshadows turbulent effects from the bed (Nepf, 1999). For cylinders as a proxy for stems, a clear increase in turbulence production, quantified as turbulent intensities u^+, v^+, with respect to vegetation density, has been consistently registered in the literature (Nepf, Mugnier and Zavistoski, 1997; Nepf, 1999; Ricardo, Franca and Ferreira, 2016). Figure 2.4-4 shows a subset of experimental normalised turbulence intensities for the longitudinal (Figure 2.4-4a) and vertical (Figure 2.4-4b) components of velocity; and vertical turbulence stresses (Figure 2.4-4c).

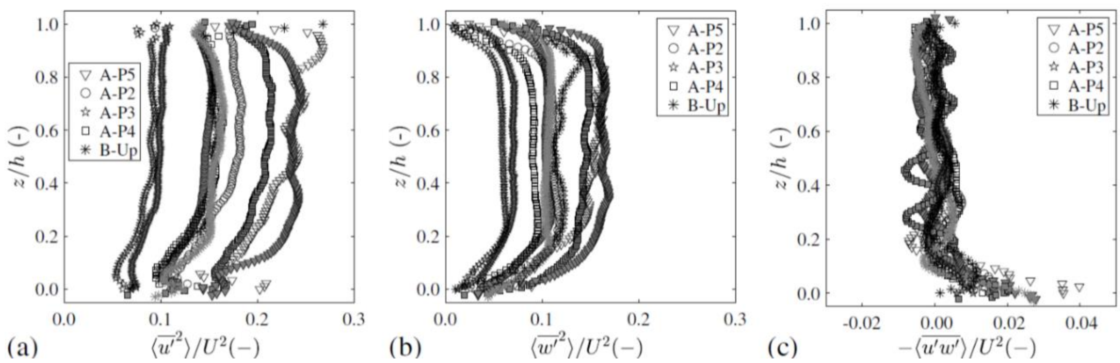

Figure 2.4-4 Vertical profiles of turbulence production a) turbulence intensity of the longitudinal component of velocity. b) turbulence intensity of the vertical component of velocity and c) space averaged Reynolds stresses between the longitudinal and vertical directions (source Ricardo, Franca and Ferreira, 2016*).*

The changes in magnitude for the profiles shown in Figure 2.4-4 correspond to different local stem densities. Sparser distributions tend to show the highest magnitudes, while the profile shapes are approximately constant. This means that a singular type of turbulence production regime is obtained for different local stem densities, and profiles only scale depending on mean distance between stems. However, these conclusions cannot be extrapolated to the case of varying distributions of diameter. Figure 2.4-4c shows that vertical momentum transfers due to turbulence are confined to the bed: $\left\langle \overline{u_i' u_j'} \right\rangle \approx 0$, for most z.

Mean flow heterogeneities are quantified via spatial and double averaging frameworks (Raupach and Shaw, 1982; Finnigan, 2000; Nikora *et al.*, 2007, 2013), and the effects of differential advection are transformed into virtual stresses in the same way that temporal fluctuations are transformed into turbulent stresses in the Reynolds decomposition. These new virtual stresses are associated with spatial fluxes of momentum and mass due to flow heterogeneities, or differential advection, and are named form-induced stresses (Giménez-Curto and Corniero Lera, 1996).

Few studies have quantified the extent of form-induced stress in emergent vegetation. They reveal that the fluxes of momentum always increase when compared to non-vegetated conditions. Ricardo, Franca and Ferreira (2016) measured form-induced stresses for a configuration with local changes in stem density. It was shown that vertical diffusion of vertical momentum is concentrated near the bed (Figure 2.4-5b), similar to vertical diffusion of longitudinal momentum (Figure 2.4-5c) due to flow heterogeneities. Conversely, the diffusion of longitudinal momentum due to differential advection is vertically constant. Different local densities generate different profiles in terms of shape and magnitude, suggesting that even for single-diameter arrays, the advection regime changes due to transport effects of large scale motions (Ricardo, Franca and Ferreira, 2016). A consequence of this is that a wider range of flow scales can result from stem interactions, which would tend to expand for arrays with non-uniform stem diameter distributions.

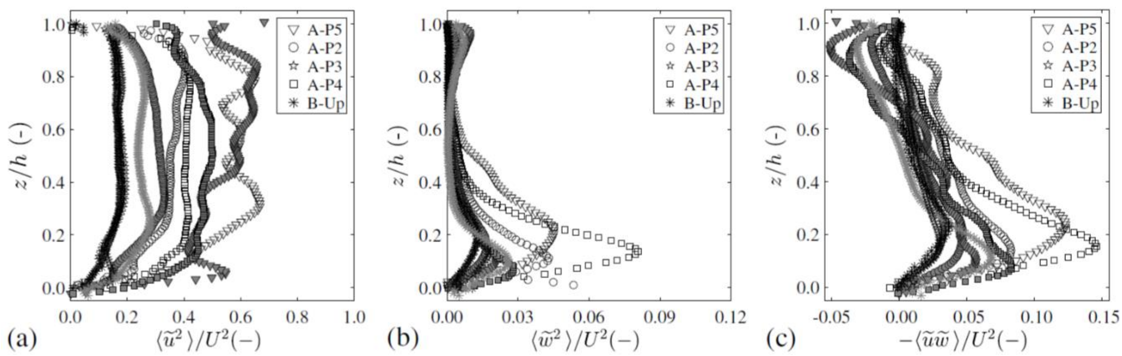

Figure 2.4-5 Vertical profiles of dispersive fluxes due to spatial heterogeneity a) form-induced stresses in the longitudinal component of velocity. b) form-induced stresses of the vertical component of velocity and c) Spatial fluxes in the vertical plane due to flow heterogeneity between the longitudinal and vertical components of velocity (source Ricardo, Franca and Ferreira, 2016)

Double-averaged Reynolds stresses depend on the local averages of the stem density m. This local adjustment suggests that turbulent stresses are independent of changes in stem density or solid volume fraction, i.e. dm/dx. Form-induced stresses were found to always increase for non-constant distributions of stems, i.e. $dm/dx \neq 0$. This reveals that flow structures are not broken down immediately after formation, regardless of local vegetation density downstream (Ricardo, 2014; Ricardo, Franca and Ferreira, 2016). These changes in spatial fluxes are caused by the additional turbulence conditions caused by wake interactions, as opposed to when a stem is isolated (Raupach, 1992; Sumner, 2010; Zhou and Mahbub Alam, 2016).

Another important component in the description of vegetated turbulence is the generation and evolution of vortex motion. Knowing that background turbulence, shear and differential advection can affect the already complex vorticity regime of a cylinder (Kiya, Tamura and Arie, 1980; Williamson, 1996a), experimental studies can help elucidate the dependency of the vortex motions on vegetation morphology. Stoesser, Kim and Diplas (2010) conducted a series of numerical experiments using Large Eddy Simulation, and found that the shedding regime of the cylinders was still largely two-dimensional, despite the interference of upstream effects. However, regular arrays were modelled, which limits the extensibility of the results to random arrays. Figure 2.4-6 shows two instantaneous streamline maps, from a PIV (Particle Image Velocimetry) visualization of the velocity field, within random cylinder array (Ricardo, 2014; Ricardo, Sanches and Ferreira, 2016). The streamlines show that the scales of vortices detached are influenced by background turbulence. Also, that depending on the modulation of the background turbulence, the vorticity of the shed vortices can either be increased or decreased, in the latter case meaning that the life span of vortices will be shorter (Ricardo, Sanches and Ferreira, 2016).

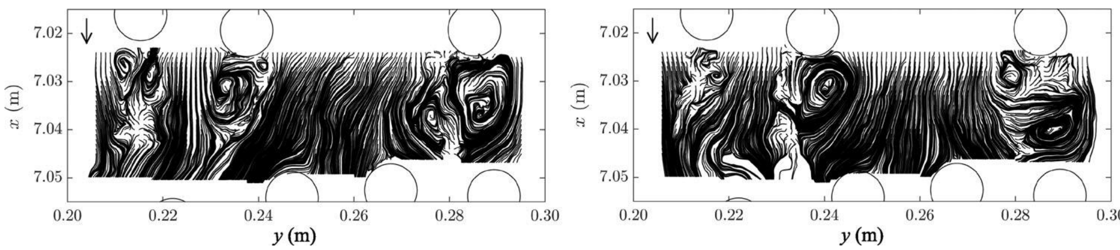

Figure 2.4-6 Instantaneous maps of stream lines indicating the change with time of the modes of rotation (Ricardo, Sanches and Ferreira, 2016)

The life span of vortices is determined by their coherence, and energy input. Although background turbulence can effectively increase the shedding rate of vortices by precipitating a laminar-turbulent transition in the recirculation zone (Roshko, 1954), this does not guarantee an increase of diffusion due to vorticity further downstream. However, it is the author's belief that, since shed vortices are still the main carriers of turbulent kinetic energy (Ricardo, Koll, *et al.*, 2014), a localised increase in diffusion will occur when a vortex encounters a stem downstream, and the spread of matter owing to this mechanism can be quantitatively more significant than the customary definition of mechanical dispersion.

2.4.1.3. Energy considerations in vegetated flows

Much of the energy considerations of turbulence due to rigid obstructions has been done in the study of atmospheric, canopy flow (Raupach and Shaw, 1982; Raupach, Antonia and Rajagopalan, 1991; Finnigan, 2000). Although the scale of the problem is different, the principles of energy transfer across different scales remains the same. (Raupach, Finnigan and Brunet, 1996) presents a turbulent kinetic energy (TKE) budget, from an early application of the double averaging methodology.

$$\frac{\partial E'}{\partial t} = P_s + P_w + P_b + T_t + T_p - \langle \varepsilon \rangle = 0 \qquad \textit{Eq. 2.4-1}$$

The terms being summed are, from left to right: P_s, shear production; P_w, wake production; P_b, buoyant production; T_t, turbulent transport; T_p, pressure transport; and $\langle \varepsilon \rangle$, dissipation. Of all these terms, only P_w has been related to the production of energy at the stem scale. P_s is neglected because it is linked to the shear layer developed above the canopy layer, a case excluded from emergent vegetation. Nonetheless, turbulent transport and shear production are still expected to be present in some form within vegetative flow (Raupach, Finnigan and Brunet, 1996).

The assumption of steady flow implies that energy transfer and therefore dissipation do not change with time (Raupach, Antonia and Rajagopalan, 1991). The empirical relations underpinning Eq. 2.4-1, were derived from velocity measurements within and above terrestrial canopies (Raupach, Antonia and Rajagopalan, 1991; Kaimal and Finnigan, 1994; Raupach, Finnigan and Brunet, 1996). It is possible to extrapolate the conclusions from these studies to cases of flow through emergent (and submerged) riparian vegetation. Figure 2.4-7 shows the vertical variation of the components of Eq. 2.4-1, for atmospheric flow. Within the vegetation, $z/h_c < 1$, wake production is a dominant production term, alongside turbulent transport. For vegetated flows, a similarity exists between the vertical dispersive flux measured by (Ricardo, Franca and Ferreira, 2016), shown in Figure 2.4-5c; and that measured in canopy flow, Figure 2.4-7, In both cases, the objective of turbulent transport seems to connect bed-generated and stem-scale turbulence production.

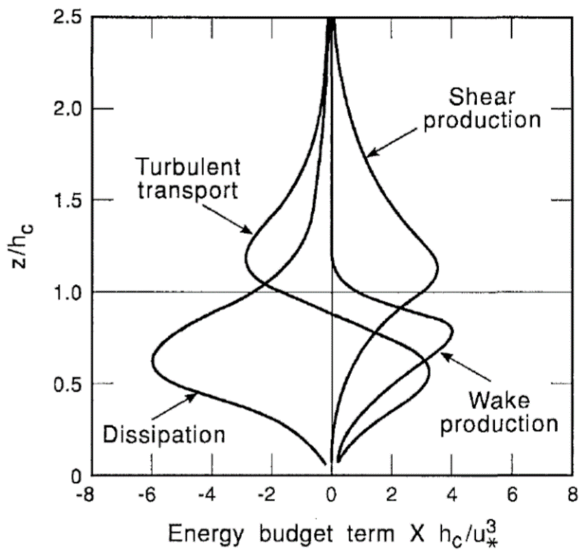

Figure 2.4-7. Vertical variation of the energy budget constituents, from velocity measurements in canopy flow. Source Kaimal and Finnigan (1994).

Nepf (1999) presented a model for isotropic turbulent diffusion, based on the equilibrium between turbulence production due to stem drag, and direct viscous dissipation. However, for low and moderate Reynolds numbers ($Re_d < 200$), viscous drag will also dissipate a portion of energy at the stem level, without the transition to turbulence (Nikora, 2000). At higher Reynolds numbers this equilibrium is still undetermined, since the universal equilibrium assumed by Nepf (1999), depends on Kolmogorov (1941a) assumption of local isotropy and homogeneity; conditions that, are unconfirmed for vegetated flows. Energy schemes like Figure 2.4-7 tend to corroborate (Ferreira, Ricardo and Franca, 2009) assertion that turbulent transport (dispersive fluxes) are of a similar order of magnitude to wake production, and are in consequence not negligible.

From Strouhal number, S_t, measurements in stem wakes, turbulent kinetic energy is concentrated in the vortex street (Raupach, Finnigan and Brunet, 1996; Ricardo, Sanches and Ferreira, 2016); as peaks are always found close to the end of the recirculation region. The downstream evolution of this spectral behaviour can inform vorticity dissipation along the wake, and therefore, the amount of energy that is transferred to the generation of smaller structures or direct viscous dissipation. These effects have not, to the author's knowledge, been explored, further results of the energy spectra from velocity statistics along the wake are needed.

2.4.1.4. Drag and shear in vegetated flows

Most measurements of drag coefficients are based on a large-scale momentum balance on canopy flow. This equilibrium includes: the effect of gravity, viscous stresses, dispersive fluxes, and mean drag force (Raupach and Thom, 1981; Finnigan, 2000). Depending on the Re_d regime, different terms will be dominant.

The drag coefficient, C_D, is mainly dependent on Re_d. Tanino and Nepf (2008a) developed a model for the individual and array drag as a function of the DA momentum equation and the effect of stem spacing. The dependency of C_D on Re_d, for artificial vegetation is reproduced in Figure 2.4-8a. For comparison, Figure 2.4-8b shows non-dimensional bulk force drag per unit leaf area, as a function of velocity, for different species of emergent riparian vegetation (Aberle and Järvelä, 2013). Quantifying bulk drag using particular features of the natural vegetation, such as leaf and plant area, has proven successful to estimate/model flow resistance models in fluvial systems (Jalonen and Järvelä, 2014). However, this bulk characterisation for natural vegetation, though useful for large scale systems, provides no insight into small-scale processes. This limits the scalability and reproducibility of results, such that different relations must be derived for seasonal variations, different growing patterns, etc.

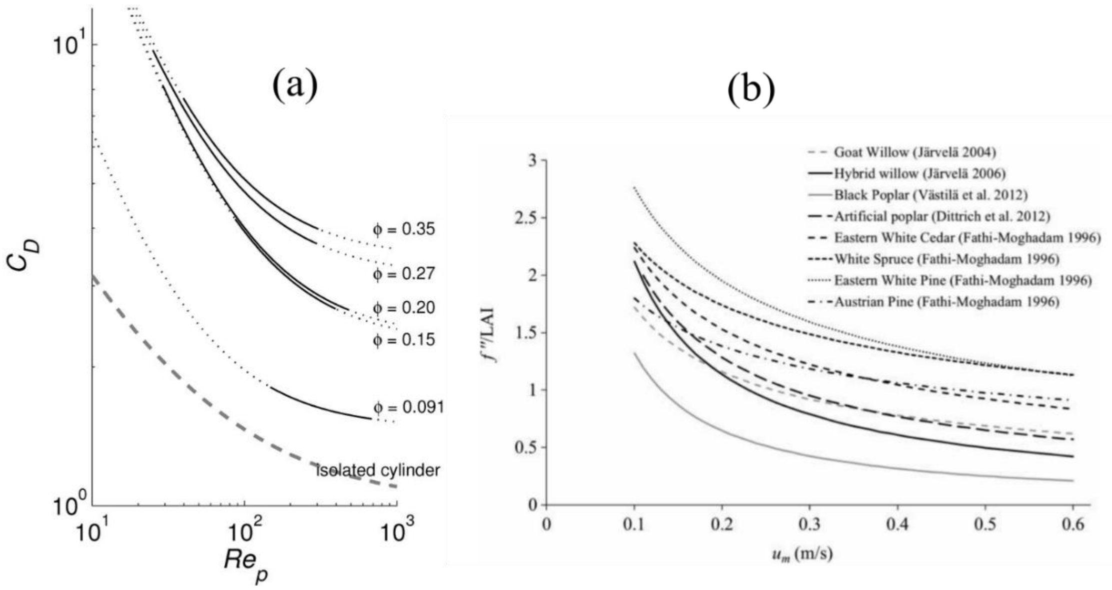

Figure 2.4-8 a) Results of experimental investigations on the dependency on solid volume fraction (stem density) of the array drag coefficient for artificial emergent vegetation (Tanino and Nepf, 2008a). b) Experimental results for the drag force (per unit leaf area) as a function of velocity, for different natural species (Aberle and Järvelä, 2013)

Evidently, the variation of non-dimensional drag with Reynolds number scales in a similar way. This indicates that a general expression for drag is scalable for different vegetation species. Indeed, following experimental datasets and models developed by Tanino and Nepf (2008a);

Ferreira, Ricardo and Franca (2009; Tinoco and Cowen (2013); A.M. Ricardo *et al.* (2014), for the quantification of array drag coefficient, Sonnenwald, Stovin and Guymer (2019b) included the effect of direct viscous dissipation as a linear dependency on solid volume fraction, φ, and obtained the expression for $\overline{C_D}$ following a re-parameterisation of Ergun (1952) initial expression

$$\overline{C_D} = 2\left(\frac{6475d + 32}{Re} + 17d + 3.2\varphi + 0.5\right) \qquad \textit{Eq. 2.4-2}$$

The results shown in Figure 2.4-8a, were obtained from a series of experiments with solid volume fractions, φ, between 0 and 0.4; and Re_d, between 1 and 700, conducted by (Tanino and Nepf, 2008a). Although an inverse proportionality is found between C_D and Re_d, the actual drag force per unit vertical length, F_D, is expected to increase with the same parameter. Increases in φ will induce increments in both F_D and C_D; this proportionality ($C_D \propto \varphi$) is expected to change at $Re_d \geq 1000$ according to Nepf (1999). To date, Tanino and Nepf (2008a) study presents the most relevant characterisation of drag for random emergent artificial vegetation. Their model neglects stresses appearing in the DANS equation and reduces the force balance to an equilibrium between hydrostatic pressure and drag force. As indicated by Ferreira, Ricardo and Franca (2009); A. M. Ricardo *et al.* (2014); and Ricardo (2014) (and suggested in Figure 2.4-7), form-induced stresses are not always negligible in random vegetation stands. Dispersive fluxes and other momentum-generating variables can be relevant in some cases. These studies also found drag force to be independent of stem arrangement, although 'patchiness' was found to have an effect on C_D, i.e. localised values of drag induced by longitudinal variation in solid volume fraction. The distribution of drag at the stem scale, and the effects of stem layout on flow resistance need to be explored further.

2.4.2. Solute Transport in Vegetated Flows

Current understanding of mixing in emergent vegetation describes dispersion to be direction-dependent. The ADE then considers the three main components of flow: D_x, D_y and D_z. Since all flows are herein analysed under the 2D hypothesis (see Section 2.4.1), all solutes are considered to be vertically well mixed in flow descriptions. The ADE can be fully described using a 2D framework.

Mixing also depends on geometry and morphology, which are the physical parameters (boundary conditions) of the vegetation. These parameters affect mixing through stem wakes, boundary layers and their interaction with the mean flow (Nepf, 1999). In consequence, each dispersion/diffusion coefficient is related to a set of hydrodynamic processes. Below is a discussion of the features of each particular component of mixing.

Molecular diffusion, D, describes the effect of mixing of a solute in static aqueous media. For fluid flow, D is several orders of magnitude smaller than other process and is therefore negligible.

2.4.2.1.Turbulent diffusion $\boldsymbol{D_t}$

Even for low Reynolds numbers ($Re_d < 40$), a transition and boundary layer separation occurs at the bed, which interacts with the mean flow and generate velocity fluctuations that diffuse mass more efficiently than molecular diffusion.

For larger Reynolds numbers, turbulence is generated at the stem wake scale. Following Prandtl's mixing length analogy, diffusive lengths are proposed to scale linearly with the 'level of turbulence'. The characteristic Lagrangian length scale of turbulence is usually d for vegetated flows (Nepf, Sullivan and Zavitoski, 1997). Integrating Kolmogorov's hypotheses with the mixing length analogy, Nepf (1999) arrived at the following expression for the non-dimensional turbulent diffusion

$$\frac{D_t}{Ud} \propto (C_d a d)^{1/3} = \frac{\sqrt{k}}{U} \qquad \textit{Eq. 2.4-3}$$

Measurements of ensemble concentration profiles showed that the stem diameter (d) can be considered as a relevant mixing scale (Nepf, Mugnier and Zavistoski, 1997; Nepf and Vivoni, 2000). As shown in Section 2.4.1, array drag and background turbulence can induce a variation in shedding frequency and consequently, length scales. Moreover, if an array with varying stem diameters is used to describe the natural variations in vegetation condition and age (Shucksmith, Boxall and Guymer, 2010; Sonnenwald *et al.*, 2017), the assumption of a unique length scale and the validity of the mixing length analogy come into question. Even when considering single diameter arrays, the assumption of a mixing length equal to stem diameter depends on spacing as stem interactions can change the size and frequency of shed vortices (Sumner, 2010).

The sole contribution from drag to turbulent diffusion, as presented in Eq. 2.4-3, results from an equilibrium between turbulence production (from stem wakes), and dissipation. This is equivalent to reducing Eq. 2.4-1 to the expression $P_w \approx \langle \varepsilon \rangle$. According to (Tennekes and

Lumley, 1972), the term $\langle \varepsilon \rangle$ scales as $\langle \varepsilon \rangle \sim u_t^3/\ell_t$, where u_t and ℓ_t are relevant turbulent velocity and length scales respectively. Both Nepf (1999) and (Tanino and Nepf, 2008b) consider the velocity scale u_t to be represented by the mean turbulent kinetic energy, k. However, it should be noted that the relation $\langle \varepsilon \rangle \sim u_t^3$ was proposed by Taylor (1935), and was conceived under the condition of isotropic turbulence; which has not, to the author's knowledge, been proven for vegetated flow.

2.4.2.2. Longitudinal Dispersion $\boldsymbol{D_x}$

This section will treat the coefficients that characterise the entirety of Longitudinal Dispersion, as described by White and Nepf (2003), and shown in Eq. 2.4-4. It should be noted that the linear superposition of the terms given in Eq. 2.4-4 presumes independence between underlying physical mechanisms. The decomposition presented in Eq. 2.4-4 is empirically based, and a rigorous derivation from first principles is still required.

$$D_x = D + D_t + D_{x,v} + D_{x,s} + D_{x,g} + D_{BL} \qquad \textit{Eq. 2.4-4}$$

Where

D: Molecular Diffusion

D_t: Turbulent Diffusion

$D_{x,v}$: Vortex trapping Dispersion

$D_{x,s}$: Secondary wake Dispersion

$D_{x,g}$: Dispersion caused by advective acceleration in the gaps between stems

D_{BL}: Dispersion caused by trapping in Laminar Boundary Layers.

The term $D_{x,g}$ represents the increase in velocity between stems to compensate for the decrease of mean velocity behind stems. Velocity fluctuations in these regions are assumed small compared to those in the actual wakes, rendering $D_{x,g}$ negligible (White and Nepf, 2003).

The tem D_{BL} corresponds to 'Boundary Layer Dispersion', as presented by Koch and Brady (1985), which makes reference to the dispersion generated by mass being trapped in the boundary layers of solid surfaces. Both the small spatial extent of stem boundary layers and the large time scales of trapping make this term negligible (White and Nepf, 2003).

We are left with the following terms defining Longitudinal dispersion.

$$D_x = D + D_t + D_{x,v} + D_{x,s} \qquad \textit{Eq. 2.4-5}$$

The following discussion will focus on obtaining each of the directional components of D_x.

2.4.2.3. Vortex trapping Dispersion $\boldsymbol{D_{x,v}}$

Vortex trapping dispersion refers to the variance in the concentration distribution induced by the alternation trapping and release of mass from primary wakes (cf. recirculation region). The contribution from $D_{x,v}$ depends on two factors: **i)** the number of times a particle is trapped within a primary wake and **ii)** the time each particle remains within this zone. Overall, $D_{x,v}$ is directly proportional to both. This can be expressed by the expression

$$D_{x,v} \propto \epsilon_w {U_\infty}^2 \bar{\tau} \qquad \textit{Eq. 2.4-6}$$

The rationale behind Eq. 2.4-6 is that the probability of trapping is equal to the proportion of the flow field occupied by primary wakes, ϵ_w. Also, the mean residence/trapping time, $\bar{\tau}$, is inversely proportional to f_s, the shedding frequency, which can be expressed in non-dimensional terms as the Strouhal number, S_t, yielding

$$D_{x,v} \propto \frac{\epsilon_w U_\infty d}{S_t} \qquad \textit{Eq. 2.4-7}$$

The Strouhal number, S_t, is defined as the ratio of f_s and the product of relevant length and velocity scales, that is, $St = f_s / U_\infty d$ (Tennekes and Lumley, 1972). Applying this to Eq. 2.4-7 the following expression for the vortex trapping dispersion is obtained

$$D_{x,v} \propto \frac{\epsilon_w U_\infty d}{St} \qquad \textit{Eq. 2.4-8}$$

2.4.2.4. Secondary wake Dispersion $\boldsymbol{D_{x,s}}$

White and Nepf (2003) derived the general expression given in Eq. 2.4-9 from the added effects of turbulence motions and reduced mean velocity behind stems (outside of the primary wake).

$$D_{x,s} = 2\sigma_w^{*2} s^* \sqrt{\frac{Sc_t}{Sc_t + 1}}\, Ud \qquad \textit{Eq. 2.4-9}$$

Where the term σ_w^{*2} is the non-dimensional variance of secondary wake velocity $\sigma_w^{*2} = \sigma_w^2/U^2$; s^* is the mean separation of stems in the longitudinal direction divided by the stem diameter $s^* = s/d$ and Sc_t is the turbulent Schmidt number which defines the ratio between eddy/turbulent viscosity and turbulent diffusion: $Sc_t = \nu_t/D_t$. A discussion on the derivation of Eq. 2.4-9 is given in Chapter 3.

2.4.2.5. Relevant results

Longitudinal dispersion is proportional to shear velocity (Nepf et al, 1997a; Elder 1959), which can be vertical (i.e. caused by bed effects) and horizontal due to differential advection. (Lightbody and Nepf, 2006; Lightbody and Nepf, 2006) presented an equation for the vertical profile of longitudinal velocity as a function of the vertical variation in canopy area, represented as $C_D a(z)$, (see Figure 2.4-3b). The model was based on Mauri and Haber (1986), solution to the triple integral given by Fischer *et al.* (1979), (see Eq. 2.3-10). Vertical changes in frontal facing area, $a(z)$, and the gradient dU/dz, were seen to generate higher shear, and therefore higher vertical dispersion.

Figure 2.4-3 shows natural vegetation to have a consistent vertical velocity profile and hence shear. From this it can be concluded that variations in the horizontal distribution of stems do not affect vertical shear, so its effects can be 'lumped' into the D_x coefficient. By aggregating vertical effects into D_x, emergent vegetation can be reliably modelled as a 2D system (Lightbody and Nepf, 2006).

Huang *et al.* (2008) studied mixing in emergent Everglade, using tracer particle injections (1 μm latex microspheres), for different types of salt marsh vegetation and different vegetation densities. The experimental results were compared with estimations using Lightbody and Nepf (2006) model, assuming a linear $U(z)$, and the wake zone formulation presented in White and Nepf (2003), and Nepf (2004). A relatively constant value of D_x with depth was registered; which supports the assumption of vegetated flows as 2D systems. However, the modelled longitudinal dispersion coefficient, D_x, was found in some cases almost an order of magnitude smaller than the actual measurement. This difference was attributed to flow heterogeneity caused by plant morphology, and the existence of physical processes still unreported in the current artificial vegetation models.

Shucksmith, Boxall and Guymer (2010) studied the effects of growth (in controlled conditions) and age of natural emergent vegetation on flow resistance, turbulence and longitudinal dispersion. Shear velocity was found to be directly, and D_x inversely, proportional to plant age.

The species used in this study were *Phragmites australis* (Reeds), and *Carex*, and it was found that the former, being more rigid and less 'leafy', presented a smaller variation of the transverse flow profile, and higher longitudinal dispersion than the latter, which was denser and more flexible. Age was also found to be inversely proportional to D_x for Reeds. No trend was found for *Carex*. Turbulence production was found to increase in the transverse direction, and decrease in the vertical one, as previously found by Nepf, Sullivan and Zavitoski (1997) and Nepf (1999), which is a consequence of turbulence being mainly produced at the stem wakes rather than at the channel bed (Leonard and Luther, 1995).

Shear is commonly associated with the formation of vortices; mass and momentum transport; and the shape and magnitude of the $U(z)$ profile; only in the exchange zone between vegetated and non-vegetated zones (Ghisalberti and Nepf, 2004, 2009; White, 2006; Nepf *et al.*, 2007; Nepf, 2012). However, it is important to note that differential advection, represented as secondary wake, $D_{x,s}$, and gap, $D_{x,g}$, dispersion is also connected to the appearance of horizontal velocity shear. A clear need for experimental results of differential advection exists, which could clarify the role of shear and gap acceleration on dispersion.

Previous measurements of D_x in artificial vegetation and natural species, as a function of vegetation density, φ, were compiled by Sonnenwald *et al.* (2017) and reproduced in Figure 2.4-9. For artificial vegetation (AV), a dependence of normalised D_x on vegetation density (φ) cannot be identified. Following the argument presented in Sonnenwald *et al.* (2017), it is possible that φ is not a robust parameter to characterise vegetation morphology. Two arrays with the same density can have radically different distributions of stem spacing and diameters, and hence distinct flow field configurations leading to different regimes of solute transport.

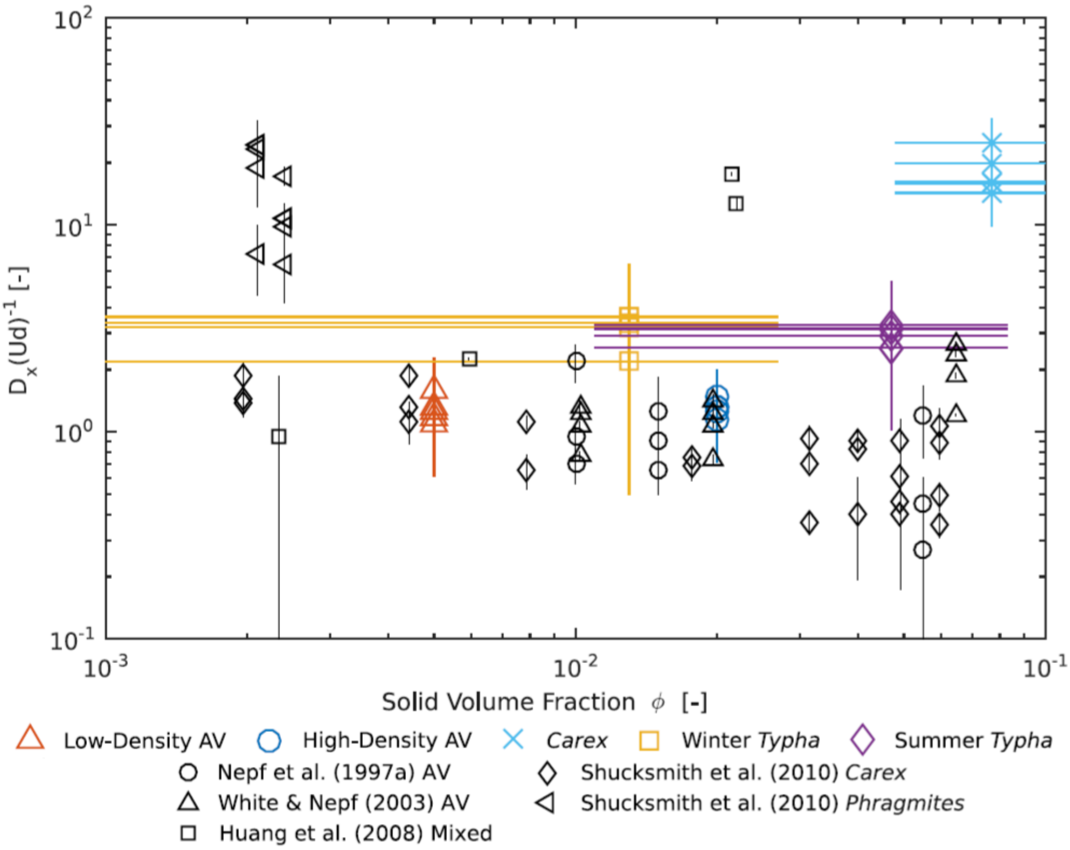

Figure 2.4-9 Comparison between the results of physical models given in the literature, for the computation of: a) vortex trapping, and b) secondary wake dispersion components, of the longitudinal dispersion coefficient D_x. Source Sonnenwald et al. (2017)

In general, the presence of stems reduces D_x^*, when compared to non-vegetated conditions, and increasing φ causes a consistent decrease in streamwise dispersion. The steps to this conclusion can be summarised as follows: stems increase turbulence at the stem scale, and overshadow bed-generated turbulence; this makes the vertical, mean velocity more uniform (see Figure 2.4-4). Also, higher turbulence along stem axes better distributes mass vertically, which, alongside a decreased vertical velocity gradient, diminish the effect of vertical shear and therefore its contribution to D_x. Increasing vegetation density will diminish vertical shear effects and ultimately decrease longitudinal dispersion.

2.4.2.6.Transverse Dispersion $\boldsymbol{D_y}$

Transverse dispersion in emergent vegetation was initially proposed by Nepf (1999) to be dependent on turbulent diffusion, represented as turbulent kinetic energy (Eq. 2.4-3). Experiments showed that turbulent diffusion on its own could not account for measurements of D_y. To complement the effect of transverse spreading, Nepf (1999) introduced mechanical dispersion as the aggregate of contributions from obstructions and path tortuosity. For a stem array, the number of collisions that a batch of particles undergoes will tend to a normal distribution due to the central limit theorem (Nepf, Mugnier and Zavistoski, 1997). The variance of a solute cloud will increase linearly with distance traversed downstream. Following a random walk approach to describe dispersion due to mechanical effects, D_y was initially defined as.

$$\frac{D_y}{Ud} = \frac{D_t}{Ud} + \left(\frac{\beta^2}{2}\right) ad \qquad \textit{Eq. 2.4-10}$$

D_t is defined as in Eq. 2.4-3. The second term on the RHS of Eq. 2.4-10 is the mechanical dispersion coefficient, where β is a proportionality constant of the first order, representing the fraction of the stem diameter (d) each particle is moved laterally when colliding with a stem, and ad is an proxy for the solid volume fraction φ.

Serra, Fernando and Rodríguez (2004) studied D_y for a random stand of emergent artificial vegetation ($d = 1\text{cm}$), at low Reynolds numbers ($10 < Re_d < 100$), and moderate to high vegetation densities ($\varphi = 0.10, 0.35$ and 0.65). Concentration measurements were obtained via Laser Induced Fluorescence. Dispersion coefficients were calculated from a Gaussian best-fit procedure of transverse concentration profiles. D_y results were found to depend on, C_D, and the ratio of mean stem spacing to stem diameter.

The results confirmed that C_D for a vegetated reach is a function mainly of Re_d (see Section 2.4.1.4). For low Reynolds numbers ($Re_d < 100$), C_D decreases with increasing Re_d, until a threshold at $Re_d \approx 100$, where C_D plateaus. Serra, Fernando and Rodríguez (2004) connected this variation of C_D, with the change from a viscous to an inertial flow regime. Also, measurements of D_y were consistently higher than predictions from Eq. 2.4-10, suggesting that this model tends to underestimate transverse dispersion. However, the model proposed in Serra, Fernando and Rodríguez (2004) was not assessed for predictive performance, so, its physical validity requires further analysis.

Building on these shortcomings, Tanino and Nepf (2008b) developed a model for transverse dispersion considering the following conditions:

The fraction of turbulent diffusion that contributes to lateral dispersion is assumed to be the length scales bigger than stem diameter, d. These scales can exist only within patches of fluid larger than d, whose occurrence depends on the variation of porosity (i.e. $1 - \varphi$) and the average of turbulence intensity occurring in these areas. The expression for D_t then has the form

$$\frac{D_t}{Ud} = \gamma_1 \left\langle \frac{u^+}{U} \right\rangle \frac{\langle s_n^2 \rangle_{snc>r^*}}{d^2} \frac{\varphi}{\pi/4} P_{snc>r^*} \qquad \textit{Eq. 2.4-11}$$

Where

$\left\langle \frac{u^+}{U} \right\rangle$: is the spatial average of the turbulence intensity, conditioned to the zones where the turbulent length scales $L_e \geq d$.

$\frac{\langle s_n^2 \rangle_{snc>r^*}}{d^2}$: is the normalised area around each cylinder containing length scales according to the previous condition.

$\frac{\varphi}{\pi/4} P_{snc>r^*}$: is the fraction of cylinders with a nearest neighbour further than r^*, which is the centre-to-centre distance necessary to allow relevant length scales.

γ_1: proportionality constant

r^* : minimum distance between cylinders to allow turbulent diffusion. Imposed $r^* = 2d$.

Mechanical dispersion depends on the interactions of close cylinders and their degree of 'packing'. (Tanino and Nepf, 2008b, 2009) developed an expression for mechanical dispersion, from a model for dispersion due to velocity heterogeneities in Stokes flow, through fibrous cylindrical elements (Koch and Brady, 1986). A net increase in mechanical dispersion is expected from interactions between pairs of adjacent stems. A higher probability of mechanical dispersion is attributed to closer stems, and higher resistance to flow. The latter is defined as the inverse of the vegetation permeability. The equation for mechanical dispersion then takes the form.

$$\frac{D_{y,m}}{Ud} = \gamma_2 P_{snc<5d} \frac{\pi}{4096} \left(\frac{d^2}{k_\perp}\right)^{3/2} \frac{1-\varphi}{\varphi^2} \qquad \textit{Eq. 2.4-12}$$

Where

$P_{snc<5d}$: is the probability of finding a stem within 5 diameters from each stem. The $5d$ threshold is defined as the maximum distance necessary to have wake interaction effects (Zhang and Zhou, 2001) and mechanical dispersion.

$k_\perp$: is the permeability of the array

$\frac{\pi}{4096}\left(\frac{d^2}{k_\perp}\right)^{3/2}\frac{1-\varphi}{\varphi^2}$: this factor represents the mean form drag as given in the initial model of (Koch and Brady, 1986).

For $0 < \varphi < 0.03$, transverse dispersion (D_y) is proportional to d, but decreases with increasing stem (edge-to-edge) spacing. For increasing φ, transverse dispersion is expected to increase rapidly. For $0.03 < \varphi < 0.2$, an increase in flow path tortuosity due to a reduced stem spacing entails a decrease in D_y. An increase in vegetation density will damp turbulence effects, and mechanical dispersion will increasingly become the main source of transverse dispersion. This last conclusion seems validated by a reported increase in D_y, for $\varphi > 0.2$, which is the result of an increase in mechanical dispersion alone (Tanino and Nepf, 2008b), due mainly to flow path tortuosity.

Figure 2.4-10 shows the variation of non-dimensional D_y and its main components: turbulence and flow heterogeneity, as a function of the surrogate density value $d/\langle s_n\rangle_A$, used to illustrate the reduction of pore space with increasing φ. As mentioned above, an initial steep increase in D_y occurs as a function of stem-induced turbulence. Increasing the density further actually limits the number of spaces where large turbulent scales can exist, therefore, turbulence-induced diffusion decreases. Finally, as turbulence is dampened to the point of not contributing to large scale transverse dispersion (turbulence will still play a role in smoothing concentration profiles, due to small-scale mixing), both mean flow heterogeneity and mechanical dispersion dominate, which explains the last, more gradual, increase in normalised dispersion.

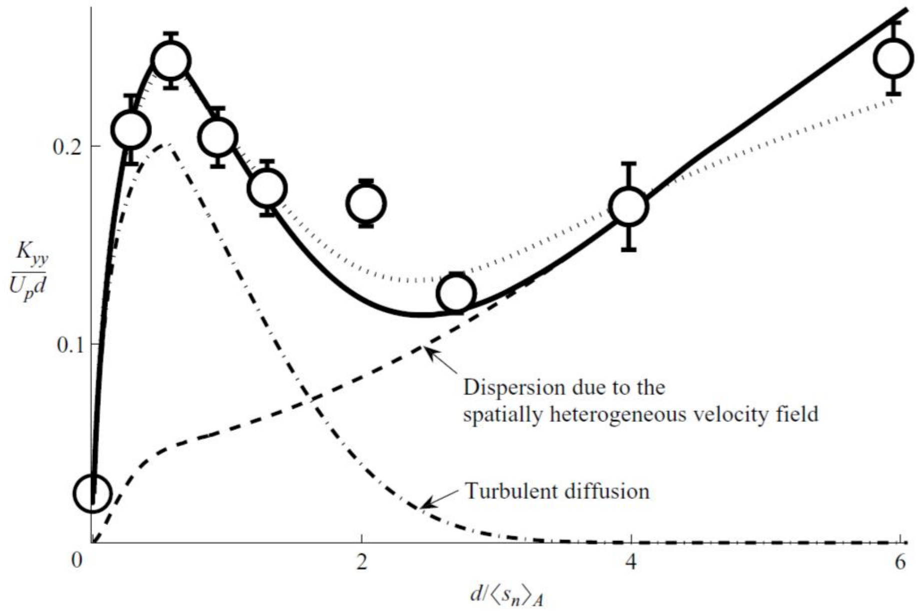

Figure 2.4-10. Components of Transverse Dispersion as a function of solid volume fraction, for turbulent flows, wherein dispersion is expected to be independent of Reynolds number. The dot-and-dash line

represent the contribution from turbulent dispersion arising from wake transitions and the dashed line represents the contribution from spatial heterogeneity. The solid line and circles represent the complete model and the experimental results respectively. Source (Tanino and Nepf, 2008b)

From experimental results, Tanino and Nepf (2008b) also assert that the variation of non-dimensional D_y with φ is independent of Re_d. This finding suggests that the model for Stokes flow (Koch and Brady, 1986), can still be useful to calculate dispersion in turbulent shear flows (see Eq. 2.4-12). Whether this independence of dispersion on flow regime is valid (more experimental evidence is needed), it does reflect a need to characterise shear flow and its variation in emergent vegetation, as a function of both φ and Re_d.

From the threshold for dominant mechanical dispersion ($\varphi \approx 0.2$), Nepf (2012) proposed an alternative expression for D_y, in sparse arrays, $\varphi < 0.1$, which is a limit where $P_{snc<5d}$ tends to zero and the contribution of mechanical dispersion is negligible. This assumption leaves a dispersion coefficient weakly dependent on Reynolds number, from which it is reasonable to expect a constant normalised dispersion coefficient $D_y/Ud = O(0.1)$.

Figure 2.4-11, shows a comparison of D_y results for different vegetation species and artificial vegetation, as a function of φ. Although Tanino and Nepf (2008b) model performs well for the artificial vegetation, the variations with Reynolds numbers analysed are limited. Also, it has consistently been found that longitudinal dispersion, D_x, is approximately one order of magnitude greater than D_y (Sonnenwald *et al.*, 2017). In this study it is also hypothesised that a distribution of stem diameter can approximate the natural variations in plant morphology caused by clustering, age and seasonal variation.

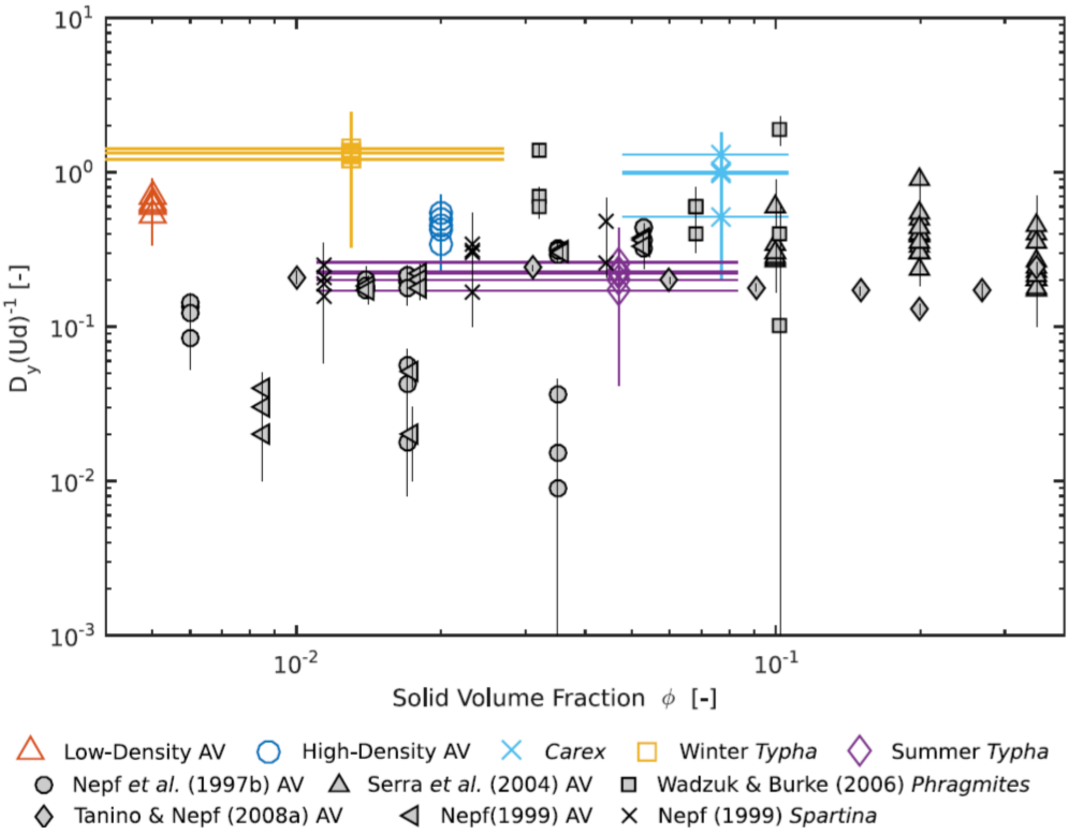

Figure 2.4-11 comparison between physical models given in the literature for the computation of transverse dispersion coefficients, D_y, for artificial and natural vegetation, source Sonnenwald et al., (2017)

D_y in flows through vegetation is greater than in shallow open channels. This trend is easily identified from the theoretical and experimental values shown in Figure 2.4-10. However, when comparing the results from different studies a trend cannot be identified, since deviations from a straight line (which would be the estimated trend in Figure 2.4-11) are up to two orders of magnitude. The differences reported in the studies analysed can have different causes: experimental conditions, effects of the advective zone, over-simplification of the vegetation morphology or unknown additional physical effects. Discussions on possible causes of error are further explored in this thesis.

Chapter 3. PRELIMINARY EXPERIMENTS

Abstract

This chapter presents a series of preliminary studies motivated by an analysis of the treatment of velocity statistics in the derivation of the most relevant model for longitudinal dispersion (White and Nepf, 2003). The first study, presented in Section 3.1, combines concentration and Surface PIV measurements in a sparse array configuration, with 4 mm-diameter cylinders, in a 300 mm-wide flume at the University of Warwick. This experiments have as an objective to quantify the main components of the White and Nepf (2003) model, namely turbulent diffusion and secondary wake dispersion, also called dispersion by differential advection in this work. The results show that the velocity heterogeneities are approximated by the secondary wake term, only for low Reynolds numbers. The trends for intermediate Reynolds numbers suggest that the secondary wake dispersion term, will underestimate the effect of velocity heterogeneities owing to the initial assumption of linear velocity superpositions, which overlooks higher order stem wake interactions.

The importance of the White and Nepf (2003) should always be, acknowledged. However, the treatment of velocity statistics, based on the conceptual framework used for the Lagrangian-to-Eulerian transformation, as well as the contribution of the mean velocity field, require further discussion. The validity of the theoretical assumptions, and their consequences on concepts such as homogeneity, stationarity (i.e. steady flow conditions) and isotropy are explored in Section 3.2. This analysis is donen by means of simultaneous 2-point velocity statistics, using ADV probes, measured in a sparse array, with 20 mm-diameter cylinders, in a 300 mm-wide flume in the University of Sheffield. The results from the ADV experiments show wakes are dominated by persistent coherent features, that are associated to large scales of the flow. Further, velocity heterogeneities are dominated by these wake effects, since, in the absence of clear momentum transfer between wakes, these tend to deform due to array configuration. A model is suggested to extrapolate coherence metrics (i.e. correlation functions) from single-point measurements to Lagrangian functions.

3.1. CHARACTERISATION OF LONGITUDINAL DISPERSION IN EMERGENT VEGETATION USING SURFACE PIV

3.1.1. Introduction

This chapter presents the results of the characterisation of velocity fields, from measurements of surface PIV, to predict longitudinal dispersion in flow through emergent vegetation. The experimental results presented correspond to joint measurements of longitudinal dispersion, from tracer tests using submersible fluorimeters (cyclops), and velocity variations from Surface Particle Image Velocimetry (PIV). The experiments were carried out in the Armfield Flume, at the University of Warwick, by other researchers, prior to the start of this PhD.

Flow field measurements and dispersion coefficients are related using the model for scalar transport given in White and Nepf (2003). A summary of the key points of the model, the relevant equations and parameters is presented. This is followed by a discussion of the information required to obtain the inputs of the model from the Surface PIV data. Subsequently, quantification of dispersion coefficients from the velocity data is presented.

Based on the predictions, and comparing the results with the measured dispersion coefficients, it is evident that a two-dimensional characterisation of the velocity field can be used to calculate dispersion processes. However, it is found that one component of the model, secondary wake dispersion, is not well predicted from the data. A discussion reveals that the analytical developments from which this component was developed, tend to overlook the effects of spatial heterogeneities in the flow field caused by the vegetated array.

3.1.2. Experimental set-up

The experiments were conducted in a 300 mm wide flume, the specific details of which are covered in Sonnenwald, Stovin and Guymer (2019a), with the camera located above the flume, as shown in Figure 3.1.2-1a. The focal plane was perpendicular to the bed, at a small enough distance to avoid projection errors, thereby eliminating the need for image distortion corrections. Surface PIV and dispersion measurements were taken for a random, synthetic vegetation array, composed of rigid stems (plastic straws), with uniform diameter d of 4 mm, a stem density of 398 stems/m^2 and a solid volume fraction φ of 0.005.

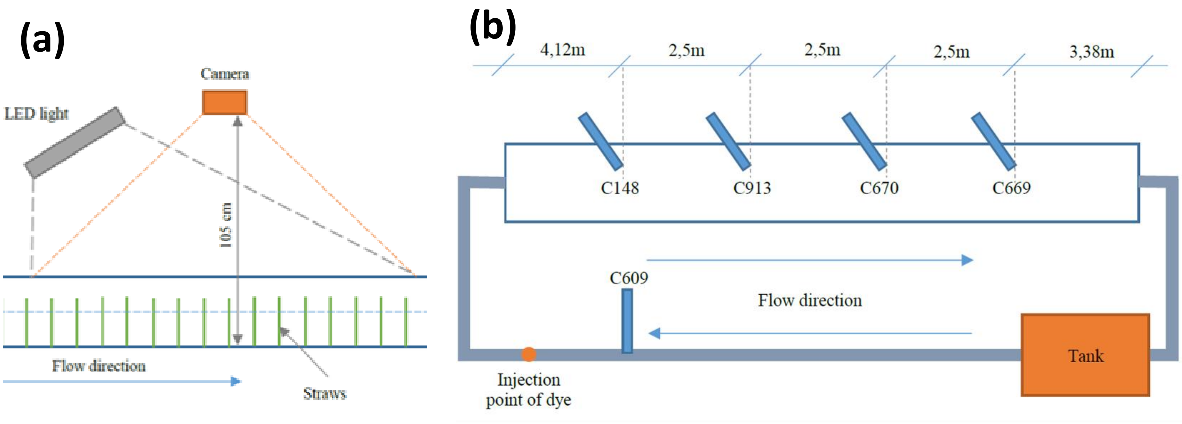

Figure 3.1.2-1. a) Surface PIV configuration, b) Locations of the fluorimeters for the measurements of concentration profiles.

Measurements of concentration and Surface PIV were taken under uniform flow conditions, with a constant depth of 150 mm for a total of 4 flow scenarios. The nominal flow rates set for the pump were validated using the travel velocities from the concentration measurements. These measured velocities will be used as reference as they better represent flow conditions within the vegetated array. The velocities and Reynolds numbers of each test are presented in Table 3.1.2-1.

Table 3.1.2-1. Nominal mean velocities and stem Reynolds numbers for the tests analysed.

TEST	U_∞ *[mm s^{-1}]*	Re_d* *[-]*
1	*14*	*57*
2	*20*	*80*
3	*40*	*158*
4	*68*	*270*

*With a kinematic viscosity of 1.01·10^{-6} m^2/s

Concentration measurements were taken with 5 fluorimeters, 4 of which were distributed uniformly along the flume, within the artificial vegetation, and one in the inlet pipe, upstream of the injection point, to confirm a fixed background concentration during the tests. The distances between fluorimeters, the location of the injection point, and the general configuration for the tracer tests are shown in Figure 3.1.2-1b. Three repeats for each test were performed, resulting in 9 values of longitudinal dispersion, D_x, for each test, calculated from an optimised routing of two consecutive concentration profiles (Eq. 2.2-6, Chapter 2). The results of longitudinal dispersion for all repeats and reaches (i.e. consecutive fluorimeters) are grouped for each test shown in Figure 3.1.2-2.

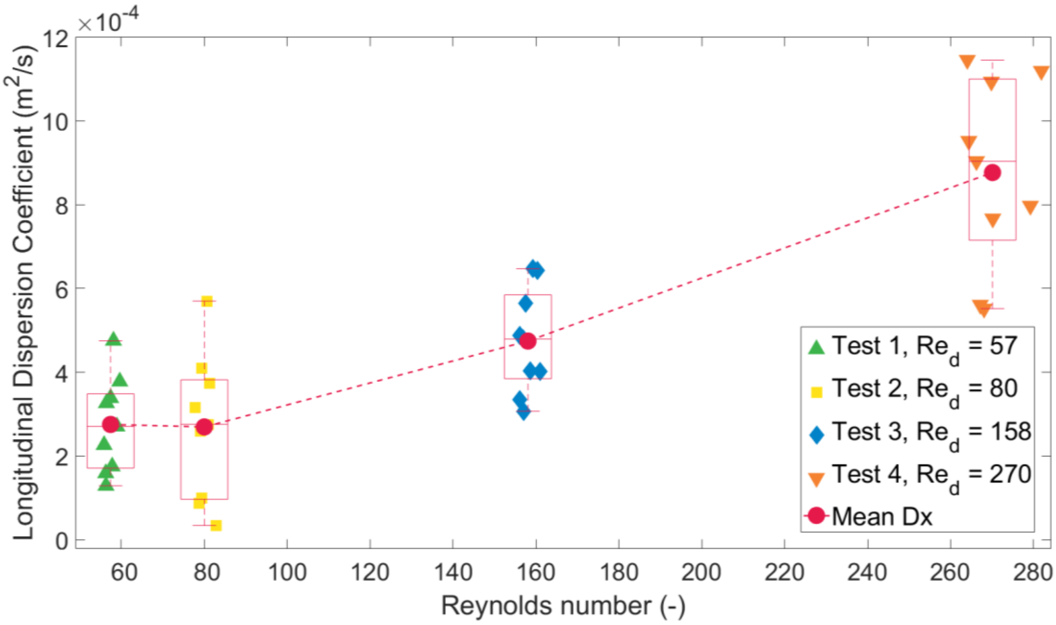

Figure 3.1.2-2. Results of Longitudinal Dispersion for all trials and all tests. External whiskers in the boxplots represent ±2.7 standard deviations from the mean of the data, the boxes represent the data between the first and third quartile, and the central line represents the median of the experimental results. Measurements of longitudinal dispersion for each test and trial are shown to illustrate variation in terms of Dispersion and Reynolds number.

The main purpose of the analysis is to perform a full characterisation of the velocity field from the Surface PIV measurements, to obtain the relevant parameters to predict the longitudinal dispersion coefficients. The specific details of this model are given in the following section.

3.1.3. Data Analysis

3.1.3.1. Theoretical Background

This section will treat the components that characterise the longitudinal dispersion coefficients, as described by White and Nepf (2003), namely

$$D_x = D + D_t + D_{x,v} + D_{x,s} + D_{x,g} + D_{BL} \qquad \textit{Eq. 3.1.3-1}$$

Where

D: Molecular Diffusion

D_t: Turbulent Diffusion

$D_{x,v}$: Vortex trapping Dispersion

$D_{x,s}$: Secondary wake Dispersion

$D_{x,g}$: Dispersion caused by convective acceleration in the gaps between stems

D_{BL}: Dispersion caused by trapping in Laminar Boundary Layers.

The term $D_{x,g}$ represents the increase in velocity (called 'local advective acceleration') that is generated in the gap between stems as a compensation for the decrease of mean velocity behind stems. White and Nepf (2003) assume, under dimensional considerations, that turbulence-induced velocity variations in these regions are small compared to those in the actual wakes, and $D_{x,g}$ is therefore negligible.

The tem D_{BL} corresponds to 'Boundary Layer Dispersion', as presented by Koch and Brady (1985). Given the small spatial extent and the large time scales of this effect, D_{BL} is considered negligible for experimental purposes. Molecular diffusion is several orders of magnitude smaller compared to other physical processes. Longitudinal dispersion in emergent (artificial) vegetation, is defined as

$$D_x = D + D_t + D_{x,v} + D_{x,s} \qquad \text{Eq. 3.1.3-2}$$

These individual contributions are the result of cross-correlation terms (e.g. $\overline{u'C'}$) generated by the consecutive time and space averaging of the ADE (see Eq. 2.3-5). Their physical meaning was explored by White and Nepf (2003), and are briefly covered here in Section 2.4.2. The following discussion will focus on quantifying each of the components of D_x.

3.1.3.1.1. Molecular Diffusion $\boldsymbol{D_m}$

The constant of molecular diffusion D_m is known for most components, including Rhodamine. The common values found in technical notes and the literature varies within the range.

$$D_{Rhodamine} = (4.6 \pm 0.5) \cdot 10^{-8}\, m^2 s^{-1}$$

3.1.3.1.2. Turbulent Diffusion D_t

Turbulent Diffusion D_t can be obtained from the turbulence kinetic energy per unit mass[2], k, see Eq. 3.1.3-3, or alternatively from the array drag coefficient, $\overline{C_D}$ shown in Eq. 3.1.3-4, as explained in Nepf (1999).

$$\frac{D_t}{Ud} = \alpha_2 \frac{\sqrt{k}}{U} \qquad \textit{Eq. 3.1.3-3}$$

$$\frac{D_t}{Ud} = \alpha[\overline{C_D} ad]^{1/3} \qquad \textit{Eq. 3.1.3-4}$$

Where α_2 and α are proportionality constants, a, is the mean frontal facing area per unit volume, and d is the mean diameter of stems.

3.1.3.1.3. Isotropic vs Anisotropic diffusion/dispersion

All dispersive/diffusive processes in Eq. 3.1.3-1 are indicated by D, and the subscripts give an indication of the physical process in each case. Two types of subscripts are used. First, coefficients with a single subscript denote **isotropic diffusion coefficients**, i.e. remain equal after any rotation of the coordinate system. The second type of coefficients refer to processes that are dominant in one direction, and whose effect in all other directions are overshadowed by isotropic effects. These are called **anisotropic/directional dispersion coefficients** (e.g. $D_{x,s}$ for secondary wake dispersion). The distinction between isotropic and anisotropic coefficients is considered relevant because the extent to which certain mechanism is Fickian, must be considered in a directional basis.

3.1.3.1.4. Primary and Secondary wakes

To understand the equations describing vortex trapping and secondary wake dispersion, it is necessary to define the spatial domain of each process. To do that, Figure 3.1.3-1 shows the extent of the primary and secondary wakes graphically, as explained in White and Nepf (2003). The **primary wake** corresponds to the region dominated by recirculation, which, at low Reynolds numbers, is bounded by closed streamlines and therefore no direct mass exchange other than that due to molecular diffusion occurs. After this initial recirculation zone characterising the primary wake, a region of velocity defect induced by the cylinder is formed,

[2] Following considerations of two-dimensionality, the turbulent kinetic energy per unit mass, k, can be defined only from the longitudinal and transverse velocity components: $k = (u^2 + v^2)/2$.

called **secondary wake**, which extends to a scale defined by the drag imposed by the stem and the solid volume fraction (White and Nepf, 2003).

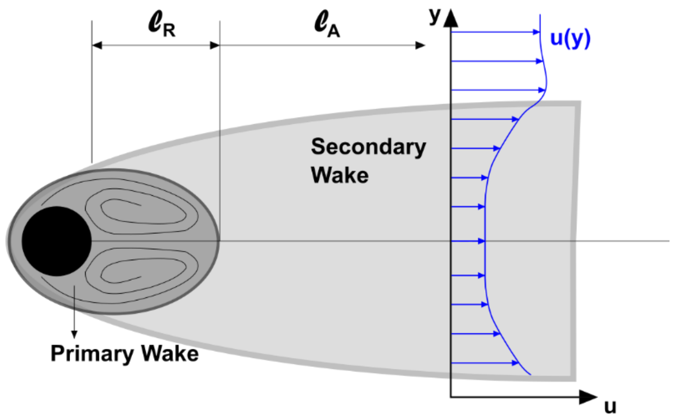

Figure 3.1.3-1. Separation of the wake generated by a single cylinder, into a primary wake, defined by the recirculation region immediately behind the stem; and a secondary wake characterised by the velocity defect further downstream. l_R: length scale of the recirculation region. l_A: Attenuation length, i.e. streamwise extension of the velocity decay caused by the stem.

3.1.3.1.5. Vortex trapping Dispersion $\boldsymbol{D_{x,v}}$

This refers to the spread of the concentration distribution induced by mass trapping in **primary wakes**. During early stages of formation ($Re_d \leq 40$; Gerrard, 1978) this region contains two symmetric vortices with opposite rotation and any mass can only escape through molecular diffusion. As Re_d increases above this threshold, mass exchange pathways are opened between the primary wake and the outer flow, thereby decreasing the retention time, $\overline{\tau}$, and dispersion. The length of this formation region grows Re_d, until periodic vortex shedding starts. The length of the primary wake, at this transition, has been found to be $2d$ (Gerrard, 1978).

As mentioned in Chapter 2, Eq. 2.3-8, White and Nepf (2003) define vortex trapping dispersion as the result of two main factors: the proportion of the flow field occupied by primary wakes, ϵ_w, and the average trapping time, $\overline{\tau}$. The former represents the vegetated array, and the latter depends on Re_d, and is represented by the Strouhal number, S_t (i.e. non-dimensional vortex shedding frequency). We know that ϵ_w can be readily measured from the Surface PIV (SPIV) data collected, so the use of the equation $\epsilon_w \propto ad$ used in White's paper is not necessary.

An advantage of having spatially and temporally resolved flow fields is that both ϵ_w and S_t can be computed directly from the SPIV data available. This calculation is explained below.

3.1.3.1.6. Secondary wake Dispersion $\boldsymbol{D_{x,s}}$

This effect has to do with the velocity perturbations induced by the stems, but outside of the recirculation zone. These are related to instabilities that induce the generation of coherent structures and turbulence production downstream of the wake and therefore a reduction in mean velocity (i.e. a velocity defect). This velocity defect is more noticeable along the stem centreline (parallel to the flow direction, see also Figure 3.1.3-9).

Particles advecting through the secondary wake will be slowed down when they are captured in vortices and recirculating locally, or simply by encountering a stem. If a single particle is followed in a Lagrangian manner through the vegetation array, the delays can be accounted for by measuring the changes in velocity along its path. Statistically, the tool that allows for such quantification is the autocorrelation function $\mathcal{R}_i(t)$, defined as

$$\mathcal{R}_i(t) = \frac{1}{v_i^+(\tau)v_i^+(\tau+t)\,T}\int_0^T v_i'(\tau)v_i'(\tau+t)\,d\tau \qquad \textit{Eq. 3.1.3-5}$$

Where $v_i'(\tau)$ represents the (Lagrangian) velocity fluctuations of a particle in the i-th direction. The general autocorrelation $\mathcal{R}_i(t)$ considers the turbulence intensities at different intervals during the particle's motion. Although no restrictions regarding isotropy or homogeneity are imposed on Eq. 3.1.3-5, there is a requirement for the interval T to be significantly larger than the characteristic integral scales of the flow. The secondary wake dispersion coefficient will be given by (Csanady, 1973).

$$D_{x,s} = v_i^+(t)\int_0^t v_i^+(\tau+t)\,\mathcal{R}_i(\tau)\,d\tau \qquad \textit{Eq. 3.1.3-6}$$

For want of space it is only necessary to know that the general expression given in Eq. 3.1.3-6 is the added effect of perturbations induced by velocity fluctuations and the heterogeneous time-averaged flow field behind stems (yet outside of the primary wake), and between stems. The latter is considered negligible based on dimensional considerations (White and Nepf, 2003). The same restriction on t being larger than the integral scales is necessary. By expressing Eq. 3.1.3-6 in terms of the time-average velocity field (White and Nepf, 2003), Eq. 3.1.3-7 is obtained. The validity of this treatment of Eq. 3.1.3-6 is discussed in detail in Chapter 3.2.

$$D_{x,s} = 2\sigma_w^{*2}s^*\sqrt{\frac{Sc_t}{Sc_t+1}}\,Ud \qquad \textit{Eq. 3.1.3-7}$$

Where the term σ_w^{*2} is the non-dimensional variance of time-averaged velocity fluctuations in the secondary wake $\sigma_w^{*2} = \sigma_w^2/U^2$, s^* is the mean separation of stems in the longitudinal direction divided by the stem diameter $s^* = s/d$ and Sc_t is the turbulent Schmidt number which defines the ratio between eddy/turbulent viscosity and turbulent diffusion: $Sc_t = \nu_t/D_t$.

Eq. 3.1.3-7, as presented by White and Nepf (2003) can be treated in several ways. In this report three approaches will be explored, which will involve the calculation of the following parameters.

a. The term σ_w^{*2} is expressed in terms of C_D, D_t, Sc_t and a, in the form of an incomplete gamma function calculated from the end of the inner wake (termed x_0^* in the paper). We can compute all those terms and find the best-fit for the gamma function defining σ_w^{*2} and solve Eq. 3.1.3-7 directly.

b. An estimate of mean velocity heterogeneities can be obtained from the dispersive fluxes computed from SPIV maps.

c. We re-formulate Eq. 3.1.3-5 and Eq. 3.1.3-6, and use an experimental proxy for $\mathcal{R}_i(t)$. To do this, we must convert the autocorrelation function for a single particle in the temporal domain, to a Eulerian cross-correlation (or simply correlation) function between consecutive points within a wake, starting at the onset of the secondary wake, i.e. $R_i(\psi)$, in the spatial domain (like the axis presented in Figure 3.1.3-2c). The validity of this Eulerian-Lagrangian similarity requires a detailed analysis, which is presented in Chapter 3.2.

In this analysis, option (a) requires empirical estimations of C_D and the other parameters, which become additional sources of uncertainty. (b) will also be explored here, as Surface PIV provides the spatially resolved velocity fields to obtain velocities along the secondary wake. Finally, option (c) requires a more detailed treatment of multi-point velocity statistics, and a detailed analysis of the necessary empirical assumptions and simplifications to relate Lagrangian and Eulerian statistics. The necessary conditions for its application are explored in Chapter 3.2.

In conclusion, we have to calculate 2 parameters to obtain $D_{x,v}$, and have three approaches to compute $D_{x,s}$. These alternatives are explained later on. For now, the focus is on the capabilities of Surface PIV for the extraction of detailed flow field information. This analysis, will be seen, is beneficial because the computation of parameters that previously had to be assumed or drawn from different studies. Further, allows the characterisation of velocity perturbations in more detail to discuss the validity of the physical assumptions given in the derivations of the current models.

3.1.3.2. Characterisation of the Flow Field and Dispersion Coefficients via SPIV

Having outlined dispersion models, this section is devoted to the methods to compute velocity-dependent measurements using (Surface) PIV. The common feature for foregoing formulations is the notion of an ensemble average of Lagrangian transport equations, which are defined for distinct solute elements throughout the motion. This approach will be followed here, and all computations will be explained for a single stem, i.e. wake. The results will be extended to the complete test section via ensemble averages.

Figure 3.1.3-2a shows the pattern of the pseudo-random vegetation array in which dispersion and velocity were measured. The Surface PIV field of view is shown in Figure 3.1.3-2b. There the stem wake of analysis is depicted in detail. According to the subdivision of the wake presented (see Figure 3.1.3-2c), three specific points have been chosen: *k, p* and *q*; which were chosen to represent the recirculation region (i.e. primary wake), the shedding or transition region, and the secondary wake, respectively. Further, the wake centreline, X_{sc}, which is used in the next section to describe the mean flow field, is presented.

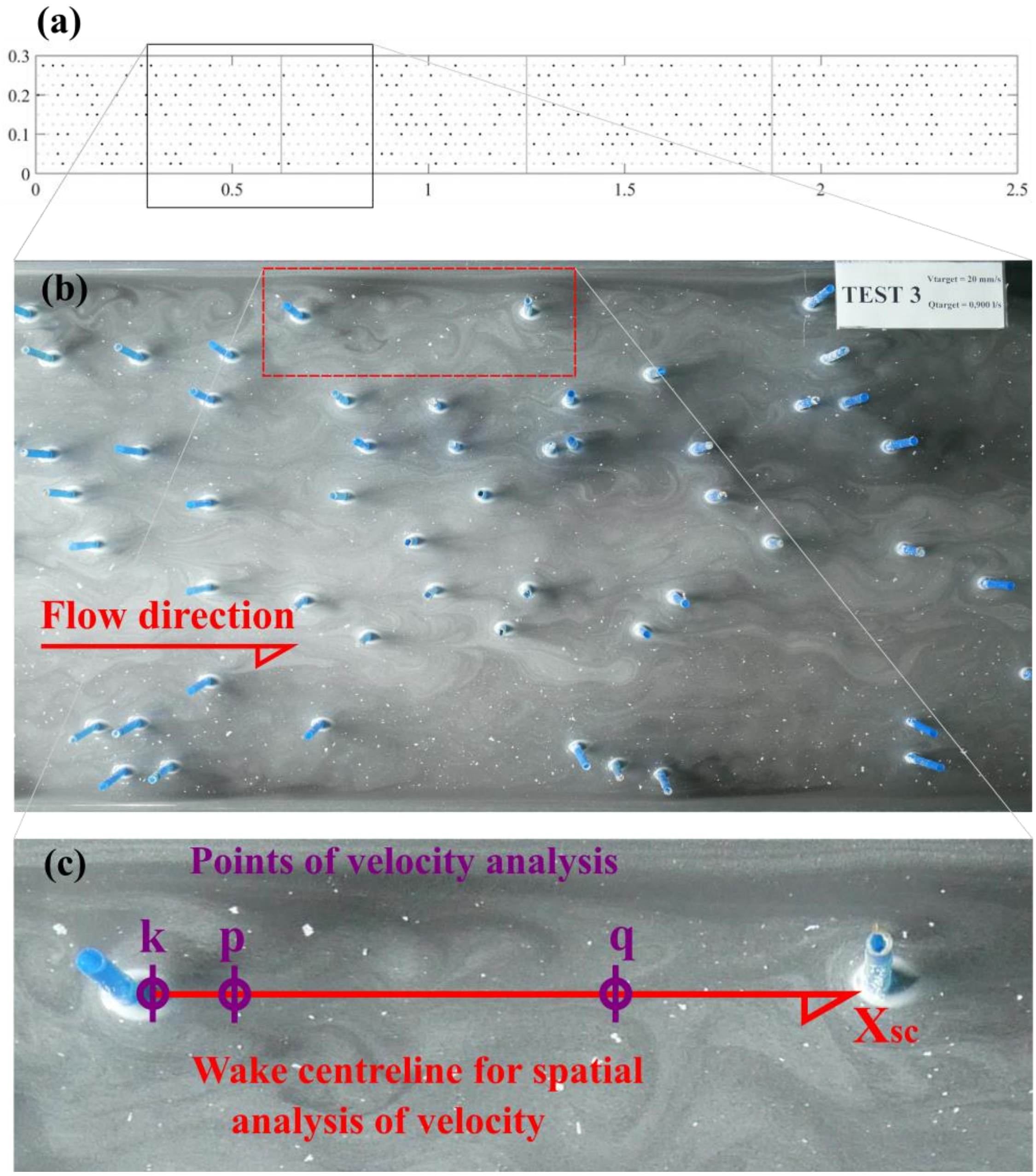

Figure 3.1.3-2. Area of study for Surface PIV. a) 2.5 m-long repeating pattern of pseudo-random vegetation. b) Sample image taken from SPIV experiments. c) Stem wake under analysis, wake centreline and location of the points for the temporal analysis of the velocity variations. Point k is located as close to the recirculation zone as possible; point p is chosen close enough to the inner wake but within the secondary wake to allow for the characterisation of velocity fluctuations for the measurement of vortex shedding frequency.

3.1.3.2.1. Computation of the volume fraction of primary wakes ϵ_w

Although the concept of a volume fraction of primary wakes, in vegetated flows, was introduced by White and Nepf (2003); a clear methodology for its calculation is required. Remembering the mathematical definition of instantaneous vorticity,

$$\Omega = \frac{\partial U}{\partial y} - \frac{\partial V}{\partial x} \qquad \textit{Eq. 3.1.3-8}$$

Corredor-Garcia *et al.* (2020) proposed a method for calculating the fraction of the flow field occupied by primary wakes, based on the reported features of increased time-avereage vorticity (cf. recirculation) and decreased mean longitudinal velocity (cf. velocity defect) evidenced in the vicinity of circular cylinders. Accordingly, this method considers a **primary wake** to be composed of the points, m, in a discrete velocity map, that comply with the following conditions.

$$\frac{U_m}{\langle U\rangle} \leq \alpha_w \quad \textit{and} \quad \frac{|\Omega_m|}{\langle|\Omega|\rangle} \geq \varepsilon_w \qquad \textit{Eq. 3.1.3-9}$$

The values U_m and Ω_m represent the time-averaged longitudinal velocity and vertical vorticity (i.e. $U_m = \overline{u}_m$, and $\Omega_m = \overline{\omega}_m$), at a particular point m in a discrete map. The term $\langle|\Omega|\rangle$ represents the **intrinsic spatial average**[3] of the time-averaged, absolute vorticity field (map); $\overline{u_m}$ and $\left|\overline{\omega_{z,m}}\right|$ represent, respectively, the time-averaged longitudinal velocity and vorticity magnitude at m; and U is the mean pore velocity. The criteria in Eq. 3.1.3-9 indicate that primary wakes are composed of points with vorticity fluxes higher than a threshold, ε_w, and longitudinal velocity lower than a predetermined value, α_w. Both constants have to be determined empirically, and are expected to vary depending on the macroscopic descriptors of vegetation. Spatial averages (i.e. $\langle U\rangle$ and $\langle|\Omega|\rangle$) are used as reference thresholds to reflect the macroscopic flow properties, and also, to smooth any possible outliers remaining after the initial filtering of erroneous velocities.

Before discussing the values of α_w and ε_w, the criteria is described graphically. Figure 3.1.3-3 to Figure 3.1.3-5 show the maps for U, ω and volume fraction of primary wakes, ϵ_w respectively. Clearly, Figure 3.1.3-3 shows that decreases in U take place not only behind stems but also expands radially near the stem (area A). Further, when two stems are sufficiently closed together, their wake effects and hence their recirculation regions combine (area B). For Figure 3.1.3-4, a key detail is the fact that mean vorticity is highest not only behind stems but a vorticity field is created stems. This can be explained by the shear induced by each stem, which guarantees a source of vorticity around a stem.

[3] Intrinsic average refers to averages considering only the extent of the pore space, omitting the space occupied by stems.

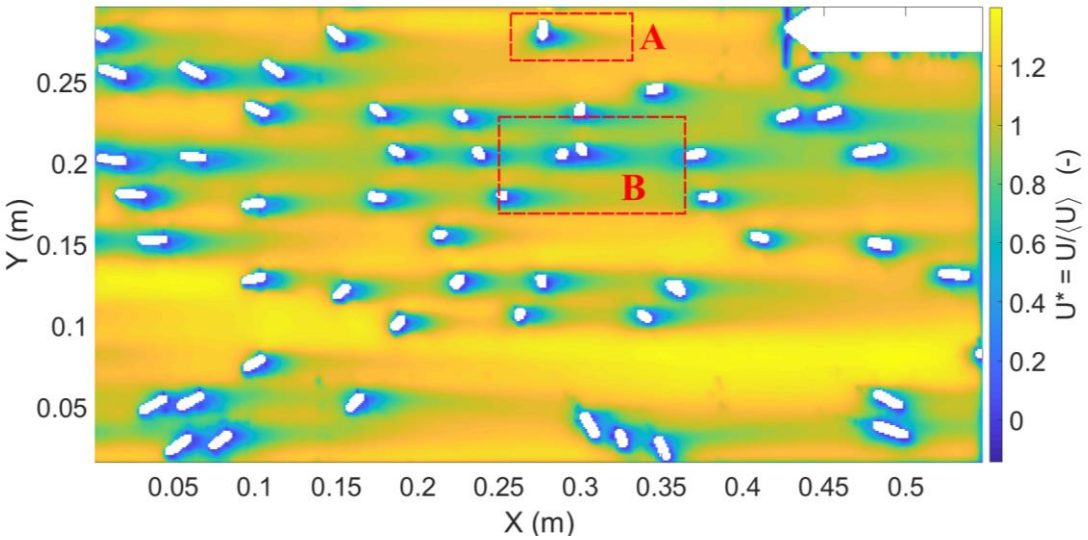

Figure 3.1.3-3. Map of non-dimensional mean longitudinal velocity for Test 3.

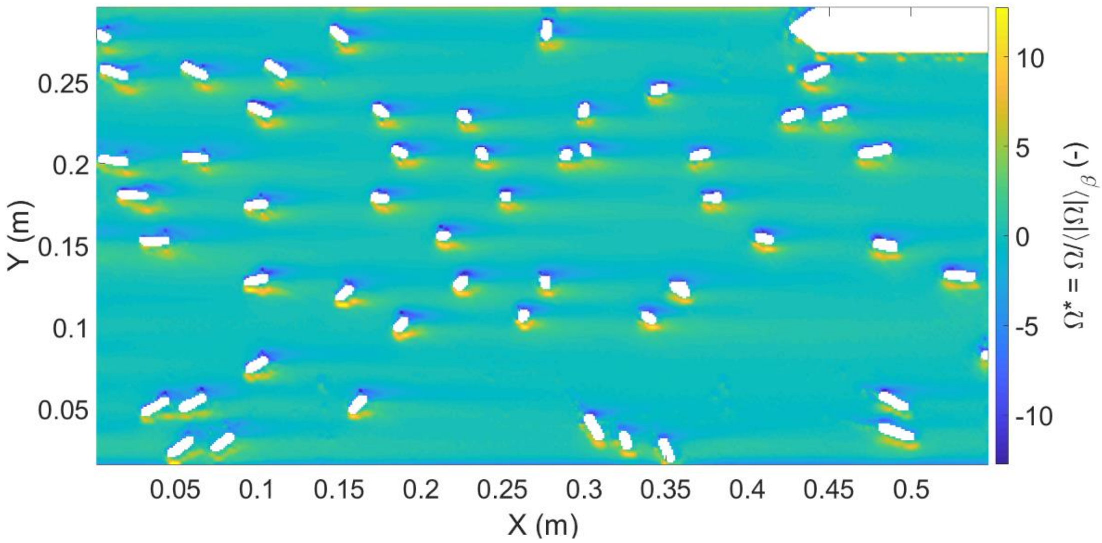

Figure 3.1.3-4. Map of non-dimensional Vorticity for Test 3.

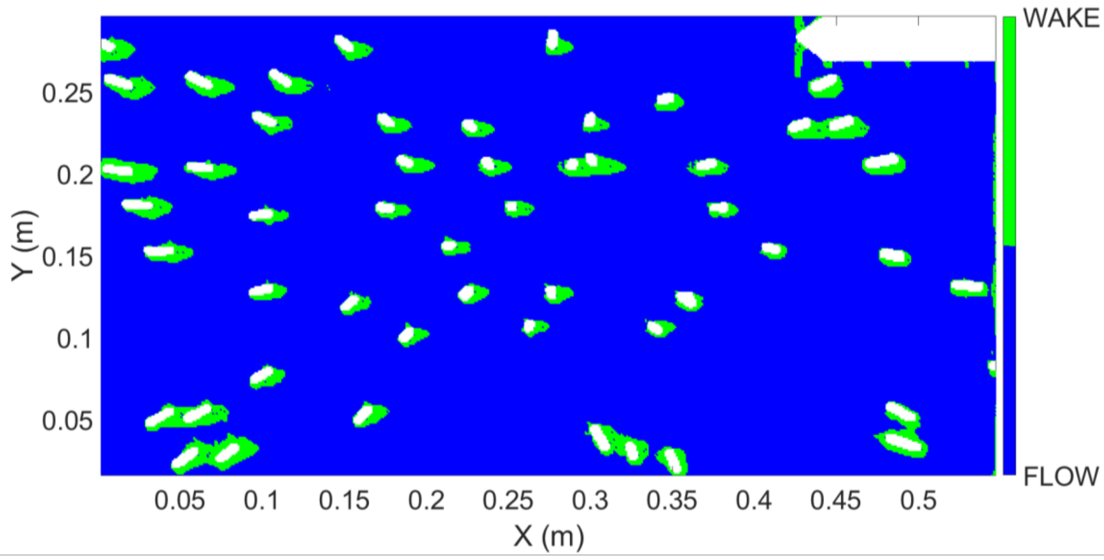

Figure 3.1.3-5. Map of primary wakes $\epsilon_w = 0.06$. With $\alpha_w = 0.5$ and $\varepsilon_w = 0.063$, for Test 3.

The appropriate arguments for the estimation of the vorticity threshold, ε_w, must be considered empirically. For the longitudinal velocity threshold, α_w, on the other hand, a detailed spatial analysis of the mean velocity can inform the natural range at which the inner wake exists. Since no precedents exist for these values, these were adjusted to have primary wakes as close to the $2d$ recirculation region found in Gerrard (1978). The next section is devoted to the calculation of the shedding frequency, which is based on the temporal variation in velocity for the points shown in Figure 3.1.3-2c.

3.1.3.2.2. Computation of the Shedding frequency and Strouhal number

The shedding frequency describes the rate at which vortices detach from the inner wake and move along the secondary wake. Behind stems, where energy from the mean flow is transferred to vortex generation, times series of velocities, $u(t)$ and $v(t)$, show periodic features from travelling vortices which leave their 'footprints' as rotational variations. To characterise vorticity and shedding frequency, the sinusoidal patterns in the $v(t)$ profile at different points along the wake centreline are used. The dominant frequency is obtained via spectral analysis, using Fourier Transforms[4] to get the spectrum (see Eq. 2.1-18, Chapter 2).

In the primary wake, the velocity damping effect will mask fluctuations[5], so variations in the velocity profiles due to vorticity will be difficult to detect (without measurements at higher frequencies). However, further downstream, when vortices detach, they will rotate, travel, and diffuse, so we can expect a decay in the sinusoidal patterns further downstream. Figure 3.1.3-6a shows the profiles of transverse velocity for points *k*, *p* and *q* (See Figure 3.1.3-2c).

[4] Note that spectral analyses can only provide evidence of the length scale and frequency of detached vortices, and cannot describe coherent structures (Hussain, 1983).
[5] (Taylor, 1935, Part I and II) proposed an empirical, linear relationship for the ratio of mean velocity to turbulence intensity, $U/u^+ = ax + b$, for dissipative turbulent flows behind honecomb and square grids.

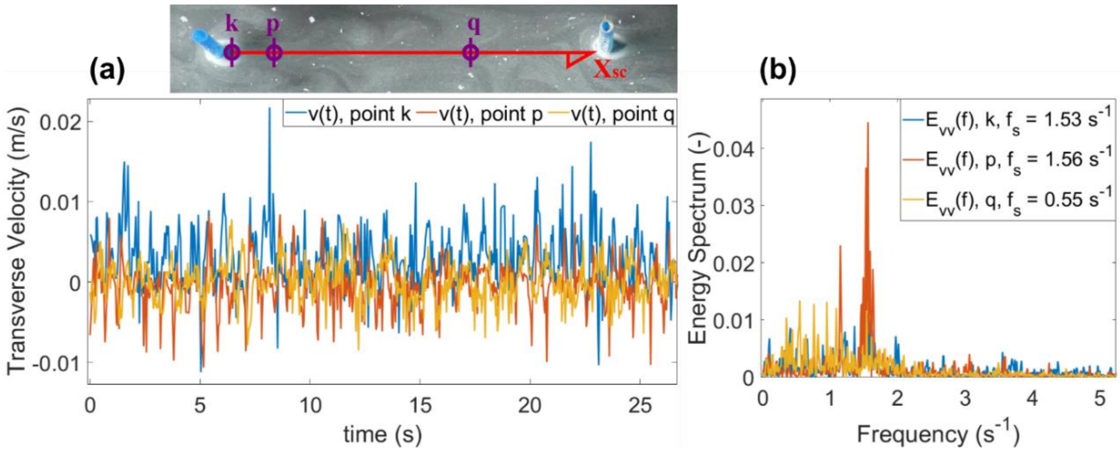

Figure 3.1.3-6. a) Variation of Transverse velocity behind the stem, for points k, p and q. b) Frequency spectra of the velocity series for points k, p and q.

As expected, for points behind a stem (Figure 3.1.3-6– point *k*) vortices are not fully formed, and the reduction in velocity decreases the signal-to-noise ratio, concealing rotational motions in recorded velocity signals. This makes dominant frequencies harder to identify. Further downstream, at the point where vortices start to detach (Figure 3.1.3-6 – point *p*), clear sinusoidal patterns in the transverse velocity time series can be discerned. Performing a spectral decomposition, the dominant frequency, f_S, which in this case corresponds to 1.56 Hz is clearly found. The amplitude (energy) of this frequency indicates that the flow structures are dominant and stable, albeit only at this location. Moving further downstream, the information for point *q* (Figure 3.1.3-6), shows that dissipation and diffusion have taken energy (i.e. rotation) from the detached structures. As a consequence, a reduction in the energy of the dominant frequencies is evident, as the larger structures are broken down into lower frequencies (i.e. energies).

The next step is to extrapolate this measurement of shedding frequency f_S of a single stem, to that of the entire array—at least a subsample of stems from the image; to obtain an estimate for the entire vegetated array. To do this a total of 30 stems were chosen at random, and their frequencies computed at the equivalent location of point *p* for each one, that is $2d$ downstream from the stem rear. The results of this ensemble average of shedding frequencies, for each test, is presented in Table 3.1.3-1.

Table 3.1.3-1. Estimation of shedding frequencies and Strouhal number, from empirical predictions using nominal and corrected estimations of velocity, and from experimental estimations using spectral frequencies.

TEST	Predicted values				Measured values from SPIV					
	1	2	3	4	5	6	7	8	9	10
	$\boldsymbol{U_\infty}$ [mm/s]	$\boldsymbol{Re_d}$ [-]	S_t* [-]	f_s [Hz]	$\langle \boldsymbol{U} \rangle$ [mm/s]	$\boldsymbol{Re_d}$ [-]	S_t* [-]	f_s ** [Hz]	S_t [-]	$\langle \lvert \overline{\boldsymbol{\omega}} \rvert \rangle$ [Hz]
1	14	57	0.13	0.5	14.5	52	0.12	0.56±0.2	0.15	0.46
2	20	80	0.15	0.8	15.2	56	0.13	0.64±0.3	0.17	0.52
3	40	158	0.19	1.9	34.0	123	0.17	1.60±0.4	0.19	0.93
4	68	270	0.21	3.5	59.0	214	0.20	2.90±0.8	0.20	1.25

*Values from the equations for S_t in Fey, König and Eckelmann (1998) and McCroskey (1977)
**Value of shedding frequency obtained as the ensemble average from a subsample of stems

Table 3.1.3-1 shows the results of the ensemble average of shedding frequency for all tests. Assuming that the discharge was correctly calibrated, the nominal values of U_∞, from continuity, and Re_d shown in Table 3.1.2-1 can be considered valid, and can thus be used to obtain shedding parameters, i.e. Strouhal number, from the empirical equations proposed by Fey, König and Eckelmann (1998) and McCroskey (1977). The obtained values are presented in column 3 of *Table 3.1.3-1*, and the shedding frequency based on this value is shown in column 4.

The measured mean velocity, $\langle U \rangle$, shown in column 5 of *Table 3.1.3-1*, was added to illustrate the variation in mean velocity within the array, from its nominal value. The value was measured as the double average of longitudinal velocity, only considering the pore space (see Figure 3.1.3-3). This change in mean velocity with respect to the nominal value can be the effect of two possible causes: surface values deviate from mid-flow velocities, or values not being correctly calibrated during the experiments. The corrected Reynolds numbers from these estimations are shown in column 6, and the empirical estimations of S_t are presented in column 7. Using the methodology explained above for the experimental estimation of f_s, based on a subsample of stems, the ensemble average is presented in column 8, and the corresponding experimental value of the Strouhal number is given in column 9. The spatial average of the time-averaged vorticity magnitude is presented in column 10.

The empirical predictions of Strouhal number based on the double-averaged velocity are lower than the values obtained using nominal mean velocity values, and both values are lower than the experimental estimations via the ensemble averages of f_s, for tests 1 – 3. Nonetheless, the differences between estimations are not large enough to induce errors in the predictions of vortex trapping dispersion, $D_{x,v}$. These estimations reveal a contradiction, the increase in shear stress has been shown to delay the onset of vortex shedding (Kiya, Tamura and Arie, 1980). The higher values of shedding frequency reported in Table 3.1.3-1 may be explained by the fact that, while for some stems the increase in shear can delay the onset of wake oscillations and hence frequency; in other stems, background turbulence can induce instabilities that will precipitate the formation of vortices. Also, stem interactions can induce pairs of stems to behave as a single obstruction, so, by having the same shedding frequency (as it is a function of the array Reynolds number) with a larger length scale, a higher Strouhal number is obtained.

The question now is: how can this analysis be extrapolated to cases where a detailed characterisation of f_s for each stem is not possible? This could arise, for instance, in CFD modelling where a detailed temporal characterisation of the flow is unattainable, but mean variations of the quantities of interest are available. To address this question, some basic information of the vorticity is necessary, which is a quantity relatable to shedding frequency. These are two different parameters describing a single process. We know that shedding frequency and absolute vorticity, are both proportional to mean longitudinal velocity and will scale accordingly, i.e. $|\overline{\omega}| \sim f_s$. As an example, consider the spatial average of mean absolute vorticity, $\langle|\overline{\omega}|\rangle$, the quantities of which are given in Table 3.1.3-1 for each test. If we compare the variation in $\langle|\overline{\omega}|\rangle$ with the changes in f_s, a proportional relationship is obtained, as shown in Figure 3.1.3-7.

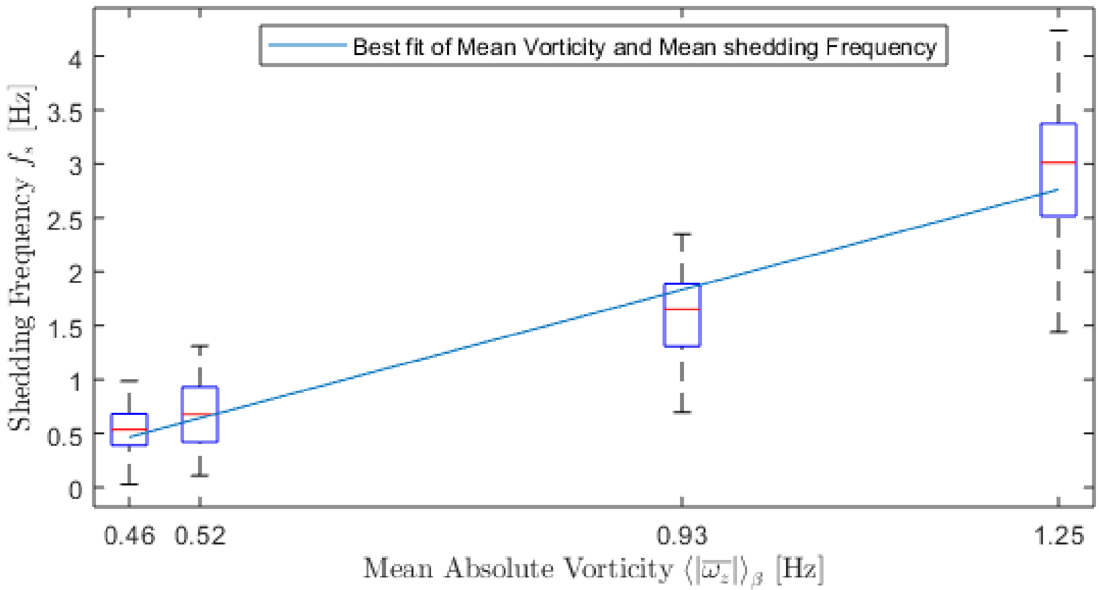

Figure 3.1.3-7. Linear best-fit of shedding frequency as a function of mean absolute vorticity.

Figure 3.1.3-7 shows a strong correlation between the increase in mean absolute vorticity and shedding frequency. This illustrates a possible relationship between a time-averaged descriptor of vorticity, or rotational motion[6], shedding frequency and subsequently Strouhal number. However, experimental limitations make this dataset insufficient to conclude a valid applicable relationship.

From this section, the following conclusions can be drawn: ***1)*** for the purposes of calculating the shedding frequency as the reciprocal of retention time, $\overline{\tau}$, for the White and Nepf (2003) model, a single value of f_s does not represent the variation in retention time in the array. A characterisation that takes into account the effects of shear and background turbulence is needed. ***2)*** Whilst the actual frequency might change for different stems within a vegetated reach, its non-dimensional parameter, Strouhal number, S_t, will not vary significantly. This means that even for high vorticity, an effective removal of mass from the inner wake will greatly depend on the mean longitudinal velocity, as this will describe the speed with which vortices are transported downstream. ***3)*** An experimental relationship between shedding frequency and a descriptor of mean vorticity can be obtained, but more data is needed to assert the validity of this statement.

3.1.3.2.3. Computation of velocity fluctuations along the wake centreline *Xsc* – Calculation of velocity fluctuation variance $\boldsymbol{\sigma_w^2}$ in the secondary wake

Eq. 3.1.3-7 presents the general expression for the effect of the secondary wake on longitudinal dispersion, as proposed by White and Nepf (2003). The most important parameter is the non-dimensional variance, σ_w^{*2}, of wake-induced velocity fluctuations, u_w''. This parameter is derived from a conditional average of the RANS equation, and dimensional simplifications, which only includes points within the secondary wake of a stem. Considering a normalized coordinate system (x^*, y^*) with origin at the end of the primary wake (i.e. point *p* from Figure 3.1.3-2c), so that its variation downstream is independent of flow upstream, White and Nepf (2003) defines the wake-induced velocity u_w'' as,

$$u_w''(x^*, y^*) = -\frac{C_D U_\infty \sqrt{Re_t}}{4\sqrt{\pi x^*}} \exp\left(-\frac{Re_t\, y^{*2}}{4x^*} - C_D a dx^*\right) \qquad \textit{Eq. 3.1.3-10}$$

Eq. 3.1.3-10 is equivalent to the expression for the mean velocity in the far wake, from a circular cylinder, presented by Schlichting (1979, Eq. 24.39), with an additional first order decay term, $C_D a dx^*$, that represents the effect of upstream drag on the stem of analysis. This expression

[6] Just as mean absolute vorticity is a parameter, we can have angular velocity, maximum vorticity or a fraction of it to describe the evolution of f_s.

takes into account two important physical phenomena. First, cylinder drag is the dominant driver of turbulence and turbulent diffusion (Nepf, 1999) through wake production (Raupach and Shaw, 1982; Finnigan, 2000). Hence, a drag coefficient will dictate the magnitude and extension of turbulent effects. Second, wake-related turbulence is unaffected by background turbulence, and decays to zero after the effect of vegetative drag is dissipated or entirely diffused.

Both assertions are based on the assumption of a local energy equilibrium, which, for a single stem (Eq. 3.1.3-10) cannot be asserted (Nikora, 2000). This is due to the fact that an energy equilibrium considering wake production similar to dissipation is done for a spatial average of the flow field (Finnigan, 2000). This, in turn, requires a spatial extent sufficiently larger than the largest spatial heterogeneities in order to comply with the averaging theorems (Monin and Yaglon, 1971, p. 207). In other words, the balance between production and dissipation should be considered at an array level, not for a single stem, especially when the balance at a specific stem is affected by the effects of adjacent stems.

The expression given in White and Nepf (2003), for secondary wake dispersion, is based on the assumption that turbulence effects and mean velocity heterogeneities are independent, and consequently considered separately. From the analytical definition of cylinder-induced variations in mean velocity, given in Eq. 3.1.3-10, a characteristic velocity scale, defined as the variance of mean velocities, can be defined by adding the perturbations caused only be secondary wakes in a vegetated reach, as presented in Eq. 3.1.3-11.

$$\sigma_w^2 = \int_{x_0^*}^{\infty} (u_w''(x) - U)^2 p(u_w'') du_w'' \qquad \textit{Eq. 3.1.3-11}$$

The mean longitudinal pore velocity U is considered equal to the average obtained from only secondary wake contributions (Eq. 3.1.3-10). This is a consequence of the assumption of negligible momentum contributions from gaps between stems presented above. White and Nepf (2003) propose the following analytical solution to Eq. 3.1.3-11, from the definition of u_w'' given in Eq. 3.1.3-10.

$$\sigma_w^2 = \frac{U^2}{16\sqrt{\pi}} \Gamma\left(\frac{1}{2}, 2x_0^* C_D ad\right) \sqrt{C_D^3 \, ad \, Re_t} \qquad \textit{Eq. 3.1.3-12}$$

To evaluate Eq. 3.1.3-12 it is necessary to know the drag coefficient, C_D, and the turbulent Reynolds number, $Re_t = Ud/\,(\nu + \nu_t)$, where the eddy diffusivity, ν_t, depends on the Reynolds stresses along the secondary wake. Experimental estimations of these quantities are presently unattainable for full vegetated arrays. Two alternatives for the scale of the velocity heterogeneities (σ_w^2), in order to compute $D_{x,s}$ are explored in this work. First, the dispersive fluxes, $\langle \overline{u}''\overline{u}'' \rangle$, available from the SPIV data, are used as a proxy for the velocity scale σ_w^2. Second, empirical estimates for C_D and Re_t, alongside a Taylor expansion approximation of the incomplete gamma function, $\Gamma(1/2\,, 2x_0^* C_D ad)$, are used to solve Eq. 3.1.3-12.

The statistical treatment of secondary wake velocities leading to Eq .7, will be analysed in detail in Chapter 3.2. For now, it should be noted that separating turbulence and mean velocities does not reflect the effects both have in the trajectory of a diffusing Lagrangian particle. To illustrate this, the points *k*, *p* and *q*, along the sample wake presented in Figure 3.1.3-2c, are selected to discuss the variations in longitudinal velocity. Figure 3.1.3-8 show the time series of longitudinal velocity of the points during a sampling interval of 30 seconds for Test 3.

The time series of longitudinal velocities elucidate some of the main features of the flow behind a stem. Points closer to the recirculation zone (points *k* and *p*) show higher variability, indicating higher turbulence production, which tends to dissipate as the area of analysis moves further downstream (point *q*). Below, the spatial variation along the axis X_{sc} of: the mean longitudinal velocity U, mean transverse velocity V, mean vorticity magnitude $|\Omega|$, turbulence intensity of longitudinal velocity u_w^+, and turbulence intensity of transverse velocity v_w^+, are shown. It is important to note that the subscript w means that the quantities described are referred to the wake centreline.

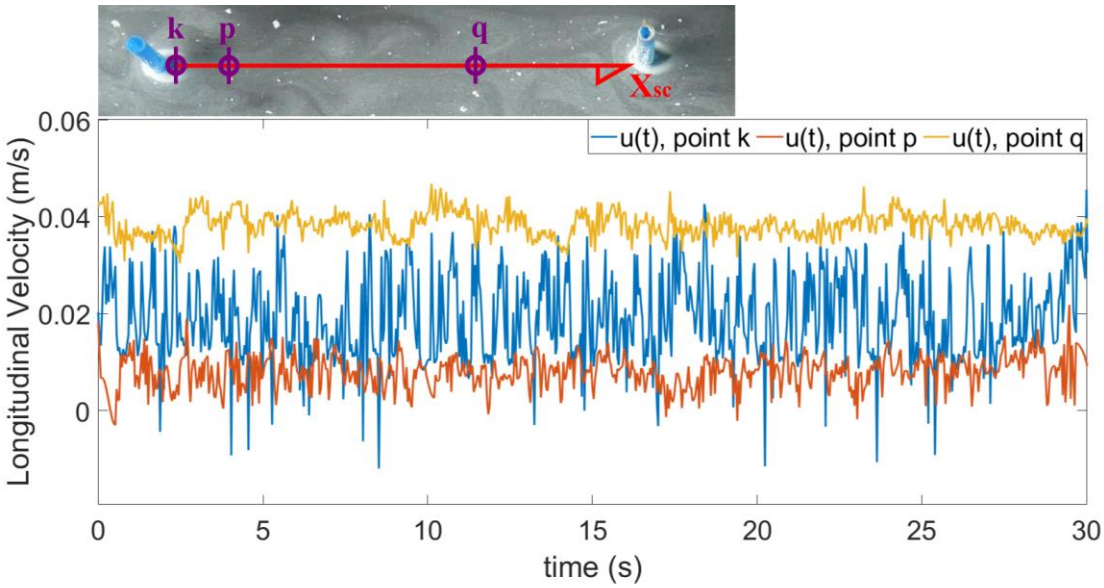

Figure 3.1.3-8. Time series of Longitudinal velocity at point k (recirculation region), p (shedding point), q (further within the secondary wake).

Spatial analysis of the wake – variation with respect of the wake centre line

Longitudinal Velocity U

The variation of time-averaged velocity along the wake centreline (see Figure 3.1.3-9) shows that an effective reduction in mean velocity occurs upstream of stems, meaning that recirculation zones (cf. primary wakes) should be considered as the entire boundary layer area around stems. This reduction in velocity is coupled with zones of velocities above advection, further downstream from the wake. The variance of mean velocities is clearly proportional to Reynolds number, which is the basis for assuming dispersive fluxes as an appropriate proxy for the velocity scale σ_w^2.

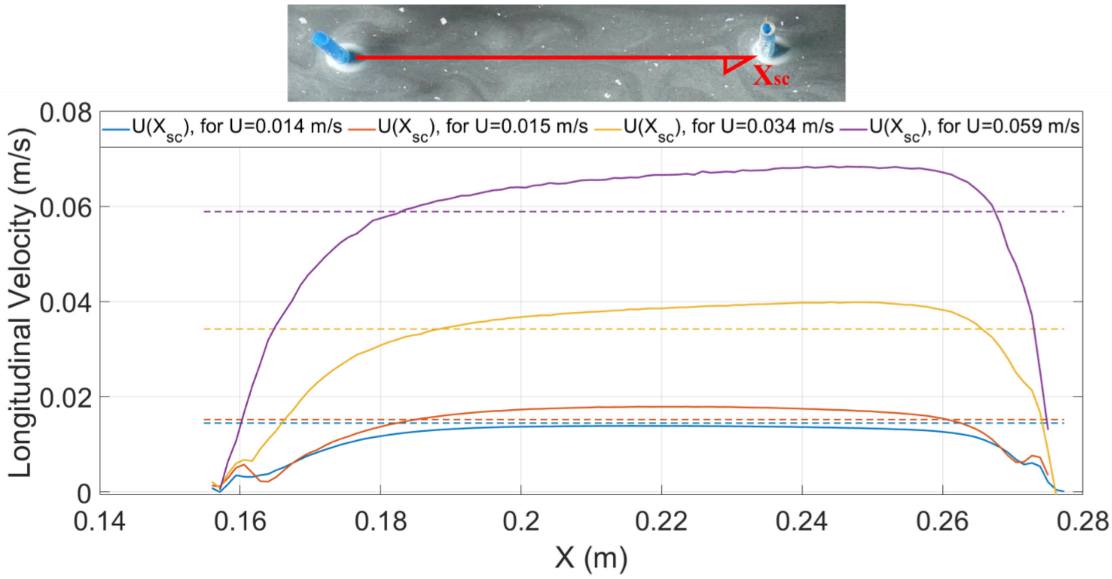

Figure 3.1.3-9. Variation of mean longitudinal velocity along the line Xsc describing the wake centreline of a single stem. Dashed lines represent mean pore velocities for each test.

Transverse Velocity V

Similar to the region of velocity damping found for longitudinal velocity in Figure 3.1.3-9, we can see an increase in negative transverse velocity (i.e. transverse velocity magnitude) as the centreline approaches a downstream cylinder. This could imply that mechanical transverse dispersion takes effect before the actual stem, or simply that this increase reflects the circulation effect of the stem.

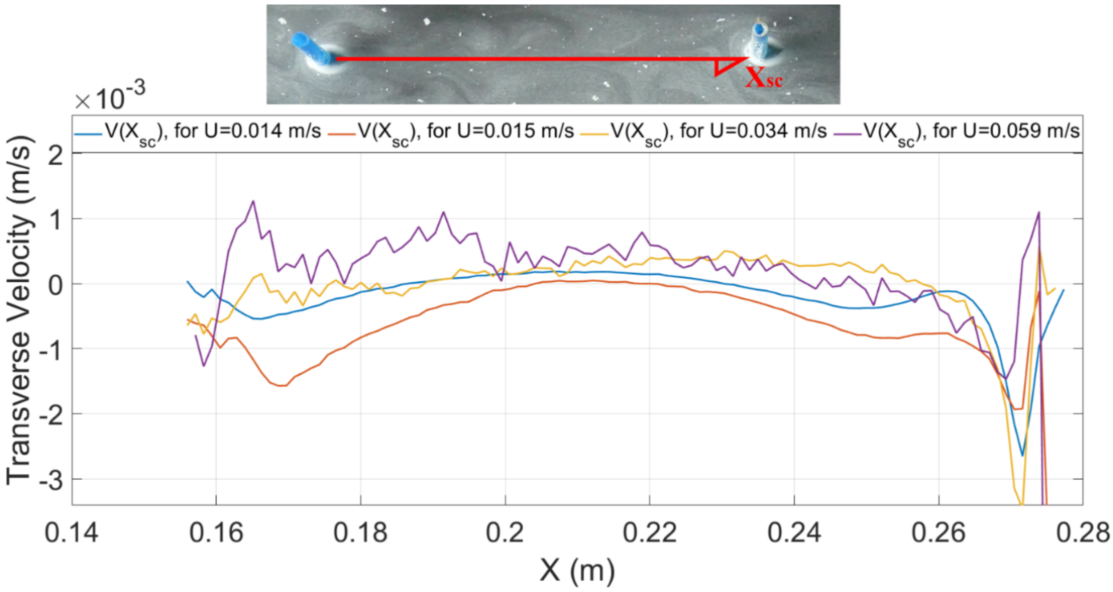

Figure 3.1.3-10. Variation of mean transverse velocity along the Xsc describing the wake centreline of a single stem.

Variation of Vorticity

As we have seen earlier, vorticity is defined in part by the longitudinal gradient in transverse velocity, and this plots of vorticity corroborate that. Additionally, vorticity appears some distance upstream of a stem, which reinforces the hypothesis that the primary wake is not limited to the rear of a cylinder.

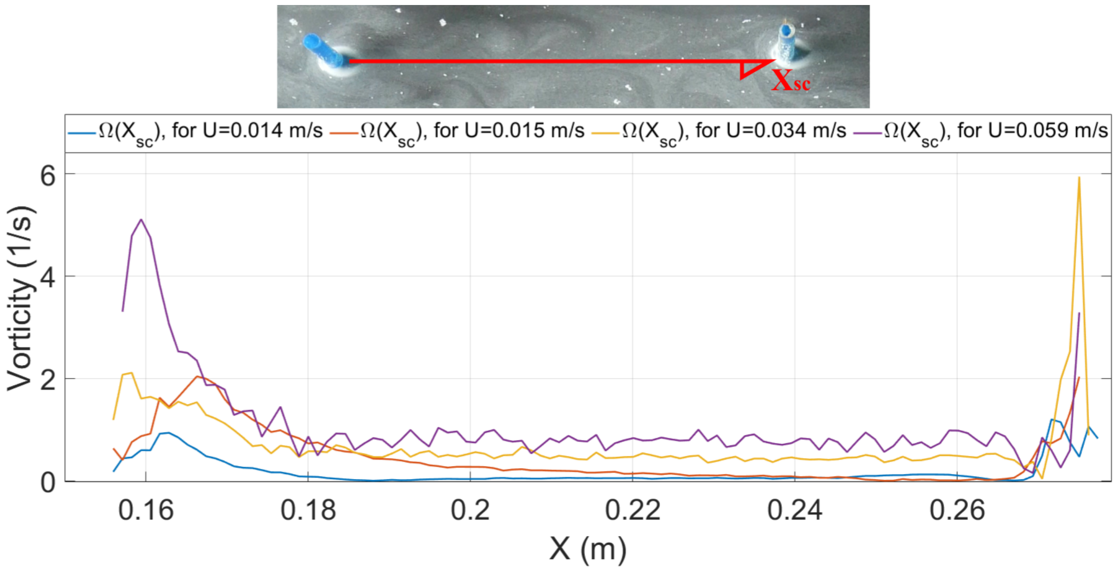

Figure 3.1.3-11. Variation of mean vorticity and mean absolute along the line Xsc describing the wake centreline of a single stem.

Variation of Streamwise Wake Turbulence Intensity u_w^+

As presented in (Paranthoën *et al.*, 1999), the peak of longitudinal turbulence intensity is found at the end of the recirculation region, along the wake centreline. Figure 3.1.3-12 corroborates these findings. Further, it can be seen that value of background (i.e. unperturbed) turbulence intensity is proportional to Reynolds number, for all the tests analysed.

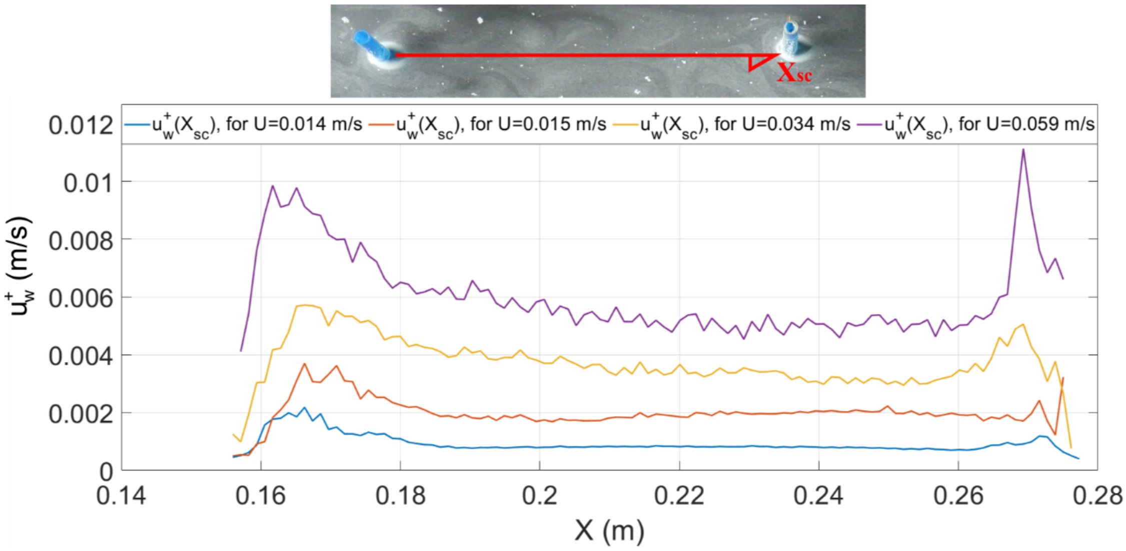

Figure 3.1.3-12. Variation of Turbulence Intensity of longitudinal velocity along the line Xsc describing the wake centreline of a single stem.

Variation of Transverse Wake Turbulence Intensity v_w^+

The smooth slope with which v_w^+ varies shows that the diffusive effect decays more slowly along the wake when compared with that of u_w^+. This implies that the evolution of the wake width and length with distance downstream is dominated by the diffusive effect of turbulence in the transverse direction.

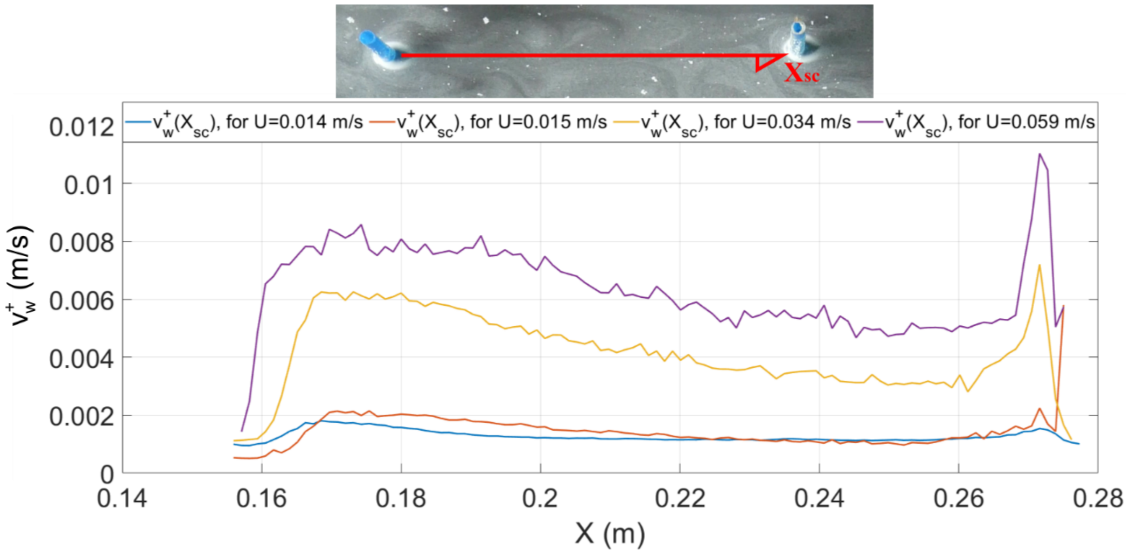

Figure 3.1.3-13. Variation of Turbulence Intensity of Transverse velocity along the line Xsc describing the wake centreline of a single stem.

Figure 3.1.3-9 to Figure 3.1.3-13 show that in general, the effect of the secondary wake downstream from a stem may be dominated by the presence of a stem further down. The decay rate of turbulence in the wake of a stem can reveal important effects related to diffusion. For the case of u_w^+, the rapid initial increase and subsequent quick decay means that diffusion due to longitudinal velocity fluctuations occurs early in the secondary wake, and further downstream, dispersion is dominated by advection, until a new stem is found. Similarly, the main contribution to mean velocity heterogeneities comes from the velocity defect zone at the onset of the secondary wake, as can be seen from Figure 3.1.3-9. However, this is the case only for low Re_d, where wake velocities reach U downstream from each cylinder. For higher values of Re_d and stem densities, local advective acceleration pathways are created to compensate the increasing resistance to flow. In other words, the assumptions leading to the expression for $D_{x,s}$, presented by White and Nepf (2003), and shown in Eq. 3.1.3-7, are expected to be valid for low Reynolds numbers and sparse configurations. The next section presents the estimation of these parameters and the comparison with experimental estimations of D_x.

3.1.4. Computation of Dispersion Coefficients from Experimental Data

After presenting the criteria to calculate the necessary parameters to compute longitudinal dispersion, this section describes how each parameter was computed from Surface PIV data, the summary of results is given in Table 3.1.4-1.

Turbulent Diffusion D_t

The proportionality constant α_2, shown in Eq. 3.1.3-3, has been found to vary between 0.1 and 0.2 for vegetated reaches with solid volume fraction less than 0.1 ($ad \leq 0.1$). A value of 0.2 was chosen.

The turbulence scale presented in Eq. 3.1.3-3, the square root of turbulent kinetic energy, $\sqrt{k}$, was obtained as the spatial average of $\sqrt{k}$ for all points within the flow field, a single estimate for each test was obtained. A list of all turbulence intensities found is given in the third column of Table 3.1.4-1.

Vortex Trapping Dispersion $D_{x,v}$

The proportionality constant β (Eq. 2.3-8, Chapter 2), has been found to be of order 1-10, for a wide range of vegetation densities, and values of 3.2 and 2.3 have been reported by Lightbody and Nepf (2006b, 2006a) and White and Nepf (2003), respectively. A value of 3.2 has been chosen to reflect that we must account for the variation in shedding frequency, and therefore increase in trapping.

ϵ_w (proportion of wakes occupied by primary wakes), is evaluated from the maps of mean longitudinal velocity and mean vorticity, according to the conditions expressed in Eq. 3.1.3-9. It was found that for the tests with low velocities, where a trapping zone is expected at the rear of the stem and will extend approximately 2 diameters downstream, the values 0.5 and 0.1 for α_w and ϵ_w, respectively, were chosen for the estimation. The values of ϵ_w found for each test are given in the 4th column of Table 3.1.4-1.

S_t (Strouhal number), the values found for the ensemble average of the frequencies found for a sample of stems in the maps are given in Table 3.1.3-1, and repeated in the 5th column of Table 3.1.4-1.

Secondary wake Dispersion $D_{x,s}$

Two alternatives for the calculation of σ_w^2 (variance of spatial velocity heterogeneities in the time-averaged velocity field caused by secondary wakes, Eq. 3.1.3-7), are explored. First, dispersive fluxes $\langle \overline{u}''\overline{u}'' \rangle$, see Eq. 2.2-42 (Chapter 2), are computed from the SPIV maps of mean longitudinal velocity and used as a proxy for σ_w^2. Second, σ_w^2 was computed from the analytical solution shown in Eq. 3.1.3-12, using the same empirical value for Re_t presented in White and Nepf (2003), and C_D was obtained from Tanino and Nepf (2008a) empirical model for array drag. The estimations from the first alternative are presented in Table 3.1.4-1, and all alternatives are compared to experimental results for D_x in Figure 3.1.4-2.

Sc_t, the turbulent Schmidt number (Eq. 3.1.3-7), expresses the ratio between eddy diffusivity and eddy viscosity; a value of $Sc_t = 1$ is typically a good assumption for a wide range of transitional and turbulent flows (Hinze, 1975).

s^* (non-dimensional mean spacing between stems, Eq. 3.1.3-7), this value is defined as $s^* = s/d$, where s is the mean (edge-to-edge) spacing between stems. To calculate the mean spacing, it was necessary to describe the spatial variation of stems along the entire bed array. This was done by performing a triangulation between all stems and finding the probabilistic distribution of the distances between them. To save consistency and space, Figure 3.1.4-1a shows a subsample of the triangulation for the SPIV window to illustrate the process, and Figure 3.1.4-1b shows the resulting spacing distribution. It is important to clarify that not all lines joining two stems represent a valid stem-to-stem spacing, e.g. the lines drawn at the edges of the triangulation. To avoid errors induced by this, all outer edges were removed from the distribution. The mean stem spacing, considering the probabilistic distribution shown in Figure 3.1.4-1b, was found to be $s = 0.051$ m, and non-dimensionalised with stem diameter yielded $s^* = 12.7$. In other words, all stems are separated on average, a distance of 13 diameters between each other.

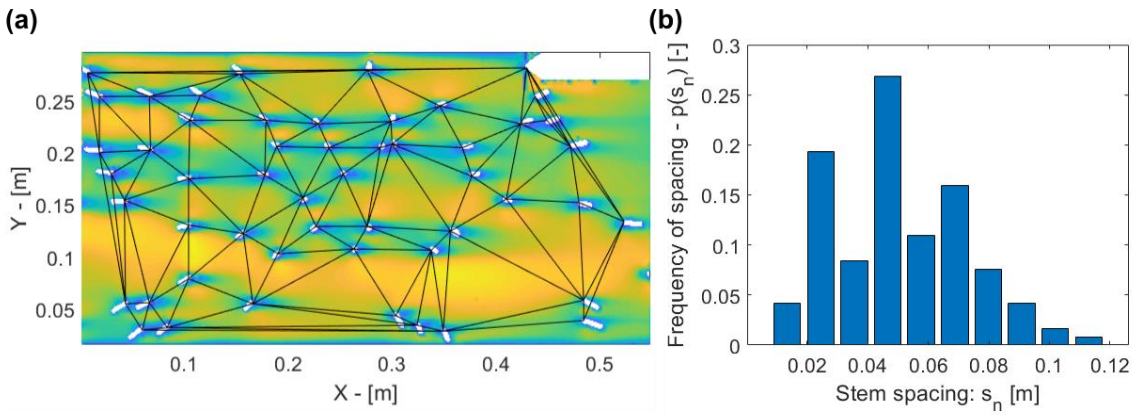

Figure 3.1.4-1. a) Triangulation between stems for the calculation of the mean stem spacing. b) Distribution of stem spacing for all tests, mean stem spacing was found to be 0.06 m.

Considering the foregoing parameters, we now proceed to calculate longitudinal dispersion as the result of the joint effects of turbulence, vortex trapping and secondary wakes. Estimates of each dispersion process are given, respectively in columns 7, 8 and 9 of Table 3.1.4-1.

Table 3.1.4-1. Parameters from SPIV maps.

TEST	U [mm s-1]	D_t $\sqrt{k}$ 1 [cm s-1]	$D_{x,v}$ ϵ_w 1 [-]	$D_{x,v}$ S_t 1 [-]	$D_{x,s}$ σ_w^2 1 [m2 s-2]	D_t [m2 s-1]	$D_{x,v}$ [m2 s-1]	$D_{x,s}$ [m2 s-1]	D_x [m2 s-1]
1	14.5	0.19	0.072	0.15	1.6e-5	1.5e-6	0.9e-4	7.9e-5	1.7e-4
2	15.2	0.18	0.072	0.17	1.9e-5	1.5e-6	0.8e-4	9.0e-5	1.7e-4
3	34.0	0.49	0.063	0.19	7.9e-5	3.9e-6	1.4e-4	1.7e-4	3.2e-4
4	59.0	0.71	0.043	0.20	1.8e-4	5.7e-6	1.6e-4	2.2e-4	3.8e-4

1 These columns specify to which dispersion component each of the computed quantities belong, e.g. the fraction of the flow field occupied by primary wakes, ϵ_w, is a quantity needed to compute the vortex trapping dispersion coefficient.

The computed values for D_x, using the experimental SPIV data, are comparable for low flow rates, but underpredict the values obtained experimentally, for $Re_d > 100$. Vortex trapping dispersion, $D_{x,v}$, decreases with increasing Reynolds number, as expected, knowing that after the threshold for shedding frequency has been surpassed ($Re_d \approx 70$) vortex shedding causes the retention time to drop rapidly.The spatial effects of secondary wakes are more prominent than vortex trapping because they make up a bigger portion of the flow field, which has been shown experimentally by Sonnenwald *et al.* (2017). Also, turbulent diffusion appears to play no role in the longitudinal dispersion of dye; this, although physically unrealistic, follows the same observations done to the diffusion model done in previous papers (Nikora, 2000; Ricardo, Franca and Ferreira, 2016; Sonnenwald *et al.*, 2017).

This under prediction of $D_{x,s}$ is the result of the value of σ_w^2 calculated for all tests, which reveals some shortcomings of the model given in Eq. 3.1.3-10 and Eq. 3.1.3-11, the most prominent being the fact that local convective acceleration becomes more prominent with increasing Re_d. The experimental results presented, and summarised in Figure 3.1.4-2, confirm the idea that velocity defect areas are the primary driver of secondary wake dispersion, for low flows. However, this conclusion is only applicable to sparse configurations ($\varphi \approx 0.005$), where minimal interaction between stems occur, and each behave as an isolated element. The low resistance to flow in sparse configurations also implies that velocity fields downstream from stems recover to uniform conditions, as further obstructions are less likely to be found. Higher densities, on the other hand will tend to generate high conveyance pathways as stem sheltering starts to occur. These local acceleration zones are expected to be more significant in the estimation of mean velocity heterogeneities for denser configurations.

An alternative to the model for $D_{x,s}$ given in Eq. 3.1.3-7, is the simplified expression by Lightbody and Nepf (2006b) for emergent vegetation with solid fractions $\varphi \leq 0.1$

$$D_{x,s} = \frac{1}{2} C_D^{3/2} U d \qquad \text{Eq. 3.1.4-1}$$

For the quantification of C_D, Tanino and Nepf (2008a) relied on the empirical expression derived by Ergun (1952),

$$C_D = 2\left(\frac{\alpha_a}{Re_d} + \alpha_b\right) \qquad \text{Eq. 3.1.4-2}$$

Where α_a and α_b are best-fit coefficients that depend linearly on stem diameter d and solid volume fraction φ.

$$\begin{aligned} \alpha_a &= 7276.43d + 23.55 \\ \alpha_b &= 32.70d + 3.01\varphi + 0.42 \end{aligned} \qquad \text{Eq. 3.1.4-3}$$

If we compute secondary wake dispersion from Eq. 3.1.4-3, using the empirical coefficients just given, we find that the effects of longitudinal dispersion are now those presented in Table 3.1.4-2.

Table 3.1.4-2. Parameters using the simplified expression for $D_{x,s}$

TEST	$\boldsymbol{U}$ *[cm s^{-1}]*	$\boldsymbol{D_t}$ *[m^2 s^{-1}]*	$\boldsymbol{D_{x,v}}$ *[m^2 s^{-1}]*	$\boldsymbol{D_{x,s}}$ *[m^2 s^{-1}]*	$\boldsymbol{D_x}$ *[m^2 s^{-1}]*
1	*14.5*	*1.5e-6*	*0.9e-4*	*1.5e-4*	*2.4e-4*
2	*15.2*	*1.5e-6*	*0.8e-4*	*1.5e-4*	*2.3e-4*
3	*34.0*	*3.9e-6*	*1.5e-4*	*1.8e-4*	*3.3e-4*
4	*59.0*	*5.7e-6*	*1.6e-4*	*2.4e-4*	*4.0e-4*

Figure 3.1.4-2 shows the results of the tracer tests in terms of mean and standard deviations (box plots), taken from the optimised dispersion coefficients shown in Figure 3.1.2-2. These results were compared with the different approaches presented: the model for $D_{x,s}$ with σ_w^2 calculated using dispersive fluxes as a proxy; using empirical estimations of C_D and Re_t for the analytical solution to Eq. 3.1.3-12 (as presented in White and Nepf, 2003); and with the simplified expression using C_D.

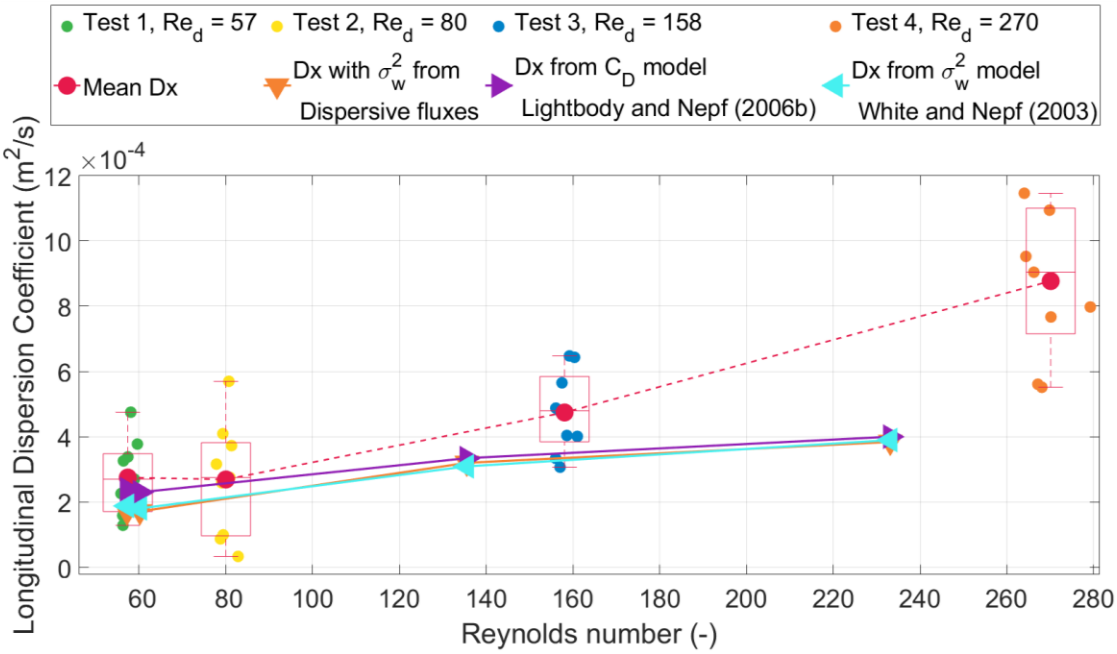

Figure 3.1.4-2. Comparisons of results from tracer tests and predictions using velocity information from SPIV data.

Results from dispersion models and experimental measurements are comparable for low Reynolds numbers, i.e. $Re_d < 100$. The simplified model for secondary wake dispersion (Eq. 3.1.4-1) predicts the experimental data marginally better this range; the results fall within the 2 central quartiles from the distribution of D_x values obtained experimentally. For the last tests, $Re_d > 100$, the difference between experiments and estimations increases with Re_d. Note that trapping behind stems is expected to decrease due to higher rates of mass transfer between the recirculation zones and the outer flow; however, the opposite trend is found from the estimates in Table 3.1.4-1. The approach for the area of primary wakes, ϵ_w, used herein is a function of Re_d, as proposed in White and Nepf (2003), however, the behaviour of this dependency requires further analysis. Seeing that boundary layers around stems define the extent and induce the trapping into primary wakes, and from Figure 3.1.3-9, it is seen that these decrease with increasing Re_d, it is in the author's believe that ϵ_w is inversely proportional to Re_d.

Another important factor to consider is the effect of wake interactions, which are overlooked in Eq. 3.1.3-10. One can imagine that a particle that has experienced turbulence from a stem, when enters the secondary wake of another stem its state of motion (i.e. diffusivity) will get amplified, so, for an actual variance of wake-induced velocity fluctuations to be physically consistent, we must add the effects of wake interactions, which are linked to the existence of *coherent structures*. This will be explored via velocity statistics in Chapter 3.2. In conclusion, the model presented by White and Nepf (2003) to characterise longitudinal mixing is reliable for low Reynolds numbers, and sparse configurations, for all alternatives to compute $D_{x,s}$. However, it has been found that some physical assumptions behind the expressions for dispersion require further analysis, particularly those associated with treating dispersion components as independent.

3.1.5.Conclusions

A complete physical characterisation of the physical parameters needed to quantify longitudinal dispersion from velocity information, obtained through Surface PIV has been presented. Specifically, the analysis focused on vortex trapping and secondary wake dispersion. For vortex trapping, the shedding frequencies measured from the velocity data were found to vary little from the values measured in the literature. Indeed, the variation in Strouhal number is found to be small compared to that of the area of primary wakes. Although the model for vortex trapping, $D_{x,v}$, is physically sound; there are still remaining questions regarding the spatial characterisation of the primary wake. An empirical definition, based on the effects of increased vorticity and longitudinal velocity defects has been proposed, but a detailed analysis of its validity is still in order. Also, it should be remarked that the computation of shedding quantities (i.e. f_s and S_t) requires a detailed spatial description of the vegetated reach, which, due to experimental or field limitations might not be always achievable. alternatives that can relate these quantities to macroscopic descriptors of vegetation, e.g. mean vorticity magnitude, for practical applications, should be explored. Figure 3.1.3-7 shows that such a relationship can be constructed with the available data, but the nature of this relationship, and the extension to other cases requires further analysis.

All approaches for secondary wake dispersion were found to perform similarly, which confirms the validity of White and Nepf (2003) solution for wake velocities, for low Reynolds numbers. However, both the assumptions and the model under predicted dispersion for $Re_d > 100$. This mismatch is also expected for larger stem densities where stems interactions are expected. For the solid volume fraction analysed here, most stems in the array are expected to behave as isolated elements (unaffected by the effects of neighbouring stems), as their mean separation is approximately 13 diameters (Sumner, 2010). For isolated stems (cylinders), the induced flow perturbation is mainly the result of the velocity defect in the secondary wake. From this premise, the White and Nepf (2003) analytical model for $D_{x,s}$ treats velocity heterogeneities as the superposition of flow perturbations from individual stems. This analysis overlooks the effects of near- and far-wake interactions, which, for denser distributions and larger Reynolds numbers can induce acceleration regions between stems and thus increase the scale of mean velocity heterogeneities, as the experimental results in Figure 3.1.4-2 suggest.

Lastly, it is in the author's opinion that the analysis behind the secondary wake dispersion component, $D_{x,s}$, (cf. differential advection) should be revised. Even though, generally, features like increased turbulence production and spatial velocity heterogeneities are correctly included in the model presented in White and Nepf (2003), some issues remain. First, assumptions of negligible contributions from background turbulence and local advective acceleration on dispersion, as depicted in the development of Eq. 3.1.3-10, do not match the persistence of these quantities seen in experimental results (see Chapter 3.2). Second, dispersion from velocity statistics is defined for a Lagrangian frame of reference, and its use on time-averaged velocity fields is not justified. Lumley (1962) showed that a direct Lagrangian-Eulerian transformation of the velocity correlation function cannot be analytically achieved. Any use of the correlation function, as proposed initially by Taylor (1922), must consider these caveats in detail.

3.2. EXPLORATION OF VEGETATED HYDRODYNAMICS USING MULTI-POINT VELOCITY STATISTICS

3.2.1. Introduction

In vegetated flows, turbulence processes are associated with the presence of stems and evolve along their wakes. Diffusion is therefore determined by turbulent characteristics along each stem wake, and their mutual interactions. This research presents a series of experiments, designed and executed to describe two-point velocity statistics along cylinder wakes (a surrogate for stem wakes), within a vegetated flow. For this, Acoustic Doppler Velocimeters (ADVs) were used to obtain simultaneous velocity measurements from a reference point in the onset of a wake and several points downstream. This procedure allows for the experimental construction of a velocity correlation curve, and subsequently the computation of early-stage diffusion profiles, relative to cylinder wakes, purely from turbulent velocity data. The results show that an approximation of quantities, such as the width of a wake and the turbulent dispersion coefficient, can be obtained from the dataset. Furthermore, the results are used to study the interactions between adjacent wakes and their impact on the overall diffusion of mass through a vegetated system.

Previous studies have explored the problem of solute transport in vegetated flows from a physical perspective. In the formulation of two-dimensional vegetated dispersion (see Section 2.4) the contribution from molecular and turbulent diffusion are considered isotropic phenomena (Nepf, Sullivan and Zavitoski, 1997; Nepf, 1999), as turbulent structures have the same extent in the streamwise and transverse direction. The additional contributions caused by the presence of stems: shear, path tortuosity and trapping are considered directional components. Specifically, the following physical phenomena are considered:

a) Streamwise Dispersion is caused by vortex trapping and differential advection. The former refers to the existence of a recirculation zone behind each stem, and the latter represents the difference in mean velocities between low velocity zones behind stems and high velocity areas between stems. Generally, vortex trapping is expected to decrease for increasing Reynolds numbers; the opposite trend is expected for differential advection. Both are also predicted to be proportional to vegetation density (White and Nepf, 2003).

b) Transverse Dispersion is caused by transverse velocity fluctuations and mechanical dispersion. The latter refers to the spread in variance of particles as they encounter physical obstructions. When compared with vegetation density, the number of collisions increases for denser vegetated reaches, thereby enhancing mechanical dispersion whilst decreasing the porous space and, the scale of turbulence and thus the effect of turbulent dispersion (Tanino and Nepf, 2008b). Transverse dispersion is mainly dependent on vegetation morphology.

Both models were developed from the Stokes' flow analysis of porous and fibrous media given in Koch and Brady (1985, 1986). This limits the applicability of the models and the physical reasoning behind them. Consequently, White and Nepf (2003) confine the validity of their model to low and moderate stem Reynolds numbers ($10 < Re_d < 1000$). Following previous experimental studies quantifying dispersion under these conditions (Serra, Fernando and Rodríguez, 2004; Huang *et al.*, 2008; Shucksmith, Boxall and Guymer, 2010; Sonnenwald *et al.*, 2017), no strong trends could be identified between dispersion metrics (i.e. coefficients) and solid volume fraction or Reynolds number. It is in the author's belief that this mismatch between experimental evidence and theoretical predictions highlights the need for better characterisations of the vegetated velocity field. Particularly regarding coherent structures, which dominate mass and momentum transfer along and between stem wakes.

A thorough study of wake interactions should take into account the effects of stem spacing and relative orientations (Sumner, Richards and Akosile, 2005), on several different parameters, e.g. sheltering and drag coefficient decay (Bokaian and Geoola, 1984), and vortex shedding/Strouhal number and fluid forces (Zhou *et al.*, 2009; Tong, Cheng and Zhao, 2015; Zhou and Mahbub Alam, 2016; Kim and Christensen, 2018). Several useful insights are extracted from these experimental and numerical studies. Overall, sheltering induces a decrease in vortex shedding frequency for downstream cylinders (thereby increasing the trapping time behind stems), as well as in incoming hydrodynamic forces. A further exploration of this is given in Chapter 7. No strong inference can be made about drag coefficients as they fluctuate depending on spacing and orientation.

These results are obtained from aerodynamics studies and thus provide useful insights on stability, resonance and acoustic noise; and some results on drag can be extrapolated to the problem of vegetated flows. However, the data for these studies is limited to the near wake

($x^* = x/d < 3$, from the cylinder centre) and does not offer information on the downstream evolution of the wakes, which is the region of interest for the study of diffusion. Further, most of these studies were undertaken using planar techniques, or point-based measurements around individual or cylinder pairs. Reproducing these studies in vegetated flows presents a challenge, as experimental limitations exist to the velocity characterisation within full vegetation arrays. For planar optical methods, such as PIV, the presence of obstructions generates shadowing and undesired refractions of light. Further, the intrusive nature of point-based measurements (LDA, ADV), makes them sensitive to optical, acoustic and physical interferences, from both the instruments and the stems. Point-based measurements are presented in this chapter, for a sparse configuration of stems, to study first and second order velocity statistics over a pair of interacting wakes. A novel experimental configuration to resolve spatial velocity fields, using planar optical techniques in vegetated arrays is presented in Chapter 4, the measured velocity fields are presented and analysed in Chapter 6 and Chapter 7.

This chapter presents an experimental study designed to obtain a velocity characterisation relevant to vegetated diffusion (i.e. two-point statistics). The flow is located within a sparse, randomly distributed vegetation[7], with cylinders as surrogates for stems. Two-point velocity statistics, necessary to describe dispersion metrics, were obtained from simultaneous measurements with fixed and mobile ADV probes. The Reynolds numbers, reference cylinders (stems) location and orientation were selected to avoid acoustic and physical interferences, whilst also providing a representative sample of points from two adjacent cylinders. The space between cylinders was selected to avoid near wake interference, but allow secondary wake interactions.

Before a description of the set-up, it should be explained that the analysis of velocity statistics from secondary wakes was motivated by a critical analysis of White and Nepf (2003) model for longitudinal dispersion. Specifically, the assumptions leading to the secondary wake dispersion component. Note that the model is the best theoretical approach to the problem so far, with a thorough phenomenological description that has served as the foundation for many subsequent analyses. Its importance should always be acknowledged. However, the treatment of velocity statistics, and their use alongside Taylor (1922) Theory of Diffusion, negates some important underlying conditions for its application, thus hindering its reproducibility.

[7] The cylinder distribution was obtained as the central third of the RandoSticks configuration described in Chapters Chapter 4 and Chapter 4, but only considering cylinders with 20 mm diameters.

Dispersion predictions based on this model, and presented in Chapter 3.1, indicate that, except for very sparse configurations ($\varphi < 100$), the extent of stem-induced velocity heterogeneities are underestimated. Section 3.2.1.1 presents a discussion of the main assumptions in question, which will then be contrasted with the experimental results. A final descriptions of the general problem of mass transfer between interacting wakes is presented at the end of the chapter.

3.2.1.1. Previous Model and Rationale for the ADV study

The purpose of this study is to use velocity statistics to inform dispersion models in vegetated reaches, an undertaking that has, to the author's knowledge, no precedent in the relevant literature. The main models for longitudinal and lateral dispersion in vegetated flows have been proposed by White and Nepf (2003), and (Tanino and Nepf, 2008b, 2009), respectively. These approaches are based on Koch and Brady (1985, 1986) models for diffusion due to mean velocity heterogeneities caused by random arrays of spheres in Stokes flow. When compared to practical cases of turbulent flow, both the theoretical bases and the derived models for vegetated dispersion present some limitations. To understand these limitations, and provide a baseline to compare the experimental results presented here, this subsection gives an overview of the model for Longitudinal Dispersion presented by White and Nepf (2003). The assumptions will be contrasted and examined in light of the experimental results presented.

White and Nepf (2003) model for Longitudinal dispersion

Let us begin by giving the definition of the wake velocity derived by White and Nepf (2003)

$$u_w''(x^*, y^*) = -\frac{C_D U \sqrt{Re_t}}{4\sqrt{\pi x^*}} \exp - \left(\frac{Re_t y^{*2}}{4x^*} + C_D a d x^* \right) \qquad \text{Eq. 3.2.1-1}$$

where $u_w''(x^*, y^*)$ is the 'velocity defect' function, representing the mean streamwise velocity in the (far) wake of a cylinder centred at the origin. The Lagrangian autocorrelation function needed to define a dispersion coefficient, from Taylor (1922) Theory of Diffusion, TTD, is defined as,

$$\mathcal{R}_i(\tau) = \lim_{N\to\infty} \frac{1}{N} \sum_{n}^{N} v_{i,n}'(0)\, v_{i,n}'(\tau) \qquad \text{Eq. 3.2.1-2}$$

where $v_{i,n}'$ is the Lagrangian velocity function, in the i-th direction, of the n-th particle in a statistical ensemble, comprising N independent particles. The application of TTD for Eq. 3.2.1-2 must comply with 2 conditions related to Lagrangian functions (Batchelor, 1949). 1) the ensemble of moving particles must be stochastic (deviations from average behaviour being the result of randomness) and 2) mutually independent (trajectories of each particle must be independent of neighbouring ones). Clearly, the velocity function $u_w''(x^*, y^*)$ cannot be applied directly to obtain a Lagrangian (relative to the particle) correlation function, $\mathcal{R}_i(\tau)$. First, u_w'' is defined over fixed spatial points (i.e. Eulerian). Second, as a mean velocity field, u_w'' is deterministic, in the sense that a trajectory (i.e. streamline) derived from u_w'', from the same starting point, would be the same regardless of the number of trials performed.

With this in mind, let us look at the change of domain proposed to compute $\mathcal{R}_i(\tau)$.

$$\mathcal{R}_i(\tau) \equiv \frac{1}{s}\int_{-s/2}^{s/2} v_{i,\zeta}'(0) v_{i,\zeta}'(\tau)\, d\zeta \qquad \text{Eq. 3.2.1-3}$$

where s represents the characteristic inter-stem space. However, Eq. 3.2.1-3 is at odds with the conditions required to compute stochastic quantities. The ensemble of N particles presented in the original expression for $\mathcal{R}_i(\tau)$ (Eq. 3.2.1-2) must, by definition, be the result of N different trials under the same initial and macroscopic turbulence conditions. Further, any two particles released consecutively must have no effect on each other. Clearly, by spreading the points in the ensemble over the initial domain s, we give each particle a distinct starting point, thereby eliminating the necessary conditions of reproducibility inherent to stochastic properties (Batchelor, 1949).

The Lagrangian product, $v_{i,n}'(0)v_{i,n}'(\tau)$, presented in the definition of $\mathcal{R}_i(\tau)$ (Eq. 3.2.1-2), is transformed into the equivalent Eulerian product

$$u_w''(x_o^*)\, u_w''(x^* + x_o^*, y^*)\, p(x^* + x_o^*, y^* \mid x_o^*, \xi^*) \qquad \text{Eq. 3.2.1-4}$$

Where $u_w''(x^*, y^*)$ is the Eulerian wake-induced, mean velocity defect function at point x^*, y^*. $\tilde{p}(x^* + x_o^*, y^* \mid x_o^*, \xi^*)$ is the "Gaussian propagator for the transverse diffusive motion", meaning the probability of finding a particle at a point $(x^* + x_o^*, y^*)$ after starting its motion at x_o^*. Where, the spread of particles is assumed to transport and spread according to a random walk model (Csanady, 1973, chap. 2). The superscript * is used to represent dimensionless variables: $x^* = x/d$, and $y^* = y/d$; and x_o^* is the start of the secondary wake, i.e. $x_o^* = 2.5$.

The transformation between the Lagrangian product, $v_{i,n}'(0)v_{i,n}'(\tau)$, and Eq. 3.2.1-4 is justified on physical grounds. Knowing that dispersion in vegetated flows is mechanical (i.e. driven primarily by advection), it is then possible to decompose the Lagrangian trajectory of a particle into an advective component and a diffusive one. Referring to Eq. 3.2.1-4, $u_w''(x^* + x_o^*, y^*)$

and $\tilde{p}$ represent the advective and diffusive component of the trajectory of any particle starting its motion at point x_o^*. The Gaussian propagator, $\tilde{p}$, given in White and Nepf (2003), is defined as

$$\tilde{p}(x^* + x_o^*, y^* \mid x_o^*, \xi^*) = \sqrt{\frac{Re_t\, Sc_t}{4\pi x^*}} \exp\left\{-\frac{Re_t\, Sc_t}{4x^*}(y^* - \xi^*)^2\right\} \qquad \text{Eq. 3.2.1-5}$$

Re_t and Sc_t are the turbulent Reynolds an Schmidt numbers, respectively, given by

$$Re_t = \frac{Ud}{\nu + \nu_t} \quad and \quad Sc_t = \frac{\nu + \nu_t}{D_y} \qquad \text{Eq. 3.2.1-6}$$

ν and ν_t are the kinematic and eddy viscosity, respectively; D_y is the transverse diffusion coefficient. The product $Re_t\, Sc_t$ defines the following version of the Péclet number for transverse dispersion.

$$Pe = \frac{Ud}{D_y}$$

Upon further inspection, it can be seen that p is the solution to an ADE-type equation, defined as

$$\frac{\partial}{\partial t}\tilde{p} = D_y \frac{\partial^2}{\partial y^2}\tilde{p} \qquad \text{Eq. 3.2.1-7}$$

With the well-known solution

$$\tilde{p} = \frac{1}{\sqrt{4\pi D_y t}} \exp\left(-\frac{y^2}{4D_y t}\right) \qquad \text{Eq. 3.2.1-8}$$

By applying the identity $dt = dx/U$ on Eq. 3.2.1-7, normalising the x and y coordinates, and solving the PDE, we obtain

$$\tilde{p}(x^* + x_o^*, y^* \mid x_o^*, \xi^*) = \frac{1}{\sqrt{4\pi D_y^* x^*}} \exp\left[-\frac{(y^* - \xi^*)^2}{4D_y^* x^*}\right] \qquad \text{Eq. 3.2.1-9}$$

which is equal to Eq. 3.2.1-8. The presentation of $\tilde{p}$ shown in Eq. 3.2.1-9, helps to illustrate a somewhat paradoxical result: to obtain the correlation function necessary to derive D_x we need to know D_y, which entails a similar statistical treatment in the transverse direction. Nonetheless, as dispersion is derived for long travel times, it will be expectedly constant, as informed in (White and Nepf, 2003). It should be added that, at the wake level, coherent structures dominate transverse mass transfer. Ignoring the contribution of coherence will not have a significant effect on the estimation of D_y in the Fickian regime; but it will impact the estimation of the time scale needed to reach this regime.

The final definition of the secondary wake dispersion coefficient is found from the integration of Eq. 3.2.1-10,

$$D_{x,s} = \sqrt{ad} \int_0^{\infty} \frac{dx^*}{u(x^* + x_0^*, y^*)} \int_{-\frac{s^*}{2}}^{\frac{s^*}{2}} d\xi u_w''(x_0^*) \times \int_{-s^*/2}^{s^*/2} dy^* \, \tilde{p}(x^* + x_0^*, y^* | x_0^*, \xi) \, u_w''(x^* + x_0^*, y^*) \qquad \text{Eq. 3.2.1-10}$$

Which was found to be an equation of the form (White and Nepf, 2003),

$$D_{x,s} \propto \frac{\sigma_w^2}{U} s \qquad \text{Eq. 3.2.1-11}$$

where σ_w^2 represents the variance of the time-averaged velocity field. The ratio σ_w^2/U and s work appropriately as velocity and length scales for Fickian Dispersion. When this value is derived from the modified velocity defect function, Eq. 3.2.1-1, a proportionality of the form $D_{x,s} \propto C_D^{3/2}$ is obtained, which can limit the applicability to a narrower set of Reynolds numbers and sparse configurations (see Chapter 3.1 and Chapter 7). Notwithstanding the discussion, the model provides a good scaling relationship of dispersion from mean velocity heterogeneities, and is in the author's opinion the best contribution to the problem of vegetated dispersion so far. Still, appropriate revisions can be made to the calculation of the relevant scale of velocity heterogeneities, σ_w^2, and thus provide better models for $D_{x,s}$, and extend its validity range.

In light of this, the ADV experiments were devised to check whether the velocity statistics in the near secondary wake match those from the modified Schlichting (1979) equation, given the presence of upstream cylinders. Also, whether secondary wakes interact linearly (i.e. their combined velocity field corresponds to that of linearly superimposed wakes), and thus whether advective acceleration in the gaps between cylinders can really be considered negligible.

3.2.2. Experimental Methods

To investigate diffusion and wake interactions, a series of Acoustic Doppler Velocimetry (ADV) measurements were performed along the secondary wakes of two adjacent 20 mm-diameter cylinders. These were located within a random, sparse (60 stems/m^2) array, generated to simulate uniform emergent vegetation, as shown in Figure 3.2.2-1. The experiments were conducted in a 12 m long by 0.3 m wide flume with a slope of 0.5%. Flow was supplied from a constant header tank and controlled by a valve located before the inlet. As experiments with the same flow rates had to be performed on different days, discharges were calibrated using a Valeport Model 801 EM Manual Current meter (Valeport, 2016). To do this, the current meter was located at a reference point, and the valve was operated until the target flow rate was obtained, and maintained over a period of five minutes. A constant flow depth of 160 mm within the test section was maintained for all experiments by adjusting the tail-gate at the flume outlet[8].

Smooth PVC plates were located at the bottom to avoid boundary layer effects. The test section was located at the centre of the flume to avoid wall effects, as shown in Figure 3.2.2-1a. After the flow inlet, the flume contains a flow straightener to ensure streamlined one-dimensional flow.

The experiments conducted have two purposes: first, to analyse diffusion along the secondary wake. This is achieved from the analysis of two-point velocity statistics, which are obtained by recording velocities simultaneously at two different points within the flow field. Second, to study whether the interaction between two adjacent secondary wakes enhances or diminishes mass and momentum transfer.

To construct 2-point Eulerian correlation functions, it is necessary to obtain the velocity statistics for fixed reference points, located at the beginning of the secondary wakes for each of the reference cylinders; for a set of points forming streamwise axes along the wakes centrelines (AA’ and BB’ in Figure 3.2.2-1b); and for points along transects covering the two adjacent wakes (00’, 11’, 22’, 33’ and 44’ in Figure 3.2.2-1b).

[8] All other experiments in this thesis were performed with a 150 mm flow depth. The additional depth was required to allow down-looking ADV probes to be fully submerged.

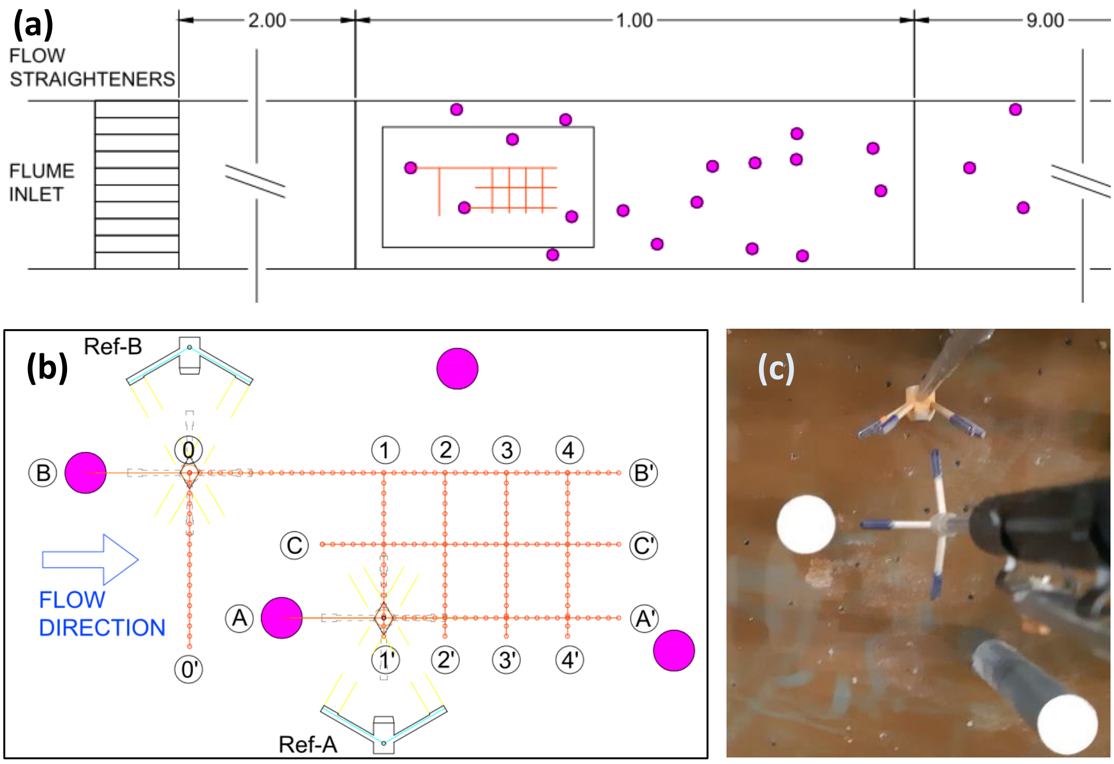

Figure 3.2.2-1. a) General plan layout of the flume and vegetation array. b) Detailed scheme of the test section and measurement points. c) Physical configuration of the ADV probes for simultaneous measurements of velocities.

The velocity measurements were taken using a side-looking and a down-looking Vectrino probe to avoid physical interferences, as shown in Figure 3.2.2-1c. For laboratory settings, ADV manufacturers (e.g. Nortek, 2018) recommend the use of additional seeding in the water to enhance the acoustic response of the probes. Polyamid 12 (Φ = 20 µm) particles were used as seeding and injected immediately after the flow straighteners, to eliminate any jet effects and residual turbulence from the injection.

To focus on the effects of the secondary wake, the fixed (side-looking) ADV probe was located 2.5d downstream from each cylinder centre, as it is estimated to be the end of the recirculation zone (Gerrard, 1978). The mobile (down-looking) ADV probe was moved downstream along all longitudinal (AA’, BB’ and CC’) and transverse (00’, 11’, 22’, 33’ and 44’) sections shown in Figure 3.2.2-1b, starting from the same point as the fixed probe. In total 2 Reynolds numbers were tested, which are presented in Table 3.2.2-1.

Table 3.2.2-1. Reynolds numbers analysed

$Re\ (-)$	250	1100
$U_\infty\ (m\ s^{-1})$	0.014	0.056

For each flow rate, two experimental runs were performed. For each run, the side-looking Vectrino was fixed at one of the reference points: start of secondary wake of cylinders A and B. In this way, both single- and two-point statistics are obtained with reference to both fixed points. This allows for a preliminary evaluation of data quality, and the study of the evolution of coherence downstream of each wake.

3.2.3. Results

Studies of secondary wake interactions from a basic hydrodynamics perspective are scarce. Before discussing the novel elements of this research, it is necessary to validate the data and compare with the baseline case of isolated circular cylinders. Therefore, this work presents a characterisation of single-point statistics, to compare in terms of Reynolds number and to identify trends from these parameters that could hint at exchanges between interacting wakes. This discussion is intended as a lead up to the exploration of diffusion along the near secondary wake, and its implications on long-term mixing, in light of previous studies.

3.2.3.1. First-order velocity statistics

For reference purposes, the single-point statistics analysed were the mean streamwise velocity, U; the streamwise and transverse standard deviations of turbulent velocities, u^{+} and v^{+}; and Reynolds stresses, τ_{xy}, specifically their non-dimensional versions U^{*}, u^{+*}, v^{+*} and τ_{xy}^{*}. For simplicity, the notation u and v represents turbulent velocities, i.e. their time-averaged components, U and V are implicitly removed.

The objective of the single-point statistics analysis is to confirm validity via comparisons with analytical predictions of wake velocities (Schlichting, 1979; White and Nepf, 2003) and experimental studies over a range of different Reynolds numbers. First, this validation is necessary to qualitatively assess the data. That is, to check that the measurements follow the patterns identified previously, either analytically or experimentally and that the orders of magnitude are similar. Second, as most previous experimental studies on vegetated diffusion have focused on the "Low to moderate" Reynolds number range ($10 < Re_d < 1000$), representative points within this range were chosen. However, due to time and physical constraints it was only possible to conduct experiments for the two stem Reynolds numbers shown in Table 3.2.2-1.

Considering the wake velocity characterisation of an isolated cylinder as a baseline case, a study of the same features for a vegetated reach can help identify differences due to the additional stems. Additionally, as will be seen later, single point statistics are necessary to compute diffusion parameters.

Regarding the figures, the longitudinal axes were chosen to match the wake centrelines of reference cylinders A and B, starting just outside the recirculation zone. The distance between cylinders A and B ensures that they fall within the *no interference zone*, according to the classification provided by (Zhou and Mahbub Alam, 2016). Hence, their recirculation zones and shedding frequencies are unaffected and independent from one another. This independence means that the wake centrelines can be analysed separately, regardless of location. For this reason, all plots of streamwise evolution of quantities are expressed generically from their cylinder centre, non-dimensionalised using the stem diameter, d: $x^* = x/d$, $y^* = y/d$. Non-dimensional transect plots show the behaviour of quantities between the two adjacent secondary wakes. The wake interactions of interest are thus confined to the secondary wake, which is responsible for most of the mixing.

3.2.3.1.1. Mean Velocity field along the wake centreline

Figure 3.2.3-1 shows the measured curves of the mean streamwise velocity along the wake centreline, $U_{CL}(x^*)$, for each of the reference cylinders. Similar curves for different Reynolds numbers have been added for comparison. It can be seen that the new experimental data appropriately falls between the range of Reynolds numbers $70 < Re_d < 1500$, at least for the steepest portion of the plot, located in the range $2 < x^* < 4$.

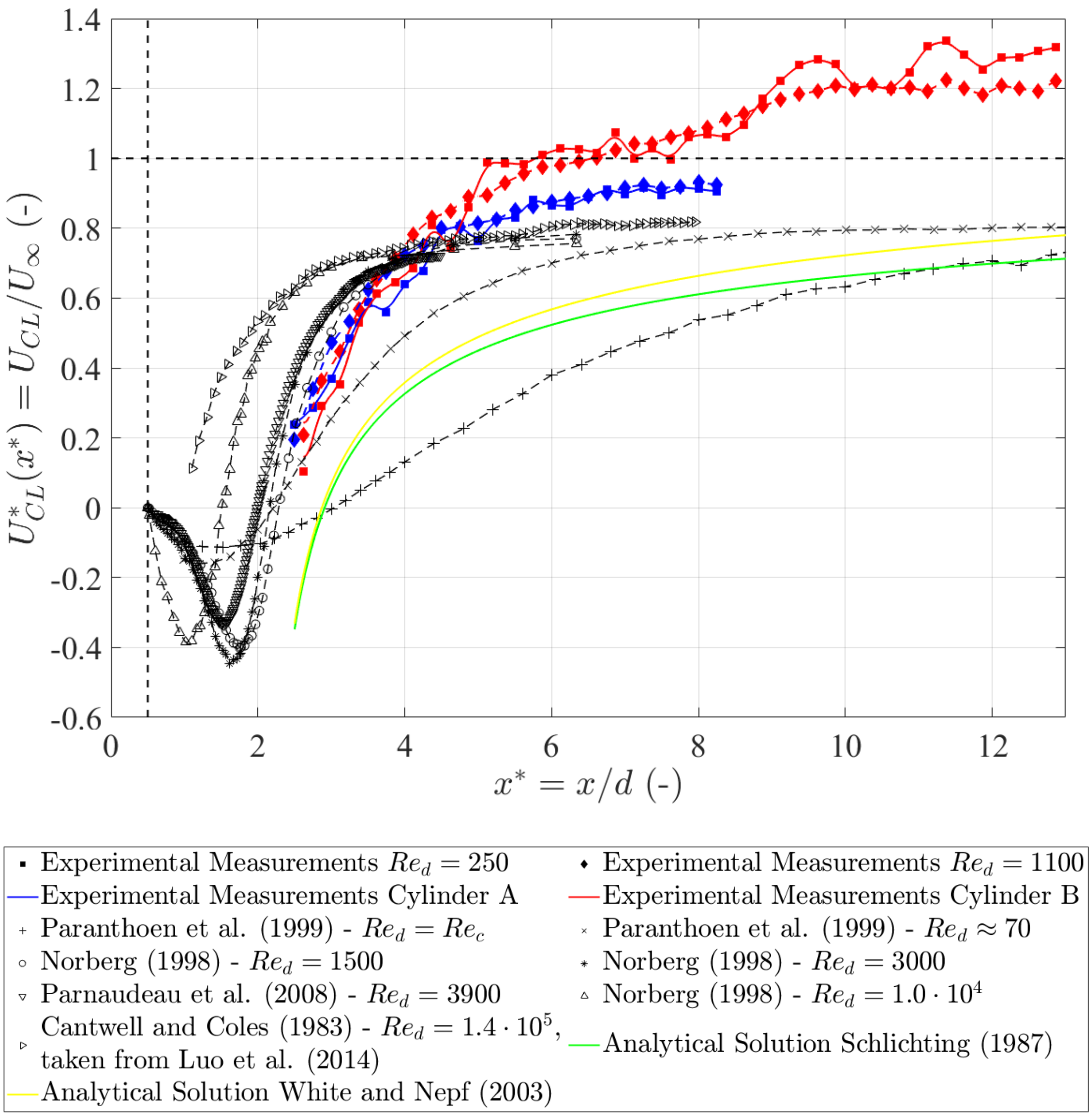

Figure 3.2.3-1. Evolution of the mean streamwise velocity along the wake centreline. Comparison with previous experimental results over a range of Reynolds numbers, comprising laminar and fully turbulent regimes.

All results from previous studies indicate that the $U^*_{CL}(x^*)$ curve plateaus at about 75% of the mean approaching velocity, U_∞[9]. In contrast, the measured profiles, $U^*_{CL}(x^*_A)$ and $U^*_{CL}(x^*_B)$ show a steady increase for the same range, rising above U_∞ for the curve of reference B. Two possible causes for this (not mutually exclusive) are contemplated: 1) the presence of downstream cylinders modifies the wake centreline. This is corroborated by the plots of mean transverse velocity along the wake centrelines, $V^*_{CL}(x^*_A)$ and $V^*_{CL}(x^*_B)$, shown in Figure 3.2.3-2. For an unmodified wake $V^*_{CL}(x^*)$ should be zero along the centreline, which is clearly not the

[9] Note that the approaching velocity U_∞ is used here to allow comparison with previous studies. This value should not be confused with the 'pore velocity', U_p presented in the following sections. The latter refers to the mean travel velocity within the vegetated array, which could not be measured for these experiments given the extent of the measurement section.

case in Figure 3.2.3-2. Also, Figure 3.2.3-3 shows an increase in mean velocity, $U^*_{CL}(y^*)$, at points close to the cylinder directly downstream from B. 2) From continuity, it is known that the decrease in mean velocity behind and around stems is coupled with local advective acceleration in the gap between stems. The transects 00' and 11' in Figure 3.2.3-3, show evidence of this, as velocity peaks at both sides of each cylinder.

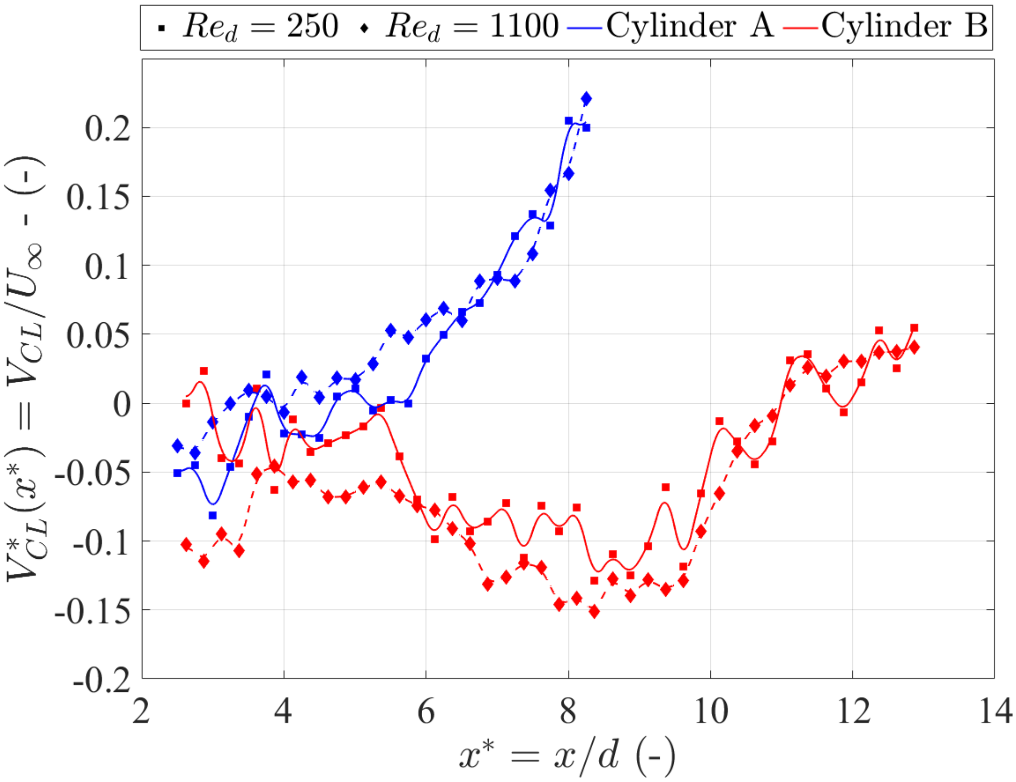

Figure 3.2.3-2. Evolution of the mean transverse velocity along the wake centreline.

The general array layout (Figure 3.2.2-1a), shows three cylinders above the test section, whose configuration seems to create a preferential pathway through the measurement area. The shape of the wake centrelines, inferred from Figure 3.2.3-2, and the magnitude of $U^*_{CL}(x^*_B) > 1$ for $x^* > 7$, appear to confirm this. Quantitatively, the local acceleration in this preferential pathway, generates velocities approximately 20% higher than the incoming velocity, $U^*_{CL}(x^*_B) \gtrsim 1.2$, as shown in Figure 3.2.3-1. Further, the evidence of acceleration zones wherein $U^*_{CL} \geq 1.2$ brings into question the assumption of gap contributions being negligible. Particularly with regards to relative displacements between low velocity and acceleration zones, which are expected to be higher than if the velocity distribution of moving particles only considered wake related effects.

The shape of the measured U^*_{CL} curves, for each wake, is constant for the range of Reynolds numbers measured. Consequently, the presence of the side-looking ADV, at the reference point, had a negligible impact on the flow field downstream, which speaks in favour of the consistency of the experiments.

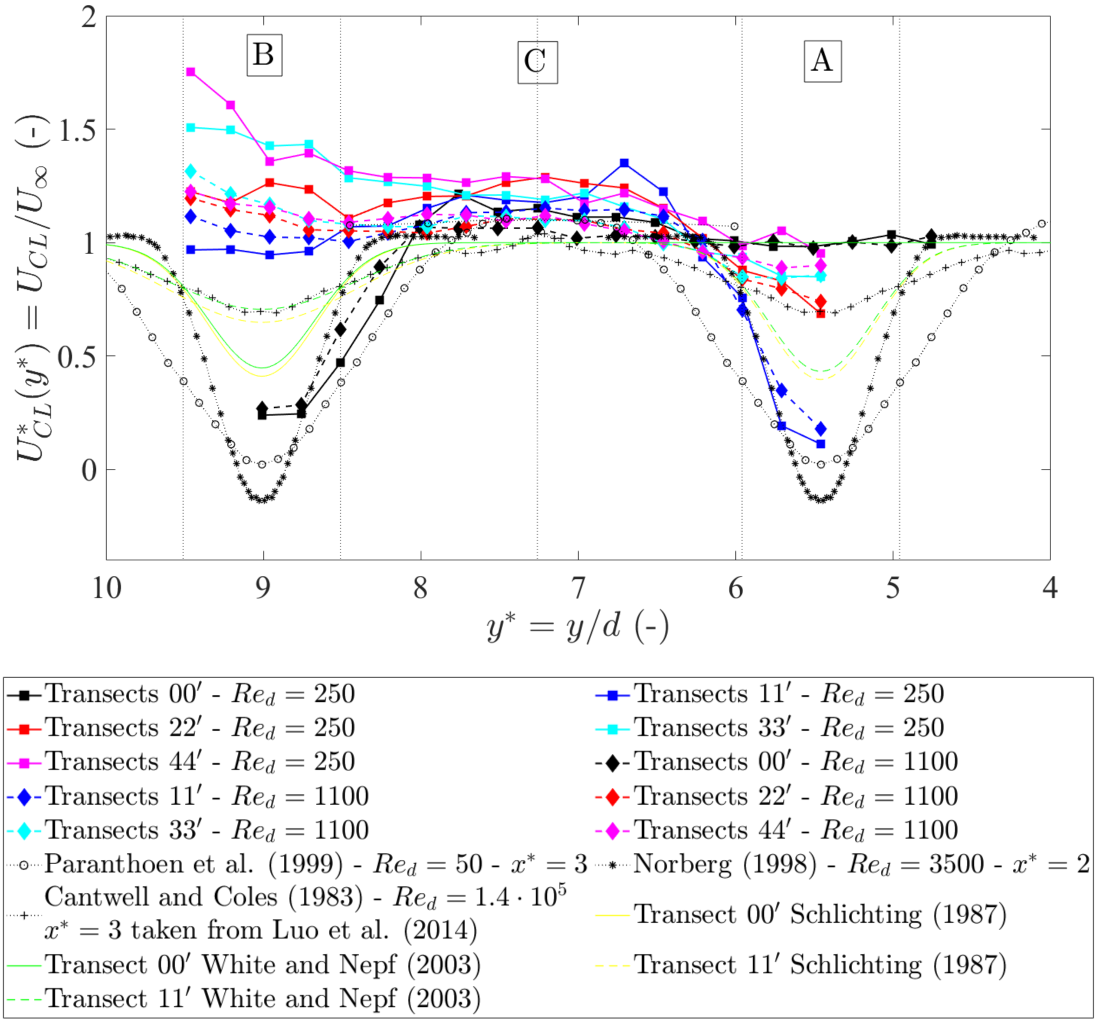

Figure 3.2.3-3. Evolution of the mean streamwise velocity along various transects over the wake length. Comparison with previous experimental results over a range of Reynolds numbers comprising laminar and fully turbulent regimes.

Figure 3.2.3-1 shows that analytical solutions are not representative of $U^*_{CL}(x^*)$ near the recirculation zone (x* < 3.0). Nonetheless, by moving the analytical solutions a distance equal to $2x^*$, they do resemble the shape of $U^*_{CL}(x^*)$, only for the secondary wake. White and Nepf (2003) relied on this resemblance to use their analytical solution for $U^*_{CL}(x^*)$ in the computation of the secondary wake dispersion coefficient. However, as will be explained later, these velocities are not representative of Lagrangian trajectories and their applicability for the calculation of either correlation functions is limited to the empirical assumptions applied.

3.2.3.1.2. Turbulence along the wake

The measured turbulent intensities along the wake (for $Re_d = 250, 1100$), shown in Figure 3.2.3-4a and b, are comparable to those measured by Cantwell and Coles (1983, presented in Luo *et al.*, 2014) for a Reynolds number several orders of magnitude greater ($Re_d = 1.4 \cdot 10^5$). The consistency of results for both cylinders and Reynolds regimes, suggests a high degree of background turbulence. This could be the result of flume characteristics, the short distance between the flow straighteners and the measurement area, or residual turbulence from the particle injection system. The shape of the turbulence intensity curves was unaffected by the location of the reference probe, hence, influence of the fixed (i.e. side-looking) ADV on the flow is unlikely.

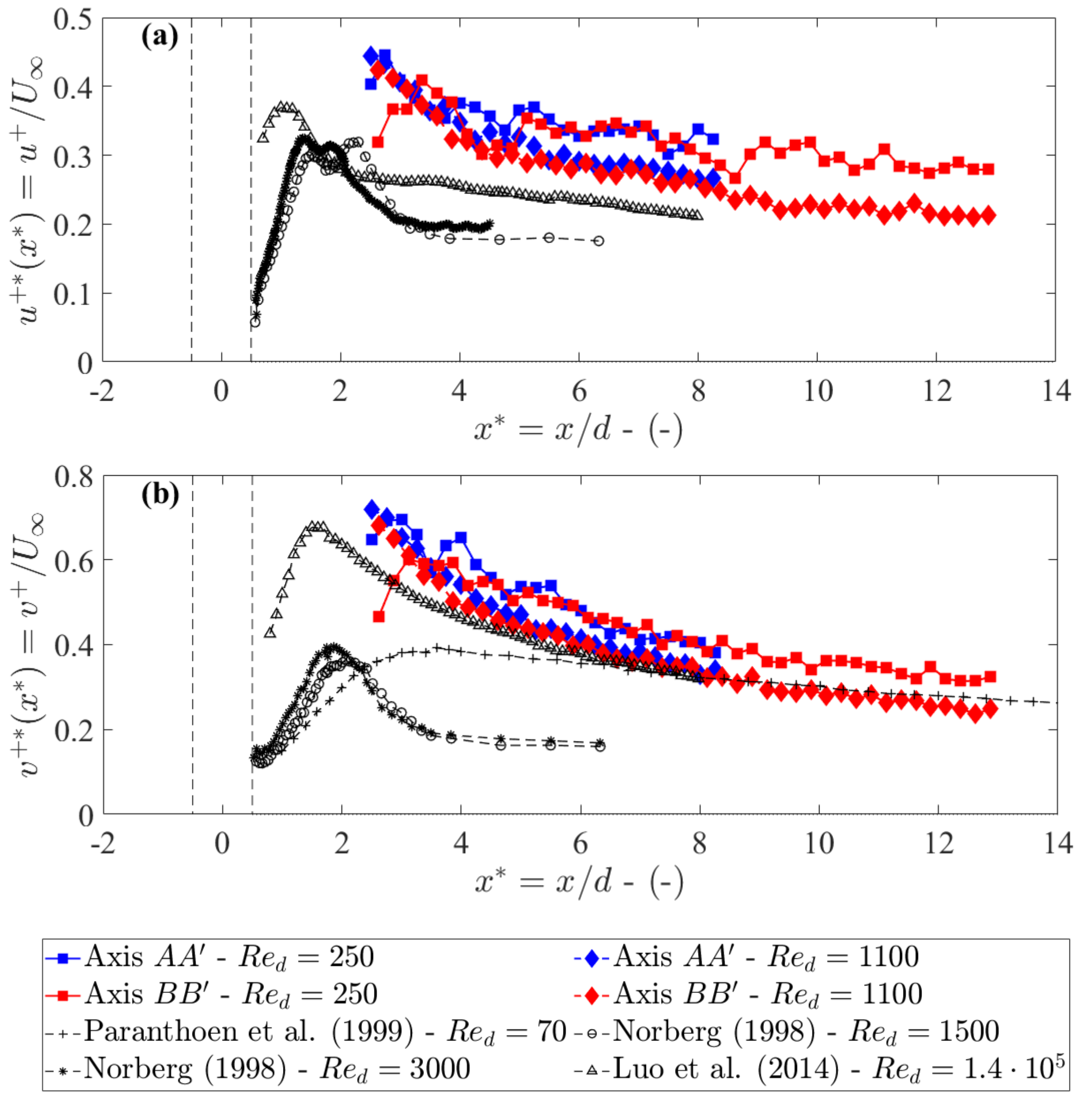

Figure 3.2.3-4. Evolution of the (a) streamwise and (b) transverse components of turbulent intensity along the wake centreline. Comparison with previous experimental results over a range of Reynolds numbers comprising laminar and fully turbulent regimes.

Incidentally, this high degree of background turbulence simulates the effect of upstream turbulence generated by vegetation on the reference cylinders. This level of upstream turbulence only seems to displace the profiles of turbulence intensity upwards, without affecting the gradient, which is an indication of dissipation and a useful quantity for the calculation of dispersion metrics. Further, the transects shown in Figure 3.2.3-5a and b suggest that turbulence production is enhanced by wake interactions, as the magnitudes at downstream transects seem higher than those expected from isolated cylinders. Transverse turbulence production is concentrated in a single peak located at $x^* \approx 3$, and then decreases monotonically. Longitudinal turbulence production is concentrated at symmetrical peaks located on either sides of the cylinder centreline, following the general outline presented by Kovasznay (1949).

Regarding isotropy, it can be noted from Figure 3.2.3-4 and Figure 3.2.3-5 that the magnitude of transverse turbulent intensity is clearly greater than the streamwise component within the wake (the peaks for u^{+*} is approximate 0.5, while that for v^{+*} is close to 0.75). This is expected due to periodic motions (vortex shedding) behind a cylinder being more effective in diffusing matter in the transverse direction. This difference between directional turbulent intensities seems to disappear with distance along the wakes. In Figure 3.2.3-5a the transverse and streamwise turbulence intensities at transects 33' and 44' have the same shape and magnitude for each Reynolds number. This convergence reflects that, as vortices break down and diffuse, dissipation decreases and the wake flow tends to be isotropic further downstream.

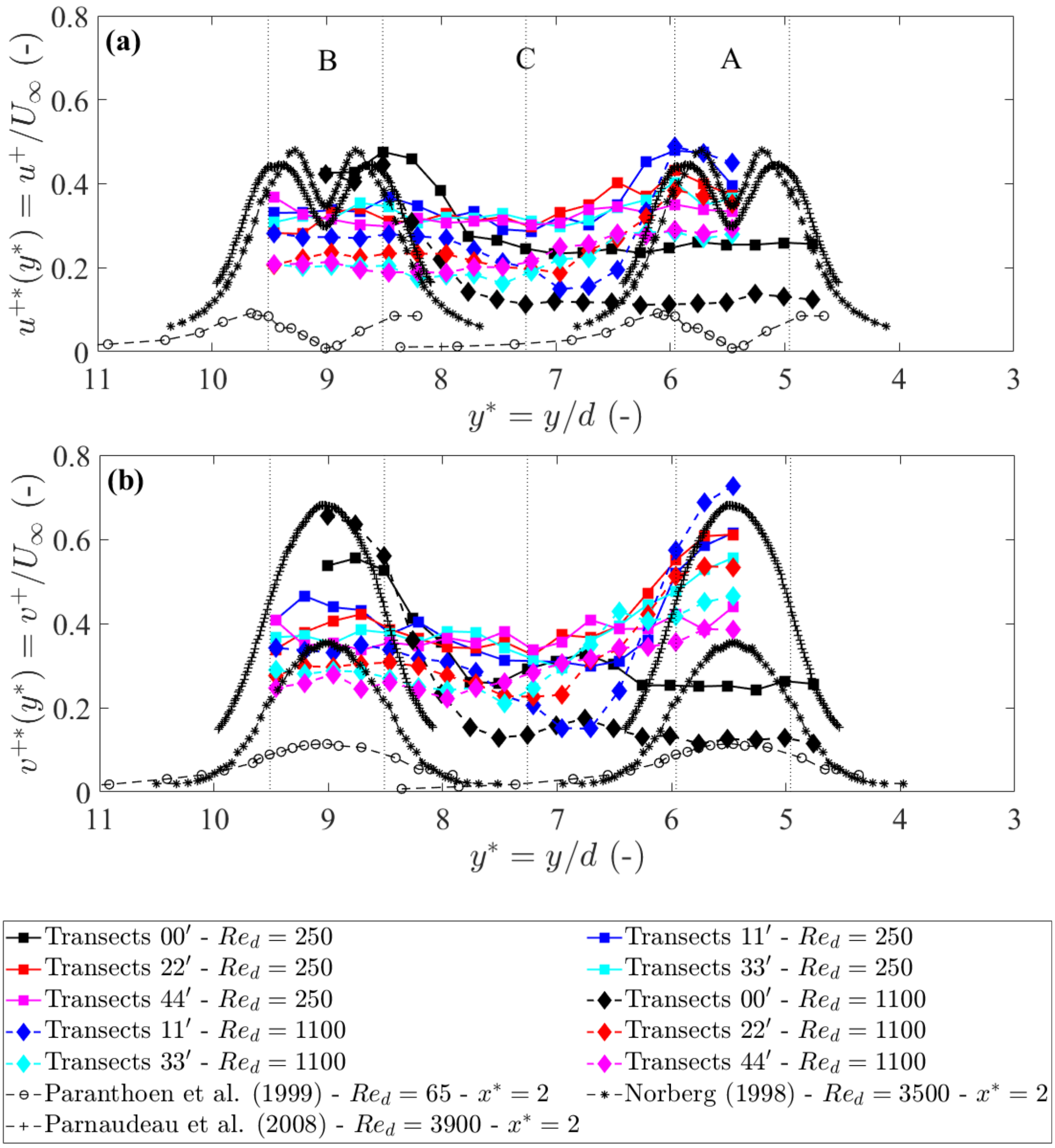

Figure 3.2.3-5. Evolution of the (a) streamwise and (b) transverse components of turbulent intensity along various transects over the wake length. Comparison with previous experimental results over a range of Reynolds numbers comprising laminar and fully turbulent regimes.

3.2.3.1.3. Momentum transfer (Reynolds stresses) along and across the wake

Reynolds stresses were measured in order to study mass and momentum transfer between the two interacting wakes. Figure 3.2.3-6 shows the evolution of this quantity across the wakes for different transects. Curves from previous experimental studies show the peak values of Reynolds stress are, expectedly, aligned with the vortices' cores, as momentum transfer occurs when the turbulent and periodic flow along the wake comes in contact with the outer flow, which is purely advective. Also, the resistance to rotation (vorticity) imposed by the outer flow generates a strong shear (and therefore dissipation) on the shed vortices, which are responsible for a large portion of mass transport along the wake.

As the shed vortices move downstream, they induce rotation on the outer flow due to shear, simultaneously losing energy due to viscous dissipation. For isolated cylinders, we expect the opposing peak values of Reynolds stress to diminish in magnitude and to grow transversely, as is evident from Figure 3.2.3-6. For the case of two interacting wakes, Figure 3.2.3-6a ($Re_d = 250$) shows that the boundaries of the two wakes come in contact at transect 11'. Given the configuration of the wakes, no clear transfer of momentum occurs, but a clear restriction on their lateral expansion occurs. Visualisations using contrasting dye (Figure 3.2.3-9) revealed that increased shear at the wakes boundaries accelerates vortex breakdown, and mass transfer occurs as packets of turbulence that detach from vortices and 'slip' into the adjacent wake. It should be noted that this behaviour cannot be considered universal, and that relative spacing and orientation are believed to play a major role in how mass is transferred between interacting secondary wakes.

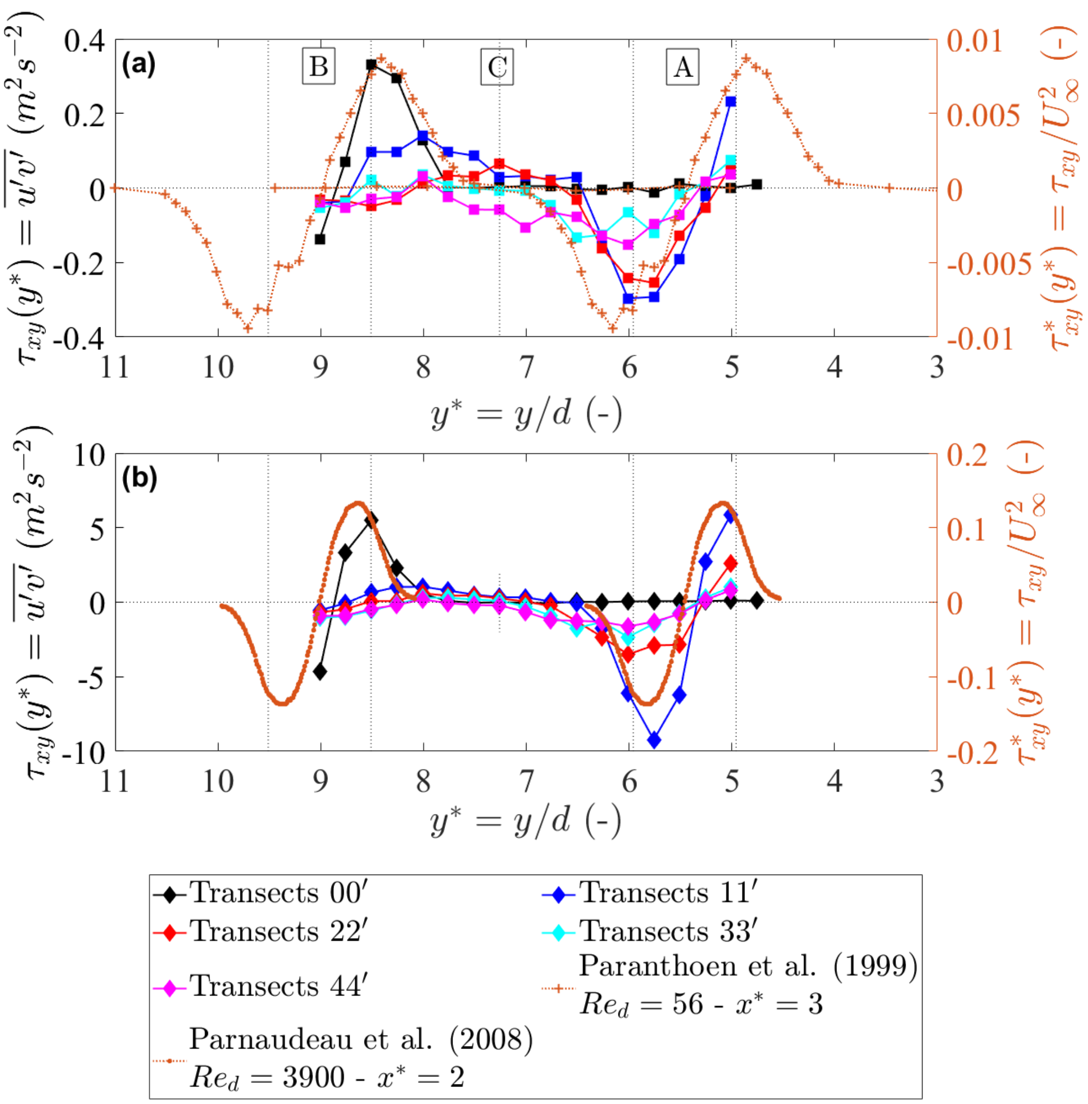

Figure 3.2.3-6. Evolution of the shear Reynold stress over the wake transects for (a) Re_d = 250, and (b) Re_d = 1100.

3.2.3.2. Two-point statistics along the wake

It is important to note that in addition to a decrease in mean velocity, cylinder wakes are dominated by periodic (coherent) motions and turbulence. This periodicity sets in at low Reynolds numbers, $Re_d \approx 40$ (Gerrard, 1978), and quickly evolves into a vortex street. Vortex formation and transport are accompanied by an early transition to turbulence, $Re_d \approx 180$ (Williamson, 1988b), caused by shear-induced instabilities in the vortices. It is expected that, for the Re_d range tested, and for most of the “low and moderate” Reynolds number range, wake-scale diffusion is dominated by turbulence due to coherent motions. A well-known model for turbulent diffusion, including effects due to turbulence decay, was presented by Taylor (1935), and is defined as

$$D_y = \frac{1}{2}\frac{d\overline{Y^2}}{dt} = v_y^+(t)\int_0^t v_y^+(\tau)\,\mathcal{R}_y(\tau)d\tau \qquad \text{Eq. 3.2.3-1}$$

Taylor's theory of diffusion (Eq. 3.2.3-1) is defined in a Lagrangian frame of reference, which means that the turbulence quantities v_y^+ and $\mathcal{R}_y(\tau)$ are defined for specific fluid particles instead of fixed points in the flow field (Eulerian frame of reference). Most experimental techniques in fluid mechanics are defined in a Eulerian fashion, and those which are not (e.g. Particle Tracking Velocimetry) are greatly limited by the resolution and frequency of data obtainable, as well as comparatively higher costs.

It would be more convenient to express Eq. 3.2.3-1 in Eulerian terms. However, a direct analytical transformation, of second-order statistics, between Lagrangian and Eulerian frameworks has no solution yet (Lumley, 1962). Any attempt at a solution must rely on either empirical assumptions, or reduce the problem to purely theoretical conditions. For stationary (c.f. steady), isotropic and homogeneous flow fields, Philip (1967) proposes that Lagrangian and Eulerian velocity pdfs are similar, such that a large ensemble would guarantee significant approximation. Koper, Sadeh and Turner (1978), proposed a general model that is not restricted to theoretical conditions, but which still requires the computation of concurrent Eulerian correlation functions at all points within the control volume. Given the experimental conditions presented here, it is necessary to rely on empirical simplifications and assumptions in order to characterise diffusion from the 2-point statistics calculated, that is, to apply Eq. 3.2.3-1.

These empirical assumptions refer to a proportionality between dispersive and advective length scales and the velocity distributions along the wake having a Gaussian pdf. The latter is applied from Philip (1967) probabilistic analysis of correlations, such that and the Eulerian functions presented below can be considered as approximations of the Lagrangian ones. Without going into details about the mathematical treatment of these assumptions, the following expressions are obtained for Taylor (1935) theory of diffusion in a Eulerian frame of reference.

$$y_x = \int_0^x \frac{v^+}{U}dx$$

Where the updated version of Eq. 3.2.3-2 is now,

$$\widetilde{D_y} = \frac{1}{2}\frac{d\overline{Y^2}}{dx} = \frac{v^+(x)}{U}\int_0^{y_x} \frac{v^+(x+\xi)}{U}\; R_{yy}(x+\xi, 0)d\xi \qquad \text{Eq. 3.2.3-2}$$

Where v_{rms} represents the spatially variable standard deviation of velocity, and the new correlation function $R_{yy}(x+\xi,0)$ expresses the connection between velocities measured at a fixed point x and a mobile point located at a distance ξ, from x. The value $\widetilde{D_y}$ is introduced as a short-term dispersion coefficient. The term two-point statistics refers in this study to the correlation functions $R_{yy}(\xi,0)$ and $R_{xx}(\xi,0)$ measured for each wake. Furthermore, the remaining components to compute Eq. 3.2.3-2 were presented in the section on single-point statistics.

The data from $R_{xx}(\xi,0)$, plotted in Figure 3.2.6-1, reveals little information about coherence processes along the wake centreline. A subtle periodicity can be seen from the time-dependent correlation $R_{xx}(0,\tau)$, which is expected to rapidly decay with distance downstream (ξ), thus the lack of correlation for the function $R_{xx}(\xi,0)$. The periodicity of $R_{yy}(0,\tau)$ and $R_{xx}(0,\tau)$ is expected to be equal. However, for the near and intermediate wake ($x^* < 20$), measurements of $R_{xx}(0,\tau)$ have been seen to present weaker periodic signals with twice the main shedding frequency (Kovasznay, 1949; Roshko, 1954). By moving the probe slightly away from the centreline ($y^* \approx 1$), the correlation signal from the longitudinal velocity, $R_{xx}(\xi,0)$, approximates the one obtained from $R_{yy}(\xi,0)$.

3.2.3.2.1. Experimental Eulerian Correlation Function

The study of correlation functions is not new, and a considerable amount of literature is devoted to it, especially from a theoretical perspective. However, the author is unaware of any prior application to the study of dispersion in interacting cylinder wakes in a vegetated reach.

Figure 3.2.3-7 shows the 2-point correlation function, of transverse velocities, $R_{yy}(\xi,0)$ for both reference cylinders and Reynolds numbers analysed. The correlation functions have a seemingly universal form, at least along the wake centreline. From the graphs presented, it can be inferred that different processes occur alongside vortex shedding. In addition to translation and rotation, vortices experience dissipation. This is evident from the decrease in absolute correlation with distance downstream, and the decrease in the frequency of the sinusoidal component of the correlation functions (width of each sinusoidal period becomes wider as the function moves downstream). These features in the correlation curve reflect the diffusion of vorticity towards the outer flow, which makes vortices larger, but reducing energy, i.e. rotation.

For $Re_d = 1100$, the periods of the curves are more clearly defined, and also, they seem to be stable further downstream. In contrast, for $Re_d = 250$, the correlation drops rapidly after the second period. The reason for this is that for higher Reynolds numbers (Figure 3.2.3-7b), vortices formed by the cylinder have a larger energy input, and can withstand dissipation for longer distances than those formed with lower energy inputs at lower Reynolds numbers (Figure 3.2.3-7a).

The first few points in the 2-point correlation curves were affected by acoustic interference: the combined acoustic pulses amplified the noise recorded. To correct for this interference, a time-dependent correlation was derived from the fixed point at the wake onset. Under the assumption of a 'first conservative cycle' of the correlation function, the initial points of the $R_{yy}(\vec{\xi}, 0)$ curve were corrected with the first half-period of the time-dependent correlation $R_{yy}(0, \tau)$.

This comparison between space- and time-dependent Eulerian correlation functions reveals the well-known existence of a dissipative regime, and the effects of shear between the vortices (coherent structures) and the outer flow. For $Re_d = 250$, the first period of both $R_{yy}(\xi, 0)$ and $R_{yy}(0, \tau)$ have a similar gradient, suggesting minimal dissipation during the measurement period. For $Re_d = 1100$, the two curves have the same intersect point ($R_{yy} = 0$), but the different gradients indicates strong vortex diffusion and dissipation.

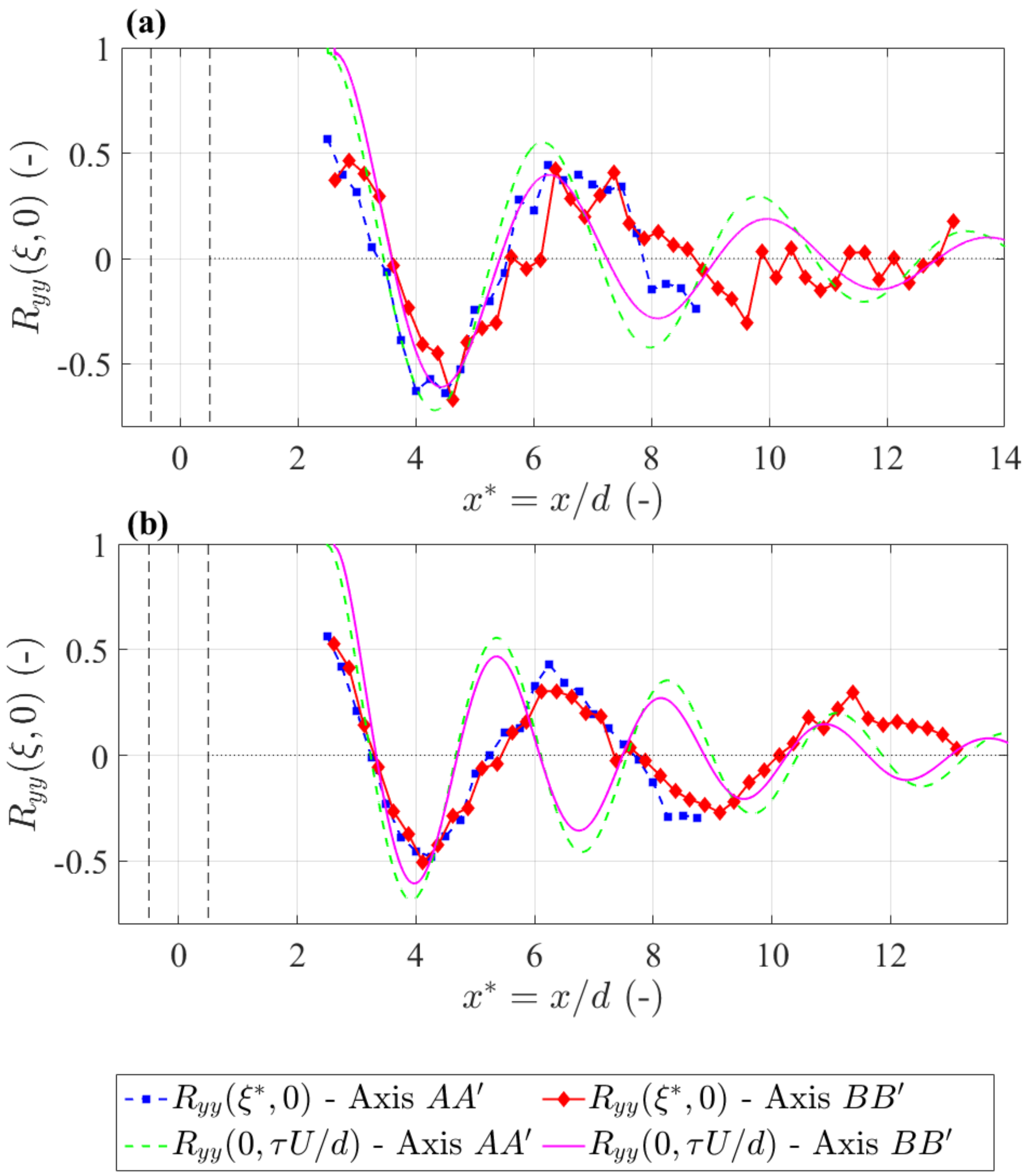

Figure 3.2.3-7. Comparison between time- and space-dependent correlation functions for transverse velocities, (a) Re_d = 250, and (b) Re_d = 1100.

3.2.3.2.2. Use of Taylor's Theory of Diffusion and the diffusion-turbulence proportionality assumption to compute diffusion in the secondary wake

To characterise diffusion from the experimental correlations, Taylor's assumption of proportionality between diffusive and velocity scales is used (i.e. between the ratios dy_x/dx and v^+/U, respectively, from Eq. 3.2.3-2). If we calculate $\overline{Y^2}$ directly from the modified Theory of Diffusion (Eq. 3.2.3-2), we obtain the variance of the transverse displacement of particles along the wake. In other words, if we release a number of particles where at the start of the secondary wake, then $\overline{Y^2}$ represents the distance-dependent variance of the distribution of particle as they diffuse and advect downstream. If, as a criterion, it is defined that the wake must contain 99.7% of the particles (i.e. the total mass of particles within 3 standard deviations from the wake centreline), then the half-width of the wake will be defined as

$$b_{1/2} = 3 \cdot \sqrt{\overline{Y^2}} \qquad \text{Eq. 3.2.3-3}$$

Figure 3.2.3-8 shows the results of using the x-dependent diffusion coefficient $\widetilde{D}_y$, (with units of m^2/m) proportional to the actual Diffusion coefficient D_y (with units of m^2/s), to obtain the wake widths for the 2 reference cylinders. Note that for $Re_d = 1100$, the predicted wake width is narrower than that for $Re_d = 250$. This goes in agreement with the phenomenological description given in Sections 3.2.3.1.3 and 3.2.3.2.1 Shear between rotating vortices and the outer streamline flow increases vortex size whilst simultaneously decreasing rotation, and ultimately dissipating energy. For higher energy inputs (i.e. higher Reynolds numbers) vortices travel faster and remain consistent for longer periods of time.

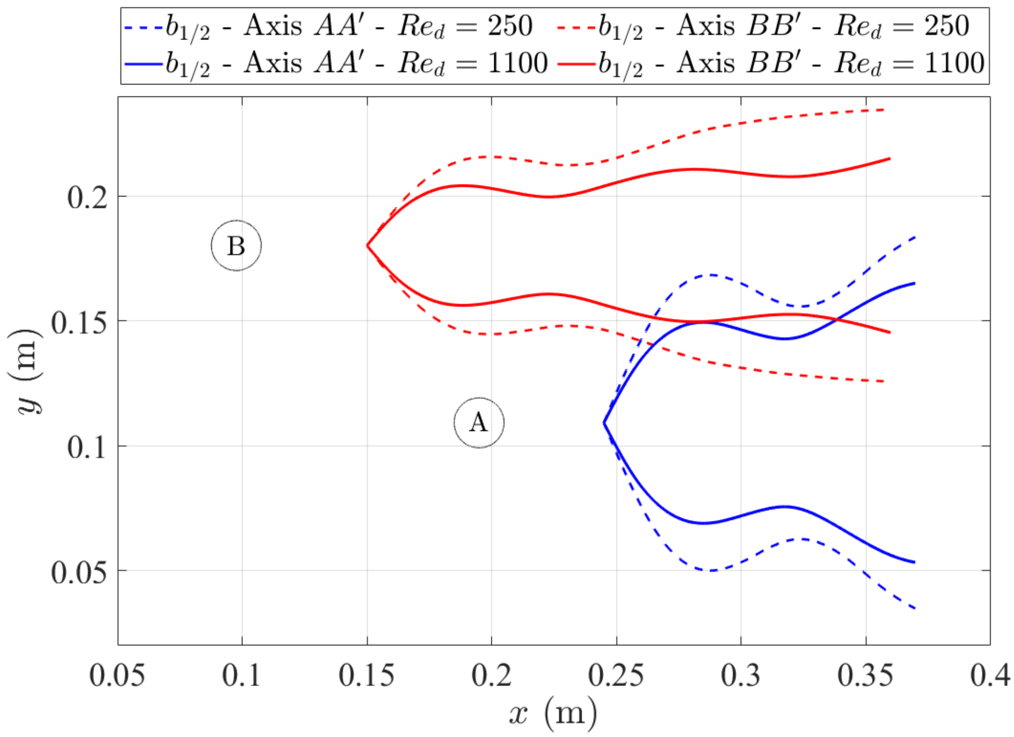

Figure 3.2.3-8. Calculated wake widths from reference cylinders A and B.

From the transects of Reynolds stresses (Figure 3.2.3-6), the zero crossing between wakes suggests no momentum transfer due to turbulence. However, statistical momentum transfer gives an incomplete picture of diffusion in vegetated flow. Mass transfer between interacting wakes depends on their relative orientation. To investigate the dynamics of diffusion, visualisation tests with food-colouring dye, to trace the wakes, were performed at the same Re_d values as the ADV experiments, a snapshot is shown in Figure 3.2.3-9.

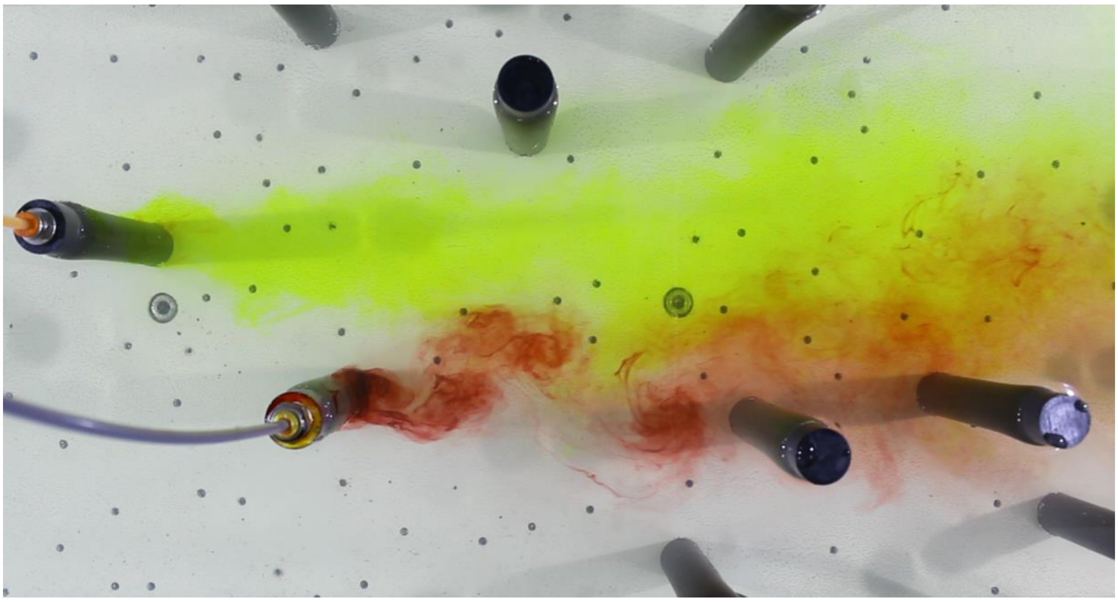

Figure 3.2.3-9. Food-colouring dye visualisation experiments to check mass transfer between the secondary wakes from reference cylinders A and B, $Re_d = 250$.

The wake from cylinder B (green in Figure 3.2.3-9) is restricted by the downstream cylinder, confirming the preferential pathway hypothesis presented above. For early shedding cycles, minimal interaction was noticed between vortices from these adjacent wakes. With distance downstream, interactions start to occur, and two main transfer mechanisms were detected from the visualisation experiments. **(a)** As vortices travel downstream, rotation generates negative pressures around them, which can drag mass from the adjacent wake. In other words, strong rotation brings adjacent mass into the vortex core. **(b)** A more effective mass transfer takes place as adjacent wakes enhances shear and thus vortex break down.

Downstream cylinders play an important role in transferring mass outside of each specific wake. As can be seen from Figure 3.2.3-9, vortices from Cylinder A (in red) break down when in contact with the downstream cylinder. Then turbulence is more effective in allowing smaller structures to be 'dragged' into adjacent wakes.

3.2.4. Further Steps

3.2.4.1. Analytical formulations to the correlation functions

Despite their complexity, the periodic motions registered in the secondary wakes analysed appear to have a well-defined mathematical structure. Both single- and two-point correlation functions seem to be composed of a decreasing envelope and a sinusoidal component with a time-varying frequency. The time-varying component reflects the effect of dissipation, and the decreasing envelope the effect of both dissipation and general loss of statistical correlation. Generally, this structure can be represented as follows

$$r(\tau) = \epsilon(\tau) \cdot cs(\beta(\tau) \cdot \tau) \qquad \text{Eq. 3.2.4-1}$$

Where the function $\epsilon(\tau)$ represents the envelope of the monotonically decreasing correlation function; $cs(\tau)$ is the periodic component defined as a linear combination of orthogonal sinusoidal functions; and $\beta(\tau)$ is a 'frequency function' representing the effect of dissipation.

The simplest case of these functions is the time-dependent correlation function measured at the reference point, $R_{yy}(0, \tau)$, which, being only time dependent, does not include a dissipation (i.e. $\beta(\tau)$) component. Csanady (1973) proposed a general expression for correlation functions of 'wave-like motions', defined as:

$$r(\tau) = e^{-m\tau} \left[\cos(n\tau) - \left(\frac{m}{n}\right) \sin(n\tau)\right] \qquad \text{Eq. 3.2.4-2}$$

Where m and n are empirical constants. It is important to note here that since n is constant, this expression does not take into account vortex dissipation due to shear. A best-fit procedure, using this analytical equation to fit the experimental fixed-point correlation function for cylinder B, $Re_d = 1100$, yields the optimised profile shown in Figure 3.2.4-1.

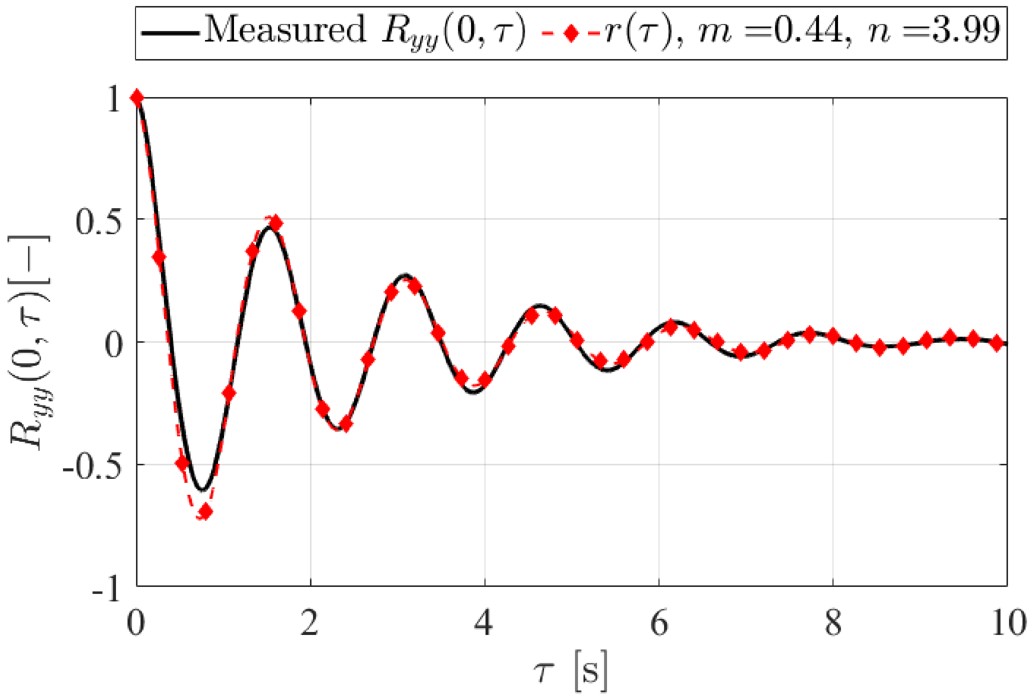

Figure 3.2.4-1. Comparison between experimental time-dependent correlation function, $R_{yy}(0,\tau)$, for the fixed point B, $Re_d = 1100$; and an optimised curve using Csanady (1973) function.

The advantage of having an analytical expression for the fixed point correlation is that a sequence of steps can be developed to compute the Lagrangian correlation function from a theoretical expression.

$$\underbrace{r(\tau)}_{I} \rightarrow \underbrace{R_{yy}(0,\tau)}_{II} \rightarrow \underbrace{R_{yy}(\xi,0)}_{III} \rightarrow \underbrace{\mathcal{R}_y(\tau)}_{IV} \qquad \text{Eq. 3.2.4-3}$$

In other words, if a satisfactory expression for $r(\tau)$ is obtained, it will be possible to obtain a valid approximation for the Lagrangian frame of reference. The following requirements should be considered: step $II \rightarrow III$ involves adding a dissipation function that stretches the domain of the correlation, also, step $III \rightarrow IV$ involves the use of Taylor's proportionality, or a similar hypothesis, to relate Eulerian and Lagrangian trajectories (see Section 3.2.3.2.2)

3.2.4.2. Phenomenological propositions (time scales)

Most models for diffusion focus on the Fickian range, including the ones discussed here (White and Nepf, 2003; Tanino and Nepf, 2008b); however, information regarding time scales necessary to attain this regime is usually scarce and empirically based. After analysing the features of the plots presented in this study; the following propositions can be presented:

Mixing in vegetation is divided into three regimes, each dominated by one of the following scales

a. Eddy scale: early stages of diffusion ($t \rightarrow 0$). In this regime, particles move with the average eddy, in such a way that two particles that start their journey from very close initial points, will not change their relative distance as both are moved by the same eddy.

b. Wake scale: Intermediate stages of diffusion ($T_1 < t < T_2$). In this regime, particles move with the vortices shed by a cylinder. The rate of separation of two particles starting from very close initial points depend on the properties of the wake alone. T_1 is the time scale required for two particles to abandon the initial eddy scale. T_2 is the time scale necessary for two particles to become completely uncorrelated, after each has experienced several wakes.

Fickian regime. ($t \rightarrow \infty$). This is the range that is attained by two particles that became uncorrelated after experiencing a sufficient number of wakes. Dispersion in this range is linear.

3.2.5. Discussion

Laboratory measurements of single- and two-point velocity statistics along the wakes of two adjacent cylinders, for moderate Reynolds numbers, $Re_d = [250, 1100]$, were made for a sparse cylinder array. Single-point statistics show that vegetated flows are predominantly heterogeneous, anisotropic and strongly dissipative. Further, it was found that in a random array, wakes tend to deform, as evidenced by the variations in transverse and longitudinal mean velocities. This suggests the creation of preferential pathways, with advective accelerations showing ≥20% velocities higher than the incident flow. Shear between wakes indicates strong momentum transfer, and it is hypothesised that vortex break down along parallel wakes is responsible for mass transfer.

It was found that strong coherent motions dominate mass transfer along the secondary wake (at least for a distance $2 < x^* < 11$ behind the cylinder). Likewise, diffusion in this region seems to be proportional to shear and thus dissipation between wakes. A further analysis of parallel wakes from coloured dye images, Figure 3.2.3-9, shows that as vortices break down due to shear, small 'packets' of turbulence are drawn into adjacent wakes due to rotation and pressure differences, but a strong continuous mass transfer does not takes place.

The White and Nepf (2003) model relies on the assumption that the random mean velocity field, caused by the presence of cylinders, can be obtained by a linear superposition of analytical wake velocities (Eq. 3.2.1-1). However, summing velocity deficits does not account for the advective acceleration generated between cylinders. Figure 3.2.3-1 to Figure 3.2.3-3 show that the presence of nearby cylinders, even for a sparse distribution, can generate increases from 20%, up to 75% in the mean velocity along a wake.

Replacing the Lagrangian velocity function, $v_i'(\tau)$ by the Eulerian wake velocity, $u_w''(x^* + x_o^*, y^*)$ neglects the contributions from periodic (coherent) and turbulent motions. Clearly, these contributions cannot be omitted on dimensional grounds, since, as Figure 3.2.3-4 and Figure 3.2.3-5 show, turbulent production in the wake can reach values of 70% and 50% of the mean streamwise velocity for the transverse and longitudinal components of turbulence, respectively. From the Figures shown, it can be seen that turbulent transitions occur in the stem-flow interfaces for values of Re_d as low as 250. So, even when a dispersion model is restricted to 'low and moderate' Reynolds numbers ($10 < Re_d < 1000$), almost the entirety of the range will involve turbulent flow.

The transects of Reynolds stresses shown in Figure 3.2.3-6 were measured to analyse wake interactions (i.e. momentum transfer) between adjacent wakes. When the experimental results of this study are compared with the transects for isolated cylinders, it is seen that wake boundaries (zero-crossing points in the Reynolds stress graphs) get displaced for $Re_d = 250$. These changes in the shapes of wakes also entail changes in their turbulence structure, which, as noted by (Zhou *et al.*, 2000) shows that wakes have non-linear interactions. Consequently, the assumption of a random velocity field as a result of a linear superposition of wake velocity functions should be revised.

The curve of $U_{CL}^*(x_B^*)$ in Figure 3.2.3-1, shows that the cylinder upstream of B generates a preferential pathway where $U_{CL}^* \gtrsim 1.2$. This suggests that acceleration zones can be a significant portion of the velocity distribution along a mean velocity path. Neglecting acceleration effects should also be revised on the fact that the simultaneous effects of accelerations and velocity defect in wakes is larger on the relative displacement of two particles, than if only wakes are considered. Theoretically this was explored in Batchelor (1951), where it was found that for two travelling particles, the velocity pdf of their relative displacement is not equivalent to their independent pdfs of travelling velocities.

The best approach to the problem can be obtained from Taylor's Theory of Diffusion, TTD, (Eq. 3.2.3-1). However, it is important to note that Taylor's Theory is also subject to a set of caveats and assumptions that must be analysed. Any empirical framework in which a frame of reference transformation is proposed, must consider the limitations of the original theory. As explored in Lumley (1962) and Philip (1967), Lagrangian and Eulerian velocity functions are equivalent so long as their distributions are identical, for which stationarity, homogeneity, isotropy and ergodicity are necessary. As shown in section 3.2.3.1, the wakes analysed present a mixture of periodic motions, rapid energy dissipation, heterogeneity and anisotropy. Notwithstanding the limitations, the assumption of proportionality between diffusive and turbulent length scales given in Taylor (1935) allows complex flow field like the one presented here tractability via the TTD. Further explorations of this theory should be undertaken to validate the findings presented here.

3.2.6. Additional Figures

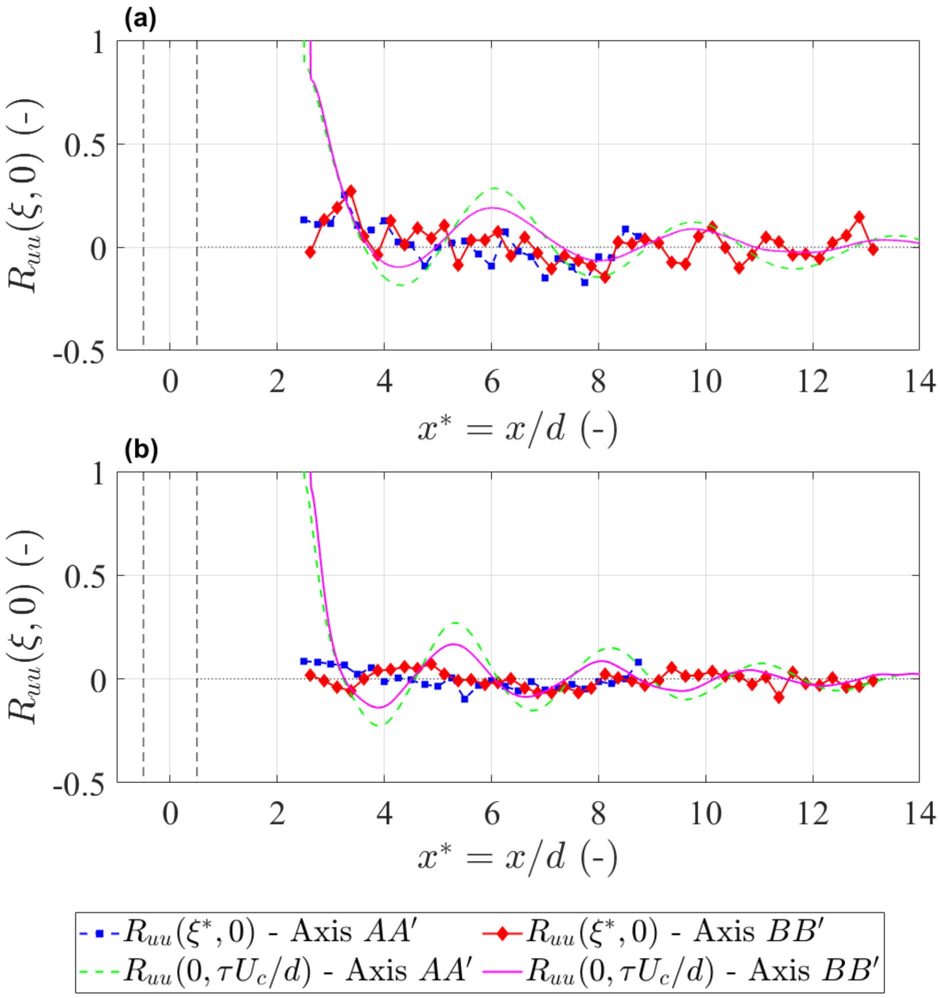

Figure 3.2.6-1. Comparison between time- and space-dependent correlation functions for streamwise velocities, (a) Re_d = 250, and (b) Re_d = 1100.

Chapter 4. EXPERIMENTAL METHODS

From: Proceedings of the 39th IAHR World Congress.
Spatio-Temporal Characterisation of Hydrodynamics and Mixing Processes in Obstructed Flows using Optical Techniques

Abstract

This study describes an artificial vegetation model, based on the morphological characteristics of real species, to study vegetated hydrodynamics and solute transport. A thorough description of the proposed morphology is given, alongside the experimental system built to provide a full experimental characterization of velocity and solute transport. Although previous studies have focused on obtaining similar descriptions of the flow within artificial vegetated arrays, most are faced with the same physical constraints, limiting the scope and level of detail of the obtained data. A custom-made LIF-PIV system is presented, with the potential to provide velocity and solute transport characterizations, that can help expand on the current understanding of mixing in emergent vegetation. Data obtained confirms the capabilities of the system.

4.1. Introduction

The experiments described here build on the methodology presented in Sonnenwald *et al.* (2017), wherein the longitudinal and transverse dispersion of a passive solute in natural and artificial vegetated systems was studied, using Laser Induced Fluorescence (LIF). Artificial vegetation systems are usually represented by arrays of circular cylinders of a single diameter. According to the characterization performed in that study, for the natural species tested, factors such as stem diameter distribution and vegetation layout (e.g. random locations, clustering) must be considered for artificial vegetation systems in order to better represent natural vegetation systems. This study aims to provide a hydrodynamic and mixing characterization on a more realistic artificial vegetation morphology, considering diameter and spacing distributions observed in real vegetation, particularly winter Typha Latifolia.

Regarding hydrodynamic characterization, the most relevant precedent for velocity measurements in vegetated flows, using Particle Image Velocimetry (PIV), is the one presented in Ricardo (2014). From that, a comprehensive description of vegetated hydrodynamics was presented (Ricardo *et al.*, 2014; Ricardo, Franca and Ferreira, 2016), despite the small flow fields obtained. This is the first study in which a comprehensive area of a vegetated flow field is illuminated, so special consideration is given to the material and layout of the obstructions, and the windows for viewing and light transmission.

This experimental set up and methods presented in this chapter underpin a series of studies performed in the configuration presented, with the aim of providing a detailed characterization of solute transport and hydrodynamics in emergent vegetation. The purpose of this chapter is therefore to describe the experimental set-up and its capability to provide high-quality concentration and velocity fields to tackle the problem of characterizing mixing in emergent vegetation. A thorough description of the configuration process, for researchers aiming to develop similar systems, is presented in Appendices A and B.

4.2. RandoSticks Vegetated Array

The inconsistency between results from natural and artificial vegetation, shown in Sonnenwald *et al.* (2017), is attributed to the use of uniform diameters to represent natural vegetation morphology. Based on this, a new configuration is proposed, which consists of a random array of circular PVC rods, with a diameter distribution resembling that of winter Typha latifolia (as measured by Sonnenwald *et al.*, 2017). This configuration is referred to as RandoSticks. It is hypothesized that including diameter distributions will account for the variety of flow scales and thus yield dispersion coefficients closer to the ones measured in real vegetation.

4.2.1. RandoSticks Distribution and Layout

Figure 4.2-1a shows the layout for the RandoSticks configuration, which consists of a 1x1 m^2 pattern of randomly located stems, replicated in the streamwise direction, for a total of 9 m of vegetation. To allow fully developed flow, seeding and fluorescent dye were injected 3 m downstream from the start of the array. To study changes in initial conditions for LIF, 7 lateral injection locations, spaced at 0.05m, from 0.35m to 0.65m, across the flume width, were defined. To comply with the 2D flow condition, dye was injected uniformly over the flow depth. Figure 4.2-1a shows the first 2 measurement sections (cameras) for LIF, the injection locations and the PIV field of view. Two additional LIF measurement stations were located at 1 m intervals after the first two, for a total of four. To acquire LIF images, 0.1 x 1.0 m^2 glass windows were constructed on the bed, at each measurement station. To avoid trapping effects, an 8 mm gap, between adjacent stem plates, was set to allow visualization. A 0.5 x 1.0 m^2 glass window with a perforated acrylic plate was fitted between the first 2 adjacent sections for PIV experiments.

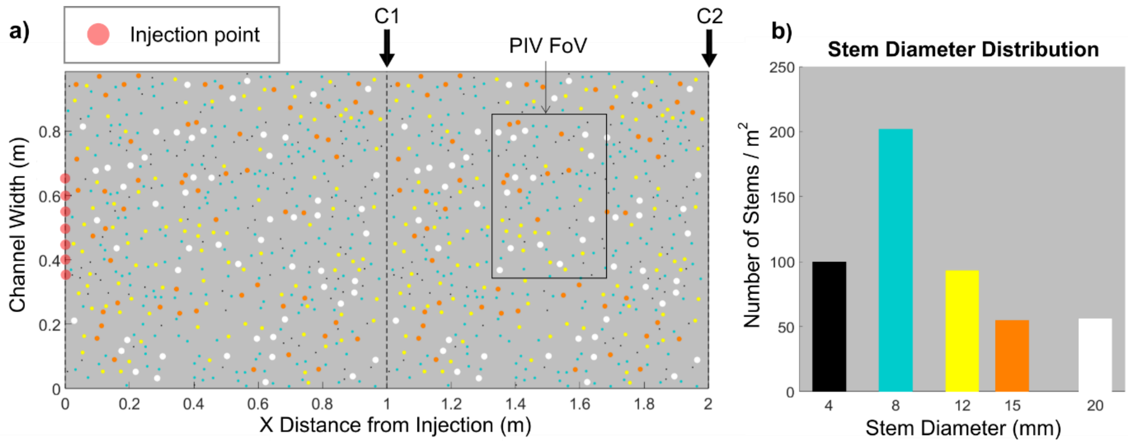

Figure 4.2-1. a) Location of the stems comprising the RandoSticks system, injection points and first two measurement stations. b) Stem Diameter Distribution of the RandoSticks configuration.

The RandoSticks diameter distribution (d =4, 8, 12, 15 and 20 mm) is presented in Figure 4.2-1b. The morphological metrics of the configuration are: (representative) mean diameter, d =10.3 mm; solid volume fraction, φ = 0.05; stem number density, m =514 stems/m^2; frontal facing area, a =5.14 m^{-1}; mean edge-to-edge stem spacing, s_n =0.041 m; mean centre-to-centre spacing, s =0.052 m.

4.2.2. Flow Conditions (Flume Slope, Flow Rates and Water Profiles)

The flume used for the experiments had a fixed slope, therefore, only a limited range of discharges generated quasi-uniform water depths. In total, 15 flow rates were tested, as presented in Table 4.2-1, The actual measured discharges are presented alongside the Reynolds numbers (with kinematic viscosity, $\nu = 1.01 \cdot 10^{-6}$ m^2/s, at 19.5 °C) from the optimised mean streamwise velocities (see Section 5.3.2). A reference depth of 150 mm, at *X* = 1.5 m from Figure 4.2-1a was set for all tests, and the water profile was measured, for all tests, using a Vernier gauge. The reference depth is located between the first two LIF sections and where the PIV measurements are taken, so that at least for that section, the same slope and flow depth can be kept consistent. An analysis of flow uniformity is given in Section 5.3.2. All tests were repeated to obtain representative samples for each case, and a total of 738 injections were performed in total, yielding a comprehensive dataset from which statistical significance is given to the results.

Table 4.2-1. Tested flow rates

Q target (l/s)	Q meas. (l/s)	U (mm/s)	Re_d	Mean Frame Rate (Hz)	Number of Tests per injection location (y_{inj})						
					0.35 (m)	**0.40 (m)**	**0.45 (m)**	**0.50 (m)**	**0.55 (m)**	**0.60 (m)**	**0.65 (m)**
0.5	0.63	5.6	57	5	-	-	3	3	3	-	-
1.0	0.84	7.0	71	5	-	3	5	6	5	3	-
1.5	1.55	10.8	110	10	3	5	7	7	7	5	3
2.5	2.54	19.9	203	10	3	3	5	12	5	4	3
3.0	3.32	24.8	253	20	3	7	13	13	13	7	3
4.0	4.10	31.0	316	20	3	7	11	12	11	7	3
5.0	4.49	35.2	359	20	3	5	9	14	10	6	3
6.0	5.98	44.7	456	28	3	7	13	14	13	7	3
7.5	7.78	58.1	593	4	3	5	5	16	5	3	3
9.0	8.81	67.7	690	27	3	8	13	15	13	8	3
10.0	10.40	79.3	809	30	3	6	10	16	10	5	3
11.0	11.40	86.4	881	30	3	8	13	13	13	8	3
12.5	12.63	96.7	986	29	5	11	16	16	16	11	5
14.0	13.40	101.7	1037	29	3	8	13	14	13	8	3
15.0	14.58	109.5	1117	9	6	6	10	21	7	3	-

The experiments described in this research were conducted in the Water Engineering Laboratory at the University of Sheffield. The existing flume is 1.22 m wide by 14.63 m long and a fixed slope of 0.138 %. Inner walls were added to limit the width of the flume to 1.0 m. The RandoSticks array started at 2.9 m after the flow straighteners at the inlet. 1.0 x 1.0 m perforated PVC plates were used to install the cylinders. For convenience, 1.0 x 0.3 m plates were used in the measurement section, which were waterproofed and levelled to avoid bed effects. All lasers were aligned horizontally at mid-depth, i.e. 75 mm above the bed. Figure 4.2-2 shows the lasers in operation, alongside an elevation view describing the flume set-up.

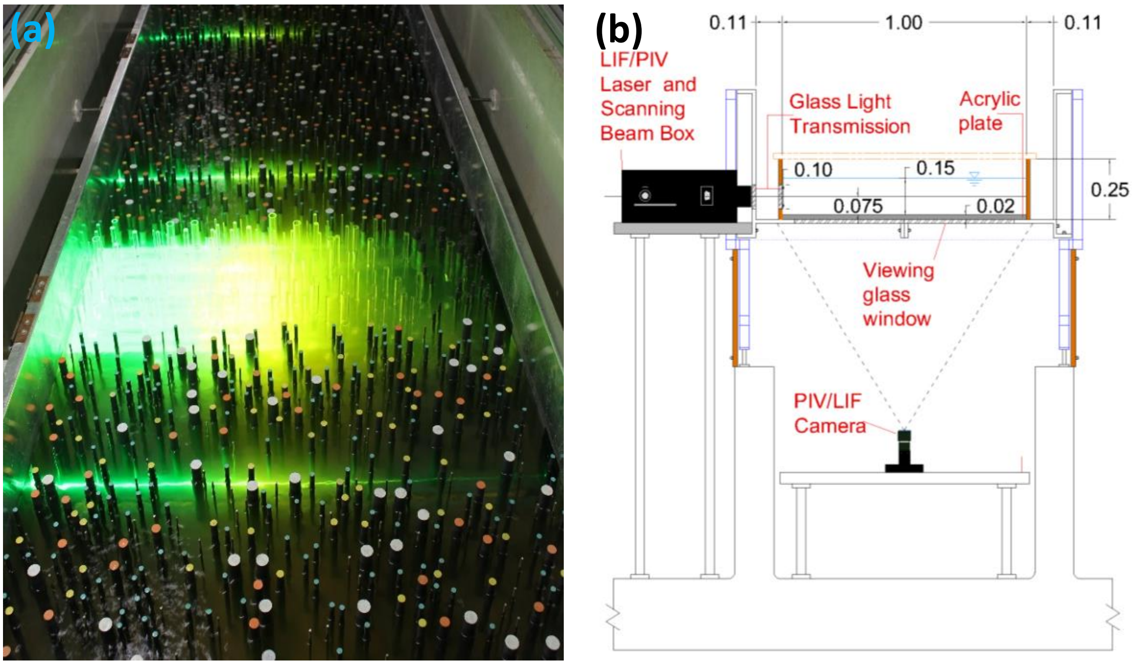

Figure 4.2-2. a) Photograph of the RandoSticks layout, illumination from laser beams (LIF) and laser sheet (PIV), and change in emission colour due to fluorescence from Rhodamine 6G. b) Elevation view showing the location of the system components.

4.3. Laser Induced Fluorescence System Description

LIF systems have 4 basic components: illumination source, fluorescent compound, image acquisition device and illumination optics (Crimaldi, 2008). This work only considers the first three for LIF. Illumination optics (i.e. scanning box) were included for PIV (see Section 4.4). Conventionally, the dye absorption peak and the laser wavelength should match, also, a camera filter to isolate the dye's emission peak should be added to isolate it from external light sources. For the experiments described in this work, Rhodamine 6G was chosen based on the available laser system, its insensitivity to photo-bleaching (Crimaldi, 1997), secondary absorption (Baj, Bruce and Buxton, 2016) and its relative stability with temperature (Zhu and Mullins, 1992).

4.3.1. Theory of Fluorescence

LIF measures quantities that are proportional to the emitted fluorescent light, I_f, which depends on the dye concentration, C, and the intensity of the laser, I_l. If the operational intensity of the light source is considerably lower than saturation level, these quantities are related by the form $I_f \propto I_l C$ (Crimaldi, 2008). Neither I_f nor I_l are easily measurable. Experimentally, I_l is equivalent to the laser output power, P, and its spatial variation depends on the laser sheet optics, and concentration-dependent absorbance. Also, if I_f is isolated from all other light sources using an appropriate filter, it will be measured as camera-dependent intensity value I. This equivalence is better expressed as

$$P \rightarrow I_l \overset{\Phi_y}{\Rightarrow} I_f \overset{\Phi_E}{\rightarrow} I \qquad \textit{Eq. 4.3-1}$$

The dye's quantum yield, Φ_y, governs the relation between I_l and I_f. The proportionality between I_f and I is described by the camera's quantum efficiency, Φ_E. For LIF experiments in optically thin systems, i.e. without light attenuation along the beam path (Vanderwel and Tavoularis, 2014), the foregoing relationship simplifies to

$$I = A_1 \Phi_E \Phi_y \varepsilon \, P \, V \, C \qquad \textit{Eq. 4.3-2}$$

Where V represents the measurement volume, ε the absorptivity coefficient, and A_1 is a proportionality constant. The variable of interest in the calibration equation is C, and all other quantities can be lumped into a single coefficient, thus removing the need to quantify P.

For systems with light attenuation (e.g. due to low laser power), Eq. 4.3-2 is insufficient to compute C, as P will change over V. Light/Power attenuation through an aqueous medium is modelled using the Bouguer-Beer-Lambert law, BBL (Ferrier, Funk and Roberts, 1993; Mayerhöfer, Pahlow and Popp, 2020) which relates the change in laser beam power, between points x_0 and x_1, to the concentration, C, and absorption coefficient, ϵ, of the medium.

$$P(x_1) = P(x_0) \exp\left[-\epsilon \int_{x_0}^{x_1} C(r)dr\right] \qquad \textit{Eq. 4.3-3}$$

4.3.2. Physical Components and Set-up

The image acquisition devices chosen for the LIF experiments were POINTGREY FL3-U3-13Y3-C cameras, with an image resolution of 1280 x 1024 px, and the following relevant technical specifications (FLIR, 2017).

Table 4.3-1. Relevant Camera Parameters.

Resolution (px)	1280 x 1024
Colour range	Monochromatic
Pixel Depth (bits)	8
Exposure Range	0.1129 µs – 0.99 s
Quantum Efficiency (%)	60 – 65*

*The range given is the maximum achievable and it is valid for wavelengths between 475 and 600 nm.

The camera was coupled with a NAVITAR NMV-4WA wide angle lens, with nominal focal length of 3.5 mm and lens aperture in the range f/1.4 to f/11 (NAVITAR, 2016). Lens aperture and focal length were fixed manually and remained constant for the experiments. To allow mainly parallel incident light beams into the lens, so that a wider intensity response was available and the images were less sensitive to focal length, an aperture of f/8 was selected.

A reference graduated ruler was used to associate pixels width specific points along the laser beam, and correct for multiphase refraction and lens distortion. The latter is common to wide angle lenses, and can be radially symmetric and solvable via an odd polynomial model, usually up to the third degree (Jiang, Zhang and Zhou, 2003; Stamatopoulos and Fraser, 2011). Regarding digital parameters, only the Shutter Speed/Time was found to be consequential. The shutter time is limited by the framerate, which for the LIF experiments ranged between 5 – 30 fps, and the chosen Shutter times were between 2.5 and 10.5 ms. As 30 fps works out to an interval of 33.33 ms, no scan time overlap occurs.

As mentioned in Section 4.2, the experiments presented in this thesis build and expand on the work presented in West (2016) and Sonnenwald *et al.* (2017); the illumination equipment used in this work was the same. The four lasers used for the LIF system (see Figure 4.2-1) are solid state, continuous wave (CW) lasers, manufactured by Changchun New Industries Optoelectronics Tech., with the following specifications.

Table 4.3-2. General specifications of the lasers used.

Operating Mode	CW
Nominal Output Power (mW)	200
Transverse Mode	TEM_{00}
Wavelength (nm)	532
Operating Temperature (°C)	$10 \sim 35$

CW lasers are generally more stable, particularly in TEM_{00} mode, i.e. with a continuous Gaussian cross-sectional distribution of intensity. The actual measured output powers were 180, 260, 285 and 242 mW. Given the power outputs, power attenuation was expected. To calibrate for attenuation, Optical Density (OD) filters were used, which are described by the percentage of light transmitted through, as defined by the power law in Eq. 4.3-4. Where OD represents the values of the optical density filter, P_o is the resulting attenuated laser power by the OD filters and P_N is the nominal output power for each laser.

$$P_o = P_N \, 10^{-OD} \qquad \textit{Eq. 4.3-4}$$

Given the lasers available for the experiments, particularly the excitation wavelength of 532 nm, the most appropriate dye was Rhodamine 6G. The peak absorption and emission wavelengths of the dye are around 525 nm and 548 nm, which visually correspond to light at the green and yellow bands of the visible light spectrum (as can be seen from Figure 4.2-2a). The concentrations of Rhodamine 6G are chosen depending on laser power and the expected attenuation response. In aqueous solutions, Zehentbauer *et al.* (2014) reported a solubility around 0.02 g/ml ($1.5\cdot10^7$ ppb), and a linear concentration-fluorescence proportionality in the range $0\text{-}10^{-4}$ g/ml ($0\text{-}7.69\cdot10^4$ ppb). During the calibration, it was found that laser attenuation becomes a problem (i.e. incident light intensity is completely depleted before reaching the opposite side of the flume) for uniform concentrations above 10^{-7}g/ml (77 ppb). The concentration for the initial injections was thus set to obtain traces in the range 0-80 ppb.

To isolate the fluorescent dye emission spectrum, a Long-Pass filter with a cut-on wavelength of 570 nm (OG570) was used. The light transmitted through the chosen sensor, though limited, was seen to be sufficient to fully describe the entirety of the laser beam.

4.3.3. Intensity-Fluorescence-Concentration Calibration

To obtain appropriate power-intensity-concentration calibration equations, known uniform concentrations of dye were added to an enclosed section of the flume containing the 4 LIF lasers. The power output from the laser was varied and images captured for each combination of these quantities. Converting the BBL law to discrete form, the variation in calibration intensity, I_n, over a pixel distance, n, can be fitted using the attenuation expression in Eq. 4.3-5.

$$I_n(C,P) = I_o(C,P)\exp(-\eta(C,P)n) \qquad \textit{Eq. 4.3-5}$$

Consider I_o as the 'output' intensity from the image, which is analogous to P_0, and η as the attenuation coefficient (analogous to the integral product in Eq. 4.3-3). The best-fit coefficients, I_o and η, vary over the uniform concentration, C, and power, P values. The absorbance, η, is a function only of concentration, and follows a linear relationship (Ferrier et al. 1993).

$$\eta(C) = \eta_w + \epsilon_o C \qquad \textit{Eq. 4.3-6}$$

Where η_w is usually considered as the attenuation coefficient due to clean water (Ferrier, Funk and Roberts, 1993). However, because filters remove all incident light from clean water, η_w will be considered to be a purely empirical value. I_o has a double dependence on concentration and power, $I_o = f(C,P)$. If desired, a surface map for $I_o(C,P)$ can be constructed, from the known quantities C and P_o, and an approximate equation derived. Alternatively, independent solutions of the form $I_o = f_C(P) = f_P(C)$ can be obtained. Performing independent best-fit procedures, the following empirical equation was obtained.

$$\frac{I}{P} = a_1 C^{b_1} + e_1 \qquad \textit{Eq. 4.3-7}$$

Where the ratio I/P is known as fluorescence efficiency (Ferrier, Funk and Roberts, 1993). A linear fit is normally expected for Eq. 4.3-7; however, it was found that adding a power dependency (i.e. b_1), allows for a closer approximation whilst adding the physical condition of null fluorescence efficiency as $C \to 0$. No significant changes were found by omitting the empirical coefficient e_1. The final calibration was obtained to be

$$I_n = a_1 P_{n-1} C_n^{b_1} \qquad \textit{Eq. 4.3-8}$$

A recursive calibration is then obtained by pairing Eq. 4.3-8 with the discrete form of Eq. 4.3-3, such that for each n, the previous attenuated power, from Eq. 4.3-9, is used to compute concentration.

$$P_{n+1} = P_0 \exp\left[-\sum_{i=0}^{n}(\eta_w + \epsilon_0 C_i)\Delta x_i\right] \quad \textit{Eq. 4.3-9}$$

4.4. Particle Image Velocimetry System Description

PIV is used to obtain instantaneous velocity maps over illuminated areas of a flow field. This is achieved by computing the relative displacements of tracer particles following the movement of the fluid, between consecutive frames captured at regular intervals. Conventional PIV systems comprise 3 main components: imaging equipment, illumination source alongside sheet optics, and seeding particles. The general principle for PIV alongside the system used for the hydrodynamic characterization of the RandoSticks configuration is presented as follows.

4.4.1. Theoretical Framework

The theory of displacement computation for PIV follows a general principle of 'pattern matching'. The intensity map $I(\overrightarrow{X_p}, t_1) \equiv I_1(\overrightarrow{X_p})$ from an array of particles, $\overrightarrow{X_p}$, passing through the illuminated plane at $t = t_1$, is compared to a subsequent recording, $I(\overrightarrow{X_p}, t_2) \equiv I_2(\overrightarrow{X_p})$ at $t_2 = t_1 + dt$. The difference between I_1 and I_2 is the displacement that particles $\overrightarrow{X_p}$ have undergone during the interval dt (Adrian and Westerweel, 2011; Raffel *et al.*, 2018).

A detailed analysis requires each I to be divided into interrogation windows, the size of which is determined such that particles within it experience the same displacement. Defining $\tau_1(\overrightarrow{X_p})$ and $\tau_2(\overrightarrow{X_p})$ as the maps corresponding to the same interrogation window within maps I_1 and I_2, respectively, the act of searching for a 'match' between t_1 and t_2, can be expressed as the cross-correlation function, $R(\vec{s})$, defined over the displacement domain $\vec{s} = (\Delta x, \Delta y)$.

$$R(\vec{s}) = \int \tau_1(\overrightarrow{X_p})\, \tau_2(\overrightarrow{X_p} + \vec{s})\, d\vec{X} \quad \textit{Eq. 4.4-1}$$

The correlation value over the displacement domain, $\vec{s}$, will be the result of different interactions between particles. Accordingly, $R(\vec{s})$ can be defined as

$$R(\vec{s}) = R_C(\vec{s}) + R_F(\vec{s}) + R_D(\vec{s}) \qquad \text{Eq. 4.4-2}$$

$R_C(\vec{s})$ is the convolution of mean light intensity over both interrogation windows, $R_F(\vec{s})$ is a random component associated intensities from non-matching particles, and $R_D(\vec{s})$ is the cross-correlation peak at, $\vec{s} = \overrightarrow{s_D}$, which matches the particles in τ_1 to their displaced versions in τ_2. The digital version of the correlation function shown in Eq. 4.4-1, for discrete interrogation windows $\tau_1[m,n]$ and $\tau_2[m,n]$, is presented in Eq. 4.4-3. The values μ_τ and $\mu_\tau[p,q]$ represent the average intensity over τ_1 and the area where τ_1 and τ_2 overlap, respectively.

$$R[p,q] = \sum_{m=1}^{M}\sum_{n=1}^{N}(\tau_1[m,n] - \mu_\tau)(\tau_2[m+p,n+q] - \mu_\tau[p,q]) \qquad \text{Eq. 4.4-3}$$

The most probable displacement of the particles between τ_1 and τ_2 (Figure 4.4-1a and b) is found as the coordinates of the peak in the correlation function shown in Figure 4.4-1c. The components of $R(\vec{s})$ are shown in Figure 4.4-1d.

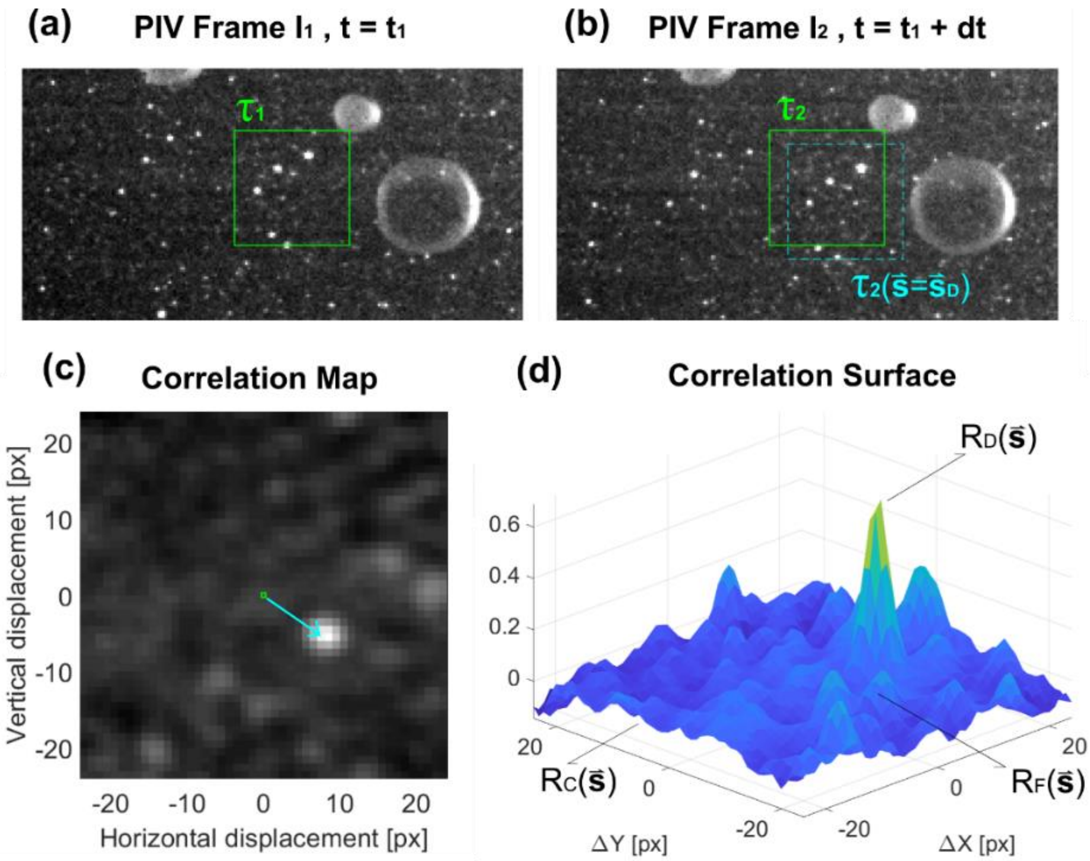

Figure 4.4-1. Displacement calculation based on cross-correlation analysis of consecutive frames, a) and b) interrogation windows for both images, with (cyan) rectangle showing the displaced particles. c) Correlation map detailing the origin (unmoved interrogation window) and the estimated displacement vector. d) 3D correlation surface detailing the components in Eq. 4.4-2.

Adrian and Westerweel (2011) found that higher particle densities increase the amplitude of the peak, and high velocity differentials within the interrogation window increases the width of $R_D(\vec{s})$, whilst decreasing its peak. Direct spatial correlation operations are done in the spectral domain via FFT computations for efficiency. Also, accuracy is improved by successive iterations with smaller interrogation windows (Scarano, 2002). These methods are now standard and implemented in commercial and open-source PIV software packages, including PIVlab® (Thielicke and Stamhuis, 2014), the one used for this project.

4.4.2. Physical Components and Set-up

To illuminate the PIV field of view, DURAN® borosilicate 3.3 glass cylinders (refractive index of 1.473 for wavelengths around 586.7 nm, Schott, 2017) were used. The value for water is 1.333. To avoid light focusing at the back of the cylinders, glass tubes were used for the 12, 15 and 20 mm diameters; and glass rods for 4 and 8 mm. The acrylic plate (refractive index = 1.495 at 532 nm wavelength, Kasarova *et al.*, 2007) shown in Figure 4.2-2b, located above the viewing glass window, was used to allow visibility, hold the glass stems in place, and allow maintenance. A 2D calibration was performed to correct for multiphase distortion. It should be noted that the components used were independent. This allows more versatility and control in complex facilities. Conversely, it also increases the degrees of freedom involved in setting up and calibrating the system.

The imaging component of the PIV system was composed of a Blackfly® BFS-U3-23S3 camera (FLIR, 2018), and a short-focal, Computar® H6Z0812 manual lens (Computar, 2018). No lens distortion was found. However, a longer focal distance between the lens and the illuminated plane was necessary to cover a field of view of 0.5 x 0.3 m. A maximum exposure time was chosen to allow more information from the darker areas, and this value was selected as a multiple of the frame rate of the camera. The camera used has a maximum resolution of 1920 x 1200 pixels. The camera shutter time and the scanning rate of the sheet generator were synchronized to avoid scan overlap (Rockwell *et al.*, 1993). The different combinations of synchronization parameters applied to each test are presented in Table 4.4-1.

Table 4.4-1. Relationship between digital camera parameters and laser sheet scan rate.

Frame Rate (fps)	Exposure time (µs)	Laser Scanning period (µs)	Number of scans per exposure
60	8335	463	18
65	7691	384.5	20
80	12501	329	38
110	9089	303	30
120	8335	463	18
125	7998	421	19
130	7691	384.5	20
160	6249	390.5	16

The camera gain was used to amplify the signal to a point, beyond which the increase in noise would have been detrimental to the image quality. The laser used for the experiments is a class 4, CNI MLL-W-532, with the characteristics given in Table 4.4-2. The laser was embedded into a sheet generator with a polygonal and parabolic mirror. The dimensions of the illumination plane produced were 700 x 15 mm, and the possible scanning rates were in the range 225 – 750 µs. This system was chosen over a pulsed laser, to avoid higher non-uniformities by the glass cylinders, and for constraints of space and cost.

Table 4.4-2. General specifications of the PIV laser used.

Operating Mode	CW
Nominal Output Power (W)	10
Transverse Mode	TEM_{00}
Wavelength (nm)	532
Beam diameter (mm)	~ 1.0
Operating Temperature (°C)	10 ~ 35

Several scans were done per frame, to obtain more stable scattering and less flickering. Although measures were taking to mitigate light attenuation, some still persisted, which were digitally corrected. Nonetheless, the system is still considered a step forward in the understanding of vegetated hydrodynamics.

Seeding particles were selected to yield the highest possible scattering, whilst moving without affecting the underlying structures of the flow. For this project, emphasis is given to the area, which requires larger particles to provide higher scattering. The selected particles were polyamide 12, of 100 µm diameter. The injection line was located 1.5m upstream of the PIV measurement section, and in order to avoid jet effects the velocity was chosen to match that of the lowest flow rate, and remained constant. In this way, it was expected that the particles assimilate the ambient flow before the PIV section. The final seeding density was achieved by calibrating the concentration of polyamide in the stirring tank.

4.4.3. Data Preprocessing

This section describes the procedure to relate points in the interrogation volume to the intensity maps, correct for light attenuation and spatial illumination differences. A regular grid of fibre-optic LEDs with marked coordinates, connected to the location of the stems, was used to correct for possible distortion, focus the lens and obtain the real coordinates of the flow field. Figure 4.4-2a shows the calibration plate used to obtain the real coordinates from the flume. Distortion was found to have a negligible effect on the velocity maps obtained.

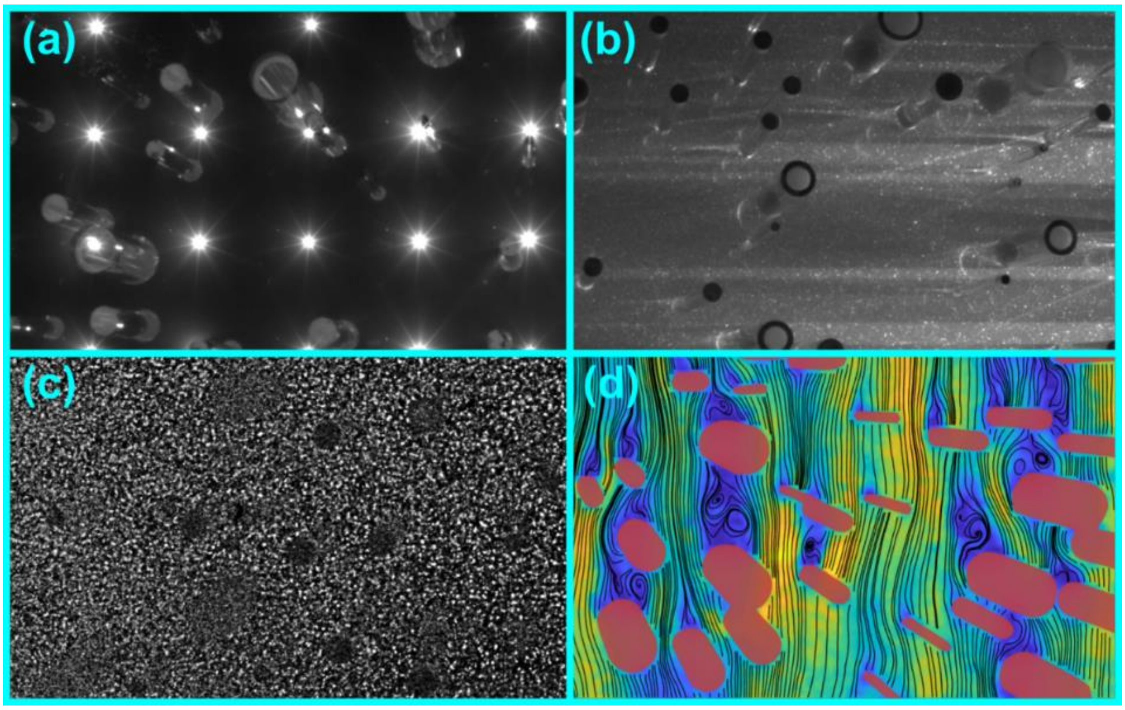

Figure 4.4-2. a) Calibration template for pixel-distance transformations b) Raw PIV recording c) PIV recording after the pre-processing algorithm. d) Streamline and velocity map from PIV recording

The main issue found was light attenuation along the direction of the laser sheet, resulting from cylinder refraction. A correction factor was used to obtain a uniform average intensity along the attenuating direction, and amplify signals in dimer areas. Further, background illumination from unseeded images was subtracted to remove local light heterogeneities.

The resulting images were then passed through the pre-processing filters included in the PIV software packages used (Thielicke and Stamhuis, 2014). For reference purposes, the PIVlab pre-processing settings used were: Contrast Limited Adaptive Histogram Equalization (60px), Highpass (16px) and denoise (3px) filters; seeded background removal, intensity capping and limit stretching. Multiple passes (3) starting from 120px, and 32, 24, 20 and 16px for the final interrogation windows

4.5. Results

It should be reiterated that the purpose of this chapter is to introduce the RandoSticks configuration, together with the experimental system built around it to comprehensively characterize concentration and velocity fields. Acknowledging the scope of this experimental study, the results presented in this section are intended to demonstrate the potential of the acquired dataset. Regarding the LIF experiments, the 4 lasers allowed for the construction of $C(t, y)$ maps, at distinct, equally spaced locations, as shown in Figure 4.5-1. Streamwise and Transverse dispersion is evident from this comparative plot, and small-scale effects caused by vortex shedding from the cylinder is also evident. This is an indication of the level of detail achieved by the experimental system. For consistency, all pulse injections were performed over 5 seconds, with the same initial concentration of Rhodamine 6G (40.2 mg/).

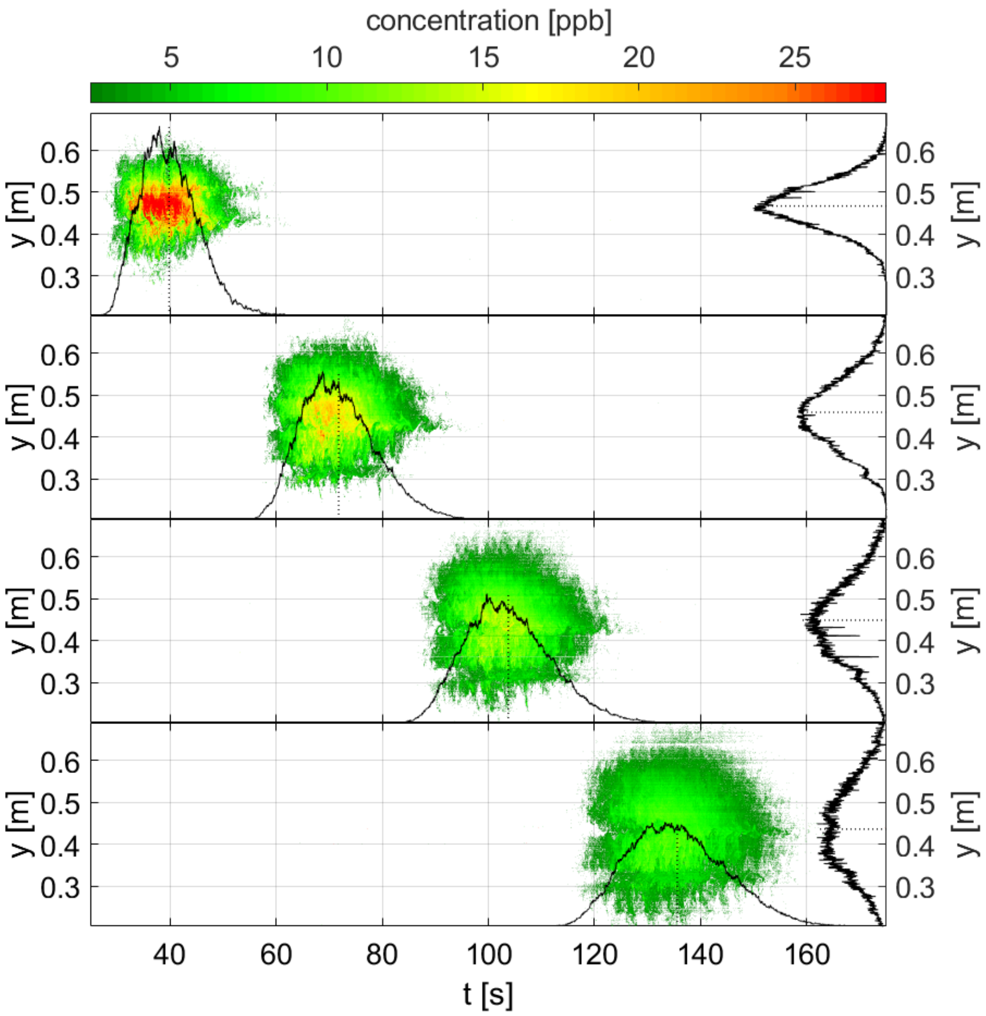

Figure 4.5-1. Concentration maps obtained for a test conducted at Re_d =316, and midpoint (y =0.5m) injection location.

Finally, the integration of the PIV system, together with the methodology introduced to deal with illumination heterogeneities and attenuation, allowed for the construction of comprehensive velocity maps over a representative area of the system. Figure 4.5-2 shows a velocity map over the entire Field of View, showing the scope of the hydrodynamic characterization, alongside a zoomed in view detailing the resolution of velocity data achieved. Although higher velocity map resolutions involved higher noise levels, compromises in terms of resolution and different frame rates still allowed for the construction of detailed hydrodynamic maps, that can help described velocity scales at different levels. For instance, velocity fields with smaller resolutions were found to perform better to obtain second-order velocity statistics (e.g. turbulent kinetic energy), whilst vorticity was better described around stems using smaller interrogation windows. Noise was generally found to decrease with lower frame rates.

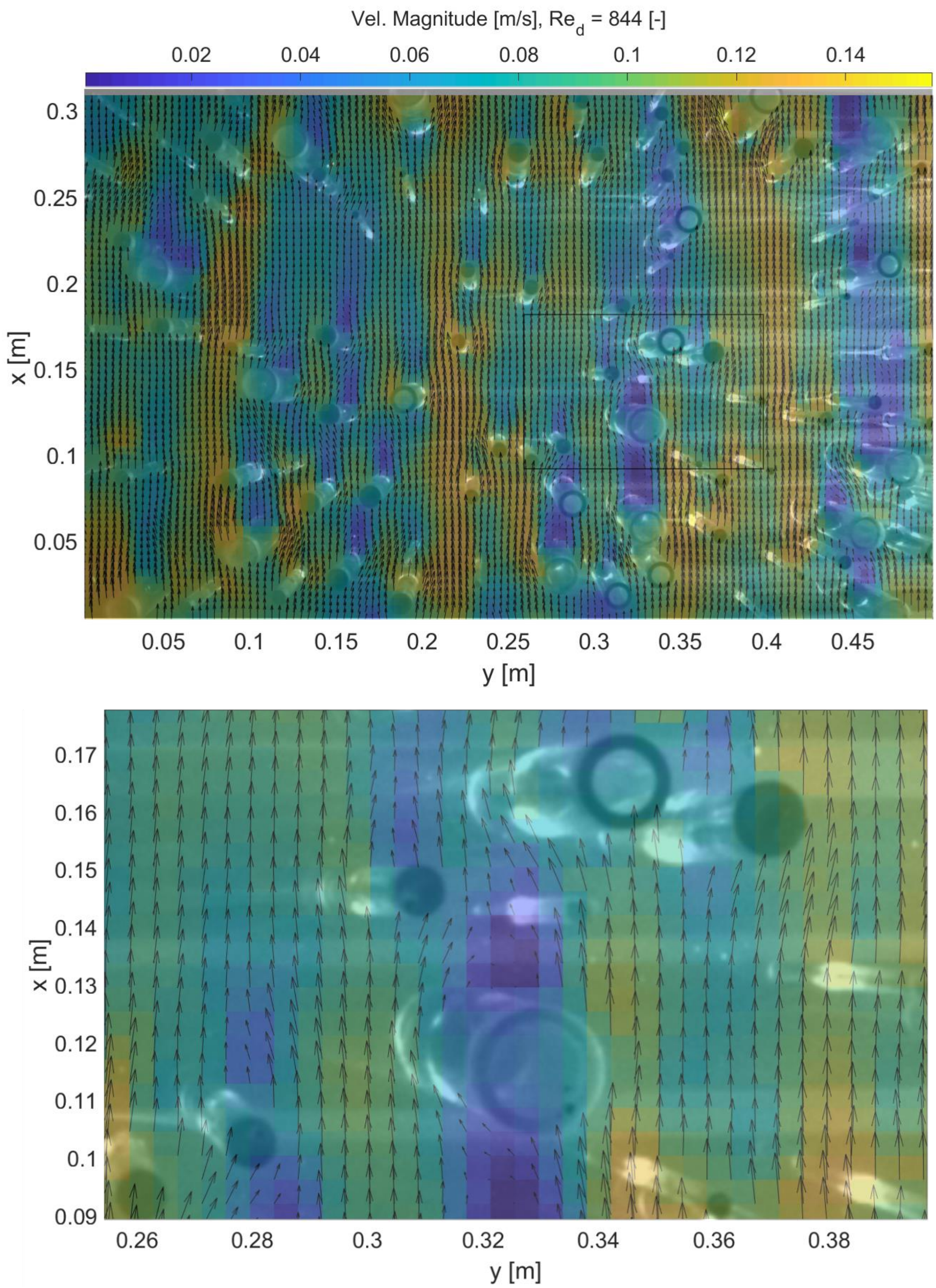

Figure 4.5-2. Velocity magnitude and vector plot over the PIV field of view.

4.6. Summary

The results presented are intended to illustrate the capabilities of the system, and its potential to generate relevant hydrodynamic and mixing data. The installation and operation of the LIF and PIV systems required the use of special equipment and novel methods, to overcome the physical challenges of obstructed flows. These methods are expected to help researchers conduct more detailed experiments in different sorts of obstructed flows. This chapter offers a summary of the methods used to obtain the experimental results analysed in the subsequent chapters. A detailed account of the steps necessary to complete the configuration described here, intended to serve researchers with the knowledge necessary to set up LIF and PIV systems are given in Appendices A and B. The primary data presented here attest to the potential of the system to yield high-quality data.

Chapter 5. 2D DISPERSION CHARACTERISTICS IN A RANDOSTICKS CONFIGURATION

Abstract

This chapter covers the principles and methods used to pre-process and analyse the concentration profiles obtained from LIF data. Given the breadth of information collected, only data from centre-point injections has been selected for a detailed analysis of the methodology. Regarding the methods used, no significant difference was found between parameters calculated from a method of moments analysis or optimisation. The only noticeable difference is in the early stages of mixing for the lowest flow rates, where asymmetry reduces the applicability of the Gaussian solution to the ADE for longitudinal dispersion. Regarding dispersion coefficients variation with Re_d: longitudinal dispersion has two distinct regimes, separated at $Re_d \approx 400$, indicating the influence of different physical processes. Transverse dispersion does not vary with Re_d. Results of dispersion are in remarkable agreement with the relevant literature, both in terms of processes and magnitudes, particularly for non-dimensional coefficients.

Section 5.1 provides a quick review of the theory and simplifying assumptions used to model dispersion. The procedure to simplify and clean the measured concentration data is detailed in Section 5.2. Transport quantities calculated from statistical moments and parameter optimisation of the governing equation are presented in Section 5.3 and Section 5.4, respectively. Section 5.5 explores the variations of longitudinal and transverse dispersion coefficients, with Reynolds number, measured in the RandoSticks configuration. A study of the influence of initial conditions on dispersion is presented in Section 5.6, followed by an exploration of memory effects in Section 5.7. The general conclusions from the RandoSticks system are presented in Section 5.8 and the dispersion results are contextualised and compared with previous studies in Section 5.9.

5.1. Introduction

5.1.1. Relevant Theory

Given the importance and ubiquitous nature of vegetated flows (e.g. floodplains, wetlands, coastal marshes, etc.), studying the transport and mixing of solutes in these environments is crucial, not only for conservation purposes but also for the design of engineered treatment systems. Assuming incompressibility, and equal densities between solute and solvent (i.e. water), the hydrodynamic transport of a passive substance can be modelled via the Advection Diffusion Equation (ADE)

$$\frac{\partial C}{\partial t} + u_i \frac{\partial C}{\partial x_i} = \frac{\partial}{\partial x_i}\left(D \frac{\partial C}{\partial x_j}\right) \qquad \textit{Eq. 5.1-1}$$

where tensor notation is used, implying that repeated subscripts represent a sum over the index space. C is the instantaneous concentration value defined in all spatial coordinates, x_i, and time, t, values; u_i represents the velocity vector and D the molecular diffusion coefficient. Since the focus of this study is on dispersion through vegetated flows, some additional assumptions may be used to simplify Eq. 5.1-1. Considering vegetation as vertical cylindrical elements such that the system is vertically similar, a relatively low water depth, and bed boundary effects being outweighed by vegetation effects (Nepf, Sullivan and Zavitoski, 1997), the system can be regarded as two-dimensional. Further, if we consider the flow to be advective (i.e. zero mean transverse, V, and vertical, W, velocities) and mixing to be directionally and spatially independent, Eq. 5.1-1 can be expressed in simplified form (see Section 2.3.1):

$$\frac{\partial C}{\partial t} + U \frac{\partial C}{\partial x} = D_x \frac{\partial^2 C}{\partial x^2} + D_y \frac{\partial^2 C}{\partial y^2} \qquad \textit{Eq. 5.1-2}$$

Eq. 5.1-2 reduces the transport to a description of the advective component, i.e. mean streamwise (x) flow velocity, represented by U; and represents mixing by the independent longitudinal, D_x, and transverse, D_y, dispersion coefficients, which integrate the effects of cross sectional shear, trapping zones, energy dissipation, turbulent and molecular diffusion together for each direction. An analytical solution to Eq. 5.1-2 requires initial and boundary conditions that can be reproduced experimentally. For conservative systems and known (measured) initial concentration profiles, Baek, Seo and Jeong (2006) propose the routing solution given in Eq. 5.1-3, assuming the "frozen cloud hypothesis"[10] in order to reduce the dependence of $C(x, y, t)$ on (y, t) only, which is more applicable to LIF measurements.

$$C(X_2, y, t) = \int_0^W \int_{-\infty}^{\infty} \frac{C(X_1, y^*, t^*)U}{4\pi(t_{c2} - t_{c1})\sqrt{D_x D_y}} \exp\left\{-\frac{U^2(t_{c2} - t_{c1} - t + t^*)^2}{4D_x(t_{c2} - t_{c1})}\right\} \times \exp\left\{-\frac{(y - y^*)^2}{4D_y(t_{c2} - t_{c1})}\right\} dt^* dy^* \qquad \text{Eq. 5.1-3}$$

where t_{c1} and t_{c2} are the times at which the centroids of the concentration profile pass by the upstream and downstream longitudinal measurement locations, defined as X_1 and X_2 respectively[11]. It should be noted that Eq. 5.1-3 describes a 'Gaussian' transport which is only valid in the Fickian regime, that is, after some time wherein local shear effects induce asymmetric behaviour in the dispersion process (Rutherford, 1994). Comments on the validity of this assumption for the collected data will be explored in Section 5.3.4.

The same assumptions regarding vegetation and mixing processes have been adopted previously for experimental estimations of D_x (e.g. Huang *et al.*, 2008; Shucksmith, Boxall and Guymer, 2010) and D_y (e.g. Serra, Fernando and Rodríguez, 2004; Tanino and Nepf, 2008b), and for the development of simplified physically-based models for the same quantities (White and Nepf, 2003; Lightbody and Nepf, 2006b; Tanino and Nepf, 2009). Previous experimental and model results, alongside a number of estimations from LIF experiments testing a range of different Reynolds numbers, stem densities and diameters; for natural and artificial vegetation, were compiled and analysed by Sonnenwald *et al.* (2017). In that study—the first where full $C(t, y)$ maps were recorded—it is shown that existing models, and measurements in artificial vegetation, are unable to accurately predict dispersion for real vegetation, which also presents a large variability of estimated dispersion metrics. It was proposed that the dependence on singular length scales (i.e. diameter and spacing) in most models, and the use of uniform diameters in previous artificial vegetation experiments, are unable to capture the complexities of real emergent vegetation.

The inconsistency between results from natural and artificial vegetation, shown in Sonnenwald *et al.* (2017), is attributed to using uniform diameters in artificial arrays, which cannot represent

[10] This hypothesis asserts that the changes in shape of the concentration profile, as it passes through the measurement point, are negligible.
Mathematically, this means that $C(X_i, t) \cong C(x_i, \bar{t}_i)$, with $x - X_i = U(\bar{t}_i - t)$. It should also be noted that this assumption is considered valid for large dimensionless times after injection (Fischer *et al.*, 1979).
[11] To avoid confusion, uppercase letters with subscripts, X_i, indicate specific spatial points; and lowercase letters with subscripts, x_i, represent spatial coordinates in tensor notation.

the heterogeneities of vegetation morphology. According to the characterisation performed in that study, for the natural species tested, factors such as stem diameter distribution and vegetation layout (e.g. random locations, clustering) must be considered for artificial vegetation systems. Based on this premise, a new configuration is proposed, which consists of a random distribution of circular PVC rods, with a diameter distribution resembling that of winter *Typha latifolia* (as measured by Sonnenwald *et al.*, 2017). This configuration will be referred to as RandoSticks. It is hypothesised that including diameter distributions will account for the variety of flow scales and thus yield dispersion coefficients closer to the ones measured in real vegetation. The objective of this chapter is then to describe macroscopic transport in the new configuration proposed, described in Chapter 4. The vegetation layout, flow rates and number of tests for each injection location are presented in Section 4.2 (Chapter 4), the concentration maps (i.e. primary data) from the LIF tests are illustrated in Section 4.5 (Chapter 4). A detailed account of the experimental set-up and calibration procedure is given in Appendix A. The hydrodynamic characterisation will be given in Chapter 6.

5.2. Concentration Data Pre-processing

5.2.1. Concentration map simplification $\boldsymbol{C(t,y) \rightarrow C(t), C(y)}$

This section presents the dimensional simplification of the measured concentration profiles. Once the LIF data has been acquired, compiled and the calibration applied, 2D concentration maps, $C(t,y)$, like the one shown in Figure 5.2-1a, are obtained. The frame rates (see Table 4.2-1) and image resolution (see Chapter 4) chosen for the production of concentration maps, allow for a detailed spatial characterisation of concentration distributions, even at scales associated with the smallest cylinders (i.e. ~ 4 mm). Since the focus of this study is on large-scale mixing characterisation, it is necessary to reduce the complexity (i.e. size) of the concentration data. These simplifications have impacts on the computation efficiency statistical parameters (e.g. Method of Moments, Section 5.3) and optimisation routines (Section 5.4). Under the assumption of directional independence, given in Section 5.1, and knowing that the axes in Figure 5.2-1 are aligned with the main dispersion directions, it is possible to reduce the measured 2D concentration maps to one-dimensional concentration profiles by taking the mean along each axes, as shown in Eq. 5.2-1.

$$C(t) = \frac{1}{Y}\int_0^Y C(t,y)\,dy \quad ; \quad C(y) = \frac{1}{T}\int_0^T C(t,y)\,dt \qquad \textit{Eq. 5.2-1}$$

The final concentration profiles obtained from the directional averaging are shown in Figure 5.2-1b and c. The simplified concentration profiles reduce both the size and degrees of freedom necessary to perform the optimisation procedures described below, to obtain dispersion coefficients, thus improving the accuracy and reducing computation time. Note that given the nature of noise from LIF images, the 1D profiles obtained will have artificial background concentration levels that must be removed before performing any analysis, to avoid biases in the estimation of statistical parameters (e.g. centroids, variances etc.). The methods and criteria adopted to limit the cloud of dye, remove background and apply mass conservation to the concentration profiles are explained in Section 5.2.2.

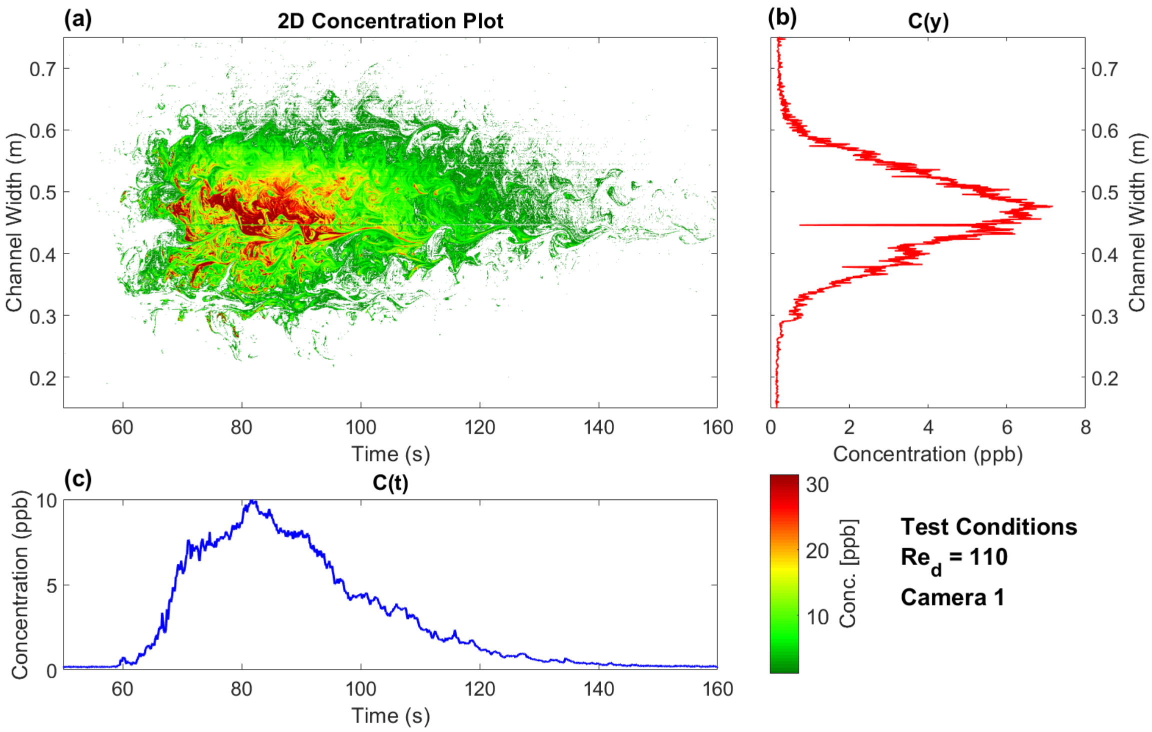

Figure 5.2-1. Derivation of 1D concentration profiles from 2D concentration maps a) Temporal-Transverse Concentration Map for camera 1, b) 1D Concentration profile in the transverse direction, c) 1D Concentration profile in the temporal domain.

5.2.2. Trace pre-processing

As shown in Figure 5.2-1, the integration process undertaken to dimensionally reduce the concentration maps can lead to an increased level of background concentration and statistical biases. To avoid this, a criterion to delimit the plume based on the features of the data (as opposed to any predetermined value) was adopted.

Consider the sample raw concentration profile, $C(y)$, shown in Figure 5.2-2a, which is obtained from the integration presented in Eq. 5.2-1. In order to differentiate the background from the plume, a moving average was performed along the profile to smooth noise and better identify features from the dataset. From the smooth profile it is possible to compute an initial guess of the background level, and the maximum (i.e. peak) concentration by averaging a sample of the smallest and highest values, respectively. Subtracting the former from the latter, an estimate of the measured concentration range is obtained. For this project, the sample was associated to the length of each profile, namely, 5% of the number of data points. This value is given as a reference, and any further application of this technique should consider the features of each specific dataset.

The lateral limits of the plume can be found as the points in the smooth profile corresponding to a specific percentage of the computed concentration range. For reference purposes the threshold was chosen to be 5%, so the limits of the plume are found as the points in the smooth curve where concentration is equal to the background plus the threshold defined. To capture as much of the plume as possible, the limits are moved away from the plume centre by a quantity equal to some fraction of a characteristic spread metric from the plume (e.g. standard deviation). The spread selected was 3 standard deviations, which includes a bias from the background. This value was found to perform well for all profiles analysed, as the background was consistent. Figure 5.2-2 shows the location of the limits following this criteria, the points beyond the limits are considered the background to be removed.

From the characteristics of LIF measurements using low-power lasers (See Chapter 4 and Appendix A), it is expected that image intensity and thus concentration will vary due to power attenuation even in the absence of Rhodamine (Ferrier, Funk and Roberts, 1993). As a consequence, the background concentration will vary along the direction of the beam path, i.e. the width of the flume. Using the coordinates and concentration values of the background, a best-fit linear function is calculated and subtracted from the entire profile. Negative values and random noise beyond the plume limits are set to zero and the Clean Concentration Profile, as shown in Figure 5.2-2a, is obtained.

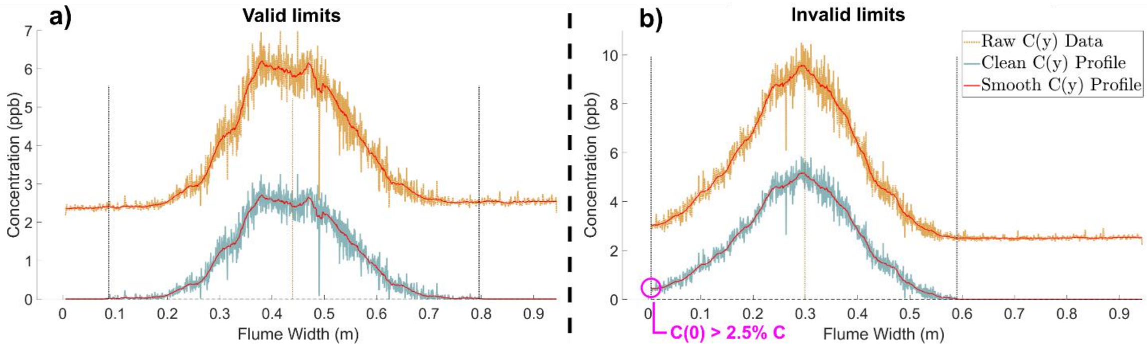

Figure 5.2-2. Comparison between raw measurements and final concentration profiles with removed background for a) Valid measurement b) Invalid measurement. Vertical lines denote the estimated limits of the plume. The background levels have been exaggerated for illustration purposes.

From the injection locations described in Section 5.1, edge cases where the computed limits fall beyond the flume width (i.e. dye reaching the side walls), are expected. For these cases, boundaries limit the spread of dye, rendering the dispersion values invalid. Figure 5.2-2b shows one of the tests where the left limit correspond to the flume walls. Numerically, a test is considered valid if the concentration value at the limits is lower than 2.5% of the peak concentration from the smooth profile; invalid otherwise. Note that smooth profiles are used to pre-process the concentration curves, and the statistical analyses described below are performed on the measured data with background removed.

5.3. Method of Moments Analysis

The statistics of concentration distributions, from pulsed injections, are similar to probabilistic functions, and thus share the same properties, summarised by the statistical moments (Fischer et al., 1979). Analytically, the general expression for the n-th degree moment, M_n, is defined as,

$$M_n = \int_{-\infty}^{\infty} t^n \, C(t) \, dt \qquad \text{Eq. 5.3-1}$$

Generally, moments from concentration distributions are functions of time, and from the dimensional reduction presented in Eq. 5.2-1, the definition is the same regardless of the domain. Eq. 5.3-1 will also apply for transverse concentration profiles by replacing t for y.

5.3.1. Mass Balance

To obtain optimised dispersion coefficients from the routing solution to the ADE model (see Eq. 5.1-3), it is necessary to guarantee mass conservation. Whether from the calibration or pre-processing phase, small deviations can occur in the concentration readings, which can yield differences in the mass balance. Conservation of mass implies that for a test with uniform velocity, all concentration profiles must have the same mass, i.e. constant zeroth, M_0, moment. For unsteady flow, the quantity to be constant is the flux: $uCdt$.

Performing a mass balance on all profiles in a test allows for a simultaneous visualisation of spread and decrease in peak concentration. Figure 5.3-1 and Figure 5.3-2 show the results of the pre-processing and mass balance on a specific LIF test, the statistical parameters of interest (centroid, variance, standard deviation and skewness) are given in Table 5.3-1 and Table 5.3-2. The specifics of these quantities will be explained in the following subsections.

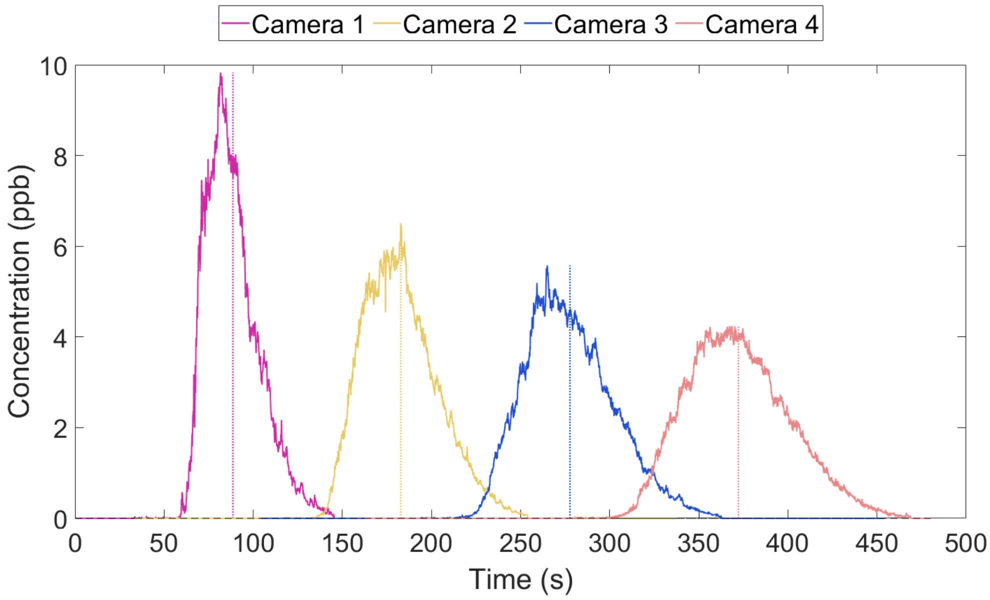

Figure 5.3-1. Longitudinal variation of time-dependent concentration profiles for $Re_d = 110$ ($q = 1.5$ l/s) and centre-line injection point, $y_{inj} = 0.50$ m.

Table 5.3-1. Statistical parameters from Concentration profiles shown in Figure 5.3-1.

	Camera 1	Camera 2	Camera 3	Camera 4
t_c (s)	88.6	182.8	277.7	372.3
σ_t^2 (s^2)	217.6	429.5	613.5	815.7
σ_t (s)	14.8	20.7	24.8	28.6
κ_t^3 $(-)$	0.79	0.50	0.46	0.37

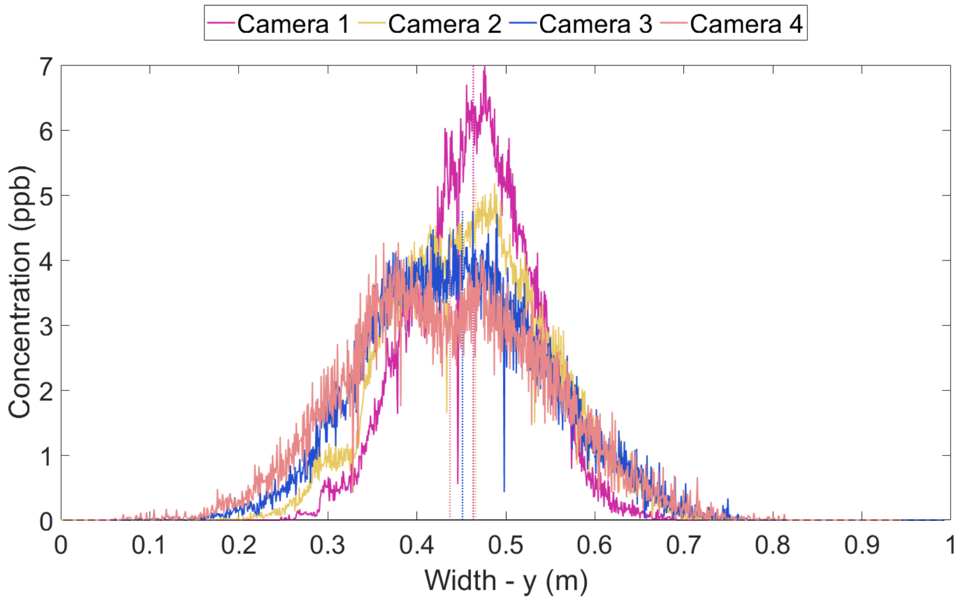

Figure 5.3-2. Longitudinal variation of y-dependent concentration profiles for $Re_d = 110$ ($q = 1.5$ l/s) and centre-line injection point, $y_{inj} = 0.50$ m.

Table 5.3-2. Statistical parameters from Concentration profiles shown in Figure 5.3-2.

	Camera 1	Camera 2	Camera 3	Camera 4
$\boldsymbol{y_c\ (m)}$	0.46	0.47	0.45	0.44
$\boldsymbol{\sigma_y^2\ (m^2)}$	0.0041	0.0069	0.0090	0.0106
$\boldsymbol{\sigma_y\ (m)}$	0.0642	0.0829	0.0946	0.1032
$\boldsymbol{\kappa_y^3\ (-)}$	-0.09	0.03	0.09	0.05

Figure 5.3-1 and Figure 5.3-2 have been corrected for mass conservation, i.e. the concentration profiles have been scaled so that M_0 is equal for all cameras. It should be noted that, although the calibration was set up to measure consistent concentrations (see Chapter 4 and Appendix A); differential advection, and local variations in fluxes resulted in calculated mass imbalances. Instrumentation-related effects were also found to induce small deviations in the measured concentrations. Nevertheless, 75 % of all tests reported mass balances better than 80% of the averaged M_0, and absolute differences below 30% were reported for 90% of the tests conducted. These percentages are deemed acceptable for vegetated flows, as shown in a detailed analysis of mass conservation given in Appendix A.

5.3.2. Concentration centroids and travel times

As mentioned in the previous subsection, concentration profiles share the same statistical properties of probabilistic distributions, therefore, centroids and measures of spread can be determined from the concentration profiles obtained. As will be explained below, these metrics will reveal information on the advective and dispersive behaviour of the flow.

The first of these metrics of interest is the centroid of the concentration distribution, which physically represents the centre of mass of the dispersive plume. Following from the general moment expression, Eq. 5.3-1, the centroid of a profile, t_c, can be found from the following expression (Fischer *et al.*, 1979).

$$\mu_t = t_c = M_1/M_0 \qquad \textit{Eq. 5.3-2}$$

Figure 5.3-1 and Figure 5.3-2 show vertical lines indicating the location of the centroids for each of the concentration profiles. The time it takes the cloud to travel from one measurement station (i.e. camera) to the next can be found as the difference of their respective centroid times as previously mentioned in Section 5.1.1. This travel time is defined as $\bar{t} = t_{c,i} - t_{c,i-1}$, where the subscript i represents measurement station. Sample values of this quantity can be found in Table 5.3-1, for the mass balanced profiles shown in Figure 5.3-1. For the case of $C(y)$, the difference, $\bar{y} = y_{c,i} - y_{c,i-1}$, now represents a displacement in the transverse direction. Figure 5.3-3 shows the travel times for each reach, for all tests performed with centre-line injections. For the whole range of Reynolds number tested travel times can be considered statistically constant; with noticeable variations only visible for the lowest flows. Acknowledging the limitations in the slope of the flume, it is important to note that differences in travel times do not account for noticeable variations in flow regime; which can be classified as uniform.

The travel times, and all further transport parameters (advection and dispersion) were computed for all valid tests, repetitions and centre-point injections. The results are grouped by reach (i.e. consecutive measurement points) and Reynolds number in Figure 5.3-3. For reference purposes, the upper and lower ends of the boxes represent the 75th and 25th percentile points, and the whiskers define the limits covering the central 99.3% (i.e. ±2.7 standard deviations from the mean) of the data, filled markers represent mean values and unfilled ones indicate outliers.

The reaches shown in Figure 5.3-3 are related to the mid-point between consecutive measurement locations. Mean values and boxplots of travel times are consistent for all reaches and each Re_d. A decrease in average travel times with Re_d is clearly evident, as expected. From the known measurement locations, X_i, the mean velocity, U, is computed using the calculated travel times. The consistency in travel times over all reaches suggests uniform flow; still, it is necessary to evaluate the flow regime in terms of U, for a correct application of the ADE presented in Eq. 5.1-2. Figure 5.3-4 shows the measured velocities, U, for all flows tested with a centre-line injection. Local changes in velocities were noticed over the measurement area, due to some restrictions of the system. Quantification of the differences shows that these are negligible for the purposes of applying a Fickian analysis of solute transport on the dataset.

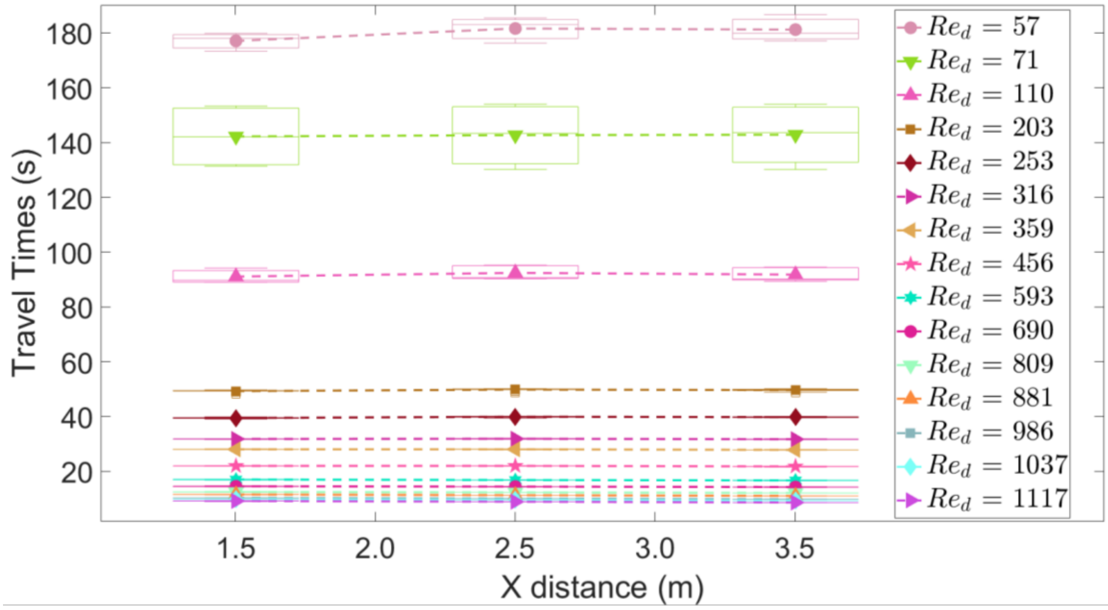

Figure 5.3-3.Variation in Travel Times as a function of Downstream distance, for tests with a centre-line injection $y_{inj} = 0.5$ m.

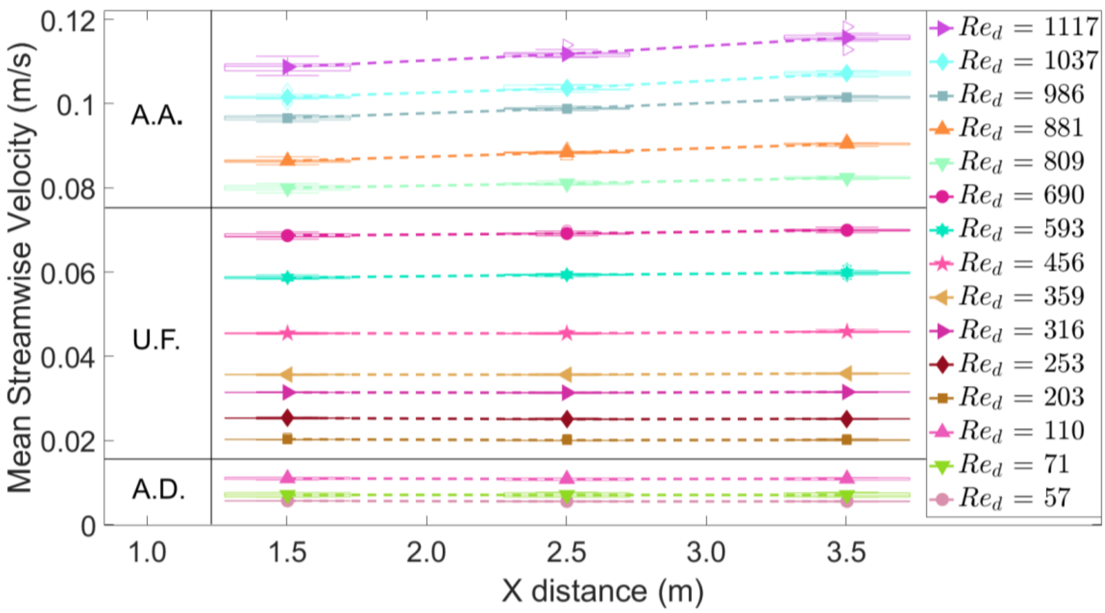

Figure 5.3-4. Results of mean (advective) velocities (U) for all flow rates tested, and centre-line injection $y_{inj} = 0.5$ m.

For all the tests summarised in Figure 5.3-4, the results show minimal variation for each reach. This reaffirms the robustness of the experimental procedure, calibration and pre-processing. Regarding the behaviour of mean velocity over the flow rates tested, it is possible to identify 3 groups: an advective deceleration (A.D.) range comprising the lowest 3 flows ($57 \leq Re_d \leq 110$); a uniform flow (U.F.) range composed of the central portion of flows ($203 \leq Re_d \leq 690$); and a final advective acceleration (A.A.) range covering the highest flow rates ($809 \leq Re_d \leq 1117$). The flume had a fixed slope, so unavoidable advective accelerations were expected given the range of flows tested. Nevertheless, after quantifying the percentage difference in velocity, ΔU, along the three reaches analysed (see Figure 5.3-4) it is noted that the highest difference is 6% for the highest flow. Table 5.3-3 shows a classification of flow regimes depending on the computed percentage difference from the mean values presented in Figure 5.3-4.

Table 5.3-3. Classification of flow rates according to longitudinal variation in mean velocity, U.

Deceleration	A.D.	$57 \leq Re_d \leq 110$	$-4\% < \Delta U < -2\%$
Uniform	U.F.	$203 \leq Re_d \leq 690$	$\lvert\Delta U\rvert \leq 2\%$
Acceleration	A.A.	$809 \leq Re_d \leq 1117$	$2\% < \Delta U < 7\%$

Albeit arbitrary, the classification presented in Table 5.3-3 shows that for Reynolds numbers below $Re_d < 809$, the change in velocity, over 3 metres, is below 4%. It can be concluded that uniform flow requirements for the experiments are valid within this range.

A similar exercise was performed for the lateral displacements of the plumes (see Figure 5.3-2 and Figure 5.10-1), to obtain mean transverse velocities, and it was found that all transverse velocities are below 2 mm/s (for the range of flows considered 'uniform', transverse velocities are below 1 mm/s). It can be concluded that lateral displacements do not play a role in the mean longitudinal motion of the dye and the tests performed comply with the assumptions of directional independence presented in Section 5.1. It should be noted that all flows are considered to behave more closely to uniform flows than non-uniform ones, on empirical grounds, based on the variation of velocities presented above. An analysis of dispersion considering the effects of these non-uniformities is a necessary exploration, and will be explored at the next research stage.

5.3.3. Concentration variance and dispersion Coefficients

It is known that shear, turbulence and physical obstructions (i.e. stems) contribute to the continuous spread of solutes (see Chapter 2). Figure 5.3-1 and Figure 5.3-2 show the expansion of the concentration profiles, alongside a decrease in peak concentration, as the dye travels downstream. Following from the similarities between concentration distributions and probability functions, the spread can be characterised with the variance, σ_t^2, σ_y^2, defined as (Fischer *et al.*, 1979),

$$\sigma^2 = \frac{M_2}{M_0} - \mu^2 \qquad \textit{Eq. 5.3-3}$$

Similar to the analysis of mean velocity, U, the computed variances from all valid tests, conducted for centre-line injections, were grouped and presented for all flow rates and all measurement stations and the results are shown in Figure 5.3-5 and Figure 5.3-6 for streamwise (temporal) and transverse variance evolution, respectively. It should be noted that, for the analysis of dispersion, the change in variance is analysed with respect to time. To allow uniformity, the plots in Figure 5.3-5 and Figure 5.3-6 are expressed in terms of a normalised time scale, t^*, defined as

$$t^* = (t_c - t_0)/\langle \bar{t} \rangle \qquad \textit{Eq. 5.3-4}$$

Where t_c is the centroid time for each profile, t_0 is the time of injection, which was constant for all tests, and $\langle \bar{t} \rangle$ is the average travel time over all reaches for each test.

For the streamwise evolution of longitudinal variances (Figure 5.3-5), their increase seems to follow a linear behaviour for the entire range of flows tested, even for those classified as non-uniform. This might suggest that all recordings fall close to the Fickian regime, and that constant advection, and therefore uniformity, could be safely assumed for the entire range of flows. The rate of spread decreases with increasing velocity. This goes in accordance with White and Nepf (2003) phenomenological description of longitudinal dispersion, which states that for increasing velocities, the effects of boundary and vortex trapping decrease. Also, it is important to note that as the flow surpasses the threshold for periodic vortex shedding ($Re_d \approx 140$), dissipation and transition to three-dimensional regimes make the rates of mass and momentum transfer between vortices and the outer flow more effective (Williamson, 1991).

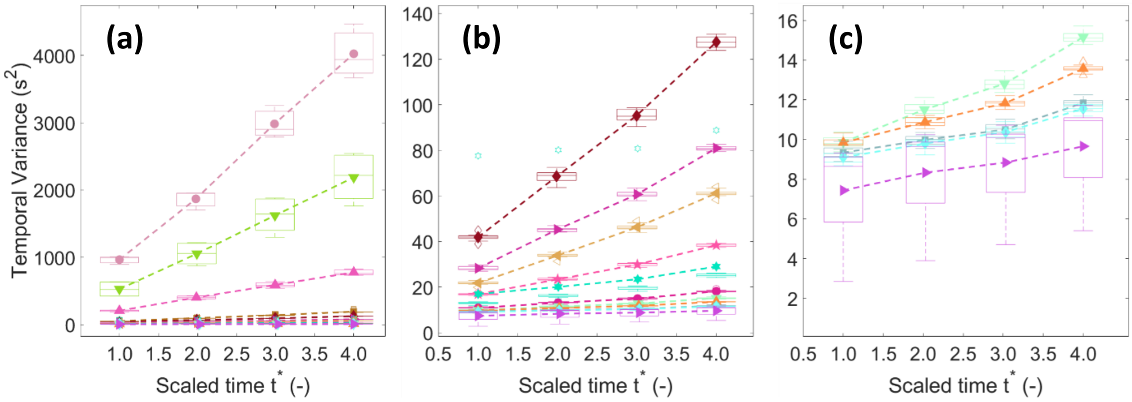

Figure 5.3-5. Temporal variance as a function of scaled time for all flow rates tested and centre-line injection $y_{inj} = 0.5$ *m. The same conventions for Figure 5.3-4 apply. (a) Complete range of* Re_d *tested, (b)* $Re_d > 250$ *(c)* $Re_d > 800$

From Figure 5.3-6, it is not possible to draw any noticeable changes in transverse variance, σ_y^2, with Reynolds number, as all results cluster around the same trend line. Smaller, local variations can be identified for high flow rates, which could hint at the possible influence of turbulence in a more uniform rate of spread. However, no conclusions can be derived from the plots of variance with scaled time since dispersion coefficients are defined in terms of travel times, which change considerably over the different flows considered (see Figure 5.3-4).

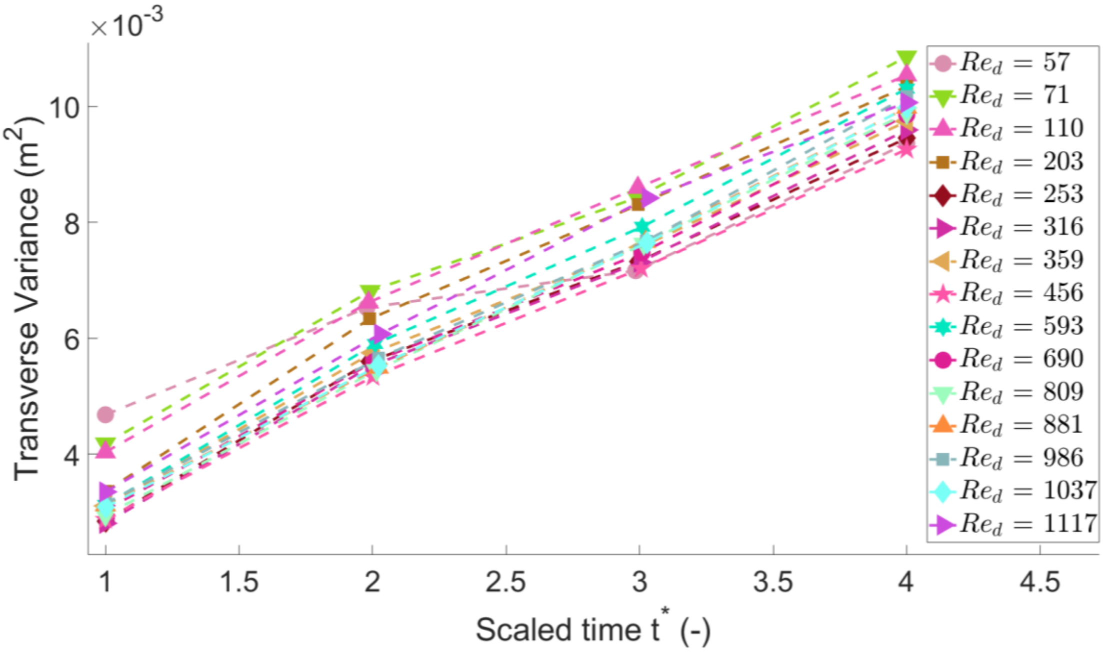

Figure 5.3-6. Transverse variance as a function of scaled time for all flow rates tested and centre-line injection $y_{inj} = 0.5$ *m.*

The main focus of the analysis of second order statistics from concentration distributions is the calculation of dispersion coefficients, defined as follows (Fischer *et al.*, 1979)

$$D_i = \frac{1}{2}\frac{d\sigma_i^2}{dt} \qquad \textit{Eq. 5.3-5}$$

Where i represents each of the directions along which dispersion is being quantified. For want of space this analysis has been omitted in this section and will be added in Section 5.4, where the results of the optimisation analysis are presented. The difference in predictive performance between dispersion coefficients calculated from the Method of Moments (MoM) and from the optimisation are not sufficient to change the conclusions.

5.3.4. Concentration skewness

An important component of the statistical analysis of concentration distributions, that is often overlooked, is the asymmetry (i.e. skewness) of the measured profiles, particularly for time-dependent plots. This analysis is not only useful to test whether concentration is measured within the Fickian regime (Fischer *et al.*, 1979), but also to explore possible cross-sectional effects on mixing such as shear, or the existence and influence of trapping zones.

This lack of analyses of this type means that there is not a standard coefficient to quantify skewness in the context of mixing. For the purposes of this study, skewness will be studied using the standardise third moment (DeGroot and Schervish, 2012), which is defined by Eq. 5.3-6

$$\kappa_t^3 = \frac{1}{M_0}\int_{-\infty}^{\infty}\left(\frac{t-\mu_t}{\sigma_t}\right)^3 C(t)\,dt \qquad \textit{Eq. 5.3-6}$$

Performing a grouped analysis of skewness coefficients on the current dataset gives the results presented in Figure 5.3-7. Clearly, low Reynolds numbers have higher initial asymmetry, suggesting that some physical processes in this regime cannot be fully described by Gaussian routing parameters. Nonetheless, the results also suggest that equilibrium has been reached along the entire measurement area, as indicated by the decreasing skewness for $Re_d < 500$, and the low skewness magnitude for $Re_d > 500$ (Rutherford, 1994, page 182 – Image in Chapter 2). This is corroborated by the linear trend found for the average longitudinal variances (see Figure 5.3-5).

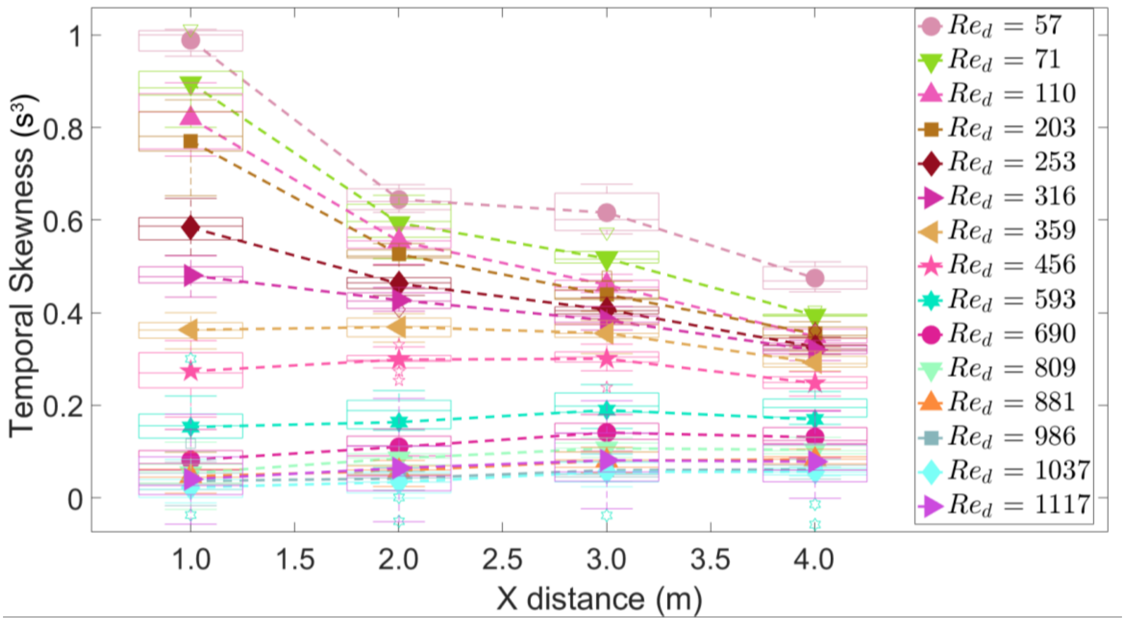

Figure 5.3-7. Evolution of skewness coefficient for time-dependent concentration profiles.

Gerrard (1978) found that remnants of the recirculation zone behind circular cylinders can be found at Reynolds numbers as high as 400, and vortices still conserve some coherence despite the accelerated shedding regime and high dissipation rates. This agrees with White and Nepf (2003) explanation of recirculation regions acting as trapping zones. Figure 5.3-7 suggests that the upper limit for trapping to be an effective driver of dispersion is around $Re_d \approx 359$, as skewness is less than half of the value for the lowest Reynolds number, and the decreasing trend stops. Despite the reasonable assumption of equilibrium, high skewness values for low and intermediate flow rates ($0 < Re_d < 400$) would suggest that dispersion due to differential advection is not Fickian by definition, and that its effect on overall mixing might be higher than the model presented in White and Nepf (2003) would suggest.

For higher flow rates ($Re_d > 400$) the increase in turbulence, paired with the transition to three-dimensional shedding regimes (Williamson, 1991), augments the rates of mass and momentum transfer, which in turn leads to reduced boundary and recirculation retention times. The result of this is a quicker transition to Fickian dispersion and thus lower skewness. In this range, two subranges can be identified: for 'intermediate' flows ($316 < Re_d < 690$), skewness does not vary considerably over the measurement stations, but the magnitude is not negligible. For the highest flows ($Re_d > 690$), skewness is statistically insignificant. The decrease in the magnitude of κ_t^3 with Re_d shows that the advective zone length decreases with Reynolds number, as shown also in (Shucksmith, Boxall and Guymer, 2010). As will be seen in subsequent sections, the correlation between optimisation performance and skewness can affect the predictive value of dispersion coefficients in the low end of the range of Reynolds numbers analysed.

Analysing skewness reveals the influence of physical processes predominantly for longitudinal dispersion. Transverse dispersion, in the absence of asymmetric hydrodynamics (e.g. partially vegetated channels) is expected to vary in a Gaussian manner, hence yielding lower values of skewness. For reference purposes, Figure 5.10-2 shows the results of the skewness coefficient for transverse concentration profiles. Small increases in asymmetry can be attributed to local patches of dye. No systematic bias was found.

5.4. Optimisation Analysis

By reducing the dimensions of the concentration values measured, the routing solution to the ADE presented in Eq. 5.1-3 can be simplified into a similar set of independent 1D routing equations,

$$C(X_2,t) = \int_{-\infty}^{\infty} \frac{C(X_1,t^*)U}{\sqrt{4\pi D_x \bar{t}}} \exp\left\{-\frac{U^2\left(\bar{t}-t+t^*\right)^2}{4D_x\bar{t}}\right\} dt^* \qquad \textit{Eq. 5.4-1}$$

$$C(X_2,y) = \int_{0}^{W} \frac{C(X_1,y^*)}{\sqrt{4\pi D_y \bar{t}}} \exp\left\{-\frac{\left(V\bar{t}-y+y^*\right)^2}{4D_y\bar{t}}\right\} dy^* \qquad \textit{Eq. 5.4-2}$$

It has been found that in addition to a substantial increase in efficiency, using independent routing equations does not affect the accuracy of the optimisation of dispersion parameters, when compared with 2D approaches. This is because fewer parameters entail fewer degrees of freedom and therefore higher chances of finding a reasonable solution. Further, employing optimisation routines was found to provide better estimations of U and D_x for longitudinal, and V and D_y, for transverse dispersion (as will be shown below), than those obtained from the Method of Moments.

Regarding travel times, $\bar{t}$, and mean velocities, U, V, the values found did not differ from those presented in Figure 5.3-4 and Figure 5.10-1. The only relevant variation was the percentage difference, ΔU, for the lowest flow rate changing from 2% to 3.5%, which is still not a significant change. In light of this, the classification presented in Table 5.3-3 remains valid.

Figure 5.4-1 and Figure 5.4-2 show the optimised dispersion coefficients. As expected, dispersion is correlated with velocity, which confirms the relationship between turbulent production and transverse dispersion (Nepf, 1999); and the proportionality between differential advection and longitudinal dispersion (White and Nepf, 2003). Also, the range of values defining dispersion for each direction are of the same order of magnitude than the ones found for natural vegetation (*Carex* and *Typha*) in (Sonnenwald *et al.*, 2017). Regarding the consistency of optimised D_x and D_y, the results seem to be normally distributed. Deviations from average values are reasonably small, and appear to increase with Re_d; although it should be noted that the number of tests also increased with Re_d (see Table 4.2-1). Moreover, dispersion coefficients are seen to fluctuate around the (expected) average across reaches, particularly for $Re_d > 400$.

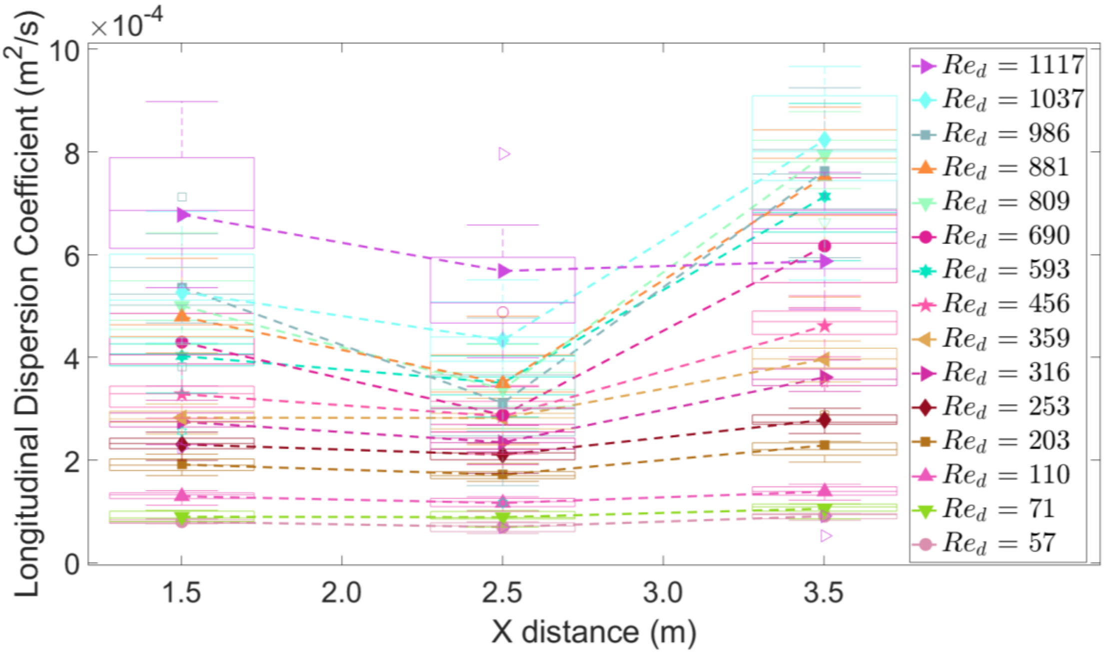

Figure 5.4-1. Results of optimised D_x for all reaches and all flow rates tested. Centre-line injection $y_{inj} = 0.5$ m.

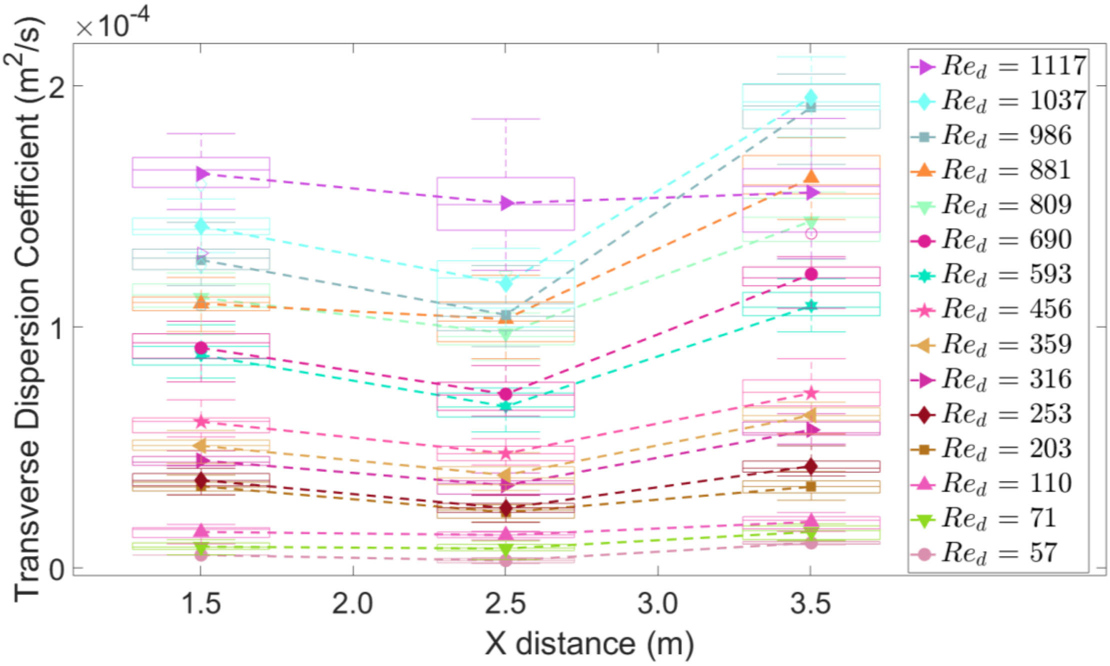

Figure 5.4-2. Results of optimised D_y for all reaches and all flow rates tested. Centre-line injection $y_{inj} = 0.5\ m$.

Figure 5.4-3 shows the comparison between downstream predictions for a sample reach, using both approaches described. A small difference on the best-fit coefficient R_t^2 (Young, Jakeman and McMurtrie, 1980) leads to a noticeable change in the quality of the downstream prediction. Similar trends were identified for the optimised transverse dispersion coefficients, as shown in Figure 5.10-3. These plots also show the effect of local variations in concentration, which can, regardless of whether they are associated with random velocity/concentration fluctuations or signal noise, affect negatively the performance of dispersion metrics. Even though the differences between dispersion metrics, found from the optimisation and Method of Moments, might not seem significant, small quantitative differences can have noticeable impacts on the predictive value of a set of dispersion parameters.

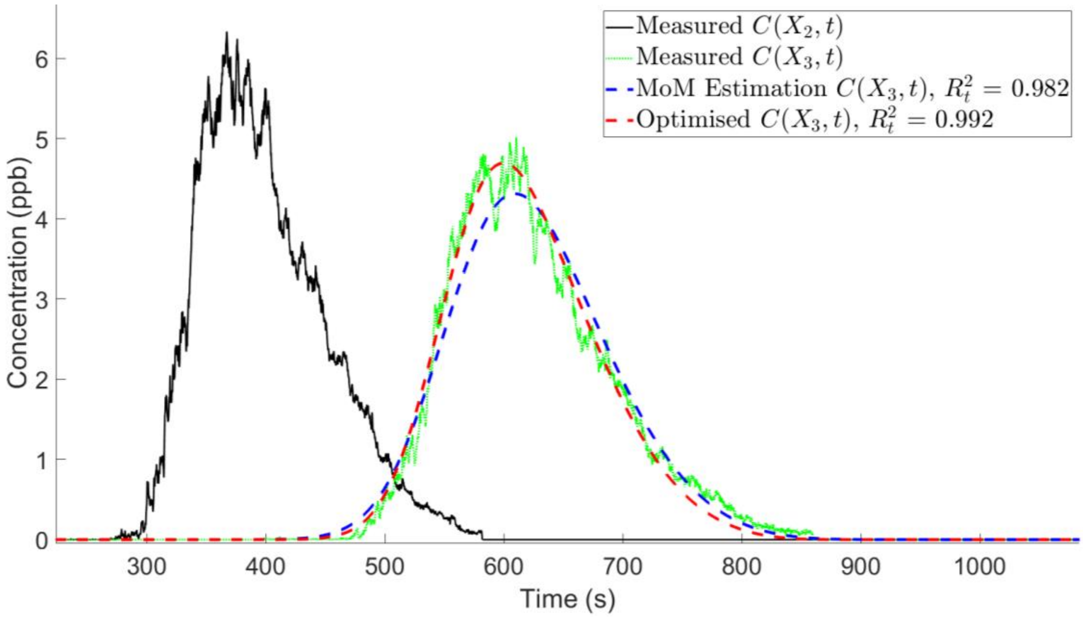

Figure 5.4-3. Difference in Routing performance between MoM and Optimised parameters for time-dependent concentration profiles. $Re_d = 57$ and centre-line injection, $y_{inj} = 0.5$ m

Figure 5.4-4 shows the comparison between the computed R_t^2 for predicted concentration profiles using MoM-derived and optimised advection and dispersion parameters. It is evident that optimisation outperforms the method of moments as a predictive tool, and the difference is noticeable for tests undertaken at $Re_d < 400$, particularly for the first reach. Comparing this subset of values to the results of skewness coefficient shown in Figure 5.3-7, a correlation between relatively 'poor' prediction performance and asymmetry can be found, despite the profiles being considered in equilibrium (Rutherford, 1994). This could be due to analytical solutions to the ADE not covering the range of physical processes driving dispersion, for the early stages of mixing, and for the lower flow rates analysed.

No significant difference between the predictive performance of either method was found for the case of transverse dispersion, as shown in Figure 5.10-4. The range of R_t^2 values for D_y is wider than for D_x, though no systematic variation was found. This higher variability seems to be caused by noise and is not associated with any apparent physical process nor the routing expression used for the optimisation. In conclusion, optimisation routines perform better to obtain reliable dispersion metrics from measured concentration profiles. Also, as it has been described, predictive performance provides information on the validity of the assumptions leading to the existing dispersion models, and the physical processes acting during the dispersion process.

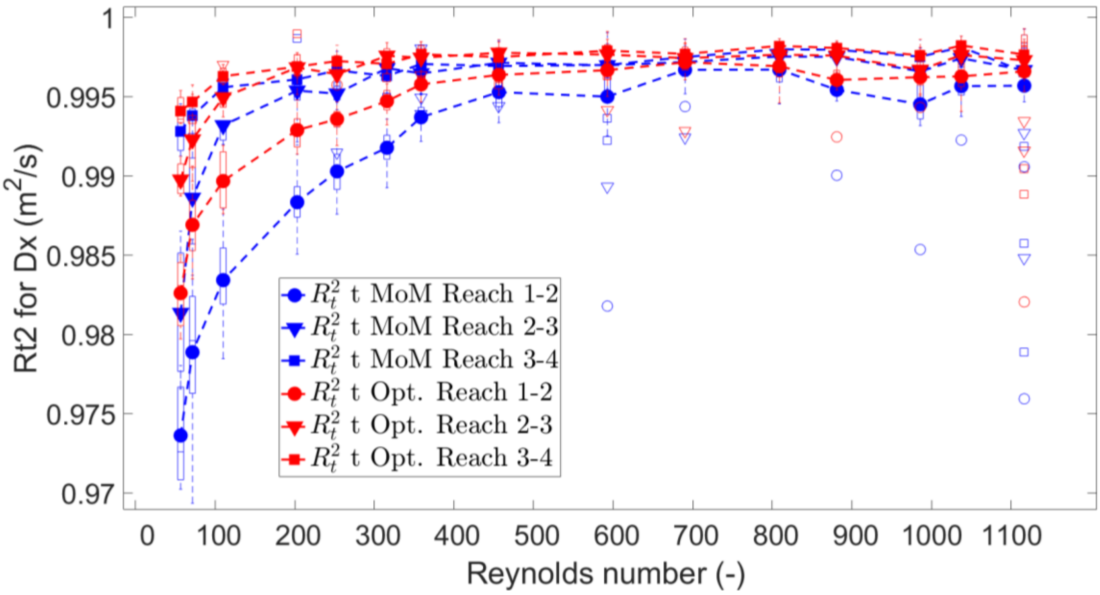

Figure 5.4-4. Comparison of prediction performance between MoM-derived and Optimised longitudinal dispersion coefficients.

5.5. Reynolds number variation of Dispersion Metrics

As far as the author is aware, this is the first study quantifying longitudinal and transverse dispersion variation for a comprehensive range of Reynolds numbers. Sonnenwald *et al.* (2017) described streamwise and transverse mixing for low Reynolds numbers ($20 < Re_d < 120$), for natural and artificial vegetation, where it was found that D_x and D_y seem to vary linearly with Re_d; though the dependency seemed to be weaker for the latter. Similarly, White and Nepf (2003), and Tanino and Nepf (2008b, 2009) independently reported similar relationships for D_x and D_y, respectively. This section extends from these studies, to present a comprehensive characterisation of dispersion, for a wider range of flows, and a more realistic vegetated array.

Figure 5.5-1 and Figure 5.5-2 show the variation of D_x and D_y for low, intermediate and high Reynolds numbers (according to the classification given in Tanino and Nepf, 2008b), for each independent reach analysed. It is possible to see that both dispersion coefficients are proportional to Reynolds number, and thus U. The relationship seems to be linear in the case of D_y, which is also roughly an order of magnitude smaller than D_x, which in turn, is not strictly linear with U (Figure 5.5-1), where two distinct regimes can be identified before and after the threshold $Re_d \approx 400$. For flows below the threshold, the calculated longitudinal dispersion coefficients appear to increase linearly, and have significantly less variability between reach estimates. For higher Re_d values, D_x increases at a different rate and the variability across reaches also increases considerably.

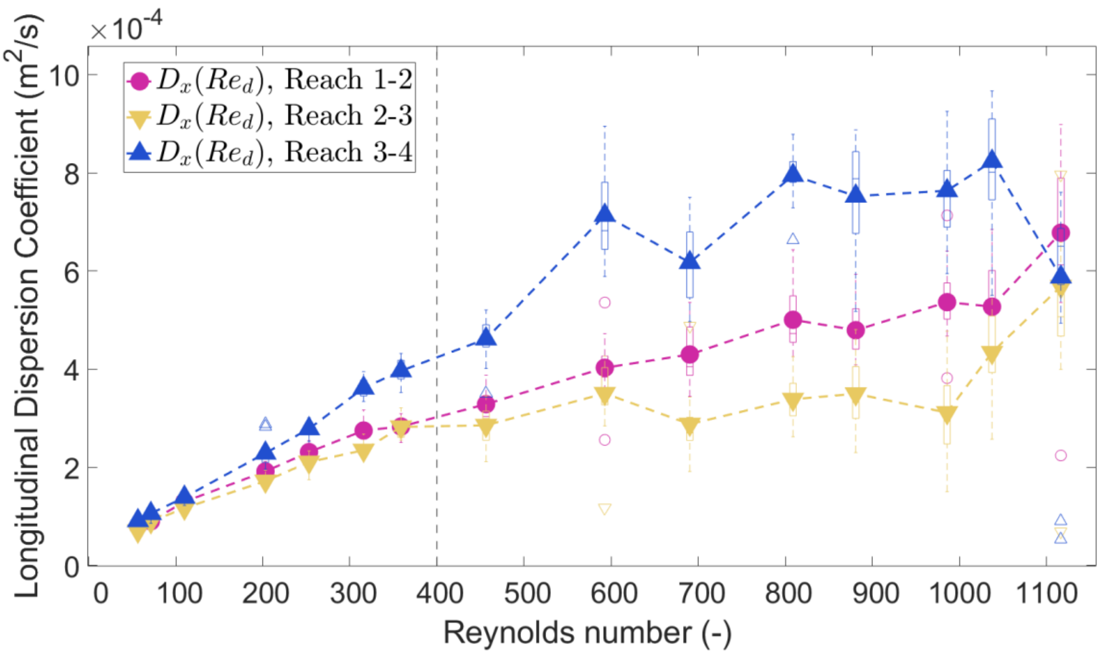

Figure 5.5-1. Variation in longitudinal dispersion, D_x, with stem Reynolds number, for a centre-line injection, $y_{inj} = 0.5$ m.

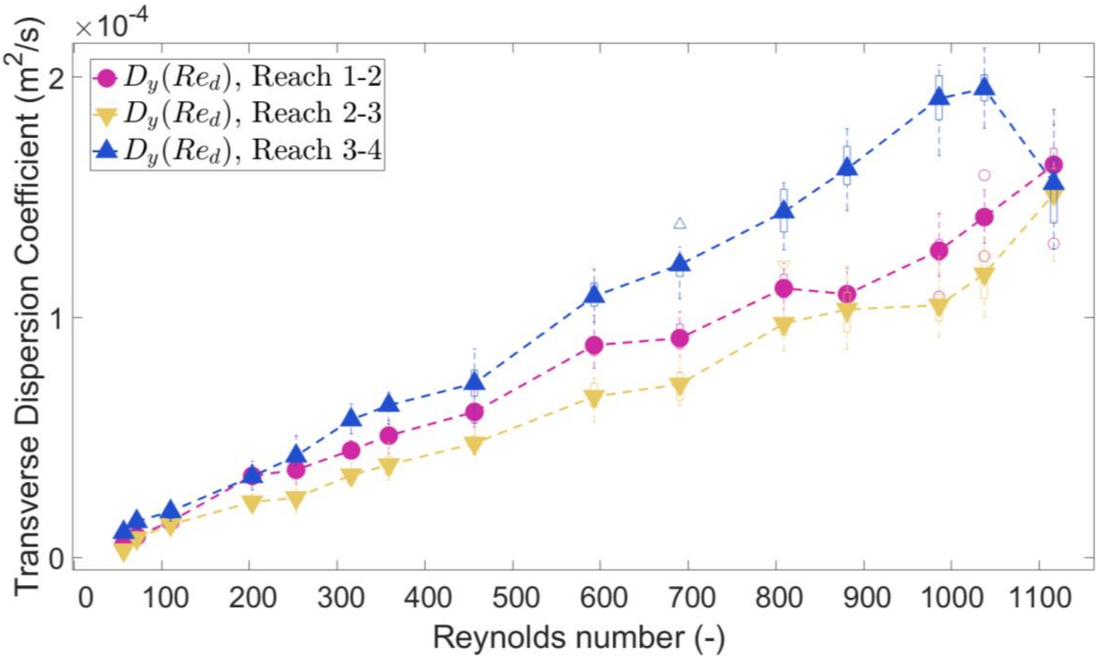

Figure 5.5-2. Variation in transverse dispersion, D_y, with stem Reynolds number, for a centre-line injection, $y_{inj} = 0.5$ m.

Figure 5.5-3 and Figure 5.5-4 show the dispersion coefficients non-dimensionalised, i.e. $D_i^* = D_i/(Ud)$, in this case using the mean diameter from the distribution shown in Figure 4.2-1b, i.e. $d = 10$ mm. If the estimations of D_x^* from Figure 5.5-3 are compared with the experimental results of White and Nepf (2003), shown in Figure 8 of that paper (which is attached in Section 5.10), a remarkable agreement is found for the closest solid volume fraction value ($ad =$

0.025), both in terms of magnitude and trend. The $ad = 0.082$ data shows the same trend, although with higher magnitude. Regarding lateral dispersion, the apparent independence between D_y^* and Re_d goes in agreement with the model proposed by Nepf (1999) and Tanino and Nepf (2009) (see Section 2.4.2.6, Chapter 2), and the results presented in Sonnenwald *et al.* (2017).

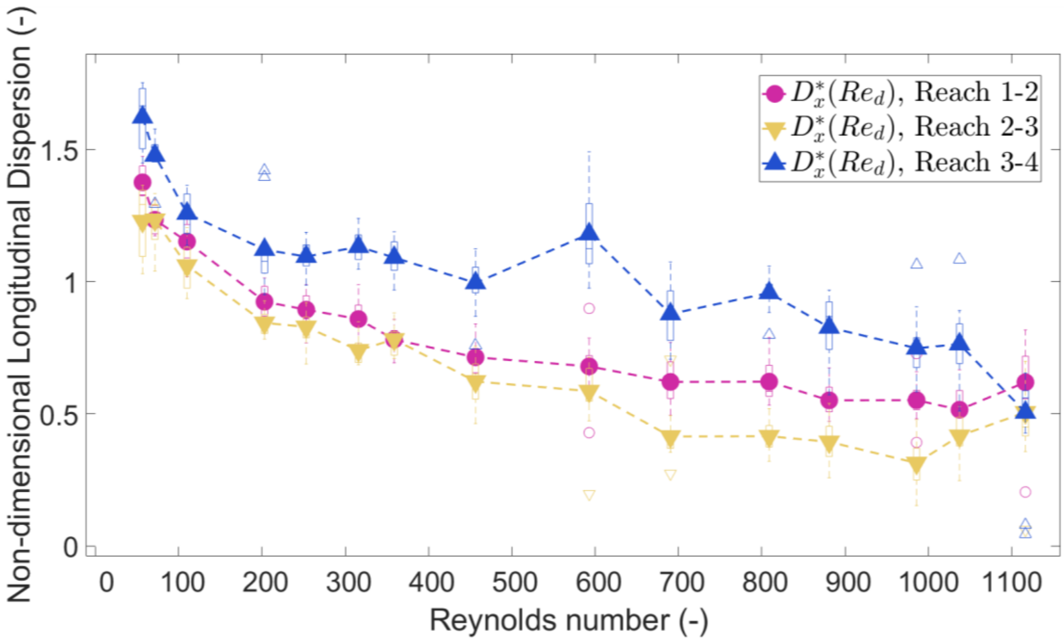

Figure 5.5-3. Variation in non-dimensional longitudinal dispersion, $D_x^* = D_x/Ud$, as a function of stem Reynolds number and for the centre-line injection, $y_{inj} = 0.5$ m.

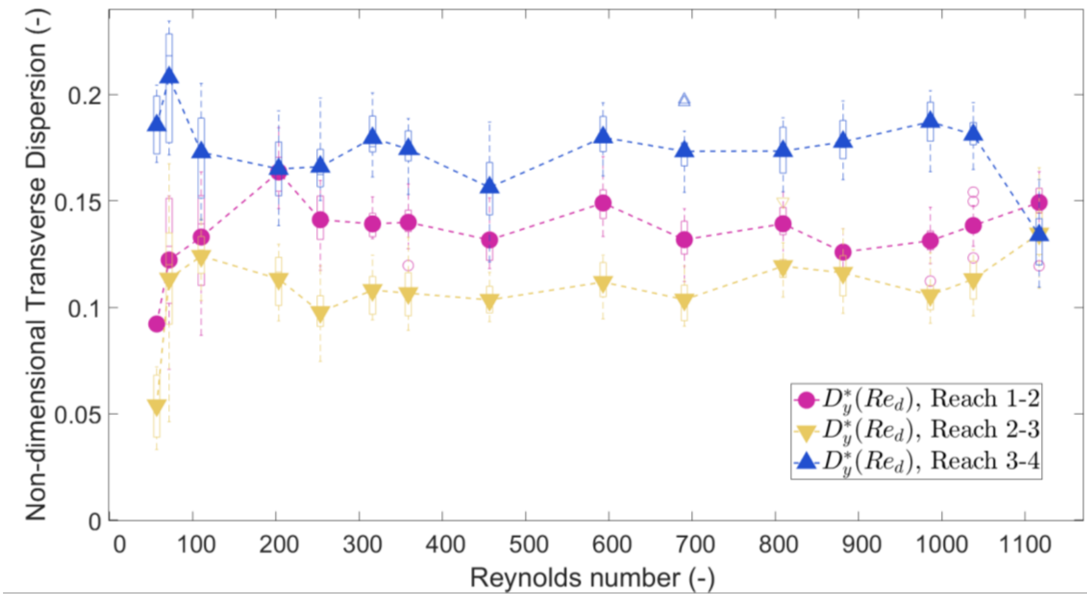

Figure 5.5-4. Variation in non-dimensional transverse dispersion, $D_y^* = D_y/Ud$, as a function of stem Reynolds number and for the centre-line injection $y_{inj} = 0.5$ m.

5.6. Cross-injection analysis (change in initial conditions)

The results presented have focused on the variation in dispersion, for a comprehensive range of Reynolds numbers, at a single injection location (i.e. centre-line). In physical terms, this means that a very specific set of initial conditions has been analysed. It is known that the existence of flow structures, generated by the presence of stems, can dominate small scale diffusion and bulk dispersion for some time after the initial release of a solute (Section 2.4.2, Chapter 2). This persistence of initial conditions over the mixing process is sometimes referred to as 'memory effects'. This section explores the effects of varying initial conditions on longitudinal and transverse dispersion. The objective is to determine whether the vegetated configuration at the injection location affect large scale dispersion, and for how long these effects persist. As shown in Figure 4.2-1a, initial conditions varied in this study by means of changing the location of the injection; such that for some time after the release of dye, the length and time scales of the flow are different depending on the closest stems. It is shown that memory effects are only relevant for a specific subset of flows, but these tend to be damped by the random flow field. Consequently, for a Randostick configuration, and the natural vegetation it is based on (*Winter Typha*), dispersion results are largely unaffected by initial conditions. The physical reasoning behind this is presented in the following section.

Figure 5.6-1 and Figure 5.6-2 show the variation of mean D_x and D_y, respectively, as a function of Reynolds number, for all injections analysed (experiments for $y_{inj} = 0.35$ m and $y_{inj} = 0.65$ m were discarded due to low sample sizes, i.e. high numbers of invalid traces). Similar to the case for $y_{inj} = 0.50$ m, longitudinal dispersion coefficients, for all injections, converge with considerably small deviations, for $Re_d < 400$; and continue with the same trend as shown in Figure 5.5-1, albeit with higher deviations. The cross-injection comparison for mean, transverse dispersion coefficients, presented in Figure 5.6-2, shows a consistent linear behaviour with Reynolds number, with a remarkably low variation. In practical terms, this indicates that, under the conditions analysed, measured dispersion coefficients are unaffected by the initial conditions of the mixing process.

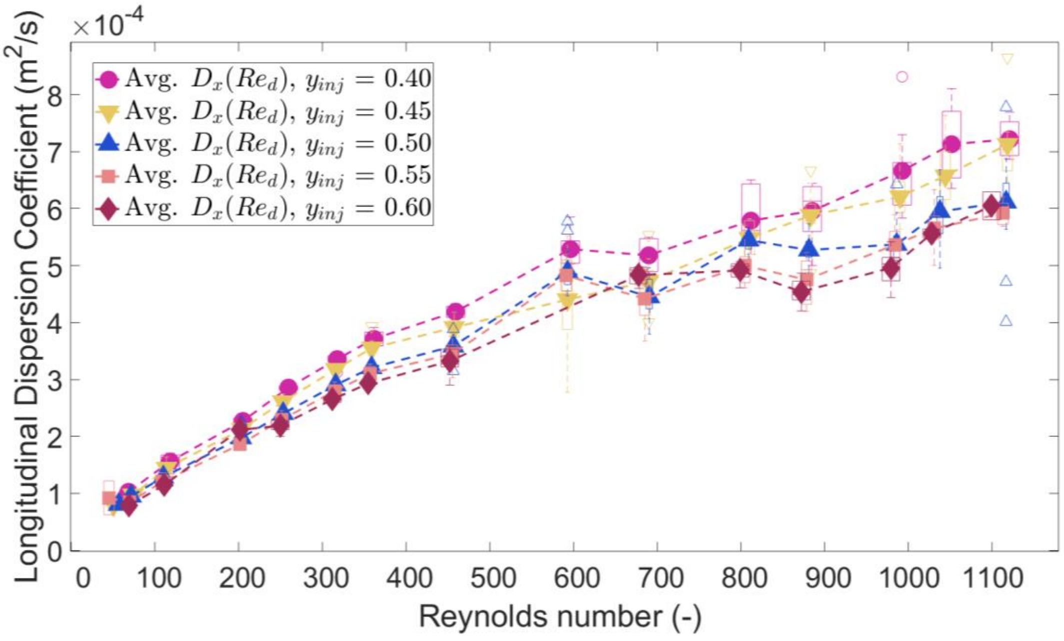

Figure 5.6-1. Variation in Average Longitudinal Dispersion Coefficient, Dx, for all injection locations.

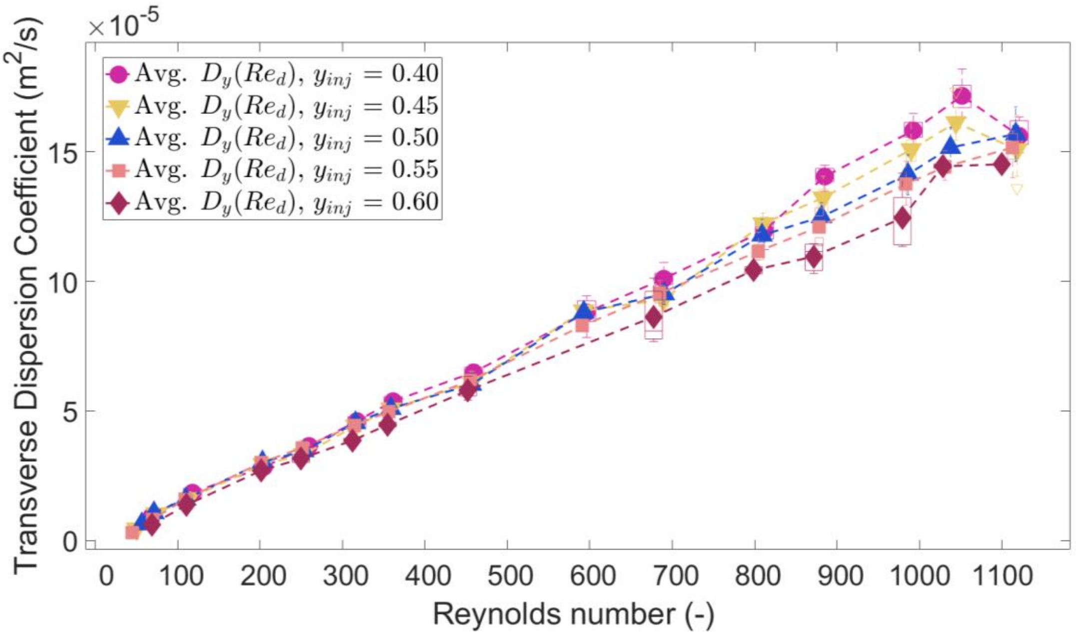

Figure 5.6-2. Variation in Average Longitudinal Dispersion Coefficient, Dy, for all injection locations.

Figure 5.6-3 and Figure 5.6-4 show the cross-injection variation of the average, non-dimensional longitudinal and transverse dispersion coefficients. Dimensional dispersion coefficients, show a consistent convergence for low Reynolds numbers, and an increased cross-injection variability for higher flows. Conversely, the non-dimensional coefficients show slightly higher deviations among cross-injection estimates for $Re_d \rightarrow 0$, though the trends do not change for the different injection positions.

Given that no significant memory effects (i.e. changes to varying initial conditions) are found for the experiments, the following conclusions gather the observations from non-dimensional dispersion coefficients. Figure 5.6-3 shows that D_x^* decreases with increasing Reynolds numbers, with a steeper decay for low Re_d values. As discussed in Koch and Brady (1985) this behaviour is caused by the presence of obstacles in a laminar flow and the change in the ratio of dispersive and advective scales. When a solute is transported in a laminar (c.f. Stokes) flow, the mass trapped in the boundaries and recirculation zones, around and behind the obstacles, can only move due to molecular diffusion, longer (retention) time scales than laminar velocity, and thus causes greater dispersion than the bulk flow. For the case of D_y^*, shown in Figure 5.6-4, transverse dispersion is independent of the advective scales, except for low Reynolds numbers, where its effect decreases. A possible explanation for this variation may be the fact that for low solid volume fractions (e.g. the Randostick configuration), mechanical dispersion (as defined in Nepf, 1999) is less effective than turbulence; which for $Re_d < 100$ is also negligible in flow around cylinders.

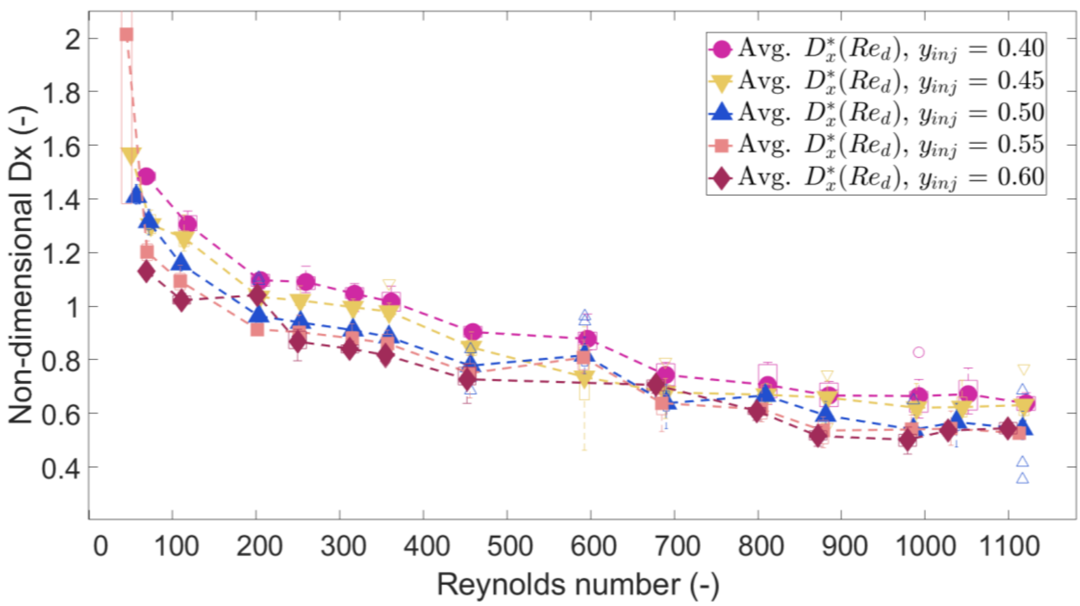

Figure 5.6-3. Variation in Average, Non-Dimensional Longitudinal Dispersion Coefficient, Dx, for all injection locations.*

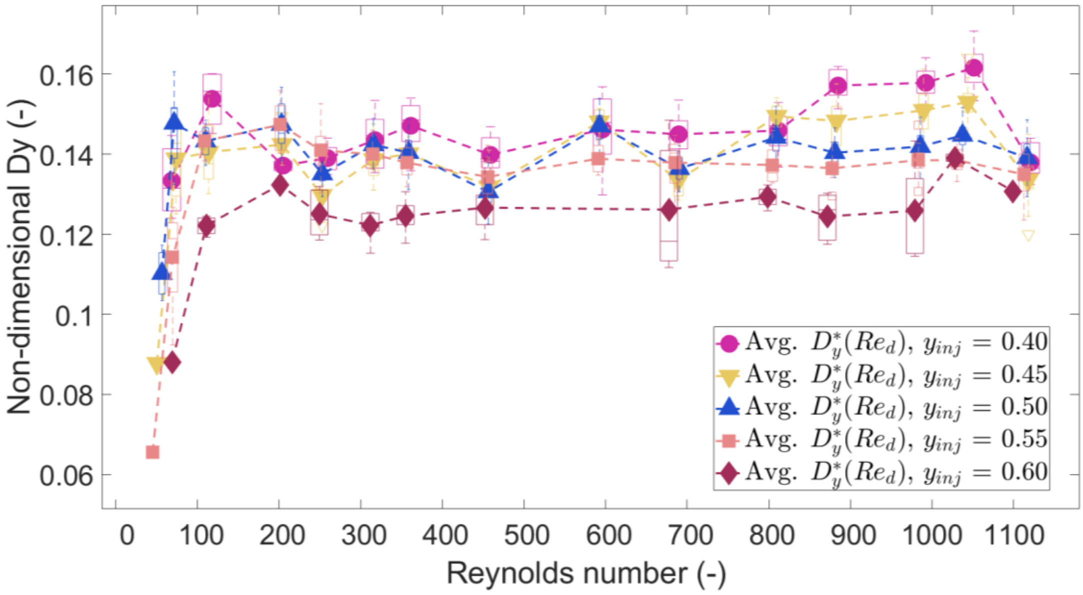

Figure 5.6-4. Variation in Average, Non-Dimensional Transverse Dispersion Coefficient, Dy, for all injection locations.*

5.7. Vegetation Analysis

This section explores the morphology of the Randostick configuration, in relation to the mixing process, to investigate how long it takes for the solute to experience a significant sample of vegetation characteristics, i.e. reach equilibrium. This can be defined as the distance after injection, needed for the scale of the cloud of dye to become significantly larger than the integral scales of the vegetated flow. This section will corroborate whether the experiments were conducted in the Fickian regime (see Section 5.3.2), and identify how long it takes for the flow to eliminate 'memory effects' caused by random initial conditions.

The selection of relevant length scales to characterise the vegetated array is still a contended topic amongst researchers. Until now, studies have used, almost exclusively, uniform distributions of diameters, which facilitated the selection of diameter as the relevant scale of the flow, as most coherent structures are shed with sizes similar to the stem diameter. For the case of random distributions of diameters, a rich ensemble of scales exists. Nominally, the bigger scales are more relevant for mass transport, although, depending on the space between stems, these scales will also break down more easily. With this in mind, any analysis of vegetation should consider diameter, density and spacing. The first two can be expressed as mean quantities, but clear criteria do not exist for the calculation of spacing.

To avoid *ad hoc* definitions of spacing, that are dependent on each configuration; it is decided that the space between stems is considered 'relevant' if it contains enough space to allow flow structures without obstruction. The amount of space available is calculated via a Delaunay triangulation (De Loera, Rambau and Santos, 2010). This technique relates neighbouring points, or in this case stems, if the circumscribed circle does not contain another stem, as shown in Figure 5.7-1a. In this way, it is possible to generate a distribution function of stem spacing defined by the side lengths of the Delaunay triangles, subtracting stem diameters. An example of a spacing distribution using this criterion, for the Randostick configuration, is shown in Figure 5.7-1b. It should be noted that this definition covers a wider range of spaces than the one given by Tanino and Nepf (2008b), which could yield biased spacing distributions by only considering the distance between each stem and its closest neighbour.

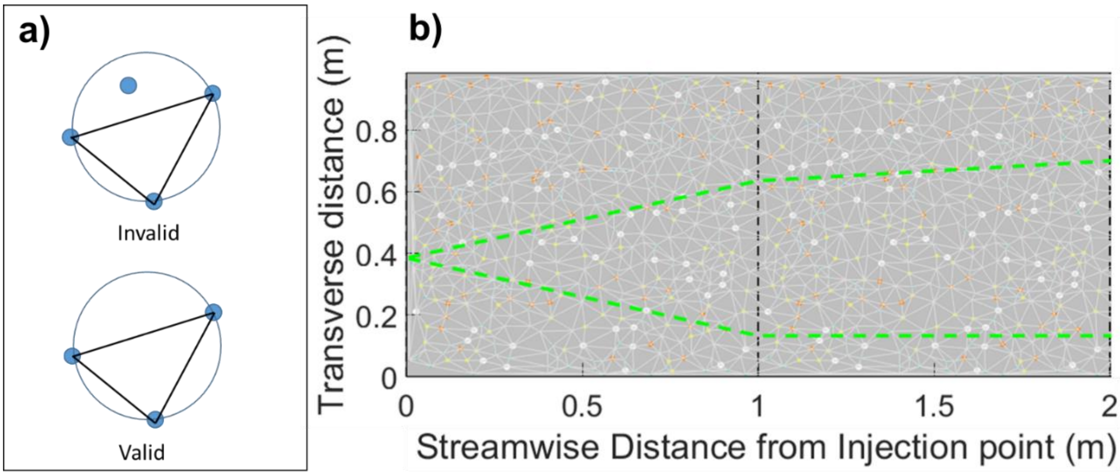

Figure 5.7-1. Definition of stem spacing, a) Delaunay criterion to determine which segments joining stems are considered valid, b) Map of stem spacing following Delaunay triangulation criteria. The dashed green line represents the limits of the moving cloud of dye.

To corroborate equilibrium with the variation in vegetation morphology – i.e. check how quickly the cloud of dye experiences the mean morphological parameters; the lateral limit of the cloud was tracked along its path. The mean vegetation parameters (solid volume fraction, φ, stem diameter, d, and edge-to-edge stem spacing, s_n) were computed for the traversed distance, as shown in Figure 5.7-2. It can be seen that, for small distances after injections, there is significant variability, but quickly the cloud becomes bigger than the relevant integral scales and adopts the mean (macroscopic) vegetation characteristics.

The evolution of traversed vegetation characteristics, presented in Figure 5.7-2, was calculated for all flow rates and all injections; and it was found that an asymptotic behaviour was obtained before the first reach, regardless of flow rate or injection point. This validates the assumption of independence, with respect to initial conditions, presented in Section 5.6. More generally, it can be concluded that for vegetated reaches with random distributions of stem locations and diameters, dispersion is independent of initial conditions. However, the distance necessary to attain mean vegetation conditions (i.e. for memory effects to fade) may vary with solid volume fraction. Grouping the skewness behaviour and optimisation performance discussed above, with the distance necessary to attain average conditions suggests that all tests achieve Fickian regime over the measurement distance.

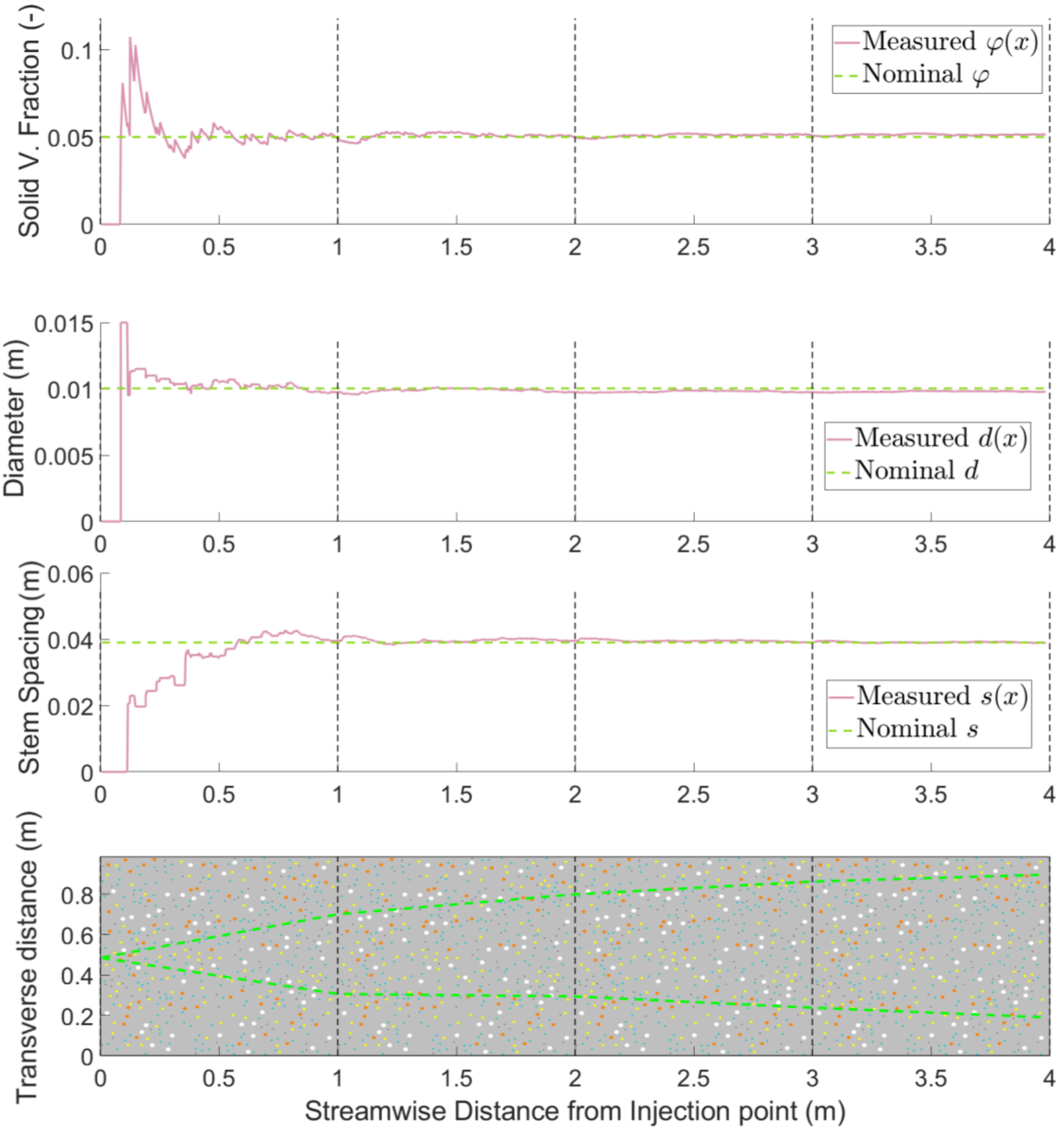

Figure 5.7-2. Variation of morphological parameters from the Randostick configuration (Solid Volume Fraction, Stem Diameter and Stem Spacing), for a test conducted at $Re_d = 456$, and centre-line injection, $y_{inj} = 0.5$ m. The probability distribution of stem spacing is presented in Chapter 7 (Figure 7.3-2).

5.8. Conclusions from the RandoSticks system

The main findings from the analysis are summarised as follows:

- Computational approaches (i.e. Method of Moments vs. Optimisation) have little impact on the determination of dispersion metrics. However, the performance of any chosen method depends heavily on the data pre-processing, as wrong estimations of the cloud limits or backgrounds can affect the performance of the methods.

- Dimensional Longitudinal and transverse dispersion coefficients are correlated with Reynolds number, which means that increases in advection, turbulence, shear and dissipation contribute to dispersion and mixing.

- Longitudinal dispersion increases at a lower rate than pure advective transport (Ud). This is due to the fact that increases in turbulence (proportional to advection), make the transfer of mass more efficient between zones with differential advection.

- Dimensionless coefficients show that at high Re_d, bulk flow is the main driver of longitudinal dispersion. For transverse dispersion, this is only weakly dependent on Re.

- Despite the existence of almost-negligible advective accelerations, the flows, for the purposes of mixing, can be considered uniform.

- Variance linearity and vegetation analysis (cloud becoming bigger than integral scales/cloud experiencing mean vegetation parameters) show that the experiments, and generally random configurations can achieve equilibrium relatively quickly, as the extents of the cloud encompass enough vegetation area to contain macroscopic descriptors of vegetation.

- Averaged dispersion coefficients, for all injection points, do not vary. This is an indication that for random configurations of vegetation (i.e. Randostick) mixing/dispersion is independent of initial conditions. In other words, memory effects do not last for more than a couple of stems.

- Notwithstanding equilibrium, for flows $Re_d < 400$, the existence of physical processes driving asymmetry/skewness persist. It should be noted that if a model is developed to parameterise skewness, this will induce changes in the quantified variances

5.9. Discussion

This section presents the results of non-dimensional longitudinal, D_x^*, and transverse, D_y^*, dispersion obtained above, and contextualises them with measurements from the literature. In summary, it is found that longitudinal dispersion is inversely proportional to Re_d, for $Re_d < 2000$; and is independent of hydrodynamics afterwards. An interdependency between Re_d and D_y^* was not found for the entire range of Reynolds numbers analysed. Previous studies measuring dispersion in real vegetation report higher magnitudes and wider variations of dispersion coefficients, for both directional components of mixing. This can be attributed initially to additional sources of dispersion like trapping caused by vegetation substrate, foliage, for the case of D_x^*. The differences for D_y^* are far less noticeable for comparable studies; however, a correlation between stem-diameter and mean spacing with mixing variations is found for natural vegetation. An explanation of some physical causes is given below.

5.9.1. Longitudinal Dispersion

As mentioned in previous sections, the Randostick configuration was inspired by the diameter distribution for Winter *Typha*, measured by Sonnenwald *et al.* (2017), which is more uniform and presented lower bed-induced dispersion than other natural species tested. Figure 3.1.2-1 shows the results of non-dimensional longitudinal dispersion, D_x^*, from the experiments conducted in the Randostick configuration, alongside a compendium of previous experimental results. The latter are presented as the mean measured values, colour-coded according to the solid volume fraction, φ, presented to the right; and the former is given in a different colour with a segmented trend line. Despite the reported cross-reach and cross-injection variation, Figure 3.1.2-1 shows that D_x^* measurements for the Randostick configuration has a smaller variation, relative to experimental results obtained from natural vegetation. However, deviations were found to be higher when compared to tests conducted with artificial vegetation.

Studies with the largest measured dispersion are usually derived from experiments in real vegetation, low Reynolds number and $\varphi > 0.1$: Sonnenwald *et al.* (2017) in *Carex*, and *Cladium* obtained by Huang et al. (2008); large longitudinal dispersion was also reported by Shucksmith, Boxall and Guymer (2010) in reeds, at $\varphi < 0.1$. Vegetation morphology seems to have no effect on non-dimensional dispersion for high Reynolds numbers ($Re_d > 1300$); that is, solute transport is dominated by advection for high Reynolds numbers, as shown by the results given in Shucksmith, Boxall and Guymer (2010) for *Carex*. For the subset of experimental values showing continuous variations in φ, a weak linear proportionality with D_x^* can be identified; which is in line with the models for longitudinal dispersion proposed by White and Nepf (2003) and Lightbody and Nepf (2006b).

We can subdivide the results presented in Figure 3.1.2-1 into two regions. The first one is limited by the interval [D_x^* , Re_d] where D_x^* ∈ [0, 5], and Re_d ∈ [0, 1300]; and is the region where the Randostick data is located. The other region is the complement of the set previously described. These two regions will be named inner and outer regions respectively.

The outer region, can in turn be divided into the high Reynolds number regime, composed of the dispersion values of *Carex*, as measured by Shucksmith, Boxall and Guymer (2010); and the high dispersion values, comprising the measurements of Summer *Carex* by Sonnenwald *et al.* (2017), reeds (*Phragmites Australis*) by Shucksmith, Boxall and Guymer (2010), and low φ measurements (≈ 0.02) in *Cladium* by Huang *et al.* (2008). Overall, if we connect the vegetation tested in this region, a continuous decreasing relationship is found. Two additional features must be highlighted: for high Re_d, longitudinal dispersion is independent of Re_d and φ, and is approximately unity, with relatively small variation. For low Re_d this subset of experiments shows D_x^* values several times bigger than those in the inner group, and also with considerably larger variations.

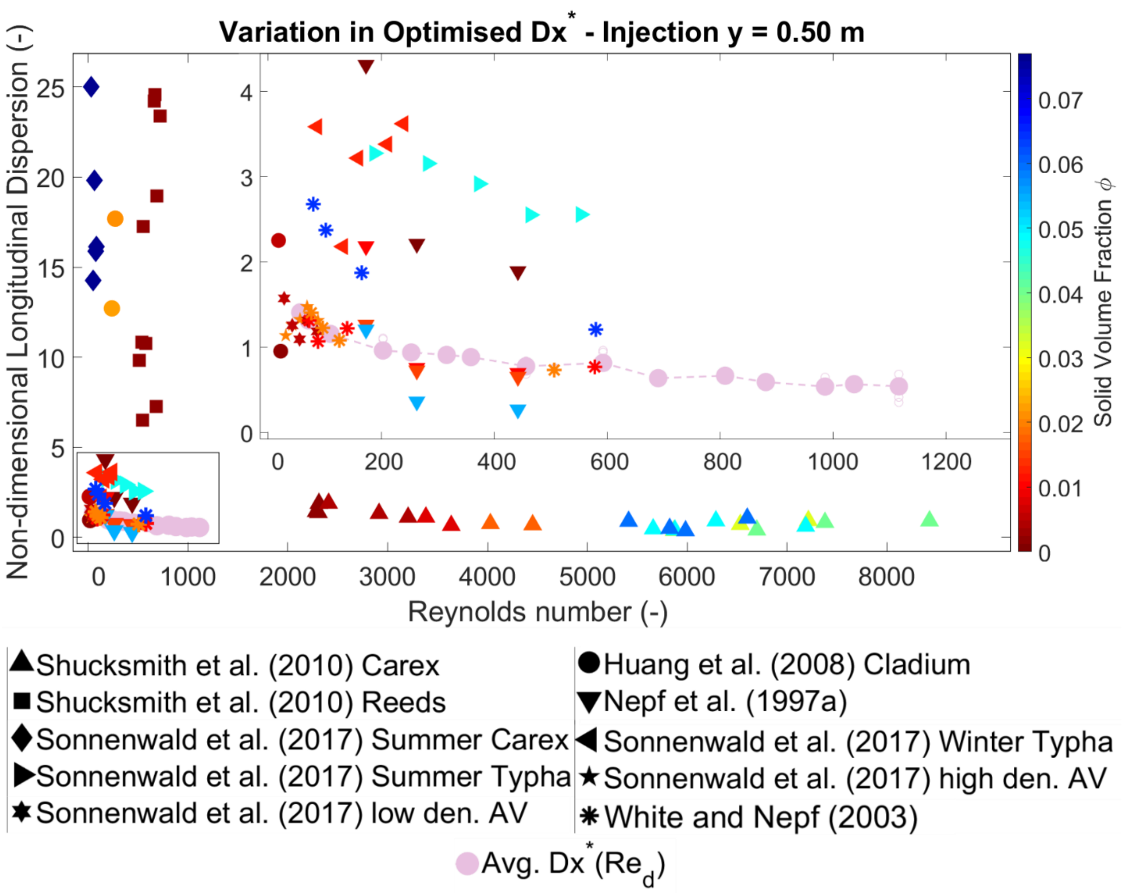

Figure 5.9-1. Comparison between values of non-dimensional longitudinal dispersion, Dx, reported from previous experiments in natural and artificial vegetation, and experimental values obtained from the Randostick configuration.

Performing a phenomenological analysis on these data groups, a strong decreasing and asymptotic behaviour is identified, which, particularly for small Re_d values (Re_d < 1200), reflects an increase in trapping caused by specific features of the vegetation types analysed. The *Carex* and reeds tested (Shucksmith, Boxall and Guymer, 2010; Sonnenwald *et al.*, 2017; respectively) are rhizomatous species, which due to the expansions of roots, increases bed effects and thus trapping via increases in bed roughness. Furthermore, patchiness in the case of reeds and the presence of flexible foliage for *Carex* increases localised trapping and involves higher drag coefficients, respectively. Similarly, the tests performed by Huang *et al.* (2008) for high φ values were carried out in tests sections with varying types of vegetation, where trapping due to similar physical effects also applies.

Previous results in the range of Reynolds numbers studied in this work comprise both natural and artificial vegetation, as can be seen in the rectangle in Figure 5.9-1. For the case of natural vegetation in this region, the two types of *Typha* analysed, representing two different seasonal growth stages (Sonnenwald *et al.*, 2017), present very similar dispersion behaviours despite considerable differences in mean diameter and φ. The smaller dispersion measured for *Cladium* Huang *et al.* (2008), in this region, reflects the effect of a reduced biomass on trapping and therefore mixing.

For artificial vegetation (AV), it is evident that both the magnitude and variation of measured dispersion are lower than for natural vegetation. However, the same decreasing trend identified for the previously described vegetation species is noticeable for AV. Physically, this can be explained by the absence of the bed-related trapping mechanisms explained above. The artificial vegetation used in Sonnenwald *et al.* (2017) experiments compares well with those from the Randosticks configuration, both in terms of magnitude and spread, for the Re_d values analysed, where trapping, and not differential advection dominates dispersion. Care must be exercised, however, when extrapolating these results for higher Re_d values, because the hydrodynamics of regular cylinder configurations vary considerable in comparison with random ones.

For the random dowel array presented in Nepf, Mugnier and Zavistoski (1997), the correlation with the Randosticks data is evident, particularly for the higher φ values tested. It should be remarked that an inverse relationship between solid volume fraction and dispersion was obtained in the random dowel array. A remarkably good agreement exists between the single-diameter, random array tested by White and Nepf (2003), and the Randostick results, both in terms of trend and magnitude; however, the spread expected in natural species is underestimated in studies using uniform configurations.

Lastly, the extreme values found from measurements in natural species and low Reynolds numbers must not be discarded as statistical anomalies. These can serve as an indication of the fact that relevant morphological scales can be of lengths comparables to groups of stems that behave as single bluff bodies, due to clustering.

5.9.2. Transverse Dispersion

In contrast to Longitudinal Dispersion (see Figure 3.1.2-1), where mixing is predominantly dependent on spatial differences in the hydrodynamic field caused by the presence of stems, and weakly dependent on vegetation morphology (i.e. φ); transverse dispersion is driven mainly by vegetation, both in terms of solid volume fraction and orientation. Figure 5.9-2 shows the results of normalised transverse dispersion, D_y^*, from the tests performed in the Randostick configuration, compared with previous results found in the literature for both natural and artificial vegetation.

Focusing again on the magnitudes and degree of spread between transverse and longitudinal dispersion, it is clear from Figure 5.9-2 that values of D_y^* cluster closer together and are an order of magnitude lower than those of D_x^*. Similarly, no strong dependency is found between dispersion values and Reynolds numbers, especially for experiments with the same morphology.

Although a delimitation of regions similar to the one shown for longitudinal dispersion is not clear for the case of transverse dispersion; important distinctions can be made in terms of specific vegetation species. Considering first, values from natural vegetation, it can be found that extreme values of transverse dispersion, i.e. $D_y^* > 0.8$, are mainly measurements in *Carex* and winter *Typha* (Sonnenwald *et al.*, 2017), alongside some spurious points from reeds (*Phragmites*) from Wadzuk and Burke (2006). Following the descriptions given in the previous section, it can be seen that both *Carex* and Winter *Typha* have a tendency to grow in patches, and stems and foliage tend to be oblique due to flexibility and natural orientation respectively. Physically, the existence of patches is associated with increased local flow path tortuosity and turbulence, which in turn allows for the existence of a wider range of mixing length scales.

As pointed out in Sonnenwald *et al.* (2017), summer *Typha* shows smaller lateral dispersion than that for winter, despite having a larger solid volume fraction; which disagrees with the behaviour proposed in Tanino and Nepf (2008b). This discrepancy can, at least partially, be explained by the fact that clusters of vegetation behave as single obstructions for the purpose of describing the flow scales driving transverse dispersion. In other words, the coherent structures formed behind patches of vegetation are bigger than those estimated from single stems, and thus, transverse dispersion will be higher for patched configurations than for more evenly distributed ones.

For the measurements performed in *Spartina Alterniflora* (Nepf, 1999), all φ tested, even those comparable with the Randostick configuration, yield slightly higher D_y^* values, than the ones obtained in this work. The same applies to the values of winter *Typha*, which are also associated with moderately higher values of D_y^* despite having lower solid volume fractions. As referred in Sonnenwald *et al.* (2017), localised increases in turbulence and tortuosity caused by plant heterogeneities might explain the difference. Nonetheless, accounting for cross-reach and cross-injection variations reduces the relative differences considerably.

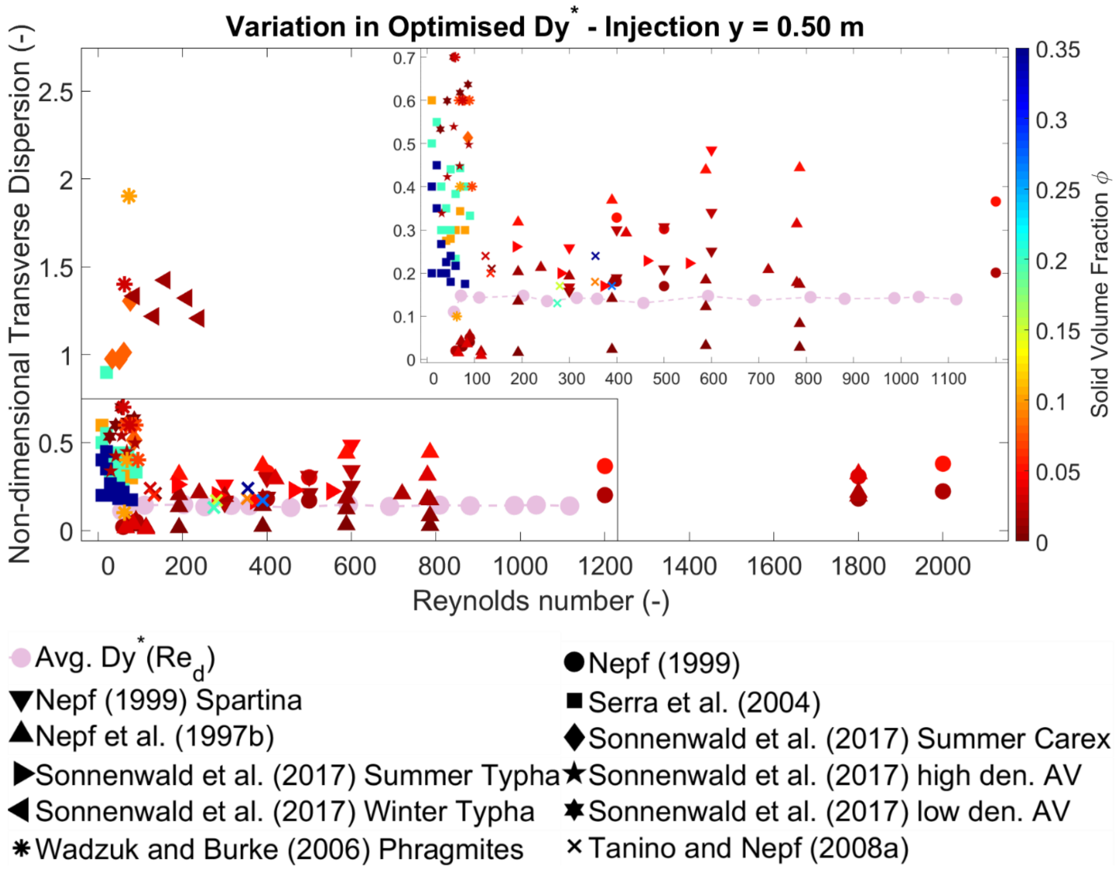

Figure 5.9-2. Comparison between values of non-dimensional transverse dispersion, Dy, reported from previous experiments in natural and artificial vegetation, and experimental values obtained from the Randostick configuration.

For artificial vegetation, the same independence of D_y^* with Reynolds number is evidenced. However, some trends can be identified for the results from single-diameter configurations (Serra, Fernando and Rodríguez, 2004; Tanino and Nepf, 2008b). As shown in the model proposed by Tanino and Nepf (2008b), lateral dispersion is initially dominated by stem-induced flow phenomena, particularly turbulence and coherent structures, which is represented as an initial peak in the function $D_y^*(\varphi)$ at $\varphi \approx 0.02$. For increasing solid volume fraction, the influence of turbulence is quickly damped by the presence of closer stems until flow path tortuosity becomes dominant, which is seen in the function $D_y^*(\varphi)$ as an intermediate decrease with a minimum point at $\varphi \approx 0.2$ and a subsequent increase with φ (Tanino and Nepf, 2008b). For the RandoSticks density ($\varphi = 0.05$), turbulence effects are expected to be dominant, and as seen in Figure 5.9-2, these do not change with Reynolds number. Not enough data is provided in artificial vegetation by Nepf (1999) and Nepf, Mugnier and Zavistoski (1997) to check the behaviour of dispersion with solid volume fraction. Overall, artificial vegetation and some tests conducted in natural reaches show a good agreement with both the trend and variation reported for the Randostick configuration.

Finally, the scatter seen in the measurements of dispersion from real vegetation suggest that scalar macroscopic descriptors of vegetation, e.g. solid volume fraction; alongside scalar descriptors of vegetation morphology, e.g. stem cylinder; are insufficient to characterise obstruction-induced vegetation. In other words, descriptors of spacing might be needed to describe hydrodynamic scales, and D^* variations might need to be explained from the variations in the stem-diameter/spacing distributions. An example of this is the need to describe the difference between patched and evenly distributed vegetated reaches, as shown here for the case of summer and winter *Typha*, which can involve considerable differences in dispersion. This can be achieved by describing the different behaviour in the spacing distribution. In conclusion, mean stem spacing might be a better way of describing vegetation morphology-associated length scales. Also, probabilistic distributions, particularly deviation descriptors can be used to predict/characterise the deviations in the estimations of dispersion.

5.10. Additional Figures

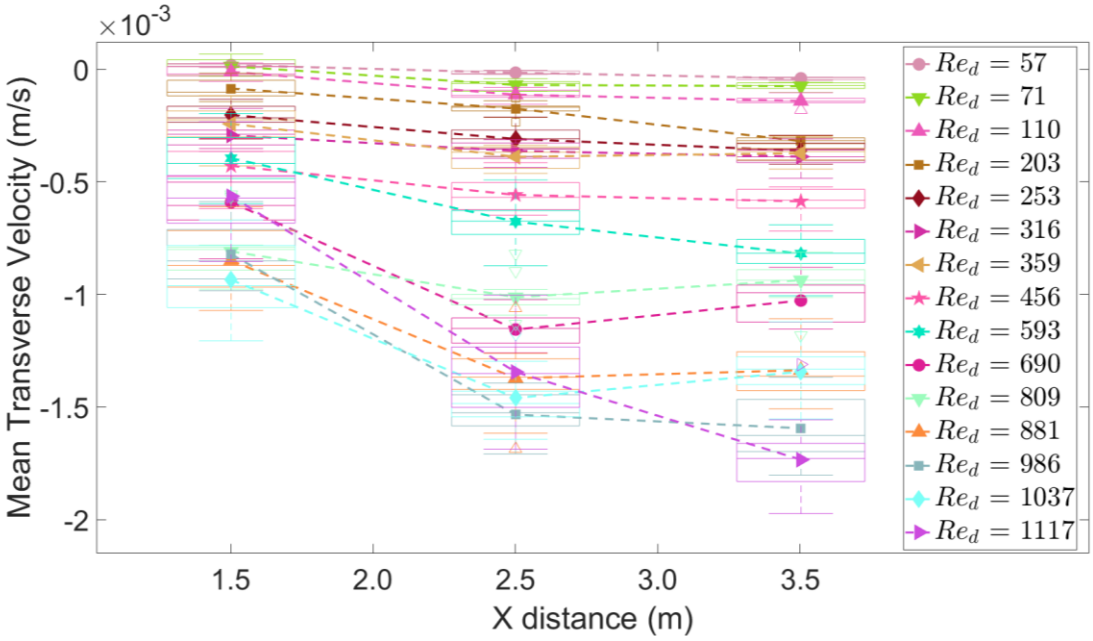

Figure 5.10-1. Results of mean Transverse velocities (V) for all flow rates tested, and centre-line injection $y_{inj} = 0.5$ m. Note that the results show a systematicity in the results of mean transverse velocity. Possible explanations include slight misalignments during the calibration stage, or secondary effects. However, this systematicity has negligible effects on the dispersion quantities estimated, and further discussions on this can be explored in future stages of the research.

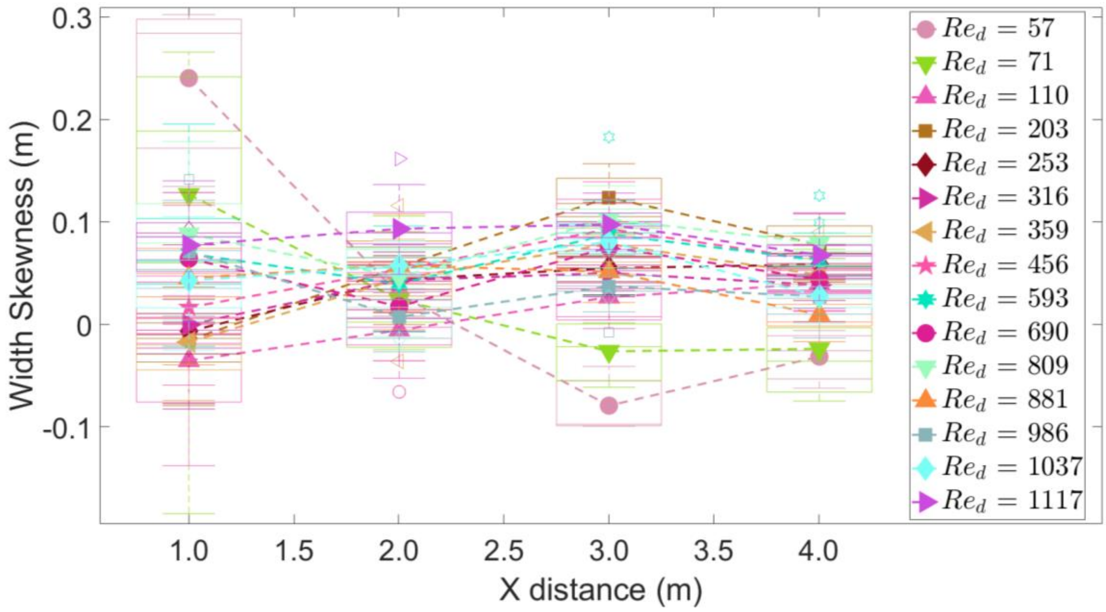

Figure 5.10-2. Evolution of Pearson's skewness coefficient for y-dependent concentration profiles, and centre-line injection $y_{inj} = 0.5$ m.

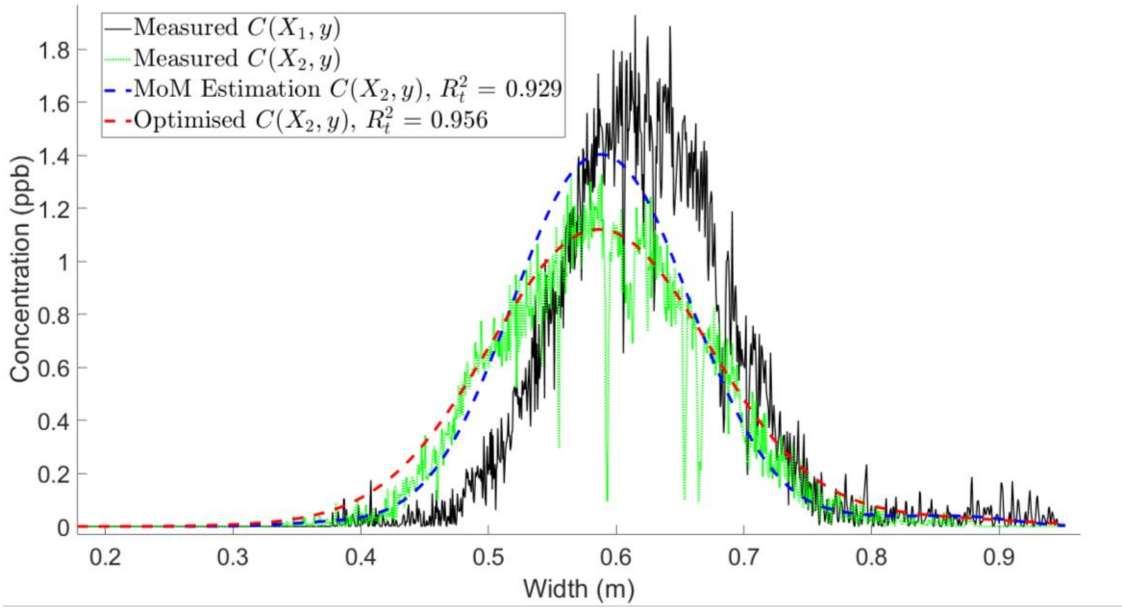

Figure 5.10-3. Comparison ofn Routing performance between MoM and Optimised parameters for y-dependent concentration profiles. $Re_d = 1037$ and $y_{inj} = 0.65$ m.

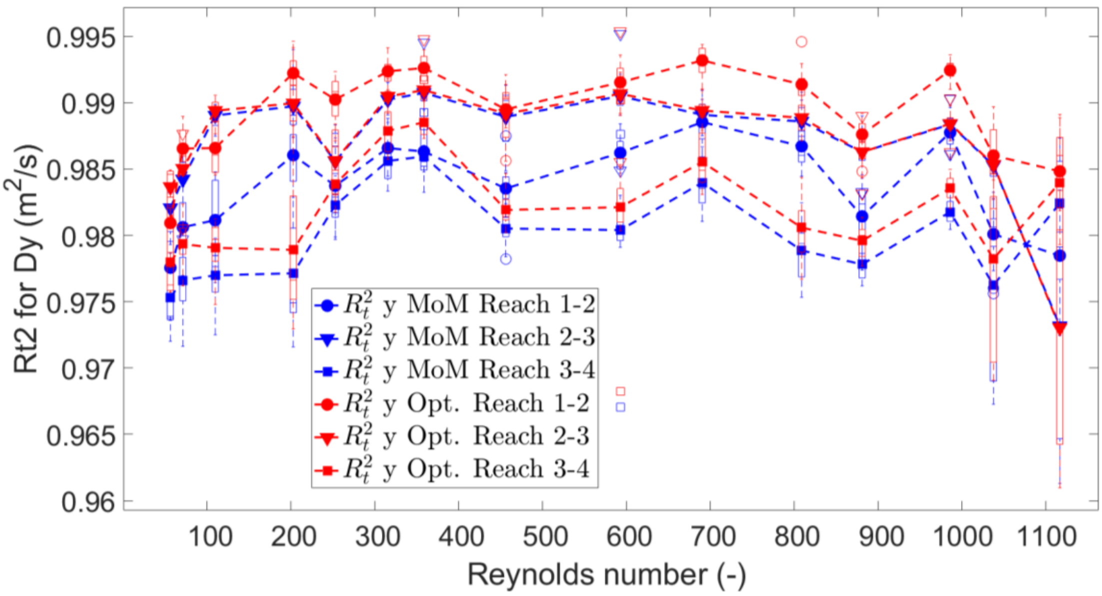

Figure 5.10-4. Comparison of prediction performance between MoM-derived and Optimised transverse dispersion coefficients.

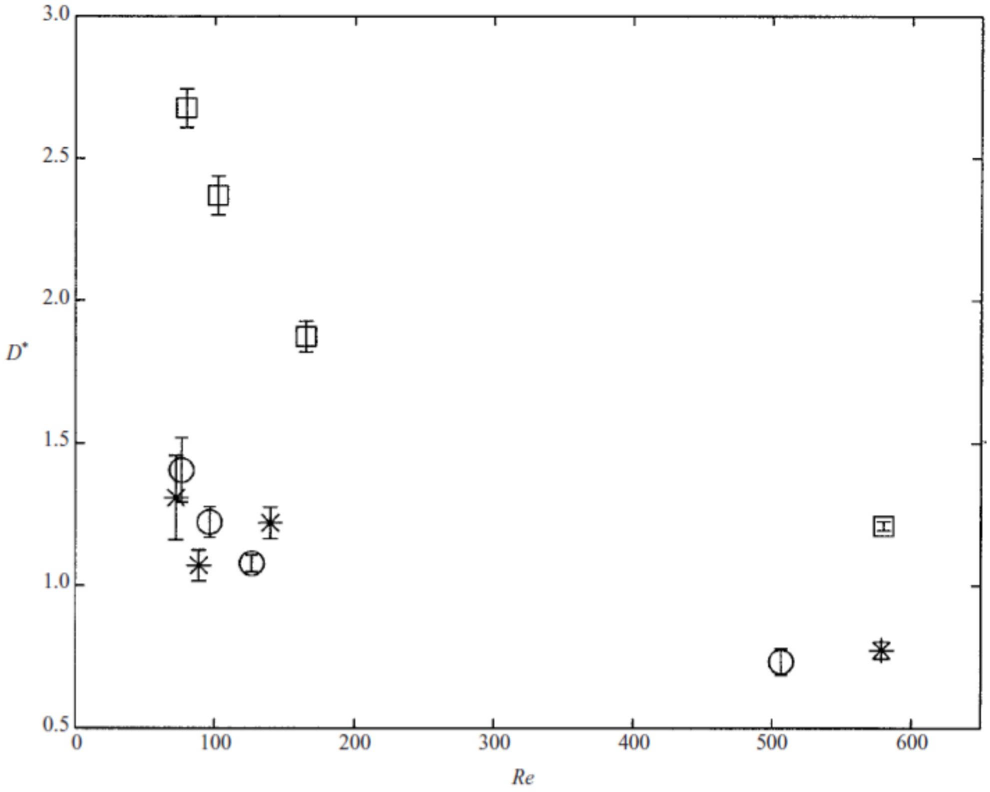

FIGURE 8. Dependence of total dispersion, $D^* = D/U_o d$, on Re for $ad = 0.013$ (*), $ad = 0.025$ (circles), $ad = 0.082$ (squares). Vertical bars give uncertainty in D^* obtained from linear regression analysis of σ_x^{*2} *vs.* t^* data. The inverse relationship between Re and D^* observed for all ad scenarios is consistent with the dependence of both D_s and D_v on the changing wake structure. The primary wake size and residence time, as well as the drag coefficient, all decrease with increasing Re. For all Re, D^* is comparable at $ad = 0.013$ and $ad = 0.025$, but increases sharply at $ad = 0.082$. This suggests that at the lower ad secondary-wake dispersion dominates, but is surpassed by vortex-trapping dispersion at the highest ad.

Figure 5.10-5. Reproduction of Figure 8, from White and Nepf (2003)

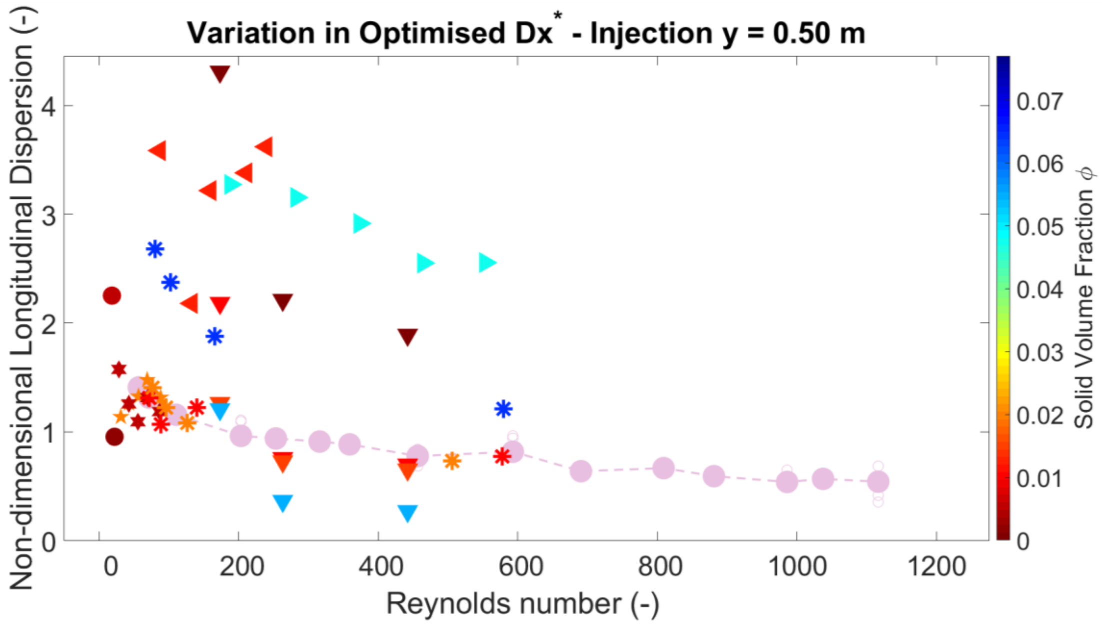

Figure 5.10-6. Area of Interest for the Non-Dimensional Longitudinal Dispersion Data. Conventions are the same than those presented in Figure 3.1.2-1.

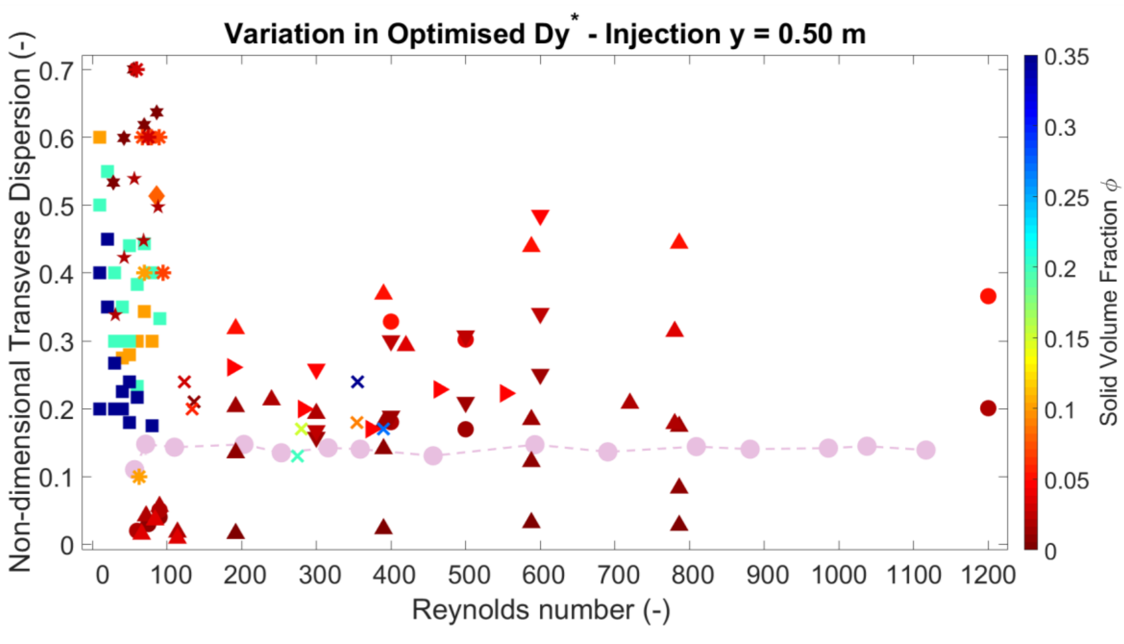

Figure 5.10-7. Area of Interest for the Non-Dimensional Transverse Dispersion Data. Conventions are the same than those presented in Figure 5.9-2.

Chapter 6. HYDRODYNAMICS IN A RANDOSTICKS CONFIGURATION

Abstract

This chapter covers the principles and methods used to post-process and analyse the velocity data, from a hydrodynamics perspective. This analysis will subsequently be applied in Chapter 7 to the study of dispersion by connecting the information presented here to the LIF results shown in Chapter 4. Given the extent and level of detail of the dataset, it is concluded that the best approach is to start from a general description using global statistics (mean, standard deviation and skewness) for the measured velocity fields, and compare their variation with Reynolds numbers. From this general description, the velocity information is further broken down into 1st order velocity maps, namely, time-averaged velocities and vorticity, and 2nd order velocity statistics maps: turbulent kinetic energy (TKE) and turbulence intensities. Alongside their transverse and longitudinal variations from directional averages. These graphs reveal the effects of obstructions on the flow, for the range of flows analysed, which are evident in the relative change of velocity magnitudes with Re_d. Regarding 1st order statistics, the relative differences in mean velocities reflect an increasing transition between velocity defect and acceleration zones, and similarly vorticity magnitudes increase with Re_d. Physically, these represent the effect of wakes, which are the product of energy abstraction from the mean flow. In the same way, the plots for 2nd order velocity statistics show the increase in turbulence and coherent motions, which are a product of a more efficient energy transfer from the larger scales (shed vortices) into ever smaller scales.

In order to contextualise this hydrodynamic analysis, the values found are presented in the context of the double-averaged momentum balance (DANS equation). The terms generated as virtual stresses are explored and their impact and relative impact on the flow is discussed in detail. Acknowledging that drag forces play an important role in vegetated hydrodynamics (in terms of energy production, dissipation and coherence), the available terms of the momentum equation and the relevant virtual stresses will be computed. Lastly, a discussion of previous derivation of vegetated drag is provided, alongside a development given here for its calculation.

Summary of the Main elements of this chapter

Components of the dataset

- Instantaneous maps (20 – 130 fps) of longitudinal and transverse velocity.
- Comprehensive vegetated flow field spanning a representative sample of stems
- Frame rates from 15 to 130 fps, and resolutions from 2 to 8 mm^2
- Record of water surface variation for drag calculations

6.1. PIV Processing Summary

Chapter 4 (Table 4.2-1) presents the range of flow rates from which dispersion, advection and water profile information was obtained, via LIF and point gauge measurements for the RandoSticks configuration. This chapter presents the results from the acquisition of hydrodynamic information using PIV measurements. The aims in collecting this dataset are: first, to complement the dispersion measurements with the intention of developing a comprehensive velocity-based mixing model for RandoSticks-type vegetated configurations (e.g. winter *Typha latifolia*). Second, to provide a full description of vegetated hydrodynamics for the same configuration, such that results can be adopted by researchers and practitioners in areas such as flow resistance, turbulence and fluvial fluid mechanics.

To define flow regimes, we must identify a relevant length scale that dominates the creation of instabilities (and therefore turbulence), and define the scenarios where they have completely propagated. It is known, for instance, that in pipe flow, laminar-turbulent transitions can be identified since the existence, magnitude and propagation (amplification and translation) of temporal instabilities can be related to the pipe radius and thus Reynolds number, given the axisymmetrical nature of the flow (Maurer and Libchaber, 1979; Landau and Lifshiftz, 1987). The same extension is not possible for open-channel flows. The instabilities should be considered in the time-space domain, and their propagation is now limited by spatially dependent dissipation (Sano and Tamai, 2016). For vegetated flows, stems dominate the processes occuring in the flow, so the definition of different flow regimes can be approximated by extending the studies of cylinder flow dynamics given in Roshko (1954), Gerrard (1978), Williamson (1991), among others.

Accordingly, the range of flows presented here was devised to span as many vegetated flow regimes as possible, given the physical limitations of the experimental rig (see Chapter 4 and Appendix A). Table 6.1-1 presents the range of flows spanning the tests conducted, for both LIF and PIV experiments, according to the classification given by Roshko (1954) for cylinder wake flows. The stable range covers purely laminar flow, with a clear separation zone with localised recirculation and no mass transfer; to periodic vortex shedding, where pure vortex dissipation dominates the flow, and turbulence is generated far away from the vortex formation zone. The transition range is characterised by an acceleration in the vortex shedding process, early transition to three-dimensional vorticity (Williamson, 1996b) and turbulence generation due to increased rates of vortex dissipation. In the irregular range, traces of periodicity remain in the shedding process, and vortex cores become turbulent during formation, i.e. 'roll up' (Gerrard, 1978).

Table 6.1-1. Range of flow rates for both LIF and PIV experiments.

Re_d	57	71	110	203	253	316	359	456	593	690	809	881	986	1037	1117
LIF	✓	✓	✓	✓	✓	✓	✓	✓	✓	✓	✓	✓	✓	✓	✓
PIV			✓		✓		✓	✓		✓		✓			
Reg.	Stable range			Transition range				Irregular range							

To understand the maps of velocity-based quantities given below, Figure 6.1-1a shows the location of the Field of View (FoV) relative to the 1m x 1m repeating stem plate. In the context of the whole flume, the FoV was located between the 1st and 2nd LIF windows (see Chapter 4). As explained in Chapter 4 and Appendix B, images were taken from beneath the flume, at a sufficient distance (0.18 m) from the laser window on the side to avoid wall effects on the flow. Figure 6.1-1b shows the stems contained in the FoV, noting that it is shown as captured from below. The distribution of stems in the FoV was chosen to be large enough to replicate the general stem distribution of the RandoSticks configuration shown in Chapter 4.

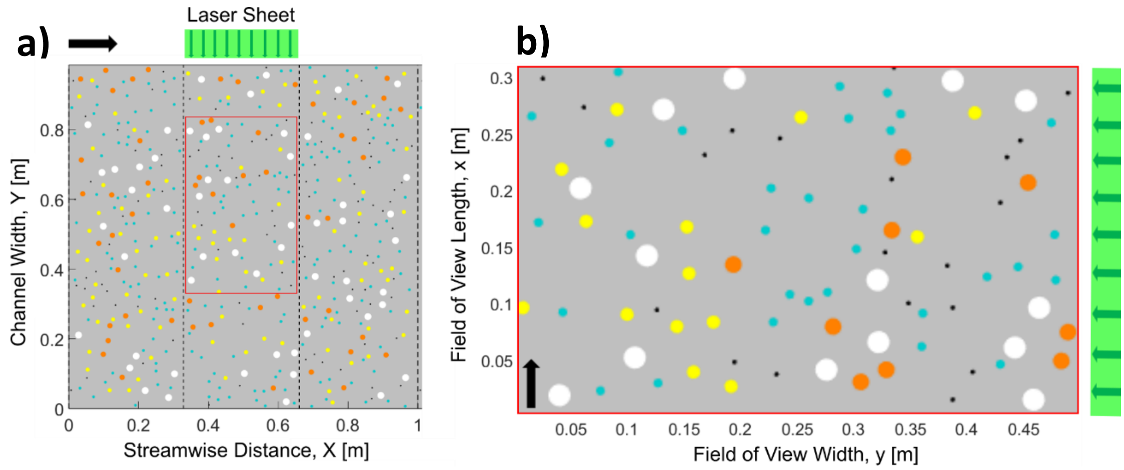

Figure 6.1-1. a) Relative location of the Field of View (red rectangle) for the PIV experiments, with respect to the general 1 m² stemplate replicated along the flume. b) Randosticks distribution within the chosen Field of View.

Once acquired, the images were pre-processed as explained in Chapter 4 and Appendix B. A further adjustment for intensity homogenisation, the displacement calculation and a global post-processing to filter spurious velocities using global statistics was performed via the open-source software PIVlab (Thielicke and Stamhuis, 2014; Thielicke and Sonntag, 2021). Depending on the specific objectives, further post-processing procedures were undertaken. Specifically, kernel-based filters were applied on each instantaneous velocity map to reduce intensity-based noise which was seen to be caused by intensity heterogeneities along the FoV, for the 2nd order velocity quantities. Time-based filters were applied on specific spatial locations (velocity pixels) to improve the calculation of single and multipoint statistics.

6.2. Global Velocity Statistics

This section explores the global probability density functions (PDFs) of post-processed instantaneous velocities $u(x, y, t)$ and $v(x, y, t)$, together with their variation of mean (μ_u, μ_v), standard deviation (σ_u, σ_v) and skewness (κ_u^3, κ_v^3), metrics, with Re_d. The purpose of this analysis is to explore the general trends of the data, particularly in terms of mean, to evaluate the variation in advection; spread, a quantity that could be used to describe dispersion; and skewness, which can serve to analyse the asymmetry caused by the trapping zones. Also, these general metrics can help to assess whether the PIV procedure and/or post-processing produces data that appears consistent with the overall trend (e.g. sudden spikes in any descriptor along a smooth Re_d-dependent behaviour can indicate possible errors in a specific test.)

Figure 6.2-1a and b show the shape of the probability functions for u and v, respectively; and Figure 6.2-1c summarises the variation of mean velocities, along with the main statistical descriptors of these distributions. The spread is analysed in terms of the root-mean-squared of the probability functions centred around zero[12], that is, the standard deviation STD. As expected, the magnitude of velocity variations increase with Re_d. The spread of the PDFs for both longitudinal and transverse velocities (i.e. σ_u and σ_v), lump together the effects of turbulence, differential advection and mechanical dispersion. Therefore, their behaviour is expected to correlate well with that of the dispersion coefficients presented in Chapter 4. Physically, the trend for $\sigma_u(Re_d)$ is larger than that for $\sigma_v(Re_d)$, as the latter comprises the increase in lateral displacements, which is in turn proportional to both advection and the range of length scales characterising the obstructions (Nepf, 1999). $\sigma_u(Re_d)$ on the other hand, captures the effects of trapping and recirculation zones, as well as local advective acceleration gaps (White and Nepf, 2003). This is also consistent with the behavior of skewness, since wakes and boundary layers will also represent a portion of the total velocities measured.

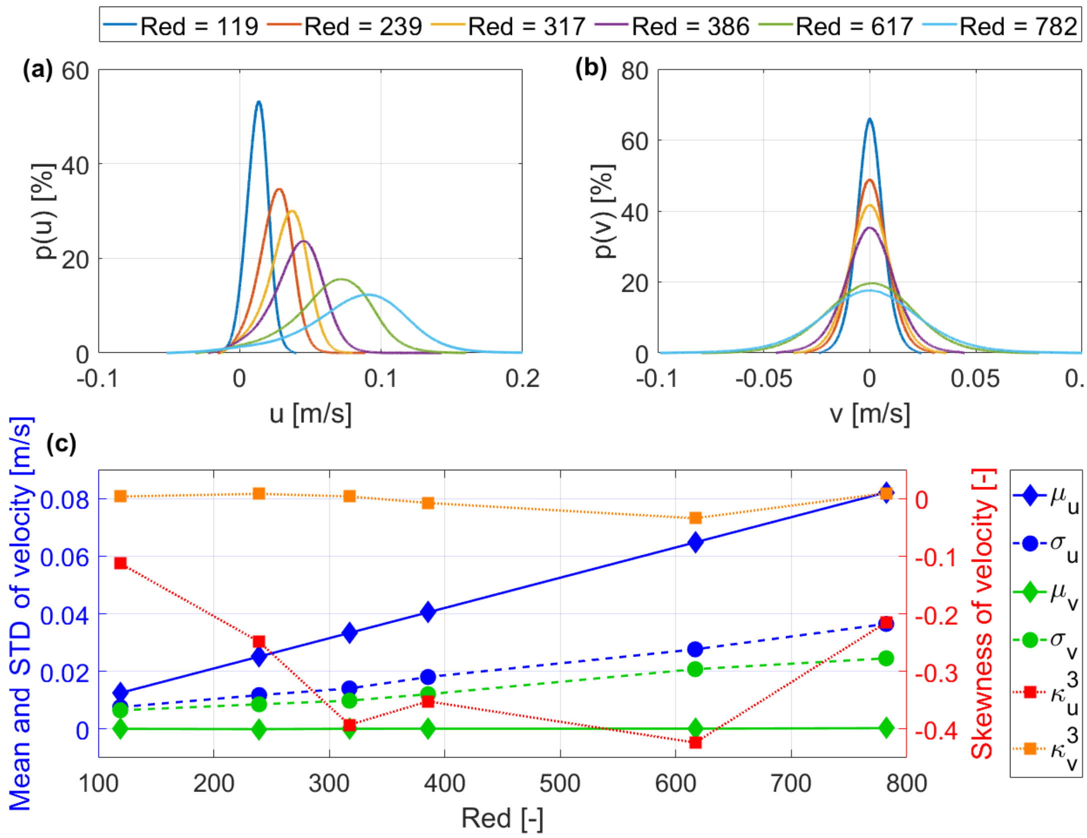

Figure 6.2-1. Variation of Global Statistics for Longitudinal and Transverse instantaneous velocities. a) variation of the pdf of u with Red. b) variation of the pdf of v with Red. Variation of mean, standard deviation and skewness for c) Longitudinal velocity and Transverse velocity.

[12] The STD of a centred distribution ($\mu = 0$) represents the square root of the second moment. Note that this is the same definition as the standard deviation. For consistency, both will be used interchangeable for the remainder of the document.

Clearly, velocity spread (σ_u and σ_v) grows with increasing advection but at a lower rate than μ_u. Similarly, the existence of recirculation/ trapping velocities, for higher flows, increases the negative skewness of the longitudinal velocity PDF, which needs to be factored in when relating velocity statistics to dispersion. Physically, isolating the κ_u^3 components from $p(u)$ helps quantify the contribution from wakes and boundary layers, for dispersion and flow resistance. The latter is explored below via the drag force and coefficients from a double-average analysis of the data.

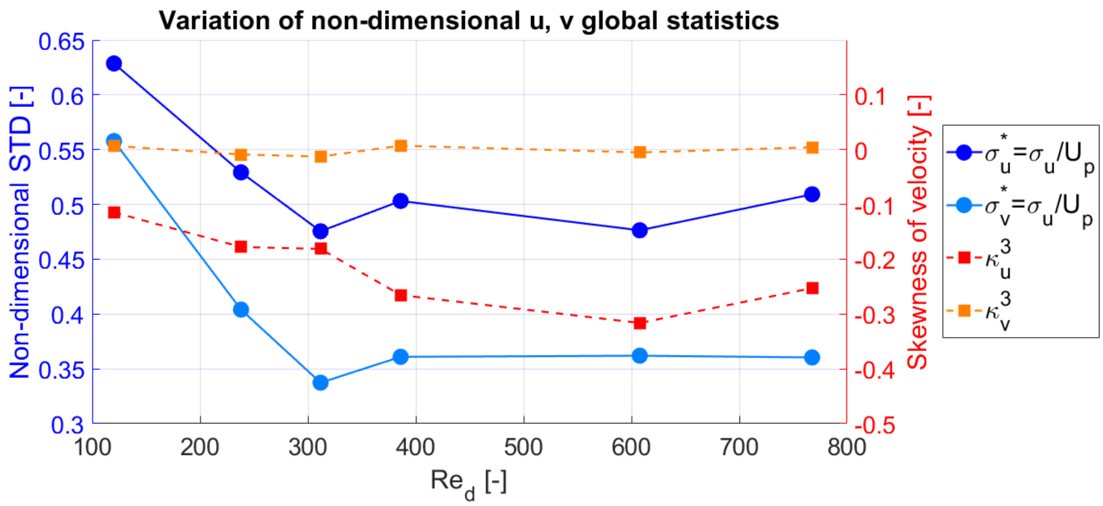

Figure 6.2-2. Variation of Normalised statistics for Longitudinal and Transverse instantaneous velocities.

A further exploration of these general trends can be achieved by comparing their evolution with respect to advection. Figure 6.2-2 shows the behaviour of spread metrics normalised with the mean velocity (i.e. advection), $\sigma_u^* = \sigma_u/U_p$, with Re_d. Note that the skewness coefficient is already a normalised quantity (see Chapter 4, Section 5.5). Similar to the study for dispersion, a better perspective on the vegetation-induced effects is achieved by comparing them with advection. The effects of turbulence, differential advection and trapping increase with Re_d, but do so at a lower rate than advection, a behaviour evidenced also for dispersion coefficients, particularly for D_x^*. However, a further analysis on σ_v vs D_y^* is required, because D_y^* was shown to be constant with Re_d. Further, as shown in Chapter 4, Section 5.7, D_y^* is approximately an order of magnitude lower than D_x^*, which conflicts with the relative differences shown in Figure 6.2-2.

As stated above, a PDF analysis is limited by the fact that the breadth of physical processes occurring in an obstructed velocity field are lumped into single descriptors. Moreover, it is known that after an initial mixing length, namely the advective length (Shucksmith, Boxall and Guymer, 2007), velocity variations (particularly transverse ones) smaller than the extent of the dispersing solute do not contribute to dispersion, so $\sigma_v^*(Re_d)$ naturally will be greater than

$D_y^*(Re_d)$. Note that the same does not apply to D_x^* as boundary layer trapping has a continuous effect on the longitudinal spread of a solute even beyond the advective length. A further physical insight into these specific hydrodynamic processes can be obtained by breaking down the velocity fields into their 1st and 2nd order statistics, and contextualising their contributions via the equations of motion. Section 6.3.1 explores the former, and Section 6.3.2 the latter.

6.3. Exploratory Analysis

This exploratory analysis covers the study of the main time-averaged hydrodynamic variables: mean velocities, vorticity and turbulent quantities. The spatial variation of these quantities (maps) provides insight into the effects of vegetation on the flow at the inter-stem scale; and the variation of these quantities with Re_d contextualises these changes in the global flow range analysed.

An expected increase in magnitudes and their relative variability with Reynolds number is confirmed by the results shown. For instance, variables presumed to increase with advection (U and 2nd order/turbulent quantities) show increases in both magnitude and spread with Re_d. Transverse motions and coherence ($V$and Ω, in Figure 6.3-2 and Figure 6.3-3), although are predictably zero for all Reynolds numbers, show a consistent increase in spread with Re_d, which physically refers to the relative magnitude of lateral displacement and the strength of coherent motions.

Overall, the results shown in this analysis confirm previous hypotheses about the effects of stems on the mean flow, and how they vary with Re_d. Particularly regarding their consistent direct proportionality with advection (i.e. Re_d) in terms of magnitudes and spread – the latter is directly linked to dispersion as will be explored later. The figures presented in this section aim to help the reader identify the main components of the flow field around stems, and their spatial variation along the streamwise and transverse directions. On their own, the values in this exploratory analysis, and their dependency with Re_d, are insufficient to develop a rigorous relationship with dispersion. A discussion on the appropriate physical frameworks to analyse dispersive quantities/fluxes is given below.

6.3.1. Mean Velocity and Vorticity Maps $\boldsymbol{U}(\boldsymbol{x},\boldsymbol{y})$, $\boldsymbol{V}(\boldsymbol{x},\boldsymbol{y})$ and $\boldsymbol{\Omega}(\boldsymbol{x},\boldsymbol{y})$

The approach proposed in this work to analyse velocity information follows a deductive approach: from a general/global analysis through progressive simplifications, in order to reveal particular physical phenomena. After the PDF analysis presented in Section 6.2, the natural next step is the study of time-averaged quantities. From the instantaneous $u(x,y,t)$ and $v(x,y,t)$ fields, applying a time average over an interval, long enough to cover the largest geometric scales of the flow, the mean maps are obtained

$$U(x,y) = \overline{u} = \frac{1}{T}\int_T u(x,y,t^*)\,dt^* \quad , \quad V(x,y) = \overline{v} = \frac{1}{T}\int_T v(x,y,t^*)\,dt^* \qquad \textit{Eq. 6.3-1}$$

Despite sacrificing information on temporal features (e.g. vortices), these maps of time-averaged quantities are obtained over a comprehensive area, with sufficient resolution to identify temporally persistent patterns in the flow. In the case of U, relevant phenomena such as wakes, recirculation zones, local advective acceleration 'gaps' and boundary layers can be identified. These areas are globally referred to as differential advection.

For the case of V, although given the nature of the flow a net displacement equal to zero is expected, the magnitudes of the spatial variations reveal the intensity of lateral displacements and thus are important for the estimation of transverse dispersion.

Note that from the time-averaged velocity maps, $U(x,y)$ and $V(x,y)$ shown below, the effects of obstructions on the velocity field are evident. However, direct map comparisons are not helpful, nor practical, when studying changes in the velocity patterns over different flow rates. To allow for a better comparison of magnitudes between different flow rates—instead of looking at independent maps; the variations of one-dimensional reductions of these velocity fields will be used. These dimensional reductions are achieved by applying directional spatial averages, as defined in Eq. 6.3-2.

$$U(y) = \langle U \rangle_x(y) = \frac{1}{X}\int_X U(x^*,y)\,dx^*, U(x) = \langle U \rangle_y(x) = \frac{1}{Y}\int_Y U(x,y^*)\,dy^* \qquad \textit{Eq. 6.3-2}$$

These averages are defined over the extent of the field of view (see Figure 6.1-1). Beside a representative map of each of the quantities analysed, their dimensional reductions, namely, $\langle U \rangle_y(x)$, $\langle V \rangle_y(x)$, $\langle U \rangle_x(y)$, $\langle V \rangle_x(y)$, are presented. Additionally, the variation of these averaged quantities with Re_d are presented as boxplots, showing their statistical distribution, alongside their (double-) averaged quantities and standard deviation.

6.3.1.1. Mean Longitudinal Velocity, $\boldsymbol{U(x,y)}$

Figure 6.3-1a shows the map of $U(x,y)$, for one of the (6) flow rates tested. Blank areas represent stems. Boundary layers zones can be seen in areas of rapid decrease in U around stems. These velocity-defect zones extend as wakes downstream of each stem. This reduction in velocity (momentum) is compensated by acceleration zones between stems[13].

Spatial variations in U are the main indicator of differential advection[14], and can, as a first approximation, identify different flow areas. Namely, wakes, recirculation zones, boundary layers and advective acceleration 'gaps'. Changes in advection and steeper transitions between velocity-defect and acceleration zones can be identified in the plot of $U(y)$, which reflects the increase in differential advection with Re_d. On its own, $U(y)$ is valuable in the quantification of transversely varying D_y, as presented in the differential model proposed by West (2016) for partially vegetated channels. That model is based on the gradient-flux relationships for dispersion coefficient estimation presented in Ghisalberti and Nepf (2005). The information presented here for $U(y)$ could be used for a inter-stem scale estimation of dispersion coefficients, given the scope and resolution of the data; however, as this work revolves around reach-scale estimations, such calculations are outside the current scope. $U(x)$ is only affected by advection, and the differences shown in Figure 6.3-1b can serve to justify the assumption of $\partial\langle U\rangle/\partial x \approx 0$, that will be presented in the study of vegetation drag (Section 6.4). The boxplot of $U(Re_d)$, (Figure 6.3-1d) shows a linear increase in differential advection (i.e. spread of U), though it should be noted that this trend is roughly half of that shown for σ_u (see Figure 6.2-1), which indicates how time-averaging smooths the effect of turbulent and coherent motions.

---

[13] Note that in Figure 6.3-1, and subsequent contour maps in this section, the cylinders are coloured according to stem diameter using the key first presented in Figure 4.2-1b (Chapter Chapter 4), flow is from bottom to top of the images.

[14] Differential advection is defined as the spatial variations in mean longitudinal velocity. For comparison, this quantity conceptually represents the secondary wake variations presented in White and Nepf (2003).

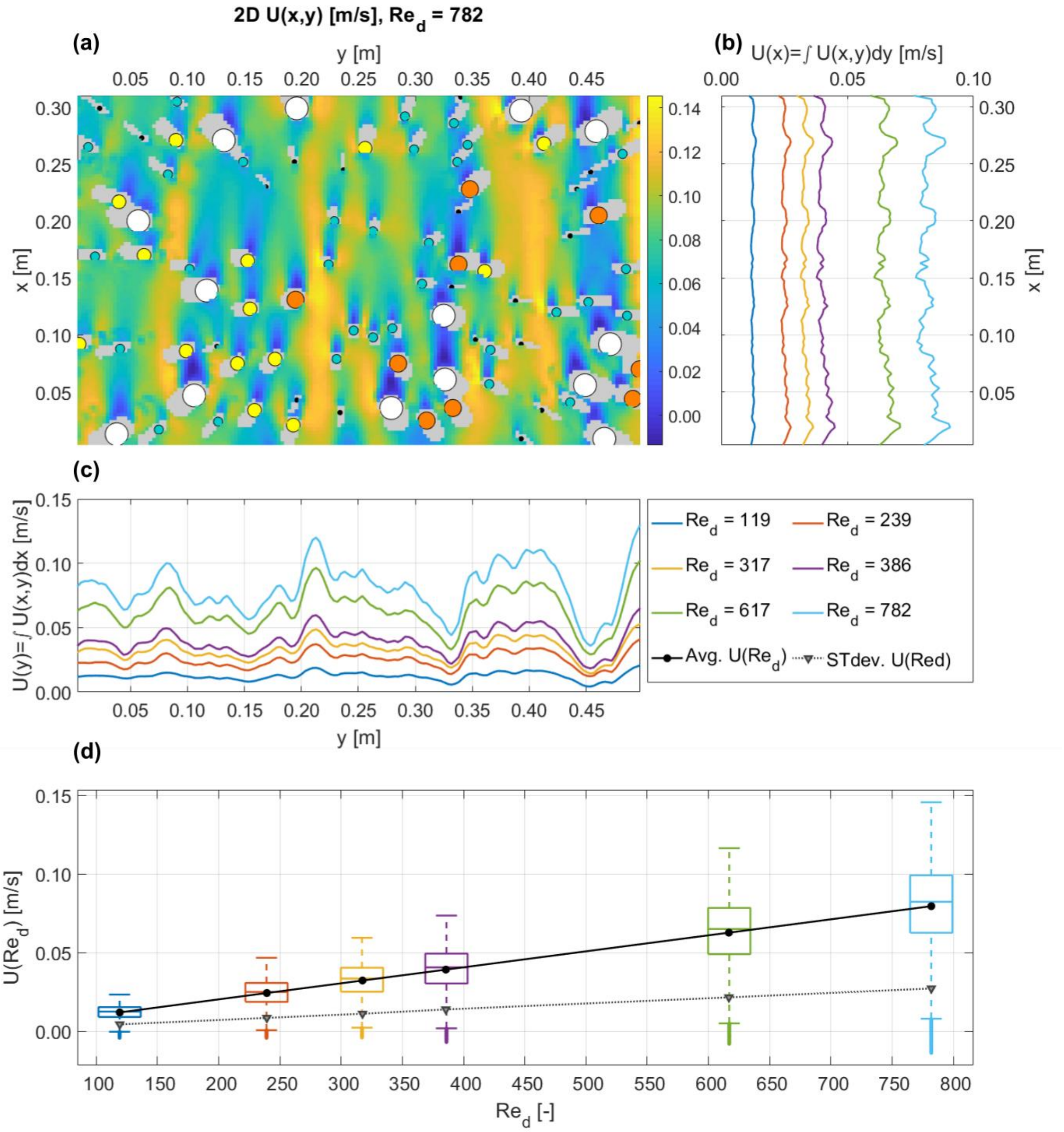

Figure 6.3-1. a) Map of time-averaged longitudinal velocity for a test carried out at Re_d=782. b) Longitudinal profiles for $U(x)$, from a transverse average of $U(x,y)$ c) Transverse profiles for $U(y)$ from a longitudinal average of $U(x,y)$ and d) Variation of U with Re_d for the range of flows tested.

6.3.1.2. Mean Transverse Velocity, $\boldsymbol{V(x,y)}$

Clearly, the behaviour of $V(x,y)$ is dominated by the presence of stems, which is illustrated by the concentration of lateral displacements on the upstream boundaries of the stems shown in Figure 6.3-2a. The magnitude of these displacements is proportional to both Re_d and (representative) stem diameter, and contrary to the case for U, the gradients of lateral velocity vary in both spatial directions. It can then be concluded that V is proportional to advection, stem diameter and the stem density. The variation in $V(x)$ and $V(y)$ shown in Figure 6.3-2b anc c present seemingly scaled versions of the same function, which, for the case of a constant vegetation distribution makes all quantities dependent on V only a function of Re_d for this set of experiments. This is in agreement with the results for D_y^* presented in Chapter 4, and the model proposed by Tanino and Nepf (2009).

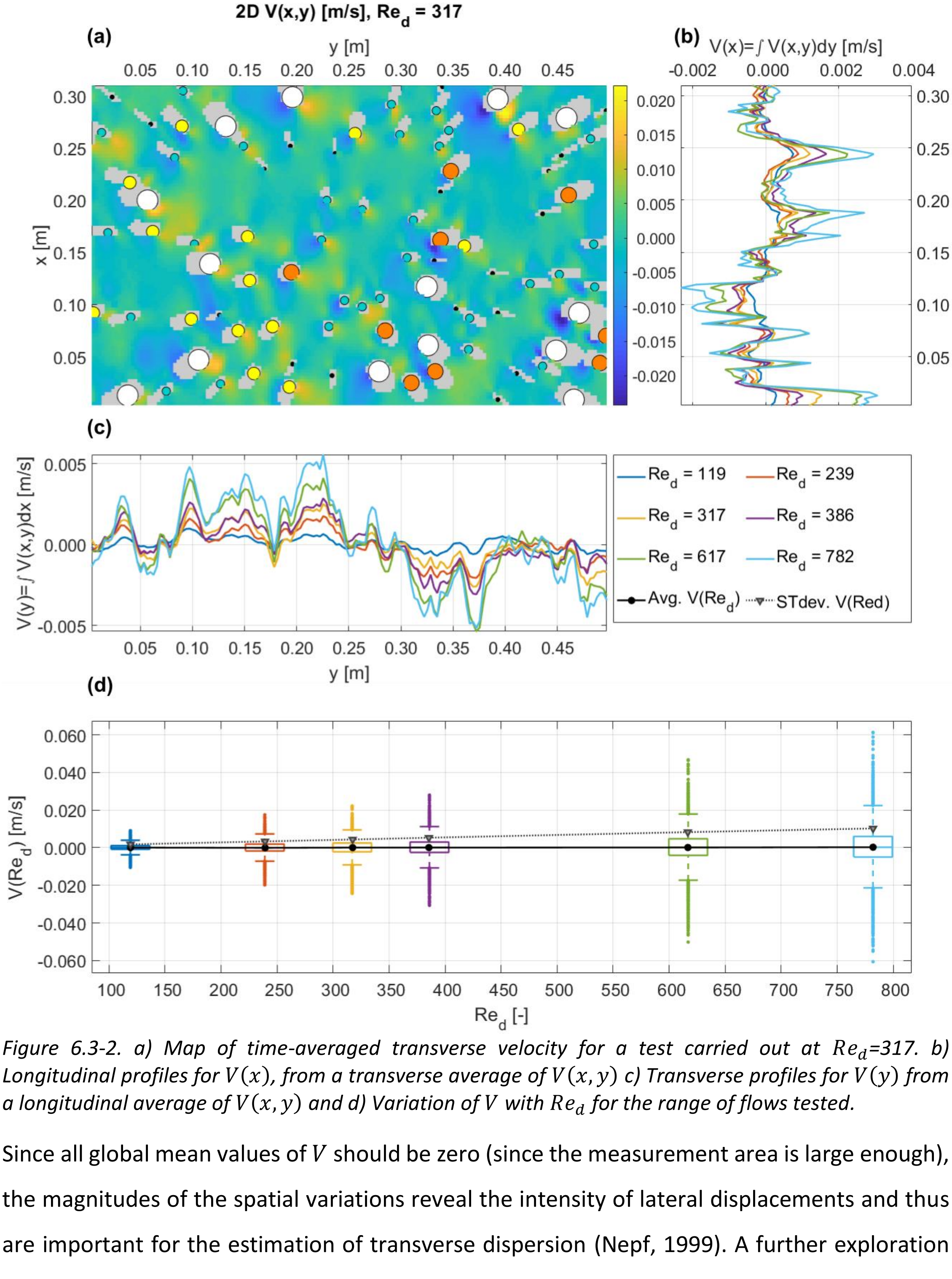

Figure 6.3-2. a) Map of time-averaged transverse velocity for a test carried out at Re_d=317. b) Longitudinal profiles for $V(x)$, from a transverse average of $V(x,y)$ c) Transverse profiles for $V(y)$ from a longitudinal average of $V(x,y)$ and d) Variation of V with Re_d for the range of flows tested.

Since all global mean values of V should be zero (since the measurement area is large enough), the magnitudes of the spatial variations reveal the intensity of lateral displacements and thus are important for the estimation of transverse dispersion (Nepf, 1999). A further exploration on the methodology necessary to compute a representative transverse mixing scale is given in Chapter 7. Figure 6.3-2d shows the overall spread of lateral velocities, which seemingly follows a linear proportional relationship with Re_d. Similar to the case of U, the spread of mean transverse velocities, shown in Figure 6.3-2d, is approximately half of that seen for σ_v (see Figure 6.2-1), this is a consequence of the time-averaging smoothing the effects of vortex-induced transverse displacements, which have characteristic periods smaller than the averaging interval, T.

6.3.1.3. Time-averaged vorticity $\boldsymbol{\Omega(x, y)}$

The combined effects of recirculation boundaries and lateral gradients generate rotational instabilities around stems, giving rise to vortex shedding (see Chapter 2). This is one of the main characteristics of flows around stems/cylinders. Vorticity is used to quantify the intensity of these rotational motions and is defined as

$$\Omega(x, y) = \left(\frac{\partial V}{\partial x} - \frac{\partial U}{\partial y}\right)$$

Since vortices are shed in an alternating manner, the values of Ω are concentrated downstream of the stems, as can be seen downstream from the stems in Figure 6.3-3a. Briefly, the magnitude of this value represents the rotation intensity of coherent structures around stems. In addition to being associated to energy production (vortices need energy to exist and move), vortices are also localised trapping mechanisms that affect dispersion. The increase in Ω with Re_d indicates stronger vortex shedding with advection. This is important as the scale of these structures determines relevant dispersion scales, and governs the rates of energy transfer and dissipation.

From a dispersion study perspective, vortices are relevant insofar as they work as solute trapping mechanisms, their characteristic scales determine the mixing lengths for the initial stages of dispersion, their magnitude is proportional to the effect of drag on the flow (Tanino and Nepf, 2008a) and their shedding frequencies determine mass exchange rates. The analysis presented at this stage is insufficient to determine length scales and shedding frequency, and will be explored in detail in Chapter 7. Nevertheless, it is important to note that the peaks seen in Figure 6.3-3a show the location of the extent of shed vortices, and their decay is representative of the dissipation they experience as they move downstream. This dissipation is much quicker than the one expected for a single cylinder (Sanches *et al.*, 2014), which is a consequence of the vortex interactions present in random cylinder arrays. Briefly, these interactions can be summarised as the result of vortex coalescence and cancelation caused by vortex fluxes having equal and opposing-sign vorticities (Ricardo, Canelas and Ferreira, 2016), the creation of preferential pathways caused by pressure fields behind stems (Sanches *et al.*, 2014). It should also be said that background turbulence increases shedding frequencies (Kiya, Tamura and Arie, 1980), whilst increasing vorticity decay rates and general dissipation, and decreasing vorticity fluxes (Ricardo, Sanches and Ferreira, 2016).

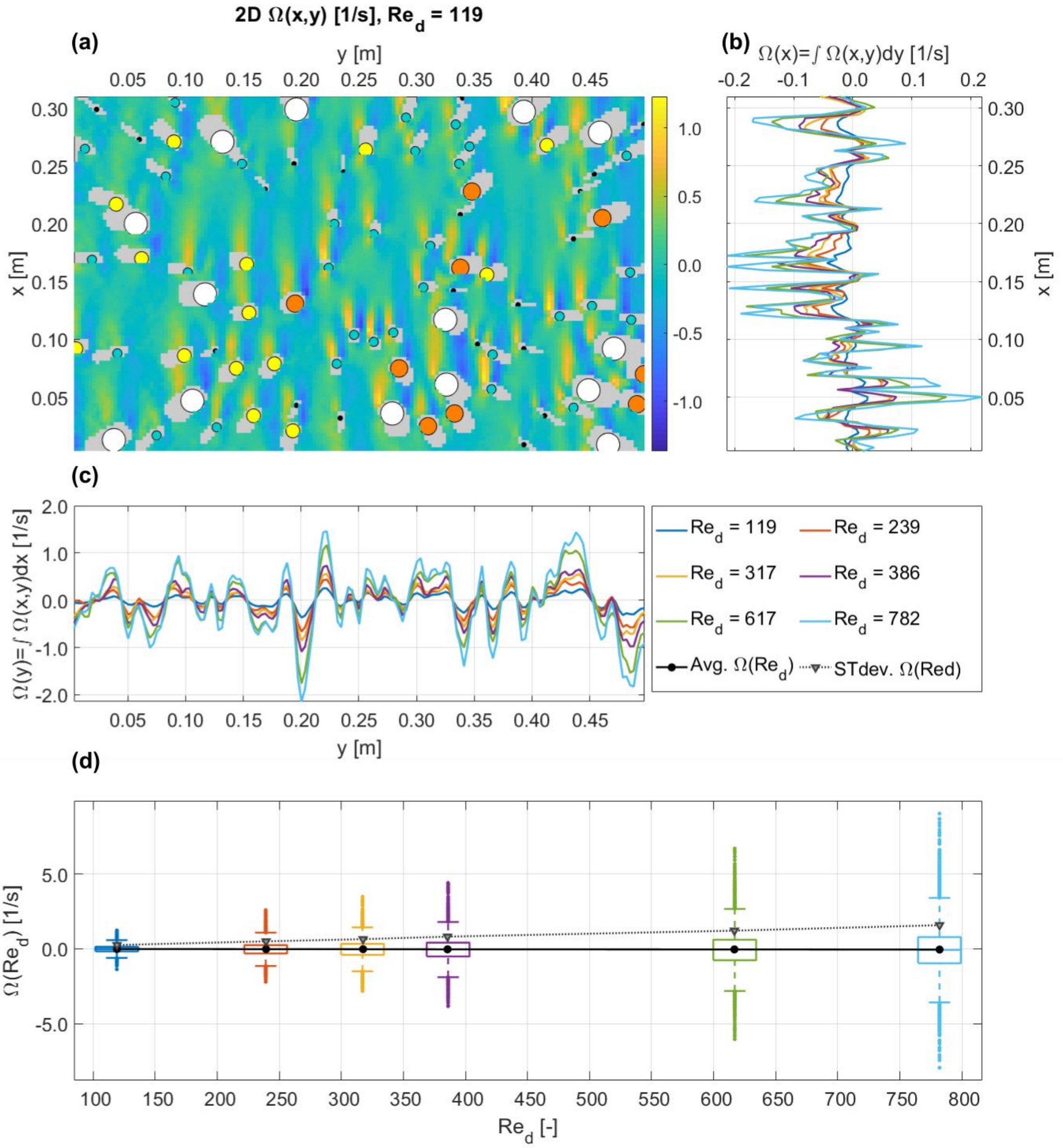

Figure 6.3-3. a) Map of time-averaged vorticity for a test carried out at Re_d=119. b) Longitudinal profiles for $\Omega(x)$, from a transverse average of $\Omega(x,y)$ c) Transverse profiles for $\Omega(y)$ from a longitudinal average of $\Omega(x,y)$ and d) Variation of $\Omega(x,y)$ with Re_d for the range of flows tested.

6.3.2. Second order velocity statistics, $\boldsymbol{TKE(x,y)}$, $\boldsymbol{U^*(x,y)}$ and $\boldsymbol{V^*(x,y)}$

First order maps give a comprehensive view of the distribution of mean travel velocities over the vegetated reach. However, the time averaging procedure 'hides' important underlying processes such as small scale turbulence, and the existence of coherent motions. The magnitude of these processes can be explored via 2nd order statistics (or measures of spread), and their spatial variations are shown in this section. It should be noted that special characteristics (time and length scales – extent and life span) of the structures that give rise to these coherent motions, and also turbulence, require a detailed spectral analysis that will be explained in Chapter 7.

Generally, the magnitudes presented in Figure 6.3-4 show the combined effects of 'random' turbulence[15] and coherent motions generated by vortex shedding. The jump between the curves for $Re_d = 386$ and $Re_d = 617$, suggests a change in the flow regime, possibly, the quicker breakdown of large scale structures, the transition to turbulent boundary layers (meaning that the detached vortices are turbulent themselves), or even the effect of seiches[16].

Second order velocity statistics are based on the deviations from the mean velocities ($u' = U - u$), and are therefore the main descriptors of turbulence magnitudes, the energy associated with time-dependent structures and momentum transfers. As water flows through the stems, pressure differentials along their surface, together with its roughness, will involve a transfer of energy from the mean flow into the creation of the aforementioned vortices. Due to direct shear between these vortices and the undisturbed flow, ever smaller structures will be formed until scales small enough to be directly dissipated into heat due to viscosity.

6.3.2.1.Turbulent Kinetic Energy

If we consider the kinetic energy per unit mass of u' and v', defined as

$$TKE = k = \frac{1}{2}\left(\overline{u'^2} + \overline{v'^2}\right)$$

We see from Figure 6.3-4 that these values are concentrated around stems, and reach peaks after some distances downstream from the stems. This distances are the recirculation zones mentioned in the section for U. The peaks of this quantity are expected near the sources of turbulent energy (which is transferred from the mean flow through drag).

The magnitude of this turbulence production is proportional to stem diameter and Re_d, and this proportionality with Re_d does not follow a linear trend. Also, from the fact that TKE production is stem localised, these values are not expected to have strong directional variations, meaning that for constants stem densities, only variations with respect to Re_d are

[15] When discussing deviations in the velocity profile, it is necessary to distinguish between 'small-scale' turbulence, which is random, and periodic (or coherent) ones, which are phase-correlated.
[16] As we had previously discussed these, we assumed, are the oscillating motions generated by the frequency of surface waves matching that of the cylinders.

relevant. The variations evidenced in some of the directional plots shown in Figure 6.3-4b and c are the consequence of illumination heterogeneities, which were found to be dependent on the attenuation caused by the stems in the far end of the illuminated plane (see Chapter 4 and Appendix B). As can be seen by comparing Figure 6.3-4c and d, the noise is already captured in the boxplot of $TKE(Re_d)$ as outliers, such that the mean trends can be considered unaffected.

Regarding the importance of TKE for dispersion characterisation, Nepf (1999), based on the equilibrium between turbulent production and dissipation, proposed the square root of TKE as the characteristic turbulent length scale, such that turbulent diffusion, D_t, is proportional to this quantity. The selection of this quantity as a representative turbulent length scale is confirmed below, as turbulence intensities have similar magnitudes and, as such, an isotropic assumption is valid, as discussed in White and Nepf (2003) and Tanino and Nepf (2008b).

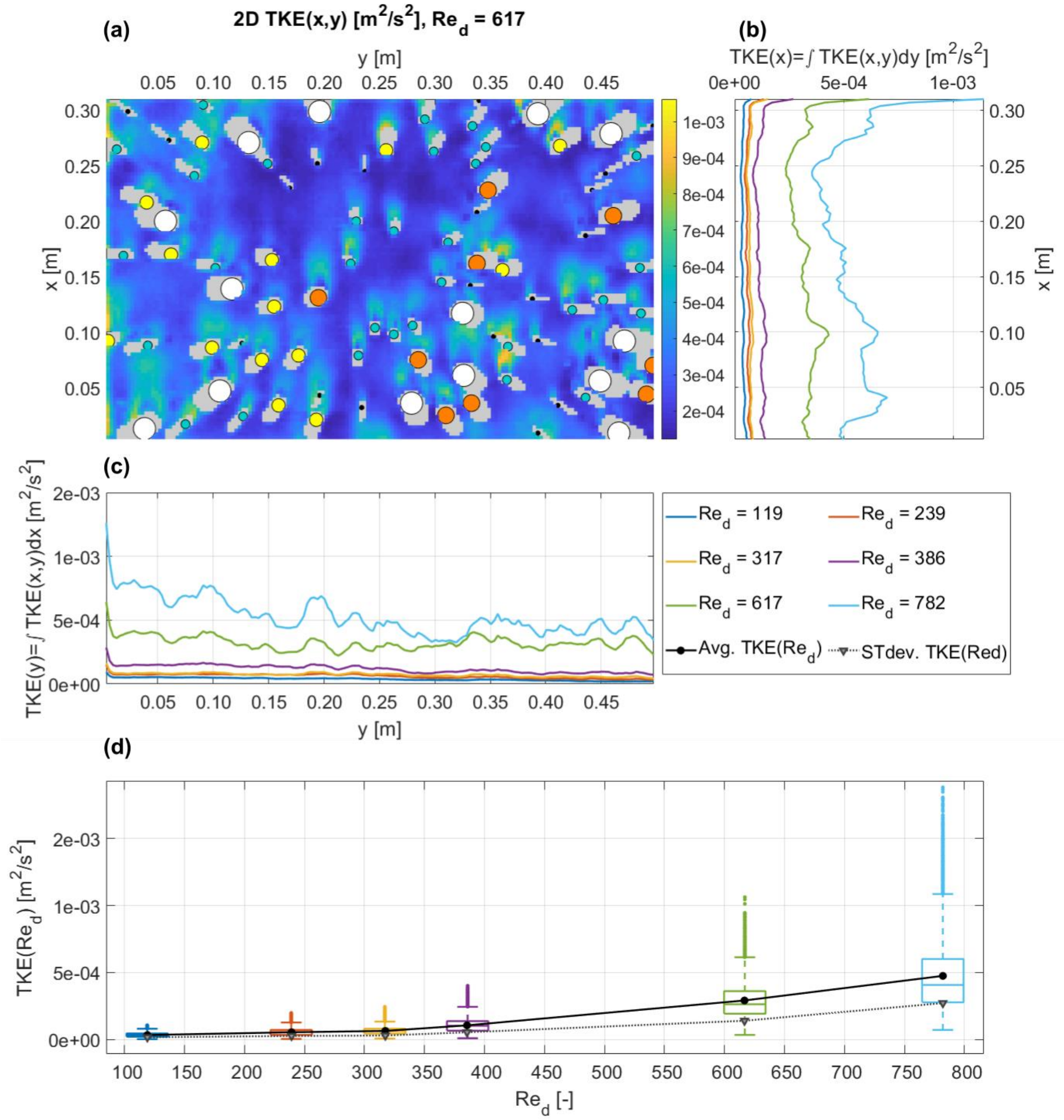

Figure 6.3-4. a) Map of $TKE(x, y)$ for a test carried out at Re_d=617. b) Longitudinal profiles for $TKE(x)$, from a transverse average of $TKE(x, y)$ c) Transverse profiles for $TKE(y)$ from a longitudinal average of TKE(x, y) and d) Variation of TKE(x, y) with Re_d for the range of flows tested.

6.3.2.2. Turbulence intensity of Longitudinal velocity, $\boldsymbol{u}^{+*}(\boldsymbol{x}, \boldsymbol{y})$

The characteristic longitudinal turbulent scale is obtained as the root-mean-square of u', and a first approximation to the longitudinal mixing length can be obtained from the product u^+L, where L is a characteristic length scale of the flow, considered to be a representative stem diameter, d for vegetated flows. Figure 6.3-5a shows the maps of this turbulent velocity scale, u^+ normalised with the advection, i.e. $u^{+*} = u^+/U_p$, conventionally called turbulence intensity, to allow a direct comparison with σ_u. The fact that high values of u^{+*} are concentrated around stems seems to confirm the hypothesis that stem diameters are the characteristic turbulent length scale of the flow. Further, the ratio of turbulence to advection decreases with Re_d, following the similar trend as σ_u (Figure 6.2-2), albeit with a ~30% difference in magnitude.

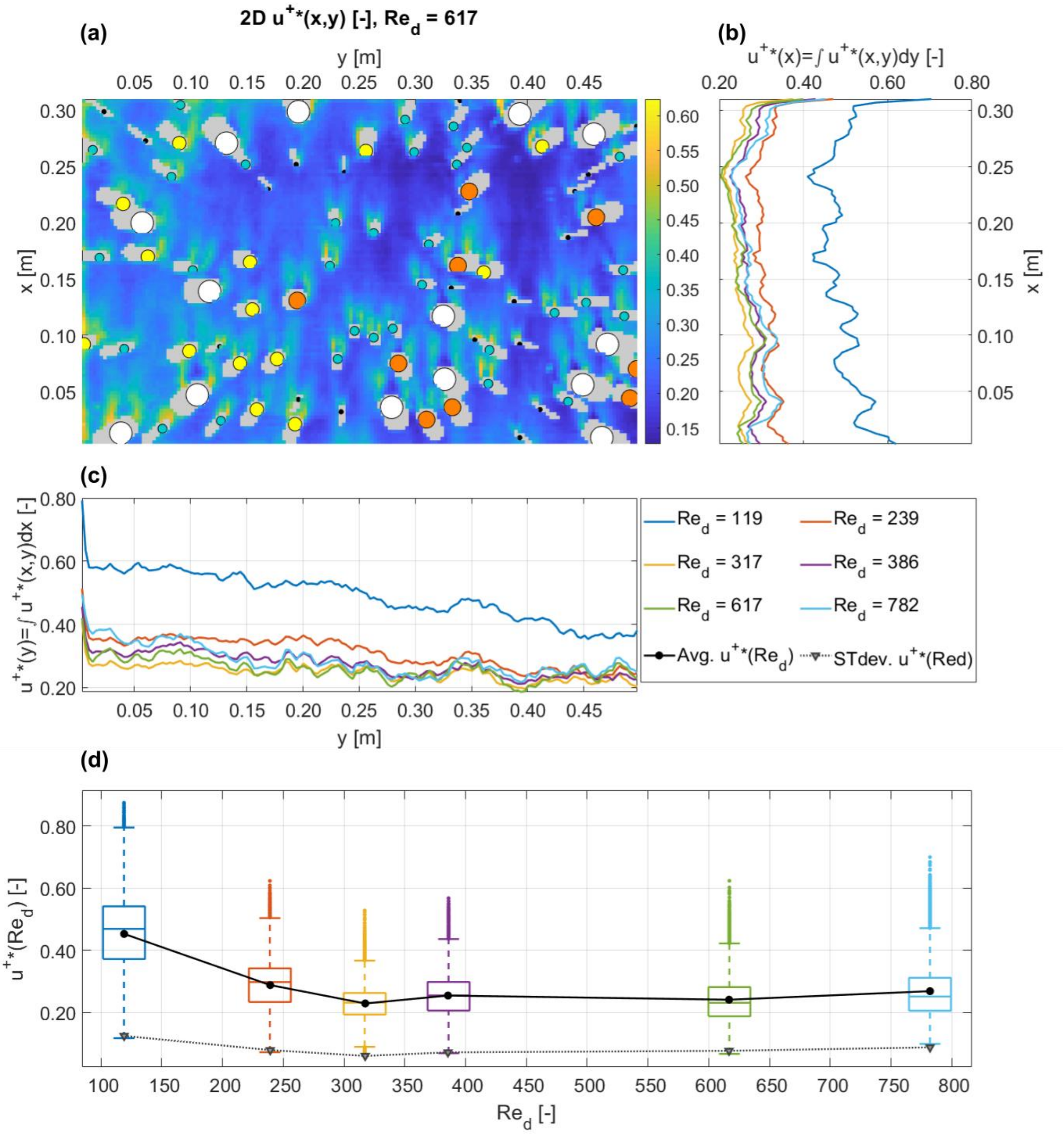

Figure 6.3-5. a) Map of longitudinal turbulence intensity, $u^{+*}(x, y)$, for a test carried out at Re_d=617. b) Longitudinal profiles for $u^{+*}(x)$, from a transverse average of $u^{+*}(x, y)$ c) Transverse profiles for $u^{+*}(y)$ from a longitudinal average of $u^{+*}(x, y)$ and d) Variation of $u^{+*}(x, y)$ with Re_d for the range of flows tested.

6.3.2.3.Turbulence Intensity of Transverse Velocity, $\boldsymbol{v}^{+*}(\boldsymbol{x}, \boldsymbol{y})$

Similar to u^{+*}, transverse turbulence intensities, v^{+*}, Figure 6.3-6, confirm the premise that the main factor contributing to turbulence scales are the stems.

It is also important to note that the negative trends of u^{+*} and v^{+*} with Re_d show that the growth of coherent structures is limited by both the space in which they can develop (stem spacing), and the increasing dissipation rates. As differential advection increases, shear and thus direct viscous dissipation also increase, limiting the role of large structures to diffusion. For areas in the far end of the illumination plane (left side on Figure 6.3-6a), light scattering, and thus the signal of the PIV image will have a lower signal-to-noise ratio, as these areas are affected by light attenuation. This effect is more noticeable for the lowest flow analysed, as seen in Figure 6.3-6c, where noise has a scale comparable to half of the mean velocity, U_p. It is then expected that the distribution $v^{+*}(Re_d)$ for $Re_d = 119$, shown in Figure 6.3-6d, slightly overestimates normalised turbulent intensities. However, both the magnitude and trend of u^{+*} and v^{+*} for this range are as expected knowing that in the periodic vortex street range, vortices are the main carriers of turbulent energy (See Chapter 2).

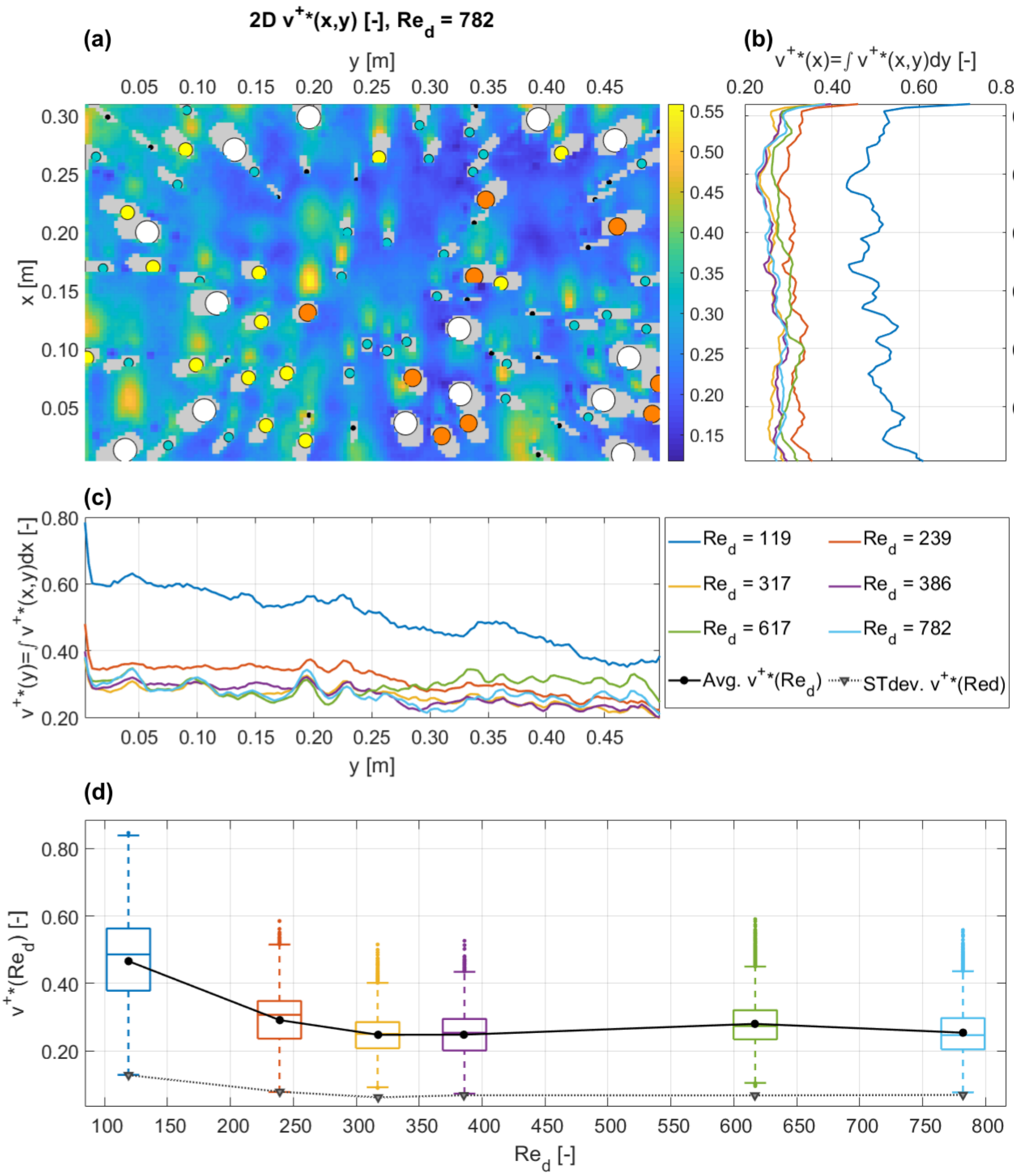

Figure 6.3-6. a) Map of transverse turbulence intensity, $v^{+*}(x,y)$, for a test carried out at Re_d=782. b) Longitudinal profiles for$v^{+*}(x)$, from a transverse average of $v^{+*}(x,y)$ c) Transverse profiles for $v^{+*}(y)$ from a longitudinal average of $v^{+*}(x,y)$ and d) Variation of $v^{+*}(x,y)$ with Re_d for the range of flows tested.

As will be presented below, the dimensional turbulence magnitudes squared (${u^{+*}}^2$ and ${v^{+*}}^2$) also represent the normal, virtual turbulent stresses, which are important for the quantification of drag forces in a vegetated array. Finally, the analysis presented in this section has served to introduce some of the main quantities that have been used to describe dispersion.

6.4. Analysis Framework – Momentum Equation

As mentioned above, an exploratory analysis can only take the study of hydrodynamic dispersion so far. The interaction between the quantities presented and other important phenomena (e.g. drag and dissipation) is overlooked when these values are considered in isolation.

Equations for the momentum, mass and energy balance serve as a pivot point to study the way in which these variables are interrelated, and help to simplify the analysis by removing degrees of freedom that, due to experimental limitations, cannot be quantified directly. Further, based on dimensional grounds, the analysis can be simplified by omitting values that are shown to have a negligible impact on the physical phenomena these equations represent (e.g. Burke and Stolzenbach, 1983).

The analysis proposed in this section is based on the momentum equation, which expresses a balance between flow acceleration and the forces acting on the flow field. Similar approaches have been undertaken before. Relevant examples are the works of Tanino and Nepf (2008b, 2008a) and Ricardo, Martinho, *et al.* (2014), in which the momentum equation is progressively simplified by applying temporal and spatial averages. These approaches replace intractable degrees of freedom by dispersive fluxes, that aggregate temporally and spatially-dependent quantities into single values that help reveal the statistical nature of some of the processes that these equations of motion represent. An illustration of this approach is presented as follows.

The general momentum equation (see Chapter 2) compares the change in instantaneous momentum (i.e. acceleration of fluid particles) to the changes in internal stresses and the effect of external forces, Eq. 6.4-1 (tensor notation is used for simplicity).

$$\underbrace{\frac{\partial u_i}{\partial t} + u_j \frac{\partial u_i}{\partial x_j}}_{\text{Change of momentum}} = \frac{\partial}{\partial x_j}\Bigg(\underbrace{-\frac{1}{\rho} p \delta_{ij} + \nu \frac{\partial u_i}{\partial x_j}}_{\text{Fluid stress}}\Bigg) + \underbrace{f_i}_{\text{External forces}} \qquad \textit{Eq. 6.4-1}$$

In this state, Eq. 6.4-1 is prohibitively complex by virtue of the random nature of $u_i(x, y, t)$. The first simplification is achieved by applying the Reynolds decomposition presented in Section 2.2.5 (Chapter 2), and time averaging the entire equation, this yields the RANS equation, Eq. 6.4-2, which now expresses the momentum balance in terms of mean quantities and one new correlation term: the Reynolds/turbulent stresses. This new term expresses the average stress that a volume of fluid experiences as a result of the transfer of tangential ($i \neq j$) and normal ($i = j$) turbulent fluctuations.

$$\underbrace{\frac{\partial U_i}{\partial t} + U_j \frac{\partial U_i}{\partial x_j}}_{\text{Change of avg. momentum}} = \frac{\partial}{\partial x_j} \underbrace{\left(-\frac{1}{\rho} P \delta_{ij} - \overbrace{\overline{u_i' u_j'}}^{\text{Reynolds stresses: avg. flux of turb. momentum}} + \nu \frac{\partial U_i}{\partial x_j} \right)}_{\text{Mean fluid stress}} + \underbrace{F_i}_{\text{Mean external forces}} \qquad \textit{Eq. 6.4-2}$$

This simplification now expresses the momentum balance in terms of (experimentally available) mean quantities. However, for the specific case of obstructed flows, the term for mean external forces, F_i, lumps together the effects of gravity and stem-induced drag. To avoid translating the complex effects of obstructions into an additional term, that still is experimentally unattainable, a further spatial decomposition of the time-averaged quantities into spatial averages and fluctuations, $U_i = \overline{u_i} = \langle \overline{u_i} \rangle + \overline{u_i}''$ and averaging over a large enough spatial domain, we obtain the double-averaged momentum equation (Nikora *et al.*, 2013), shown in Eq. 6.4-3.

$$\underbrace{\epsilon_f \langle U_j \rangle \frac{\partial \langle U_i \rangle}{\partial x_j}}_{\text{Change of avg. momentum}} = \frac{\partial}{\partial x_j} \epsilon_f \underbrace{\left(-\frac{1}{\rho} \langle P \rangle \delta_{ij} - \overbrace{\left\langle \overline{u_i' u_j'} \right\rangle}^{\text{Reynolds stresses}} - \overbrace{\langle \overline{u_i}'' \overline{u_j}'' \rangle}^{\text{Dispersive flux}} + \left\langle \nu \frac{\partial U_i}{\partial x_j} \right\rangle \right)}_{\text{Mean fluid stress}}$$

$$\underbrace{+ \epsilon_f \langle F_i \rangle + \overbrace{\frac{1}{\rho V} \overline{\int_{A_c} n_i p dA}}^{\text{Form drag}} - \overbrace{\frac{1}{V} \overline{\int_{A_c} n_j \nu \frac{\partial u_i}{\partial x_j} dA}}^{\text{Viscous drag}}}_{\text{Mean external forces}} \qquad \textit{Eq. 6.4-3}$$

The resulting double-averaged momentum equation (DANS) now includes the effects of pressure (form) and viscous drag on the momentum balance, as independent terms. Also, spatial changes in mean velocities (i.e. differential advection) are summarised as the correlation term, $\langle \overline{u_i}'' \overline{u_j}'' \rangle$, namely form-induced stresses (Giménez-Curto and Corniero Lera, 1996) or dispersive fluxes (Raupach, Coppin and Legg, 1986). The value ϵ_f represents the porosity and is the complement to the solid volume fraction, φ (i.e. $\epsilon_f = 1 - \varphi$). Limiting the analysis to the experimental conditions presented here, the steady flow condition removes all time-dependent terms, the mean external force corresponds to the gravity, and the integration representing the form and viscous drag terms are carried out over the interfaces between cylinders and the flow.

Provided that sufficient velocity information is available, and the physical conditions allow for empirical simplifications in Eq. 6.4-3, the total drag force acting on the flow can be calculated from the foregoing momentum balance. Discussions on the assumptions needed to obtain vegetated drag have been presented by Tanino and Nepf (2008a); Ferreira, Ricardo and Franca (2009); and Ricardo, Martinho, *et al.* (2014). Their methodology will be discussed in Section 6.6, and adopted for the calculation of flow resistance for the data presented here. For now, it is important to focus on the role of both virtual stresses, generated as correlation terms, on the flow, particularly their evolution with Re_d and their magnitude in relation to advection.

6.5. Virtual Stresses

From the procedure illustrated in Eq. 6.4-1 to Eq. 6.4-3, the covariances of temporal and spatial velocity fluctuations, obtained after each average, have been called virtual stresses. This interpretation of statistical quantities as stresses derives from the fact that, by being symmetric, tensor quantities (e.g $\tau_{ij} = -\overline{u_i' u_j'}$), can be subdivided into tangential and normal components that act on each volume of fluid (Tennekes and Lumley, 1972). Accordingly, their effect on fluid volumes will, over the averaging interval, be analogous to those caused by shear and pressure. These virtual stresses also represent the average turbulent and dispersive momentum transfers, in a similar way that viscous stresses represent molecular momentum transfers (Pope, 2000). For instance, cross terms like $\overline{u'v'}$ represent the average flux of streamwise turbulent momentum in the transverse direction, and vice versa.

Normal virtual stresses represent the magnitude of each fluctuating component, and thus can serve to identify characteristic dispersive length scales. For the case of Reynolds stresses, the square root of terms $\overline{u_i' \, u_i'}$ gives the representative turbulent length scale in the i-th direction[17]. For mixing in a Fickian range (see Chapter 2 and Chapter 4), turbulent diffusion can be computed as the product of this characteristic turbulent scale, and a representative length scale of the flow. Similarly, the square root of dispersive fluxes of the form $\langle \overline{u_i}'' \overline{u_i}'' \rangle$ can be understood as a characteristic differential advection scale (c.f. secondary wake scale, White and

[17] This is due to $\overline{u_i'} = 0$.

Nepf, 2003). To analyse the role of these virtual stresses on the vegetated flow, Figure 6.5-1 shows the variation of all virtual stresses with Re_d for the experiments conducted.

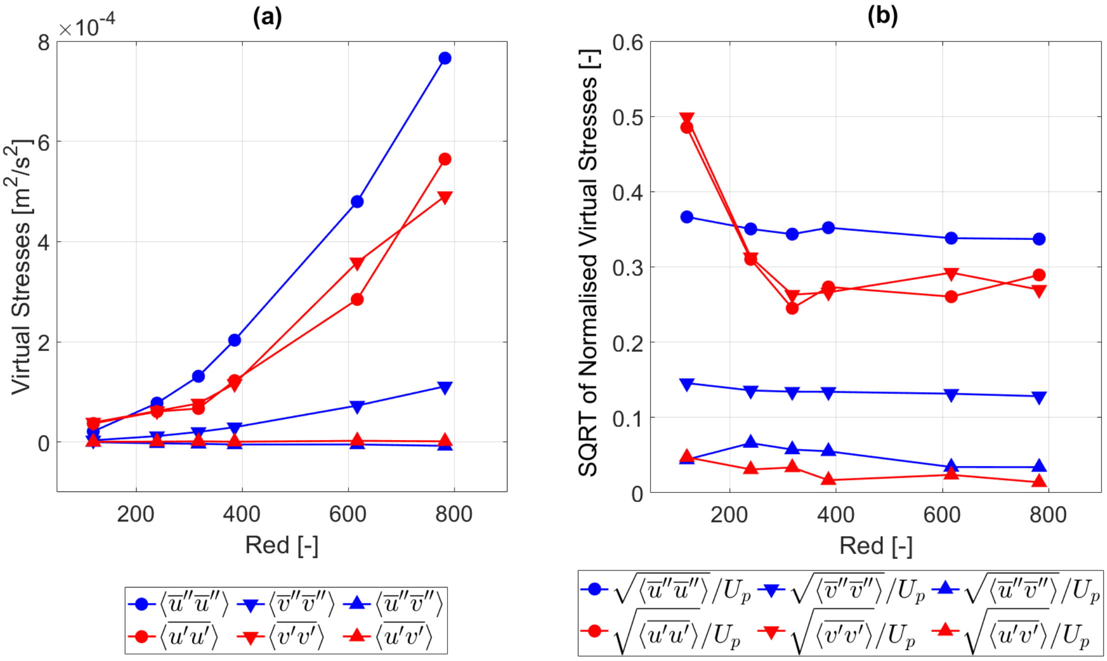

Figure 6.5-1. Variation of the virtual stresses, generated from the time-space averaging procedures, with Re_d. a) Variation of dimensional form-induced stresses (blue) and Reynolds stresses (red) with Reynolds numbers. b) Variation of (square-root) virtual stresses, non-dimensionalised by the pore velocity (U_p), form-induced (blue) and Reynolds (red). (●) streamwise stresses, (▼) transverse stresses, (▲) cross-products.

Figure 6.5-1a shows the variation of the virtual stresses measured in the RandoSticks configuration, for the range of flows tested. As expected, normal Reynolds stresses have comparable magnitudes for all Re_d (see Figure 6.3-5 and Figure 6.5-1), as these values represent the magnitudes of the characteristic turbulent scales. The same does not occur for form-induced stresses, which show that, whilst changes in transverse mean velocities are limited by the size of the obstructions, longitudinal dispersive fluxes represent the increasing difference between boundary layer velocities, velocity defect zones behind isolated and clustered stems and convective acceleration gaps (stripes of high momentum between stem clusters). In order to obtain a reliable comparison with advection, the scale of the virtual stresses are normalised using advection, $\langle \overline{u_i}'' \overline{u_i}'' \rangle^* = \langle \overline{u_i}'' \overline{u_i}'' \rangle / U_p^2$, and then the square root is calculated. The results are presented in Figure 6.5-1b. It can be seen that for form-induced stresses, their proportion to advection steadily decreases with Re_d. Physically this means that as pore velocity increases, it does so at a slightly higher rate than differential advection and lateral displacements. Note that form-induced stresses are not isotropic, with differential advection being ~2.5 times larger than characteristic lateral displacements. Given the relative magnitudes of normal Reynolds stresses, turbulent length scales can be considered isotropic, in the context of the double-averaging domain. A compensation seems to occur for $Re_d > 300$, as normalised turbulence scales are proportional to advection, and increase at a similar rate as normalised dispersive fluxes decrease. For the $Re_d < 300$ range, the proportion of turbulent length scales to advection (Figure 6.5-1b) decreases 50%. The first measurement at $Re_d = 119$ is expected to be a maximum since stable periodic shedding starts around this value (Gerrard, 1978). The growth of the largest turbulent scales is limited to the inter-stem scale so the asymptotic behaviour is expected in the context of vegetated flows. It should be noted, that the proportion of the scales for $Re_d < 200$ can be affected by the noise resulting from illumination heterogeneity (see Chapter 4 and Appendix B). Notwithstanding the effect of noise, the trends are expected to behave similarly for an ideal experimental case.

Regarding 'tangential' virtual stresses ($i \neq j$), for horizontal velocity components (i.e. u and v), Figure 6.5-1 shows their negligible contribution, notable when compared to normal virtual stresses and advection. Form-induced stresses, $\langle \overline{u}''\overline{v}'' \rangle$, do not show a trend with Re_d. Also, their small magnitudes indicate a lack of correlation between directional mean velocity variations. Physically, this reflects the difference in directional length scales: mean transverse velocities vary at the scale of the representative cylinder diameter (cf. Nepf, 1999), while mean longitudinal velocities vary at scales given by the difference between the trapping and acceleration zones, i.e. at the wake scale. The same independence with Re_d and inconsequential magnitudes are evidenced in Reynolds stresses, $\langle \overline{u'v'} \rangle$.

Figure 6.3-5 and Figure 6.3-6 show that the peak longitudinal turbulent scales are measured near the cylinder separation points, whilst for transverse turbulent velocity they are present after the formation region (Kovasznay, 1949; Gerrard, 1978). Although their contribution to reach-scale momentum is, from Figure 6.6-2, negligible; Reynolds stresses still play a role in vegetated hydrodynamics at the stem and inter-stem scales.

As mentioned above, shear Reynolds stresses represent the correlation between turbulent velocity components. Given that vegetated dynamics are governed by stems, turbulent correlations are expected to vary spatially as the flow structures (vortices), that drive the magnitude of the fluctuations, undergo rotational, diffusive and dissipative processes. As shown in Figure 6.3-5 and Figure 6.3-6, the peaks in turbulence intensities occur near the shedding regions, behind the stems, although not at the same specific locations for each velocity component.

Let us introduce the quantity $\tau^*_{xy}(x,y)$, defined as the Reynolds (stress) correlation, and calculated as the following correlation coefficient

$$\tau_{xy}^{*} = \frac{\overline{u'v'}}{u^{+}\ v^{+}} \qquad \textit{Eq. 6.5-1}$$

This expresses the cross-directional turbulent momentum transfer as a proportion of the total magnitude of turbulent momentum at each point x, y in the field of analysis. A map of this quantity is presented in Figure 6.5-2a, alongside their directional and general variation for all tests, similar to the Figures in Section 6.3. Graphically, Reynolds correlation coefficients show peaks of opposing sign near the vortex formation region, illustrating the cause of this cross-directional momentum transfer. Note also that no transfer occurs between wakes when zones of opposite sign interact, as the area denoted by A in Figure 6.5-2a shows. The opposite occurs with wakes for which the same transfer signs interact, and the wakes seem to coalesce (see area B in Figure 6.5-2a). This collision-coalescence behaviour is similar to the one reported by (Ricardo, Canelas and Ferreira, 2016; Ricardo, Sanches and Ferreira, 2016) for the case of vorticity fluxes. The extent of this transfer zones increases downstream proportional to Re_d. It is the author's view that τ_{xy}^{*} can serve as a good indicator of the extent, magnitude and deformation of cylinder wakes.

The remaining elements in the virtual stress tensors (i.e. elements including $i, j = 3$), were not measured in the current experiments. Previous studies in emergent vegetation provide evidence on the effects of these stresses. Differences in structure length scales induce a lack of correlation between vertical and streamwise turbulent fluctuations, i.e. $\langle\overline{u'w'}\rangle \sim 0$ (Tanino, 2008). Specifically, u' is expected to have a dominant coherent component from the vortex street, whilst w' will have a dominant depth-scale variation. Initially, form-induced stresses between streamwise and vertical components, i.e. $\langle\overline{u}''\overline{w}''\rangle$, were expected to be around 1% of the corresponding Reynolds stresses (Kaimal and Finnigan, 1994, chap. 3.3; Tanino and Nepf, 2008b). However, in results discussed by (Ferreira, Ricardo and Franca, 2009) and subsequently presented formally by (Ricardo, Martinho, *et al.*, 2014), it was found, from PIV data, that these stresses can be comparable in magnitude (depending on stem density). Nonetheless, when compared to other momentum components, these stresses are indeed negligible (Coppin, Raupach and Legg, 1986; Poggi, Katul and Albertson, 2004b, 2004a; Ferreira, Ricardo and Franca, 2009). Finally, for vertical Reynolds and form-induced stresses, the comprehensive experimental dataset presented by Ricardo, Franca and Ferreira (2016) showed that, if only cylinder effects are considered, form-induced stresses, $\langle\overline{w}''\overline{w}''\rangle$, are negligible compared to Reynolds stresses, $\langle\overline{w'w'}\rangle$. Also, normal and shear vertical virtual stresses tend to zero towards the depth boundaries, i.e. bed and surface ($z = 0, h$). This is important for the simplification of terms in the momentum equation and subsequent calculation of drag, as will be shown in the following section.

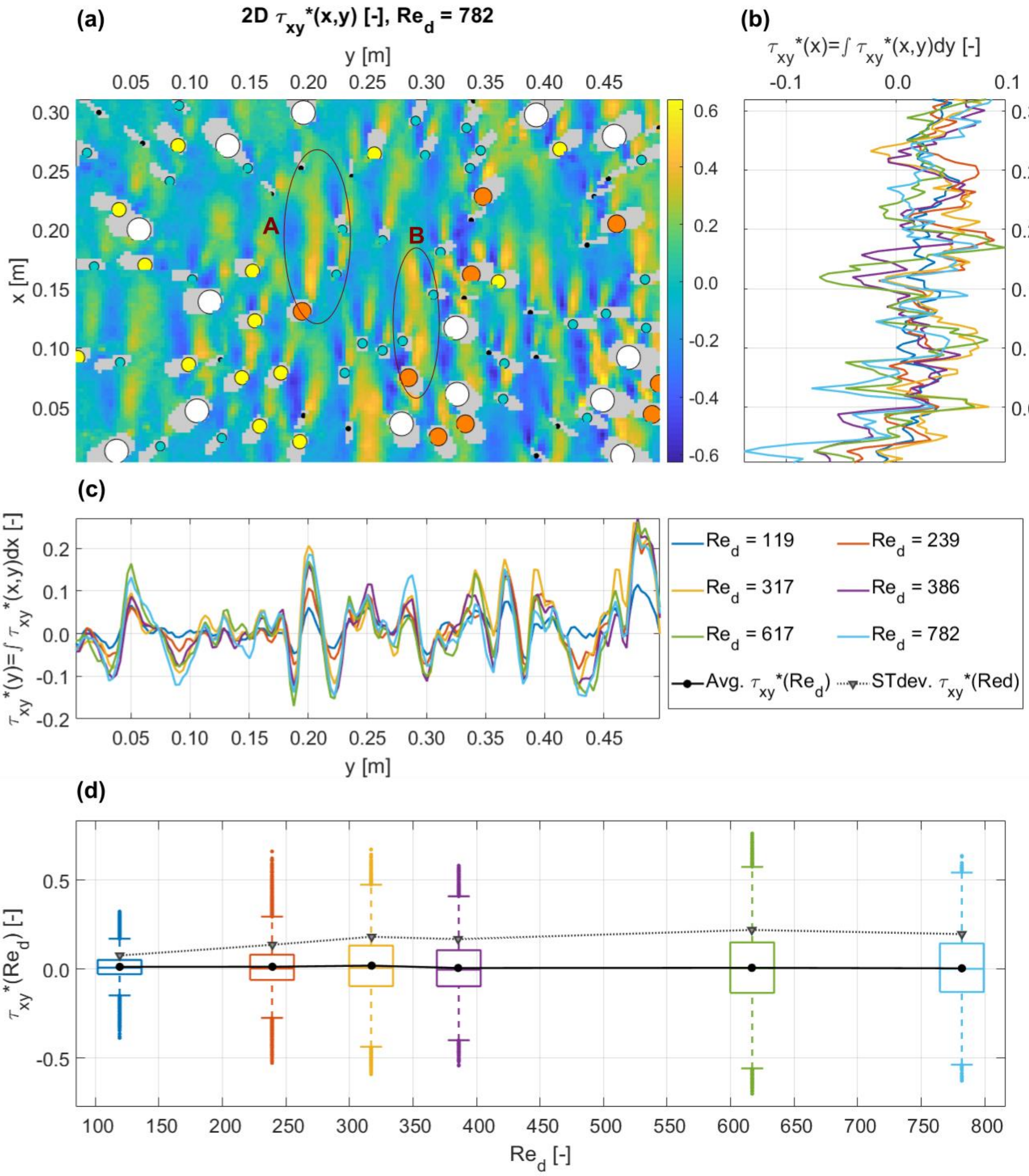

Figure 6.5-2. a) Map of Reynolds coefficients, $\tau_{xy}^{*}(x,y) = \langle\overline{u'v'}\rangle/(u^{+}\,v^{+})$, for a test carried out at Re_d=782. b) Longitudinal profiles for $\tau_{xy}^{*}(x)$, from a transverse average of $\tau_{xy}^{*}(x,y)$ c) Transverse profiles for $\tau_{xy}^{*}(y)$ from a longitudinal average of $\tau_{xy}^{*}(x,y)$ and d) Variation of $\tau_{xy}^{*}(x,y)$ with Re_d for the range of flows tested.

6.6. Vegetated Drag in a RandoSticks configuration

From the general momentum balance, based on the DANS framework, presented in Section 6.4, and following the discussion on virtual stresses given in Section 6.5, it is possible to calculate the vegetated drag using measurements obtained via PIV and the surface water profiles during the tests. The formulation presented in this section is based on the independent developments of Tanino and Nepf (2008a); and Ricardo, Martinho, *et al.* (2014). Both undergo different sets of analytical and empirical simplifications and arrive at slightly different models. However, some common assumptions are sufficient to compare them on the same terms, and be applicable to the RandoSticks configuration presented here. It will be seen that under experimental conditions similar to those described here (see Chapter 4), both formulations for cylinder drag are equivalent.

The assumptions and equations for vegetated drag discussed here are based on the derivations presented in Tanino and Nepf (2008a) and Ricardo, Martinho, *et al.* (2014). The vegetation is generally assumed to be composed of vertical cylindrical elements; further, the flow is studied along the main direction of the flow, using averaging domains large enough to avoid net lateral displacements, $\partial\langle\cdot\rangle/\partial y \approx 0$. Finally, the flow is considered steady and viscous stresses are small enough (compared to the contribution from stem drag) to be considered negligible. These assumptions are reproduced in the RandoSticks experiments presented here.

Using the double-averaging framework (Nikora *et al.*, 2013) for the momentum equation, as shown in Eq. 4.3, we see that, even after the simplifying assumptions presented above, the streamwise component of the DANS equation ($i = 1$ in Eq. 4.3) is still indeterminate, since solving for the drag terms still leaves the pressure term and many virtual stresses unresolved. An expression for the hydrodynamic pressure is found by integrating the vertical component of the DANS equation, the vertical variation in pressure is found as the sum of a hydrostatic component and a variation thereof (Ricardo, 2014), described as.

$$\epsilon_f \langle \overline{p} \rangle (x,z) = -\rho g_z \int_z^{h(x)} \epsilon_f dz + \rho \aleph(x,z) \qquad \textit{Eq. 6.6-1}$$

As mentioned above, ϵ represents the porosity of the vegetated reach, g_z is the vertical component of the gravitational acceleration, and the term $\aleph(x,z)$ represents the deviation from the hydrostatic pressure and is defined as the sum of various virtual stresses with vertical components and their gradients. Following the discussion presented in Ferreira, Ricardo and Franca (2009), together with PIV measurements of virtual stresses along vertical planes presented in Ricardo, Martinho, *et al.* (2014), it is possible to conclude, on dimensional grounds, that the vertical distribution of pressure is hydrostatic.

$$\langle \overline{p} \rangle (x,z) = -\rho g_z (h - z) \qquad \textit{Eq. 6.6-2}$$

This result was already given by Tanino and Nepf (2008a), wherein the assumption of a horizontal bed had been given, namely $g_z = -g$. This pressure term is used in the streamwise momentum balance. All stress terms involving lateral velocities (v' and $\overline{v}''$) become zero. Further, on empirical grounds, it is assumed that normal and shear vertical virtual stresses are negligible (Tsujimoto *et al.*, 1992; Kaimal and Finnigan, 1994, p. 85; White, 2002). Consequently, the Tanino and Nepf (2008a) version of vegetated drag omits all contributions from virtual stresses, such that the change in water depth, h, defines the contribution of vegetated drag, namely

$$\langle \overline{f_D} \rangle_V m = -\rho g (1-\varphi) \frac{dh}{dx} \qquad \textit{Eq. 6.6-3}$$

The term $\langle \overline{f_D} \rangle_V$, represents the vertical average of the average drag in the direction of the average flow per unit length of stem, $\langle \overline{f_D} \rangle$, and m is the stem number density. In addition to omitting contributions from virtual stresses, Eq. 6.6-3 does not account for compensations in advection as a consequence of the non-uniform cross section. This has implications for experimental works in which boundary conditions are imposed on the flow, e.g. using a tailgate to maintain a reference water depth at specific points, or adjusting the slope to keep water depth differences under a certain threshold.

A more general formulation for vegetated drag was obtained by Ricardo (2014) for horizontal beds. An expression derived from this methodology, that can be applied to sloping beds in vegetated reaches, and under laboratory condition (i.e. ignoring surface stress effects) is defined in Eq. 6.6-4. Note that the streamwise and vertical contributions of the gravitational acceleration are given in generality (i.e. g_x and g_z) because a condition on the channel's geometry has not been imposed. For a flume with an inclination angle β, these terms become $g_x = g(\sin\beta)$ and $g_z = -g(\cos\beta)$.

$$\begin{aligned} \frac{1}{\rho}\langle \overline{f_{Dx}} \rangle = & -\frac{\partial h}{\partial x}\left(U_p^2 - g_z h\right) - \frac{\partial h}{\partial x}\left(\langle \overline{u'u'} \rangle + \langle \overline{u}''\overline{u}'' \rangle\right) \\ & + h\left(g_x - 2U_p \frac{\partial}{\partial x} U_p\right) - h\frac{\partial}{\partial x}\left(\langle \overline{u'u'} \rangle + \langle \overline{u}''\overline{u}'' \rangle\right) \end{aligned} \qquad \textit{Eq. 6.6-4}$$

The LHS of Eq. 6.6-4 represents the total volume average drag in the direction of flow per unit mass of fluid. To unify notation, it is important to understand the difference between the different terms defining drag. The net cylinder drag force per unit of fluid mass over the double-averaging interval, f_x, is defined as the sum of the last two integral terms in Eq. 6.4-3. The term

$\langle\overline{f_D}\rangle$, defined above, represents the drag caused by the average cylinder. $\langle\overline{f_{Dx}}\rangle$ is equivalent to f_x but now considering the flow depth and the mass of fluid. In other words, the term $\langle\overline{f_D}\rangle_V$ represents the average drag force per unit of submerged stem length, and $\langle\overline{f_{Dx}}\rangle$ represents the total drag force over the entire averaging volume. For future references, the relationship between the foregoing definitions for drag can be expressed as,

$$\frac{1}{\rho}\langle\overline{f_{Dx}}\rangle = h\,\langle f_x\rangle_h = \frac{hm}{\rho(1-\varphi)}\langle\overline{f_D}\rangle_V \qquad \textit{Eq. 6.6-5}$$

The terms defining vegetated drag force in Eq. 6.6-4 are grouped to represent the different contributions to drag in the simplified vegetation model presented. Note that by joining the terms with U_p, it can be seen that drag is balanced by the gradients of pressure ($\sim \partial h/\partial x$), kinetic energy ($\sim U_p^2$), and potential energy ($\sim g_x$). The effects of the virtual stresses are obtained by joining the 2nd and 4th terms on the RHS of Eq. 6.6-4 and using the product rule of differentiation; the result can be understood as the change in the energy transfer rate between the mean flow and the creation of coherence and random turbulence.

When the general definition of vegetated drag given in Eq. 6.6-4 is compared to Tanino and Nepf (2008a), Eq. 6.6-3, it can be seen that the latter is limited to drawdown water profiles for horizontal or mildly sloped beds, i.e. H2 and M2 (Chow, 1959, p. 225). Uniform flow and moderate backwater profiles are fringe conditions under this model. Even for the cases in which Eq. 6.6-3 is considered valid, flow resistance in the form of drag, does not include the effects of potential energy or changes in pore velocity—even though the latter is expected to be minimal for moderate, steady profiles. Figure 6.6-1 shows the water depth and pore velocity gradients for the RandoSticks configuration considered here, to illustrate their mutual compensation. The former was measured using a moving Vernier gauge, over a distance of 6 metres, covering the LIF and PIV sections, at 0.5 m intervals. The velocity gradients were obtained from the linear best-fit of travel velocities measured from the LIF experiments (see Chapter 4). The extent of the PIV section is not large enough to provide significant conclusions on pore velocity gradients. No significant changes in velocity (advective deceleration) can be seen for the backwater profiles, and this extends for most of the flows tested: changes over each measurement reach, 1 m, are below 2% of the mean pore velocity for $Re_d < 800$. For the maximum Re_d tested, the changes in advection represent 4% of the mean pore velocity. The behaviour of the velocity gradients shown in Figure 6.6-1, therefore justify the argument advanced in Chapter 4 of Fickian dispersion for each of the LIF reaches analysed[18]. Based on this, it is proposed that for experimental studies in vegetated flows, changes in velocity regimes should be used to determine whether flow is uniform instead of water profiles. As will be shown below, this justification extends to momentum contributions.

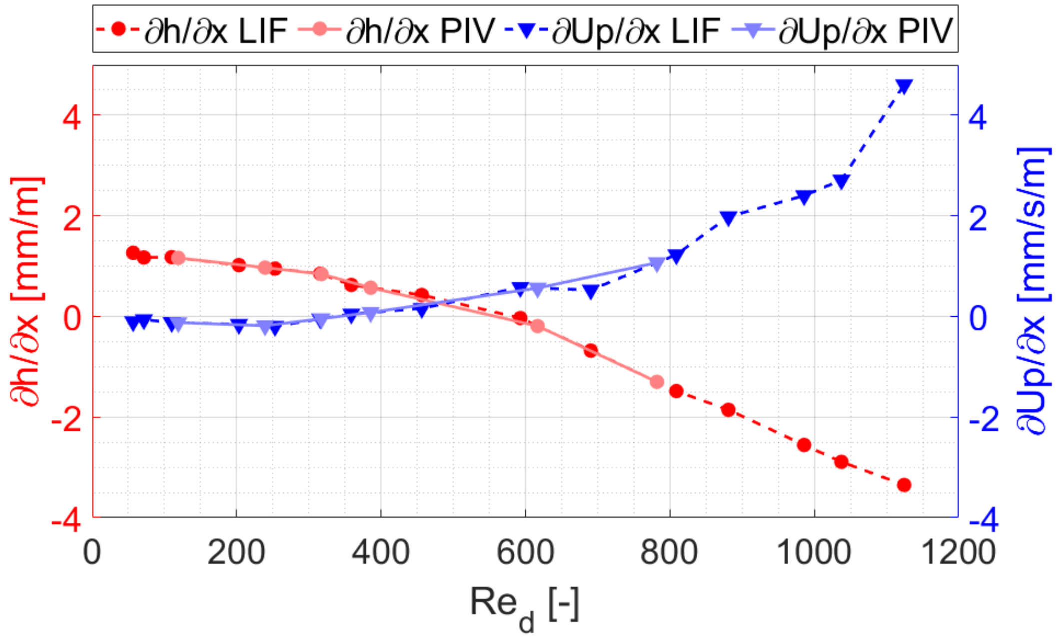

Figure 6.6-1. Variation of water depth and pore velocity gradients from the LIF and PIV experiments. PIV trends were obtained from a Re_d-based interpolation.

Although comparable on dimensional grounds, the gradients shown in Figure 6.6-1 are not equivalent in terms of momentum contributions (see Eq. 6.6-4). This result is in line with most estimation of drag based on the DANS equation (Tanino and Nepf, 2008a; Ricardo, Martinho, *et al.*, 2014) and gradually varied flow profiles (Busari and Li, 2016), among others. If the 1st and 3rd terms on the RHS in Eq. 6.6-4 are decomposed, and the 2nd and 4th are grouped following the product rule of differentiation, we can compare the contribution of different sources to the total vegetated drag in a RandoSticks configuration, the momentum balance becomes

$$\frac{1}{\rho}\langle\overline{f_{Dx}}\rangle = -U_p^2\frac{\partial h}{\partial x} - g(\cos\beta)h\frac{\partial h}{\partial x} + g(\sin\beta)h - 2hU_p\frac{\partial}{\partial x}U_p - \frac{\partial}{\partial x}\left[h\left(\langle\overline{u'u'}\rangle + \langle\overline{u}''\overline{u}''\rangle\right)\right] \qquad \textit{Eq. 6.6-6}$$

The first 4 terms shown in the RHS of Eq. 6.6-6 were calculated from the LIF data, and the remaining one was computed from the PIV results discussed here; their trends with Re_d are

[18] From continuity, the gradients shown in Figure 6.6-1 should intersect at zero, which marks the point for uniform flow; however, given the uncertainty in water depth and velocity measurements, relative to their magnitudes, these differences are considered negligible.

presented in Figure 6.6-2. As mentioned above, all terms expressing momentum contributions due to changes in kinetic energy (1st and 4th term on the RHS of Eq. 6.6-6), and volume virtual stresses (5th term on the RHS of Eq. 6.6-6) are negligible. The constant contribution of potential energy ($\sim g\sin\beta$), with Re_d, reflects the effect of the fixed slope, which serves to put into perspective its relative effects compared to the pressure gradient ($\sim -g\partial h/\partial x$).

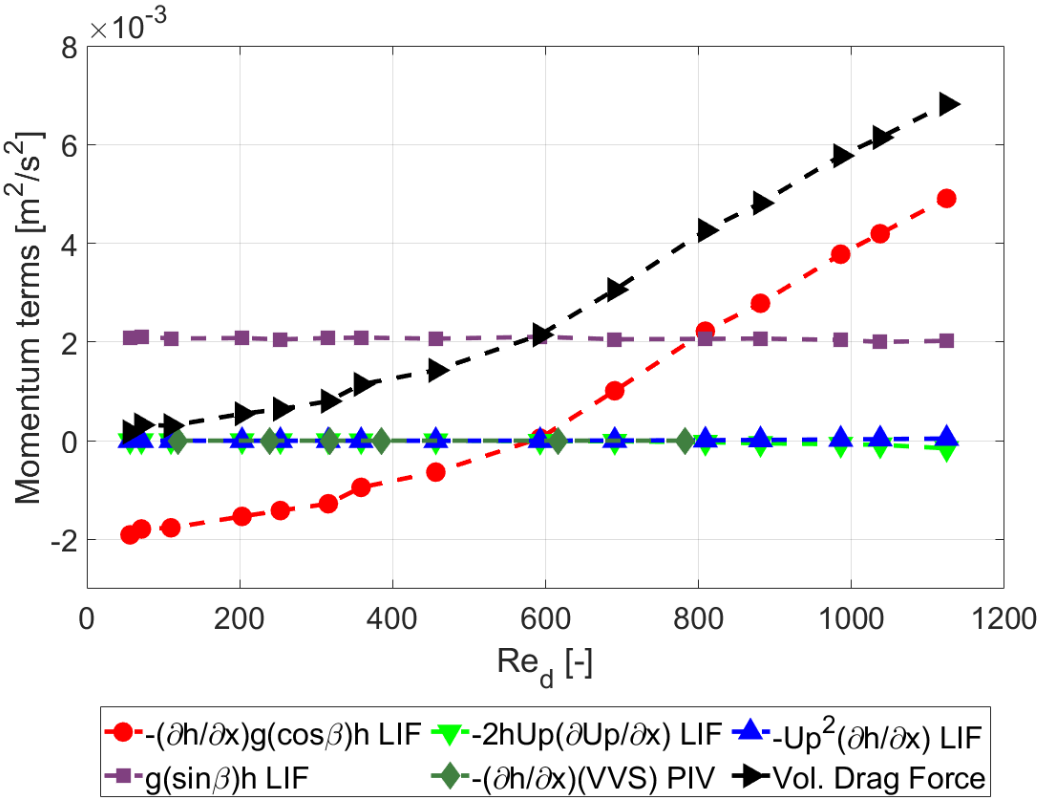

Figure 6.6-2. Comparison between terms contributing to the Streamwise momentum balance shown in Eq. 6.6-4. VVS: Volume Virtual Stresses (i.e. second term on the RHS of Eq. 6.6-4)

The momentum balance terms shown above supports the general definition of drag force given in Sonnenwald, Stovin and Guymer (2019b), for reaches with homogeneous vegetation density and constant stem distribution along the flow direction.

$$\langle\overline{f_D}\rangle_V = -\frac{\rho\epsilon}{m} g S_f \qquad \textit{Eq. 6.6-7}$$

Where S_f represents the friction slope (i.e. slope of the energy line) of the vegetated reach. Note that for 'patched' reaches or vegetated flows with non-moderate water profiles[19], the

[19] The natural criterion to determine whether a profile is moderate is the Froude number, F_R. All RandoSticks experiments were carried out in obvious subcritical conditions ($F_R < 0.1$). As the flow approaches critical conditions, kinematic energy terms, and thus changes in virtual stresses are expected

inclusion of porosity terms (Ricardo, 2014), kinetic energy and virtual stresses terms (see Eq. 6.6-4) is necessary. The drag coefficients, $C_D = 2\langle\overline{f_D}\rangle_V/(\rho d U_p^2)$, derived from the measured drag forces in the RandoSticks configuration are shown in Figure 6.6-3.

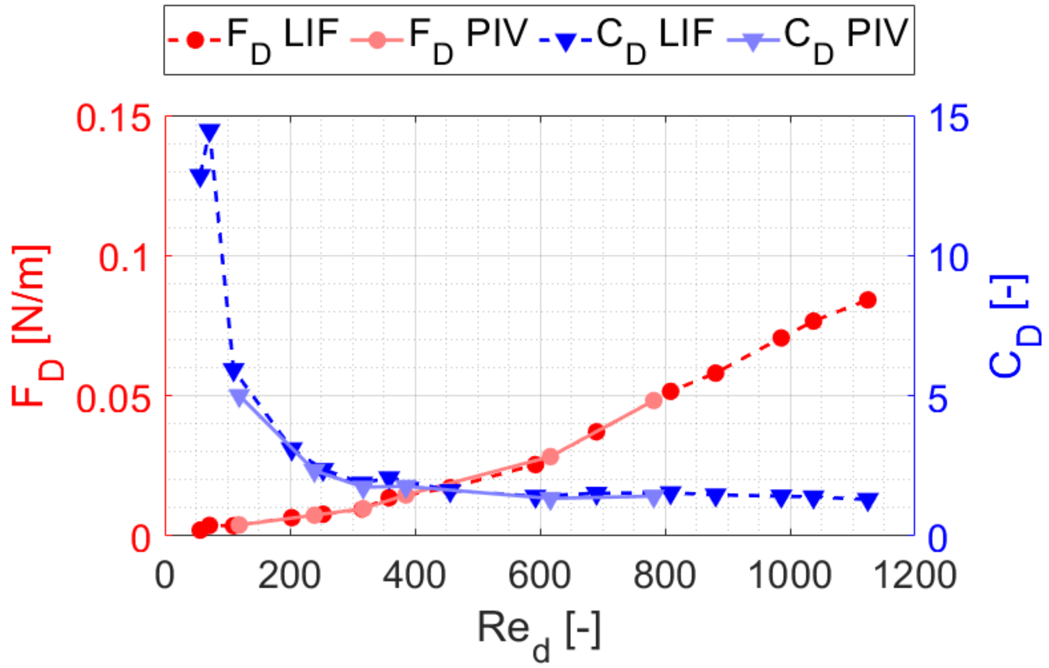

Figure 6.6-3. Variation of average drag force per unit stem length, and drag coefficient for the LIF and PIV experiments.

Before comparing the $C_D(Re_d)$ from Figure 6.6-3, with previous experimental data and models, it is necessary to describe flow resistance for the RandoSticks configuration specifically. A tentative suggestion is that the threshold for drag under inviscid conditions is located in the interval $400 < Re_d < 500$. For flows below this threshold, the contribution to flow resistance from negative pressures behind circular stems, caused by vortex shedding, is considerably higher than the reference stagnation pressure at the front of the stems (Schlichting and Gersten, 2017, chap. 1). Similarly, viscous effects are expected to be the dominant drivers of drag for Re_d before the onset of vortex shedding. As advection increases, viscosity effects rapidly become irrelevant.

The peak in the C_D curve could reflect the transition from stable mass transfer from oscillating recirculation zone to actual vortex shedding leading to negative pressure behind stems. This seems to be justified by the fact that the peak is located around $Re_d \approx 70$, which has been found to be the start point of periodic vortex shedding (Gerrard, 1978). The existence of this peak, currently a hypothesis, is subject to the possibility of vortex streets developing. In other

to be consequential. A subtle increase in this term, to support this assumption, can be seen in **Error! Reference source not found.** for the highest Re_d values.

words, pressure drag from shedding is dominant below the inviscid threshold, as long as stem densities are sparse enough for the vortex streets to develop. At higher stem densities, which involves larger surface areas for that specific range of Reynolds numbers, the proportion of viscous drag will be larger than shedding-related pressure drag, thus overshadowing the peak measured in Figure 6.6-3. This seems to be the case for drag in cylinder arrays at higher φ values than the RandoSticks configuration, as shown in Figure 6.6-4. Further experimental work at similar densities is required to support this hypothesis.

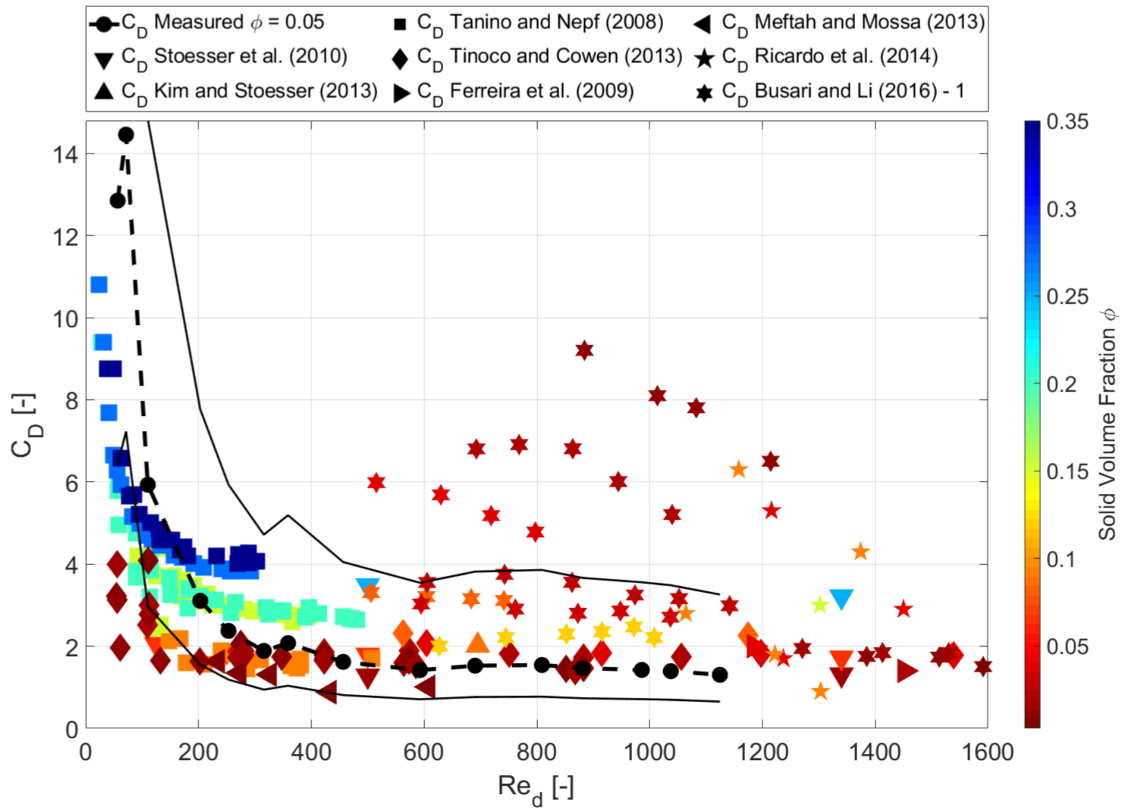

Figure 6.6-4. Comparison between vegetated drag coefficient obtained using the RandoSticks configuration (for both LIF and PIV measurements). Comparison with previous experimental results in vegetated reaches using equivalent cylindrical elements to represent stems. Solid black lines represent the deviation in the C_D values caused by using the extreme stem diameters as the characteristic length scales (i.e. 4mm and 20mm).

Figure 6.6-4 shows that all data taken from different experiments, but with similar solid volume fractions, tend to follow the same trends, with little uncertainty when the mean diameter is used to calculate C_D. The noticeable deviation from the main trend that some data points show, can be experimentally justified. The cylinder array used in Ricardo, Martinho, *et al.* (2014) was placed on top of a gravel-sand bed, and some of the tests included reaches with non-uniform cylinder distributions (thus non-constant φ). These additional sources of flow resistance are expected to contribute to the total drag measured. For the case of Busari and Li (2016), the experiments involved regular arrays of rectangular cylinders, which present higher drag coefficients (White, 1991). Drag coefficients obtained from numerical simulations in random (Koch and Ladd, 1997) and staggered (Stoesser, Kim and Diplas, 2010) arrays, for similar volume fractions, agree well with the RandoSticks data. Experimental regular (Ben Meftah and Mossa, 2013) and staggered (Kim and Stoesser, 2011) arryas show little difference with the random ones for low φ values; however, discrepancies with random configurations are expected to occur for increasing stem densities, as the effects of sheltering will change the behaviour of the pressure gradients (Nepf, 1999).

When the RandoSticks data is compared to results with equivalent φ values, a good agreement is found, particularly for inviscid conditions ($Re_d > 500$). Note that the mean diameter was used for the calculation of the drag coefficient, if other values from the stem-diameter distribution (see Figure 6.1-1, Chapter 4) are used, a 50% reduction to a 150% increase in the error bars for the RandoSticks C_D values are obtained. The implications of selecting different characteristic stem scales, require a detailed analysis, including physical justifications, that is considered outside of the scope of the present work. For the time being, a good physically-justified representative stem scale is obtained as the diameter necessary to make the solid volume fraction equivalent to the stem number density, m, given that $\langle \overline{f_D} \rangle_V$ is obtained by normalising the net cylinder drag by the number of stems per unit area. If this diameter is used for the RandoSticks configuration, a 10% reduction in the experimental values shown in Figure 6.6-4 is obtained, which does not show a considerable difference to the values originally presented.

The original attempt at characterising drag was done by Ergun (1952), who related $\langle \overline{f_D} \rangle_V$, normalised by μU_p, where μ is the fluid dynamic viscosity, to the pressure drop along arrays of staggered cylinders. Further works by Koch and Ladd (1997) and Tanino and Nepf (2008a) noticed that this pressure drop follows a trend with Re_d in which cylinder drag is the result of the additive effects of viscous and inertial contributions. The latter represents the asymptotic drag for the inviscid regime, and the former is dominant for low Re_d. Based on these considerations Tanino and Nepf (2008a) found the following formulation for the drag coefficient

$$C_D = 2\left(\frac{\alpha_0}{Re_d} + \alpha_1\right) \qquad \textit{Eq. 6.6-8}$$

For most of the information presented in Figure 6.6-4, experimental estimations of α_0 and α_1 have been presented. The compiled results are presented in Sonnenwald, Stovin and Guymer

(2019b). There, it is shown that the viscous term (α_0) shows no correlation with stem density, whilst a linear relationship with stem diameter seems to exist. For the inertia term (α_1), proportionality is found with both φ and d. When comparing estimations of Eq. 6.6-8 from the RandoSticks configuration, to the ones from the literature, it is necessary to consider the caveat that previous experiments limit cylinder arrays to uniform diameters. The proportionalities described in Sonnenwald, Stovin and Guymer (2019b) between viscous and inertial terms, and morphological descriptors of the array require some considerations for the case of the RandoSticks. The representative diameter used here is the mean of a distribution that spans diameters 40% smaller and 100% bigger, so, the dependency of α_0 with d would suggest that larger diameters will involve higher drag coefficient values, therefore the $C_D(Re_d)$ curve will be steeper for low Re_d values. Regarding inertia, the double dependency of α_1 with φ and d, would also suggest an increase relative to uniform arrays with equivalent descriptors, and although this is true, the magnitude of α_1 would also make this increase negligible. When the best-fit curve, based on Eq. 6.6-8 and the experimental results for the RandoSticks configurations, is compared to the coefficients from previous experiments—interpolated to match the RandoSticks features; as shown in Figure 6.6-5 it is possible to see that these considerations hold true.

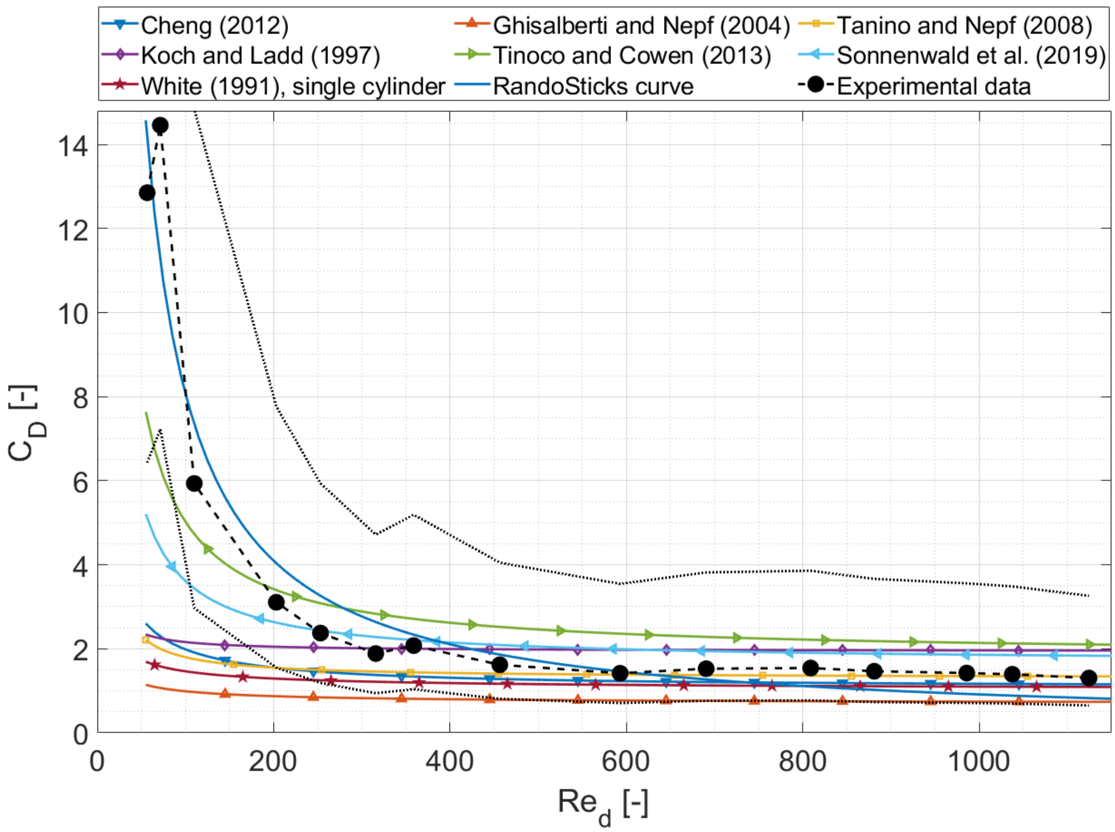

Figure 6.6-5. Comparison between Ergun (1952)*-based curves for the characteristics of the RandoSticks configuration. Dotted lines (:) represent the uncertainty in experimental C_D if the minimum (4 mm) and maximum (20 mm) diameters in the RandoSticks configuration is used as representative length scale.*

6.7. Conclusions

A detailed spatial characterisation of the hydrodynamics in a RandoSticks configuration has been provided. Starting from a global statistical analysis of the experimental flow fields, the general descriptors of the velocity probability distributions revealed some information about the general behaviour of vegetated velocity fields. Skewness was found to reveal the influence of boundary layers in the distribution of longitudinal velocities, and the increasing importance of differential advection on dispersion. The spread of the velocity distributions is comparable to advection for $Re_d < 200$, showing the importance of velocity heterogeneities and turbulence production on mass transport. For larger Re_d the magnitude of advection, U_p, increases more rapidly than the spread of the velocity distributions, thus making dispersion more advective.

Further analysis using contour maps, showing the distribution of several hydrodynamic quantities, revealed some noteworthy phenomena in and around stems. Turbulence is produced near the stems, where the peaks of turbulent kinetic energy are found, which is in agreement with the increase in vorticity magnitudes with Reynolds number. Further, the behaviour of double-averaged quantities, particularly Reynolds stresses, showed that certain key aspects of turbulent flows, such as isotropy, can be concluded only in a double-averaged sense. Dispersive fluxes are a strong indicator of velocity heterogeneities, especially for longitudinal velocities. Shear Reynolds stresses, although dimensionally negligible, can be used to study the behaviour of interacting secondary wakes. The main conclusions of this chapter can be summarised as follows.

- The presence of trapping zones even at high Re_d indicates that skewness should be used to parameterise the global distribution of velocities in velocity fields.

- Not all quantities follow the same proportionality trend with respect to Reynolds number. Second order turbulent quantities have a sharp transition at $Re_d \approx 500$, whereas first-order deviations follow a smooth increasing curve with Re_d.

- Relevant turbulence length scales grow proportionally to advection and can be considered isotropic only in a double-averaging context. Isotropy cannot be assumed locally.

- Dispersive quantities, associated with differential advection play a more important role than turbulence.

- Virtual stresses are for the most part negligible, except for normal streamwise components. Shear Reynolds stresses, although non-important on the context of the DANS eq. and drag calculations, still play an important role in determining transfer rates of momentum at the local level and are shown to be a good indicator for the existance and evolution of stem wakes.

- Previous drag models, derived for homogeneous cylinder arrays also apply for the RandoSticks configuration. Drag forces and coefficients follow the same overall trends as those found for previous studies under similar conditions. When comparing the individual contributions from viscous and inertial effects, it was seen that the diameter distribution changes the behaviour of the C_D curve for low Reynolds numbers. It is possible that the $C_D(Re_d)$ model derived based on Ergun (1952), might not be applicable for RandoSticks-type distributions at certain regimes.

Chapter 7. INTRODUCTION OF VEGETATED HYDRODYNAMICS INTO SOLUTE TRANSPORT FOR A RANDOSTICKS CONFIGURATION

Abstract

This chapter connects the dispersion coefficients measured in Chapter 4, to the velocity scales and trends identified in Chapter 6. As a further exploration of the effect of the RandoSticks morphology on the flow, a statistical characterisation of the velocity field is provided via time- and space-dependent autocorrelation functions. Spectral analysis from these functions reveals the existence of a broader range of scales, associated with both the turbulent and mean flow field. The behaviour of these scales, as well as the correlation functions, suggests that artificial cylinder arrays, at least those that include diameter distributions, do not behave as superimposed elements. Conversely, a significant level of interactions occurs, from synchronisation to clustering. A final comparison of dispersion and hydrodynamic scales shows that turbulent fluxes are dominant in the periodic vortex shedding regime, including the oscillation of recirculation areas, $40 < Re_d < 100$. Above this range, constant dispersive fluxes are dominant in both directions, as these seemingly approach inviscid conditions. Transverse dispersion is seen to be influenced by turbulent fluxes over a very narrow Re_d range, and its dependence remains largely on vegetation density. Finally, this analysis shows that in each of these regimes, singular hydrodynamic scales govern dispersion, which hints at the possibility of D_x^* and D_y^* being a linear combination of the hydrodynamic quantities presented here. If this is true, the challenge of determining dispersion coefficients in vegetation flows, will be equivalent to finding empirical/analytical expression for $\langle \overline{u'u'} \rangle$ and $\langle \overline{u}''\overline{u}'' \rangle$.

Summary of the Main elements of this chapter

- *Single-point (time-dependent) correlation functions from a sample of points over the array, to study shedding parameters and time-dependent length scales. The distance between these points and their reference cylinders is chosen to be close to the end of the recirculation zone (Gerrard, 1978).*

- *Spatial correlations over sections from instantaneous velocity series, as obtained in Ricardo (2014), to study the existence of persistent features, and relevant spatial length scales. The time-average is seen to obscure/hide smaller scales of motion.*
- *Probabilistic distribution of length scales from the time- and space-dependent velocity statistics were obtained. These indicate the influence of RandoSticks morphology on the characteristic structures of the flow. Time-dependent and mean flow-related features (i.e. length scales) are revealed, by this analysis, to be wider than morphological RandoSticks descriptors.*
- *A comparison of normalised dispersion coefficients with relevant hydrodynamic scales identified the Re_d ranges where each different component (i.e. physical driver) was dominant.*

7.1. Introduction

Using the information presented in Chapter 4 and Chapter 6, a series of proportionality relationships between velocity and dispersion measurements has been developed. From this, it is possible to: 1) evaluate the impact of each hydrodynamic quantity on large scale mixing, and 2) isolate the main components contributing to dispersion. Consequently, representative analytical and empirical mixing models for real-life applications can be derived.

The relationship between solute transport and vegetated hydrodynamics is evaluated alongside their variation with Reynolds number, as the primary independent parameter. Physical constraints only allowed one iteration of the RandoSticks configuration, so no variation in terms of solid volume fraction was studied. For reproducibility, dispersion coefficients are non-dimensionalised using advection, U_p, and mean stem diameter, d, as characteristic velocity and length scales, respectively. Hydrodynamic quantities are normalised using the mean velocity U. Note that the selection of these characteristic scales, at least for vegetated hydrodynamics, depends on the main structures of the flow—by 'main' it is meant the flow structures containing most of the turbulent kinetic energy.

Vegetated flows contain a rich variety of structures, which is a product of the wide variability in stem diameter and inter-stem spacing—and, as will be seen later, also of stem clustering and sheltering. Thus, finding characteristic length scales, as it pertains to the flow and not the vegetation morphology, requires a detailed statistical characterisation of the velocity recordings measured.

The concept of a statistical characterisation of velocity was presented by Taylor (1922), as a framework to obtain turbulent diffusion by treating velocities as stochastic quantities. Diffusion, defined as the change of spread, with time, of a set of particles moving in a turbulent flow, was found to be the product of representative velocity and length scales. Physically, the latter represents the distance after which a particle is statistically independent from its initial condition[20], i.e. the distance/time after which its (turbulent) velocity autocorrelation function approaches zero.

Taylor's theory of diffusion is based on velocity statistics in a Lagrangian frame of reference, and direct analogy with Eulerian quantities is almost solely achievable in theoretical conditions (Lumley, 1962). Probabilistic approximations require detailed knowledge of the locations of a statistically significant ensemble of particles, over the correlation domain in a Eulerian frame of reference (Philip, 1967).

For the case of the RandoSticks configuration, neither the velocity frame of reference, nor the extent of the measurement window, are appropriate to compute Lagrangian correlation and diffusion functions. However, Eulerian single- and multi-point velocity statistics, from the PIV measurements (see Chapter 6), can still be used to estimate the temporal and spatial extent of the main coherent structures of the flow. Consequently, proxy velocity and length scales can be computed and used to compare with the dispersion coefficients obtained from the LIF experiments (see Chapter 4). A discussion of these characteristic proxy scales will be given in this chapter before concluding with the relationship between dispersion and hydrodynamic scales.

Section 7.2 presents the methodology employed to select and describe time- and space-dependent velocity statistics from a sample of reference points and transects over the PIV field of view. From these results, characteristic frequencies and length scales are obtained, which are presented in Section 7.3, and compared with the distribution of morphological scales of the RandoSticks configuration, namely diameters and inter-stem spacing. Finally, Section 7.4

[20] It should be noted that, although similar, the ideas of a diffusion length scale and mixing length are fundamentally different. The former, as was said, was proposed by Taylor as a way to describe the distance/time after which a particle moving in turbulent motion losses statistical connection with its initial conditions. Physically this diffusion scale is proportional to the size of the average eddy and as such is a feature of the turbulent motion itself, irrespective of the particle. The mixing length, proposed by Prandtl, is a conceptualisation of the same principle, but expressing the distance/time over which a particle with certain initial conditions absorbs those of the surrounding medium. Note that the latter necessarily involves molecular characteristics of the particle (e.g. heat conductivity) and is not representative of the turbulent motion (Taylor, 1935).

relates these length scales to the characteristic velocity values found in Chapter 6, and to the mixing coefficients presented in Chapter 4.

7.2. Statistical Characterisation of Velocity

Briefly, the statistical concept of a length scale alluded to earlier, comes from Taylor's statistical analysis of turbulence in a Lagrangian frame of reference. The turbulent diffusion coefficient can be expressed as the product of a characteristic velocity, v_i^+ (root-mean-square of the turbulent component of a velocity series[21]) and length, Λ_i, scale. This length scale defines the time/distance after which a Lagrangian particle losses correlation with its initial condition. This correlation coefficient is computed between the turbulent velocity history of the particle, $v_i'(t)$, and shifted versions of itself, $v_i'(t-\tau)$, over the diffusing interval $\tau \in (0,t)$, as shown in Eq. 7.2-1 (Taylor, 1935)

$$\mathcal{R}_i(t,t-\tau) = \frac{\overline{v_i'(t)v_i'(t-\tau)}}{v_i^+(t)\, v_i^+(t-\tau)} \quad \Rightarrow \quad \mathcal{R}_i(\tau) = \frac{\overline{v_i'(t)v_i'(t-\tau)}}{\overline{v'^2}} \qquad \textit{Eq. 7.2-1}$$

Where $\mathcal{R}_i(t,t-\tau)$ is the Lagrangian correlation coefficient, in the i-th direction, expressed for the general case in which the velocity statistics of the particle change along its path. The simplified version shown on the RHS of Eq. 7.2-1 represents mean and turbulence characteristics independent of time, i.e. steady and homogeneous. It is known that $\mathcal{R}_i(0) = 1$, and, $-1 < \mathcal{R}_i(\tau) < 1$, for all other values of τ. Further, $\mathcal{R}_i(\tau)$ will continuously decrease until $\mathcal{R}_i(\tau) = 0$ as $\tau \to \pm\infty$. The rate at which the correlation function approaches this asymptotic value is determined by the average size of the turbulent eddies or, as will be seen later, of organised flow structures such as vortices. Given that the contribution of $\mathcal{R}_i(\tau)$ is negligible above the size of this average eddy, the characteristic scale, Λ, is obtained by integrating $\mathcal{R}_i(\tau)$ over the diffusing domain. Connecting this to the Theory of Diffusion alluded to above, Eq. 7.2-2, shows the progression between the statistical functions and the product of velocity and length scales.

$$D_t = v_i^+(t) \int_0^t v_i^+(t-\tau)\mathcal{R}_i(t,t-\tau)\, d\tau \Rightarrow v_i^+ \left(v_i^+ \int_0^t \mathcal{R}_i(\tau) d\tau \right) \Rightarrow v_i^+ \Lambda_i \qquad \textit{Eq. 7.2-2}$$

---

[21] The superscript + is used as a shorthand for $a^+ \equiv \sqrt{\overline{(a-\overline{a})^2}}$. So, in terms of velocities, this quantity will represent standard deviations, and will be the same for the velocity value, u, and its turbulent component, u'. See the List of Symbols for reference.

The mixing length analogy $\upsilon_i^+\Lambda_i$ requires the condition $t \rightarrow \infty$. Contrary to the highly theoretical flow fields from which these expressions were derived, vegetated flows are governed by the existence of vortices, which are examples of 'coherent structures'. These are defined as persistent flow masses with phase-correlated properties (e.g. vorticity, lateral velocities), that are the main carriers of turbulent kinetic energy (Hussain, 1983). These structures will manifest themselves on the velocity statistics of vegetated flows. Therefore, a different treatment is needed to reveal these scales from the correlation functions presented below.

Obtaining $\mathcal{R}_i(\tau)$, and hence estimates of υ_i^+ and Λ_i, from experiments is currently unfeasible, as measuring Lagrangian velocities over the dispersion domains (e.g. the one presented in Chapter 4) is prohibitively complex. Instead, approximations have been proposed from time- and space dependent velocity series, from Eulerian measurements, like the ones described in this work (see Chapters 3.2 and Chapter 6).

Three main types of velocity statistics, in a Eulerian frame of reference have been considered in the literature. First, statistics of time-dependent velocity series, from single points in a flow field. From these, length scales can be derived by adopting Taylor's 'frozen turbulence' hypothesis. Studies of this kind are commonplace in experimental hydrodynamics, and are achievable by inexpensive point-based instruments, e.g. ADV, LDA. The second type is used to reveal 'persistent spatial features' from time averages of correlations defined over spatial sections of the flow. This methodology was proposed by Ricardo (2014, chap. 7), and was used as a method to estimate the spatial extent of coherent structures. The third type of velocity statistics are multipoint correlations (cf. two-point statistics), as presented in Raupach, Antonia and Rajagopalan (1991), which are more appropriate for the study of the spatial evolution and decay of flow structures.

The study of multipoint correlations is expansive and including it here negates the potential for a detailed characterisation of turbulent motion, beyond just the quantification of length scales. This statistical framework allows for the study of structure functions, and coherence modes. These analyses warrant an independent study from a purely turbulence perspective, which is beyond solute transport, thus, these will be the subject of further work.

It was found that the first two correlation types provide lower and upper limits for the characterisation of RandoSticks length scales. In Chapter 3.2, multi-point correlations show the effect of dissipation and thus larger estimations of characteristic periods, than those from single-point, second-order statistics. However, as will be seen below, second-order statistics provide smaller estimations of the scale of 'persistent spatial features'. This data has shown some issues (see TKE plots from Chapter 6) which implies that an appropriate and more thorough post-processing is needed to derive conclusions regarding intermediate and small-scale turbulence.

Given the variety of stem sizes and spacing, in order to obtain reasonable estimates of length scales, a representative number of measurements, spanning different diameters, were required. In total, 32 reference cylinders were chosen, and the diameter breakdown was designed to follow the distribution shown in Chapter 4, Figure 4.2-1b. As it is known that vortices fully develop 2 diameters downstream from the cylinder back (Gerrard, 1978), reference points for the measurement of time-dependent statistics were selected for each cylinder, following this criterion. For the spatial correlations, transverse (y) and streamwise (x) sections, relative to the reference points mentioned above, were selected. Figure 7.2-1 shows the cylinders in the measurement area, relative to the PIV measurements. Streamwise sections were chosen along the wake of the reference cylinders, and are represented as light-red vertical lines; within this sections, points marked in dark red show the reference points chosen for time-dependent statistics. Transverse sections are shown as horizontal light-red lines, and were selected as the longest transects for the same x-coordinate of the reference point.

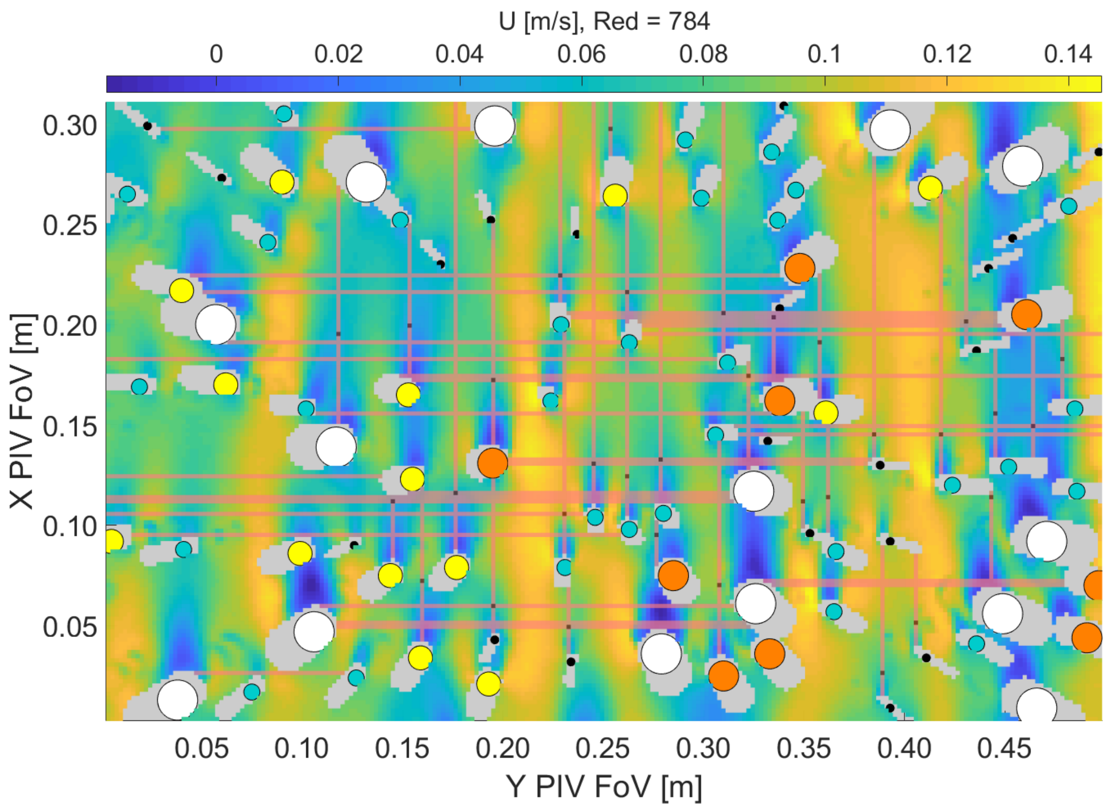

Figure 7.2-1. Sample Mean Velocity Maps in the PIV Field of View (FoV) showing: Reference cylinders and 1) Lateral and streamwise transects for space-dependent correlation functions (light red), and (2) points within these sections, 2d downstream from selected cylinders, for time-dependent correlations (dark red points).

Although seemingly random, the final selection of the reference cylinders was obtained from a balance between the length of the resulting sections, particularly transverse ones and their location. Longer transects allow a broader range of wakes, from which to obtain information. Having the reference points well distributed over the measurement area allows a characterisation of the whole flow field. The mathematical definitions of the time-dependent (dark-red points) and space-dependent (light-red lines) correlations are given in the following sub-sections.

For reference, all flow rates analysed were captured using a framerate of 130 fps. The construction of velocity maps was done via PIVlab, wherein 3 iterations with interrogation windows 120, 48 and 16, with 50% overlap were applied. The final velocity resolution was 149x239 elements, from 1200x1920 images. The measurement area for each velocity points is then 2.1 mm^2. A median filter was applied to the longitudinal and transverse sections of velocity, to avoid influence from small scale turbulence and random noise, and to highlight the periodic features of velocity.

7.2.1. Single-Point Velocity Statistics: time-dependent Autocorrelations

Experiments were conducted under steady flow conditions, for all Re_d, and the time records were defined longer than the characteristic flow scales. Consequently, velocities from each reference point (x_0, y_0), were safely measured in steady flow conditions. Eq. 7.2-3 shows the definition of the time-dependent correlation function.

$$R_{xx}(\tau; x_0, y_0) = \frac{\overline{u'(x_0, y_0, t)u'(x_0, y_0, t-\tau)}}{\overline{u'(x_0, y_0, t)^2}} \qquad \textit{Eq. 7.2-3}$$

Given the random nature of stem locations, and the criteria followed to select reference points, all values of length scales will be treated as realisations of a random process, with the same weight. Therefore, the dependency on the spatial point is dropped and the correlation functions will be considered as random values only dependent on time, i.e. $R_{yy}(\tau)$.

To illustrate the variation of scales with flow rate, and space (within the field of view), Figure 7.2-2a and b show the longitudinal and transverse, time-dependent correlation functions for the same point, over the range of Re_d tested. Given the spatial resolution of the velocity measurements, coherence features from 4 mm cylinders are usually overshadowed by vortices from larger cylinders. Relevant scales from these cylinders were therefore largely excluded. This will be explored further in Section 7.3.

Clearly, transverse velocity series, v (Figure 7.2-2b) better illustrates the fluctuations from coherent structures than u (cf. Figure 7.2-2a). Figure 7.2-2c and d, show the changes in time-dependent correlation functions, for different points in the flow field, and the same value Re_d. The legend shows the diameter breakdown of the correlation function shown. The numbers represent the diameter of the reference cylinder in mm. Since each $R_{xx}(\tau)$ is intended to represent a random function, the nomenclature is added to indicate that each cylinder analysed was unique, but the actual location should bear no relevance on the random process described.

Note that the correlation functions shown in Figure 7.2-2 and Eq. 7.2-1 are distinct from each other, and so is the statistical treatment needed to obtain relevant information. The derivation of length scales from the latter is obtained as the integration over the time domain. However, the same cannot be applied to the functions $R_{xx}(\tau)$ and $R_{yy}(\tau)$ shown above, as the persistence features remain somewhat constant with time. Further, depending on the length of the recording, the integration can yield zero or a negative value.

An alternative way to compute the characteristic length scale from the correlation functions shown in Figure 7.2-2, is to use the characteristic period, i.e. the interval between the first two consecutive positive peaks. This is not new, in fact, the reciprocal of this characteristic period is the shedding frequency, f_s, which has been previously measured experimentally. This frequency represents the main periodic patterns existing in the time-dependent velocity series, caused by coherent motions. Previous experiments have computed this value directly from the velocity measurements, by counting phase-similar patterns over an interval (Kiya, Tamura and Arie, 1980); matching Lissajous ellipses in an oscilloscope (Kovasznay, 1949; Roshko, 1954) or performing spectral analyses, using FFT, on the velocity series (Abroug *et al.*, 2022). Here, the the Energy Spectra of the correlation function is used. From Parseval's theorem (Pope, 2000), a normalisation of the spectra is obtained. Further, the shedding frequency, f_s, is found as the single characteristic frequency containing the maximum of the turbulent kinetic energy. The normalised energy spectrum, for each velocity component, is defined in Eq. 7.2-4

$$R_x(\tau) = \int_{-\infty}^{\infty} e^{i2\pi f\tau}\,\tilde{E}_x(f)df \quad , \quad \tilde{E}_x(f) = \int_{-\infty}^{\infty} e^{-i2\pi f\tau}\,R_x(\tau)d\tau \qquad \textit{Eq. 7.2-4}$$

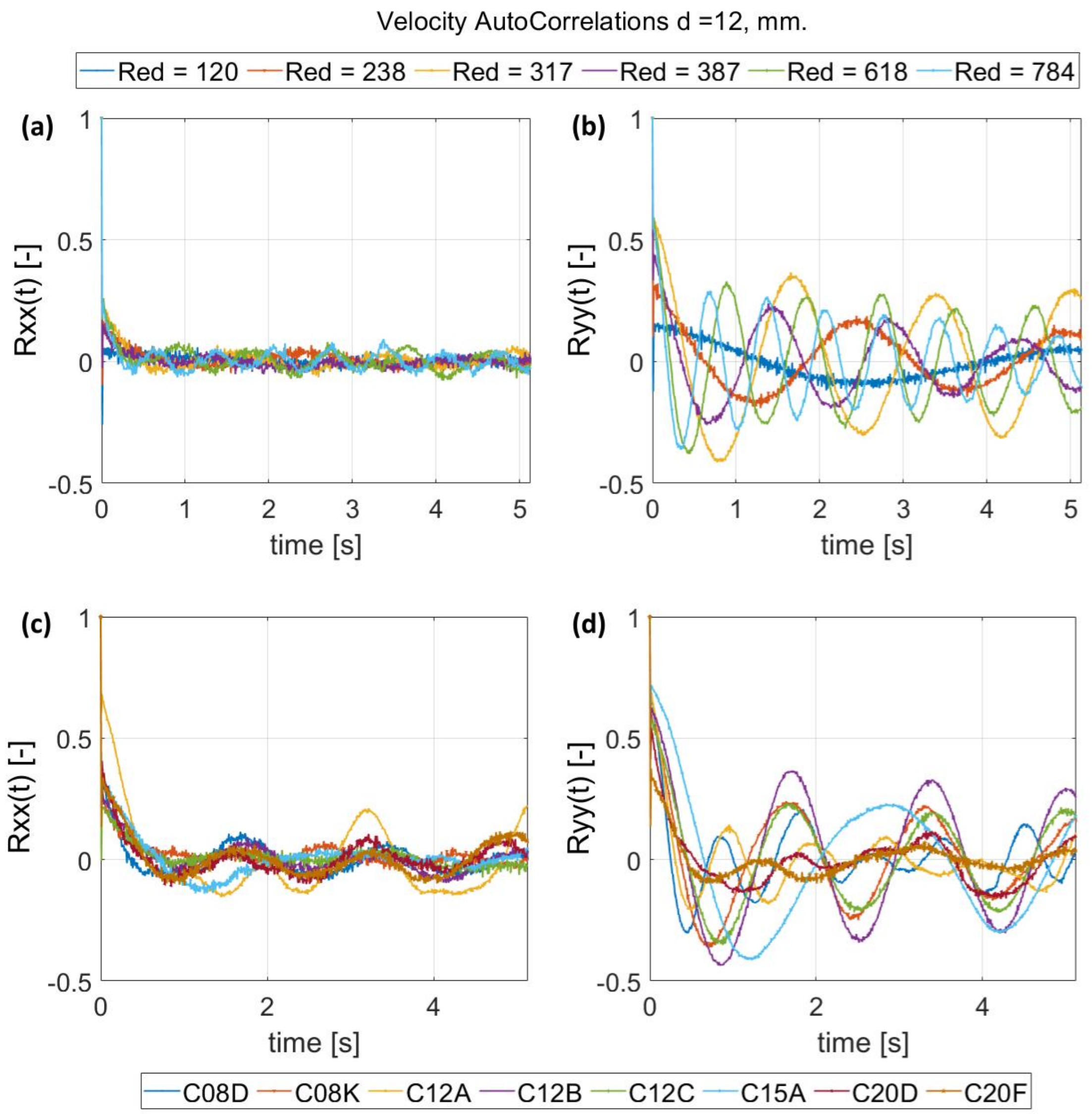

Figure 7.2-2. Single-Point, Time-Dependent Functions. Upper: a) Streamwise and b) Transverse velocity Autocorrelations from a single point, within the wake of a 12 mm cylinder, over the range of Red values measured. Lower: c) Streamwise and d) Transverse velocity Autocorrelations for points relative to a random sample of cylinders, Re_d = 317. The number in the labels for plots b and c represent each diameter in mm.

From the definitions in Eq. 7.2-4, some properties are useful to remember. A direct relationship between real-domain and symmetry exists between correlations and their spectra. That is, symmetry in one implies the other one is real, and vice versa. The spectrum, $\tilde{E}$ is normalised and positive for all f, because $R_{xx}(0) = 1$, and this is its maximum (Tennekes and Lumley, 1972).

Some principles must be applied when the spectrum is calculated in a discrete domain (i.e. from finite, digital recordings). The Fourier Transform pair shown in Eq. 7.2-4 is better represented as the one-sided Spectrum, $E_{xx}(f) = 2\,\tilde{E}_{xx}(f)$, with $\{f \mid f > 0\}$ for E_{xx} and E_{yy}. For discrete records, unambiguous, one-sided spectra are defined in the domain $\{f \mid 0 \leq f < f_{\text{Nyquist}}\}$. It was found that normality in E is better preserved if a two-sided correlation function is computed.

Using these definitions, the spectra from the correlations shown in Figure 7.2-2 are computed, and presented in the same order in Figure 7.2-3. The characteristic period, T, of the correlation functions shown can be computed from the shedding frequency seen in the energy spectra. This is found as the value f_s, for which $E_{yy}(f_s) = \max\left(E_{yy}(f)\right)$.

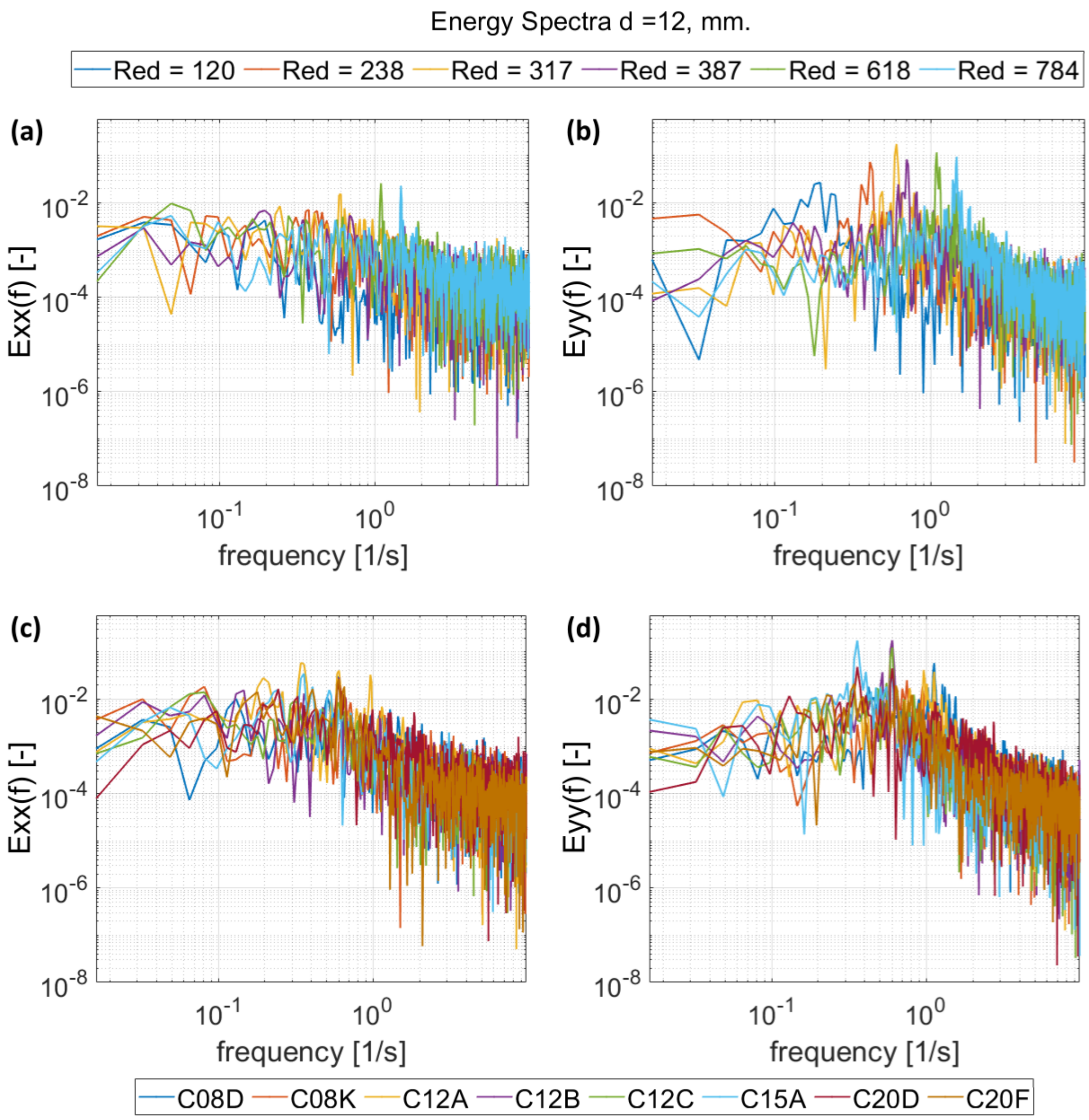

Figure 7.2-3. Energy Spectra from the Single-Point, Time-Dependent Autocorrelation Functions shown in Figure 7.2-2. Upper: a) Streamwise and b) Transverse velocity Energy Spectra from a single point, within the wake of a 12 mm cylinder, over the range of Red values measured. Lower: c) Streamwise and d) Transverse velocity Energy Spectra for points relative to a random sample of cylinders, Red = 317.

From the energy spectra shown in Figure 7.2-3b, it can be seen that the shedding frequency, i.e. the peaks of the Energy Spectra circled in Figure 7.2-3b, increases with Re_d, as expected in the range of flow rates tested (Roshko, 1954). The values represent the main frequency of the periodic component shown in Figure 7.2-2b. The spectra of the longitudinal velocity (Figure 7.2-3a) show a few distinguishable dominant frequencies, particularly for $Re_d > 400$. These are comparable to the same values measured for the Transverse Spectra.

Note that the repeated patterns, defined by f_s from transverse velocities, actually group two shed vortices, whereas those for longitudinal velocities correspond to one. This was found experimentally by Roshko (1954) and Kovasznay (1949), who noticed that a secondary frequency, $f_2 = 2f_s$, is picked up by the streamwise velocity signal, u', when it is measured along the wake centreline of a given cylinder. Particularly in the near wake. A combination of turbulence and noise seem to affect the identification of secondary frequencies from streamwise velocity series, $u'(t)$. For some values, the secondary dominant frequency from the $E_{xx}(f)$ spectra was actually measured, but the sample size was not large enough to derive statistically significant estimates.

From the spectra of all reference points, the variation of shedding frequency, f_s, with Re_d is studied and presented in Figure 7.2-4, where the estimates are shown together with the average and the linear best-fit (BF) over the Re_d range. As was mentioned before, for some velocity records the coherent component can be obscured by larger (random) turbulence amplitudes and noise, such that a dominant frequency cannot be discerned. To avoid ambiguous shedding frequency measurements, which can bias the behaviour of $f_s(Re_d)$, a criterion was imposed to only consider shedding frequencies for which the spectral component, $E_{xx}(f_s)$, represents more than 5% of the total energy density.

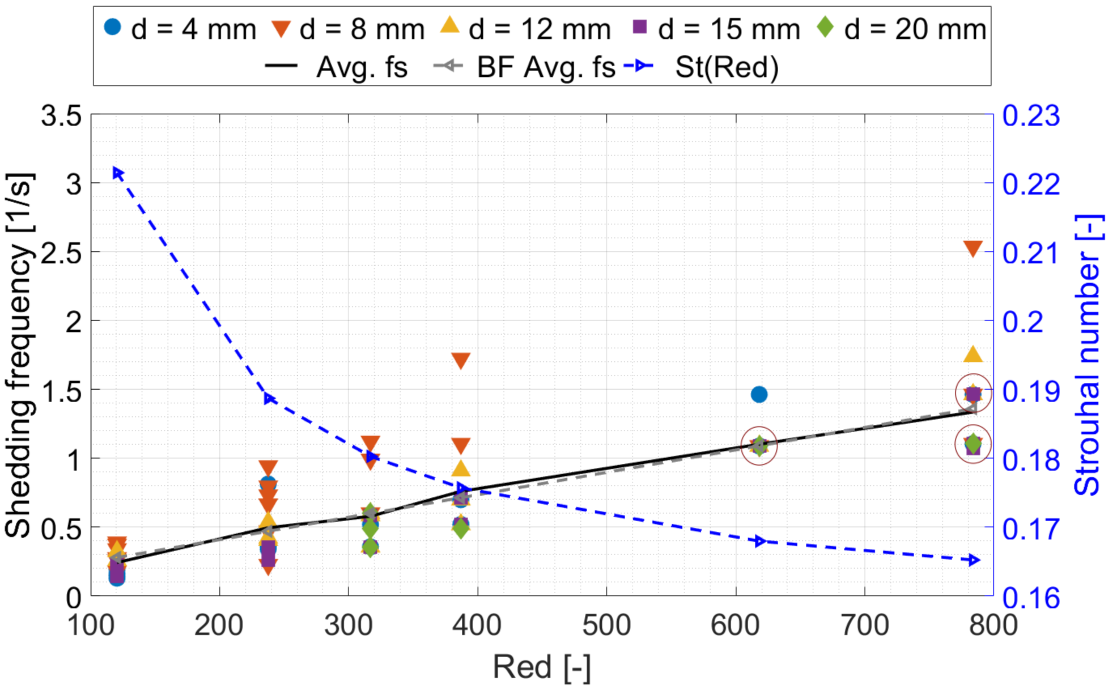

Figure 7.2-4. Variation in computed shedding frequency with respect to reference diameter and flow rate. Variation in non-dimensional frequency: Strouhal number as a function of Reynolds number.

For f_s values in the range $Re_d > 400$, the flow developed seiches, which are the lateral fluctuations of the water surface, caused by a synchronisation of the vortex shedding and the natural oscillation of the water surface. This is a self-sustaining process, which also involves a synchronisation of the shedding frequency of all cylinders in an array (Viero, Pradella and Defina, 2017). This conclusion is derived from uniform-diameter configurations, and data on this phenomenon, for stem diameter distributions is needed. Nevertheless, Figure 7.2-4 suggests that vortex shedding synchronisation occurs to a large extent in the RandoSticks configuration. The spread of f_s values for $Re_d > 400$ decreases considerably, and all frequencies seem to group around the same value in a unimodal ($Re_d \approx 617$) and bimodal ($Re_d \approx 782$) way. These 'groups' are shown circled in Figure 7.2-4. Defina and Pradella (2014) found that in order for seiches to occur, the water surface and shedding frequencies of the array must be similar (up to a tolerance of 35%). It is reasonable to expect, therefore, that water surface fluctuations do not bias the measurements of f_s. This is based on their criteria, however, more information/analysis is needed to provide a conclusive answer to this.

The average shedding frequency was computed for each flow rate, given the validity criteria established earlier. From the behaviour of the average curve for $f_s(Re_d)$, shown in black in Figure 7.2-4, it was found that a linear best-fit is the most appropriate to model its behaviour. To keep consistency with the formulation of Reynolds number, the mean cylinder diameter was used to compute the non-dimensional shedding frequency, i.e. the Strouhal number, $S_t =$

$f_s d/U_p$. Results from single cylinders and uniform cylinder arrays have shown that S_t is predominantly proportional to Re_d, for the range of flows analysed in this study, and is in the range $0.18 < S_t < 0.22$. The values shown in Figure 7.2-4 are within that range, but a clear inverse proportionality with Re_d is found. A possible reason is the appearance of a lock-in regime, in which the shedding frequencies of all cylinders synchronise, which also explains why the spread of estimates of f_s is much smaller for $Re_d > 400$.

The characteristic period of the main coherent structures—i.e. the main periodic feature of the correlations in Figure 7.2-2—is found as the reciprocal of the shedding frequency: $\mathrm{T} = 1/f_s$. The term T represents the time it takes for the same spatial features, of the relevant structure, to be recorded in the measurement point. In other words, it is the time it takes vortices to travel across a specific point. From Taylor's frozen cloud turbulence hypothesis (Taylor, 1938), meaning that no significant decay occurs during the interval T, the size of the passing vortex is defined by $\Lambda_t = U_p \mathrm{T}$.

7.2.2. Multi-Point Velocity Statistics: Spatial Autocorrelations

A direct calculation of spatial flow scales from time records of velocity requires the flow to satisfy Taylor's criteria, namely, stationarity, homogeneity and isotropy (and ergodicity). These conditions are not met in the RandoSticks experiments and vegetated flows in general. As a consequence, length scales found from the characteristic period, T, are dependent on the location of the measurement point, along the wake of the reference cylinder. Differences in estimations of T, for different measurement points, are caused by shear-related energy dissipation and vorticity diffusion. The use of $2d$ as a measurement distance, behind the reference cylinders comes from previous estimations of the location of the 'shedding' point. Namely, the distance after which the recirculation area behind a single cylinder has fully 'rolled up' and detaches as shed vortices (Gerrard, 1978). The measured signals will then have strong coherent components as the flow structures have not undergone substantial dissipation. Regarding length scale estimations (see Section 7.3), these should be read as reference values.

A more direct estimation of spatial flow scales from persistent flow features can be obtained from a direct spatial analysis of velocity statistics. To achieve this, the same methodology presented in Ricardo (2014, chap. 7) will be followed to find the spatial features from the RandoSticks experiments. To apply this methodology, instantaneous, spatial fluctuations of velocities are needed to define the spatial autocorrelations over the longitudinal and transverse sections defined in Figure 7.2-1. From the double-averaged, Reynolds decomposition, it is known that instantaneous velocities, $u(x,y,t)$ and $v(x,y,t)$, can be represented as the addition of the following quantities

$$u = \langle\overline{u}\rangle + \overline{u}'' + u' \quad , \quad u = \overline{\langle u\rangle} + \langle u\rangle' + u'' \qquad \textit{Eq. 7.2-5}$$

Where, from the convention used so far, single and double primes—u' and u''—represent deviations from time, $\overline{u}$, and space, $\langle u\rangle$, averages, respectively (see Chapter 2, Section 2.2.5). The term u'' can be understood as a series of snapshots, showing the instantaneous distribution of flow structures over the recording period. By definition, these structures are isolated from the mean velocity (i.e. advection) component. Hence, the extent to which the velocity, u'', between points (x_0, y_0) and $(x_0 + x,\ y_0 + y)$ are statistically correlated, is an indication that both points are within the same flow structure.

The final definition of the spatial autocorrelation functions is obtained as a direct analogy to the definition given in Eq. 7.2-3, but using the instantaneous spatial fluctuations, u'' and v'', over the directional spatial domains shown in Figure 7.2-1, instead of time. Further, to only capture persistent features, a time average over all instantaneous spatial autocorrelations is performed (Ricardo, 2014, chap. 7), as shown in Eq. 7.2-6 and Eq. 7.2-7.

$$\overline{R_{xx}(x; x_0, y_0)} = \overline{\left(\frac{\langle u''(x_0, y_0, t)u''(x_0 + x, y_0, t)\rangle_X}{\langle u''(x_0, y_0, t)^2\rangle_X}\right)} \qquad \textit{Eq. 7.2-6}$$

$$\overline{R_{xx}(y; x_0, y_0)} = \overline{\left(\frac{\langle u''(x_0, y_0, t)u''(x_0, y_0 + y, t)\rangle_Y}{\langle u''(x_0, y_0, t)^2\rangle_Y}\right)} \qquad \textit{Eq. 7.2-7}$$

Again, in order to generate a distribution with enough statistical significance, and given the selection criteria for the transverse and longitudinal sections (see Figure 7.2-1), the dependency on the origin point (x_0, y_0) is dropped. Consequently, each correlation function of the form $\overline{R_{xx}(x)}$ will be considered as a single realisation of a random variable, with equal probability of occurrence within the measurement area.

In the results presented in Ricardo (2014, chap. 7), the lateral sections were located within viewing gaps generated as discontinuities in the random cylinder array, to allow lateral illumination through the area of interest. Although these gaps were designed to have spacing values similar to those of the cylinders upstream, thus maintaining the geometric features of the array, these values are believed to not be representative of the real inter-stem behaviour of the structures. As a result, the measurements actually represent values from fully developed wakes, neglecting the effects of vortex breakdown and dissipation caused by shear from downstream cylinders. For the RandoSticks experiments, these problems are avoided as the PIV area is fully representative of the general array, and these physical effects are present in the measurements. The differences from the experimental set-up, as well as some consequences of this methodology are evident from the results, as will be seen below.

Following the same criteria of Figure 7.2-2 and Figure 7.2-3, Figure 7.2-5a and b show the spatial autocorrelation of a random transverse section, over the Re_d range, and Figure 7.2-5c and d show the same functions for a sample of transverse sections, for the same Reynolds number, $Re_d = 317$. Likewise, the energy spectra of these correlation functions is shown, in the same order, for the same functions, in Figure 7.2-6. Note that the energy contributions of these persistent spatial features are defined over the lateral, γ, and streamwise, κ, wavenumber domains. In analogy with the frequency spectra defined in Eq. 7.2-4, the energy spectra over the wavenumber domains are defined as follows.

$$\tilde{E}_{xx}(\gamma) = \int_{-\infty}^{\infty} e^{-i2\pi\gamma y}\, \overline{R_{xx}(y)} dy \quad , \quad \tilde{E}_{xx}(\kappa) = \int_{-\infty}^{\infty} e^{-i2\pi\kappa x}\, \overline{R_{xx}(x)} dx \qquad \textit{Eq. 7.2-8}$$

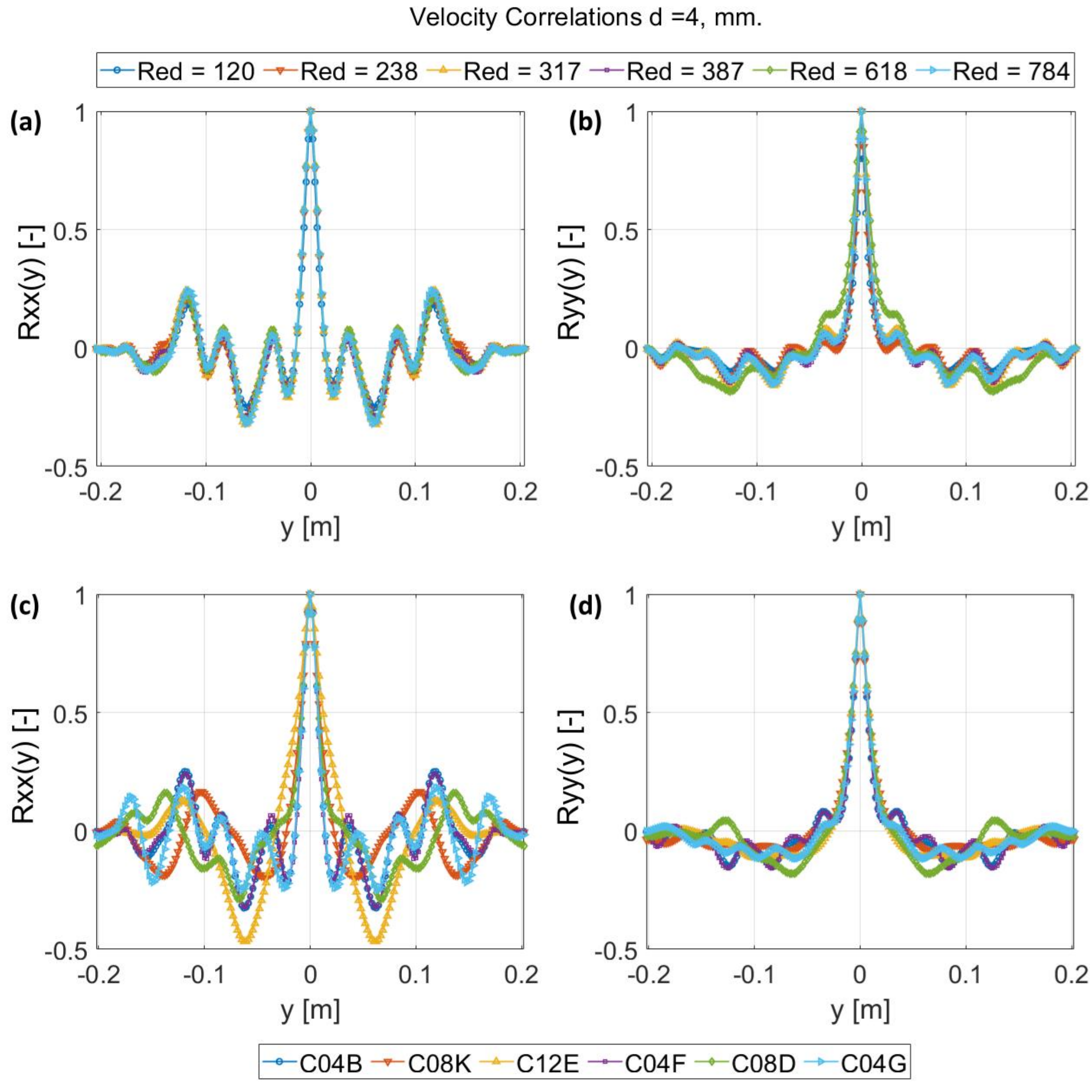

Figure 7.2-5. Multi-Point, Time-averaged and Space-dependent functions along transverse sections. Upper: a) Streamwise and b) Transverse velocity autocorrelations from a single transverse section, (within the wake of a 4 mm cylinder) over the range of Re_d values measured. Lower: c) Streamwise and d) Transverse velocity autocorrelations for a random sample of transverse sections, Re_d = 317.

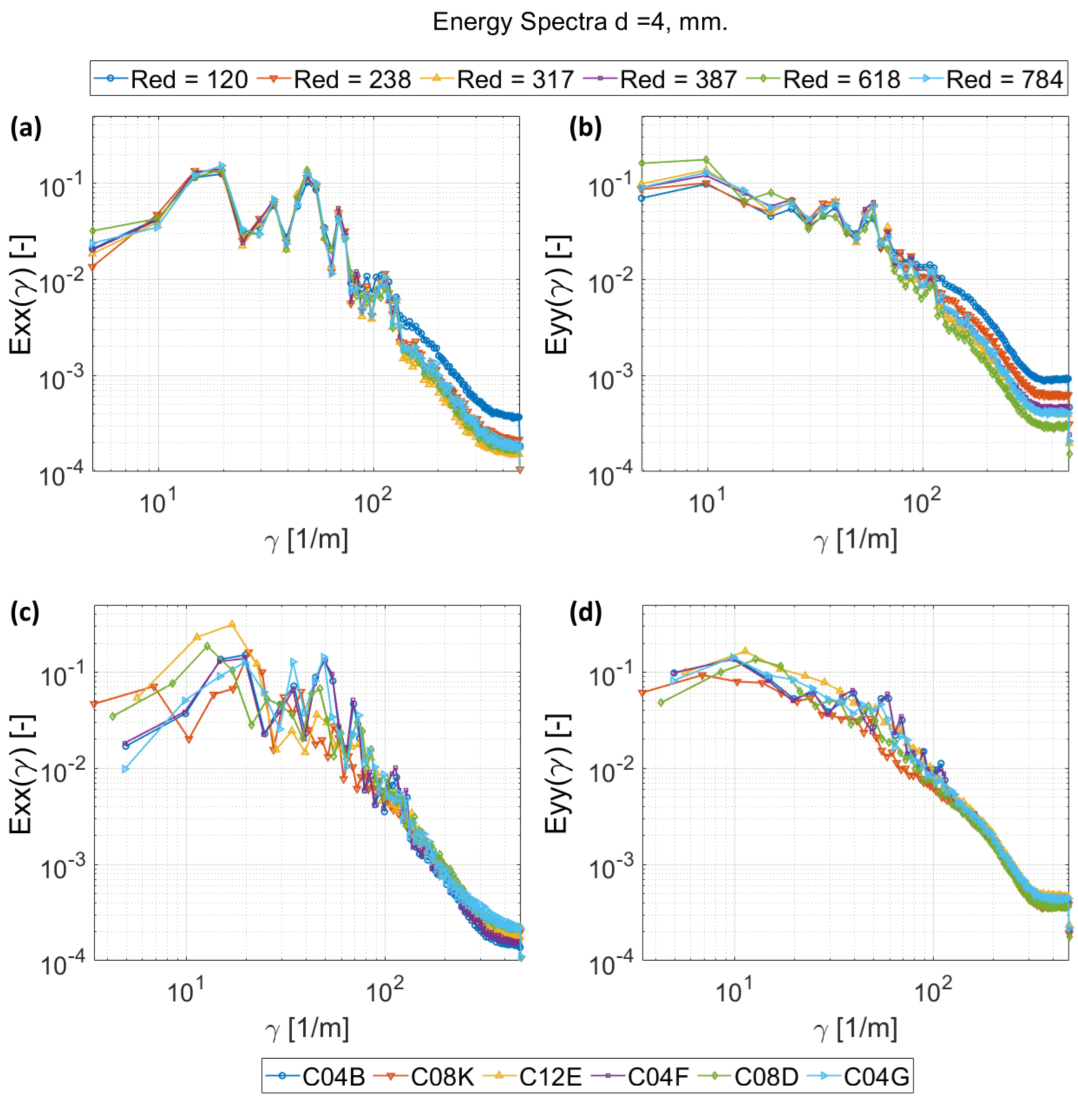

Figure 7.2-6. Energy Spectra from transverse Sections shown in Figure 7.2-5. Upper: a) Streamwise and b) Transverse velocity Energy Spectra from a single transverse section, (within the wake of a 4 mm cylinder) over the range of Red values measured. Lower: c) Streamwise and d) Transverse velocity Energy Spectra for a random sample of transverse sections, Re_d = 317.

From Figure 7.2-5 and Figure 7.2-6, some relevant conclusions can be drawn. A better identification of periodicity is achievable from the streamwise velocity autocorrelations, $\overline{R_{xx}(y)}$, as the amplitude of the coherence features is higher than those for the $\overline{R_{yy}(y)}$ functions. Persistent spatial features do not change with flow rate, neither in terms of wavenumber nor amplitude. When comparing different transects over the measurement area, it can be seen that each has different characteristic periods (including more than one per transect). These features are visible for both velocity directions, though more defined for the streamwise component.

These conclusions from the $\overline{R_{xx}(y)}$ and $\overline{R_{yy}(y)}$ functions are confirmed by their respective spectra, shown in Figure 7.2-6. The spectra for $E_{xx}(\gamma)$, Figure 7.2-6a and c, show distinct peaks in the Integral (i.e. Energy-containing) range, wherein multiple dominant coherent wavenumbers can be seen for the same function.

Further, the difference in the existence of dominant wavenumbers is also noticeable from the proportion of the total energy they contain. For the streamwise spectra, $E_{xx}(\gamma)$, the few prominent peaks in the integral range contain a significant portion of the total turbulent kinetic energy. This can be seen by comparing the portion of the total spectra contained in the inertial subrange ($\gamma \gtrsim 100$), which is lower for $E_{xx}(\gamma)$ than for $E_{yy}(\gamma)$. The total energy for the latter seems to be distributed across γ wavenumbers, in a manner that resembles Kolmogorov's second universality hypothesis[22] (Pope, 2000, p. 231), particularly the -5/3 slope in the inertial range (approximately the intermediate slope in Figure 7.2-5b and d). However, certainty in this conclusion requires some physical conditions to be met: large Reynolds numbers and local isotropy and homogeneity (Nikora, 2000). Inferences on the validity of the power law for the RandoSticks flow demands a detailed analysis of the turbulence structure, which is outside the scope of this thesis and will the covered in further works. For now, it should be remarked that a few dominant wavenumbers, and thus characteristic scales can be obtained from the $E_{yy}(\gamma)$ function, given the distribution of energy across different wavenumbers.

The spatial statistics presented in Ricardo (2014, chap. 7) only focus on the transverse velocity autocorrelations, which show the relevant structures more clearly than the similar functions presented here (Figure 7.2-5b and d). Differences in the experimental approach, in conjunction with the time average, are hypothesised to explain the lack of similarity between both studies. First, the use of uniform diameters guarantees that vortices have similar scales, and given the average spacing, it is more likely that these develop independently (i.e. groups of adjacent cylinders are less likely to form clusters). Furthermore, measurement transects were taken within discontinuities[23] in the vegetated array, which allows travelling structures to fully develop, as these are less susceptible to shear-induced dissipation. Conversely, the transverse sections in the RandoSticks measurement area will record the passage of structures of different scales, given the diameter distribution, in the inter-stem space. The time average over

[22] Reminder of Kolmogorov's second universality hypothesis: the range of energy transfer between the integral (energy containing) range and the dissipation rate is a function solely of dissipation. Acknowledging the assumption of universal isotropy at these small flow scales, the transfer rate can be expressed by a power law with a slope of -5/3.
[23] These discontinuities were designed to allow lateral illumination within the vegetated array for PIV measurements.

instantaneous spatial correlations will then obscure some of the smallest scales (footprints of the smaller coherent structures), in favour of the larger ones.

Focusing on the differences between velocity components evident from Figure 7.2-5, a comparison between the correlation functions $\overline{R_{xx}(y)}$ and $\overline{R_{yy}(y)}$ is required. It was noted that coherence components (i.e. sinusoidal patterns) are better identified from the streamwise correlation functions, $\overline{R_{xx}(y)}$, than from the transverse ones, $\overline{R_{yy}(y)}$. The opposite is true from the time correlation functions, and the results presented by Ricardo (2014).

From the definition of the spatial autocorrelations (Eq. 7.2-6 and Eq. 7.2-7), it can be seen that before the time average, bivariate correlations of the form $R_{xx}(y,t)$ and $R_{yy}(y,t)$ are obtained. To obtain a general picture of the time-dependence of these functions, the mean and standard deviation, across the t domain was performed, as shown in Figure 7.2-7. It can be seen that, as expected, coherence components have higher amplitudes for transverse velocities, $R_{yy}(y)^{+}$, evidenced by the larger spread of the standard deviation lines. It can be safely concluded that the time component of the $R_{yy}(y,t)$ function encodes the information of travelling vortices, of multiple sizes (see Figure 7.2-2d) but that the time averaging obscures them. The prevalent coherence components in these functions is a result of patterns being more consistent over time, especially for u velocities (because wakes and advective acceleration zones are time-averaged features).

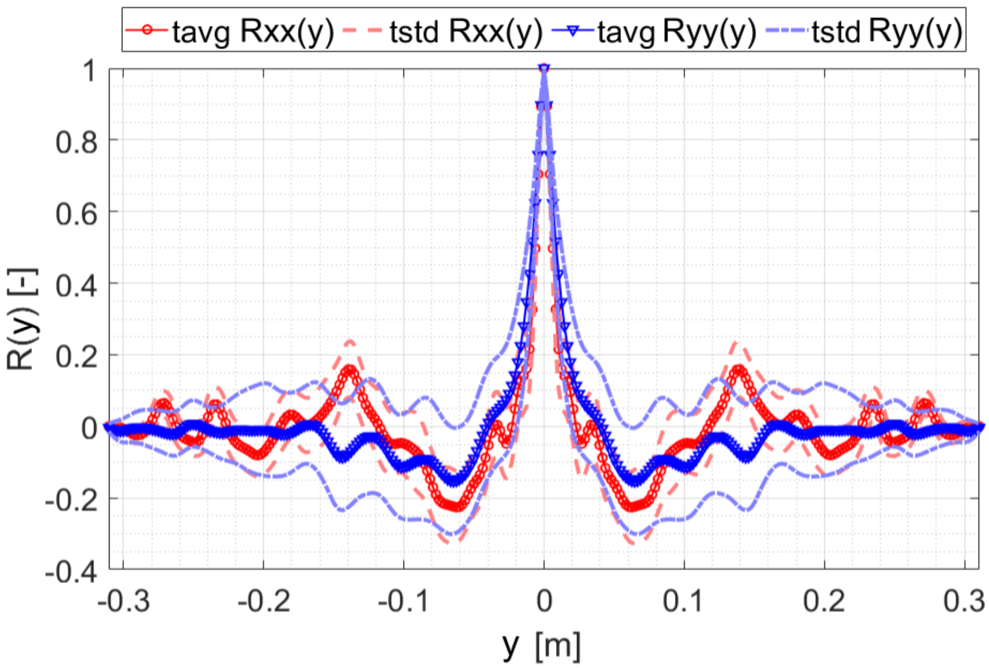

Figure 7.2-7. Comparison of the effects of time averaging on the spatial autocorrelation functions.

As mentioned, the 'persistent', i.e. time constant, features present in the spatial correlations, are indications of wakes and large velocity defect zones. The extent and prevalence of these spatial features depend on the geometry of the array, and are independent of the scales of moving flow structures, as these are hidden by the time average. As a result, estimates of characteristic length scales, defined as the reciprocal of the dominant wavenumbers, should be interpreted as attributes of the vegetated array; not the turbulence structure. This will be evident in Section 7.3, where the length scales from time- and space-dependent correlations are compared in terms of probability distributions. The space-dependent length scales will be seen to be generally higher than time-dependent ones, as the former are actually showing larger zones of differential advection, most likely the result of adjacent cylinders forming clusters. The role these scales play in the description of vegetated dispersion is connected to dispersive fluxes, which are related to shear and local trapping zones. Both are dominant drivers of dispersion for $Re_d < 400$ (see Chapter 4).

To complement the analysis of spatial correlations, the statistics from streamwise sections, defined along the wakes of reference cylinders, were computed. These correspond to the functions $\overline{R_{xx}(x)}$ and $\overline{R_{yy}(x)}$, defined in Eq. 7.2-6. Note that, as before, the dependency on reference points (x_0,y_0) is dropped to give each correlation function, and all characteristic scales therefrom, the same statistical importance.

Restating the criteria to show the behaviour of velocity statistics, Figure 7.2-8a and b show the spatial autocorrelation functions, for both velocity components, along a random cylinder wake (Figure 7.2-1), over the Re_d range. Figure 7.2-8c and d show the variation of wake autocorrelations over a sample of wakes across the measurement area, for $Re_d = 317$. Figure 7.2-9 shows the wavenumber spectra of the spatial autocorrelation functions presented in Figure 7.2-8, in equivalent order.

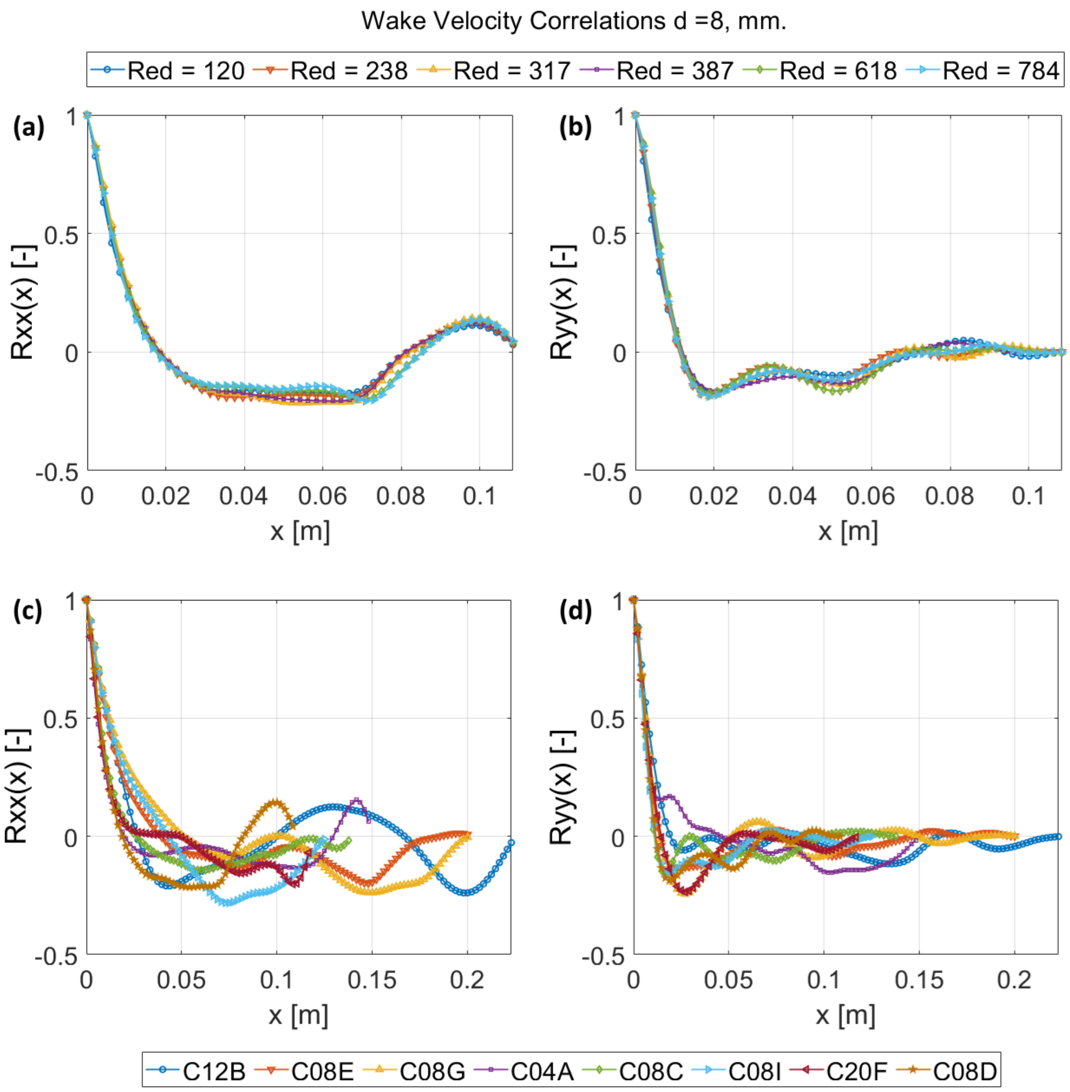

Figure 7.2-8. Multi-Point, Time-averaged and Space-dependent functions along longitudinal (wake) sections. Upper: a) Streamwise and b) Transverse velocity autocorrelations from a single streamwise section, (i.e. the wake of an 8 mm cylinder) over the range of Red values measured. Lower: c) Streamwise and d) Transverse velocity autocorrelations for a random sample of streamwise sections, Re_d *= 317.*

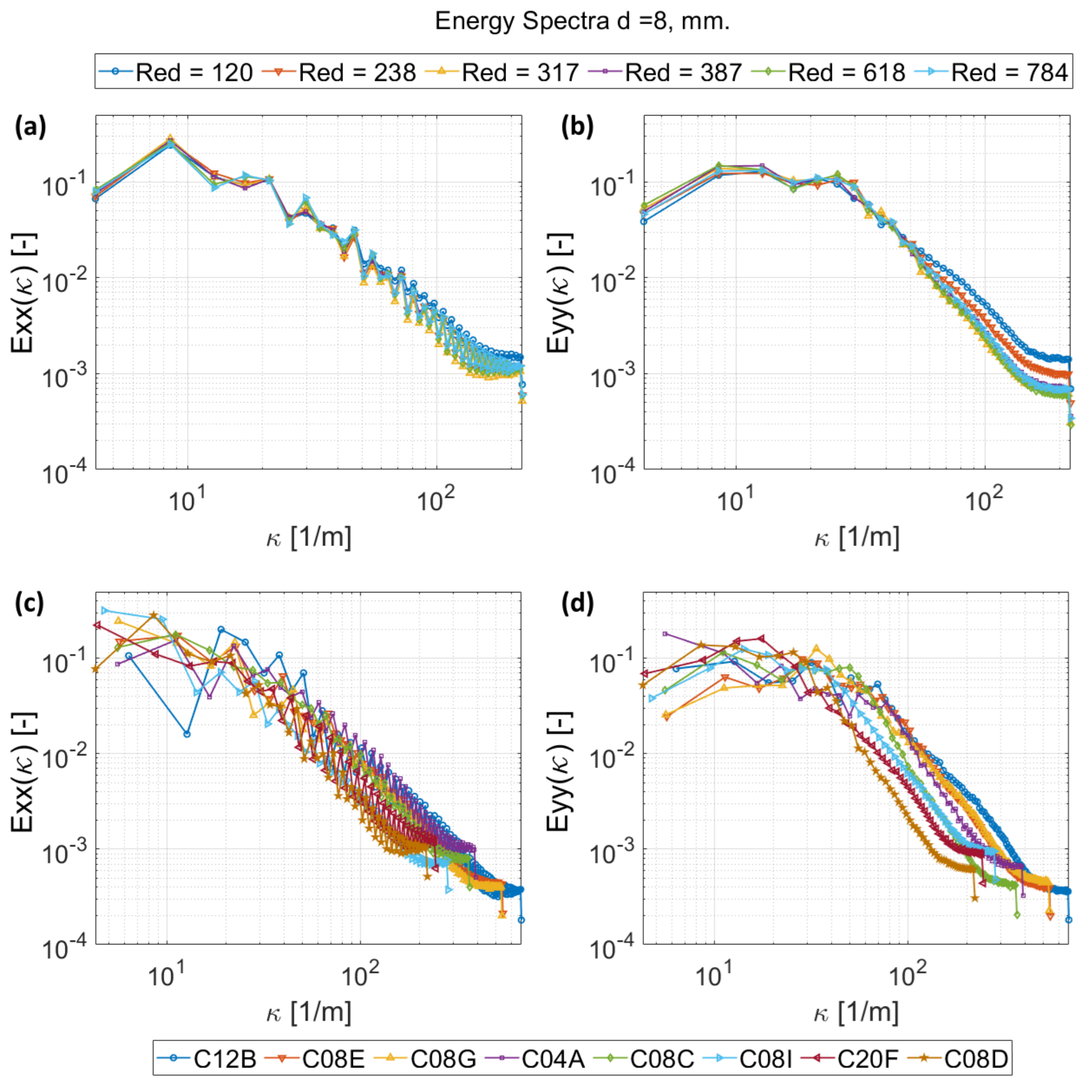

Figure 7.2-9. Energy Spectra from streamwise (i.e. wake) sections shown in Figure 7.2-8. Upper: a) Streamwise and b) Transverse velocity Energy Spectra from a single streamwise section, (along the wake of an 8 mm cylinder) over the range of Red values measured. Lower: c) Streamwise and d) Transverse velocity Energy Spectra for a random sample of streamwise sections, Red = 317.

As explained before, the 'persistent features' captured from spatial statistics are actually properties of the mean flow field, and not of the turbulence structure. In this sense, the variations in $\overline{R_{xx}(x)}$ and $\overline{R_{yy}(x)}$ actually represent common features of the wakes analysed. Given the range of Re_d analysed, a well-defined formation region, behind cylinders is expected. The point after which the correlation is zero, can be understood as the length of the recirculation region, as they contain the same structure. Also, the time averaging obscures the spatial evolution of flow structures, as the direction of motion is along the correlation direction, so a similar problem as that seen for $R_{yy}(y)$ occurs.

Similar to the case for $R_{yy}(y)$, the shape of the wake autocorrelations is independent of flow rate. Physically, this means that persistent features over the autocorrelation domain (i.e. the wake centreline) present negligible changes over the range of Re_d reported. The evidence of travelling vortices is eliminated by the time average, and only steady features such velocity-defect and advective acceleration zones are present in the $\overline{R_{xx}(x)}$ and $\overline{R_{yy}(x)}$ curves. In the context of dispersion, particularly the effects of vortex trapping (White and Nepf, 2003), the non-dependency of spatial streamwise features with Re_d means that the extent of primary wakes remains unchanged for the Re_d domain tested. Therefore, trapping-induced dispersion will be a function solely of shedding frequency (i.e. S_t). Indeed, Gerrard (1978, fig. 4) reports that, for the Re_d values tested here, the length of the recirculation/trapping zone for an isolated cylinder lies within the range ($1 < x/d < 2$). As it can be seen from the variation in shedding frequency, a combination of the lock-in regime leading to seiches, and the possible effects of clustering, lead to the conclusion that the recirculation region behind stems will remain largely unchanged.

For the cases when a dominant periodic feature is identifiable, this is usually not a significant component of the energy spectrum (i.e. the dominant mode does not represent more than 5% of the total energy spectrum) therefore most length scales derived for this analysis are overlooked. For reference, the characteristic wavenumbers, i.e. those associated with the dominant modes, are defined as: $\kappa_s \mid E_{xx}(\kappa_s) = \max|E_{xx}(\kappa)|$ and $\gamma_s \mid E_{xx}(\gamma_s) = \max|E_{xx}(\gamma)|$

7.3. Characteristic RandoSticks Length Scales

At the end of Section 7.2.1, the characteristic length scale of the flow, from time-dependent correlation functions, was defined as the product of the characteristic shedding period, T, and advection, U_p: $\Lambda_t = \mathrm{T}U_p$, where Taylor's frozen-turbulence hypothesis is assumed, and the period, T, is found as the reciprocal of the shedding frequency, f_s. Similarly, length scales from spatial autocorrelations, Λ_{xy}, are found as the reciprocal of the wavenumbers, κ_s and γ_s, from the dominant components (i.e. peaks) in the corresponding energy spectra. The criteria to select the relevant length scales was defined as those that contained more than 5% of the total turbulent kinetic energy. Also, to avoid possible biases in the characterisation of length scales, a geometric limit, equivalent to the flow depth, was imposed on the length scales.

Following these criteria, and acknowledging that the measurement points and transects are related to a sample of reference cylinders, Figure 7.3-1a and b show the valid length scales from time- and space-dependent autocorrelations, over all Re_d values tested and disaggregated by diameter.

The disaggregation by diameter and Reynolds number is done to study possible patterns in the length scales, with respect to these parameters. If no interactions are assumed between adjacent stems, such that the results from isolated cylinders are applied to the reference points presented in Figure 7.3-1a, a single value of Λ_t, proportional and unique to each diameter, independent of Re_d, would be expected. Overall, no strong dependency on either d or Re_d is evident from Figure 7.3-1a.

Length scales calculated from 4 mm cylinders show the largest spread. This is a consequence of the velocity resolution, which obscures small coherent components. Further, given the relative size difference, most cylinders of this size are expected to be influenced by the wakes of upstream stems, and their characteristic periods overshadowed by larger vortices. A weak increasing trend between stem diameter and mean length scale is found for $8 \leq d \leq 15$, although the spread in the Λ_t estimations negates the possibility of establishing a unique value.

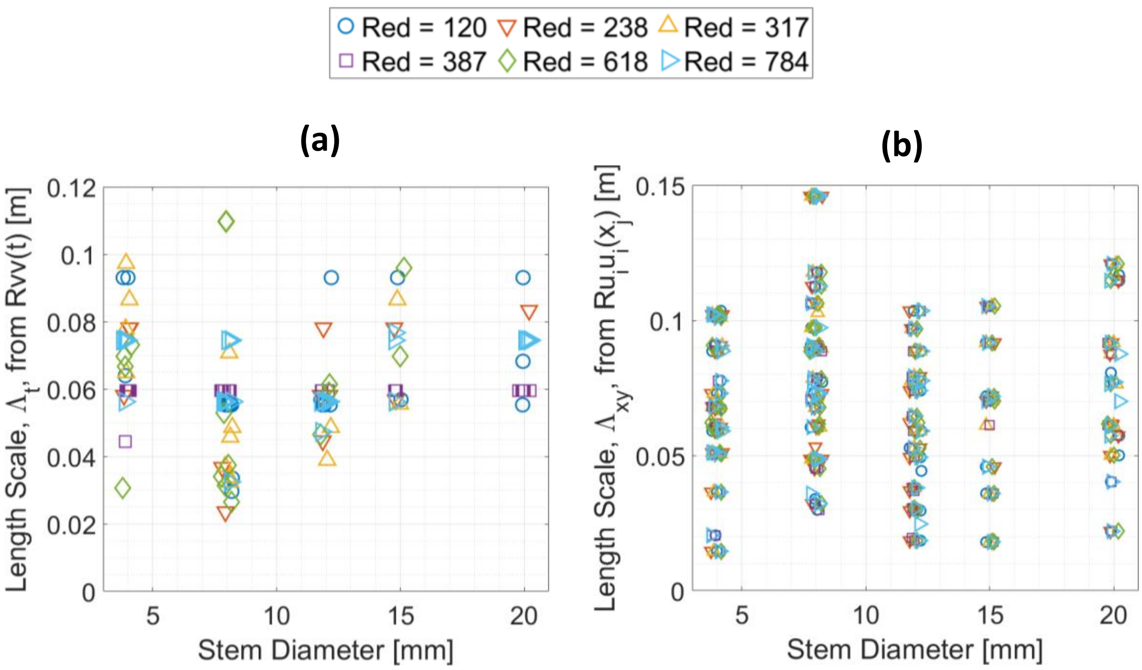

Figure 7.3-1. Distribution of characteristic scales from a) time-dependent and b) spatial autocorrelation functions, per reference cylinder and flow rate.

No statistical difference is found for Λ_t estimates between $d = 15$ and $d = 20$ mm. Two possible explanations exist: first, the lock-in regime that generates seiches (Defina and Pradella, 2014)—i.e. the self-sustaining process whereby shedding and natural surface oscillation frequencies match and generate lateral surface fluctuations—makes frequencies across different cylinders consistent. Second, some of these estimates neglect the reference cylinder entirely and are actually associated to groups of adjacent stems, hence the values $\Lambda_t > 20$ mm.

For $Re_d = 387$, no variation in the estimation of Λ_t was found along Re_d or d, and all values assemble around $\Lambda_t \approx 0.06$ m; which is a common estimates across flow rates and diameters. For the time being, this is attributed to the possible existence of a preferential cluster size, although a data quality assessment is first necessary to check possible measurement issues for $Re_d = 387$.

The spread in length scale estimations is more noticeable for Λ_{xy}, where no clear trends can be established, rendering a clear random behaviour to this variable. Overall, this conclusion also applies for Λ_t, and also validates the original assumption of independence between correlation functions and reference points.

Taking advantage of this random behaviour, a comparison between the distributions of morphological (i.e. diameter and spacing) and statistically derived length scales, is presented in Figure 7.3-2.

In Section 7.2.1, the existence of a secondary frequency, $f_2 = 2f_s$, was presented. This has been experimentally reported from studies on isolated cylinders, and is attributed to the coherence signal recorded by streamwise velocities in points along the wake centreline, close to the formation region. Physically, this records the size of individual shed vortices—note that $\mathrm{T}_2 = \mathrm{T}/2$, from the foregoing definition—rather than phase-correlated patterns. Such quantities were rarely spotted in the RandoSticks experiments. However, for comparison purposes, the cumulative distribution of scales based on the T_2 period, Λ_{t2}, are calculated from its theoretical definition, and presented in Figure 7.3-2.

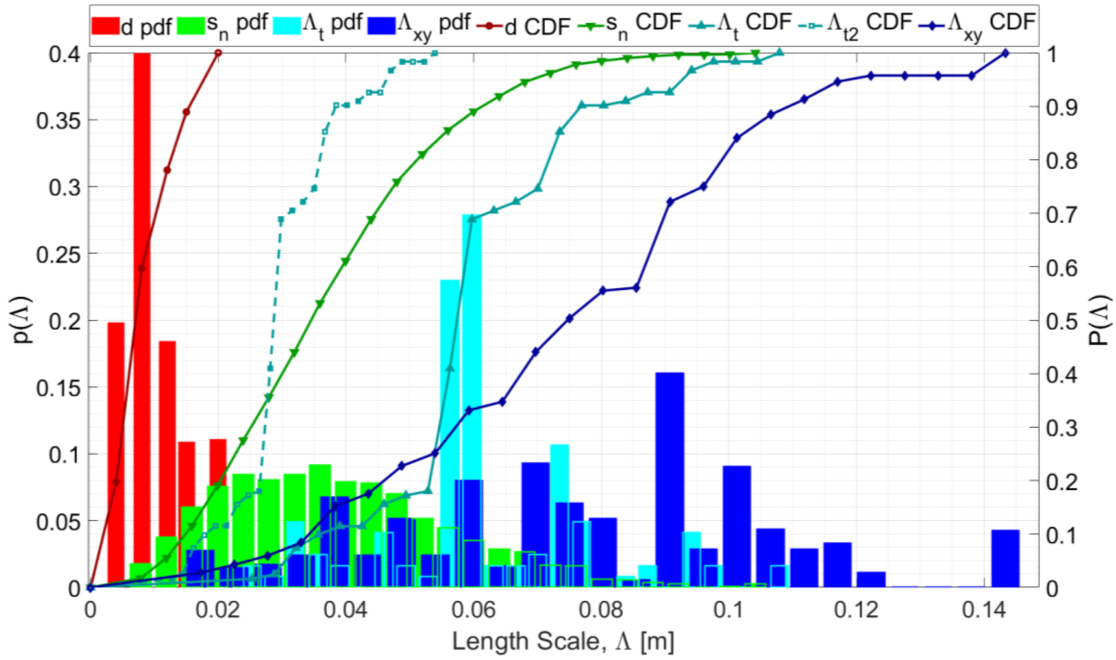

Figure 7.3-2. Comparative Summary of Characteristic Geometric and Hydrodynamic Length Scales from the RandoSticks configuration and experiments.

The diameter distribution is presented according to Figure 4.2-1b, Chapter 4. The inter-stem (edge-to-edge) spacing, s_n, was calculated using Delaunay criteria, as mentioned in Section 5.7, Chapter 4. Flow scales and representative diameters are largely uncorrelated, which means that a minority of stems operate as isolated cylinders.

Comparing estimates of the characteristic time-dependent length scales, Λ_t (c.f. vortex size), with the inter-stem distribution, s_n, it can be seen that the lower and upper limits for both are similar. However, roughly 85% of all Λ_t are located within the top 25% of the inter-stem spacing distribution. This suggests two things: 1) the necessary distance between cylinders, for vortices to develop, is approximately 0.05 m, i.e. $5d$ or $2.5d_{max}$. 2) for inter-stem distances, $s_n < 0.05$ m, most adjacent cylinders interact, thus, depending on the incidence angle, the resulting vortices will have a scale proportional to the space occupied by both (Sumner, 2010). Note that these two hypotheses are not mutually exclusive. Moreover, if Zdravkovich (1987) threshold for cylinder-pair interference is assumed, $s/d < 5$, then, using the spacing limit defined above, $s_n \approx 0.05$m, the characteristic diameter matches the average of the RandoSticks distribution, i.e. $d = 0.01$ m.

Assuming these two results, such that all adjacent cylinders within $s_n \approx 0.05$ m form 'clusters', a larger conclusion can be drawn. The local deceleration/trapping zones caused by the clusters, have to be balanced by advection acceleration zones/avenues. This equilibrium should be achieved to maintain mean flow conditions. It is then reasonable to expect that, given the morphology of the array, a universal criterion for the formation scale of clusters exists. A detailed analysis of the relationship between cylinder distance, interference and flow scales, is necessary to validate the foregoing assumptions about clustering. This analysis, however, will involve a detailed localised characterisation of the RandoSticks experiments, rather than a simplified probabilistic one. In other words, cylinder locations, insofar as relative distances and incidence angles are concerned, should be considered in the formation of flow structures. This, again will be the objective of further work.

Length scales from spatial statistics, Λ_{xy}, show a larger spread than Λ_t, and also, are more uniformly distributed across the range of possible length scales. Indeed, roughly 60% of Λ_{xy} values overlap with the inter-stem spacing distribution. This indicates that the persistent features recorded cover from single cylinder wakes, to the largest possible clusters in the measurement area.

Both scales shown above, Λ_t and Λ_{xy}, represent lower and upper limits for the existing characteristic features of the flow field. These, respectively, represent turbulence-dependent and advection-dependent scales. From a dispersion framework, flow scales, Λ_t give an indication of turbulent diffusion, but advection scales (related to Λ_{xy}) are associated to dispersive fluxes and thus large-scale dispersion. Although possible, a full two-point statistics analysis would have provided little additional information on characteristic scales. This exercise will be undertaken in future work, wherein a full characterisation of scale diffusion, life-span and interactions of flow structures will be the focus. These higher-order statistics are not expected to provide new insights to the study of solute transport.

This analysis of characteristic length scales from velocity statistics is presented to illustrate the need to compare the geometry of the artificial vegetation layout (to represent real emergent vegetation), with the distribution of flow structure scales that cause dispersion at the smaller scales of flow. Physically, these scales govern how quickly a cloud of solute will assimilate the average morphological characteristics of the flow. For the case of the RandoSticks experiments presented in this work, the non-dimensional characteristic flow scale is expected to remain constant for all experiments, given that no variations in vegetated morphology were explored. This, in other words, means that effects like clustering and sheltering are believed to cause flow scales larger than those expected from diameters or inter-stem spacing, which would explain the differences between measurements done in real and artificial vegetation, as those presented in Figure 5.9-1 and Figure 5.9-2.

Even though this analysis started with the intention of finding scales, proportional to the RandoSticks morphology, that could be used to non-dimensionalise dispersion values; a breadth of knowledge on the RandoSticks behaviour has been revealed. One of the main findings is that different statistical characterisations of vegetated flow can reveal different properties from the flow generated through it. For example, travelling vortices are often generated by interacting stems, and recirculation regions rarely change their dimensions over the range of flows tested.

The discrepancy between actual flow scales and RandoSticks geometry suggests that the previous assumptions for non-dimensionalisation lengths might not entirely be true in emergent vegetation. However, the spread of the mixing coefficients clearly shows that a wide range of vegetated/flow scales does not necessarily reflect a wide spread in the dispersion coefficient. Since solutes were seen to quickly assimilate average vegetation characteristics, flow scales can be understood as the necessary size of the cloud to adopt 'average conditions'. Beyond that, any value can be used to non-dimensionalise dispersion.

7.4. Mixing as a function of RandoSticks Hydrodynamics

The previous section focused on describing the flow structures within the RandoSticks configuration, to see how these reflect the morphological characteristics of the artificial vegetation array. To complete the analysis, this last section will compare the characteristic non-dimensional dispersive and hydrodynamic scales to see how changes in the contributions from the latter, with Reynolds number, affect dispersion. Proportionality rules will be derived and these will be associated with the flow characteristics of the array found in the previous sections in this chapter.

Previous empirical and analytical models for dispersion use turbulent kinetic energy and drag coefficient to relate the transfer of energy, from the mean flow, towards the creation of turbulent terms. These have been considered as dominant drivers of two-dimensional dispersion. Consequently, it is important to acknowledge the Production/Dissipation hypothesis, in the context of turbulent diffusion, presented in the works of Nepf (1999) and Tanino and Nepf (2008b). Before dispersion is analysed, the proportionality between space-averaged turbulent kinetic energy and drag coefficient will be verified experimentally.

Based on the balance between energy production, associated entirely with form drag caused by the vegetation elements (Finnigan, 1985), and an estimation of the dissipation rate associated with Kolmogorov's universality hypotheses (Tennekes and Lumley, 1972, p. 68), Nepf (1999) proposes the turbulent diffusion in a cylinder array, D_t, using the square-root of TKE as the main velocity scale, as shown in Eq. 7.4-1

$$\frac{D_t}{U_p d} \propto \left\langle \frac{\sqrt{TKE}}{U_p} \right\rangle = \gamma (\varphi C_D)^{1/3} \qquad \textit{Eq. 7.4-1}$$

where γ represents a proportionality constant. For the relationship in Eq. 7.4-1 to be consistent with the theory, Re_d should be large enough for small-scale isotropy (Pope, 2000, chap. 6), and for Taylor's frozen turbulence hypothesis (Taylor, 1938), to be valid, as explained by Nikora (2000). Further, changes in the impact of viscosity and shedding on drag, caused by the addition of a diameter distribution, could hinder the applicability of the Production $\sim$ Dissipation hypothesis presented in Nepf (1999). Nevertheless, both terms can be obtained from the PIV and surface measurements, and the comparison performed. Figure 7.4-1 shows the variation of the production, $(\varphi C_D)^{1/3}$, and dissipation, $\langle\sqrt{TKE}/U_p\rangle$, terms in Eq. 7.4-1, alongside an estimation of their proportionality constant, γ.

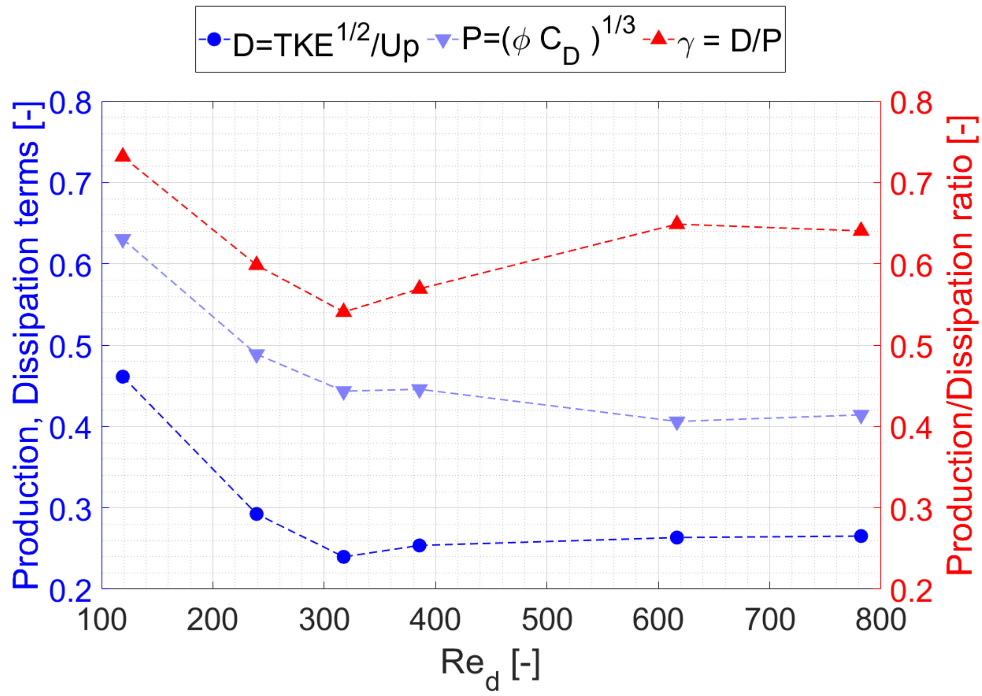

Figure 7.4-1. Experimental validation of the Production ~Dissipation hypothesis presented in Nepf (1999), for the calculation of the turbulent diffusion term.

The dissipation and production terms can be seen to follow a similar trend for the flow rates tested, although the proportionality is not constant. It is expected that γ will reach an asymptotic value for the inviscid range. Given the vegetation density of the RandoSticks presented here, which can be classified as 'sparse' ($\varphi = 0.05$) lateral dispersion is expected to be largely determined by turbulence. This, and the variation of Eq. 7.4-1 in the context of the D_y^* measurements will be presented below, respectively.

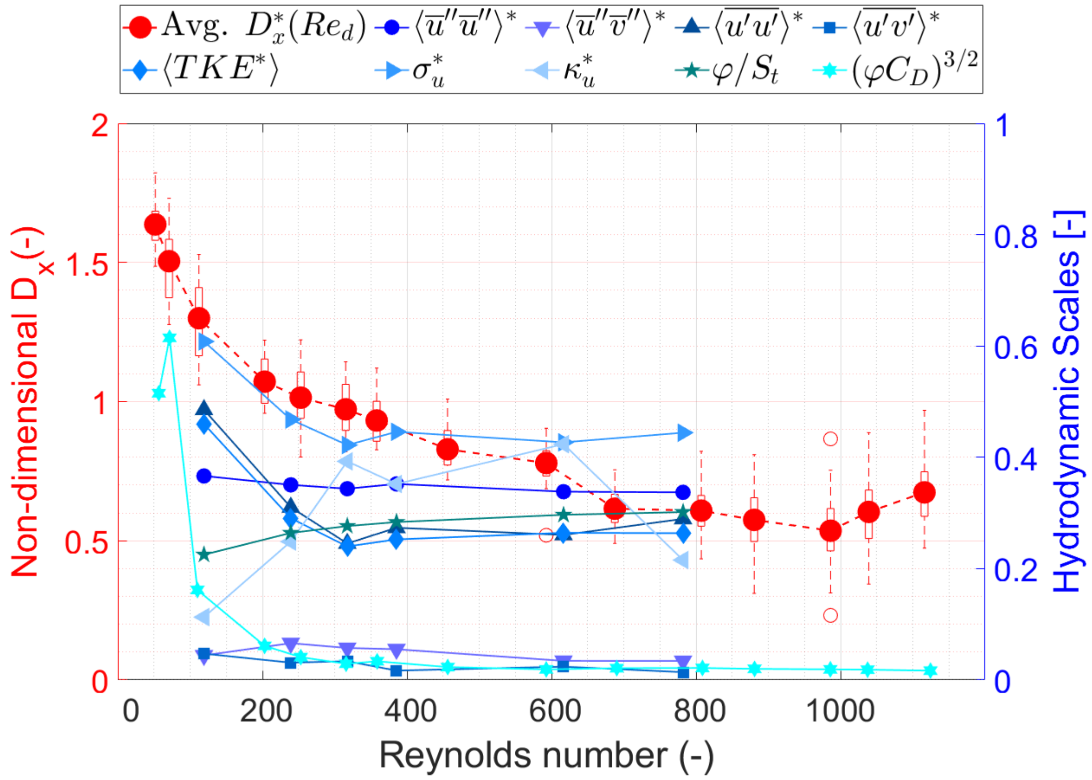

Figure 7.4-2. Variation of normalised longitudinal dispersion with Reynolds number and effects of different hydrodynamic scales on the trend for D_x^*.

Focusing on the general statistical descriptors of the velocity fields, $u(x, y, t)$, as shown in Figure 6.2-1, Chapter 6, it can be seen that the normalised, global standard deviation of the longitudinal velocity, σ_u^*, shows a trend similar to that of D_x^*, for $Re_d < 600$. After this value, the dispersion trend seems to be influenced by the change in skewness magnitude, κ_u^*—note that this value is negative for all Re_d tested. Focusing on the combination of these two global statistical descriptors, it can be seen that the behaviour of the skewness shows that for $Re_d < 200$ and $Re_d > 600$, the velocity tends to a symmetric distribution. For the first range ($Re_d < 200$), the larger dispersion is caused solely by the scale σ_u^* being a larger proportion of advection. The range $200 < Re_d < 600$, contains the largest registered skewness, κ_u^*, with a relatively uniform behaviour. The same occurs for σ_u^*. The trend of D_x^* follows the same trend as the previous range, despite changes in σ_u^* and κ_u^*. Physically, while the high values of κ_u^* in this range indicate a large proportion of trapping velocities, these are compensated by acceleration zones. The tendency of the velocity distribution, to be more symmetrical, at $Re_d > 600$, is an indication of the existence of zones of higher local acceleration, as a compensation for trapping areas. This is also supported by the fact that vortices reach turbulence conditions before they detach from the cylinders.

In absence of a general analytical model for two-dimensional dispersion, all hydrodynamic scales, shown in Figure 7.4-2, are assumed to be independent components of D_x^* in a first-order relationship.

The effect of shear fluxes (both dispersive and turbulent) is largely negligible compared to the other ones. Clearly, dispersion drivers change over different Re_d intervals. Focusing on the PIV data, turbulent fluxes, $\langle\overline{u'u'}\rangle^*$, caused by temporal fluctuations, are dimensionally dominant in the range $100 < Re_d < 200$. It can also be seen that for Re_d between 100 and 300, these fluxes steadily decrease until a relatively stable value of $\langle\overline{u'u'}\rangle^* \approx 0.26$, with a seemingly positive gradient, is achieved. For $Re_d > 200$, dispersive fluxes, $\langle\overline{u}''\overline{u}''\rangle^*$, are dominant, and are relatively constant for the range of flows tested. It should be noted that the trends of D_x^*, and $\langle\overline{u'u'}\rangle^* + \langle\overline{u}''\overline{u}''\rangle^*$ for the range, $Re_d < 300$, are closely related. However, for larger values ($300 < Re_d < 600$), in which the sum of dispersive and turbulent fluxes is constant, D_x^* shows the same decreasing behaviour, up to $Re_d \approx 600$.

A notable difference between the hydrodynamic scales presented in Figure 7.4-2 and previously reported results, can be seen in the variation of the vortex trapping component, φ/S_t. When the cylinders comprising a vegetated array are modelled as superimposed elements, without non-linear interactions[24], the change in shedding frequency, represented by S_t, follows the same as that for isolated cylinders. For the range of flow rates presented here, it means that $S_t \propto Re_d$. Although this proportionality is not strictly linear (McCroskey, 1977; Gerrard, 1978). This assumption underlies the vortex trapping dispersion term, $\propto \varphi/S_t$, presented in White and Nepf (2003). Figure 7.2-4 shows that S_t from the RandoSticks experiments has the opposite behaviour, suggesting that trapping times actually increase. Whilst there are no explanations for this incongruence, it should be clarified that this vortex trapping term is defined as acting within primary wakes[25], which are hypothesised to change marginally with Re_d, as Figure 7.2-8a and b indicate. The proportion of primary wakes have been found to be in the order $0.01 < O < 0.1$, for sparse arrays Corredor-Garcia *et al.* (2020). Therefore, its contribution to D_x is expected to be considerably smaller than turbulent and dispersive fluxes. The possibility that

[24] This means that all cylinders in the array preserve the same behaviour as if they were in isolation. Particularly regarding vortex streets, and second order velocity statistics. The only change considered is in the mean velocity around cylinders; but interactions like sheltering or wake synchronisation are ignored.
[25] i.e. vortex formation regions behind stems.

non-linear interactions, which are evident from the statistical analyisis of periodic and space-dependent structures (see Sections 7.2 and 7.3), require a new definition of the trapping term, which can capture the behaviour of D_x^* for $300 < Re_d < 600$. This should also be considered for future work.

Finally, a few conclusions can be drawn from the behaviour of D_x^*, for Re_d outside of the PIV experiments, i.e. $Re_d < 110$ and $Re_d > 800$. The dependency of D_x^* on drag coefficient, which has been proposed to be $\propto (\varphi\ C_D)^{3/2}$ (White and Nepf, 2003; Lightbody and Nepf, 2006b) follows the same trends of the dispersive and turbulent fluxes, within the PIV experimental range. Although negligible over $110 < Re_d < 800$, scales defined from the drag coefficient are expected to become relevant in the range $Re_d < 110$, where it is responsible for shaping the mean flow field[26]. Furthermore, it is known that at these low Re_d, with static trapping areas, molecular diffusion is the relevant scale ensuring any solute experiences the average flow field (Koch and Brady, 1985). It is then expected that D_x^* is defined by $C_D^{3/2}$ and D_m in this range. For the case of $Re_d > 800$, the behaviour of the dispersive and turbulent scales, suggests inviscid conditions. Indeed, evidence of transitions to three-dimensionality (Williamson, 1991), increasing and irregular vortex shedding, and transition to turbulence inside the formation region (Gerrard, 1978), tends to confirm this hypothesis.

[26] This is particularly true for $Re_d \lesssim 40$, where time-dependent velocity fluctuations are absent, and the recirculation zones behind cylinders are static.

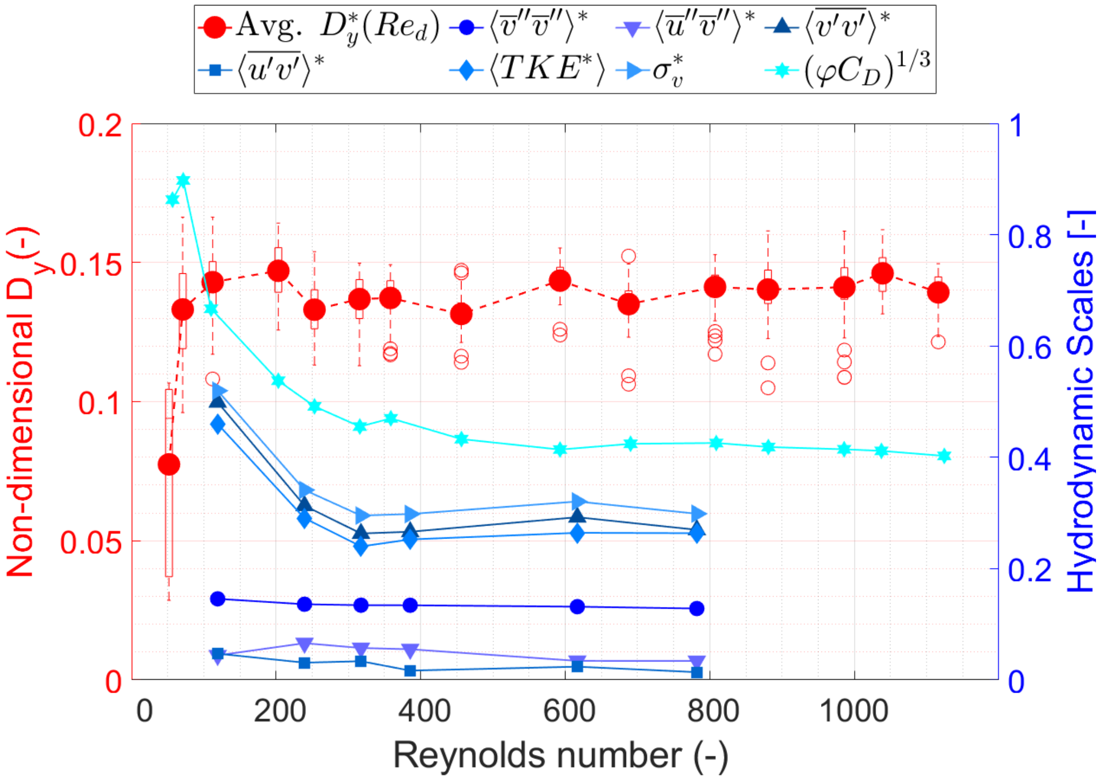

Figure 7.4-3. Variation of normalised transverse dispersion with Reynolds number and effects of different hydrodynamic scales on the trend for D_y^*.

In contrast to the variation of D_x^*, which shows various distinct regimes in the longitudinal spread of a passive solute; the variation of lateral dispersion, D_y^*, can be divided into two distinct ranges. For $Re_d < 250$, a rapid increase in transverse spread is evident with Re_d. This is caused by turbulence production, connected to the behaviour of both $C_D^{1/3}$ and $\langle TKE^*\rangle$[27] (see Figure 7.4-1). If this range is extrapolated towards $Re_d \to 0$, the following regimes are found.

a) $1 < Re_d \lesssim 10$: Stokes flow
b) $10 \lesssim Re_d \lesssim 40$: Increase of the closed recirculation region behind cylinders
c) $40 \lesssim Re_d \lesssim 70$: Oscillation of recirculation region. Start of mass transfer with outer flow
d) $70 \lesssim Re_d \lesssim 100$: Periodic vortex shedding, Karman street.
e) $100 \lesssim Re_d \lesssim 250$: Convective acceleration of shed vortices.

These regimes are based on the results of Gerrard (1978) and (Coutanceau and Bouard, 1977). For flows before the start of the oscillating wake ($Re_d \approx 40$), streamlines around cylinders are

[27] Note that $\langle TKE^*\rangle = \left\langle \frac{\sqrt{TKE}}{U_p} \right\rangle$, is equivalent to $\sqrt{\langle TKE\rangle}/U_p$. This is a consequence of the global (space-averaged) isotropy found for Reynolds stresses (see Figure 6.5-1, Chapter 6).

similar to those obtained from potential flow solutions, for which analytical models exist (e.g. Crowdy and Marshall, 2006), and minimal variation caused by turbulence is expected. Further, for ranges (a) and (b), lateral dispersion increases at a rate similar to that of transverse dispersive and turbulence fluxes. A peak in transverse turbulence fluxes is thus expected at $Re_d \approx 70$, where vortices, functioning as solute 'carriers', start detaching and travelling downstream. Slight increases in lateral dispersion would then be the consequence of an acceleration in the shedding rate of vortices (regimes d and e), which will, simultaneously diffuse and break down downstream. An equilibrium can be expected at $Re_d \approx 250$, defined by the morphological features of the array. For the case of the RandoSticks configuration, the statistical analysis presented above suggests that this equilibrium is related to well defined interactions between cylinders, in the form of synchronised shedding and sheltering, which present negligible variations with flow rate.

Finally, it should be noted that increases in advection mean that the travel time/distance necessary for a cloud of solute to reach this equilibrium, also referred above as 'average conditions', will be significantly shorter. This independence with Re_d, prevalent for most of the flow rate regime is in agreement with the model presented by Tanino and Nepf (2008b, 2009).

7.5. Conclusions

This chapter aimed to connect the independent results from dispersion coefficients (Chapter 4), and vegetated hydrodynamics (Chapter 6). The starting point was an analysis of the effects of the RandoSticks morphology, on its flow structure, via time- and space-dependent velocity statistics. The existence of temporally correlated structures, and their variation, indicates a richer vortex distribution than is expected from uniform-cylinder arrays. Spatial statistics have revealed the different interactions of cylinders of varying diameters, and their behaviour with Re_d. Finally, plots of normalised longitudinal and transverse dispersion and hydrodynamic scales were analysed. This revealed the existence of different flow regimes, in which the dominant drivers of dispersion change, and give clues as to possible proportionalities between the different hydrodynamic scales. These could be used to obtain empirical models for solute transport in emergent vegetation. The specific findings from this chapter are:

- Statistical velocity functions over the RandoSticks configuration are useful to reveal persistent features from the flow. For time-dependent correlations, measured at specific points, these features correspond to coherent structures generated by vortex shedding. In contrast to previous results in uniform-diameter arrays, coherent structures of a wide array of sizes were found. These were not limited to the cylinder diameters, but their scale suggests that cylinder interactions, particularly sheltering and wake synchronisation, play an important role in the turbulence structure of the RandoSticks configuration.

- For the case of spatial statistics, defined following Ricardo (2014, chap. 7) methodology, the time average over instantaneous spatial correlations obscures the existence of coherent structures. The 'persistent features' measured via this spatial analysis, actually reveal properties of the mean flow. These are closely related to dispersive fluxes. Their independence of flow rate, suggest that these features can be physically interpreted as the extent of velocity defect and advective acceleration zones. Some of these areas, given their size, are believed to represent clusters.

- The method for spatial velocity statistics (Ricardo, 2014) cannot be extrapolated to more complex arrays, such as the RandoSticks configuration. The relevant scales were found to be features of the mean flow field, rather than characteristic vortex sizes. Studying the standard deviation, across time, of these correlation functions reveals that all vortex-related components are smoothed by the averaging.

- Spatial velocity statistics along the wakes of the reference cylinders show no variation of relevant scales with Reynolds number. These scales specifically refer to the lengths of the formation region. Energy spectra from these sections show no dominant spatial structures.

- Only a subset of length scales was considered relevant (c.f. valid), namely, those whose spectral component contained more than 5% of the total turbulent kinetic energy, and were smaller than the flow depth. The former criterion is admittedly arbitrary, but was found to be useful to obtain statistically relevant length scales. Although further work is needed to validate this criteria, the results show no dependency of Λ on either cylinder diameter or flow rate.

- Length scales obtained from the statistical analysis seem to be uncorrelated with those from the morphological characterisation of the array, namely, cylinder diameter and inter-stem spacing. A larger proportion of flow scales is contained within the largest

25% of inter-stem values. This suggests that a considerable proportion of flow structures, and 'persistent features' are generated as a consequence of cylinder interactions, particularly clusters.

- The relationship between S_t and Re_d for the RandoSticks configuration is the opposite to what has been both measured from isolated cylinders, and proposed in analytical models of dispersion. For large Re_d, a synchronisation between surface wave oscillation and shedding frequency, known as seiching, was found. This occurs when both periodic phenomena are in-phase, and thus, no systematic error is expected from this. Assuming no issues with the sampling, the increase in trapping times can be the result of sheltering delaying the formation of vortices, and the existence of large trapping areas for groups of cylinders located within $5d$ of each other.

- The trends for the turbulent energy production$\sim$dissipation relationship, presented by Nepf (1999), are similar enough to be connected. The proportionality has smaller variations that are expected to 'stabilise' for inviscid flow conditions.

- The comparison between longitudinal dispersion and hydrodynamic scales shows dominant drivers of dispersion at different Re_d regimes. Large dispersion values, caused predominantly by the mean flow distribution, and a molecular diffusion dependency, is found for $Re_d < 40$. In this range, $C_D^{3/2}$, is the dominant term. Once turbulence becomes dominant, $40 < Re_d < 200$, the D_x^* curve follows a trend similar to that of $\langle \overline{u'u'} \rangle$. After $Re_d \approx 300$, the constant dispersive fluxes become dominant. The role of trapping requires a careful analysis of the time scales. The White and Nepf (2003) model for vortex trapping has limited applicability for the RandoSticks configuration, and possible arrays with diameter distributions.

- Two main regimes for D_y^* were found. Turbulence is found to be dominant for $Re_d < 250$. No dependency with Re_d is found for larger flows. This goes in agreement with previous results stating the main dependency of D_y^* with solid volume fraction.

Chapter 8. CONCLUSIONS

This work started under the premise that the difference between estimates of dispersion in real vegetation, and results from empirical and analytical models, are the results of simplified laboratory configurations, from which most of the current theory is derived. Adding the stem diameter variability was a step towards capturing the complexities of real vegetated systems, while still allowing for a detailed characterisation of hydrodynamics and mixing over a wide range of scales: from single stems, to representative areas of the flow. For this, the novel experimental system, and the comprehensive result dataset were crucial. The results from the physical interpretation of these results, and the comparison with existing evidence, are summarised in this chapter. From these, the main findings are summed up graphically, where the different identified flow regimes and dominant processes are discussed. It is expected that these findings become the baseline for the development of future dispersion models in vegetation.

8.1. Summary of Results

Chapter 3

- This chapter presented results from 2 experimental datasets: concentration and Surface PIV measurements from a pseudo-random, artificial, emergent vegetation array, with 4 mm diameter stems, in a 300 mm-wide flume at the University of Warwick; and two-point velocity statistics in a 300 mm-wide flume, with a reduced version of the RandoSticks configuration, using only 20 mm diameter stems, at the University of Sheffield. The objectives of these independent studies were to study the hydrodynamic assumptions leading to the main longitudinal dispersion model, and to analyse the behaviour of wake interactions, through velocity statistics, and their implications on the mixing of passive solutes.
- The hydrodynamic quantities included in White and Nepf (2003) model for longitudinal dispersion were calculated from SPIV-derived data. The results underpredict dispersion coefficients for flows where vortex shedding becomes the dominant driver of mass and momentum transfer.
- Spatial velocity statistics can be used to outline the extents of the cylinder wakes.

- Single-point and two-point correlation functions along wake centrelines and transects for two interacting cylinders show the existence and life-span of dominant structures in vegetated flow fields. Pseudo-empirical approximations can be obtained from single-point statistics by applying appropriate dissipation corrections.
- Interacting cylinders change the shape of the wake (centreline). Also, the effects of stems on the mean velocity field extend beyond the immediate vicinity of the stems.
- Finally, it is found that appropriate empirical assumptions are needed to represent Lagrangian diffusion models using Eulerian statistics. Omitting the role of coherent structures in estimates of turbulent diffusion and secondary wake dispersion will tend to underestimate their effects on longitudinal mixing.

Chapter 5

- Two distinct regimes, separated at Re_d approx. 400, can be found from the variation of D_x with Re_d, suggesting different physical processes driving dispersion.
- The ratio of transverse diffusive to advective transport (i.e. D_y^*) does not vary with Re_d.
- For the range $Re_d < 400$, skewness variation and predictive performance of dispersion coefficient seem to indicate that dispersion in this range is not strictly Fickian.
- Variation in Initial Conditions do not change the behaviour of the dispersion coefficients.
- D_x^* results from the Randosticks configuration compare well with previous results for artificial vegetation; and slightly under predicts mixing when compared to results from real vegetation. Closer agreement with some natural species is found for D_y^*.

Chapter 6

- The x-skewness from the global u velocity distribution suggests the existence of relevant trapping zones, even at high Re_d.
- Turbulent fluxes seem isotropic in a double-averaged sense, but not locally.
- Apparent discontinuity in (random) turbulence quantities, at $Re_d \approx 500$. 1st order quantities follow a smooth trend.
- Turbulent fluxes are smaller than x-dispersive fluxes, but larger than y-dispersive ones.
- Shear virtual stresses are negligible, in a double-averaged sense. Locally can indicate zones of momentum transfer.
- Models for C_D from homogeneous arrays apply acceptably for the RandoSticks.
- Drag coefficients and forces follow the same trend as results from artificial vegetation
- Disaggregating viscous and form C_D, suggests that Ergun's model is valid for the RandoSticks for some Re_d ranges.

Chapter 7

- Time-dependent correlations reveal scales of coherent structures, for a richer range of scales than just the diameters sizes.
- y-space correlations reveal 'persistent features' inherent to the mean flow field, i.e. wakes, trapping and acceleration zones. These are independent of flows.
- x-space correlations reveal scales of recirculation regions. Also independent of Re_d.
- Spatial correlations, following Ricardo (2014) method, obscure coherent structures.
- Time and space-dependent statistics provide lower and upper limits to length scales.
- This broad range of scales, and thus higher than morphological ones suggests cylinder interactions and the formation of clusters.
- Only a subset of length scales is statistically relevant. A heuristic is proposed, i.e. minimum 5% of the spectra and below a geometric boundary (e.g. flow depth).
- Flow-based length scales are uncorrelated with morphological ones.
- Based on length scales Cumulative Distribution Functions, a considerable proportion of flow structures and 'persistent features' are generated by interacting cylinders, e.g. clusters.
- Found $S_t(Re_d)$ relationship is opposite to single-cylinder results of vortex and trapping models.
- Seiching occurs for $Re_d > 400$. This occurs in lock-in frequencies, so no biases are assumed.
- Increase in trapping times, from $S_t(Re_d)$, can be explained physically as sheltering-induced delayed shedding, and large trapping zones for cylinders within $s_n < 5d$ of each other.
- The production~dissipation relation proposed by Nepf (1999) seems somewhat valid. Expected to be true as inviscid flow is approached.
- Different drivers of dispersion over distinct Re_d ranges, for D_x^* and D_y^*.
- Turbulence flux, $\langle\overline{u'u'}\rangle$ dominant for $100 < Re_d < 200$. Dispersive flux constant. $\langle\overline{u'u'}\rangle$ decreases until asymptotic at $Re_d \approx 300$.
- $\langle\overline{u'u'}\rangle$ and $\langle\overline{u}''\overline{u}''\rangle$ constant, but dispersive flux dominant for $Re_d > 300$.
- It is hypothesised that $\langle\overline{u}''\overline{u}''\rangle$ and D_m dominant for $Re_d < 40$, and $C_D^{3/2}$ main term.
- Hypothesised that $\langle\overline{u'u'}\rangle$ reaches a peak at $Re_d \approx 70$ (periodic shedding). D_x^* expected to be similar to $\langle\overline{u'u'}\rangle$ for $40 < Re_d < 200$, also, $\langle\overline{u}''\overline{u}''\rangle$ reaches asymptote in this range.
- Turbulence, $\langle\overline{v'v'}\rangle$ dominant for D_y^*, i.e. both curves expected similar, in $Re_d < 250$
- D_y^* independent of Re_d for $Re_d > 250$, in agreement with previous results.

8.2. Dispersion processes in a RandoSticks configuration

The figure shown below summarises the findings from dispersion and velocity measurements. The general trends of the non-dimensionalised dispersion coefficients, alongside the main drivers of mass transport are presented. These findings are extrapolated to ranges outside of the current experiments, based on previous studies.

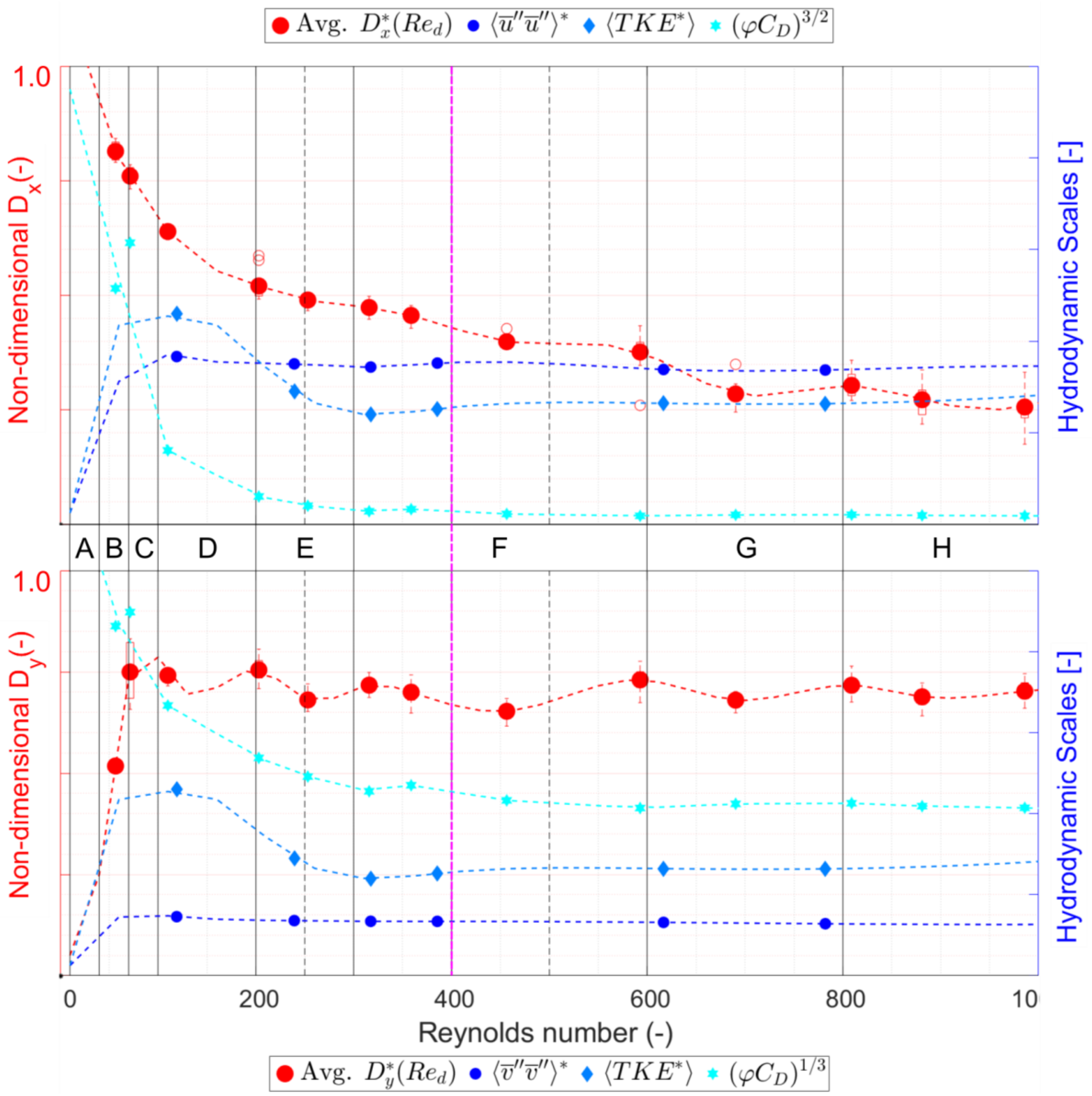

Flow ranges

- **Stokes flow range ($1 < Re_d < 10$):** In this range viscosity dominates the velocity profile. Longitudinal dispersion is dominated by the time scales of molecular diffusion, since, in the absence of turbulence, that is the only mechanism for mass to exit boundary layers.
- **A – Increase of recirculation area ($10 < Re_d < 40$):** Flow instabilities appear in the stem boundary layers, generating enclosed and stable recirculation areas. An incipient transition to turbulence occurs, which reduces the trapping times and thus longitudinal dispersion. Both velocity heterogeneities and turbulence increase in this range, thereby dominating mass transport.
- **B – Starts of mass exchanges and oscillatory wakes ($40 < Re_d < 70$):** Further decrease in longitudinal dispersion is observed as mass transport pathways are opened between recirculation zones and the outer flow. Oscillatory instabilities are associated with increased rates of mass and momentum transfer, thus, turbulence starts to become dominant for both longitudinal and transverse dispersion in this range. For part of this range, and all previous ones, it can be seen that the trends of longitudinal dispersion and the factor $(\varphi C_D)^{3/2}$ proposed by White and Nepf (2003), are correlated. Therefore, the model can be concluded to be valid within this range.
- **C – Periodic vortex shedding ($70 < Re_d < 100$):** Shed vortices become the main carriers of energy, and thus of mass and momentum transfer. Periodic oscillations are more relevant to dispersion than mean flow heterogeneities. In this range, the temporal features of these coherent structures dominate lateral dispersion, which confirms the results presented by Tanino and Nepf (2008b), for this range. The importance of temporal features and the existence and life span of flow structures indicates that from this range and larger flows, the statistical treatment of velocity correlations, requires the inclusion of turbulence terms.
- **D – Dominant periodic features ($100 < Re_d < 200$):** Consistent acceleration of vortex shedding and increased shear promote vortex break down and thus transition to three-dimensionality. These combined effects reduce the contribution of turbulent structures to the lateral and longitudinal spread of mass. Instead, increased turbulence production further reduces trapping times, and helps spread mass.
- **E – Dominant dispersive fluxes ($200 < Re_d < 300$):** Early transition to three-dimensional vortex shedding regimes, due to both quicker vortex break down and early, sporadic transition to turbulence in the vortex formation region, limits the effect turbulence has in dispersion. On the other hand, increased shear and wider differences between local

advective acceleration gaps and velocity defect zones indicate that dispersive fluxes (cf. mean flow heterogeneities) become the dominant drivers of dispersion in both directions.

- **F – Constant turbulent and dispersive fluxes ($300 < Re_d < 600$):** In this range, the ratio between turbulent and dispersive fluxes to advection becomes constant, which signifies the transition to a purely advective dispersion regime. As the profile of non-dimensional longitudinal dispersion suggests, this value tends to plateau in this range.
- **G – Decrease in global streamwise velocity skewness ($600 < Re_d < 800$):** The slight decrease in the curve of non-dimensional longitudinal dispersion is correlated to the decrease in the skewness of the global longitudinal velocity PDF. This normalisation of the u probability function represents a decrease in the proportion of the flow field occupied by trapping zones and boundary layers.
- **H – Inviscid flow ($Re_d > 800$):** From the evidenced gathered, longitudinal and transverse dispersion plateau in this range, at least as far as it is significant for ecohydraulics. Turbulence is effective in locally spreading matter to experience average vegetated conditions, thus shear, and effects that generate skewness in concentration distributions become less relevant. Traces assimilate Gaussian shapes shortly after injection. It is hypothesised that for ranges E – H, dispersion length scale analogy can be applied to the flow. For this further alternatives to accurately capture vegetation morphology into significant length scales are needed.

Chapter 9. FURTHER WORK

Throughout this project, the experimental data has shown unprecedented potential to explore the underlying, multiscale processes governing flow and dispersion in vegetated flow. The experimental results can provide researchers with a benchmark dataset for comparison and validation of numerical models, as well as the detailed information to test and explore some of the fundamental questions of turbulence. Some of the

- Recently, a comprehensive CFD study estimating longitudinal and transverse dispersion in random, cylinder array configurations; spanning different densities, spacing and diameter distributions—including the RandoSticks presented in this work—has been undertaken by Stovin *et al.*, (2022). A natural extension of this work is to validate the results for similar flows, and thus help develop a numerical tool that can provide reliable results for a wider range of experimental conditions and real-life scenarios.
- Due to limits in terms of scope and time, detailed analysis of coherent structures, and the application of decomposition functions on the flow fields measured herein cannot be conducted. It is believed that the dataset obtained presents a valuable opportunity to determine the main time- and space-persistent modes in a cylinder array. Further, this can serve to explore the evolution, life-span and and energy relations of array flow structures and their role on the transport of mass.
- This study revealed the existence of multiple flow scales, which are believed to be caused by various levels of interactions between neighouring cylinders. A detailed analysis of the cylinder interactions, beyond the comprehensive study of Sumner (2010), and extending to different diameters, and multiple stems needs to be performed. This potential study should look at relevant thresholds for the creation of clusters, their impact on sheltering and the creation of preferential flow paths; and which would benefit greatly from the experimental lessons in this study and the conclusions derived.
- The novel experimental system presented required the use of bespoke physical solutions to illuminate areas within obstructed flow fields, alongside heuristic techniques for the correction of light heterogeneities. Although the results have been shown remarkable, the author believes that this study will serve as a hinging point for further discussions on solutions for PIV and LIF applications in complex context.

REFERENCES

Aberle, J. and Järvelä, J. (2013) 'Flow resistance of emergent rigid and flexible floodplain vegetation', *Journal of Hydraulic Research*, 51(1), pp. 33–45. doi: 10.1080/00221686.2012.754795.

Abroug, I. *et al.* (2022) 'The Hydrodynamic Behavior of Vortex Shedding behind Circular Cylinder in the Presence of Group Focused Waves', *Fluids*, 7(1), pp. 1–16. doi: 10.3390/fluids7010004.

Adrian, R. J. (1986) 'Multi-point optical measurements of simultaneous vectors in unsteady flow-a review', *International Journal of Heat and Fluid Flow*, 7(2), pp. 127–145. doi: 10.1016/0142-727X(86)90062-7.

Adrian, R. J. and Westerweel, J. (2011) *Particle Image Velocimetry*. 1st edn. New York: Cambridge University Press.

Arcoumanis, C., McGuirk, J. J. and Palma, J. M. L. M. (1990) 'On the use of fluorescent dyes for concentration measurements in water flows', *Experiments in Fluids*, 10(2–3), pp. 177–180. doi: 10.1007/BF00215028.

Baek, K. O., Seo, I. W. and Jeong, S. J. (2006) 'Evaluation of Dispersion Coefficients in Meandering Channels from Transient Tracer Tests', *Journal of Hydraulic Engineering*, 132(10), pp. 1021–1032. doi: 10.1061/(asce)0733-9429(2006)132:10(1021).

Baj, P., Bruce, P. J. K. and Buxton, O. R. H. (2016) 'On a PLIF quantification methodology in a nonlinear dye response regime', *Experiments in Fluids*. Springer Berlin Heidelberg, 57(6), pp. 1–19. doi: 10.1007/s00348-016-2190-0.

Batchelor, G. K. (1949) 'Diffusion in a Field of Homogeneous Turbulence', *Australian Journal of Scientific Research, Series A: Physical Sciences*, 2, pp. 437–450.

Batchelor, G. K. (1951) 'Diffusion in a Field of Homogeneous Turbulence. II. Eulerian Analysis', *Mathematical Proceedings of the Cambridge Philosophical SOciety*, 48(2), pp. 345–362. doi: 10.1017/S0305004100027687.

Batchelor, G. K. (2000) *Introduction to fluid dynamics*. 3rd edn. Cambridge, UK: Cambridge University Press. doi: 10.1007/978-0-8176-8352-8_23.

Beer, T. and Young, P. C. (1983) 'Longitudinal Dispersion in Natural Streams.', *Environmental Engineering*, 109(5), pp. 1049–1067. doi: 10.1061/(asce)0733-9372(1983)109:5(1049).

Berger, E. and Wille, R. (1972) 'Periodic Flow Phenomena', *Annual Review of Fluid Mechanics*, 4(1), pp. 313–340. doi: 10.1146/annurev.fl.04.010172.001525.

Berkooz, G., Holmes, P. and Lumley, J. L. (1993) 'The proper orthogonal, decomposition in the analysis of turbulent flows', *Annual Review of Fluid Mechanics*, 25, pp. 539–575. doi: 10.1146/annurev.fluid.25.1.539.

Bindhu, C. V. and Harilal, S. S. (2001) 'Effect of the excitation source on the quantum-yield measurements of Rhodamine B laser dye studied using thermal-lens technique', *Analytical Sciences*, 17(1), pp. 141–144. doi: 10.2116/analsci.17.141.

Bioquest, A. (2019) *Fluorescence Spectrum Viewer*. Available at: https://www.aatbio.com/fluorescence-excitation-emission-spectrum-graph-viewer (Accessed: 19 July 2021).

Bokaian, A. and Geoola, F. (1984) 'Proximity-induced galloping of two interfering circular cylinders', *Journal of Fluid Mechanics*, 146, pp. 417–449. doi: 10.1017/S0022112084001932.

Boxall, J. B. and Guymer, I. (2007) 'Longitudinal mixing in meandering channels: New experimental data set and verification of a predictive technique', *Water Research*, 41(2), pp. 341–354. doi: 10.1016/j.watres.2006.10.010.

Burke, R. and Stolzenbach, K. (1983) 'Free surface flows through salt marsh grass', *Publication MITSG 83-16*. Cambridge, Massachusetts: MIT, pp. 1–252. Available at: Aquatic Plant Uptake.

Busari, A. O. and Li, C. W. (2016) 'Bulk drag of a regular array of emergent blade-type vegetation stems under gradually varied flow', *Journal of Hydro-Environment Research*, 12, pp. 59–69. doi: 10.1016/j.jher.2016.02.003.

Cantwell, B. and Coles, D. (1983) 'An experimental study of entrainment and transport in the turbulent near wake of a circular cylinder', *Journal of Fluid Mechanics*, 136, pp. 321–374. doi: 10.1017/S0022112083002189.

Chow, V. T. (1959) *Open-Channel Hydraulics*. 1st edn. McGraw Hill.

Computar (2018) 'Specifications H6Z0812 Camera Lens'. Computar. Available at: https://computar.com/resources/files_v2/219/H6Z0812_Spec0604.pdf.

Coppeta, J. and Rogers, C. (1998) 'Dual emission laser induced fluorescence for direct planar scalar behavior measurements', *Experiments in Fluids*, 25(1), pp. 1–15. doi: 10.1007/s003480050202.

Coppin, P. A., Raupach, M. R. and Legg, B. J. (1986) 'Experiments on scalar dispersion within a model plant canopy part II: An elevated plane source', *Boundary-Layer Meteorology*, 35(1–2), pp. 167–191. doi: 10.1007/BF00117307.

Corredor-Garcia, J. L. *et al.* (2020) 'On the Use of Surface PIV for the Characterization of Wake Area in Flows Through Emergent Vegetation', in Kalinowska, M., Mrokowska, M., and Rowiński, P. (eds) *Recent Trends in Environmental Hydraulics. GeoPlanet: Earth and Planetary Sciences*. Cham, Switzerland: Springer-Verlag, pp. 43–52.

Coutanceau, M. and Bouard, R. (1977) 'Experimental determination of the main features of the viscous flow in the wake of a circular cylinder in uniform translation. Part 1. Steady flow', *Journal of Fluid Mechanics*, 79(2), pp. 231–256. doi: 10.1017/S0022112077000135.

Crimaldi, J. P. (1997) 'The effect of photobleaching and velocity fluctuations on single-point LIF measurements', *Experiments in Fluids*, 23(4), pp. 325–330. doi: 10.1007/s003480050117.

Crimaldi, J. P. (2008) 'Planar laser induced fluorescence in aqueous flows', *Experiments in Fluids*, 44(6), pp. 851–863. doi: 10.1007/s00348-008-0496-2.

Crowdy, D. and Marshall, J. (2006) 'Conformal Mappings between Canonical Multiply Connected Domains', *Computational Methods and Function Theory*, 6(1), pp. 59–76. doi: 10.1007/bf03321118.

Csanady, G. T. (1973) *Turbulent Diffusion in the Environment*. 1st edn. Dordrecht, Holland: D. Reidel Publishing Company. doi: 10.1007/978-94-010-2527-0.

Currie, I. G. (2012) *Fundamental Mechanics of Fluids*. 4th edn. Boca Raton, FL: CRC Press, Taylor and Francis Press.

Defina, A. and Pradella, I. (2014) 'Vortex-induced cross-flow seiching in cylinder arrays', *Advances in Water Resources*. Elsevier Ltd, 71, pp. 140–148. doi:

10.1016/j.advwatres.2014.06.002.

DeGroot, M. H. and Schervish, M. J. (2012) *Probablity and Statistics*. 4th edn. Boston, Massachusetts: Pearson Education.

Dimotakis, P. E., Miake-Lye, R. C. and Papantoniou, D. A. (1983) ‘Structure and dynamics of round turbulent jets’, *Physics of Fluids*, 26(11), pp. 3185–3192. doi: 10.1063/1.864090.

Distelhoff, M. F. W. and Marquis, A. J. (1998) ‘An LIF line scan system for the measurement of scalar concentration in a continuously operated stirred tank’, *Experiments in Fluids*, 25(1), pp. 77–88. doi: 10.1007/s003480050210.

Van Dyke, M. (1988) *An Album of Fluid Motion*. 4th edn. Stanford, California: The Parabolic Press.

Ergun, S. (1952) ‘Fluid flow through packed columns’, *Chemical Engineering Progress*, 48, pp. 89–94.

Ferreira, R. M. L., Ricardo, A. M. and Franca, M. J. (2009) ‘Discussion of “Laboratory Investigation of Mean Drag in a Random Array of Rigid, Emergent Cylinders” by Yukie Tanino and Heidi M. Nepf’, *Journal of Hydraulic Engineering*, 135(8), pp. 690–693.

Ferrier, A. J., Funk, D. R. and Roberts, P. J. W. (1993) ‘Application of optical techniques to the study of plumes in stratified fluids’, *Dynamics of Atmospheres and Oceans*, 20(1–2), pp. 155–183. doi: 10.1016/0377-0265(93)90052-9.

Fey, U., König, M. and Eckelmann, H. (1998) ‘A new Strouhal-Reynolds-number relationship for the circular cylinder in the range 47<Re<2×105’, *Physics of Fluids*, 10(7), pp. 1547–1549. doi: 10.1063/1.869675.

Finnigan, J. J. (1985) ‘Turbulent transport in flexible plant canopies.’, in Hutchinson, B. A., Hicks, B. B., and Reidel, D. (eds) *The forest-atmosphere interactions*, pp. 443–480. doi: 10.1007/978-94-009-5305-5_28.

Finnigan, J. J. (2000) ‘Turbulence in Plan Canopies’, *Annual Review of Fluid Mechanics*, 32(1), pp. 519–571. doi: 10.1146/annurev.fluid.32.1.519.

Fischer, H. B. (1967) ‘The Mechanics of Dispersion in Natural Streams’, *Journal of the Hydraulics Division, Proceedings of the American Society of Civil Engineers*, 93(6), pp. 187–216.

Fischer, H. B. (1973) ‘Longitudinal Dispersion and Turbulent Mixing in Open-Channel Flow’, *Annual Review of Fluid Mechanics*, 5, pp. 59–78. doi: 10.1146/annurev.fl.05.010173.000423.

Fischer, H. B. *et al.* (1979) *Mixing in inland and coastal waters.* 1st edn. San Diego, CA: Academic Press.

FLIR (2017) ‘Technical Reference FLIR FLEA 3, USB3 Vision’. FLIR, pp. 1–128. Available at: https://www.ptgrey.com/support/downloads/10120.

FLIR (2018) ‘Technical Reference Blackfly®s BFS-U3-23S3’. FLIR.

Gavrilenko, V. I. and Noginov, M. A. (2006) ‘Ab initio study of optical properties of rhodamine 6G molecular dimers’, *Journal of Chemical Physics*, 124(4). doi: 10.1063/1.2158987.

Gerrard, J. H. (1966) ‘The mechanics of the formation region of vortices behind bluff bodies’, *Journal of Fluid Mechanics*. University of Sheffield Library, 25(2), pp. 401–413. doi: 10.1017/S0022112066001721.

Gerrard, J. H. (1978) ‘The Wakes of Cylindrical Bluff Bodies at Low Reynolds Number’, *Philosophical Transactions of the Royal Society of London. Series A, Mathematical and Physical Sciences*, 288(1354), pp. 351–382.

Ghisalberti, M. and Nepf, H. (2005) 'Mass transport in vegetated shear flows', *Environmental Fluid Mechanics*, 5(6), pp. 527–551. doi: 10.1007/s10652-005-0419-1.

Ghisalberti, M. and Nepf, H. M. (2004) 'The limited growth of vegetated shear layers', *Water Resources Research*, 40(7), pp. 1–12. doi: 10.1029/2003WR002776.

Ghisalberti, M. and Nepf, H. M. (2009) 'Shallow flows over a permeable medium: The hydrodynamics of submerged aquatic canopies', *Transport in Porous Media*, 78(3 SPEC. ISS.), pp. 385–402. doi: 10.1007/s11242-009-9434-x.

Giménez-Curto, L. A. and Corniero Lera, M. A. (1996) 'Oscillating turbulent flow over very rough surfaces', *Journal of Geophysical Research: Oceans*, 101(C9), pp. 20745–20758. doi: 10.1029/96JC01824.

Gray, W. G. and Lee, P. C. Y. (1977) 'On the theorems for local volume averaging of multiphase systems', *International Journal of Multiphase Flow*, 3(4), pp. 333–340. doi: 10.1016/0301-9322(77)90013-1.

Guymer, I. (1998) 'Longitudinal Dispersion in Sinuous Channel with Changes in Shape', *Journal of Hydraulic Engineering*, 124(1), pp. 33–40. doi: 10.1061/(asce)0733-9429(1998)124:1(33).

Higham, J. (2017) 'The application of modal decomposition techniques for the analysis of environmental flows'. Sheffield, UK: The University of Sheffield. Available at: http://etheses.whiterose.ac.uk/17296/.

Hinterwaldner, I. (2015) 'Model building with wind and water: Friedrich Ahlborn's photo-optical flow analysis', *Studies in History and Philosophy of Science Part A*. Elsevier Ltd, 49, pp. 1–17. doi: 10.1016/j.shpsa.2014.10.003.

Hinze, J. O. (1975) *Turbulence*. 2nd edn. McGraw Hill.

Holmes, P. *et al.* (2012) *Turbulence, Coherent Structures, Dynamical Systems and Symmetry*. 2nd edn. New York: Cambridge University Press.

Huang, Y. H. *et al.* (2008) 'Advection, dispersion, and filtration of fine particles within emergent vegetation of the Florida Everglades', *Water Resources Research*, 44(4), pp. 1–13. doi: 10.1029/2007WR006290.

Hussain, A. K. M. F. (1983) 'Coherent structures - Reality and myth', *Physics of Fluids*, 26(10), pp. 2816–2850. doi: 10.1063/1.864048.

Jadhav, R. S. and Buchberger, S. G. (1995) 'Effects of vegetation on flow through free water surface wetlands', *Ecological Engineering*, 5(4), pp. 481–496. doi: 10.1016/0925-8574(95)00039-9.

Jalonen, J. and Järvelä, J. (2014) 'Estimation of drag forces caused by natural woody vegetation of different scales', *Journal of Hydrodynamics*, 26(4), pp. 608–623. doi: 10.1016/S1001-6058(14)60068-8.

Jiang, J., Zhang, G. and Zhou, F. (2003) 'Distortion correction for a wide-angle lens based on real-time digital image processing', *Optical Engineering*, 42(7), p. 2029. doi: 10.1117/1.1580155.

Jirka, G. H. and Uijttewaal, W. S. J. (2004) 'Shallow Flows: a definition', in Jirka, G. H. and Uijttewaal, W. S. J. (eds) *Shallow Flows*. Delft: CRC Press, Taylor and Francis Press, pp. 3–11.

Kähler, C. J. (2004) *The significance of coherent flow structures for the turbulent mixing in wall-bounded flows*. Georg-August-University zu Göttingen.

Kaimal, J. C. and Finnigan, J. J. (1994) *Atmospheric boundary layer flows. Their structucture and measurement*. 1st edn. New York: Oxford University Press.

Karasso, P. S. and Mungal, M. G. (1997) 'PLIF measurements in aqueous flows using the Nd: YAG laser', *Experiments in Fluids*, 23(5), pp. 382–387. doi: 10.1007/s003480050125.

Karman, T. and Howarth, L. (1938) 'On the Statistical Theory of Isotropic Turbulence', *Proceedings of the Royal Society of London. Series A-Mathematical and Physical Sciences*, 164(917), pp. 192–215.

Kármán, T. V. (1911) 'On the mechanism of the drag a moving body experiences in a fluid (2013 reprint)', *Progress in Aerospace Sciences*. Elsevier, 59, pp. 16–19. doi: 10.1016/j.paerosci.2013.04.001.

Kasarova, S. N. *et al.* (2007) 'Analysis of the dispersion of optical plastic materials', *Optical Materials*, 29(11), pp. 1481–1490. doi: 10.1016/j.optmat.2006.07.010.

Keane, R. D. and Adrian, R. J. (1992) 'Theory of cross-correlation analysis of PIV images', *Applied Scientific Research*, 49(3), pp. 191–215. doi: 10.1007/BF00384623.

Khabbouchi, I. *et al.* (2014) 'Effects of free-stream turbulence and Reynolds number on the separated shear layer from a circular cylinder', *Journal of Wind Engineering and Industrial Aerodynamics*. Elsevier, 135, pp. 46–56. doi: 10.1016/j.jweia.2014.10.005.

Khintchine, A. (1934) 'Korrelationstheorie der stationären stochastischen Prozesse', *Mathematische Annalen*, 109(1), pp. 604–615. doi: 10.1007/BF01449156.

Kim, S. J. and Stoesser, T. (2011) 'Closure modeling and direct simulation of vegetation drag in flow through emergent vegetation', *Water Resources Research*, 47(10), pp. 2–15. doi: 10.1029/2011WR010561.

Kim, T. and Christensen, K. T. (2018) 'Flow interactions between streamwise-aligned tandem cylinders in turbulent channel flow', *AIAA Journal*, 56(4), pp. 1421–1433. doi: 10.2514/1.J056186.

Kinnmark, I. P. E. and Gray, W. G. (1984) 'An exposition of the distribution function used in proving the averaging theorems for multiphase flow', *Advances in Water Resources*, 7(3), pp. 113–115. doi: 10.1016/0309-1708(84)90038-1.

Kiya, M., Tamura, H. and Arie, M. (1980) 'Vortex shedding from a circular cylinder in moderate-Reynolds-number shear flow', *Journal of Fluid Mechanics*, 141, pp. 721–735. doi: 10.1017/S0022112080001899.

Koch, D. L. and Brady, J. F. (1985) 'Dispersion in fixed beds', *Journal of Fluid Mechanics*, 154, pp. 399–427.

Koch, D. L. and Brady, J. F. (1986) 'The effective diffusivity of fibrous media', *AIChE Journal*, 32(4), pp. 575–591. doi: 10.1002/aic.690320407.

Koch, D. L. and Ladd, A. J. C. (1997) 'Moderate Reynolds number flows through periodic and random arrays of aligned cylinders', *Journal of Fluid Mechanics*, 349, pp. 31–66. doi: 10.1017/S002211209700671X.

Kolmogorov, A. N. (1941a) 'Dissipation of energy in the locally isotropic turbulence', *Dokl. Akad. Nauk SSSR. English Translation in Proceedings of the Royal Society of London. Series A. Vol 434,* *pp. 15-17*, 32, pp. 16–18.

Kolmogorov, A. N. (1941b) 'The Local Structure of Turbulence in Incompressible Viscous Fluid for Very Large Reynolds Numbers', *Dokl. Akad. Nauk SSSR. English Translation in Proceedings of the Royal Society of London. Series A. Vol 434, pp. 9-13*, 30.

Kompenhans, J. and Hoecker, R. (1989) 'Investigation of turbulent flows by means of particle image velocimetry', in *Proceedings of the Fifth International Symposium on Flow Visualization*. Prague, p. 6.

Kompenhans, J. and Reichmuth, J. (1986) 'No Title', in *Advanced Instrumentation for Aero Engine Components*. Goettingen, Germany: AGARD Conference Proceedings, pp. 1–35.

Koper, C. A., Sadeh, W. Z. and Turner, R. E. (1978) 'A relation between the lagrangian and eulerian turbulent velocity autocorrelations', *AIAA Journal*, 16(9), pp. 969–975. doi: 10.2514/3.60991.

Kovasznay, L. S. G. (1949) 'Hot-wire investigation of the wake behind cylinders at low Reynolds numbers', *Proceedings of the Royal Society of London. Series A. Mathematical and Physical Sciences*, 198(1053), pp. 174–190. doi: 10.1098/rspa.1949.0093.

Landau, L. D. and Lifshiftz, E. M. (1987) *Fluid Mechanics*. 2nd edn. Oxford, UK: Pergamon Press.

Law, A. W. K. and Wang, H. (2000) 'Measurement of mixing processes with combined digital particle image velocimetry and planar laser induced fluorescence', *Experimental Thermal and Fluid Science*, 22(3–4), pp. 213–229. doi: 10.1016/S0894-1777(00)00029-7.

Leonard, L. A. and Luther, M. E. (1995) 'Flow Hydrodynamics in Tidal Marsh Canopies', *Limnology and Oceanography*, 40(8), pp. 1474–1484. Available at: https://www.jstor.org/stable/2838503.

Lightbody, A. F. and Nepf, H. M. (2006a) 'Prediction of near-field shear dispersion in an emergent canopy with heterogeneous morphology', *Environmental Fluid Mechanics*, 6(5), pp. 477–488. doi: 10.1007/s10652-006-9002-7.

Lightbody, A. F. and Nepf, H. M. (2006b) 'Prediction of velocity profiles and longitudinal dispersion in emergent salt marsh vegetation', *Limnology and Oceanography*, 51(1 I), pp. 218–228. doi: 10.4319/lo.2006.51.1.0218.

Liu, H. T. *et al.* (1977) 'Application of a Fluorescence Technique to Dye-Concentration Measurements in a Turbulent Jet', in *Proceedings of the Symposium on Flow Measurements in Open Channels and Fluid Conduits*, pp. 423–431.

Liu, J. T. C. (1988) 'Contributions to the Understanding of Large-Scale Coherent Structures in Developing Free Turbulent Shear Flows', *Advances in Applied Mechanics*, 26(C), pp. 183–309. doi: 10.1016/S0065-2156(08)70289-8.

De Loera, J. A., Rambau, J. and Santos, F. (2010) *Triangulations: Structures for Algorithms and Applications*. 1st edn. Berlin: Springer Verlag.

Lumley, J. L. (1962) 'The Mathematical Nature of the Problem of Relating Lagrangian and Eulerian Statistical Functions in Turbulence', in *Mecanique de La Turbulence*. Paris: Éditions du Centre National de la Recherche Scientifique, pp. 17–26.

Luo, D. *et al.* (2014) 'Comparative assessment of PANS and DES for simulation of flow past a circular cylinder', *Journal of Wind Engineering and Industrial Aerodynamics*. Elsevier, 134, pp. 65–77. doi: 10.1016/j.jweia.2014.08.014.

Maurer, J. and Libchaber, A. (1979) 'Rayleigh-Bénard experiment in liquid helium; frequency locking and the onset of turbulence', *Le Journal de Physique*, 40, pp. L419–L423.

Mauri, R. and Haber, S. (1986) 'Applications of Wiener's Path Integral for the Diffusion of Brownian Particles in Shear Flows', *SIAM Journal on Applied Mathematics*, 46(1), pp. 49–55.

Mayerhöfer, T. G., Pahlow, S. and Popp, J. (2020) 'The Bouguer-Beer-Lambert Law: Shining Light on the Obscure', *ChemPhysChem*, 21, pp. 2029–2046. doi: 10.1002/cphc.202000464.

McCroskey, W. J. (1977) 'Some current research in unsteady fluid dynamics', *Journal of Fluids Engineering*, 99(1), pp. 8–39.

Ben Meftah, M. and Mossa, M. (2013) 'Prediction of channel flow characteristics through square arrays of emergent cylinders', *Physics of Fluids*, 25(4), pp. 1–21. doi: 10.1063/1.4802047.

Monin, A. S. and Yaglon, A. M. (1971) *Statistical Fluid Mechanics: Mechanics of Turbulence Vol. 1*. 1st edn. Cambridge, Massachusetts: MIT Press.

NAVITAR (2016) 'Lens Specifications - NMV4WA'. Navitar Machine Vision Lenses. Available at: https://navitar.com/products/imaging-optics/low-magnification-video/navitar-machine-vision/navitar-machine-vision-12-format/.

Nepf, H. (2004) 'Vegetated Flow Dynamics Introduction : Scales of Morphology and Flow in a Tidal Marsh', *Coastal and Estuarine Studies*, 59, pp. 137–163.

Nepf, H. M. (1999) 'Drag , turbulence , and diffusion in flow through emergent vegetation', *American Geophysical Union*, 35(2), pp. 479–489. doi: http://dx.doi.org/10.1029/1998WR900069.

Nepf, H. M. *et al.* (2007) 'Transport in aquatic canopies', in Gayev, Y. A. and Hunt, J. C. (eds) *Flow and Transport Processes with Complex Obstructions. NATO Science Series*. Dordrecht: Springer, pp. 221–250. doi: 10.1007/978-1-4020-5385-6_6.

Nepf, H. M. (2012) 'Flow and transport in regions with aquatic vegetation', *Annual Review of Fluid Mechanics*, 44, pp. 123–142. doi: 10.1146/annurev-fluid-120710-101048.

Nepf, H. M., Mugnier, C. G. and Zavistoski, R. A. (1997) 'The effects of vegetation on longitudinal dispersion', *Estuarine, Coastal and Shelf Science*, 44(6), pp. 675–684. doi: 10.1006/ecss.1996.0169.

Nepf, H. M., Sullivan, J. A. and Zavitoski, R. A. (1997) 'A model for diffusion within an emergent plant canopy', *Limnology and Oceanography*, 42(8), pp. 1735–1745.

Nepf, H. M. and Vivoni, E. R. (2000) 'Flow structure in depth-limited, vegetated flow', *Journal of Geophysical Research: Oceans*, 105(C12), pp. 28547–28557. doi: 10.1029/2000jc900145.

Nikora, V. *et al.* (2007) 'Double-Averaging Concept for Rough-Bed Open-Channel and Overland Flows: Applications', *Journal of Hydraulic Engineering*, 133(8), pp. 884–895. doi: 10.1061/(asce)0733-9429(2007)133:8(884).

Nikora, V. *et al.* (2013) 'Spatially Averaged Flows over Mobile Rough Beds: Definitions, Averaging Theorems, and Conservation Equations', *Journal of Hydraulic Engineering*, 139(8), pp. 803–811. doi: 10.1061/(asce)hy.1943-7900.0000738.

Nikora, V. I. (2000) 'Comment on "Drag, turbulence, and diffusion in flow through emergent vegetation" by H. M. Nepf', *Water Resources Research*, 36(7), pp. 1985–1986. doi: 10.1029/2000wr900071.

Nishihara, G. N. and Terada, R. (2010) 'Spatial variations in nutrient supply to the red algae Eucheuma serra (J. Agardh) J. Agardh', *Phycological Research*, 58(1), pp. 29–34. doi: 10.1111/j.1440-1835.2009.00555.x.

Nortek (2018) 'Vector (ADV) Manual'. Nortek.

Paranthoën, P. *et al.* (1999) 'Characteristics of the near wake of a cylinder at low Reynolds numbers', *European Journal of Mechanics, B/Fluids*, 18(4), pp. 659–674. doi: 10.1016/S0997-7546(99)00105-3.

Philip, J. R. (1967) 'Relation between Eulerian and Lagrangian statistics', *Physics of Fluids*, 10, pp. S69–S71. doi: 10.1063/1.1762507.

Poggi, D., Katul, G. G. and Albertson, J. D. (2004a) 'A note on the contribution of dispersive fluxes to momentum transfer within canopies', *Boundary-Layer Meteorology*, 111, pp. 615–621. doi: 10.1023/B:BOUN.0000016563.76874.47.

Poggi, D., Katul, G. G. and Albertson, J. D. (2004b) 'Momentum Transfer and Turbulent Kinetic Energy Budgets Within a Dense Model Canopy', *Boundary Layer Meteorology*, 111, pp. 589–614.

Pope, S. B. (2000) *Turbulent Flows*. 1st edn. Cambridge University Press.

Raffel, M. *et al.* (2007) *Particle Image Velocimetry: A Practical Guide*. 2nd edn. Berlin: Springer Verlag.

Raffel, M. *et al.* (2018) *Particle Image Velocimetry: A practical guide*. 3rd edn. Berlin: Springer Verlag.

Raupach, M. R. (1992) 'Drag and drag partition on rough surfaces', *Boundary-Layer Meteorology*, 60(4), pp. 375–395. doi: 10.1007/BF00155203.

Raupach, M. R., Antonia, R. A. and Rajagopalan, S. (1991) 'Rough-wall turbulent boundary layers', *Applied Mechanics Review*, 44(1), pp. 1–25. doi: https://doi.org/10.1115/1.3119492.

Raupach, M. R., Coppin, P. A. and Legg, B. J. (1986) 'Experiments on scalar dispersion within a model plant canopy part I: The turbulence structure', *Boundary-Layer Meteorology*, 35(1–2), pp. 21–52. doi: 10.1007/BF00117300.

Raupach, M. R., Finnigan, J. J. and Brunet, Y. (1996) 'Coherent Eddies and Turbulence in Vegetation Canopies: The Mixing-Layer Analogy', *Boundary-Layer Meteorology*, 78, pp. 351–382.

Raupach, M. R. and Shaw, R. H. (1982) 'Averaging procedures for flow within vegetation canopies', *Boundary-Layer Meteorology*, 22(1), pp. 79–90. doi: 10.1007/BF00128057.

Raupach, M. R. and Thom, A. S. (1981) 'Turbulence in and above plant canopies.', *Annual Review of Fluid Mechanics*, 13(1), pp. 97–129.

Reynolds, O. (1883) 'An experimental investigation of the circumstances which determine whether the motion of water shall be direct or sinuous and the law of resistance', *Philosophical Transactions of the Royal Society*, 174(1883), pp. 935–982.

Reynolds, O. (1895) 'On the Dynamical Theory of Incompressible Viscous Fluids and the Determination of the Criterion', *Proceedings Mathematical and Physical Sciences*, 451(1941), pp. 5–47.

Ricardo, A. M., Martinho, M., *et al.* (2014) 'Experimental Characterization of Drag on Arrays of

Rough Cylinders', *3rd IAHR Europe Congress, Book of Proceedings*, (3), pp. 1–10.

Ricardo, A. M., Koll, K., *et al.* (2014) 'The terms of the turbulent kinetic energy budget within random arrays of emergent cylinders', *Water Resources Research*, 50, pp. 4131–4148. doi: 10.1002/2013WR014596.

Ricardo, A. M., Canelas, R. B. and Ferreira, R. M. L. (2016) 'Characterization of vortex interaction with Lagrangian coherent structures', *River Flow - Proceedings of the International Conference on Fluvial Hydraulics, RIVER FLOW 2016*, (August 2018), pp. 135–140. doi: 10.1201/9781315644479-25.

Ricardo, A. M. da C. (2014) 'Hydrodynamics of turbulent flows within arrays of circular cylinders'. École Polytechnique Fédérale de Lausanne, p. 242.

Ricardo, A. M., Franca, M. J. and Ferreira, R. M. L. (2016) 'Turbulent Flows within Random Arrays of Rigid and Emergent Cylinders with Varying Distribution', *Journal of Hydraulic Engineering*, 142(9), pp. 1–6. doi: 10.1061/(asce)hy.1943-7900.0001151.

Ricardo, A. M., Sanches, P. M. and Ferreira, R. M. L. (2016) 'Vortex shedding and vorticity fluxes in the wake of cylinders within a random array', *Journal of Turbulence*. Taylor & Francis, 17(11), pp. 999–1014. doi: 10.1080/14685248.2016.1212166.

Rockwell, D. *et al.* (1993) 'High image-density particle image velocimetry using laser scanning techniques', *Experiments in Fluids: Experimental Methods and their Applications to Fluid Flow*, 14(3), pp. 181–192. doi: 10.1007/BF00189509.

Roshko, A. (1954) 'On the Development of Turbulent Wakes from Vortex Streets', *National Advisory Committee for Aeronautics*, 1191, pp. 1–25.

Rotta, J. (1990) *Die Aerodynamische Versuchsanstalt in Göttingen, ein Werk Ludwig Prandtls*. Göttingen, Germany: Vandenhoeck & Ruprecht.

Rutherford, J. C. (1994) *River Mixing*. 1st edn. Chichester: Wiley.

Sanches, P. M. *et al.* (2014) 'Impact of the distance between cylinders on vortex statistic', in *V Conferencia Nacional de Mecanica dos Fluidos, Termodinamica e Energia*. Porto, Portugal: APMTAC.

Sano, M. and Tamai, K. (2016) 'A universal transition to turbulence in channel flow', *Nature Physics*, 12(3), pp. 249–253. doi: 10.1038/nphys3659.

Sarathi, P. *et al.* (2012) 'A calibration scheme for quantitative concentration measurements using simultaneous PIV and PLIF', *Experiments in Fluids*, 52(1), pp. 247–259. doi: 10.1007/s00348-011-1219-7.

Scarano, F. (2002) 'Iterative image deformation methods in PIV', *Measurement Science and Technology*, 13, pp. R1–R19.

Schlichting, H. (1979) *Boundary-Layer Theory*. 7th edn. New York: McGraw Hill.

Schlichting, H. and Gersten, K. (2000) *Boundary-Layer Theory*. 8th edn. Berlin: Springer-Verlag.

Schlichting, H. and Gersten, K. (2017) *Boundary-Layer Theory*. 9th edn. Berlin: Springer-Verlag.

Schmid, P. J. (2010) 'Dynamic mode decomposition of numerical and experimental data', *Journal of Fluid Mechanics*, 656, pp. 5–28. doi: 10.1017/S0022112010001217.

Schott (2017) 'DURAN® Datasheet. Tubing, rods and capillaries made of borosilicate glass 3.3'. Mitterteich, Germany: Schott AG, pp. 1–17.

Schröder, A. *et al.* (2011) 'Eulerian and Lagrangian views of a turbulent boundary layer flow using time-resolved tomographic PIV', *Experiments in Fluids*, 50(4), pp. 1071–1091. doi: 10.1007/s00348-010-1014-x.

Schröder, A. *et al.* (2015) 'Near-wall turbulence characterization using 4D-PTV Shake-The-Box', in *11th International Symposium on Particle Image Velocimetry - PIV15*. Santa Barbara, CA.

Serra, T., Fernando, H. J. S. and Rodríguez, R. V. (2004) 'Effects of emergent vegetation on lateral diffusion in wetlands', *Water Research*, 38(1), pp. 139–147. doi: 10.1016/j.watres.2003.09.009.

Shilton, A. (2000) 'Potential application of computational fluid dynamics to pond design', *Water Science and Technology*, 42(10–11), pp. 327–334. doi: 10.2166/wst.2000.0673.

Shucksmith, J., Boxall, J. and Guymer, I. (2007) 'Importance of advective zone in longitudinal mixing experiments', *Acta Geophysica*, 55(1), pp. 95–103. doi: 10.2478/s11600-006-0042-7.

Shucksmith, J. D., Boxall, J. B. and Guymer, I. (2010) 'Effects of emergent and submerged natural vegetation on longitudinal mixing in open channel flow', *Water Resources Research*, 46(4), pp. 1–14. doi: 10.1029/2008WR007657.

Smart, P. L. and Laidlaw, I. M. S. (1977) 'An evaluation of some fluorescent dyes for water tracing', *Water Resources Research*, 13(1), pp. 15–33. doi: 10.1029/WR013i001p00015.

Socolofsky, S. A. and Jirka, G. H. (2002) *Environmental Fluid Mechanics Part I : Mass Transfer and Diffusion*. 2nd edn. Karlsruhe, Germany: Institut fur Hydromechanik, Universitat Karlsruhe.

Sonnenwald, F. *et al.* (2017) 'Transverse and longitudinal mixing in real emergent vegetation at low velocities', *Water Resources Research*, 53(1), pp. 961–978. doi: 10.1002/2016WR019937.

Sonnenwald, F., Stovin, V. and Guymer, I. (2019a) 'A stem spacing-based non-dimensional model for predicting longitudinal dispersion in low-density emergent vegetation', *Acta Geophysica*. Springer International Publishing, 67(3), pp. 943–949. doi: 10.1007/s11600-018-0217-z.

Sonnenwald, F., Stovin, V. and Guymer, I. (2019b) 'Estimating drag coefficient for arrays of rigid cylinders representing emergent vegetation', *Journal of Hydraulic Research*, 57(4), pp. 591–597. doi: 10.1080/00221686.2018.1494050.

Sorokin, P. P. and Lankard, J. R. (1966) 'Stimulated Emission Observed from an Organic Dye, Chloro-aluminum Phthalocyanine', *IBM Journal of Research and Development*, 10(2), pp. 162–163. doi: 10.1147/rd.102.0162.

Stamatopoulos, C. and Fraser, C. S. (2011) 'Calibration of long focal length cameras in close range photogrammetry', *Photogrammetric Record*, 26(135), pp. 339–360. doi: 10.1111/j.1477-9730.2011.00648.x.

Stoesser, T., Kim, S. J. and Diplas, P. (2010) 'Turbulent Flow through Idealized Emergent Vegetation', *Journal of Hydraulic Engineering*, 136(12), pp. 1003–1017. doi: 10.1061/(asce)hy.1943-7900.0000153.

Stovin, V. R. *et al.* (2022) 'The Impact of Cylinder Diameter Distribution on Longitudinal and Transverse Dispersion Within Random Cylinder Arrays', *Water Resources Research*, 58(4), pp. 1–23. doi: 10.1029/2021WR030396.

Sumner, D. (2010) 'Two circular cylinders in cross-flow: A review', *Journal of Fluids and Structures*. Elsevier, 26(6), pp. 849–899. doi: 10.1016/j.jfluidstructs.2010.07.001.

Sumner, D., Richards, M. D. and Akosile, O. O. (2005) 'Two staggered circular cylinders of equal diameter in cross-flow', *Journal of Fluids and Structures*, 20(2), pp. 255–276. doi: 10.1016/j.jfluidstructs.2004.10.006.

Suzuki, H. *et al.* (2013) 'Fractal analysis of turbulent mixing in fractal-generated turbulence by planar laser-induced fluorescence', *Physica Scripta*, 88(T155), pp. 1–5. doi: 10.1088/0031-8949/2013/T155/014062.

Synge, J. L. and Schild, A. (1978) *Tensor Calculus*. 1st edn. New York: Dover Publications.

Tanino, Y. (2008) *Flow and Solute Transport in Random Cylinder Arrays: a Model for Emergent Aquatic Plant Canopies*. MIT.

Tanino, Y. and Nepf, H. M. (2008a) 'Laboratory Investigation of Mean Drag in a Random Array of Rigid, Emergent Cylinders', *Journal of Hydraulic Engineering*, 134(1), pp. 34–41. doi: 10.1061/(asce)0733-9429(2008)134:1(34).

Tanino, Y. and Nepf, H. M. (2008b) 'Lateral dispersion in random cylinder arrays at high Reynolds number', *Journal of Fluid Mechanics*, 600, pp. 339–371. doi: 10.1017/S0022112008000505.

Tanino, Y. and Nepf, H. M. (2009) 'Laboratory investigation of lateral dispersion within dense arrays of randomly distributed cylinders at transitional Reynolds number', *Physics of Fluids*, 21(4), pp. 1–10. doi: 10.1063/1.3119862.

Taylor, G. I. (1915) 'Eddy Motion in the Atmosphere', *Philosophical Transactions of the Royal Society of London. Series A, Mathematical and Physical Sciences*, 215(523), pp. 1–26.

Taylor, G. I. (1922) 'Diffusion by continuous movements', *Proceedings of the London Mathematical Society*, s2-20(1), pp. 196–212. doi: 10.1112/plms/s2-20.1.196.

Taylor, G. I. (1935) 'Statistical Theory of Turbulence I-V', *Proceedings of the Royal Society of London. Series A, Mathematical and Physical*, 151(873), pp. 421–444.

Taylor, G. I. (1938) 'The Spectrum of Turbulence', *Proceedings of the Royal Society A: Mathematical, Physical and Engineering Sciences*, 164(919), pp. 476–490.

Taylor, G. I. (1953) 'Dispersion of soluble matter in solvent flowing slowly through a tube', *Proceedings of the Royal Society of London. Series A. Mathematical and Physical Sciences*, 219(1137), pp. 186–203. doi: 10.1098/rspa.1953.0139.

Taylor, G. I. (1954) 'The dispersion of matter in turbulent flow through a pipe', *Proceedings of the Royal Society of London. Series A. Mathematical and Physical Sciences*, 223(1155), pp. 446–468. doi: 10.1098/rspa.1954.0130.

Tennekes, H. and Lumley, J. L. (1972) *A First Course in Turbulence*. 1st edn. Cambridge, Massachusetts.

Thielicke, W. and Sonntag, R. (2021) 'Particle Image Velocimetry for MATLAB: Accuracy and enhanced algorithms in PIVlab', *Journal of Open Research Software*, 9, pp. 1–14. doi: 10.5334/JORS.334.

Thielicke, W. and Stamhuis, E. J. (2014) 'PIVlab – Towards User-friendly, Affordable and Accurate Digital Particle Image Velocimetry in MATLAB', *Journal of Open Research Software*, 2, pp. 1–10. doi: 10.5334/jors.bl.

Tinoco, R. O. and Cowen, E. A. (2013) 'The direct and indirect measurement of boundary stress and drag on individual and complex arrays of elements', *Experiments in Fluids*, 54(4), pp. 1–16. doi: 10.1007/s00348-013-1509-3.

Tong, F., Cheng, L. and Zhao, M. (2015) ‘Numerical simulations of steady flow past two cylinders in staggered arrangements’, *Journal of Fluid Mechanics*, 765, pp. 114–149. doi: 10.1017/jfm.2014.708.

Torres, L. A. *et al.* (2013) ‘Calibration of a planar laser induced fluorescence technique for use in large scale water facilities’, *Measurement: Journal of the International Measurement Confederation*. Elsevier Ltd, 46(8), pp. 2597–2607. doi: 10.1016/j.measurement.2013.04.066.

Townsend, A. A. (1980) *The structure of turbulent shear flow*. 2nd edn. Cambridge, UK: Cambridge University Press.

Troy, C. D. and Koseff, J. R. (2005) ‘The generation and quantitative visualization of breaking internal waves’, *Experiments in Fluids*, 38(5), pp. 549–562. doi: 10.1007/s00348-004-0909-9.

Tsujimoto, T. *et al.* (1992) ‘Turbulent open-channel flow over bed covered by rigid vegetation’, *Journal of Hydroscience and Hydraulic Engineering*, 10(2), pp. 13–25.

Valeport (2016) ‘Model 801 - EM Flow Meter. Data Sheet.’ Valeport Ltd. Available at: https://www.valeport.co.uk/content/uploads/2020/04/Model-801-EM-Flow-Meter-Datasheet-April-2020.pdf.

Vanderwel, C. and Tavoularis, S. (2014) ‘On the accuracy of PLIF measurements in slender plumes’, *Experiments in Fluids*, 55(8), pp. 1–16. doi: 10.1007/s00348-014-1801-x.

Viero, D. P., Pradella, I. and Defina, A. (2017) ‘Free surface waves induced by vortex shedding in cylinder arrays’, *Journal of Hydraulic Research*, 55(1), pp. 16–26. doi: 10.1080/00221686.2016.1217948.

Wadzuk, B. M. and Burke, E. (2006) ‘A diffusion model for low Reynolds number flows through a constructed stormwater wetland’, in *Proceedings of the 7th International Conference on HydroScience and Engineering*. Philadelphia, PA.

Webster, D. R., Roberts, P. J. W. and Ra’ad, L. (2001) ‘Simultaneous DPTV/PLIF measurements of a turbulent jet’, *Experiments in Fluids*, 30(1), pp. 65–72. doi: 10.1007/s003480000137.

West, P. (2016) *Quantifying Solute Mixing Across Low Velocity Emergent Real Vegetation Shear Layers*. University of Warwick.

West, P. O. *et al.* (2021) ‘Modelling transverse solute mixing across a vegetation generated shear layer’, *Journal of Hydraulic Research*, 59(4), pp. 621–636. doi: 10.1080/00221686.2020.1818307.

Westerweel, J. (1993) *Digital Particle Image Velocimetry, Theory and Application*. Delft University of Technology. Available at: http://repository.tudelft.nl/islandora/object/uuid:85455914-6629-4421-8c77-27cc44e771ed/datastream/OBJ/download.

Whitaker, S. (1985) ‘A Simple Geometrical Derivation of the Spatial Averaging Theorem’, *Chemical Engineering Education*, 19(1), pp. 18–21 and 50–52.

White, B. (2006) *Momentum and Mass Transport by Coherent Structures in a shallow Vegetated Shear Flow*. MIT.

White, B. L. (2002) *Transport in Random Cylinder Arrays : A Model for Aquatic Canopies*. MIT.

White, B. L. and Nepf, H. M. (2003) ‘Scalar transport in random cylinder arrays at moderate Reynolds number’, *Journal of Fluid Mechanics*, 487, pp. 43–79. doi: 10.1017/S0022112003004579.

White, F. M. (1991) *Viscous fluid flow*. 2nd edn. New York: McGraw Hill.

Willert, C. E. and Gharib, M. (1991) 'Digital particle image velocimetry', *Experiments in Fluids*, 10(4), pp. 181–193. doi: 10.1007/BF00190388.

Willert, C. and Kompenhans, J. (2010) 'PIV Analysis of Ludwig Prandtl's Historic Flow Visualization Films'. Hannover, Germany: Deutsches Zentrum für Luft- und Raumfahrt (DLR), Technische Informationsbibliothek (TIB), pp. 1–4. doi: 10.5446/12719.

Williamson, C. H. K. (1988a) 'Defining a universal and continuous Strouhal-Reynolds number relationship for the laminar vortex shedding of a circular cylinder', *Physics of Fluids*, 31(10), pp. 2742–2744. doi: 10.1063/1.866978.

Williamson, C. H. K. (1988b) 'The existence of two stages in the transition to three-dimensionality of a cylinder wake', *Physics of Fluids*, 31(11), p. 3165. doi: 10.1063/1.866925.

Williamson, C. H. K. (1991) 'Three-Dimensional Aspects and Transition of the Wake of a Circular Cylinder', *Turbulent Shear Flows 7*, 7, pp. 173–194. doi: 10.1007/978-3-642-76087-7_14.

Williamson, C. H. K. (1996a) 'Three-dimensional vortex dynamics in bluff body wakes', *Experimental Thermal and Fluid Science*, 12(2), pp. 150–168. doi: 10.1016/0894-1777(95)00085-2.

Williamson, C. H. K. (1996b) 'Three-dimensional wake transition', *Journal of Fluid Mechanics*. University of Sheffield Library, 328, pp. 345–407. doi: 10.1017/S0022112096008750.

Williamson, C. H. K. (1996c) 'Vortex dynamics in the cylinder wake', *Annual Review of Fluid Mechanics*, 28, pp. 477–539. doi: 10.1146/annurev.fl.28.010196.002401.

Wilson, N. R. and Shaw, R. H. (1977) 'A Higher Order Closure Model for Canopy Flow', *Journal of Applied Meteorology*, 16(11), pp. 1197–1205. Available at: https://www.jstor.org/stable/26178224 A Higher Order Closure Model.

Würth, C. *et al.* (2012) 'Determination of the absolute fluorescence quantum yield of rhodamine 6G with optical and photoacoustic methods - Providing the basis for fluorescence quantum yield standards', *Talanta*. Elsevier B.V., 90, pp. 30–37. doi: 10.1016/j.talanta.2011.12.051.

Young, P., Jakeman, A. and McMurtrie, R. (1980) 'An instrumental variable method for model order identification', *Automatica*, 16(3), pp. 281–294. doi: 10.1016/0005-1098(80)90037-0.

Young, W. R. and Jones, S. (1991) 'Shear dispersion', *Physics of Fluids A*, 3(5), pp. 1087–1101. doi: 10.1063/1.858090.

Zdravkovich, M. M. (1987) 'The effects of interference between circular cylinders in cross flow', *Journal of Fluids and Structures*, 1(2), pp. 239–261. doi: 10.1016/S0889-9746(87)90355-0.

Zehentbauer, F. M. *et al.* (2014) 'Fluorescence spectroscopy of Rhodamine 6G: Concentration and solvent effects', *Spectrochimica Acta - Part A: Molecular and Biomolecular Spectroscopy*. Elsevier B.V., 121, pp. 147–151. doi: 10.1016/j.saa.2013.10.062.

Zhang, H. J. and Zhou, Y. (2001) 'Effect of unequal cylinder spacing on vortex streets behind three side-by-side cylinders', *Physics of Fluids*, 13(12), pp. 3675–3686. doi: 10.1063/1.1412245.

Zhou, Y. *et al.* (2000) 'Complex turbulent wakes generated by two and three side-by-side cylinders', *International Journal of Heat and Fluid Flow*, 21(2), pp. 125–133. doi: 10.1016/S0142-727X(99)00077-6.

Zhou, Y. *et al.* (2009) 'Reynolds number effect on the wake of two staggered cylinders', *Physics of Fluids*, 21(12), pp. 1–14. doi: 10.1063/1.3275846.

Zhou, Y. and Mahbub Alam, M. (2016) 'Wake of two interacting circular cylinders: A review', *International Journal of Heat and Fluid Flow*. Elsevier Inc., 62, pp. 510–537. doi: 10.1016/j.ijheatfluidflow.2016.08.008.

Zhu, Y. and Mullins, O. C. (1992) 'Temperature Dependence of Fluorescence of Crude Oils and Related Compounds', *Energy and Fuels*, 6(5), pp. 545–552. doi: 10.1021/ef00035a003.

Appendix A. LIF METHODOLOGY

Laser Induced Fluorescence (LIF) is a measurement technique, based on optical principles, used extensively in environmental fluid mechanics, for qualitative and quantitative descriptions of velocity and scalar fields. This chapter focuses on the application of LIF for concentration measurements of a passive species in a vegetated flow. Also, this section is intended to be an account on how the system was set up, and what should be considered before, during and after the calibration procedure, alongside some recommendations for future—and more efficient—applications of the technique.

Section A.1 offers a summary of previous applications of the technique, alongside an overview of the theory behind fluorescence-dependent concentration measurements, including the treatment of some of the most common issues in LIF experiments. A description of the experimental system installed in the Water Laboratory in the University of Sheffield is given in Section A.2, including the infrastructure (flume, visualisation windows, flow system). Section A.3 presents a description of the LIF components, alongside a step-by-step process of assembling and configuring the LIF instrumentation, and acquiring calibration information,. The results of the calibration procedure are shown in Section A.4. Finally, the performance of the calibration procedure is examined and recommendations for future applications of the technique are given in Sections A.5 and A.6.

A.1. Theoretical Framework

A.1.1. Literature Review

Using solutions of different opacities than that of background fluids in order to visually assess flow phenomena, has been a crucial tool in fluid mechanics: from visualisations of shear in Newtonian fluids, to turbulent transitions in Reynolds experiments. Recently, advances in optical systems, computers and dyes with fluorescent properties (Sorokin and Lankard, 1966), have allowed for the development of Laser Induced Fluorescent (LIF) as a non-intrusive and more comprehensive tool for the analysis of flow phenomena. In the early applications of this technique, associating dye concentrations with the persistence of flow structures served to qualitatively (Dimotakis, Miake-Lye and Papantoniou, 1983) and quantitatively (Liu *et al.*, 1977) study the dynamics of axisymmetric turbulent jets.

More recently, LIF has been applied in a wide variety of flows. Distelhoff and Marquis (1998) used Linear LIF to radially and angularly resolve the concentration gradients in a stirring tank. Exploiting the temporal trapping of dye 'patches' in coherent structures, Torres *et al.* (2013) studied the mixing field between the background flow and a co-flowing turbulent jet in a flume. Turbulent mixing at smaller scales, for conventional rectangular and fractal generated turbulence, were measured by Suzuki *et al.* (2013). Descriptions of two-dimensional macroscopic solute transport in emergent (natural and artificial) vegetation using LIF was presented in Sonnenwald *et al.* (2017). Similarly, West *et al.* (2021) presented measurements of dispersion in a sheared flow generated by a partially vegetated channel, which were then used to validate a Finite Difference Model for transverse mixing. Finally, LIF has been shown to work well with other techniques (PIV, PTV) to simultaneously describe concentration and velocity fields (Webster, Roberts and Ra'ad, 2001; Sarathi *et al.*, 2012).

As LIF is used to explore a wider range of flows, researchers have also studied the most common limitations and sources of uncertainty. It has been found that in some cases, dye molecules are incapable of fluorescing after an initial (usually high-energy) excitation. This phenomenon, called photo-bleaching, was studied by Crimaldi (1997) for Fluorescein and Rhodamine 6G, where it was found that the latter is far less susceptible to it, and overall, velocity can affect small scale concentration measurements if photo-bleaching is an issue. Another persistent problem is secondary absorption, which occurs when emitted (fluorescent) light is reabsorbed and subsequently re-emitted by dye molecules, thereby biasing the concentration dependent fluorescence values. Baj, Bruce and Buxton (2016) found that secondary absorption could account for as much as 50% of the acquired signal, depending on the image size and the topology of the concentration field. Re-emitted fluorescence seemed to be higher in zones of ambient fluid than in highly concentrated 'blobs' of dye. A correction method for reabsorption based on the quantum yield of the dye was also presented. Vanderwel and Tavoularis (2014) explored the effect of laser sheet thickness on secondary absorption, finding that, as a rule of thumb, it should be at least 1/3 of the plume thickness to avoid biases. Also, a correction test for reabsorption was presented, consisting of an isolated fluorescent cell along the test section.

A detailed study of the behaviour of Rhodamine 6G, in different organic solvents and a complete range of aqueous dilutions was presented by Zehentbauer *et al.* (2014). There it was found that a shift in the band of the emission spectrum is found and associated with an increase in concentration. This, it is explained, is the result of a change in the molecular and electromagnetic structure of the dye, associated with the distances and organisation of molecules. In this sense, secondary absorption was found to be a problem for high concentrations. A range of the concentration thresholds and the explanation of the behaviour is given in Section A.3.4. and Table A.3-5.

There is not a unique approach to setting up LIF experiments, the specific instrumentation, components, techniques and methodology depend on the physical phenomena to measure, and the particular objectives. Nonetheless, all applications of Laser Induced Fluorescence follow the same principle, and the components can be divided into 4 main groups: illumination source, fluorescent compound, image acquisition device and illumination optics (Crimaldi, 2008). Depending on the flow phenomena to analyse, a prior assessment of concentration ranges and the extent of the image area can be made; and depending on this, the appropriate components can be chosen.

Regarding the illumination sources for LIF, 2 types of lasers have been predominantly used in previous applications: continuous-wave (CW) argon-ion, and pulsed Nd:YAG lasers. The latter function by emitting short, high-intensity pulses, containing energy outputs several orders of magnitude than the former, although this output can be variable for consecutive pulses (Law and Wang, 2000). CW lasers, on the other hand, yield more stable outputs, particularly when operated in TEM00 mode, i.e. with a Gaussian cross-sectional distribution of intensity. Conventionally, lasers in LIF experiments are used in either 488 and 514 nm, for fluorescein; and 532 for Rhodamine 6G and WT (Crimaldi, 2008).

The laser operating wavelength should be selected to match the peak of the absorption spectrum of the fluorescent dye, and the optical systems (cameras and filters) should consider the emission spectrum. In addition to the factors related to the other components of the LIF system, the independent properties of the fluorescent dye (fluorophore) to consider are: quantum efficiency (Arcoumanis, McGuirk and Palma, 1990), fluorescence response to changes in pH and temperature (Smart and Laidlaw, 1977; Coppeta and Rogers, 1998), potential for photo-bleaching and secondary absorption, fluorescence-concentration response (i.e. linearity) and health and safety provisions. Commonly, Fluorescein and Rhodamine 6G have been the dye of choice for most previous experiments (Crimaldi, 2008). For the experiments described in this work, Rhodamine 6G was chosen based on the available laser system (see Section A.3.4), its insensitivity to photo-bleaching (Crimaldi, 1997), and its relative stability with temperature (Zhu and Mullins, 1992).

Although independent light-sensitive diodes have been used to measure concentration-dependent fluorescence (Distelhoff and Marquis, 1998); cameras are predominantly used to record intensity. Initial experiments used PLIF to qualitatively analysed flow phenomena, for which normal film cameras suffice (e.g. Dimotakis, Miake-Lye and Papantoniou, 1983). More recently, with the advent and availability of digital cameras, concentration fields can be resolved quantitatively. When using CCD cameras, the main parameters to consider are the image resolution (for spatial variation), frame rate (for temporal resolution of the flow field) and pixel depth, i.e. the amount of information to resolve the camera greyscale (Crimaldi, 2008). In addition to the camera itself, lenses are filters are necessary to improve the light response of the filter and focus on emitted light. A detailed description of this components, in the context of the equipment used for this work is given in Section A.3.1.

Despite the fact that for the LIF experiments presented here did not use special optic equipment to generate light sheets, e.g. scanning mirrors, cylindrical lenses, beam expanders and collimators, etc. These should be considered depending on the extent of the area to visualise. Factors light transverse attenuation, and planar light intensity should be considered in conjunction with the saturation level of the fluorophore. For Rhodamine 6G, for instance, the saturation level is considerably higher than the intensity achieved by scanning a CW laser with a rotating mirror, e.g. 3 orders of magnitude for a 2.5 W laser (Troy and Koseff, 2005). Care must be taken with pulsed lasers as these can yield higher planar intensities than the saturation levels of some dyes (Crimaldi, 2008).

A.1.2. Theory of Fluorescence

As mentioned above, LIF experiments function by integrating a light source, a fluorescent dye and an image acquisition device; and the quantities measured are light intensity values proportional to the emitted fluorescent light, which is in turn dependent on the dye concentration, and the intensity of the light source. Considering I_f as the intensity of the light emitted by the excited fluorophore, its dependency on concentration, C, and intensity from the light source, I_l, can be represented by the following expression (Crimaldi, 2008).

$$I_f \propto \frac{I_l}{1 + I_l/I_{sat}} C \qquad \textit{Eq. A.1-1}$$

With I_{sat} representing the saturation intensity of the dye. Clearly, if the operational intensity of the light source is considerably lower than I_{sat}, the proportionality relationship presented in

Eq. A.1-1 simplifies into an expression of the form $I_f \propto I_l C$. In practice, however, neither I_f nor I_l are easily measurable, and it is necessary to rely on alternative values to express the relationship given above. The amount of light intensity radiated by a laser depends on the output power, P, and its spatial variation depends on the laser sheet optics, and concentration-dependent absorbance. So, laser power is used as a surrogate for excitation light intensity, I_l. Similarly, fluorescent light intensity, I_f, is not directly measured as the amount of radiated energy at each point in the area of interest, but as a non-dimensional greyscale value, I, dependent on the camera's specific settings.

Eq. A.1-2 shows the relationship between the values used to represent excitation and fluorescent light. P and I_l are equivalent parameters, I_l and I_f are interrelated according to Eq. A.1-1, with the value Φ_y representing the quantum yield of the dye. I_f and I are proportional, and could be described by using the camera's quantum efficiency, Φ_E.

$$P \rightarrow I_l \overset{\Phi_y}{\Rightarrow} I_f \overset{\Phi_E}{\rightarrow} I \qquad \textit{Eq. A.1-2}$$

For LIF experiments in which the intensity of the light source does not change along the beam path, named optically thin (Vanderwel and Tavoularis, 2014), so that absorption does not generate light attenuation, it is possible to connect directly the definitions given above in a single expression. Eq. A.1-2 shows the calibration expression connecting dye concentration, measured fluorescence intensity and light intensity; V represents the volume of the measurement section, ε is the absorptivity coefficient, and A_1 is a general constant summarising the camera configuration. The variable of interest in the calibration equation is C, and all other quantities can be lumped together into a single coefficient, thus removing the need to quantify I_l or P.

$$I = A_1 \Phi_E \Phi_y \varepsilon \, I_l \, C \, V \qquad \textit{Eq. A.1-3}$$

For optical systems in which light attenuation must be considered (e.g. due to low laser power), the direct calibration approach presented in Eq. A.1-3 is clearly insufficient to compute concentration from image-related intensity values. In this case, excitation light intensity must also be measured over the area of interest, and for each point, values of P or I_l, together with the recorded fluorescent intensity, I_f, must be used to compute concentration. Light attenuation through an aqueous medium is modelled using the Bouguer-Beer-Lambert law, which relates the change in radiated intensity, dI_l, from a light beam as it passes through a differential section dr of a solution of dye, to concentration, and the absorption coefficient ϵ.

$$\frac{dI_l}{I_l} = -\epsilon C\, dr \qquad \text{Eq. A.1-4}$$

Note that since P and I_l are equivalent quantities, and I_f and I_l are linearly related, any of these values can be used in Eq. A.1-4. The solution of this differential equation leads to an exponential decay model of the form given in Eq. A.1-5, where the integral in the attenuation coefficient allows for the description of intensity change in a variable concentration field. Sections A.4 and A.5, show the procedure to determine the coefficients describing attenuation and the fluorescence equation.

$$I_l(r_1) = I_l(r_0)\exp\left[-\epsilon \int_{r_0}^{r_1} C(r)dr\right] \qquad \text{Eq. A.1-5}$$

A.2. Experimental Facility (System Layout)

As was mentioned in Section A.1, the LIF experiments undertaken build on the methodology presented in Sonnenwald *et al.* (2017), who evaluated the longitudinal and transverse dispersion of a passive solute in a vegetated system composed of rigid cylindrical stems with a uniform diameter distribution. This study addresses the effects of mixing on a more realistic vegetation morphology, considering diameter and spacing distributions as those observed in *Summer Typha*. In order to isolate the effects of vegetation from any other possible sources of uncertainty, the system was built to replicate the channel geometry found in the base study. This section explains the infrastructural components of the system, a description of the instrumentation and their configuration and operation is given in Section A.3.

A.2.1. Flume set-up

The system described in Sonnenwald *et al.* (2017) and West (2016), University of Warwick, corresponds to a horizontal flume, 1 m wide by 24 m long, where the vegetation is placed 10 m downstream from a set of flow straighteners, with a fixed injection point located 2 m after the start of the vegetation and at mid-width. Two measurement stations were located at 1 and 2 metres downstream from the injection point. The experiments described in this research were conducted in the Water Engineering Laboratory at the University of Sheffield. The existing flume is 1.42 m wide by 14 m long, with a maximum allowable water surface of 0.6 m and a fixed slope of 0.14 %.

Figure A.2-1 shows a diagram of the flume measurement section, and an elevation view detailing the location of lasers and image acquisition devices. In order to replicate the general geometry presented in West (2016), internal partitions were built and installed to reduce the flow width to 1m, also because it facilitates the manufacturing of the perforated plastic plates used to install the stems. The injection point was located 4.9 m downstream from the flow straighteners at the flume inlet, and 2 m after the start of the vegetated section. The 4 measurement stations are located at 1 metre intervals downstream from the injection point, with lasers at aligned horizontally at 75 mm above the bed (half of the projected 150 mm flow depth), as shown in Figure A.2-1.

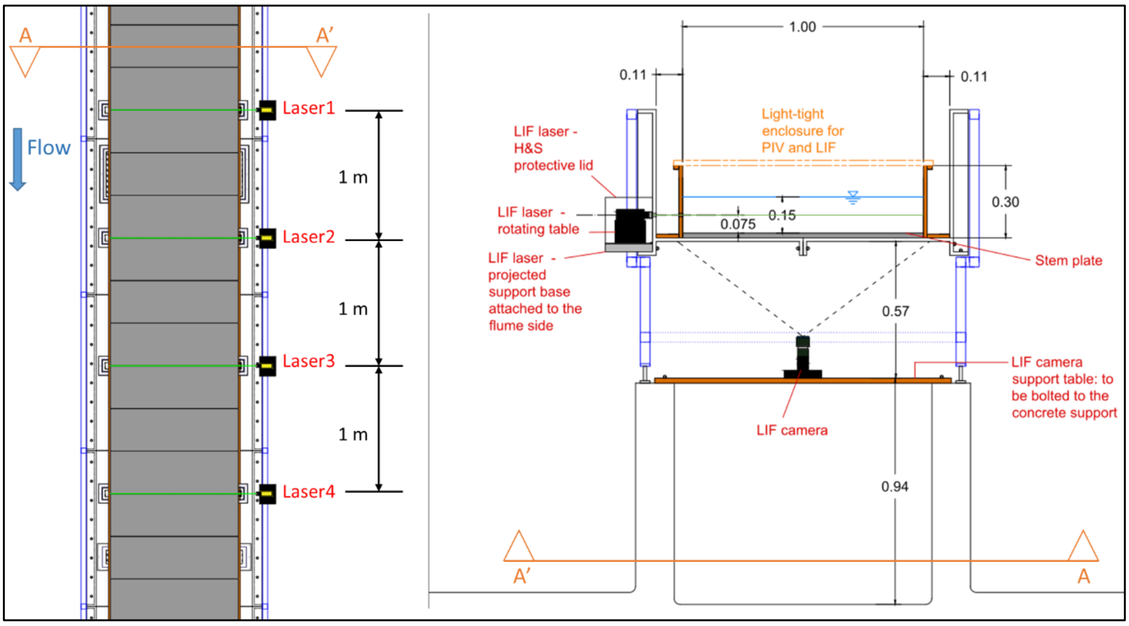

Figure A.2-1. Plan and elevation view of the LIF measurement section.

In order to acquire images and allow for a full resolution of the laser beam, 0.1 m x 1.0 m glass windows were constructed on the bed, at each measurement station, where an 8 mm gap, between adjacent perforated stem plates, was set to allow visualisation from underneath the flume. Between the first 2 LIF windows, a PIV section was constructed and a plate of transparent, perforated Perspex was placed to allow visualisation and velocity measurements through the emergent artificial vegetation, as shown in Figure A.2-2.

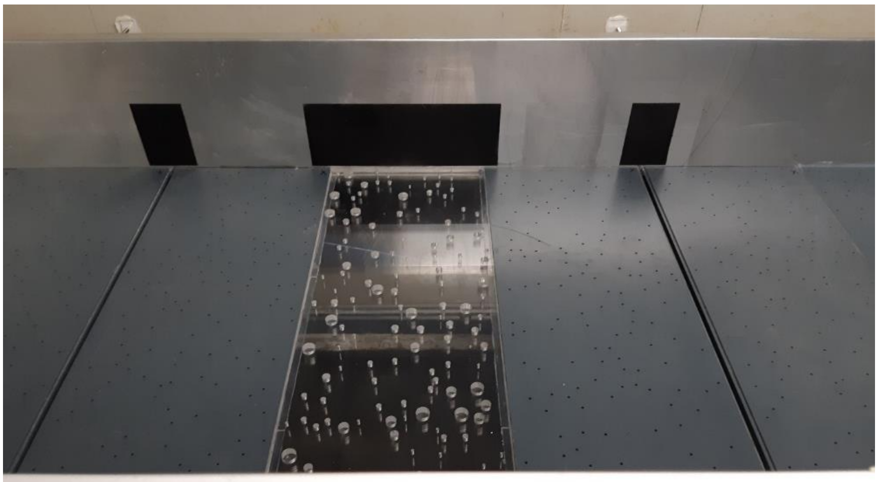

Figure A.2-2. Physical configuration of LIF windows (1 and 2) and PIV window, before the artificial vegetation was 'planted'.

A.2.2. Bed slope measurement

As shown in Figure A.2-1 and Figure A.2-2, perforated PVC stem plates were used to install the artificial vegetation. Due to manufacturing limitations, and transport convenience, 1.0 m by 0.3 m plates were used in the measurement section, and outside, 1.0 m by 1.0 m plates were used. In order to avoid bed-induced effects and substantial changes to the bed slope, the plates were installed and levelled as much as possible.

After the windows were located, the flume waterproofed, the stem plates located; the outlet was closed and the flume filled in order to measure water depth variations. Since the water was stationary, the surface could be used as reference and measure height variations throughout the bed. Figure A.2-3 shows the two-dimensional variations in bed height measured with a moving Vernier gauge. Local variations in height are noticeable between adjacent plates from Figure A.2-3. However, if these variations are compared to the total height difference along the flume, as shown in Figure A.2-4, it is reasonable to expect that they will not affect the flow for a couple of reasons. First, local variations in height, even the most noticeable ones (e.g. $Length \approx 0.75$ m in Figure A.2-4) are no bigger than 5 mm, which is still considerably smaller than the projected flow depth, 150 mm. Second, the standard deviation of the differences between measured bed heights and computed ones from a Least Squares regression is 1.3 mm, and the previous argument applies. If the focus is on the measurement section (i.e. length between $4.5\ m$ and $10\ m$) it can be seen that the variations in bed height are in general lower. Lastly, even if these local differences in bed height are assumed to generate boundary layer effects that affect the bulk flow, it should be remembered that the presence of stems has been shown to reduce the vertical extent of bed effects (Nepf, Mugnier and Zavistoski, 1997).

The measurements of bed height shown in Figure A.2-3 and Figure A.2-4 were used to compute a plane in a Least-Squares regression fashion, and obtain values of mean longitudinal and transverse slopes. The former was found to be,

$$S_x = 1.38\, mm/m$$

Which, although fixed, will allow for the existence of uniform flow for at least a subset of experiments. The computed transverse slope was

$$S_y = -0.06\, mm/m$$

And it is considered small enough to not affect the one dimensional nature of the bulk flow.

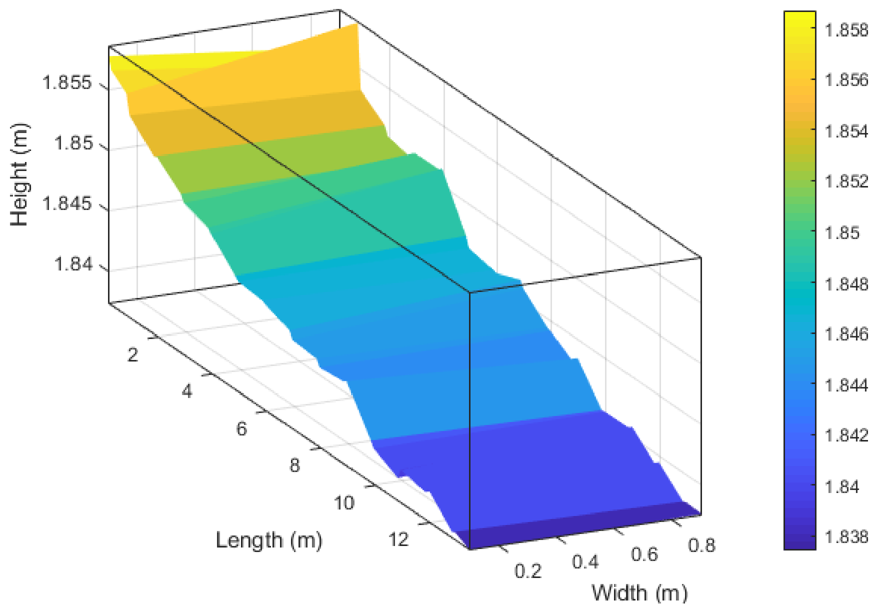

Figure A.2-3. Bed height measurements.

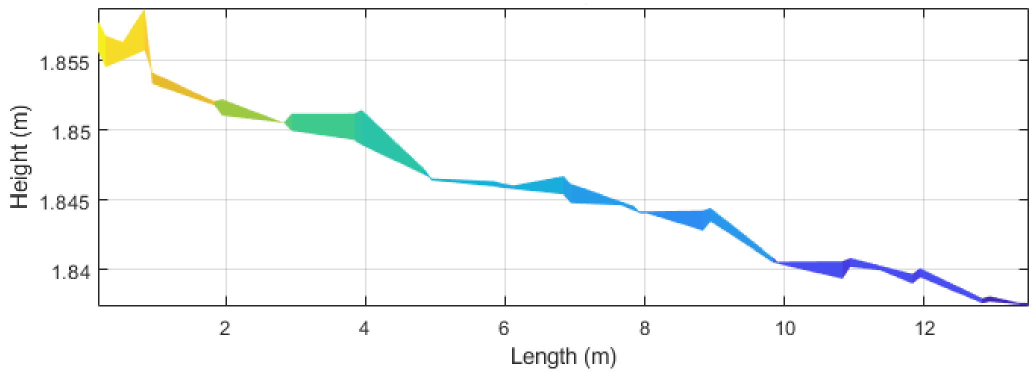

Figure A.2-4. Longitudinal variation in bed height.

A.3. Configuration of Physical Components

Independent of the application, LIF requires 3 fundamental components: an image acquisition device, a laser as an illumination source, and a fluorescent dye. The selection of these components requires a careful examination not only of their specific capabilities, but the way they mutually interact, as it affects the performance of the entire system. Moreover, the way in which these components are integrated into the existing infrastructure requires thorough planning. This section goes over the technical specifications of the components acquired for the experiments, their joint capabilities, and the tasks necessary to properly configure the system.

A.3.1. Camera Configuration

The image acquisition devices chosen for the experiments were POINTGREY FL3-U3-13Y3-C cameras with the following relevant technical specifications (FLIR, 2017).

Table A.3-1. Relevant camera parameters

Resolution (px)	1280 x 1024
Colour range	Monochromatic
Pixel Depth (bits)	8 and 16
Exposure Range	0.1129 µs – 0.99 s
Quantum Efficiency (%)	60 – 65*

*The range given is the maximum achievable and it is valid for wavelengths between 475 and 600 nm.

It should be noted that monochromatic cameras are preferred for all LIF configurations, since the interest is in the magnitude of fluoresced light (i.e. number of photons) reaching the camera sensor, for a narrow emission spectrum, thus, greyscale cameras will offer higher performance than conventional RGB ones (Crimaldi, 2008). Consider also that the photo sensor response, i.e. the conversion of fluoresced light into a digital signal, depends on the camera's quantum efficiency.

When it comes to image resolution, for pixel depth (i.e. number of bits used to resolve the camera's greyscale) and exposure range (time the shutter is open), generally, higher values mean better capabilities. However, they often come at the cost of performance, specifically transfer rate speeds and frame rate (Crimaldi, 2008). The chosen features for the experiments are given in Section A.3.2.

The camera was coupled with a NAVITAR NMV-4WA wide angle lens, having a nominal focal length of 3.5 mm and maximum lens aperture of f/1.4, and a minimum one of f/8 (NAVITAR, 2016). Figure A.3-1a shows one of the cameras used for data acquisition, with the lens and a rotating table for alignment purposes. Figure A.3-1b shows the camera configuration in relation with the LIF window. The lens features, aperture and focal length, had to be fixed manually and the cameras enclosed prior to the calibration to avoid accidental misalignments. Further, the success of the image acquisition process depends heavily on the correct camera alignment and a correct configuration of the field of view. Accordingly, the remainder of this subsection is devoted to explaining this process.

Intuitively, the gaps between plates above the LIF window were chosen as narrow as possible to avoid trapping effects in the flow; however, from Figure A.3-1b it can be seen that the resulting Field of View (FoV) is limited, requiring pinpoint precision when aligning the laser and making it difficult to apply pixel-distance transformations to the images. Also, as will be seen below, the FoV should be aligned as close to the image central pixel row as possible, to avoid the need for complex distortion calibrations.

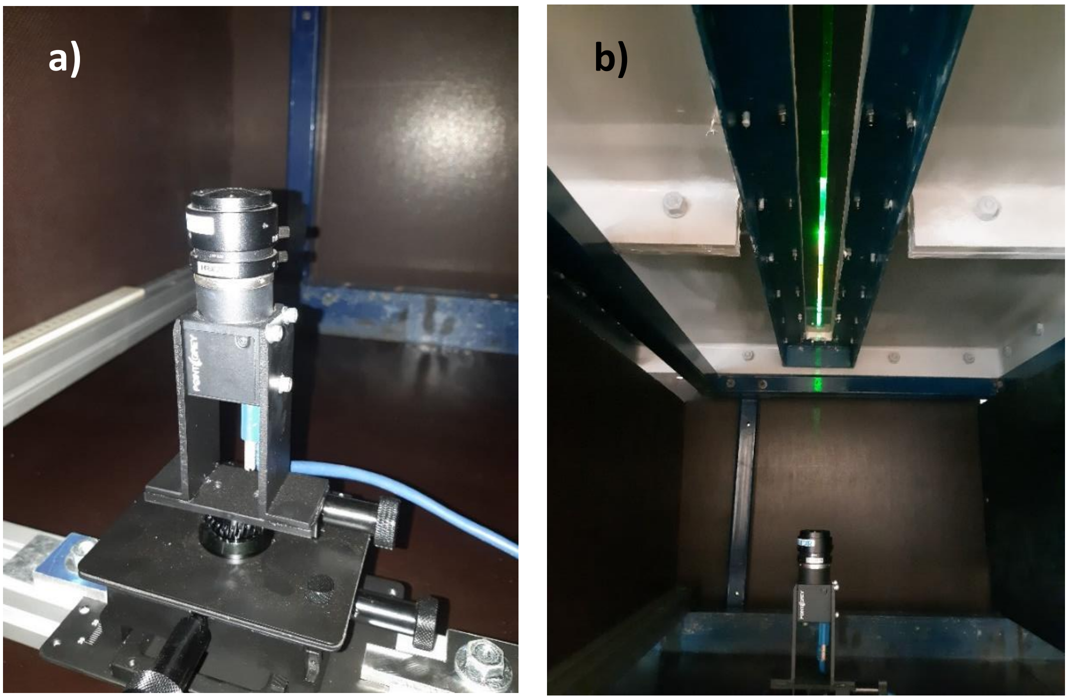

Figure A.3-1. a) Photo of the camera used for the experiments (Pointgrey camera + NAVITAR lens + rotating base), b) Camera location in reference to the LIF window.

The pixel-distance characterisation consists of locating a reference template in the FoV (where the laser will be located), with clear spatial markings to associate pixels to specific points along the laser beam. A first iteration of this procedure was tried with a dry flume, a uniform LED illumination system and a graduated 1m long ruler; the components were organised as shown in Figure A.3-2. The extent of the LIF window gap limits the light reaching the camera from sources outside of the thin FoV. In order to circumvent this problem, the LED lights were aligned next to the window, pointing upwards (see Figure A.3-2b), so that light would bounce on the ruler (Figure A.3-2a) and be redirected down towards the camera. This arrangement proved to be successful in obtaining a spatial characterisation of the LIF images, as shown in Figure A.3-3, where the recorded images for the 4 cameras used are shown, and the graduation of the ruler and the limits, are clearly visible.

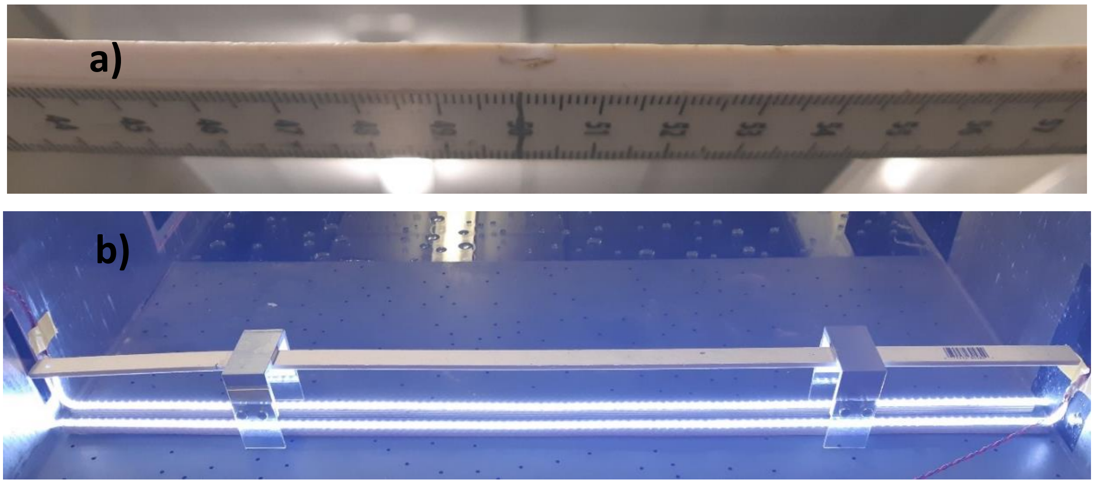

Figure A.3-2. Dry illumination system for pixel-distance calibration. a) graded ruler, b) layout of the LED illumination and ruler on an LIF window.

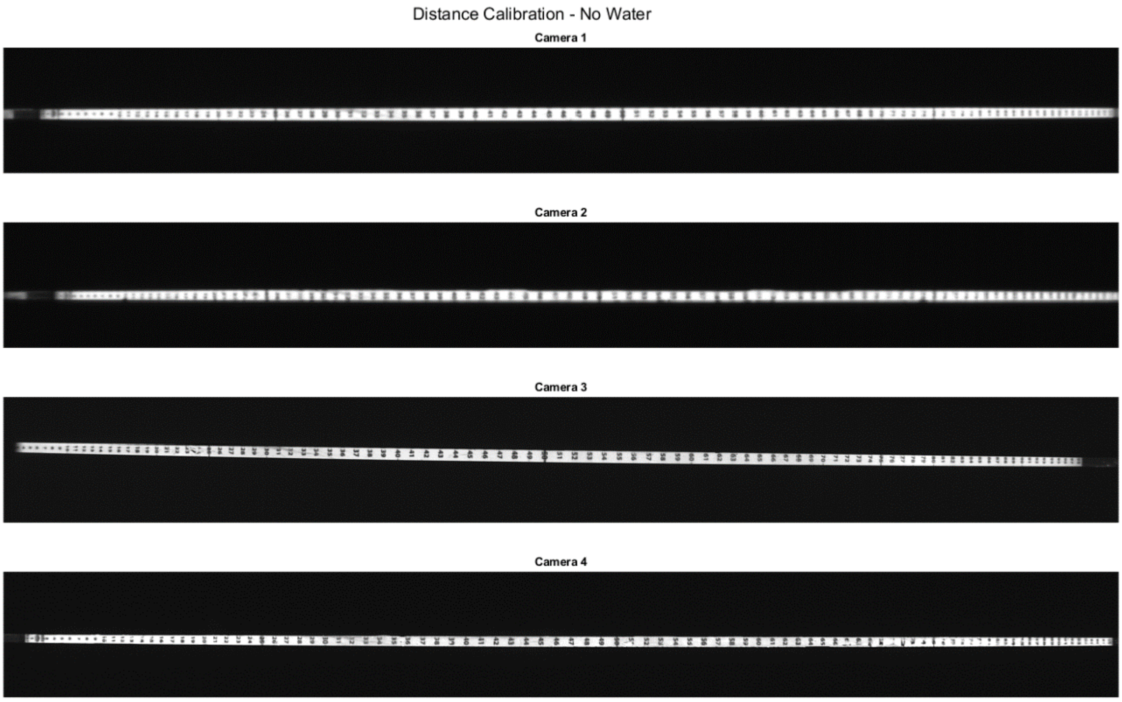

Figure A.3-3. Illuminated ruler without water in the flume, for the 4 cameras.

Despite the success of the configuration described, it is important to note that the space between the FoV and the camera lens is occupied by water, air and glass, where the former 2 represent considerable portions of the light path, therefore light refraction was expected to be an issue. To test the extent to which refraction can affect the pixel-distance characterisation, and obtain correct images, it was necessary to add a water depth that covered the FoV. For electrical Health and Safety reasons, the DC-supplied LED illumination system could not be submerged. Instead, the LED strips were located underneath a table covering up the FoV (see Figure A.3-4b), and metal plates were placed to reflect light onto a ruler hanging from the sides of the flume as shown in Figure A.3-4.

The images obtained from the underwater illumination system, for the 4 cameras, are shown in Figure A.3-5. A comparison between the results of the dry and underwater pixel-distance configuration images (Figure A.3-3 and Figure A.3-5), reveals that light reflection is an issue, evident in the fact that towards the edges of the image (where the light incident angle is more oblique), the ends of the ruler move away from the centre—in some cases beyond the window thereby eliminating a portion of the beam towards the edges.

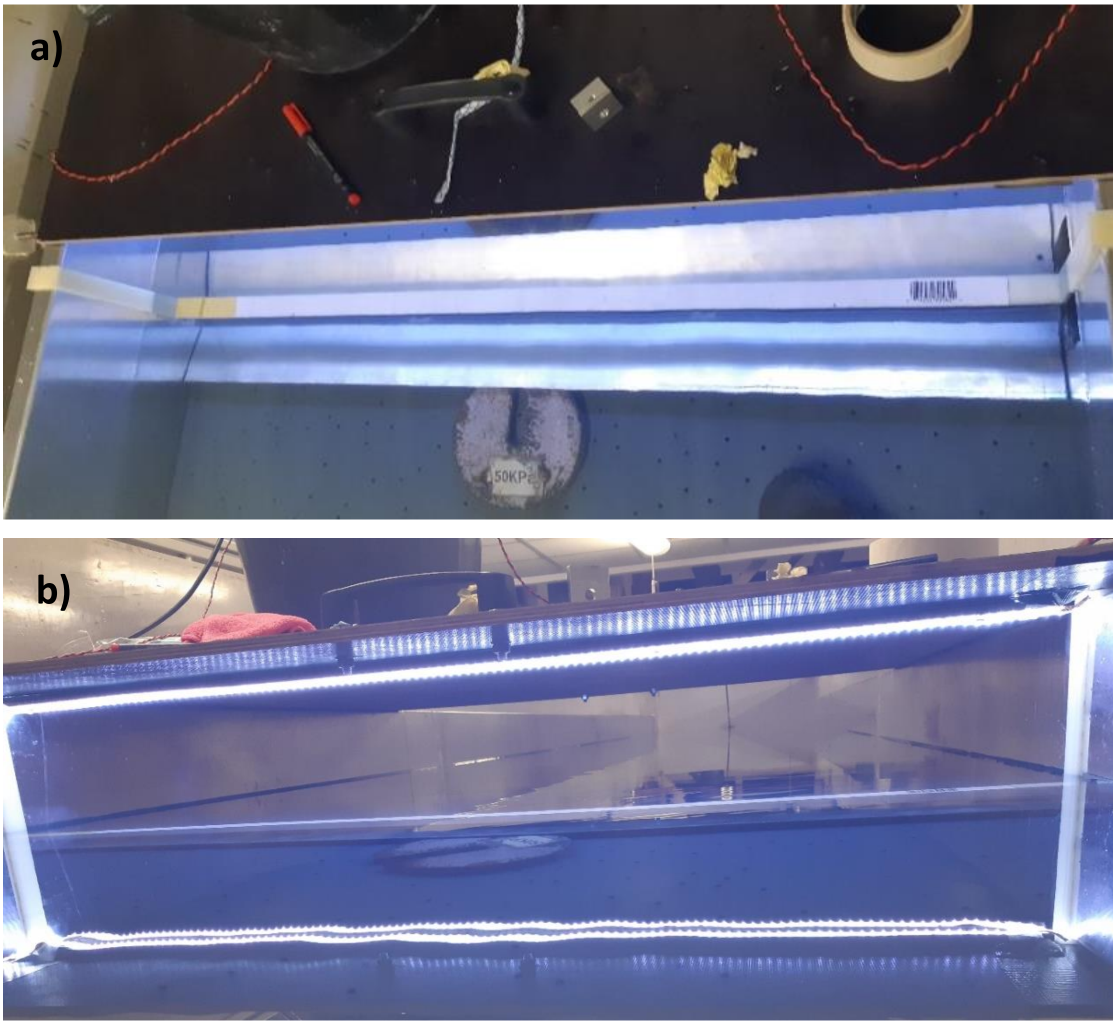

Figure A.3-4. Underwater illumination system for pixel-distance calibration.

After the camera is realigned to allow visualisation of the entire beam, and the images of the underwater template have been acquired, it is necessary to derive an expression for the pixel-distance transformation of the beam. From the images shown in Figure A.3-5, it is possible to associate each real point on the ruler, to a pixel location, and obtain an expression to transform each point along the beam. It is clear that the pixel distance between ruler marks changes when the ruler approaches the fringes of the image. These differences are related to the barrel distortion caused by the wide-angle lens used. This type of distortion has been found to be radially symmetric and solvable via an odd polynomial model, usually up to the third degree (Jiang, Zhang and Zhou, 2003; Stamatopoulos and Fraser, 2011).

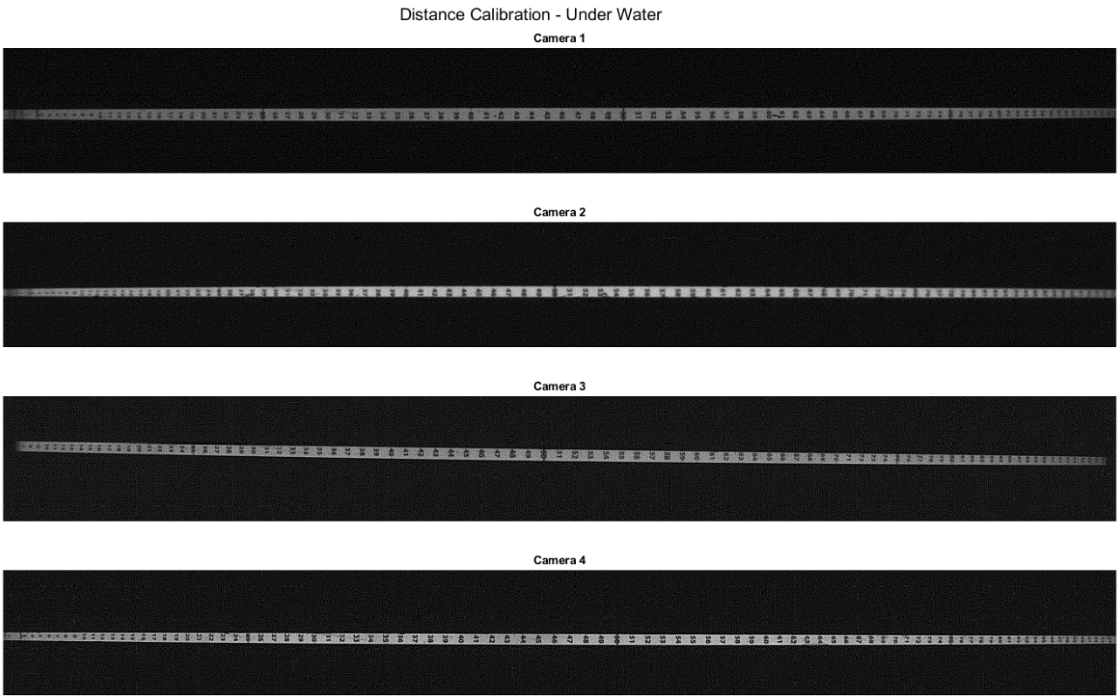

Figure A.3-5. Illuminated ruler with water in the flume, for the 4 cameras.

A full distortion correction is not necessary since we are only interested in the transverse variation of beam intensity (with respect to the flume), which normally does not occupy more than a couple of pixels in the longitudinal direction. Consequently, characterising the pixel-distance transformation only for columns of pixels is sufficient to find a full transformation. It should be remarked that this analysis is valid as long as the LIF window is aligned to the central row of pixels, as Figure A.3-5 indicates. Figure A.3-6 shows the result of using a 3rd degree polynomial to compute the transverse distance from each pixel column, based on the image readings.

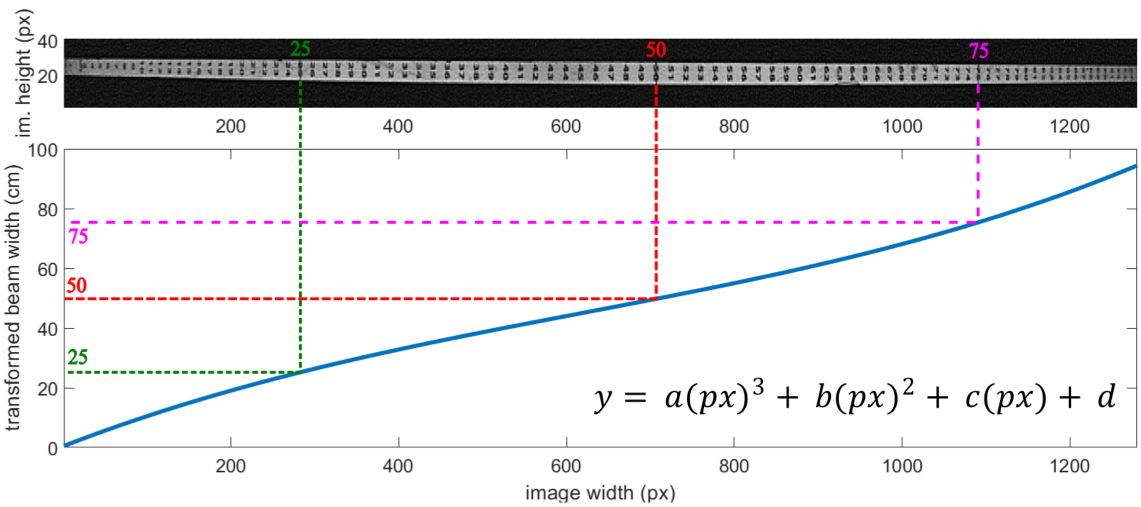

Figure A.3-6. Pixel-distance transformation procedure. The actual width distance, y, is a 3rd degree polynomial function of the pixel width.

A.3.2. Defining camera parameters

The previous section covered the specifications of the image acquisition system, the alignment of the Field of View and pixel-distance transformation to associate image pixels to points in the flume. This section describes the effects of different physical and digital camera parameters, and the criteria adopted to select the values used.

A.3.2.1. Physical parameters

The NAVITAR NMV-4WA lens attached to the camera allows for manual variations in lens aperture and focal length. The lens and the manually adjustable settings for focal length and iris aperture are shown in Figure A.3-7a, where it can be seen that both are analogous: the focal length (upper line) has no distinctions, and the lens aperture marks the points for the scale

$$\{f/11\,, f/8\,, f/5.6\,, f/4\,, f/2.8\,, f/2\,, f/1.4\}$$

Where $f/11$ is the smallest aperture, and $f/1.4$ is the lens fully open. It is important to note that focal length and lens aperture are correlated, and the performance of the optical system depends on choosing an appropriate combination. It is known that depending on lens aperture, light from different incident angles will reach the sensor. For open lenses (low f values) more light will reach the sensor and thus saturation values will most likely be reached. Figure A.3-7b shows the resulting images measured from a known concentration of Rhodamine 6G ($\sim$ 50 ppb) and varying lens apertures with low laser power. For the system configuration, it is preferable to have a lens aperture closer to $f/11$, because a smaller iris will allow less light and the incident light beams will be predominantly parallel, therefore, a wider light intensity response is available and the images will be less sensitive to focal length. In light of this, the following manual parameters were selected for the calibration and the experiments.

Lens Aperture: f/8 for all cameras

Focal Length: No division was provided in the lens. The optimal focal length for each camera was chosen by visually evaluating which position yielded the clearest pixel-distance calibration images (see Figure A.3-5).

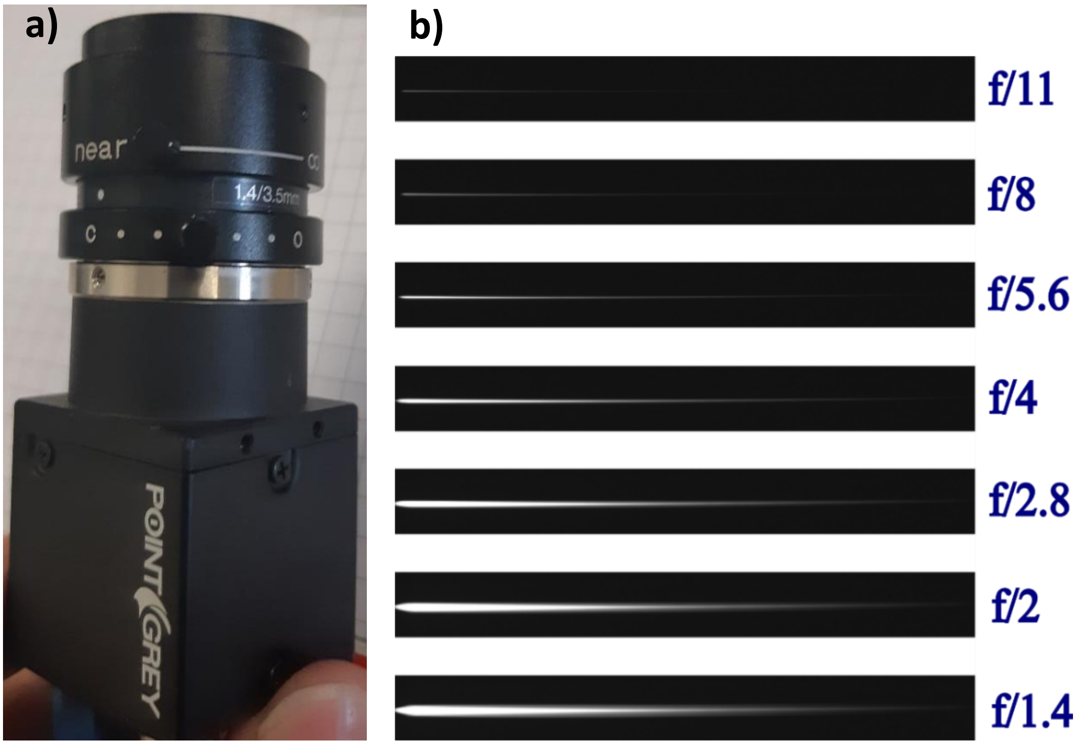

Figure A.3-7. a) Manual settings for focal length [near - ∞] and aperture [c · · · o]. for aperture, the range is continuous, but it contains markings for [f/11, f/8, f/5.6, f/4, f/2.8, f/2, f/1.4], b) Results for the variation of lens aperture on a fixed concentration of Rhodamine 6G, at low laser power.

A.3.2.2. Digital Configuration

Generally, high performance cameras allow for the digital adjustment of many optical parameters (Strobe modes, brightness, Gamma correction, Gain, Exposure, etc.), and can be operated depending on the application. For this experiment, all operation modes were set to manual, for reproducibility, and it was found that the set of key parameters was reduced to the following ones.

Exposure/Shutter time: Exposure is the time interval the camera shutter remains open allowing light through. As will be noted in Section A.3.5, the amount of (fluorescent) light is proportional to dye concentration, so the Exposure/Shutter time should be selected in such a way that the light measured from the expected concentrations do not reach saturation levels and the greyscale range (i.e. pixel depth) is used as optimally as possible. When selecting the exposure time, it is important to consider the desired framerates; if the exposure time is higher than the time it takes to scan a single frame, the camera will automatically adjust the shutter thereby changing the desired greyscale range. The framerate range for the experiments was 5 – 30 fps, and the chosen Exposure times were

$$2.5\,,4.5\,,6.5\,,8.5\,,10.5\ \text{ms}$$

Clearly, no scan time overlap occurs.

Gain: This parameter is the amplification applied to the light intensity read by a pixel sensor as it passes through an A/D converter. It should be noted that this amplification results in a simultaneous increase in brightness and signal-to-noise ratio. After testing the effect of this on recorded images, it was concluded that no increase in quality was obtained by increasing Gain.

Sharpness: Sharpness is a filter applied to the images with the objective of reducing blurring, particularly at the edges. Since the fluorescent readings were taken for a laser beam that occupied a couple of pixels transversely, 'sharpening' the edges of the images did not change the integration process (see Sections A.1 and A.4). However, the influence of blurring must be taken into account for PLIF when information in the edges of a laser sheet is to be described.

A.3.3. Laser Configuration and Alignment

Whilst the selection of image acquisition devices depends on its own capabilities and the features of the experiment, the choice of lasers depends also on the fluorescent dye. Questions of whether the laser wavelength matches the absorption spectrum, light intensity is below the saturation level of the dye and above the weak excitation limit of the dye, and the existence of power attenuation must be considered (Crimaldi, 2008). Furthermore, possible photochemical effects such as photo-bleaching (Crimaldi, 1997) and secondary absorption (Baj, Bruce and Buxton, 2016), must be taken into account when selecting the laser wavelength and emission power.

As mentioned in Section A.1, the experiments presented in this thesis build and expand upon the work presented in West (2016) and Sonnenwald *et al.* (2017); similarly, the instrumentation used in this work was the same. The four lasers used for the LIF system (see Figure A.2-1) are solid state, continuous wave (CW) lasers, manufactured by Changchun New Industries Optoelectronics Tech., with the nominal specifications presented in Table A.3-2.

Table A.3-2. General specifications of the lasers used.

Operating Mode	CW
Nominal Output Power (mW)	200
Transverse Mode	TEM_{00}
Wavelength (nm)	532
Operating Temperature (°C)	10 ∼ 35

In addition to wavelength and power output, it is important to check the operating mode as continuous wave lasers tend to have lower light intensity per exposure than pulsed lasers (Karasso and Mungal, 1997). For applications in which the laser beam must be integrated transversely or be scanned to resolve 2D flow fields, it is important to check that the transverse mode is TEM_{00}. This, in short, means that the laser beam expands transversely in a continuous and Gaussian manner. Lastly, operating temperature must be considered for CW lasers as long-time exposures can induce changes in temperature and thus the fluorescence response.

As seen in Section A.1, incident light intensity is proportional to laser power, which must be quantified in order to characterise attenuation. Table A.3-3 shows the results of power measurements from the lasers, registered in downstream order.

Table A.3-3. Measured output laser powers, lasers are numbered in downstream order.

Laser No	Output Power (mW)
1	180
2	260
3	285
4	242

The lasers used did not have a variable power output, which is necessary to describe the calibration equation (see Section A.1). Alternatively, it is possible to reduce the output power with the use of Optical Density (OD) filters, which are described by the percentage of light transmitted through. The output power for a filtered laser head is modelled with Eq. A.3-1.

$$P_o = P_N\, 10^{-OD} \qquad \textit{Eq. A.3-1}$$

Where OD represents the values of the optical density filter, P_o is the resulting attenuated laser power by the OD filters and P_N is the nominal output power for each laser as presented in Table A.3-3. Figure A.3-8a shows one of the lasers operating at the lowest laser power, attached to the laser head is a strip containing the OD filter strips. The OD values of the filters used for all lasers are show in Table A.3-4.

Table A.3-4. Percentages of transmitted power for each Optical Density filter.

Optical Density OD (-)	**% of transmitted Power** P_o/P_N
0.0	100
0.1	79
0.2	63
0.4	40
0.6	25
1.0	10

In addition to creating a set of output powers to characterise the calibration equation (Section A.1), lowering the output power serves to allow for the alignment procedure. After the LIF window has been aligned in the camera's Field of View (see Section A.3.2) it is necessary to align the laser beam so that it is visible throughout the LIF window from the camera. Figure A.3-8b shows the aligned laser as seen from underneath the flume and Figure A.3-8c shows the measured image from the camera, as it goes from left to right. The light intensity can be seen to diminish along the laser beam. Even for the lowest laser power analysed, the power output is well beyond the safe 1 mW threshold, and thus lasers must be classified as class 3B and be totally enclosed, as Figure A.3-8d shows. Recent laser safety regulation rejects open beam alignment, and consequently the alignment presented in Figure A.3-8 was done remotely using the cameras, and using a rotating base for the lasers, any small adjustment or 'tweaking' of the laser was done with its power supply turned OFF.

Figure A.3-8. a) Installed LIF lasers (2-4) in enclosure, b) Laser head with strip of Optical Density filters, c) Image of Aligned laser within LIF window.

A.3.4. Fluorescent Dye Selection and Concentration Range

The characteristics of the chosen lasers must be taken into account when selecting the type of fluorescent dye to be used and vice versa. Also, the photochemical properties of the dye with respect to pH and temperature sensitivity (Smart and Laidlaw, 1977), reactivity with other chemicals, susceptibility to photo-bleaching (Crimaldi, 1997) and general solubility, must be considered. Further, some general characteristics are desirable from the dye to optimise the optical response from the camera, namely, quantum efficiency and sufficient separation between absorption and emission spectra.

Given the laser available for the experiments, particularly the excitation wavelength of 532 nm, the most appropriate dye is Rhodamine 6G. The peak absorption and emission wavelengths of the dye are around 525 nm and 548 nm, which visually correspond to light at the green and yellow bands of the visible light spectrum. Figure A.3-9 shows a partitioned tank with 4 sections wherein 1 is filled with a small concentration of Rhodamine 6G (R6G) and the remaining ones with water, and laser is fired across the 4 sections; it can be clearly seen the difference in emission intensity and colour band. Another feature noticeable from Figure A.3-9 is the difference in emitted intensity between the laser excitation and the fluoresced dye, which illustrates the high quantum yield[28] of Rhodamine 6G—approximately 0.83 in water (Würth *et al.*, 2012), which tends to be higher than that of Rhodamine B and Rhodamine WT (Bindhu and Harilal, 2001).

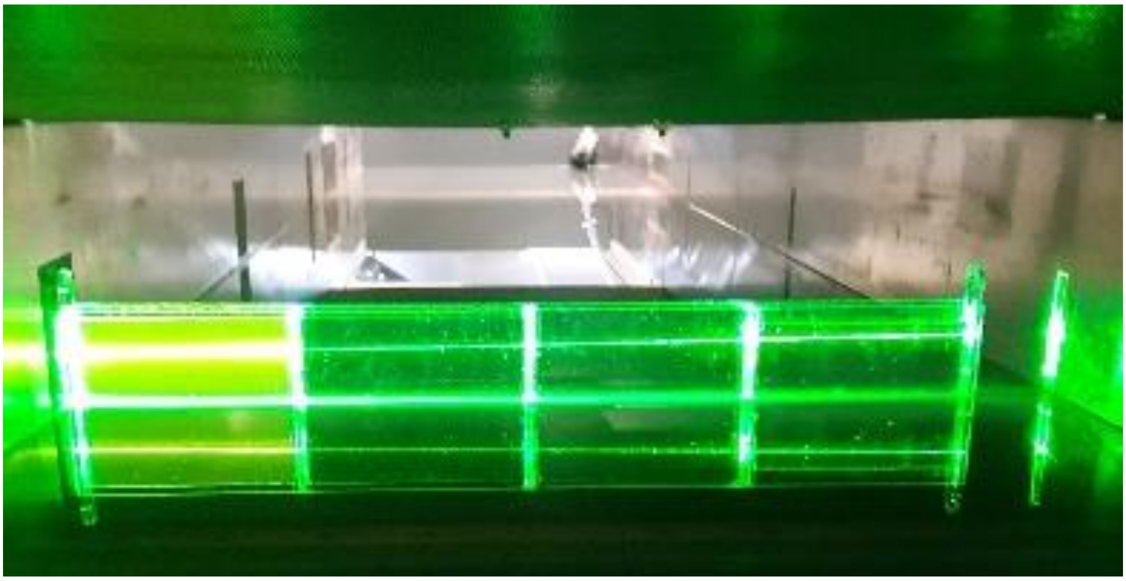

Figure A.3-9. Comparison of emission colour spectra (wavelength) between Rhodamine 6G and water.

Figure A.3-10 shows a comparison between the Absorption and Emission Spectra for Rhodamine 6G (Bioquest, 2019). Note that the excitation source (i.e. laser) falls close to the peak absorbance wavelength, which is the desired case as more of the incident energy is transformed into fluoresced light. The further an excitation wavelength is from the peak absorption the least efficient the emission will be (i.e. the emission spectrum will be scaled down. For comparison purposes, Figure A.3-11 shows the same spectra for Rhodamine WT; the same excitation source is located further from the peak, therefore a lower peak emission is

[28] For reference purposes, it is necessary to clarify the difference between quantum efficiency and quantum yield. The former refers to the ratio of converted electrons to incident photons in a photo-sensor, and the latter refers to the ratio of emitted to incident/absorbed photons in a fluorophore. Accordingly, quantum efficiency is commonly used to describe optical devices and quantum yield is associated to fluorescent dyes.

expected and higher concentrations are required to compensate for the low emission and the inverse proportionality between concentration and quantum yield.

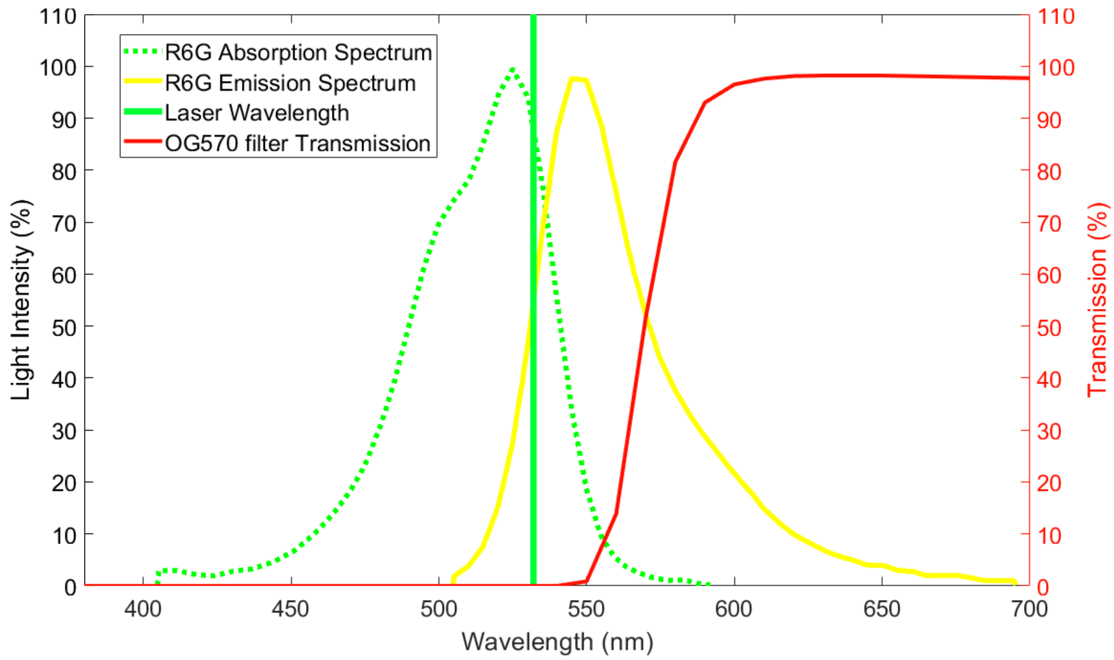

Figure A.3-10. Absorption/Excitation and Emission spectra for Rhodamine 6G in relation to the laser wavelength and the transmission from the camera lens filter.

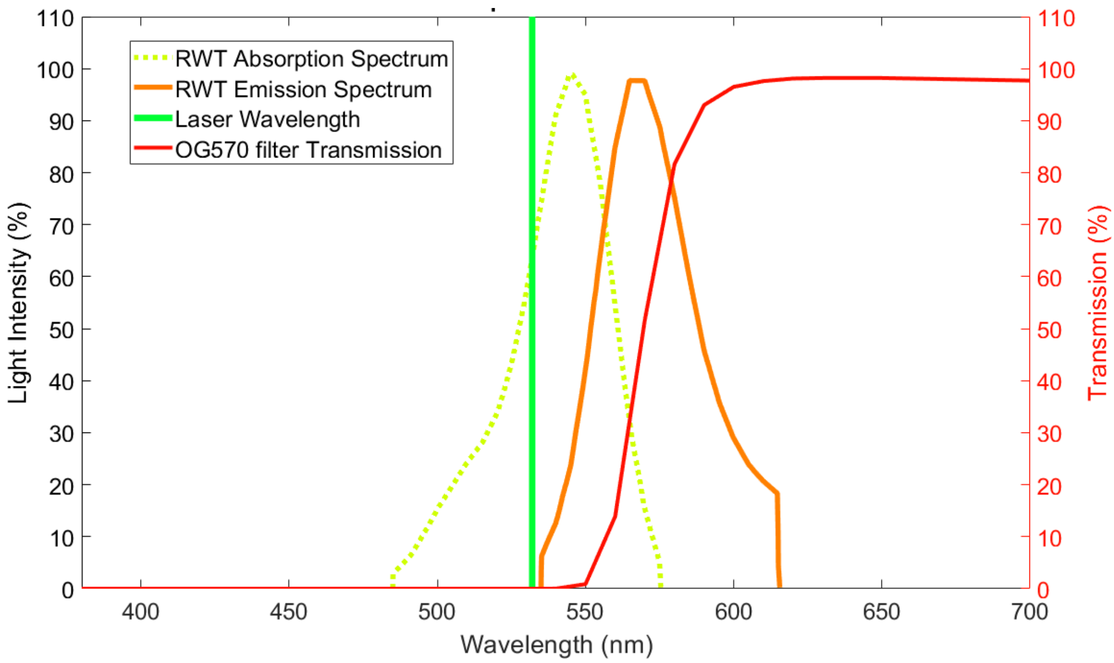

Figure A.3-11. Absorption/Excitation and Emission spectra for Rhodamine WT in relation to the laser wavelength and the transmission from the camera lens filter.

The concentration ranges for these applications must be chosen depending on the incident laser power, and the expected response between concentration and laser intensity. For R6G in aqueous solutions, Zehentbauer *et al.* (2014) reported that the solubility limit of R6G in water is around 0.02 g/ml ($1.5 \cdot 10^7$ ppb), and that concentration and fluorescent intensity are linearly proportional in the range $0 — 10^{-4}$ g/ml ($0 — 7.69 \cdot 10^4$ ppb).

During the calibration, it was found that laser attenuation becomes a problem (i.e. incident light intensity is completely depleted before reaching the opposite side of the flume) for concentrations above 10^{-7} g/ml (77 ppb). For references purposes Table A.3-5 shows some relevant concentration thresholds for R6G, that any researcher could find helpful in future applications of the technique.

Table A.3-5. Rhodamine 6G concentrations of interest.

Reference Concentration	**g/ml**	**ppb**
Lowest measured concentration	10^{-9}	0.77
Upper limit of calibration range	$1.04 \cdot 10^{-7}$	80
Upper limit of $I - C$ proportionality	10^{-4}	$7.69 \cdot 10^4$
Saturation limit of R6G (in water)	0.02	$1.54 \cdot 10^7$
Red-shifting of the peak emission wavelength (structural reconfiguration of R6G molecules)	$2 \cdot 10^{-4}$	$1.54 \cdot 10^5$
Dominant emission peak shifts to $\sim$ 600 nm. Negative $I — C$ proportionality	$4 \cdot 10^{-4}$	$3.08 \cdot 10^5$

Particular attention should be paid to the last 2 reference concentrations given in Table A.3-5. Zehentbauer *et al.* (2014) found the existence of two overlapping peaks in the emission spectrum starting at $2 \cdot 10^{-4}$ g/ml ($1.54 \cdot 10^5$ ppb) with the second one (approximately at 600 nm) becoming dominant with increasing concentration. Before this threshold, the peak emission wavelength remains constant around 548 nm. This consistency indicates that no changes occur in the photochemical or structural properties of R6G molecules, which are also sufficiently isolated for secondary absorption to not be a problem. The red-shift (i.e. a change in dominant emission towards higher wavelengths) is associated with a rearrangement of R6G molecules that induces a change in its electromagnetic properties; a detailed description of this process in given in Gavrilenko and Noginov (2006).

A.3.5. Camera Lens Filter

To avoid interferences, the image acquisition device must be coupled with a filter that only allows light within the band corresponding to the fluorescent dye emission spectrum. For the LIF experiments presented in this document, a Long-Pass filter with a cut-on wavelength of 570 nm (OG570) was used, shown in Figure A.3-12a. Ideally, the transmission curve of the filter should cover as most of the emission spectrum whilst excluding the excitation wavelength. Figure A.3-12 shows the transmission curve of the chosen filter and the emission spectrum of R6G. Although it is successful in excluding the excitation wavelength from the laser, it admittedly only includes a portion of the emission spectrum.

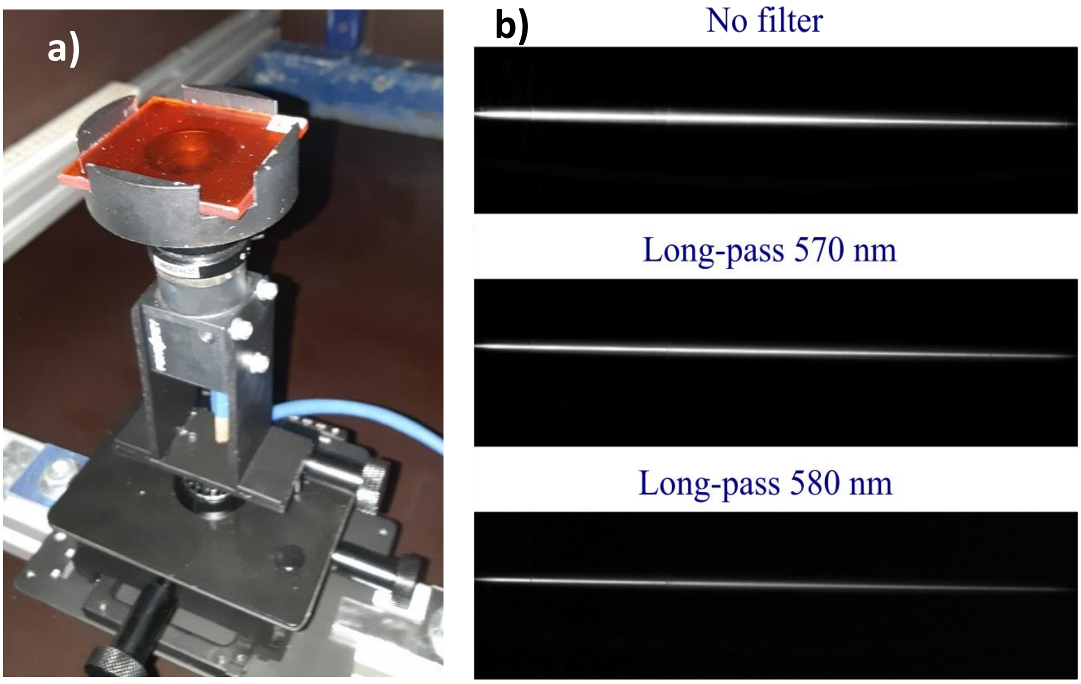

Figure A.3-12. a) Long pass filter selected for the Calibration/Experiments OG570, b) Effect of long-pass filters on the exclusion of non-fluorescent light.

Nevertheless, the light transmitted through the chosen sensor, though limited, was seen to be sufficient to fully describe the entirety of the laser beam. Figure A.3-12b shows a comparison between the images obtained using different filters: clearly, non-filtered images are over-saturated as parallel emissions from fluorescent light and laser reflections merge when reaching the camera sensor. The difference between filtered images, as shown in Figure A.3-12b, has to do with the proportion of the emission spectrum that is allowed through the glass filter. For a combination of concentration and laser power in which attenuation is significant, the choice of filter can obscure information towards the further end of the beam.

A.4. Calibration Results

Once enough calibrations have been performed, and a comprehensive dataset with an optimal intensity response and a sufficiently inclusive concentration range is at hand, it is necessary to calculate the necessary parameters to obtain accurate scalar maps. This section is devoted to the numerical treatment of the calibration data, and the results of the process undertaken. The sample results shown are for a single camera. First, let us define M_{mn} to be numeric matrix defining any image from the calibration dataset, so that m represents a pixel row and n a pixel column. Consider then

$$1 \leq m \leq N_{rows}$$
$$1 \leq n \leq N_{beam}$$
Eq. A.4-1

Where N_{beam} is the number of columns necessary to describe the length of the beam. This implies that, first, the laser's start and end points have been identified (see Section A.3.4) and the images trimmed accordingly, and second, that the LIF window was aligned with the image's central horizontal axis as much as possible.

With this in mind, the matrix M_{mn} will represent the greyscale value of intensity measured by the image at pixels (m,n). Recognising that images for varying concentrations and input laser power were obtained, let us now define $M_{mn}^{(c,p)}$ as the image taken for the c-th concentration and p-th laser power value. This new definition requires the distinction of c and p as indices of the arrays of concentration and power values, as opposed to the actual values of concentration and power output, which will be identified, admittedly rather oddly, as $C^{(c)}$ and $P_o^{(p)}$. The indices c and p must allow for the boundary cases of zero concentration and power (which are necessary to remove background and characterise white noise, respectively), thus, we have

$$0 \leq c \leq N_c$$
$$0 \leq p \leq N_p$$
Eq. A.4-2

Evidently, N_c and N_p represent the number of Rhodamine 6G injections and output powers tested. Figure A.4-1 shows an arrangement of LIF images, that is, an array of matrices of the form, $M_{mn}^{(c,p)}$. As mentioned in Section A.3.4, power output was varied by attaching filters with different Optical Densities to the laser head, which have different transmission percentages; accordingly, the columns in Figure A.4-1 show the differences in power output expressed as percentage of the nominal power transmitted by the OD filters; rows present variations in concentration. For the $M_{mn}^{(c,p)}$ images presented in Figure A.4-1, some intuitive conclusions can be derived.

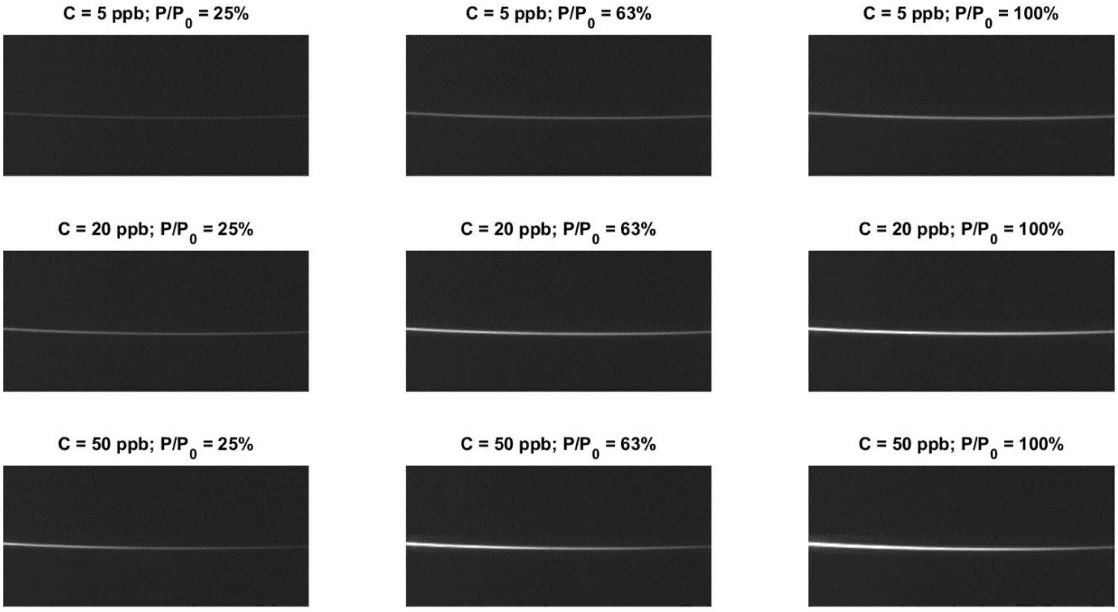

Figure A.4-1. Calibration images taken for a subsample of concentration and power values.

The proportionalities of measured intensity with concentration and power seem to follow what is theoretically expected. Additionally, it is possible to see that the beam occupies by a few pixels in the vertical direction for each longitudinal point, consequently an integration procedure is in order to obtain the total laser power at each discrete longitudinal point. The following equation

$$B_n^{(c,p)} = \frac{1}{W+1} \sum_{i=-W/2}^{W/2} M_{mc+i\,,n}^{(c,p)} \qquad \textit{Eq. A.4-3}$$

Expresses the integration procedure necessary to reduce the image into the one-dimensional array, $B_n^{(c,p)}$, representing the total beam intensity at each pixel n, for the combination of concentration and power (c, p). The summing window $W + 1$ must be a known value obtained from visual inspection. Although there is no upper limit for W, it is recommended that a value just sufficient to describe the beam is chosen to avoid noise-induced biases. Finally, mc represents the location of the peak intensity (i.e. centre of the beam) for the n-th column.

Normally, cameras have either a pre-set or controllable brightness setting that defines a baseline darkness value (so that the sensor measurement does not reach zero even in the absence of light sources). This means that even for the case of zero concentration and/or zero laser power, the following relation holds

$$B_n^{(0,p)}, B_n^{(c,0)}, B_n^{(0,0)} \neq 0 \qquad \textit{Eq. A.4-4}$$

Also, remembering that the filters used to isolate the emission spectrum exclude radiation for zero concentration, the following relation must hold

$$B_n^{(0,p)} \approx B_n^{(c,0)} \qquad \textit{Eq. A.4-5}$$

The strict equality is avoided in virtue of the random nature of white (or in this case dark) noise. Under these considerations, it naturally follows that the expression

$$I_n^{(c,p)} = B_n^{(c,p)} - B_n^{(0,p)} \qquad \textit{Eq. A.4-6}$$

Defines the longitudinal variation of intensity caused only by fluorescence. Figure A.4-2 shows the procedure described by Eq. A.4-3 to Eq. A.4-6 on the images shown in Figure A.4-1. Undoubtedly, intensity and power attenuation are present for the dataset analysed, which tends to have an exponential decay. Also, it can be safely concluded that at least for the ranges of concentrations and power shown, laser power is not depleted before reaching the far end of the flume.

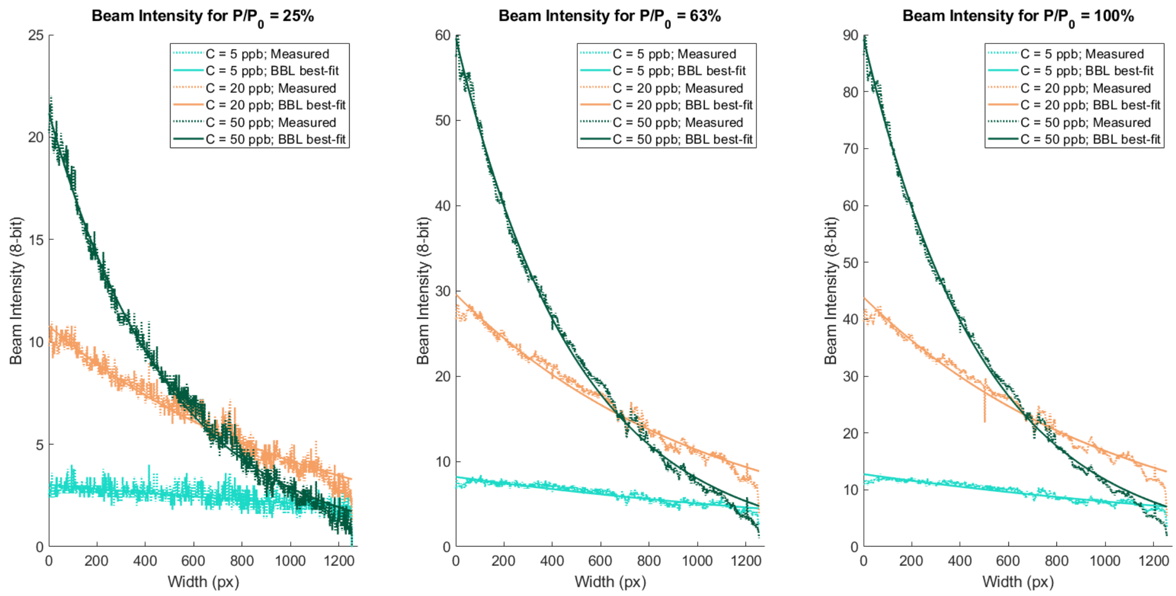

Figure A.4-2. Beam intensity for the images shown in Figure A.4-1.

As seen in Section A.1, the loss of intensity/power of light as it traverses through a medium can be modelled by the Bouguer-Beer-Lambert law, BBL (Ferrier, Funk and Roberts, 1993; Mayerhöfer, Pahlow and Popp, 2020), which says that, in the absence of strong density-related reflections, or electromagnetic effects, the amount of light intensity, $I(x)$, transmitted through a point x, along the path of a light beam is defined as

$$I(x) = I_o \exp(-\eta x) \qquad \textit{Eq. A.4-7}$$

Where I_o is the incident light intensity and η is called the attenuation/absorption/extinction coefficient, which is conventionally only dependent on the concentration of the solute through which light travels, and is constant provided that concentration remains constant.

The enclosed calibration section was fitted with recirculation components, to mix the fluorescent dye throughout, and obtain uniform concentrations, which are necessary to derive calibration parameters. Considering then that concentrations were uniform when the images in Figure A.4-1 were taken, it is possible to fit an exponential decay function describing the BBL law (Eq. A.4-7) to the experimental recordings of intensity shown in Figure A.4-2. Indeed, the fitted curves (shown as solid lines in Figure A.4-2) approximate remarkably well the variation of intensity along the beam path. Converting the BBL law equation to discrete form and applying the nomenclature used thus far, the fitted curves are of the form

$$I_n^{(c,p)} = I_o^{(c,p)} \exp(-\eta^{(c,p)} n) \qquad \textit{Eq. A.4-8}$$

The best-fit coefficients, $I_o^{(c,p)}$ and $\eta^{(c,p)}$, represent the non-attenuated light intensity and the absorption coefficient for the concentrations and power values tested. Focusing first on the array of attenuation coefficients measured, $\eta^{(c,p)}$, plotting its variation with respect to C and P will help to elucidate the behaviour of any functional form. Figure A.4-3 shows plots of η as a function of Concentration, for the different power output values tested. Evidently, the attenuation coefficient follows a linear behaviour with concentration and shows no discernible difference with output laser power—which is clear from the fact that all points and best-fit curves tend to collapse on a single line. The linear best-fit curves shown in Figure A.4-3 for $\eta(C)$ are in agreement with the general equation given by (Ferrier, Funk and Roberts, 1993),

$$\eta(C) = \eta_w + \epsilon_o C \qquad \textit{Eq. A.4-9}$$

However, it is important to point out that whilst in (Ferrier, Funk and Roberts, 1993) η_w is considered to be the attenuation coefficient due to clean water, and thus can be used as a check for the performance of the calibration[29], in reality, care must be exercised when comparing it with reference values since, as has been seen, the use of lens filters eliminates the incidence of fluorescence due to pure water. In conclusion, η_w will be considered to be a purely empirical value from now on.

[29] Ferrier, Funk and Roberts (1993) proposes an independent test for the estimation of n_w that consists in using a partitioned tank (similar to the one shown in Figure A.3-9) to measure fluorescence in particular partitions after sections of clean water.

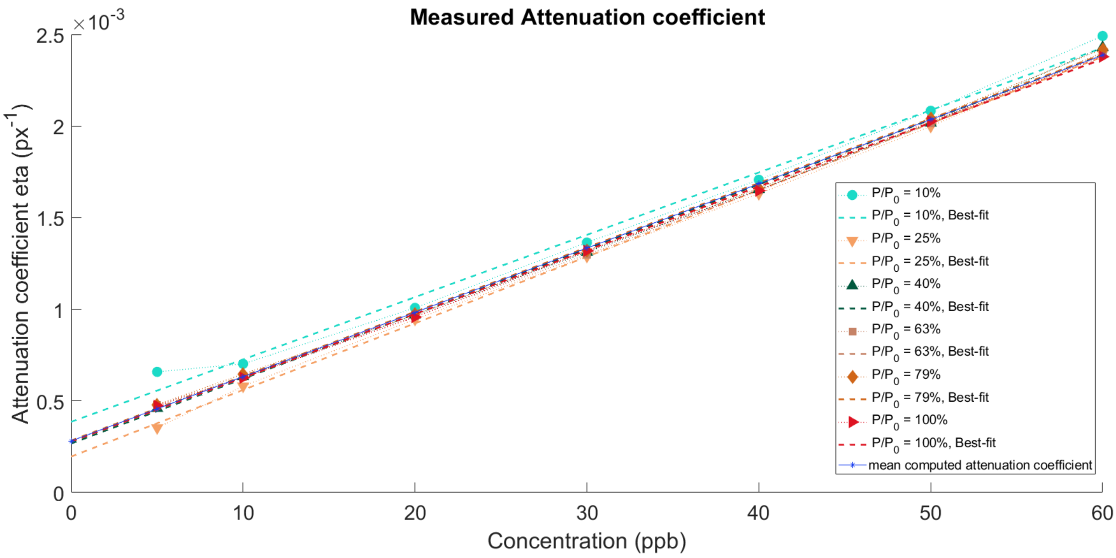

Figure A.4-3. Variation of attenuation coefficient with concentration.

The other set of best-fit parameters from the BBL law, $I_o^{(c,p)}$, clearly has a double dependence on concentration and power and thus, conclusions similar to the ones for η cannot be applied. This double dependence can be represented analytically as

$$I_o = f(C, P) \quad \textit{Eq. A.4-10}$$

If desired, a surface map representing Eq. A.4-10 can be constructed using the measured values $I_o^{(c,p)}$, and the known quantities $C^{(c)}$ and $P_o^{(p)}$, and an approximate equation derived. However, approaches of this sort require sample sizes much higher than the ones attainable from an LIF calibration, moreover, optimisation procedures tend to be sensitive to the number of additional parameters used.

Physically, we know that for the ranges of concentration and power values tested—and indeed for most cases—fluorescent intensity is linearly proportional to both concentration and power. Extending to the general case, and knowing that C and P are independent variables, we can expand Eq. A.4-10 into the following expressions

$$I_o^{(c,p)} = f_c\left(P_o^{(p)}\right) \quad \textit{Eq. A.4-11}$$

$$I_o^{(c,p)} = g_p\left(C^{(c)}\right) \quad \textit{Eq. A.4-12}$$

Eq. A.4-11 and Eq. A.4-12 have the advantage of allowing a simultaneous check of each function form, and any possible erroneous data points. This is because, by having independent parameters, variations in the functions f_c and g_p, with respect to C and P, respectively must only involve differences in scale. For instance, if it was found that if either, or both, functions are linear, then f_1 and f_2 (i.e. f_c for $c = 1$ and $c = 2$, respectively) will be linear expressions, although f_2 will have a higher slope.

Figure A.4-4 and Figure A.4-5 show the experimental expressions for Eq. A.4-11 and Eq. A.4-12, respectively. As expected, intensity and laser power are linearly related, with lower errors for low concentrations. Regarding the relationship between Intensity and concentration, although a linear trend could be used to describe the function at the expense of some variation for high output powers, it was found that a Power relation of the form

$$I = g_P(C) = a_0 C^{b_0} \qquad \textit{Eq. A.4-13}$$

Performs much better in describing the variation between concentration and intensity. Furthermore, the pseudo boundary condition for zero concentration, allows for a better description of intensities and concentrations at very low fluorescence.

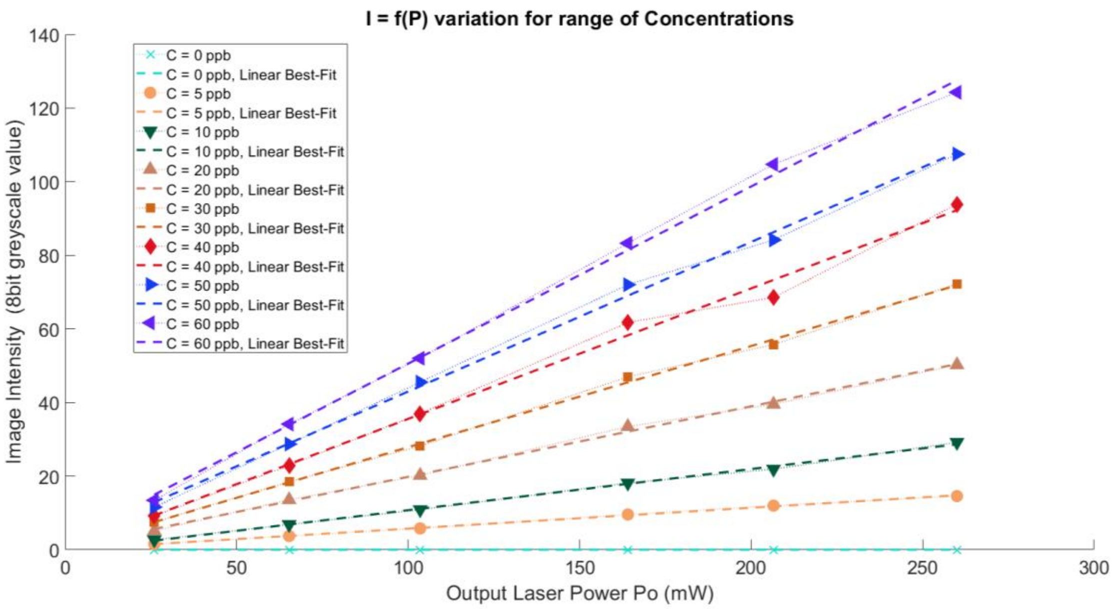

Figure A.4-4. Variation of intensity values with Output Power as a function of concentration. Experimental results show a clear linear dependence.

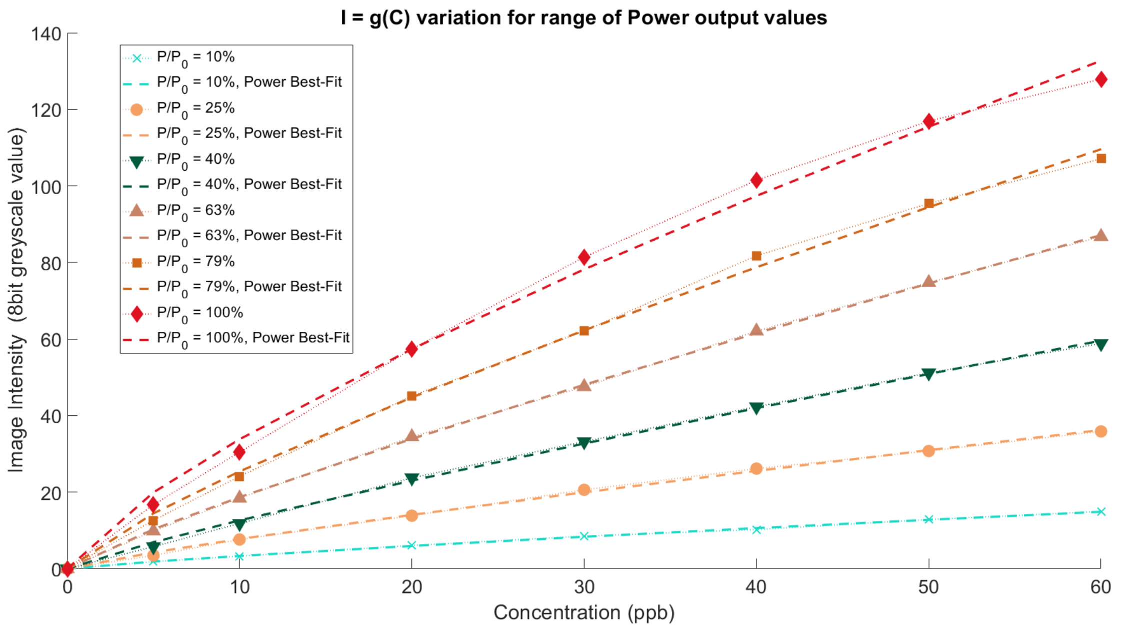

Figure A.4-5. Variation of intensity values with Concentration, as a function of Power output. Experimental results show a slight power function dependency.

Another important point regarding the linear relationship found in Figure A.4-4, is that it allows for the quantification of a surrogate for the quantum yield. With this in mind, consider the relation

$$\frac{\partial I}{\partial P} \approx \frac{I}{P} = \alpha \equiv \alpha(C) \qquad \textit{Eq. A.4-14}$$

Which defines the *Fluorescence Efficiency*, α, of the dye at different concentrations. Clearly, the experimental values of α can be found by computing the slope for each line in Figure A.4-4. Also, following the functional form defined in Eq. A.4-13, we can express the full calibration equation for single-line LIF experiments, as

$$\frac{I}{P} = a_1 C^{b_1} + e_1 \qquad \textit{Eq. A.4-15}$$

The experimental results of this expression are shown in Figure A.4-6, for the 4 cameras used. It should be noted that the coefficients found for the expression yield curves that fit remarkably well with the measured values of the fluorescent efficiency, α. Again, the choice of the third parameter e_1 is more a matter of convenience than precision. Physically, fluorescence efficiency expresses how effective is the dye in converting incident power into emitted light, which it naturally increases with concentration. It is then natural to assume/expect that as we approach $C \to 0$, α also becomes zero, since in the absence of dye, there is no conversion of incident power into fluorescent light.

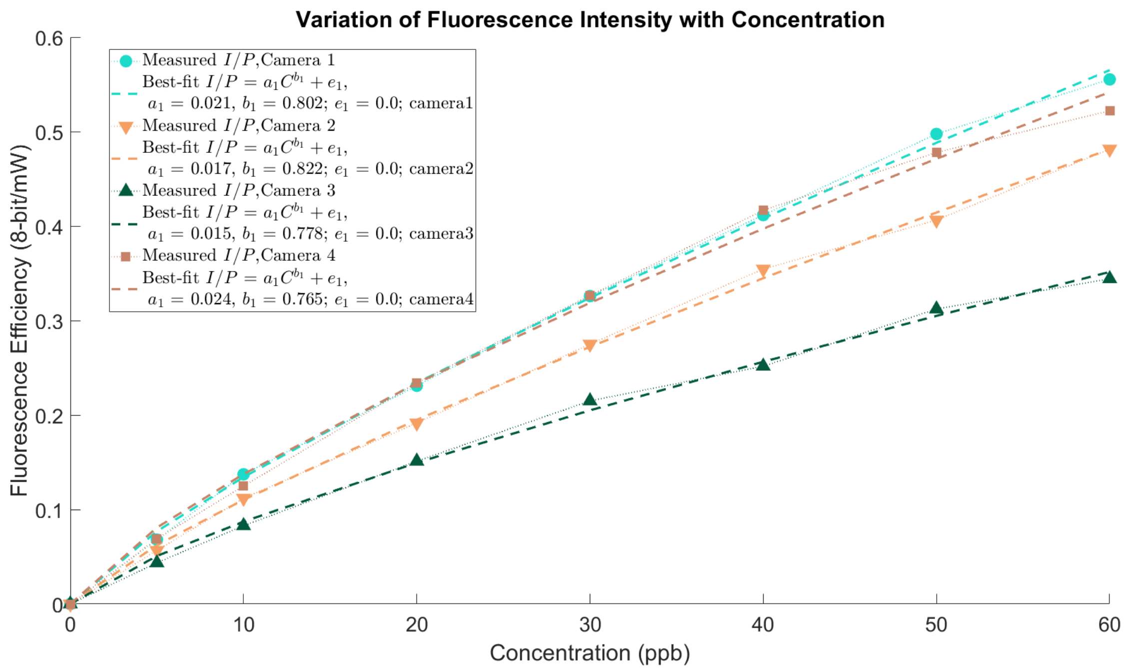

Figure A.4-6. Variation of Fluorescence efficiency with concentration. General Parameters for the camera calibration equation.

With this in mind, the final expression derived for the calibration procedure, which can be converted into an explicit equation to find I, P or C is given by

$$I = a_1 P C^{b_1} \qquad \textit{Eq. A.4-16}$$

Up to this point, the derivation of the calibration parameters has been completed. The conversion of intensity values into spatially variable distributions of concentration is done via a simultaneous application of Eq. A.4-16, and the use of Eq. A.4-9 and the BBL to define a stepwise expression for the calculation of power and concentration for concentration-varying fields. The following section shows the application of this technique to the recovery of uniform concentration profiles from the calibration data. A discussion on the limitations and possible sources of error is given, and further recommendations and assessments of the technique applied are given in the subsequent section.

A.5. Calibration Performance Analysis

In the previous section, the calibration equation relating laser power, measured intensity and concentration was obtained from experimental data. As mentioned in Section A.1, when laser power attenuation is an issue, as can clearly be seen from Figure A.4-2, obtaining concentration values requires a description of power extinction alongside the calibration equation. Discretising the general formulation for the BBL law, given in Eq. A.1-5, the following equation is obtained (Ferrier, Funk and Roberts, 1993).

$$P_{n+1} = P_0 \exp\left[-\sum_{i=0}^{n} (\eta_w + \epsilon_0 C_i) \Delta x_i\right] \qquad \textit{Eq. A.5-1}$$

If the calibration parameters described in Eq. A.4-16 and Eq. A.5-1, are known, it is possible to obtain concentration values from the measured beam intensities. Naturally, the first check of the calibration procedure is to reapply the calculated parameters to the calibration data, so that variations in laser power and fluorescence efficiency can be analysed. Uniform concentrations should be obtained.

Figure A.5-1 shows the computed laser power variation for the same subsample of data, from which the intensities shown in Figure A.4-2 are drawn. Given the physical characteristics of the flume, and the output power from the lasers used, it can be seen that attenuation is highly dependent on concentration, to the point where it is possible for laser power to deplete during the beam path, as it is the case for the plot of $P/P_0 = 63\%$.

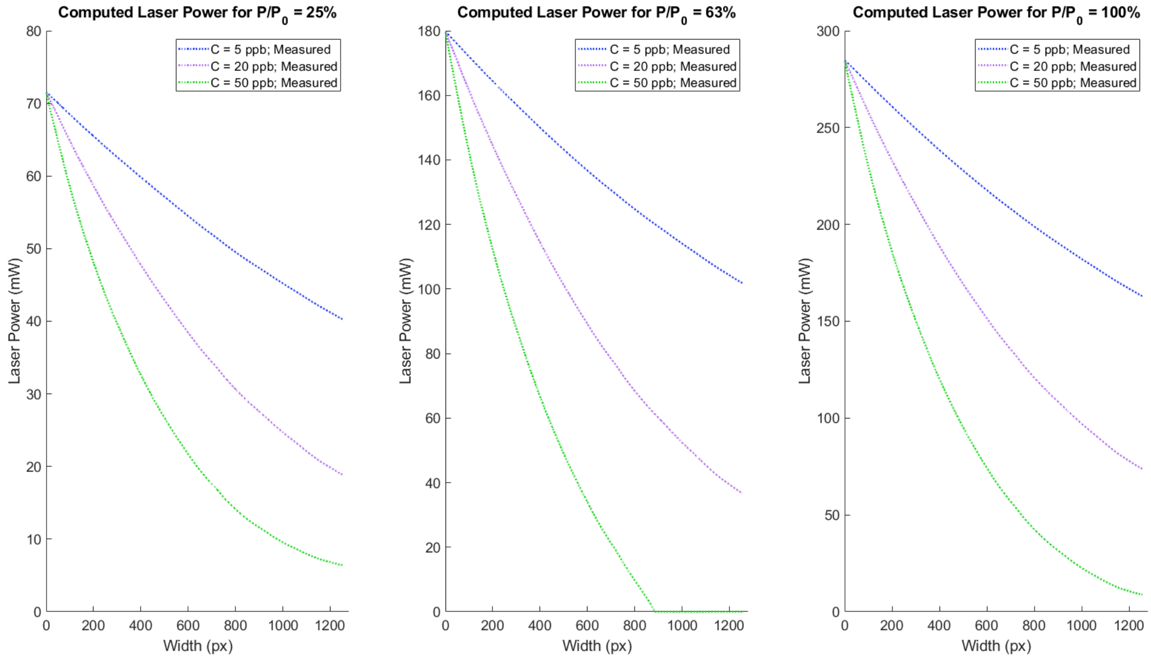

Figure A.5-1. Computed Laser Power for the subsample of calibration values analysed.

The effects of low laser power, particularly in conjunction with high Rhodamine 6G concentrations, are more visible when computing fluorescence efficiency from the calibration data (see Eq. A.4-15), as shown in Figure A.5-2. Since calibration images are taken with uniform concentrations of dye, changes in intensity and laser power should be equivalent for all points along the beam path, and α should, in consequence, be constant. When comparing Figure A.5-1 and Figure A.5-2, it is clearly seen that deviations in the assumed constant value of fluorescence efficiency occur at the same points that laser power reaches minimum values. It should be noted that when laser power approaches zero, variations in fluorescence efficiency become sensitive to noise in measured intensity.

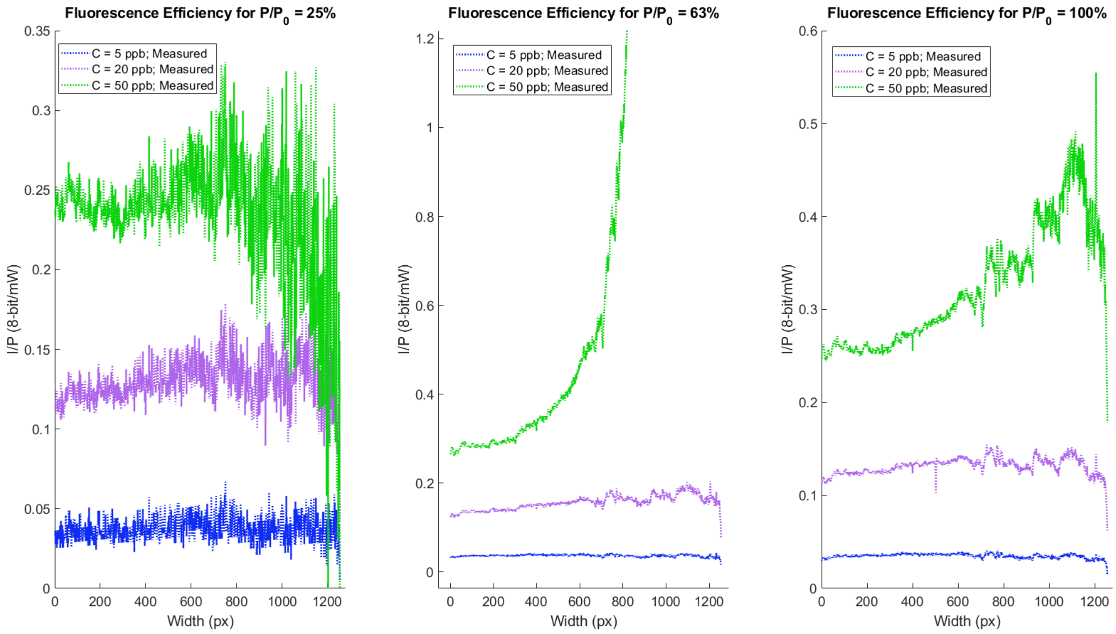

Figure A.5-2. Computed Fluorescence Efficiency for the subsample of calibration values analysed.

When concentration is computed from this dataset, as shown in Figure A.5-3, it is clear that the errors in estimated fluorescence efficiency carries over to concentration. It can also be seen that calculated concentrations from nominally low values are uniform as initially expected. Regardless of the apparent instability caused by extremely low values of laser power, these are particular cases in which the entire flow field contains a uniform high concentration of dye, such that the laser beam will attenuate more than it would through a cloud of dye during the experimental phase. Furthermore, the linear behaviour of the concentration-dependent attenuation coefficient shown in Figure A.4-3 seems to confirm the reliability of the calibration information derived.

Another point to consider is the specific non-negative restriction on concentration values imposed by the semi-linear definition of fluorescence efficiency given in Eq. A.4-15. This feature of the calibration equation will generate a positive bias on background noise, which nonetheless seem not to generate any considerable errors in the computed concentration maps. Also, despite the fact that calibration equations of the form described in Eq. A.4-10 have been reported to be linear; linearity is not strictly followed for the general calibration equation found in this document. This is due to possible differences in actual concentrations measured (i.e. monitored) and estimated ones (from injections).

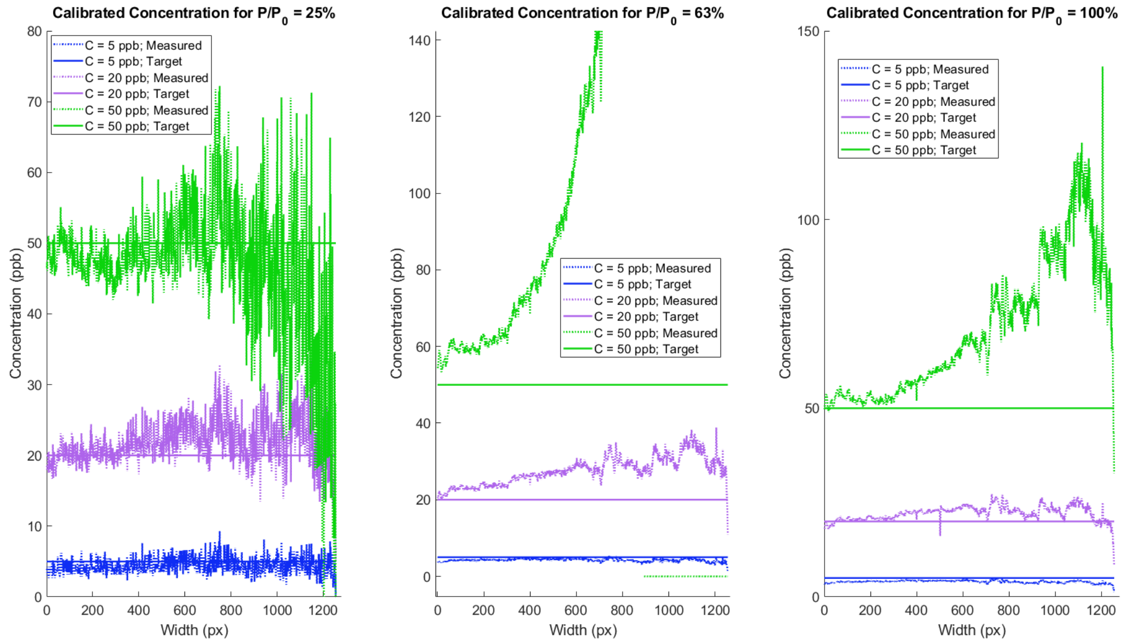

Figure A.5-3. Computed Calibrated Concentrations for the subsample of calibration values analysed.

A.6. Recommendations for future applications of the technique

- The lasers used have power outputs smaller than all references found, which explains the immense variation of the attenuation response with relatively small variations in concentrations. Based on the present work, it is recommended that LIF applications in similar flow fields (e.g. beam path length = 1 m) incorporate lasers with at least a power output of 1W.
- Although *in situ* calibrations are preferred to avoid uncertainties and errors associated with changes in the set up used; the use of calibration cells could help improve control over quantities like dye concentrations and laser beam attenuation.
- Pixel-distance calibrations and camera alignment should be done prior to obtaining calibration data, in this way, a better control over the FoV can be gained.
- Given the facility with which digital cameras can be operated, it is advised to generate Multi-parametric calibration equations, $I_o^{(c,p)} \rightarrow I_o^{(c,p,s,g,\dots)}$, that could include changes in parameters such as camera exposure time, camera gain (to control intensity-associated noise) and different pixel depths.

Appendix B. PIV METHODOLOGY

Particle Image Velocimetry (PIV) is an optical technique used to calculate spatially and temporally-resolved velocity fields in illuminated flows. This section focuses on the use of this technique for the study of hydrodynamics in flows through emergent artificial vegetation (i.e. cylinders). The aim of this chapter is therefore to give a brief overview of PIV, and discuss the main technical challenges encountered during the set-up stage, and the solutions applied. The study of the hydrodynamic data acquired and its relation to mixing is explored in Chapter 6 and Chapter 7. Previous studies have included isolated obstructions similar to the ones used here to represent vegetation. To the author's knowledge, this study is the first one to apply PIV to the investigation of obstructed flows at a reach scale, so that the results can be extrapolated to the full extent of the vegetated field proposed.

Section B.1 presents a brief overview of the development of PIV as a technique, some relevant previous applications, and the theory behind cross-correlation computations between PIV frames (the basis for displacement calculations). The section of the flume where PIV measurements were taken is outlined in Section B.2, followed by a description of the PIV components and their *in situ* configuration in Section B.3. The specific challenges related to non-uniform illumination and cylinder-induced reflection/refraction problems, and their treatment is discussed in Section B.4. The merits and limitations of this particular application are summarised and recommendations for future use are presented in Section B.5.

B.1. Background

PIV is used to obtain instantaneous velocity maps over illuminated areas of a flow field. This is achieved by computing the relative displacements of tracer particles following the movement of the fluid, between consecutive frames captured at regular intervals. For a fully functional PIV system, it is then necessary to consider 3 main components: imaging equipment, illumination source alongside sheet optics, and seeding particles. The level of detail that can be attained from any application depends on the specific equipment chosen, as well as the flow field. For this project, this will be described in more detail in Section B.3. Below is an overview of the relevant evolution of PIV, followed by a concise description of the statistical theory.

B.1.1. Historical Overview

As described in Chapter 4 and Appendix A (LIF), optical techniques in fluids originate from the observation and qualitative descriptions of flow phenomena and, as technology advances, these processes can be quantified. Initial explorations by Ludwig Prandtl and Friedrick Ahlborn (Rotta, 1990), using early photography equipment and metallic trace particles, identified the existence of vortical structures in the flow behind blunt bodies. These were revealed from the streak patterns in both time-integrated and double-exposure photographs (Hinterwaldner, 2015). These early experiments were mainly qualitative. Advances in illumination stability and frequencies (Kompenhans and Reichmuth, 1986), allowed the recording of multiple particle exposures in the same frame, and use image autocorrelation methods to compute velocity maps (Adrian, 1986). This workaround to low camera transfer rates proved effective in the study of several flows (e.g. boundary layers, Kompenhans and Hoecker, 1989), although issues such as velocity ambiguity remained (Raffel *et al.*, 2018).

The biggest leap in the quantification of velocity vector maps, occurred largely due to the availability of high-speed, digital cameras, so that independent exposures could be saved as discretised maps, and cross-correlated (Keane and Adrian, 1992). Thus eliminating ambiguity and improving spatial resolution (Willert and Gharib, 1991; Westerweel, 1993). Digital equipment has also allowed a quantitative analysis of Prandtl's early PIV recordings (Willert and Kompenhans, 2010). A comprehensive review of the technological milestones and theoretical development for PIV can be found in Raffel *et al.* (2007) and Adrian and Westerweel (2011), respectively.

Although the description given here corresponds to conventional (i.e. 2D) PIV, as technology advances, its uses and capabilities continuously expand. For instance, recent developments have allowed the recording of out-of-plane velocity components via Stereoscopic PIV (Kähler, 2004) and full 3D fields through Tomographic PIV (Schröder *et al.*, 2011). More recently, full 3D (mid-density) Lagrangian flow fields can be derived from techniques such as Shake-The-Box (Schröder *et al.*, 2015).

B.1.2. Theoretical Framework

The development of PIV encompasses both the equipment and techniques necessary to transform illuminated frames into velocity fields. Raffel *et al.* (2018) divides the PIV system into the following subsystems: 1) Seeding, 2) Illumination, 3) Recording, 4) Calibration, 5) Evaluation and 6) Post-processing; which also corresponds to the sequence of any PIV test. Parts 1 to 4 are related to the specifications and configuration of the physical PIV components, which are described in Section B.3. Part 5 refers to the theoretical treatment of the images to transform particle patterns into velocity vectors, which will be explained below. Part 6 refers to the process of identifying, eliminating and replacing erroneous velocities, for which knowledge of the statistical behaviour of velocity is necessary, thus it will be covered in Chapter 6.

The statistical methods used to compute the probable displacements of particles, depend on the physical equipment, its configuration, and the objectives of the experiments. For instance, the density of seeding particles in the illuminated plane (also called interrogation volume) will determine the frame of reference for the description of velocities. For low densities, where the distance between particles is considerably larger than their individual displacement between frames, individual trajectories can be described, and Particle Tracking Velocimetry (PTV) is used to compute Lagrangian velocities. In intermediate and high densities, where particles are closer than their individual and group displacement, the displacement of groups of particles, i.e. patterns, is considered, and conventional PIV methods are used to obtain velocities in a Eulerian frame of reference. Further, the type of camera will determine whether consecutive exposures can be saved in separate frames, in which case the displacement calculation method will be different. For this project, a single CCD camera was used and a Eulerian description of velocities is pursued, therefore only cross-correlation methods (single-exposure double-frame recordings) for high-density PIV will be considered. For information on the other techniques, or a more complete description of the concepts presented here, the reader can refer to Raffel *et al.* (2018) and Adrian and Westerweel (2011).

The theory of displacement computation for PIV follows a general principle of 'pattern matching', that will be explained, first, for a continuous (cf. analogous) domain, and the extension to the digital (cf. discrete) domain, naturally follows. Initially, consider $\overrightarrow{X_p}$ as the array of particles passing through the illuminated plane during the recording. From this array, the map of light scattered during a exposure at $t = t_1$ is defined as $I(\overrightarrow{X_p}, t_1) \equiv I_1(\overrightarrow{X_p})$, a subsequent recording taken at $t_2 = t_1 + dt$, is $I(\overrightarrow{X_p}, t_2) \equiv I_2(\overrightarrow{X_p})$. The difference between I_1 and I_2 is the displacement that particles $\overrightarrow{X_p}$ have undergone during the interval dt.

The intensity maps cover the entire illuminated area, so that the full set $\overrightarrow{X_p}$ refers to the entire flow field. In order to optimally construct a velocity field, it is necessary to divide I into interrogation windows, the size of which should be determined in such a way that particles within must experience the same displacement. Defining $\tau_1(\overrightarrow{X_p})$ and $\tau_2(\overrightarrow{X_p})$ as the maps corresponding to the same interrogation window within maps I_1 and I_2, respectively, the act of searching for a 'match' between the locations of $\overrightarrow{X_p}$ at times t_1 and t_2, can be expressed as the cross-correlation function, $R(\vec{s})$, defined over the displacement domain $\vec{s} = (\Delta x, \Delta y)$.

$$R(\vec{s}) = \int \tau_1(\overrightarrow{X_p})\, \tau_2(\overrightarrow{X_p} + \vec{s})\, d\vec{X} \qquad \textit{Eq. B.1-1}$$

The correlation value over the displacement domain, $\vec{s}$, will be the result of the additive effects of the different interactions between particles, which are the main source of illumination in both interrogation maps. Accordingly, $R(\vec{s})$ can be defined as

$$R(\vec{s}) = R_C(\vec{s}) + R_F(\vec{s}) + R_D(\vec{s}) \qquad \textit{Eq. B.1-2}$$

The definition given in Eq. B.1-2 breaks down the correlation into independent effects. $R_C(\vec{s})$ is the convolution of mean light intensity over both interrogation windows, $R_F(\vec{s})$ is a random component associated to the contribution of intensities from non-matching particles, and $R_D(\vec{s})$ is the cross-correlation peak obtained when the displacement vector $\vec{s}$ equals the peak location $\vec{s} = \overrightarrow{s_D}$, which matches the particles in τ_1 to their displaced versions in τ_2.

For the actual digital recordings at intermediate and high densities, individual particles cannot be statistically identified. The continuous maps for each frame take the form of a random illumination array as expressed in Eq. B.1-3[30]. So, the two frames $I_1(\overrightarrow{X_p})$ and $I_2(\overrightarrow{X_p})$ are respectively expressed as $I_1[m,n]$ and $I_2[m,n]$. Similarly, the discrete versions of the interrogation windows are expressed as $\tau_1[m,n]$ and $\tau_2[m,n]$. The values m and n are the local indices representing the row and column pixels of each digital image.

$$I(\overrightarrow{X_p}, t_1) \rightarrow I_{mn}(t_1) \equiv I_1[m,n] \qquad \textit{Eq. B.1-3}$$

Figure B.1-1a shows two sample image recordings taken during the set-up stage of the configuration shown in Section B.2, before locating the glass stems. The frames I_1 and I_2 shown

[30] The equivalence $A_{mn} \equiv A[m,n]$ expresses the value of indices m and n in array (matrix) A. Second notation is used when sub-indices are necessary to identify the array, and avoid ambiguity (See Nomenclature Section).

are a sequence of captured images of a seeded flow, where the motion of particles can clearly be seen, and the green rectangles show the interrogation windows τ_1 and τ_2.

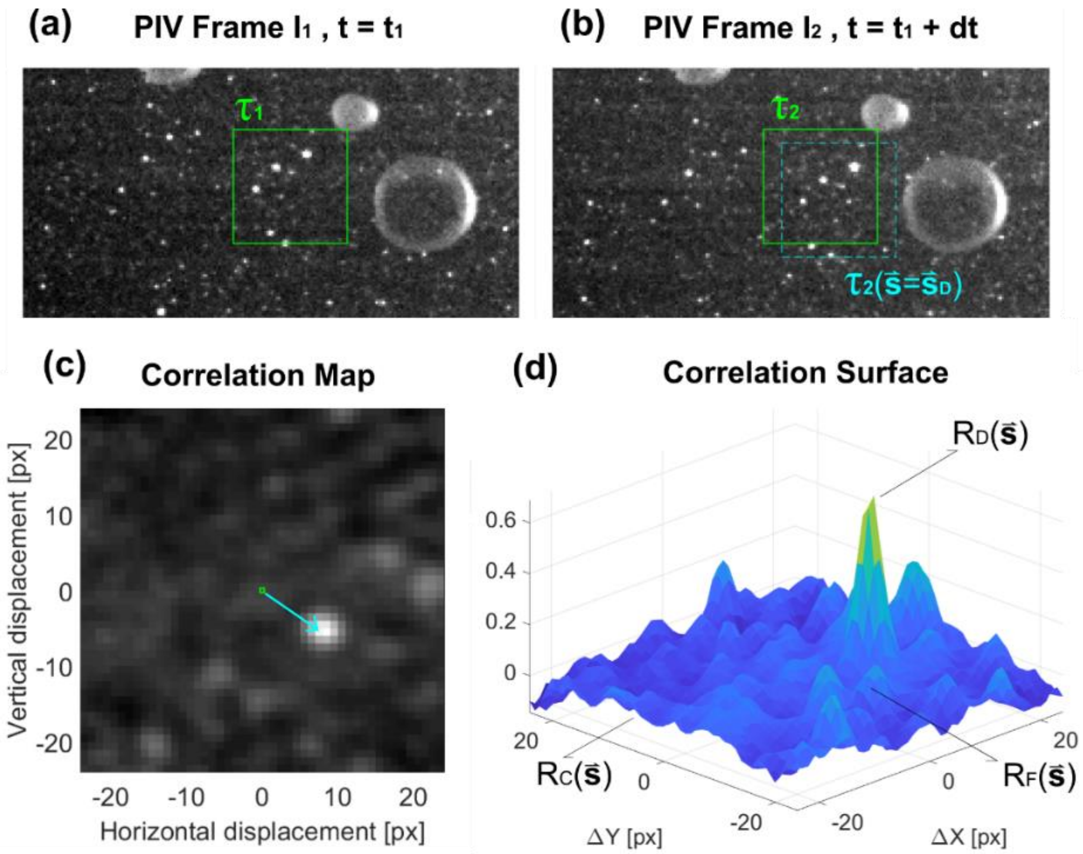

Figure B.1-1. Displacement calculation based on cross-correlation analysis of consecutive single-exposure frames, a) consecutive frames detailing the displacement of groups of particles, b) correlation map detailing the origin (unmoved interrogation window) and the estimated displacement vector, c) 3D surface of the correlation map detailing the components of the correlation function.

The discrete version of the correlation function shown in Eq. B.1-1 is presented in Eq. B.1-4. The values μ_τ and $\mu_\tau[p,q]$ represent the average intensity over τ_1 and the area where τ_1 and τ_2 overlap, respectively. Note that the subtraction of average intensities implicitly removes the convolution component presented in Eq. B.1-2 ($R_C[p,q] = 0$), so that the result of $R[p,q]$, shown as the correlation map in Figure B.1-1b, only includes the random effect of non-matching particles, and the displacement peak.

$$R[p,q] = \sum_{m=1}^{M} \sum_{n=1}^{N} (\tau_1[m,n] - \mu_\tau)(\tau_2[m+p, n+q] - \mu_\tau[p,q]) \qquad \textit{Eq. B.1-4}$$

The most probable displacement of the particles between τ_1 and τ_2 is found as the coordinates of the peak in the correlation function shown in Figure B.1-1b. The displacement of the interrogation window that matches the most probable displacement is shown as the cyan dashed rectangle in Figure B.1-1a, frame I_2. It can easily be seen that the particles[31] have the same locations relative to the windows in the green rectangle and the cyan rectangle in I_1 and I_2, respectively.

The random and peak components shown in Figure B.1-1c reveal some important details about the optimal configuration of PIV experiments. Clearly, as the peak-to-noise ratio increases, the reliability of the displacement represented by the peak increases. This can generally be accomplished, to a degree, through the physical PIV components, after which point all further improvements must be done digitally. A breadth of digital methods for optimising the correlation peak exist, which are now standard and embedded in most PIV packages and explained in any PIV textbook; for particular cases, however, *ad hoc* methods must be developed. Section B.4 explains a method used in this project to address the challenges of obstruction-induced light attenuation. Below, a concise account of the physical alternatives for noise-to-peak ratio improvement is presented.

Adrian and Westerweel (2011) proposed 4 main physical factors to consider in order to optimise the detectability[32] (D_o) of the main peak, namely, particle image density (N_{sp}), in-plane displacement (ΔX_p), out-of-plane displacement (Δz_p), and shear/local gradients (Δu_p). Higher densities increase the amplitude of both the peak and noise, however, peak detection improves at a higher rate than noise (i.e. $D_o \propto N_{sp}$). Larger in-plane displacements increase the probability of particles leaving the interrogation window/frame (i.e. $D_o \propto \Delta X_p^{-1}$). Larger out-of-plane movements imply lower probability of finding particles in subsequent frames (i.e. $D_o \propto \Delta z_p$). Shear changes the relative distances between particle, thus it increases the width of $R_D(\vec{s})$, whilst decreasing its peak ($D_o \propto \Delta u_p$).

The actual choice of these 4 factors involves some important trade-offs. Increased particle densities can also increase the probability of shear. Low in-plane displacements can lead to automatic autocorrelation peak detection , i.e. $\max\left(R_D(\vec{s})\right)$ at $\vec{s} = 0$, and thus overlook a proportion of small scale velocities. Larger laser thicknesses can increase noise through low-scattering particles away from the laser sheet centre. As clarified in Adrian and Westerweel (2011), these 4 factors should be considered as a guide, and any compromise should be adjusted to the characteristics of the experiment and the objectives.

[31] Note that the density shown in Figure B.1-1a is lower than that used for the experiments described in Chapter Chapter 6.

[32] Defined as the ratio of between the two highest peaks found in $R(\vec{s})$

It should be noted that direct spatial correlation operations are computationally costly and are commonly replaced by correlations in the spectral domain, via FFT computations. Nonetheless, the theoretical principle remains the same. Also, improvements in the estimation of the displacement vector can be achieved by successive iterations decreasing the size of the interrogation windows, to refine velocity estimations and improve accuracy and spatial resolution (Scarano, 2002). Overall, the theory presented here is an overview intended to convey the basics of displacement estimation, between consecutive frames. These methods are now standard and implemented in commercial and open-source PIV software packages, including PIVlab® (Thielicke and Stamhuis, 2014), the one used for this project (see Chapter 6).

B.2. Experimental Facility

The infrastructure of the experimental set-up is the link between the flow and the measurements obtained from it, as the quality of the data also depends on how the PIV components are integrated into the experimental infrastructure. Therefore, the aim of this section is to describe the elements of the experimental facility that are required to achieve the objectives of the dataset. These are, among others, to obtain velocity fields in vegetated fields, at scales relevant to the mixing processes analysed in Chapter 5[33].

Contrary to the LIF system described in Chapter 4 and Appendix A, which was an extension of the system proposed in Sonnenwald *et al.* (2017), the set-up described here does not have, to the author's knowledge, a published antecedent. The closest system to measure velocities in vegetated/obstructed flows is the one presented in Ricardo (2014). From that, a comprehensive description of vegetated hydrodynamics was presented (Ricardo, Franca and Ferreira, 2016; Ricardo, Sanches and Ferreira, 2016), despite the small flow fields obtained. This is the first study in which a comprehensive area of a vegetated flow field is illuminated, hence special consideration should be given to the material and layout of the obstructions, and the windows for viewing and light transmission.

[33] The objectives for the hydrodynamic data are actually of far-reaching significance than just mixing. The purposes of the PIV experiments are also to describe the energy and length and time scales of coherent structures. Drag forces and coefficients using the water surface variation and the double-averaged framework.

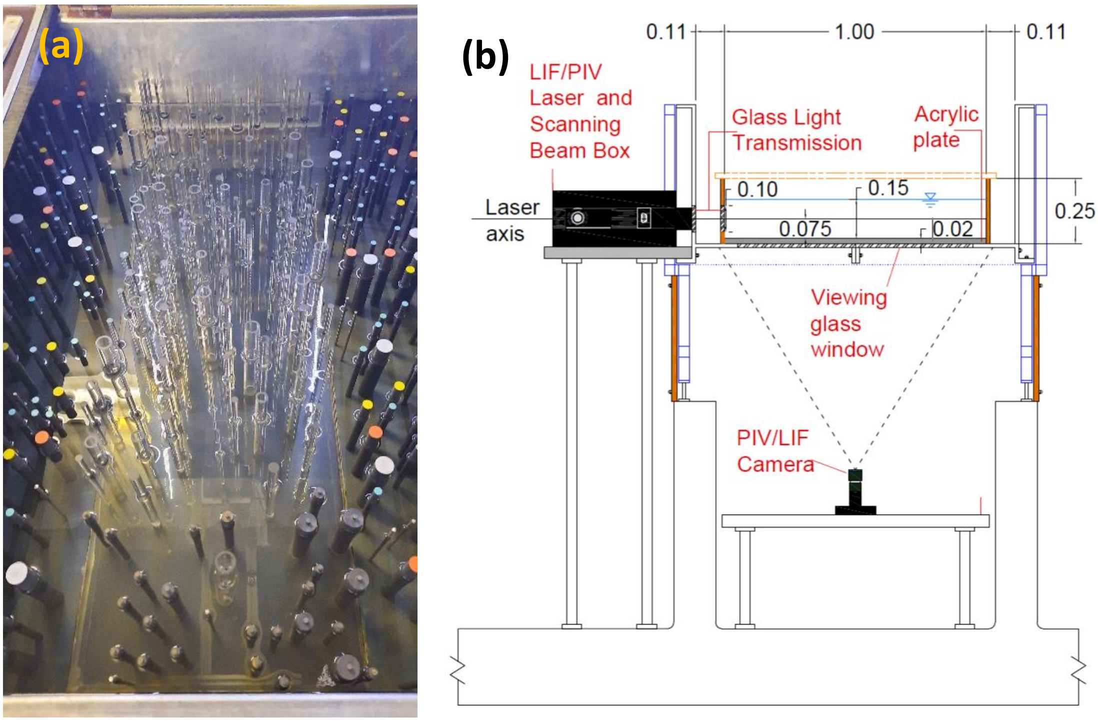

Figure B.2-1. a) Viewing window and elements in the Field of View, b) elevation view showing the location of the components.

Figure B.2-1a shows the PIV measurement section, including the viewing window, constructed at the bottom of the flume; the perforated acrylic plate, over the window; and the glass rods and cylinders used to allow the laser sheet to illuminate the width of the flume. Further, at the top of Figure B.2-1a, it is possible to see the illumination window at the side of the inner wall of the flume. A full diagram showing the locations of both illumination windows, the viewing glass, the acrylic plate, the PIV equipment and the laser sheet is presented in Figure B.2-1b.

The chosen solution for inter-stem illumination was to use transparent stems, and illuminate the area with a laser sheet from the side. The most accessible material found for the stems was DURAN® borosilicate 3.3 glass, with a refractive index of 1.473 for wavelengths around 586.7 nm (Schott, 2017). The value for water is 1.333. To avoid the excessive light focusing at the back of the stems glass tubes were used as for the 12, 15 and 50 mm diameters; for stability purposes, 4 and 8 mm stems were glass rods (for the stem diameter distribution, see Chapter 5).

The acrylic plate shown in Figure B.2-1, located above the viewing glass window, was used to allow visibility, hold the glass stems in place, and allow maintenance; whilst having a refractive index similar to that of the viewing glass, i.e. 1.495 at 532 nm wavelength (Kasarova *et al.*, 2007). In order to avoid condensation and obstructing bubbles during the experiments, the narrow space between the glass window and the acrylic plate was filled with water. It is important to note that the multiple phases between the illuminated plane and the camera lens (i.e. water, acrylic, glass and air) will affect the calibration of the PIV image (see Section B.4). However, these phases are static and thus any distortion will remain unchanged for all tests. This is not the case when imaging is done from above and surface waves and reflections will add random distortions to the intensity recordings. Mitigation measures to control surface wave reflections, using acrylic sheets over the water surface, within the field of view were undertaken by Ricardo (2014).

B.3. Configuration of Physical PIV Components

Section B.2 describes the infrastructure used to install the physical components of the PIV system. The solutions proposed to achieve the goals of the experiment will influence the physical and digital settings of the PIV equipment. This section details the configuration of the PIV elements, their specifications and, for reproducibility purposes, the settings found to yield the best quality for the tests carried out.

B.3.1. Main components of a PIV system

A rendering of the integration between the PIV system and the infrastructure described in Section B.2, is presented in Figure B.3-1. There, the PIV components of the system (camera, illumination and seeding) are shown in operation within the flow field. It should be noted that the components used were independent, as opposed to many all-inclusive, commercially-available PIV systems. This has the advantage of giving the user control over the components and is more versatile when implemented in complex facilities, as it allows local modifications to better suit the needs of the researcher. Conversely, it also increases the degrees of freedom associated with setting up the optimal configuration of the components, so that more iterations might be needed to obtain the optimal set of configuration parameters.

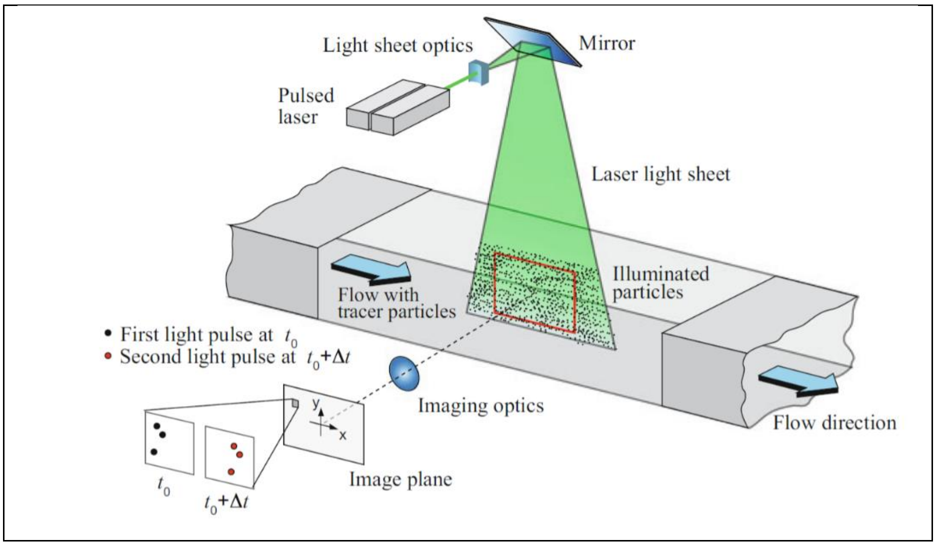

Figure B.3-1. PIV system configuration source Raffel et al. (2018)

Synchronisation of the PIV elements

Elements in Figure B.3-1 were installed independently and need to be integrated. This integration involves configuring each component to obtain appropriate intensity maps, for optimal displacement calculation (see Section B.1.2). Specifically, the settings for each device must be selected in conjunction with the other elements, the flow and the level of information desired. The particular settings that required continuous synchronisation, depending on the flow field and the objectives, were:

a. Camera frame rate.
b. Camera exposure time
c. Laser scanning rate.
d. Seeding particle displacement

Clearly, a complete configuration of the system in Figure B.3-1 includes more variables than the ones shown above. However, to avoid excessive iterations of parameters, certain restrictions were imposed on the system, both in terms of experimental limitations, and user-defined limits due to availability of materials and practicality. The following parameters were chosen to be independent of the synchronisation

i. Camera (lens) aperture, focal length and zoom.
ii. Laser type and power output.
iii. Seeding injection location and velocity.
iv. Seeding particle size and particle image density
v. Camera gain, Gamma distribution, black level, pixel depth, etc.
vi. Size of interrogation volume (cf. laser sheet size).
vii. Camera location.
viii. Laser sheet location.
ix. Flow rates.

Although the camera parameters shown in (v) were tuned for each test, these did not influence the synchronisation settings (list a - d). The remaining factors were fixed before the actual experimental stage. The justification for the choices in i – vii, is presented in Sections B.3.2 to B.3.4 for each of the PIV components. The laser sheet location (viii) and the subset of flow rates for PIV tests (ix, see Chapter 6) were chosen to maintain consistency with those specified for the LIF experiments (see Chapter 5).

Note that a prior selection of the flow rates provides approximate values for the mean particle displacements that can be expected in the flow field, and which can be used as initial estimations of the seeding particle velocity. This follows from previous knowledge of the interrogation volume and camera resolution[34]. Having an estimate of the mean particle velocity, a convenient frame rate can be proposed to obtain displacements that simultaneously avoid autocorrelation estimates of velocity and large in-plane displacements (see Section B.1.2). In summary, the configuration of synchronous parameters was achieved by proposing a frame rate that would yield reasonable displacements for each flow rate. Then, exposure time is calculated as a factor of the inter-frame period (inverse of frame rate), and laser scanning period is, in turn, computed as a factor of the exposure time[35]. This would guarantee that the cut-off of the scanning periods was, as much as possible, the same for all frames, thus avoiding scan overlap (Rockwell *et al.*, 1993).

B.3.2. Camera Configuration

The imaging component of the PIV system was composed of a Blackfly® BFS-U3-23S3 camera (FLIR, 2018), and a Computar® H6Z0812 manual lens (Computar, 2018). The main factors considered for the selection of the camera were the global shutter and the CMOS imaging sensor, which, as CCD cameras, digitalises the acquired images but higher transfer rates, thus allowing for higher frame rates. The lens is not wide-angle (i.e. short focal length), so that the image is minimally distorted and non-linear corrections are unnecessary (see Appendix A); the main drawback is that a longer focal distance (distance between lens and plane of view) is necessary. Figure B.2-1b, shows the camera location, with the distance (i.e. 1.13 m) necessary to cover a field of view of 0.5 x 0.3 m. Figure B.4-1a shows a photograph of the camera set-up.

[34] In theory, the camera resolution is another variable in the configuration of the system, but due to the relatively large size of the interrogation volume, choosing the maximum resolution is the obvious best choice.
[35] In other words, the ratios inter-frame period/exposure time, and exposure time/laser scanning period, should yield integers.

The description and effects of the manual lens (i in Section B.3.1) and the digital camera parameters (a, b and v in Section B.3.1) have already been explained in Appendix A. To avoid accidental misalignments of the camera, the lens parameters were selected and fixed during the initial set up, and remained constant for the experiments. For reproducibility and repeatability, the specific settings were

Lens Aperture: f/8

Focal Length: 1.2 m

The camera used has a maximum resolution of 1920 x 1200 pixels. The digital settings of the camera are divided into synchronisation (a and b, Section B.3.1) and optimisation parameters (v in Section B.3.1). The latter, refers to settings such as signal Gain, Gamma correction, black level, etc., that are independent of the illumination or flow, and can be used to enhance the intensity signals once the synchronisation parameters have been set. It was found that only gain and Gamma correction had a noticeable effect on the image quality. The Gain value is usually camera-specific, and dependent on the other digital parameters, and Gamma values between 0.8 and 1 yielded the best quality images. Regarding synchronisation parameters, these were not unique for each experiment; rather, different combinations were tried for the same flow, so that further analysis could be conducted on data quality. Table 4.4-1 shows the range of synchronisation parameters used, and based on each exposure time selected, the number of scans per image. An account of the parameters used and their quality, as it pertains to velocity maps, is presented in Chapter 6.

Table B.3-1. Relationship between digital camera parameters and laser sheet scan rate.

Frame Rate (fps)	Exposure time (µs)	Laser Scanning period (µs)	Number of scans per exposure
60	8335	463	18
65	7691	384.5	20
80	12501	329	38
110	9089	303	30
120	8335	463	18
125	7998	421	19
130	7691	384.5	20
160	6249	390.5	16

From Table 4.4-1, if the frame period (inverse of frame rate) is compared to exposure time, it can be seen that these are equal for frame rates ≥ 80 fps. Ideally, the frame rate should be small enough to 'freeze' particles by avoiding motion blur. The short illumination intervals in pulsed systems achieves this. For scanned systems, the control should be done through either shutter speeds or frame rate. Note that some of the areas were dimmed due to the obstructions, so, the maximum possible exposure time (under the foregoing conditions) was chosen to allow more information from the darker areas. The camera gain was used to amplify the signal to a point, beyond which the increase in noise would have been detrimental to the image quality. Figure B.3-2 shows a sample raw PIV image, where the exposure has been set to allow saturation on the brighter side of the image (i.e. right hand side, closer to the laser). For the same level of seeding, a clear difference in the level of information obtained from darker areas (left-side of the image), can be observed.

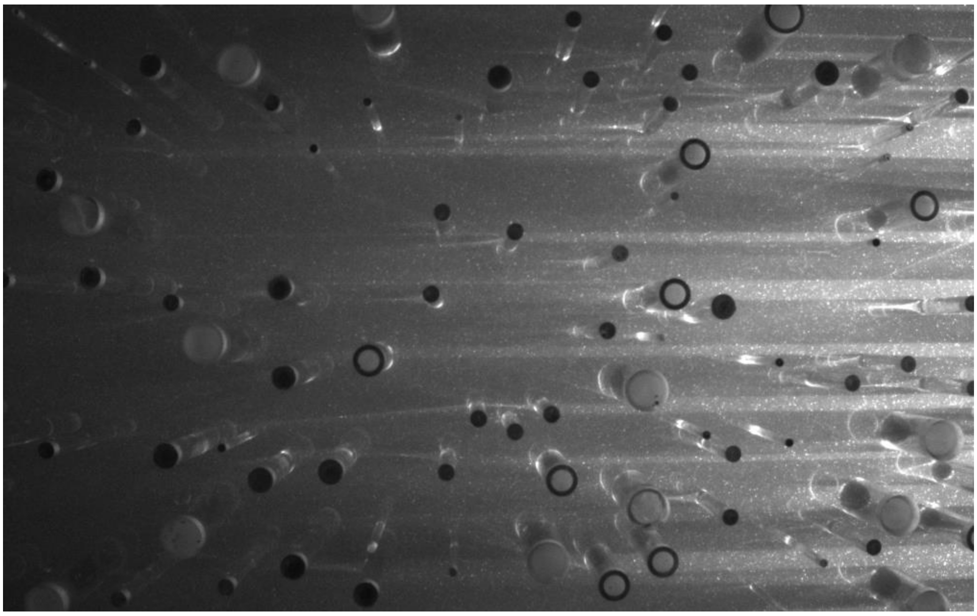

Figure B.3-2. sample image taken from the area of interest.

B.3.3. Illumination equipment

To illuminate 2D planes, 2 main techniques have been used: high-energy intermittent pulses and continuous scanned systems. Although the latter is more widely used for PIV experiments, these systems usually have divergent planes, which have non-uniform, transverse intensity distributions (dimer light towards the outer edges), even for collimated[36] planes. This can be neglected in non-obstructed, small interrogation volumes where the differences are not

[36] It should also be noted that the addition of optical equipment, such as collimators, for the desired illumination planes, was limited due to spatial restrictions around the flume.

reflected in the digital recording. For the experiments described here, these non-uniformities could be exacerbated by the glass stems. Moreover, the higher-intensity pulses could result in light focusing behind stems and reaching saturation levels. Consequently, it was considered that a more stable laser sheet output could be achieved by selecting a scanning system with a continuous high-power laser.

Table B.3-2. General specifications of the PIV laser used.

Operating Mode	CW
Nominal Output Power (W)	10
Transverse Mode	TEM_{00}
Wavelength (nm)	532
Beam diameter (mm)	~ 2
Operating Temperature (°C)	10 ~ 35

Specifically, the laser used for the experiments is a CNI MLL-W-532, class 4 laser, with the characteristics given in Table 4.4-2. The laser is embedded into a sheet generator, shown in Figure B.3-3a, which creates a 2D illumination plane by directing the beam towards a rotating polygonal mirror. The sheet is formed when the beam is reflected at different angles, from the faces of the polygonal mirror, into a parabolic mirror then projects the beam in the same direction for all reflected points, as can be seen in Figure B.3-3a. A complete scan is achieved when the polygonal mirror rotates a full face, hence, the rotation speed of this mirror determines the scanning rate of the sheet. The dimensions of the illumination plane produced were 700 x 10 mm, and the possible scanning rates are in the range 225 – 750 µs. A photo of the scanned sheet over the experimental area is shown in Figure B.3-3b.

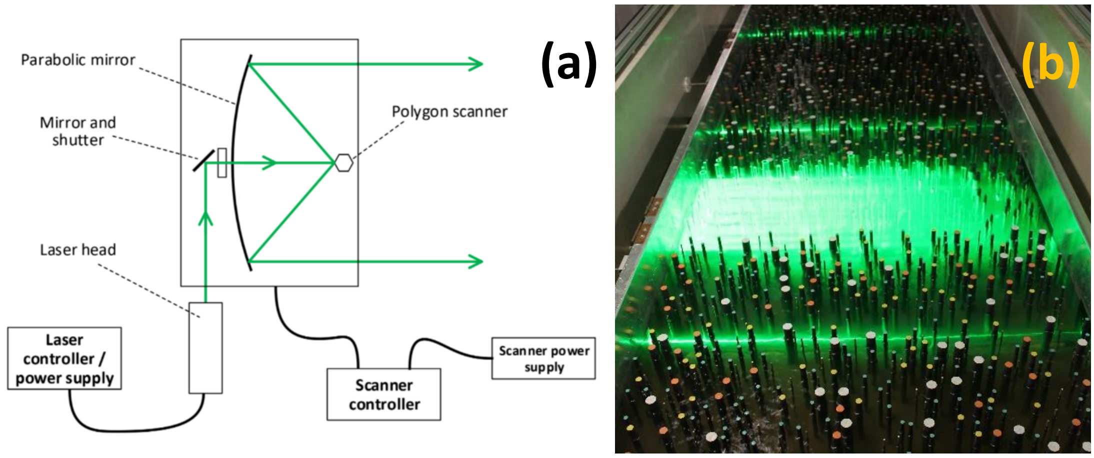

Figure B.3-3. a) Description of laser and illumination optics, b) photograph of the output illumination plane.

As mentioned in Section B.3.2, the scanning rate of the laser sheet generator should be considered together with the frame rate and exposure time of the camera. The chosen scanning rates are presented in Table 4.4-1, alongside the number of scans for a single exposure. By having several scans per single frame, the intensity will be more stable as a particle is exposed to more scanning periods and an average intensity is recorded, which will prevent flickering of the particles.

An important factor from the illumination, but which is independent of the specific equipment selected, is light refraction and reflection caused by the glass cylinders. This was an issue anticipated before the setting up stage, and although measures were taking to mitigate light attenuation, some still persisted, the digital solutions to which are presented in Section B.4. Nevertheless, the information obtained, as it pertains to inter-stems velocities, is still considered a step forward in the understanding of vegetated hydrodynamics.

B.3.4. Seeding particles

Owing to the fact that PIV is a non-intrusive and indirect technique, i.e. velocity is measured from tracers in the flow. Seeding particles should be selected to yield the highest possible scattering, whilst moving without affecting the underlying structures of the flow. For PIV in water, polyamide is the most common material for seeding particles, for which a range of diameters are available depending on the application (Raffel *et al.*, 2018).

Selection of seeding diameter depends, among other things, on the level of scattering desired and the scale of the flow structures studied (Adrian and Westerweel, 2011). For this project, emphasis is given to the area, as it should cover sufficient stems to be representative of the vegetated field. This dictates the experimental configuration shown in Figure B.2-1, particularly the size of the interrogation volume. The desired larger measurement area requires higher levels of scattering. This is achieved by larger particles, that are also better identified spatially. Given the features of the experiments, the selected particles were polyamide 12, of 100 µm diameter. However, larger particles are also denser, which, in conjunction with trapping zones and velocity defect areas around stems, can lead to settling.

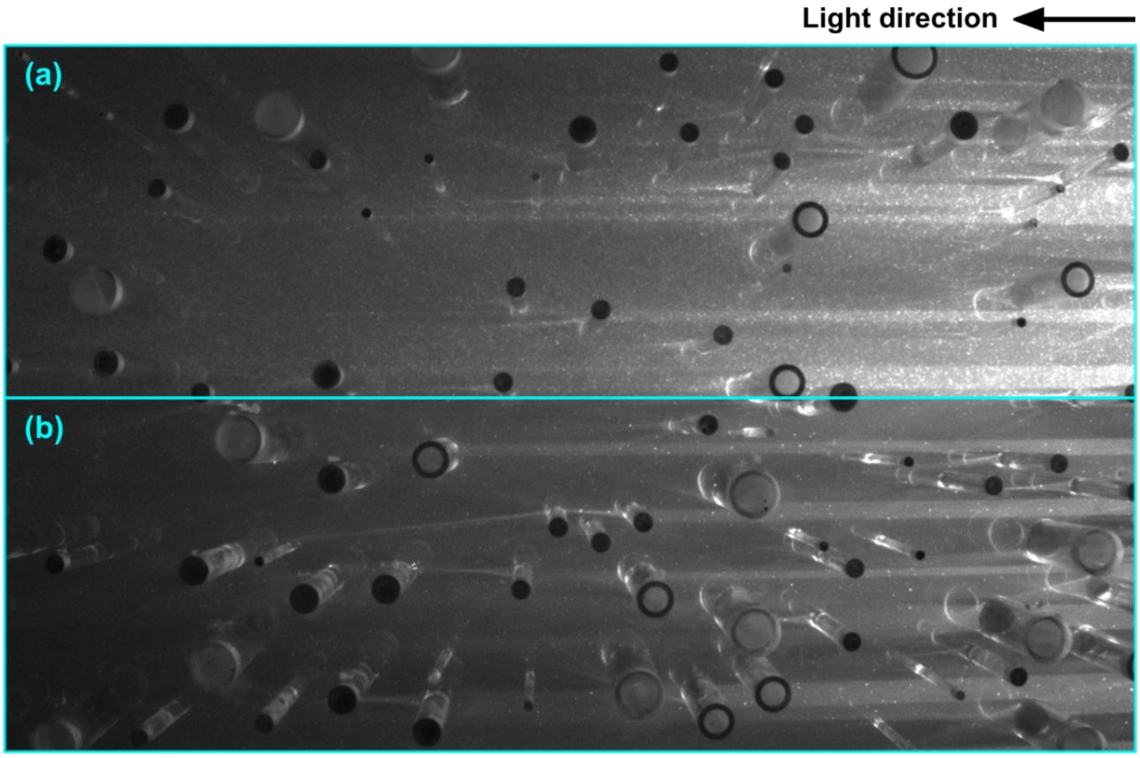

Figure B.3-4. Comparison between different seeding levels, a) high seeding density, used for the experiments b) low density.

The next parameter to consider regarding seeding, is the particle image density (number of particles per image area). Figure B.3-4 shows a comparison between low (Figure B.3-4b) and high (Figure B.3-4a) levels of particle density, in which a sample of the target density is shown as the upper part. The seeding injection system consisted of as stirring tank, connected to a set of continuous-flow pumps leading the seeded water to a transverse, line injection source located 1.5 m upstream from the measurement area. The level of desired seeding, shown in Figure B.3-4a, is a function of the concentration in the stirring tank and the injection velocity. To avoid the injection of seeding influencing the flow field, the injection velocity was chosen to match that of the lowest flow rate, and remained constant. The final seeding density was therefore achieved by calibrating the concentration of polyamide in the stirring tank.

B.4. Image Calibration and Preparation

All previous sections include information on the setting up of a PIV system, specifically the physical configuration necessary to obtain velocities in a comprehensive area of a vegetated flow field. This section describes, first, the tasks undertaken to relate the optimal intensity maps obtained, to actual points in the interrogation volume. Second, the digital optimisation of the intensity maps, to correct the effects of light attenuation. A distinction between light heterogeneity correction, and image pre-processing to improve contrast should be made. The first is explained in this section, as it is specific to this application of the technique; the second draws from standard image correction methods, which are implemented on most PIV software packages, and will be covered in Chapter 6.

B.4.1. Calibration of PIV Images

It was mentioned in Section B.2 that images were obtained through a multiphase viewing window, namely air-glass-acrylic-water. The light trajectory through this multiphase media (from the scattering particle to the camera) will be affected by the refractive indices, which need to be considered in the transformation between spatial and image domain, and vice versa. Furthermore, possible distortion effects caused by the image equipment, specifically camera lens, need to be corrected.

A complete description of the multiphase effect on the intensity map can be obtained by locating a template, with distinct markers that convey spatial information of the interrogation volume and also provide information of the vegetation distribution. In other words, a template with marked coordinates that are also connected to the location of the stems. Similarly, a template with a rectangular grid, with known spacing, can be used to determine whether distortion is present in the images, and develop a transformation function to recover a rectangular grid from the deformed images.

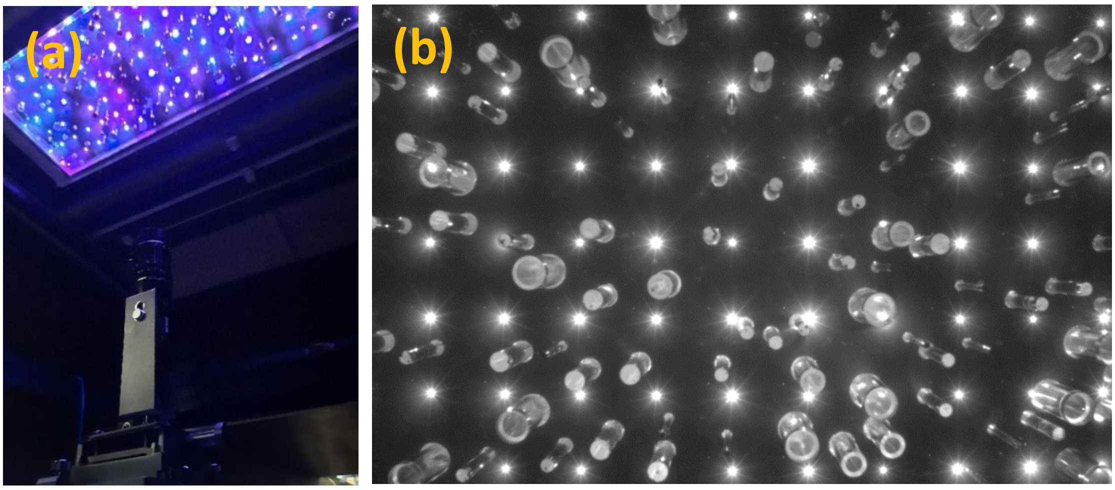

Figure B.4-1. a) camera and LED calibration plate, b) recorded image with the calibration plate in place.

Indeed, each issue, flow field location and distortion correction, was addressed with calibration plates. These were manufactured by generating a regular grid of fibre-optic LEDs on a dark plate, which was located inside the flume, at the same height, in water, at which the laser sheet was aligned, to replicate test conditions. The calibration plate used to obtain the real coordinates had orifices to allow the glass stems and express the location of each LED, in relation to them. The calibration plate for distortion correction was unperforated so that more LED points were available in order to generate an accurate transformation function. Figure B.4-1a shows the calibration plate used to obtain the real coordinates from the flume, from which the image shown in Figure B.4-1b is obtained. The calibration images were binary maps obtained by changing the camera settings, such that the LEDs were the only source of light. The distortion evaluated from the solid calibration plate was small enough to be considered negligible.

B.4.2. Correction of light intensity attenuation (pre-prepocessing)

When considering the effects of glass stems on the illuminated plane, the main issue is the light attenuation resulting from continuous shadowing caused by light refraction over the surfaces of the stems. This attenuation occurs mainly in the direction of the scanned plate, as shown in Figure B.3-4, where the laser sheet comes from the right-side and attenuation occurs towards the left of the image. In addition to selecting appropriate camera settings to reveal information from shadowed areas of the image, the attenuation information should be used to obtain a correction factor that can yield a uniform intensity map. This will then be used as input for the PIV software used to obtain the information in Chapter 6.

To obtain optimal PIV images (uniform intensity, and optimal contrast, e.g. Figure B.1-1a), light intensity values due to differences in background illumination should be removed, such that only particle reflections remain. A method is proposed to eliminate heterogeneous background illumination, and make scattered intensity uniform over the entire image. Consider an image containing only the background illumination, without seeding, I_{mn}, which was recorded from prior knowledge of the possibility of light refraction due to obstacles. Define as $\overline{I_m}^n$, the average of the image over the direction opposite to that of laser illumination, in other words, the mean laser intensity attenuation. From prior knowledge of the distribution of I_{mn}, define y_I as a target mean intensity. From this target intensity and the average attenuation, the mean correction factor, α_m, is defined

$$\alpha_m = y_I/\overline{I_m}^n \qquad \textit{Eq. B.4-1}$$

Operating the correction array, α_m, over the original background image, the corrected intensity map, I_{mn}^*, given in Eq. B.4-2 is obtained. It should be noted that the selection of an appropriate target value y_I might require a few iterations to ensure that I_{mn}^{*} has minimal saturated areas, whilst enhancing information from dimly-lit zones.

$$I_{mn}^{*} = \alpha_m \cdot I_{mn} \qquad \textit{Eq. B.4-2}$$

Once a satisfactory set of y_I and α_m values is obtained, this correction can be applied to any seeded PIV image, i_{mn}, to obtain corrected intensity maps, i_{mn}^{*}.

$$i_{mn}^{*} = \alpha_m \cdot i_{mn} \qquad \textit{Eq. B.4-3}$$

Note that the correction applied will also amplify intensity signals from particles, depending on the background illumination. Particle intensities from darker portions of the image will be amplified more. Once both the background and seeded PIV recordings are corrected, a subtraction of the form $i_{mn}^{*} - I_{mn}^{*}$, will yield intensity maps wherein intensity is solely related to particle illumination. Figure B.4-2, shows a graphical representation of this preliminary correction. After the images have been corrected and the unseeded background subtracted, an additional filter is applied, in which the average of the PIV images without background is calculated and subsequently removed from the recording. This additional step is intended to remove streaks from blurring, and refine the intensity signals from particles. The resulting image will then be passed through the filters contemplated in the pre-processing of the PIV software packages used (Thielicke and Stamhuis, 2014).

(a)

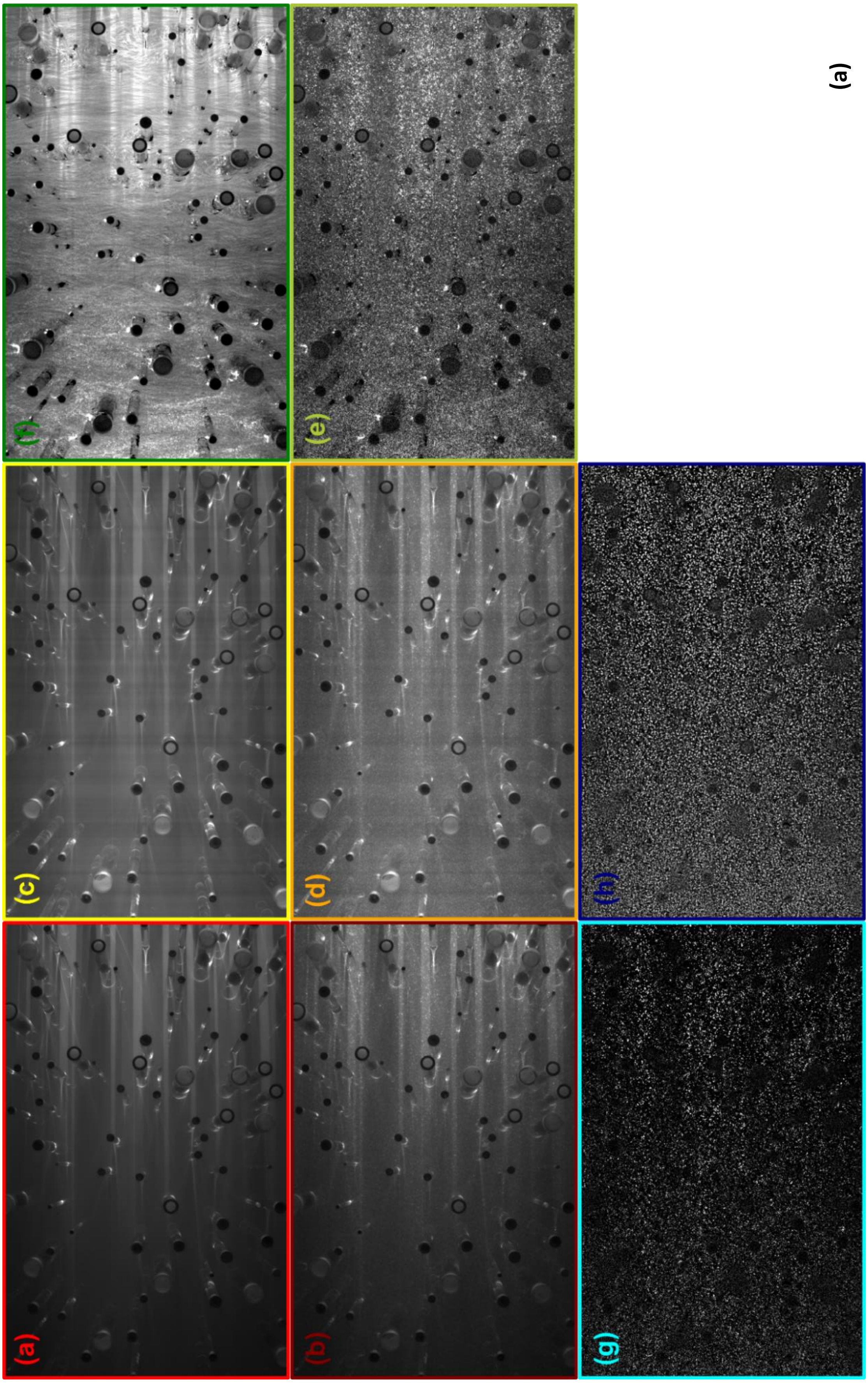

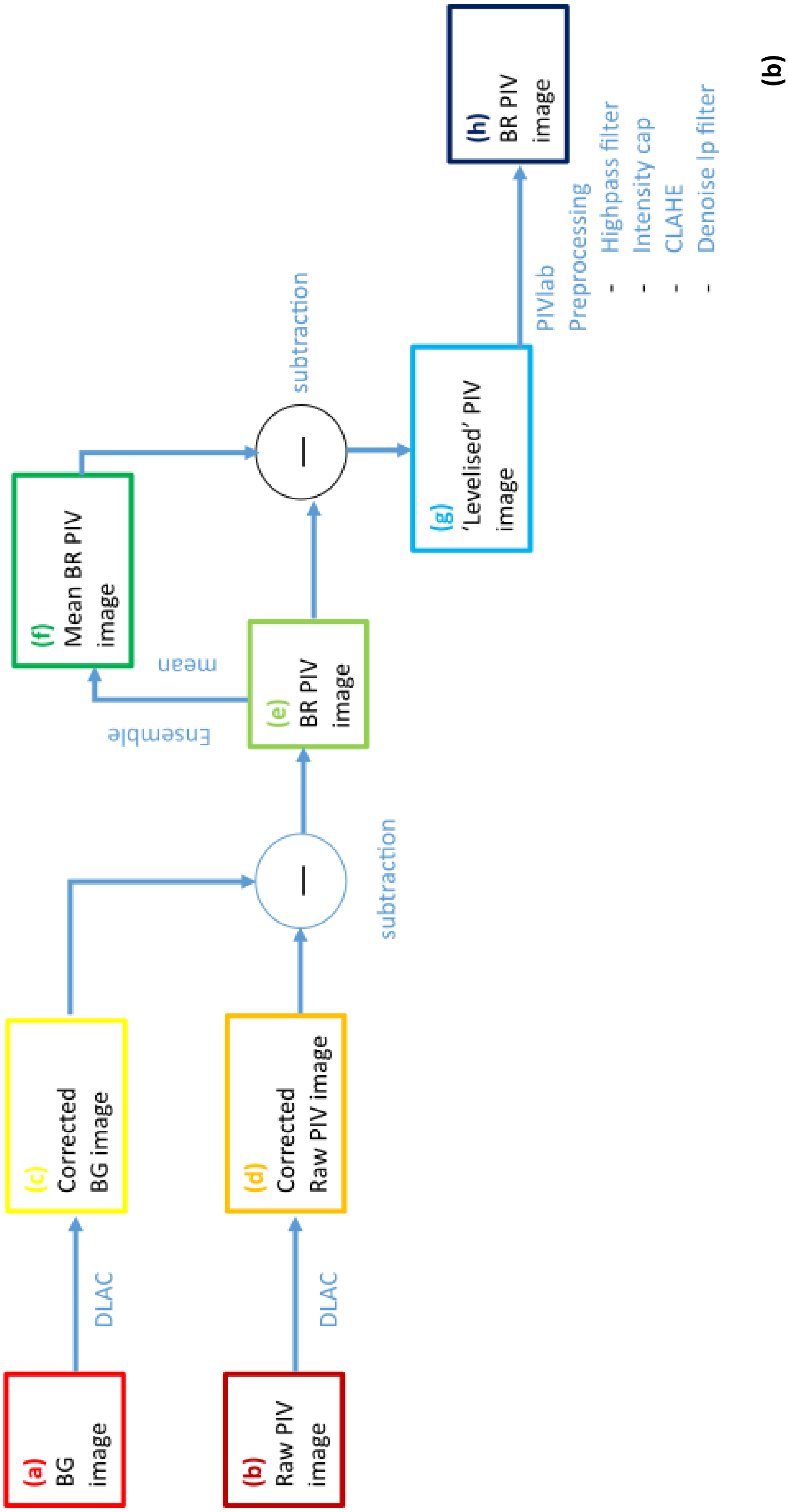

Figure B.4-2. a) Graphical Description and (b) Flow Diagram describing the sequence of steps for light intensity attenuation correction (pre-preprocessing).

B.5. Recommendations

This work is a significant step forward in the study of obstructed flow fields. It should be an inspiration for alternative improvements, and, hopefully, a discussion on technique improvement can be had. Simultaneously, the alternatives tried for this study are considered sufficient to unveil the larger portion of the hydrodynamic processes occurring in vegetated flows, specifically with regards to mixing in emergent vegetation. This can be verified in Chapters 6 and 7, where the evolution of hydrodynamic quantities around stems follows that expected from previous works on cylinder flows.

Finally, the alternatives presented in this work to digitally minimise the effects of illumination heterogeneity, across the field of view, caused by the presence of glass rods and cylinders, must be regarded as heuristic. Their effectiveness can only be asserted in this configuration (see Chapter 4). Among the possible experimental alternatives to the system proposed here, consideration should be given to:

- Localised illumination centred around specific cylinders (radial illumination)
- Oblique illumination angle and reflective surface at the opposite end.